REPORT DOCUMENTATION PAGE

Form Approved OMB No. 0704-0188

Public reporting burden for this collection of information is estimated to average 1 hour per response, including the time for reviewing instructions, searching existing data sources, gathering and maintaining the data needed, and completing and reviewing the collection of information. Send comments regarding this burden estimate or any other aspect of this collection of information, including suggestions for reducing the burden, to Department of Defense, Washington Headquarters Services, Directorate for Information Operations and Reports (0704-0188), 1215 Jefferson Davis Highway, Suite 1204, Arlington, VA 22202-4302. Respondents should be aware that notwithstanding any other provision of law, no person shall be subject to any penalty for failing to comply with a collection of information if it does not display a currently valid OMB control number.
PLEASE DO NOT RETURN YOUR FORM TO THE ABOVE ADDRESS.

1. REPORT DATE *(DD-MM-YYYY)*	2. REPORT TYPE	3. DATES COVERED *(From – To)*
24-01-2011	Conference Proceedings	6 September 2010 - 10 September 2010

4. TITLE AND SUBTITLE

Fifth International Conference "Ultrawideband and Ultrashort Impulse Signals" (UWBUSIS'10)

5a. CONTRACT NUMBER

FA8655-10-1-5072

5b. GRANT NUMBER

CSP 10-5072

5c. PROGRAM ELEMENT NUMBER

61102F

6. AUTHOR(S)

Dr. Nikolay N. Kolchigin

5d. PROJECT NUMBER

5d. TASK NUMBER

5e. WORK UNIT NUMBER

7. PERFORMING ORGANIZATION NAME(S) AND ADDRESS(ES)

V.N. Karazin Kharkiv National University
4 Svobody Sq.
Kharkiv 61077
Ukraine

8. PERFORMING ORGANIZATION REPORT NUMBER

CSP 10-5072

9. SPONSORING/MONITORING AGENCY NAME(S) AND ADDRESS(ES)

EOARD
Unit 4515 BOX 14
APO AE 09421

10. SPONSOR/MONITOR'S ACRONYM(S)

AFRL/AFOSR/RSW (EOARD)

11. SPONSOR/MONITOR'S REPORT NUMBER(S)

AFRL-AFOSR-UK-PC-2010-0023

12. DISTRIBUTION/AVAILABILITY STATEMENT

Approved for public release; distribution is unlimited. (Approval given by local Public Affairs Office) © Copyright 2010 held by the Institute of Electrical and Electronics Engineers, IEEE Operations Center, 445 Hoes Lane, P.O. Box 1331, Piscataway, NJ 08855-1331. The Department of Defense has permission to use for government purposes only. All other rights are reserved by the copyright holder.

13. SUPPLEMENTARY NOTES

14. ABSTRACT

The Final Proceedings for Fifth International Conference , 6 September 2010 - 10 September 2010

1. Theory investigations, numerical simulations
2. Generation, radiation, and receiving
3. Electromagnetic compatibility
4. Electromagnetic metrology
5. Propagation and scattering in natural and artificial materials (complex media, radio absorbers, biomaterials, nanostructures, meta-materials etc.)
6. Applications (communication, medicine, etc.)
7. Radar and Ground Penetrating Radar

15. SUBJECT TERMS

EOARD, ultrawideband, ultrashort pulse interactions

16. SECURITY CLASSIFICATION OF:			17. LIMITATION OF ABSTRACT	18, NUMBER OF PAGES	19a. NAME OF RESPONSIBLE PERSON
a. REPORT	b. ABSTRACT	c. THIS PAGE			BARRETT A. FLAKE
UNCLAS	UNCLAS	UNCLAS	SAR	290	19b. TELEPHONE NUMBER *(Include area code)* +44 (0)1895 616144

UWBUSIS 2010

PROCEEDINGS OF 2010 5th INTERNATIONAL CONFERENCE ON ULTRAWIDEBAND AND ULTRASHORT IMPULSE SIGNALS

September 6 – 10, 2010
Sevastopol,Ukraine

IEEE Catalog Number
ISBN

CFP10587-PRT
978-1-4244-7468-4

UWBUSIS 2010

IEEE

2010 5th International Conference on

ULTRAWIDEBAND AND ULTRASHORT IMPULSE SIGNALS

PROCEEDINGS



September 6 – 10, 2010
Sevastopol,Ukraine

EuMA

National Antenna Association
* Ukraine *

U.R.S.I.

XTERA

2010 5th International Conference on

ULTRAWIDEBAND AND ULTRASHORT IMPULSE SIGNALS



September 6 – 10, 2010

Sevastopol, Ukraine

ORGANIZED AND SPONSORED BY

V.N. Karazin Kharkiv National University

IEEE AP/C/EMC/SP Kharkov Joint Chapter of Ukraine Section

Sevastopol National Technical University

IN COOPERATION WITH

National Antenna Association of Ukraine

Kharkiv National University of Radio Electronics

Radio Astronomy Institute of NASU

Institute of Radio Physics and Electronics of NASU

We wish to thank the following for their contribution to the success of this conference:

European Office of Aerospace Research & Development, Air Force Office of Scientific Research, United States Air Force Research Laboratory (www.london.af.mil)

US Army International Technology Center-Atlantic (http://www.usaitca.army.mil)

European Microwave Association

Ukrainian URSI Committee

2010 5th International Conference on Ultrawideband and Ultrashort Impulse Signals

IEEE Catalog Number: CFP10587-PRT
ISBN: 978-1-4244-7468-4

Copyright and Reprint Permission: Abstracting is permitted with credit to the source. Libraries are permitted to photocopy beyond the limit of U.S. copyright law for private use of patrons those articles in this volume that carry a code at the bottom of the first page, provided the per-copy fee indicated in the code is paid through Copyright Clearance Center, 222 Rosewood Drive, Danvers, MA 01923. For other copying, reprint or republication permission, write to IEEE Copyrights Manager, IEEE Operations Center, 445 Hoes Lane, P.O. Box 1331, Piscataway, NJ 08855-1331. All rights reserved. Copyright ©2010 by the Institute of Electrical and Electronics Engineers

HONORARY CHAIRMAN:

Prof. Yakov S. Shifrin,
IEEE Life Member, Kharkiv National University of Radio Electronics,
President of Ukrainian National Antenna Association, Kharkiv, Ukraine

CHAIRMAN:

Prof. Nicolay N. Kolchigin
IEEE Senior Member, Theoretical Radiophysics Dept.
V.N. Karazin Kharkiv National University, Kharkiv, Ukraine

CO-CHAIRMEN:

Prof. Victor A. Katrich
IEEE Member, V.N. Karazin Kharkiv National University, Kharkiv, Ukraine

Prof. Aleksander G. Luk'yanchuk
Sevastopol National Technical University, Sevastopol, Ukraine

VICE-CHAIRMEN:

Dr. Vyacheslav V. Khardikov
V.N. Karazin Kharkiv National University, Kharkiv, Ukraine

Dr. Anna. V. Shishkova
IEEE Member, V.N. Karazin Kharkiv National University, Kharkiv, Ukraine

Dr. Dmitriy D. Ivanchenko
V.N. Karazin Kharkiv National University, Kharkiv, Ukraine

Prof. Yuriy B. Gimpilevich
Sevastopol National Technical University, Sevastopol, Ukraine

UWBUSIS'10 TECHNICAL PROGRAM COMMITTEE

Prof. L. Yu. Astanin (*Russia*)
Prof. C. E. Baum (*USA*)
Prof. L. F. Chernogor (*Ukraine*)
Prof. F. F. Dubrovka (*Ukraine*)
Prof. N. N. Gorobets (*Ukraine*)
Prof. I. Ya. Imoreev (*Russia*)
Prof. A. A. Konovalenko (*Ukraine*)
Prof. V. F. Kravchenko (*Russia*)
Prof. K. A. Lukin (*Ukraine*)
Prof. I. I. Magda (*Ukraine*)
Prof. S. A. Masalov (*Ukraine*)
Prof. V. M. Shulga (*Ukraine*)
Prof. S.N. Shulga (*Ukraine*)
Prof. D. M. Vavriv (*Ukraine*)
Prof. F. Y. Yanovskiy (*Ukraine*)
Prof. Qiu Jinghui (*China*)

UWBUSIS'10 ORGANIZING COMMITTEE

CONFERENCE SECRETARY:

Bogdan A. Kochetov

Dr. Mariya S. Antyufeyeva, *designer*
Dr. Nataliya K. Blinova
Dr. Alexander Yu. Butrym
Dr. Alexander N. Dumin
Oleg V. Kazanskiy
Dr. Yu Zheng
Dr. Nona G. Maksimova
Dr. Genadiy Pochanin
Svetlana V. Pshenichnaya
Nataliya L. Rzhevceva
Dr. Igor B. Shirokov
Dr. Igor L. Vetrov

http://www-radiophys.univer.kharkov.ua/uwbusis/

CHAIRMEN'S WELCOME

Honorary Chairman



Yakov S.Shifrin

Chairman



Nikolay N. Kolchigin

Dear colleagues,

We are happy to welcome all our participants in the beautiful Crimea city of great ancient history – Sevastopol, which hosts for five days (6-10 September, 2010) the fifth International Conference 'Ultrawideband and Ultrashort Impulse Signals' (UWBUSIS'10). The venue of the conference is one of the largest technical university of Ukraine, Sevastopol National Technical University. The main organizers of the conference are as usually Kharkov IEEE Joint Chapter, Karazin Kharkiv National University and National Antenna Association of. Kharkov University is the well known academic centre of East Ukraine founded as early as in 1804.

Our conference is intended to provide the international forum for discussing recent advances in the theory investigations, computer modeling, experiments, technology and applications of the ultrawideband and ultrashort impulse signals. The conference started as a workshop in 2002. It was the first conference in the field of UWB among the countries of Former Soviet Union, which activated later on the similar successful conferences in Russia and others countries of former USSR. In 2002 we met 47 participants. Since then, the number of participants and scientists interested in UWB problems continually grows. This year the Technical Program Committee had invited 10 papers and accepted 74 contributed ones from Ukraine, Russia, Belarus, USA, China, Germany and France

We enjoyed working with all the members of Local Organizing Committee and Technical Program Committee and we thank them a lot for their immense work and efforts. We appreciate deeply co-organizers and sponsors for their information, material and financial contribution to the success of the conference. A special gratitude we express to European Microwave Association (EuMA) for repeatedly sponsoring the young scientists contest that undoubtedly will promote UWB among new scientists generation. Due to support of EuMA we announced the contest for best presentation among young scientists (up to 35 years old) with 1000 EUR awarding funds. We are extremely thankful to the managers and staff of Sevastopol National Technical University for their hospitality and organization help. We would like also to kindly thank the editing group that prepared the conference proceedings and supported Website of UWBUSIS'10.

We would like to thank all the participants – these are you who have made UWBUSIS'10 possible. We wish all the UWBUSIS participants successful work at the meetings, establishing and renewal pleasant and fruitful contacts with colleagues. Let the conference brings you new ideas, discovers new horizons and leave vivid recollections about nice time in the sunny Crimea.

Sincerely yours,
Yakov Shifrin, Nikolay Kolchigin

TABLE OF CONTENTS

INVITED PAPERS

01. POLARIMETRIC SUPPRESSION OF EARLY-TIME SCATTERING FOR LATE-TIME TARGET IDENTIFICATION Carl E. Baum 12

02. THE FORMATION AND RADIATION OF HIGH-POWER SHORT RADIO PULSES: NEW APPROACHES TO MODELING AND ANALYSIS OF MICROWAVE COMPRESSORS Amosova A. I., Krivchikova A. A., Pazynin V. L., Sirenko Y. K. 16

03. SPECTRAL THEORY ANALYSIS OF UWB-OSCILLATIONS IN FREQUENCY SINTHESIZERS BASED ON PHASE-LOCKED LOOPS Kravchenko V. F., Kravchenko O. V., and Safin A. R. 22

04. THE LIGHTNING RETURN-STROKE INITIATION POINT AS AN ULTRA-WIDEBAND SOURCE Gardner R. L.. 30

05. CELLULAR EFFECTS OF ULTRAWIDEBAND ULTRASHORT PULSED RADIATION AND MICROWAVE RADIATION EXPOSURE Shckorbatov Y. G., Kolchigin N. N., Grabina V. A., Pasiuga V. N. 34

06. RADIATION AND RECEPTION OF THE SHORT SIGNALS BY THE LONG ANTENNAS Immoreev I. Ya. 40

07. IMPROVEMENT OF CHARACTERISTICS OF UWB DOUBLE RIDGED HORN ANTENNAS Dubrovka F. F. and Sushko A. Ju. 45

08. UWB NOISE ACOUSTIC ATMOSPHERIC RADAR Sinitsyn R. B. and Yanovsky F. J. 48

09. MODE EXPANSIONS IN TIME DOMAIN Butrym A. Yu. 49

NEW HYBRID METHODS

01. NEW KRAVCHENKO TRANSFORMS AND DIGITAL UWB SIGNAL PROCESSING Kravchenko V. F. and Churikov D. V. 54

02. ATOMIC DISTRIBUTIONS IN SAR PROBLEMS Kravchenko V. F. and Churikov D. V. 59

03. NEW ANALITYCAL KRAVCHENKO WAVELETS IN SPECTRAL ESTIMATION OF UWB SIGNALS Churikov D. V. 62

04. ULTRAWIDEBAND SIGNALS CONSTRUCTED FROM GENERALIZED WEYL-HEISENBERG BASES Petrov D. A.. 65

05. THE ANALYSES OF PROCESS OF GENERATION AND RESONANCE SCATTERING OF WAVES ON CUBICALLY POLARISABLE LAYERED STRUCTURE Angermann L., Yatsyk V. V. and Yatsyk M. V. 68

06. TRANSIENT WAVE PROPAGATION IN RADIALLY INHOMOGENEOUS BICONICAL LINE Kochetov B. A. and Butrym A. Yu. 71

07. OPTIMIZATION OF SIGNAL PROCESSING OF OWN RADIO-THERMAL RADIATION OF EXTENDED SOURCE IN WIDEBAND AND SUPER-WIDEBAND APERTURE SYNTHESIS SYSTEMS Volosyuk V. K., Pavlikov V. V. 74

08. SPACE-TIME SPECTRAL TRANSFORMATIONS OF WIDEBAND AND SUPER-WIDEBAND SIGNALS AND THEIR COHERENCE FUNCTIONS Volosyuk V. K. 77

THEORETICAL INVESTIGATION, NUMERICAL SIMULATION. PROPAGATION AND SCATTERING IN NATURAL AND ARTIFICIAL MEDIA

01. MULTIELEMENT SYSTEMS OF DOUBLE SLOTS IN RECTANGULAR WAVEGUIDE WITH PARTIAL DIELECTRIC FILLING Blinova N. K., Lyakhovsky A. A., Yatsuk L. P. 82

02. DIFFRACTION PROBLEM BY A SYSTEM OF RECTANGULAR SLOTS IN A COMMON WALL OF RECTANGULAR WAVEGUIDES Kaliberda M. E. and Pogarsky S. A. 85

03. INVESTIGATION OF PHASE CODED SIGNALS BASED ON GENERALIZED FRANK CODES Prudyus I. N., Sumyk M. M., Yankevych R. V. 88

04. DUAL REGULARIZATION IN ONE-DIMENSIONAL INVERSE SCATTERING PROBLEM Gaikovich K. P., Gaikovich P. K., Galkin O. E., Sumin M. I. 90

05. EFFECTS OF UWB AND CHAOTIC SIGNALS ON SELECTED OSCILLATORS Ropiak C. A. and Gardner R. L. 93

06. THE INFLUENCE OF ILLUMINATING WAVE POLARIZATION STATE ON THE ELECTROMAGNETIC FIELD DISTRIBUTION INSIDE THE DIELECTRIC CYLINDER Stasjuk N. N. and Gorobets N. N. 96

07. EVOLUTIONARY EQUATIONS FOR ELECTROMAGNETIC FIELDS IN UNBOUNDED SPACE FILLED WITH LAYERED INHOMOGENEOUS NONLINEAR TRANSIENT MEDIUM WITH LOSSES Dumin O. M., Tretyakov O.A., Katrich V. A., Dumina O. O., Nesterenko M. V., Kholodov V. I. 99

08. TIME-DOMAIN DESCRIPTOR MODELS FOR CIRCUITS WITH MULTICONDUCTOR TRANSMISSION LINES AND LUMPED ELEMENTS Rutkas A. G. and Vlasenko L. A. 102

09. ULTRAWIDEBAND SIGNALS AND PROCESSES Chernogor L. F. and Lazorenko O. V. 105

10. ULTRA WIDEBAND SIGNALS SPECTRAL ANALYSIS Syvozalizov N. A. 109

11. MATHEMATICAL MODELS OF RIGOROUS DIFFRACTION THEORY AND SIGNALS THEORY Khoroshun V. V. 111

12. HILBERT TRANSFORM APPLICATION TO THE IMPULSE SIGNAL PROCESSING Batrakov D. O., Golovin D. V., Simachev A. A. and Batrakova A. G. 113

13. QUASI-RESONANCE ACCOUNTING IN REPRESENTATION OF WIDEBAND FREQUENCY RESPONSE OF TWO-DIMENSIONAL OPEN RESONANCE STRUCTURES Andreev M. V. and Borulko V. F. 116

14. IMPULSE SIGNAL PROPAGATION IN OPEN DIELECTRIC CIRCULAR WAVEGUIDE Legenkiy M. N. and Butrym A. Yu. 119

15. SPECTRUM CONTROL IN OPEN RESONATORS: TIME-DOMAIN SIMULATION Shafalyuk O. S., Sirenko Y. K. and Velychko L. G. 122

16. POINTWISE RADIATOR IN FDTD METHOD Varyanitza-Roshchupkina L. A. 125

17. MODELING THE ELECTROMAGNETIC IMPULSE INTERACTION WITH A HUMAN SKIN TAKING INTO ACCOUNT A DISPERSION Simachova O. N. 129

18. PRESENTATION OF THE FIELD SURFACE WAVE GENERATED BY AN ANTENNA AT THE INTERFACE OF TWO HOMOGENEOUS MEDIA Rudenchik A. E., Volkomirskaya L. B., Reznikov A. E. and Bezrukova E. G. 132

19. PULSE EXCITATION OF A CAVITY WITH DISPERSIVE MEDIUM THAT REFRACTIVE INDEX IS POSITIVE AND NEGATIVE M. S. Antyufeyeva, O. A. Tretyakov..... 134

APPLICATIONS (GPR, RADARS, COMUNICATION, MEDICINE)

01. A PROLATE-SPHEROIDAL IMPULSE-RADIATING ANTENNA SYSTEM TO LAUNCH AND FOCUS 100-PS PULSES FOR MELANOMA TREATMENT Prashanth Kumar, Serhat Altunc, Carl E. Baum, C. Jerald Buchenauer, Christos G. Christodoulou and Edl Schamiloglu .. 138

02. DATA RATE IN IMPULSE ULTRA WIDEBAND RADIO NETWORKS Bunin S. G. 141

03. USE OF THE ULTRAWIDEBAND FMCW SIGNAL FOR HF COMMUNICATION RADIOCHANNEL DIAGNOSTICS Ilyin N. V., Khakhinov V. V. and Ponomarchuk S. N. 144

04. MEASUREMENT OF COORDINATES OF THE TARGETS PLACED BEHIND OF RADIO-TRANSPARENT BARRIER WITH MULTI-STATIC ULTRA-WIDE BAND RADAR Myakinkov A. V. and Smirnova D. M. 147

05. DETECTION AND COORDINATE MEASUREMENT OF TARGETS BY ULTRA-WIDE BAND RADAR WITH ANTENNA ARRAY Myakinkov A. V. and Smirnova D. M. 150

06. SEARCH ALGORITHM FOR LOCAL OBJECTS IN GPR IMAGE Shkvyrya Y..... 153

07. MULTIFREQUENCY MICROWAVE TOMOGRAPHY OF ABSORBING INHOMOGENEITIES Gaikovich K. P., Gaikovich P. K., Maksimovitch Ye. S., Badeev V. A..... 156

08. UWB BABY MONITOR Ziganshin E. G., Numerov M. A., Vygolov S. A..... 159

09. PROPOSALS TO BUILD A PROMISING ULTRA-WIDEBAND WIRELESS COMMUNICATIONS Shostko I. S., Almakadma T. 162

10. WIRELESS SECURE COMMUNICATIONS USING UWB NOISE WAVEFORMS WITH CODE SPECTRUM MODULATION Kalinin V. I. 165

11. WIRELESS FIELD BUS COMMUNICATION WITH SOFTWARE DEFINED IR-UWB IN A MANUFACTURING ENVIRONMENT Masini M., Alpert T., Lang F., Grözing M. and Berroth M. 168

12. PRACTICAL APPLICATION OF UWB GEORADAR TECHNIQUE FOR INVESTIGATIONS OF CULTURAL HERITAGE OBJECTS Yastrebov Yu. V., Kostyleva V. V., Nikolaev V. A., and Barilko M. S. 171

13. ESTIMATION OF DIELECTRIC PERMITTIVITY OF MEDIUM BY ANALYSIS OF UWB RADIOLOCATION SIGNALS FROM LOCAL OBJECT Yastrebov Yu. V., Kostyleva V. V. and Nikolaev V. A. 174

14. RECONSTRUCTION OF PERMITTIVITY PROFILE OF STRATIFIED STRUCTURES WITH LOSSES ON BASIS OF DIVERGENT BEAM PROBING USING MULTIFREQUENCY DATA IN WIDE FREQUENCY BAND Alexin S. G. and Drobakhin O. O. 177

15. ESTIMATION POWER AND SPATIAL CHARACTERISTICS OF ULTRAWIDEBAND RADAR FOR STATEMENT OF PROTECTING HANDICAPS Vlasik S. N., Yermakov G. V., Zima I. I. 180

16. THE USAGE OF EXTREMAL COHERENT INTEGRATION IN THE ALGORITHMS OF PROCESSING OF REFLECTED SYGNALS Mitrofanov D. G. 183

17. SPREADING SEQUENCE SELECTION SCHEME FOR NBI SUPPRESSION IN DS-UWB SYSTEMS Wang C., Ying R., Wei Y. and Yang Y. 186

18. WAY OF AN ESTIMATION TRAJECTORY INSTABILITY OF FLIGHT OF THE AIR TARGETS Prohorkin A. G. 189

19. BIOLOGICAL EFFECTS OF ULTRAWIDEBAND RADIATION Shckorbatov Y. G., Kolchigin N. N., Pasiuga V. N., Kazansky O. V.....192

20. THE DEVICE FOR REMOTE MONITORING OF HUMAN'S HEARTBEAT Shirokov I. B., Slesareva A. V., Korepanov A. L.....195

21. SUSCEPTIBILITY ANALYSIS OF COMPLEX INFRASTRUCTURE TARGETS Gardner R. L. and Stoudt D. C.....197

22. THE MOTION TRAJECTORY RESTORING FOR RADAR OBSERVATION OF LIVING OBJECTS Ochotnikov D. A. 201

GENERATION, RADIATION, RECEIVING

01. PULSE EXCITATION OF ACOUSTIC OSCILLATIONS OF A CELL Harlanov A. V.....206

02. HIGH SPEED AND EFFICIENT SELECTIVELY SENSITIVE PHOTODETECTORS St. Collin, F. Pardo, S. V. Averin, N. Bardou and J. L. Pelouard.....209

03. ELECTROMAGNETIC WAVES RADIATION BY THIN VIBRATORS WITH ASYMMETRICAL SURFACE IMPEDANCE Nesterenko M. V., Dakhov V. M., Katrich V. A., Berdnik S. L. and Pshenichnaya S. V.....212

04. THE RADIATOR OF Ku-BAND BASED ON INVERTED DIELECTRIC WAVEGUIDE Mayboroda D. V., Pogarsky S. A., Saprykin I. I., Pshenichnaya S. V.....215

05. PROPER MODE OF EXCITATION FOR LARGE CURRENT RADIATORS Pochanin G. P. and Pochanina I. Ye.....218

06. GENERATOR OF WIDE-BAND PULSES WITH AMPLITUDE UP TO 20 KV AND PULSE REPETITION RATE UP TO 10^4 PULSES DESIGNED FOR OPERATION WITH VARIOUS RADIATORS Boyko M. I., Bortsov A. V., Evdoshenko L. S., Ivanov V. M.....221

07. INFLUENCE OF THE SCREEN ON THE RANGE PROPERTIES OF RAREFIED ARRAYS OF NEAR-OMNIDIRECTIONAL RADIATORS Gorobets N. N. and Bulgakova A. A.....223

08. THE GENERATION BY GUNN DIODES BASED ON THE GAN, INN, ALN TED'S IN BIHARMONIC REGIME Storozhenko I. P. and Arkusha Yu. V. 226

UWB ANTENNAS

01. AN ULTRAWIDEBAND 1−20 GHZ MODIFIED LOG-PERIODIC FEED Dubrovka F. F. and Dolzhenko D. S.....230

02. THE PLASMA ANTENNAS MOUNTED ON FRAGMENTS OF MOBILE OBJECTS Ovsyanikov V. V., Ol'shevs'kiy O. L., Popel' V. M., Romanenko Y. D., Ponomarenko Y. V., Moroz S. N. 233

03. COMPLEX PULSE RADIATION OF CIRCULAR TSA ARRAY WITH STEERING POLARITIES OF ELEMENT EXCITATION Kolchigin N. N., Kazansky O. V., Ivanchenko D. D., Liang Jing Feng, He Shi, Zheng Yu.....236

04. ARRAYED «VIVALDI» RADIATORS CHARACTERISTICS Yukhanov Y. V., Bolov R. B., Privalova T. Y., Kondrat'eva A. P., Kurochkin A. P., Los' V. F.....240

05. THE CHARACTERISTICS ANALYSIS OF PATCH ANTENNA ARRAY Ku-BAND Golovin V. V., Tyschuk Y. N., Luk'yanchikov A. V. and Toloknova E. U.....243

06. A NOVEL MINIATURIZED ULTRA WIDEBAND LOG-PERIODIC ANTENNA Luan Shan, Liu Xiaofeng and Qiu Jinghui 246

07. THE DIRECTIVITY CHARACTERISTICS OF AN ANTENNA ARRAY RECEIVING THE UWB SIGNAL Konovalenko A. A., Tokarsky P. L., Erin S. N. 249

ELECTROMAGNETIC COMPATIBILITY. ELECTROMAGNETIC METROLOGY

01. STANDARD COMPLEX FOR REPRODUCTION AND TRANSMISSION OF UNIT SIZES OF PULSE ELECTRIC AND MAGNETIC INTENSITIES IN ULTRASHORT PULSE RANGE Sakharov K. Yu., Mikheev O. V., Turkin V. A., Dobrotvorsky M. I., Aleshko A. I. 254

02. SOFTWARE FOR PROCESSING METROLOGICAL CERTIFICATION RESULTS OF SHORT IMPULSE GAUGES Skoblikov O. Y. 256

03. THE "TEM" METHOD OF CALIBRATION OF THE PULSE HIGH VOLTAGE DIVIDER Kniaziev V. V., Kravchenko V. I., Niemchenko Yu. S., Lisnoy I. P. 259

04. SOME APPROACHES TO THE DEVELOPMENT OF ABSORBING MATERIALS FOR ULTRAWIDEBAND SYSTEMS Bibikov S. B., Smolnikova O. N., Menshova S. B., Prokof'ev M. V., Orlov V. V. 262

05. PARAMETRIC STUDY OF IMPULSE HIGH VOLTAGE DISCHARGE Berdin S. A., Galchenko D. A,. Zagvozdkin B. V., Karelin S. Yu., Magda I. I., Mukhin V. S., Soshenko V. A. 266

06. IMPULSE SUB-NANOSECOND REFLECTOMETRY Berdin S. A., Karelin S. Yu., Korenev V. G., Magda I. I., Mukhin V. S., Naboka A. M., Soshenko V. A. 270

07. SCALE ELECTRODYNAMIC MODELING OF ULTRA WIDEBAND SYSTEMS Titov A. N., Gribanov A. N. 273

08. SAMPLING DURATION FOR NOISY SIGNAL CONVERSION Ruban V. P., Pochanin G. P. 275

09. WIDE-BAND MEASURING COMPLEX DESIGNED FOR REMOTE CONTROL OF THERMAL RADIO RADIATION PRODUCED BY COKE-OVEN BATTERIES Bykov V. N., Grichaniuk A. M., Ivanchenko D. D., Krayushkin V. A., Zhyravsky A. A., Fedorova S. V., Hudokormov A. P., Rjapovol E. V., Berezhnaya T. D. 278

CELEBRATING ANNIVERSARIES

To 90th anniversary of Prof. Yakov S. Shifrin 284

AUTHORS LIST 285

INVITED PAPERS

POLARIMETRIC SUPPRESSION OF EARLY-TIME SCATTERING FOR LATE-TIME TARGET IDENTIFICATION

Prof. Dr. Dr.-Ing. E.h. Carl E. Baum

The University of New Mexico
Department of Electrical and Computer Engineering
MSC01 1100, 1 University of New Mexico
Albuquerque, NM 87131-0001, U.S.A.
E-mail: carl.e.baum@ieee.org

Abstract

One can suppress the strong signal amplitude of the early-time scattering, relative to the late-time signal containing the natural resonances (for target identification) using various techniques. This paper discusses the use of polarization for the early-time suppression.

1. INTRODUCTION

For target identification/classification, an important technique uses the singularity expansion method (SEM) [10]. The backscattering delta-function response is characterized by the scattering dyadic

$$\overleftrightarrow{\Lambda}_b(\vec{1}_i;s)=\sum_\alpha \vec{c}_\alpha(\vec{1}_i)\vec{c}_\alpha(\vec{1}_i)e^{s_\alpha t}u\left(t-t_0\right)+ \\ +\ entire\ function\ (temporal\ form), \tag{1.1}$$

$\vec{c}_\alpha(\vec{1}_i)\bullet\vec{1}_i=0$, direction of incidence.

As discussed in [4], the scattering problem in general must have an entire function (not describable by complex resonances) to characterize the early-time scattering. Note that the scattering dyadic multiplies the incident field to give (with a delay and $\left[4\pi r\right]^{-1}$) the scattered field.

To recognize the target by its complex natural frequencies s_α, one sometimes encounters a problem with a large early-time transient signal in the presence of a low-level late-time resonant signature. This introduces a dynamic-range problem in the transient-signal recording devices (such as digitizers). One would then like to avoid the early-time signal in the recording to accurately measure the late-time waveform.

One can approach the problem of early-time suppression in various ways. One can use limiters [9] to chop off the early-time peak(s). This raises practical questions concerning the response time of the limiter (early-time feed through) and the recovery time (hopefully before the beginning of the late-time signal). Another possibility would have linear (passive and/or active) analog filters. If the early-time signal is sufficiently narrow in time, then special low-pass filters (i.e., integrators [8]) can reduce the early-time amplitude relative to the late-time amplitude. One can also use an incident (interrogating) wave which is designed by its frequency content to maximize the return of the late-time resonances.

The present paper considers the use of the polarization properties of the scattering. If the early-time polarization is sufficiently different from the late-time polarization [6], then one can in effect "cross polarize" (in a general sense) the radar to the early-time scattering, while letting the late-time scattering (or useful portions of this) through to the recorder.

Note that we are here concentrating on physical (analog) processes so as to avoid differencing of large numbers (digital processing) from digitized waveforms.

2. ANTENNA POLARIZATION

Figure 1 shows the various combinations of transmit and receive polarizations. While this is shown for two nearby antennas for clarity, these combinations are also possible in a single antenna (such as a reflector impulse radiating antenna (IRA)) [1-3].

As will become useful, we do not need to fix $\vec{1}_h$ as horizontal (parallel to local earth). We can rotate the antenna(s) by some angle ψ_h (positive or counterclockwise as seen from the front). There are, of course, electrical ways to combine the signals with appropriate weights (e.g., attenuators) to achieve the same effect.

978-1-4244-7468-4/10/$26 ©2010 IEEE

3. NULLING SOME EARLY-TIME RESPONSES BY POLARIMETRY

Consider now some typical early-time scatter-ing examples [5, 12]. This leads to polarimetric ways to suppress such signals in the radar.

3.1. FLAT PLATE, BROADSIDE

This produces a strong specular reflection with a waveform proportional to the time-derivative of the incident field. Most importantly, the scattering is polarization independent, i.e., the scattered field has the same polarization as the incident field (with a minus sign). Denoting by V the various voltage signals in the radar, then form

$$V = V_{h,h} - V_{v,v} = 0 \tag{3.1}$$

for this type of scattering. This holds for any rotation of the radar through the angle ψ_h.

If one has such a polarization-independent scattering, another approach considers h,v (= v,h) scattering (crosspol). In this case one can use only one linear polarization for incidence and rely on the zero crosspol for such early-time scattering. Then one looks at $V_{h,v}$ for the late-time scattering. One may wish to rotate the antenna, since then only one transmit polarization is needed. One can also combine h,h and v,v transmission to give a linear polarization at any desired angle ψ. The object is to maximize the late-time crosspol scattering.

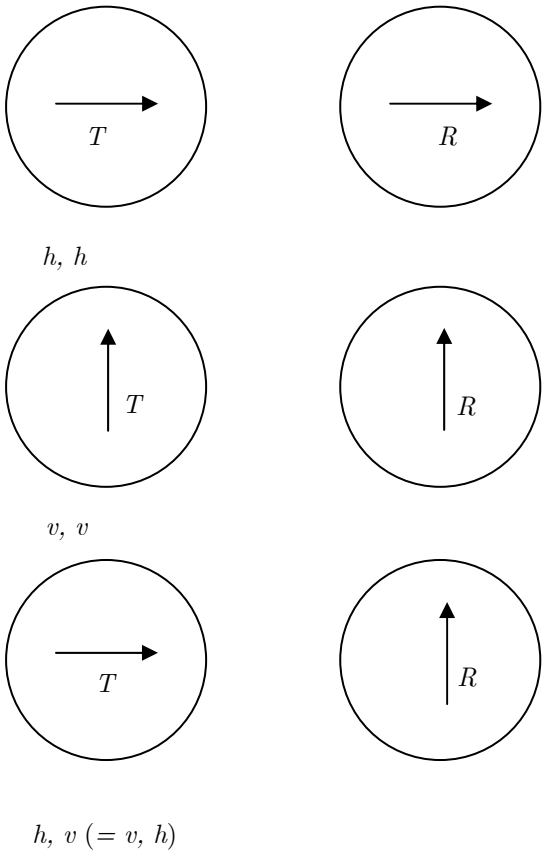


Fig. 1. Antenna polarization.

3.2. CURVED SURFACE: CONVEX

In this case we have the Gaussian curvature r_0^{-1} related to the two radii of curvature at the specular point as

$$r_0 = \left[r_1\ r_2\right]^{1/2} \tag{3.2}$$

The early-time scattering is a replica (delta function convolution) of the incident waveform [11 (Section 1.4.3), 5 (Section 5)]. The scattering is polarization independent, so the results of Section 3.1 apply.

3.3. LONG WEDGE, NORMAL INCIDENCE

Letting the edge be normal to the direction of incidence, we have a strong scattering with polarization $\vec{1}_e$ parallel to the edge. The frequency dependence is such that a delta function gives a scattering proportional to $t^{-1/2}u(t)$ [12]. Clearly we need to look in the polarization perpendicular to this. This can be acomplished by rotating the antenna by an angle ψ with

$$\begin{aligned} &\cos(\psi) = \vec{1}_e \bullet \vec{1}_h, \\ &\vec{1}_e = \pm\left[\vec{1}_h \cos\left(\psi\right) + \vec{1}_v \sin\left(\psi\right)\right]. \end{aligned} \tag{3.3}$$

Alternately, we can form

$$V = \sin\left(\psi\right)V_{h,h} - \cos\left(\psi\right)V_{v,v} = 0\,. \tag{3.4}$$

3.4. SHORT WEDGE, NORMAL INCIDENCE

With a finite-length edge at normal incidence we have an early-time signal which replicates the incident waveform [12]. The results of Section 3.3 still apply.

3.5. CONE

In this case, with the first scattering coming from the cone tip, the scattered field is proportional to the time integral of the incident field [12]. While one can null this, the amplitude of the scattered field is small (stealth) compared to the previously discussed cases.

4. SEPARATION OF POLARIZATIONS

One difficulty with this approach concerns the obtaining of two separate (h,h and v,v or appropriate combinations) polarization signals, such as is the case for early-time polarization-independent backscattering. (See Section 3.1 and 3.2.) Of course, one can perform two separate target interrogations, one with each of the two orthogonal transmit polarizations. This gives a

problem. One can always combine the results in a computer, but this has a dynamic-range problem for recovering the late-time information.

One would like an analog way to perform this combination of the two. One could place one signal, say $V_{h,h}$ in a delay line. By transmitting vertical at a later time to illuminate the target at a time after the late-time scattering from the first pulse, we can have a second signal in the *v* channel. With the delay time in the h channel equal to the delay of the *v* channel, the two signals can be differenced in real time in an analog fashion, giving the desired early-time cancellation. A similar technique can be used in transmit by splitting the signal from a pulser into the two channels and inserting a delay line in the *v* channel (same delay as in the h receive line). With two "identical" delay lines, imperfections (attenuation, dispersion) are balanced in the two channels. With ideally no early-time crosspol, there are late-time signals outside the time widow of interest, but one might ignore these. Of course, there may be some early-time crosspol, but this can be small by comparison.

For the case of a dominant signal early-time polarization (Sections 3.3 and 3.4) the situation is somewhat simpler. In this case one transmits and receives a polarization orthogonal to the scatterer early-time polarization. This can be accomplished by antenna rotation using an appropriate linear combination of h and v channels, now operated simultaneously in time.

5. Analog Signal Combination

The concern here is the required dynamic range of the digital recording devices. By reducing the early-time signal relative to the late-time signal before they reach the recorder, we lessen the dynamic-range problem.

The signal combination then needs to be done in an analog fashion by combining signals in circuits, transmission lines, etc. In some cases an inverter (which can be made with coaxial cables and chokes (ferrite)) is required to reverse the sign of a signal. Signals can also be multiplied by a positive constant by an attenuator (or amplifier). Care is needed so as to have the desired frequency-response characteristics.

6. Late-Time Polarization Differences from Early-Time Polarization

After minimizing the early-time scattering signal, we still need to observe the late-time complex resonances. This requires that the polarization properties of at least some of the late-time damped sinusoids differ significantly from the early-time polarization properties. As discussed in [6] there are a variety of polarizations associated with the various substructures on a target of interest. One then chooses those which are different from the early-time polarization. The cases of linear polarization can be promising for the required differences.

7. Application to Clutter Reduction

The discussion here has been in terms of reducing the early-time scattering signals. However, targets are often in the presence of other scatterers which produce signals which we call *clutter*. We need to reduce these for our target identification. Similar techniques can be applied. For this purpose, the early-time scattering can be regarded as just another source of clutter. The clutter from the additional scatters also has polarization properties. So we can consider "cross polarizing" to this clutter as well. An example, given in [7], considers a periodic array of vertical posts (fence posts, wall studs, etc.). There, the consideration was in terms of removing this clutter by a SAR technique by subtracting this as background when scanning a target behind the post array. Here we can note that the post array will typically scatter more in vertical than in horizontal polarization. Hence, one may preferentially look for the $V_{h,h}$ scattered signal. The polarization of the target early-time signal and the late-time resonances also need to be considered.

8. Concluding Remarks

Now we add another dimension to our attempts to suppress early-time relative to late-time scattering, namely polarization. The examples discussed here show the various forms this might taken, including various combinations of two linear polarizations. This will have various requirements for hardware realization. While the discussion here is in terms of backscatter (monostatic), the concepts apply to bistatic (or multistatic) radar, and to synthetic aperture radar (SAR) as well.

Here we have used scattering theory to illustrate various examples of interest. This can be generalized to an experimental technique as well. By measuring the early- and late-time polarization properties of targets of interest one can experimentally optimize the early-time suppression using techniques such as discussed in Sections 3 and 4.

The present technique need not be used alone. It can be combined with others, such as analog filtering, nonlinear limiters, etc.

References

1. C. E. Baum, "Configurations of a TEM Feed for an IRA", Sensor and Simulation Note 327, April 1991.
2. E. G. Farr et al, "Multi-Channel Impulse Radiating Antennas with Polarization Diversity", Sensor and Simulation Note 430, December 1998.
3. L. H. Bowen et al, "A Dual-Polarity Impulse Radiating Antenna", Sensor and Simulation Note 479, October 2003.

4. C. E. Baum, "Representation of Surface Current Density and Far Scattering in SEM and EEM With Entire Functions", Interaction Note 486, February 1992; ch. 13, pp. 273-316, in P. P. Delsanto and A. W. Saenz (eds.), *New Perspectives on Problems in Classical and Quantum Physics, Part II, Acoustic Propagation and Scattering, Electromagnetic Scattering*, Gordon and Breach, 1990.
5. C. E. Baum, "Some Simple Formulae for Transient Scattering", Interaction Note 558, February 2000.
6. C. E. Baum, "Combining Polarimetry with SEM in Radar Backscattering for Target Identification", Interaction Note 585, May 2003.
7. C. E. Baum, "Symmetry in Target Recognition", Interaction Note 587, August 2003.
8. C. E. Baum, "Second Time Integral of the Impulse Response for Enhancing the Late-Time Target Response for Target Identification", Interaction Note 590, April 2004.
9. L. M. Atchley, E. G. Farr, and W. D. Prather, "The Response of Commercial Limiters to Transient Signals", Measurement Note 59, April 2005.
10. C. E. Baum et al, "The Singularity Expansion Method and Its Application to Target Identification", Proc. IEEE, 1991, pp. 1481-1492.
11. K. S. H. Lee (ed.), *EMP Interaction: Principles, Techniques, and Reference Data*, Taylor & Francis, 1986.
12. C. E. Baum, "Continuous Dilation Symmetry in Electromagnetic Scattering", ch. 3, pp. 143-183, in C. E. Baum and H. N. Kritikos (eds.), *Electromagnetic Symmetry*, Taylor & Francis, 1995.

THE FORMATION AND RADIATION OF HIGH-POWER SHORT RADIO PULSES: NEW APPROACHES TO MODELING AND ANALYSIS OF MICROWAVE COMPRESSORS

Amosova A. I., Krivchikova A. A., Pazynin V. L., Sirenko Y. K.

A. Usikov Institute of Radiophysics and Electronics
National Academy of Sciences of Ukraine, Kharkov, Ukraine
E-mail: yks@ire.kharkov.ua

Abstract

New approaches to analysis and synthesis of microwave power compressors and radiators of high-power short radio pulses are discussed in the paper. These approaches are based on time-domain methods and allow us to study both particular dynamic processes occurring in different nodes (in resonator drives, locks, wave beams distributed switches, radiators, etc.) and the general devices operation principles.

Keywords: mathematical modeling, computational experiment, time-domain method, microwave power compressor, short radio pulse.

INTRODUCTION

A compressors' energy efficiency increase requires a detailed study of the accumulation processes and energy escape processes in open resonators, excited by long quasimonochromatic pulses.

Within the bounds of experimental approaches supported only by general ideas about electrodynamics characteristics of the storage single nodes (a resonator itself, coupling window with feeding waveguide, commutator) and approximate computations, satisfying solution of this problem can be obtained by the significant timetable and material resources. The point is that the microwave pulse compressor is the resonant structure, which is able to work only when the functional characteristics of particular nodes and the excitation parameters are well chosen. The variation of any parameter usually induce an avalanche, uncalculatable on simplified models of changes which can radically worsen the characteristics developed device.

Mathematical modeling and computational experiment allow us to consider a lot of cases, to analyze in detail the physics of the process, realized in the compressors of all structures today (see, for example [1–6]), to solve synthesis [7] and optimization problems, to obtain specific estimates in that size which sufficiently to produce available laboratory models operatively and without large resources consumption. Powerful and universal time-domain methods are the best for such modeling [8]. These methods algorithms supplied with exact absorbing conditions [9,10] allow us to analyze the limited spatial regions and to obtain reliable estimates for arbitrary time intervals of variable t, which characterize the physics of the transient processes under possible resonant waves scattering. Special time-domain and frequency-domain methods combined for the study of open resonance structures of complex geometry [11,12] are developed.

Algorithms from [9–12] are realized in specialized program packages that allow us to model and analyze the power compressors and powerful short radio-pulse resonance radiators with almost any type of storage devices (waveguide and open resonators with metal, translucent and frequency-selective mirrors), and locks (distributed grating switches for compressors in multimode waveguides and resonance radiators, interference and resonance switches for compressors with unimodal diverting waveguides). This programs have been involved in the computational experiments, the result of which are presented in the paper. We place the part of illustrated materials without the detailed comments to conclude abut the direction of research and its main results. We use SI for all physical parameters except t that is measured in meters – it is the product of the natural time and the velocity of the propagation of light in vacuum.

1. COMPRESSOR ON H_{01}-WAVE OF RECTANGULAR WAVEGUIDE

Rectangular regular waveguides of the direct flow compressor (see Fig. 1: $a = 1.28$, $b = 3$,

978-1-4244-7468-4/10/$26 ©2010 IEEE

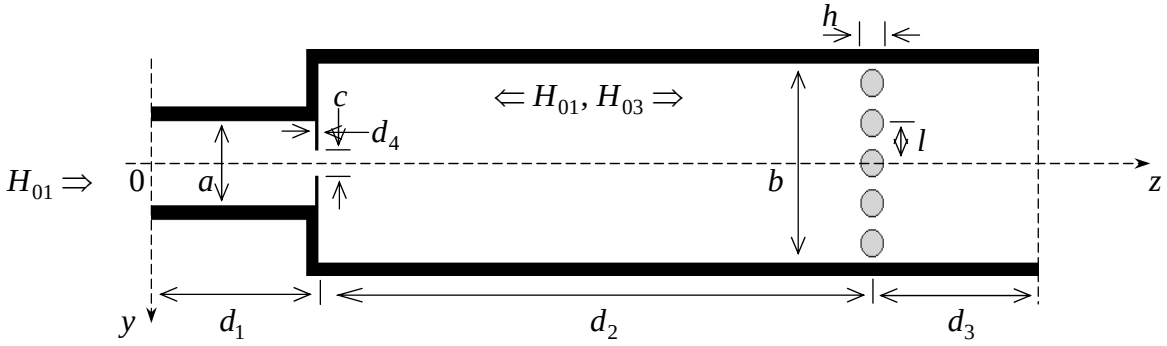


Fig. 1.

$d = d_1 + d_2 + d_3 = 16$, $d_1 = 3$, $d_2 = 10$, $d_3 = 3$, $d_4 = 0.06$, $l = 0.6$, $h = 0.4$; $z = 0$ and $z = d$ are virtual boundaries defining computational domain of model problem) supports of one (left, feeding waveguide) or three (right, outlet waveguide) H_{0n}-waves in the frequency band $3.2 < k < 4.1$. Lock (commutator) is the periodical system of the discharge tubes ($\varepsilon = 3.8$, 0.02 is the walls thickness). Its range characteristics in the accumulation mode (A – tubes are filled with $\varepsilon = 1.0$ and $\sigma_0 = 5.7 \cdot 10^4$) and in the escape energy mode (B – tubes are empty, $\varepsilon = 1.0$ and $\sigma_0 = 0$) are shown in the Fig. 2.

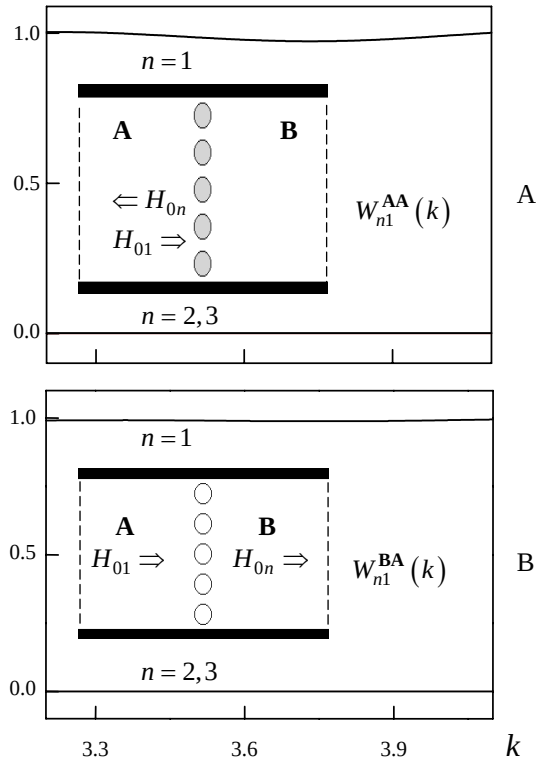


Fig. 2.

Here $k = 2\pi/\lambda$ is a wave number; ε and σ_0 are relative dielectric conductivity and a specific conductivity; $W_{n1}^{\mathbf{AA}}(k)$ ($W_{n1}^{\mathbf{BA}}(k)$) is the part of energy which is fit on the reflected (transmitted) H_{0n}-wave when lock excited by H_{01}-wave from the domain $\mathbf{A}$.

To determine the potential compressor's working frequencies $k \approx \mathrm{Re}\,\bar{k}$ (frequencies 1–7 at Fig. 3) in the frequency band $3.2 < k < 4.1$ we excite it by the pulse H_{01}-wave $E_x^i(g,t)$:

$v_1(0,t) = 4\sin\left[\Delta k\left(t-\tilde{T}\right)\right]\left(t-\tilde{T}\right)^{-1}\cos\left[\tilde{k}\left(t-\tilde{T}\right)\right]\times$

$\times\chi\left(\bar{T}-t\right)$; $\tilde{k} = 3.65$, $\Delta k = 0.5$, $\tilde{T} = 50$, $\bar{T} = 100$.

After that spectral amplitudes $\left|\tilde{E}_x(g_1,k)\right|$ of free oscillating field $E_x(g,t)$; $t > 100$, $g = \{y,z\} = g_1$ must be analyzed (see Fig.3).

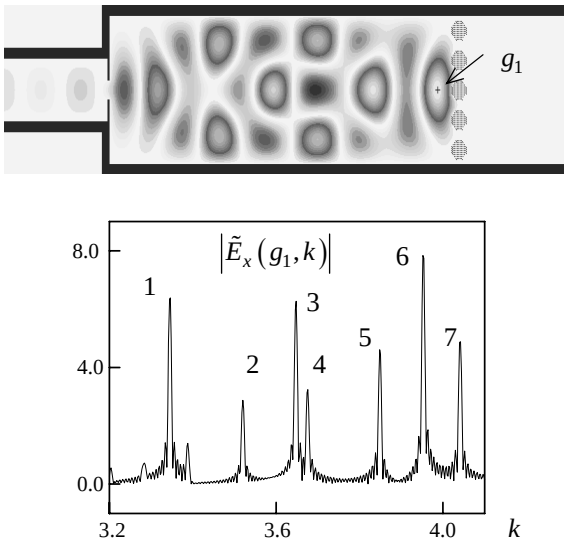


Fig. 3.

Here $\chi(...)$ is a Heaviside step function, $v_1(0,t)$ is amplitude of the incident H_{01}-wave in the plane $z=0$. $\mathrm{Re}\,\bar{k}$ are real values of the eigenfrequencies $\bar{k}$, appropriating to the high Q-quality free oscillations in the storage device. Spectral characteristics of this oscillations (configuration of the oscillations field and their quality $Q=\mathrm{Re}\,\bar{k}/2\left|\mathrm{Im}\,\bar{k}\right|$) are determined using the compressor exciting by the narrowband Gaussian pulse $E_x^i(g,t)$: $v_1(0,t)=$ $=\exp\left[-\left(t-\tilde{T}\right)^2/4\tilde{\alpha}^2\right]\cos\left[\tilde{k}\left(t-\tilde{T}\right)\right]\chi\left(\bar{T}-t\right)$; $\tilde{k}\approx\mathrm{Re}\,\bar{k}$, $\tilde{\alpha}=20$, $\tilde{T}=100$, $\bar{T}=200$ (see corresponding methodology in [11,12]). $H_{0,1,12}$-oscillation that corresponds to the frequency 6 (see Fig. 4).

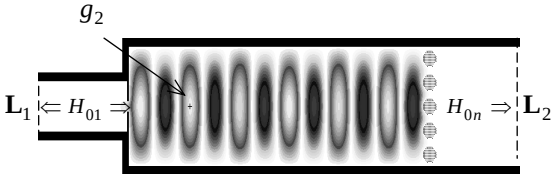


Fig. 4.

Its Q-quality ($\mathrm{Re}\,\bar{k}\approx 3.953$, $\mathrm{Im}\,\bar{k}\approx 0.0003$) is enough to construct the working compressor.

2. Factors that Significantly Influencing the Energy Accumulation Process

We can get full information about accumulation modes which can be realized in the compressor (see Fig. 5: A – $c=0.4$, B – $c=0.36$, C – $c=0.32$, D – $c=0.28$) obtaining complex eigenfrequencies $\bar{k}=\mathrm{Re}\,\bar{k}+i\,\mathrm{Im}\,\bar{k}$ for the $H_{0,1,12}$-oscillations in storage devices with different sizes of window between the feeding waveguide and the resonator and exciting compressor with the long quasi-monochromatic pulses $E_x^i(g,t)$: $v_1(0,t)=P(t)\cos\left[\tilde{k}\left(t-\tilde{T}\right)\right]$; $\tilde{k}=\mathrm{Re}\,\bar{k}$, $\tilde{T}=1.0$, $P(t)=0.1-5-3000-3004.9$.

Here $P(t)=t_1-t_2-t_3-t_4$ is the trapezoidal envelope curve. It is equal to zero when $t<t_1$, $t>t_4$ and equal to unity when $t_2<t<t_3$; $u_1(0,t)$ and $u_1(d,t)$ are the amplitudes of the reflected and transmitted H_{01}- waves in planes $z=0$ and $z=d$. Obviously, that functions $v_1(0,t)$, $u_1(0,t)$, and $u_1(d,t)$ determines the efficiency of the accumulation energy process in each point of time t, and the function $E_x(g_2,t)$ determines the peak amplitude of signal, which can be obtained as a result of compression.

Even small deviation of the central frequency $\tilde{k}$ of the feeding pulse H_{01}-wave from value $\tilde{k}=\mathrm{Re}\,\bar{k}$ may be lead to complete loss of compressor's ability to accumulate energy in the resonant volume. The data, presented in Fig. 6 ($c=0.32$; $E_x^i(g,t)$: $v_1(0,t)=P(t)\cos\left[\tilde{k}\left(t-\tilde{T}\right)\right]$; $P(t)=0.1-5-$ $-5000-5004.9$, $\tilde{T}=1.0$; A – $\tilde{k}=\mathrm{Re}\,\bar{k}=3.95625$, B – $\tilde{k}=3.953$), confirms this: the mistake in the definition of $\tilde{k}$ equal approximately to 0.082% transforms the compressors storage in the banal, well reflecting heterogeneity.

3. Characteristics of the Compressor

Here are some calculated characteristics of the compressor with $c=0.32$. $H_{0,1,12}$ is the type of working oscillation, $k_{work}=\mathrm{Re}\,\bar{k}=3.95625$ is the operative frequency, $Q\approx 7912.5$ ($\mathrm{Im}\,\bar{k}\approx -0.00025$) is the quality of accumulation resonator. Changing the duration of pumping T_1^i in the interval $2500<T_1^i<10000$ the efficiency of the energy accumulation $\eta_{accum}\left(T_1^i\right)=\left[W_1^i-W_1^s-W_2^s\right]/W_1^i$ and the achieved level of field intensity in the loop of the working fluctuation field $\alpha\left(T_1^i\right)=\max\limits_{0<t<T_1^i}\left|E_x^i(g,t)\right|/\max\limits_{t>0}\left|E_x(g_2,t)\right|$ changes like that:

	$T_1^i=2500$	5000	7500	10000
$\eta_{accum}\left(T_1^i\right)$	0.691	0.8	0.736	0.637
$\alpha\left(T_1^i\right)$	0.509	0.774	0.906	0.981

Here $W_1^i\left(T_1^i\right)=\int_0^{T_1^i}\left[-P_1^i(t)\right]dt$, $W_1^s\left(T_1^i\right)=$ $=\int_0^{T_1^i}P_1^s(t)\,dt$ and $W_2^s\left(T_1^i\right)$ is the energy stored in the input, reflected and transmitted pulses; $-P_1^s(t)$, $P_1^s(t)$ and $P_2^s(t)$ are the instant power which is fed and radiated across the virtual boundaries $\mathbf{L}_1$ and $\mathbf{L}_2$ (see Fig. 7). In the case illustrated by Fig. 7 and Fig. 8, the exciting pulse $E_x^i(g,t)$: $v_1(0,t)=P(t)\cos\left[\tilde{k}\left(t-\tilde{T}\right)\right]$; $\tilde{k}=k_{work}$,

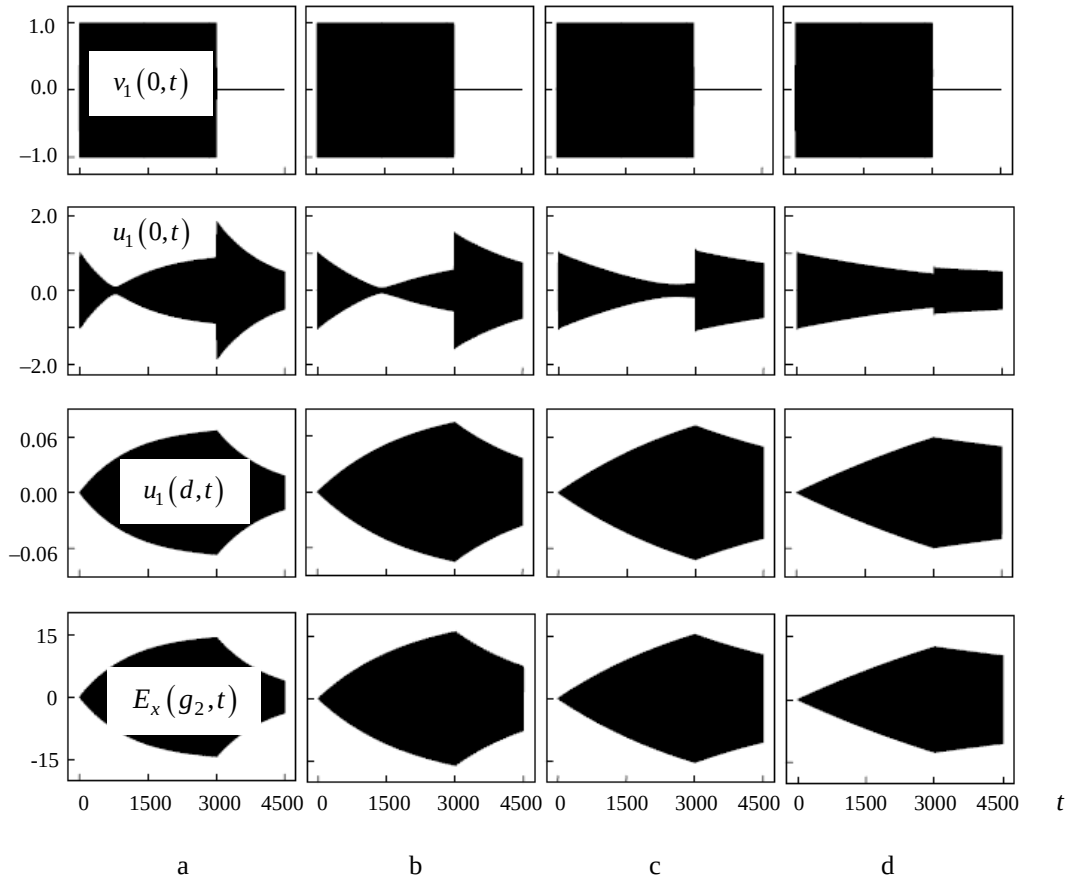

1.0
0.0
–1.0
$v_1(0,t)$
2.0
0.0
–2.0
$u_1(0,t)$
0.06
0.00
–0.06
$u_1(d,t)$
15
0
-15
$E_x(g_2,t)$
0
1500
3000
4500
t
a
b
c
d

Fig. 5.

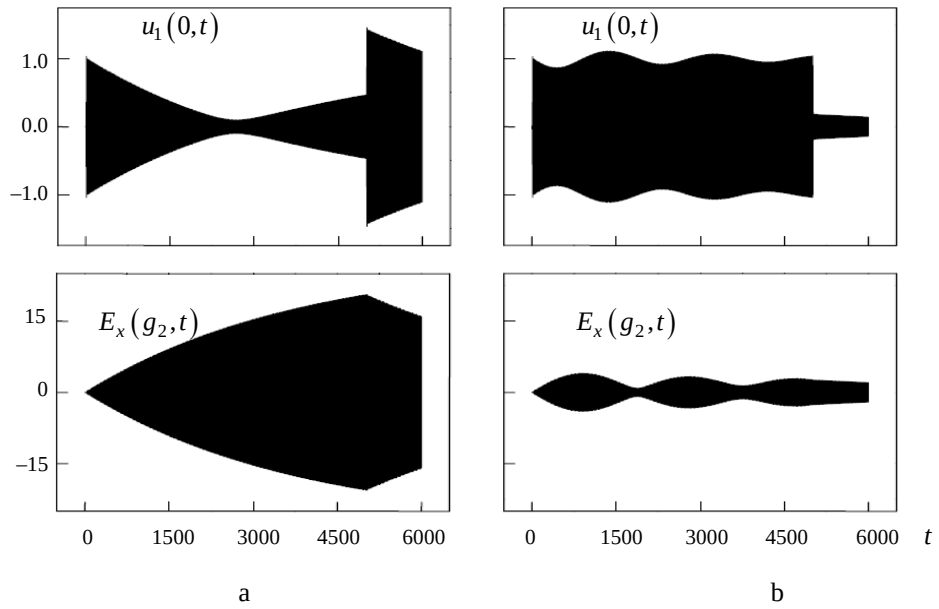

$u_1(0,t)$
$u_1(0,t)$
1.0
0.0
–1.0
15
0
–15
$E_x(g_2,t)$
$E_x(g_2,t)$
0
1500
3000
4500
6000
t
a
b

Fig. 6.

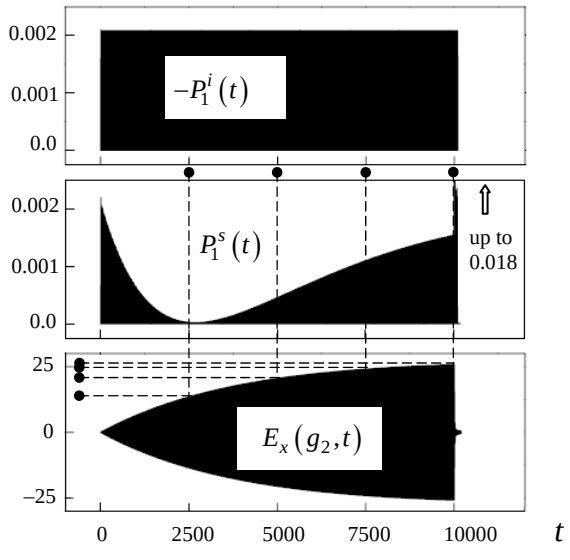


Fig. 7.

$P(t) = 0.1 - 5 - 10100 - 10104.9$, $\tilde{T} = 1.0$ feeds the structure until $t \approx 10105$, but the accumulation of energy completely stops until the moment $t = 10001$.

The values of the function $\sigma_0(t)$ that characterizes the filling of gas-discharge tubes material absorption are varying from $\sigma_0 = 5.7 \cdot 10^4$ up to $\sigma_0 = 0$ on the interval $10000 \le t \le 10001$ when compressor opens up.

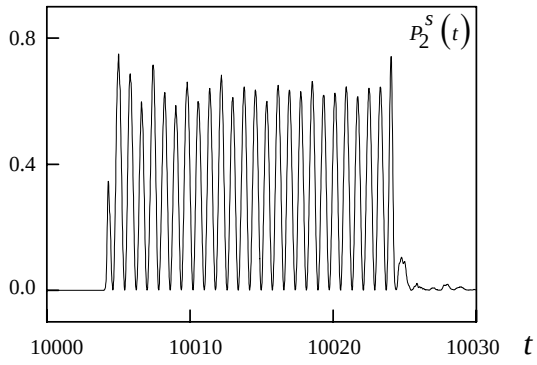


Fig. 8.

The effective duration of the signal which transmitting through the virtual boundary $\mathbf{L}_2$ is equal to $T_2^s = 21.5$ (see Fig. 8). It is not much more than twice the length of accumulation resonator. $\beta = T_1^i / T_2^s \approx 465$ it is the degree of compression; $\eta = W_2^s / W_1^i(T_1^i) \approx 0.6238$ it is the coefficient of efficiency; $\vartheta = \beta \cdot \eta \approx 290$ it is the power amplification. Here, $W_2^s = \int_{10004}^{10025.5} P_2^s(t)\,dt$, and the integration intervals has determined by the effective duration of the generated pulse. Denote, that the amplitudes of the functions $P_2^s(t)$ are greater approximately up 325 and 16250 times on this interval, than maximal amplitudes of oscillations of the functions $P_1^i(t)$ and $P_2^s(t)$ on the interval $0 < t < 10000$. The coefficient of efficiency of compressor's is less than the accumulation efficiency $\eta_{accum}(T_1^i)$. The part of energy are distributed between short intensive ejection in the reflected signal (see Fig. 7) and long lived tail which is attend the main pulse.

We can determine the working wavelength $\lambda_{work} \approx 1.588[m]$ via the value $k_{work} = 3.95625[rad/m]$. The length of the accumulative camera for compressor which operates with such λ_{work} is equal to $d_2 = 10.0[m]$.

The accumulation time is $33.3564[\mu s]$ that characteristics mentioned above must be obtained. Herewith the duration of the generated pulse will be equal to $71.7163[ns]$. Obviously, that all results obtained with this approach, are easily transformed on any other geometrically similar structures. For example, to work with the wavelength $\lambda_{work} \approx 8[mm]$ it is necessary the storage device with the length $50.38[mm]$ and with the accumulation time of $168.042[ns]$. The pulse duration formed in such compressor will be equal to $361.291[ps]$.

4. CONCLUSION

At first compressor's work has been completely computed in the frames of the strict model. It is the compressor at the segments of the rectangular waveguides with the outrageous diaphragm as the coupling window, and the system of quartz gas-discharge tubes as the commutator. That sort of models allow us to analyze correctly the space-time transformations of electromagnetic field in open resonant structures with high Q-quality. The results of this work are directly proved that prior and comprehensive electrodynamics modeling must be used for a construction of effective working compressors in region of centimeter and millimeter wavelengths.

REFERENCES

1. Artemenko S. N., Kaminskiy V. L., Yushkov Y. G. 1993, 'Derivation of energy from the large axially symmetrical resonators across oversize coaxial line', *J. Technical Physics*. **63**, 2, 105–112.
2. Vikharev A. L., Kovalev N. F., Petelin M. I. 1996, 'Wave beams distributed switches and microwave

pulses compressors', *Letters to J. Technical Physics*. 22, 19, 41–46.
3. Tantawi S. G., Ruth R. D., Vlieks A. E., Zolotorev M. 1997, 'Active high-power RF pulse compression using optically switched resonant delay lines', *IEEE Trans. MTT*. 45, 1486–1492.
4. Vikharev A. L., Gorbachev A. M., Ivanov O. A., Isaev V. A., Kuzikov S. V., Kolysko A. L., Petelin M. I. 1998, 'Active microwave pulses compressor on the axially symmetrical mode of circular waveguide', *Letters to J. Technical Physics*. 24, 20, P. 6–11.
5. Artemenko S. N., Avgustinovich V. A., Kaminskiy V. L., Chumerin P. Y., Yushkov Y. 2000, 'Experemental research of 25-megawatt three-centimeter wavelengths range microwave compressor prototype', *J. Technical Physics*. 70, 12, 102–105.
6. Vikharev A. L., Gorbachev A. M., Ivanov O. A., Isaev V.A., Kuzikov S. V., Kolysko A. L., Movshevich B. Z, Hirshfield J., Gold S. H. 2008, 'Active Bregg microwave pulse compressor of 3-cm wavelength range', *Higher School News. Radio-Physics*. 51, 7, 597–616.
7. Kuzmitchev I. K., Melezhyk P. M., Pazynin V. L., Sirenko K. Y., Sirenko Y. K., Shafalyuk O. S., Velychko L. G. 2008, 'Model synthesis of energy compressors', Radiophysics Electronics. 13, 2, 33–54.
8. Taflove A., Hagness S. C. 2000, *Computational Electrodynamics: The Finite-difference Time-domain Method*, Artech House, Boston.
9. Sirenko Y. K., Sirenko K. Y. 2005, 'Exact "absorbing" conditions in the initial boundary-value problems of the theory of open waveguide resonators', *J. Computational Mathematics Mathematical Physics*. 45, 3, 490–506.
10. Sirenko Y. K., Strom S., Yashina N. P. 2007, *Modeling and Analysis of Transient Processes in Open Resonant Structures. New Methods and Techniques*, Springer, New York.
11. Sirenko Y. K., Velychko L. G., Erden F. 2004, 'Time-domain and frequency-domain methods combined in the study of open resonance structures of complex geometry', *Progress Electromagnetics Research*. 44, 57–79.
12. Sirenko Y. K., Velychko L. G., Shafalyuk O. S. 2006, 'Time-domain analysis of open resonators. Analytical grounds', *Progress Electromagnetics Research*. 61, 1–26.

SPECTRAL THEORY ANALYSIS OF UWB-OSCILLATIONS IN FREQUENCY SINTHESIZERS BASED ON PHASE-LOCKED LOOPS

[1] Kravchenko V. F., [2] Kravchenko O. V., and [3] Safin A. R.

[1] Kotel'nikov Institute of Radio Engineering and Electronics RAS, Moscow, Russia
E-mail: kravchenko_vf@fromru.com
[2] Bauman Moscow State Technical University, Moscow, Russia
E-mail: olekravchenko@gmail.com
[3] Moscow Power Engineering Institute (Technical University), Moscow, Russia
E-mail: safin_ansar@mail.ru

Abstract

In this report a general theory of phase-locked loop (PLL) for N-dimensional UWB-signals (for example radar and optical signals) is given. On the first step a discretization method for solving differential equations of the PLL systems is presented. It is shown that there are a lot of zones of synchronous in discretized PLL and a technical realization of this device (in PLL with samples). A spectral theory of analysis of oscillations in PLL with samples is given. It is shown a lot of different physical properties in PLL with samples. The effect of shape of the input signals (harmonic signals, splines and atomic functions) at the border zones of operating modes being entered into PLL with samples is examined.

Keywords: Phase-locked loop, discretization, atomic functions.

1. INTRODUCTION

Phase locked loops (PLL) are widely used in the tasks of generating high precision oscillation (frequency synthesis) [1-5] for ultra wideband (UWB) radar, the optimal reception of digital and continues UWB-signals [1], the organization of parallel computations in multiprocessor (cluster) systems [3]. Special place in the theory of the PLLs occupy systems with samples [1,6,7] (or pulse PLL systems), in which information about error in the circle of auto regulation handled in separate instants in comparison with continues systems. This is achieved using a special type of pulse-phase discriminator (PPD).

The important feature [6-8] inherent PLL with samples presence of a great number of synchronous zones of fractional multiplicity of frequency is. As it is shown in [8] its usage for tasks of synthesis of frequencies is limited by that in physical synchronous zones of fractional multiplicities the spectrum of generated oscillations is polluted of parasite components because samples of an entry signal are allocated non-uniformly on time axis. At the approach to boundaries of physical synchronous zones the spectrum of generated signals fails. One of methods of struggle against «spectrum pollution» in the given paper, usage of various forms of entry signals is researched. Now the wide circulation for tasks of a UWB-radar-location [9-10], digital signal and image processing [9-12] was received by the theory of atomic functions (AF). However in the literature questions of generating of the signals grounded on AF practically were not discussed to it by it in operation is given particular attention with reference to tasks of reception of oscillations with a pure spectrum in PLL with samples.

Operation structure the following. In the beginning units of the continuous PLL theory [1-5] are resulted. It is shown that in continuous PLLs there is only one physical synchronous zone mode limited to a bar of synchronism. Further two sorts of PLL with samples (are considered at handle of the period and frequency of oscillations of the set up generator). It is shown that one of such models, namely: at handle of the period it is possible to receive by discretization of the differential equation for continuous PLL. Research of dynamic processes by Lamerej-Kenigs diagram's is carried out. Research of PLL's with samples dynamic processes detects a considerable quantity of physical synchronous zone modes – allowed bands of division and frequency multiplication. The detailed analysis of PLL's dynamics in the main physical synchronous zones of fractional multiplicities is given. At a following stage introduction in theory of AF and principles of creation of the difficult signals, them made them is given. Further application of the signals made from AF, for generating of oscillations with a pure spectrum in PLL with samples is researched. It is shown that usage of such signals expands physical synchronous zones modes of fractional multiplicities of frequency at low coefficient of regulation. At the final stage the spectral theory of the analysis of output PLL oscillations with samples in multiplicity synchronous zones $1/1$, $1/n$ и $n \in \mathbb{Z}$ is given

978-1-4244-7468-4/10/$26 ©2010 IEEE

2. ELEMENTS OF THE THEORY OF PHASE LOCKED LOOP SYSTEMS

2.1. CONTINUES PLL

The basic idea of synchronisation by means of PLL consists of measurement of a current mismatch of oscillation phases of the voltage control oscillator (VCO) and the generator of main oscillation with the subsequent usage of a signal of an error for frequency and phase VCO correction. The Block diagramm of the elementary continuous PLL is presented on Fig. 1. We will consider base principles of its operation. In the phase discriminator (PD) the current phase of main oscillation $\varphi_S(t)$ is compared to a phase $\varphi_G(t)$ of oscillations VCO and the error signal $e(t)$ is worked out. Having passed through a loop filter (LF) this signal arrives to VCO. Under the influence of controlling power $g(t)$ correcting mistuning is brought, and, being added to own frequency free VCO, it operates towards reduction of an initial mismatch of phases $\varphi(t) = \varphi_S(t) - \varphi_G(t)$ of VCO oscillations and a main signal.

Mathematical model of the PLL is the differential equation which in general form so we can write so [4]

$$\frac{p\varphi}{\Omega} + K(p)F(\varphi) = \gamma \qquad (1)$$

Here, $\Omega = S \cdot E$ is the greatest mismatch correction (or band-matching, since if $\left|\omega_{FR} - \omega_S^{\,0}\right| \le \Omega$ in PLL observed synchronous mode), generating in system depending on the steepness S of adjusting frequency characteristics of the householder in VCO and amplitudes of the input and VCO E. Here $\gamma = \dfrac{\omega_{FR} - p\varphi_S}{\Omega}$ is dimensionless mistuning the natural frequency ω_{FR} VCO on the current frequency $\omega_S = p\varphi_S$ of reference vibration and $K(p)$ is operator coefficient transmission in LF, $p \equiv d/dt$ is symbolic notation of differential operator and $F(\varphi)$ is discriminatory characteristic of PD. For simplicity we use a sinusoidal characteristic of PD, i.e. $F(\varphi) = \sin\varphi$. In Fig. 2a the dependence of the normalized frequency asynchronous oscillations ω_{as}/Ω on the mistuning γ. It is seen that in the band-matching Ω i.e., if $\gamma \le 1$, asynchronous oscillation frequency is equal to zero, while increasing γ, i.e. when leaving the band matching frequency asynchronous oscillations increases according to expression $\omega_{as}/\Omega = \sqrt{\gamma^2 - 1}$. In Fig. 2b matching area is shown $\gamma_s = (\omega_{sym} - \omega_s)/\Omega$ (in mathematical literature adopted the term "Arnold toungue") on plane of control parameters.

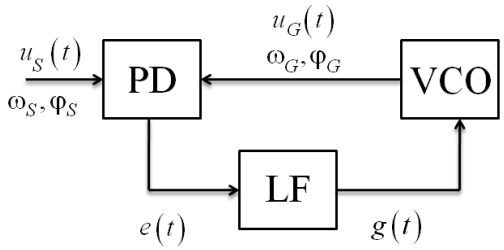
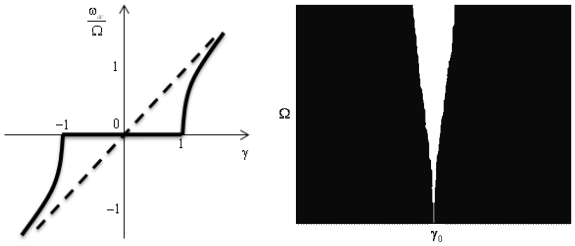


Fig. 1. Block diagram of the PLL.



a) b)

Fig. 2. The dependence of normalized frequency asynchronous oscillations ω_{as}/Ω of mistuning (a); physical matching zone (Arnold tongue) in plane of parameters (Ω, γ) (b).

Difference equation of sampling PLL in the management of the oscillation period of VCO can be obtained by discretization of differential equation of continuous PLL (1) for the sampling step equal to 1.

2.2. PLL WITH SAMPLES WORKING PRINCIPALS

Here, we analyze PLL with samples working principals. The structural scheme of such a system is presented on the Fig. 3a. Assume that signal input $u_S(t)$ is harmonica (it could by a signal coming from some reference generator) with given U_0 and given frequency $\omega_S = 2\pi / T_S$, where T_S is the signal period with initial phase θ_0. The general expression for $u_S(t)$ is following:

$$u_S(t) = U_0 \cdot \sin\left[\omega_S t + \theta_0\right] = U_0 \cdot \sin\left[\varphi_S(t)\right]. \quad (2)$$

In the PPD scheme (Fig. 3b) samples u_k of the signal input $u_S(t)$ are formed in moments t_k corresponding to the leading edge of oscillations of the impulse forming block (FB). Control voltage coming to the input VCO g_k in the case of filterless PLL equals e_k. The control of the moment t_{k+1} of the next sample can be performed in two ways: period control and oscillation frequency control of VCO. In the first case voltage g_k determines linearly the interval $T_{k+1} = t_{k+1} - t_k$ to the next sample. Thus, VCO oscillation period is

$$T_{k+1} = t_{k+1} - t_k = T_{FR} - S_T g_k, \qquad (3)$$

where T_{FR} is VCO free period (when $g_k \equiv 0$), S_T is the slope of modulation characteristic of VCO period controller. From (3) it follows the dependence $t_{k+1} = f\left(t_k\right)$ with the account of (2).

Then

$$t_{k+1} = t_k + T_{FR} - T_M \sin\left[\omega_S t_k + \theta_0\right], \qquad (4)$$

where $T_M \triangleq S_T \cdot U_0$ is the maximum deviation of oscillation frequency generated by VCO. For phase samples $\varphi = \omega_S t + \theta_0$ and maximal phase deviation $K \triangleq \omega_S T_M$ we receive

$$\varphi_{k+1} = \varphi_k + 2\pi B - K \cdot \sin\varphi_k, \qquad (5)$$

where $B = T_{FR} / T_S = \omega_S / \omega_{FR}$ is initial frequency mismatch between signal and VCO free oscillations. Lets divide finite-differential equation (5) by 2π and pass finally to coordinate $x_k = \varphi_k / 2\pi$ .Then

$$x_{k+1} = x_k + B - \left(K/2\pi\right) \cdot \sin\left(2\pi \cdot x_k\right). \qquad (6)$$

Received finite-differential equation (6) is a mathematical model of PLL with samples with VCO oscillation period control. To control VCO oscillation frequency there exist the following finite-differential equation:

$$x_{k+1} = x_k + \frac{B_\omega}{1 - K_\omega \sin\left(2\pi \cdot x_k\right)}. \qquad (7)$$

Thus, we received mathematical models of PLL with samples in the form of two-parametrical finite-differential equations (or discrete mapping) with VCO period control (6) and oscillation frequency control (7). Mapping (6) can be derived by sampling differential equation of continuous PLL with sample interval equal to 1.

Next we analyze the dynamic of PLL with samples. For simplicity we consider VCO Period control case.

3. Dynamical Processes in Phase Synchronization System with Samples

3.1. Lamerej-Kenigs Diagramms

Consider methods of investigation of mappings (6) и (7) dynamics. Discrete mappings (finite-difference equations) are considered on the cylindrical surface. This practice is usual in the theory of continuous phase synchronization systems [6]. Such presentation allows to use graphical form of dynamical process under the method of Lamerej-Kenigs diagrams. An examples of such diagram is shown in Fig. 4 for some mapping $x_{k+1} = f\left(x_k\right)$ (axes are x_{k+1} and x_k). Under this method time process x_k depending on k is constructed (Fig. 4b).

Firstly, consider the precise VCO tuning to signal frequency ($B = 1$), when one sample is made for one period of input signal. Lamerej-Kenigs diagram is presented in the Fig. 5a and time process is in the Fig. 5b. There exist three fix points: $\widehat{x} = 0$, $\widehat{x} = 0,5$ and $\widehat{x} = 1$. It is necessary to estimate their stability by multiplier.

It is possible to find multipliers of fixed points (the slope of mapping function

$$f\left(x_k, B, K\right) = x_k + B - (K / 2\pi) \cdot \sin\left(2\pi \cdot x_k\right)$$

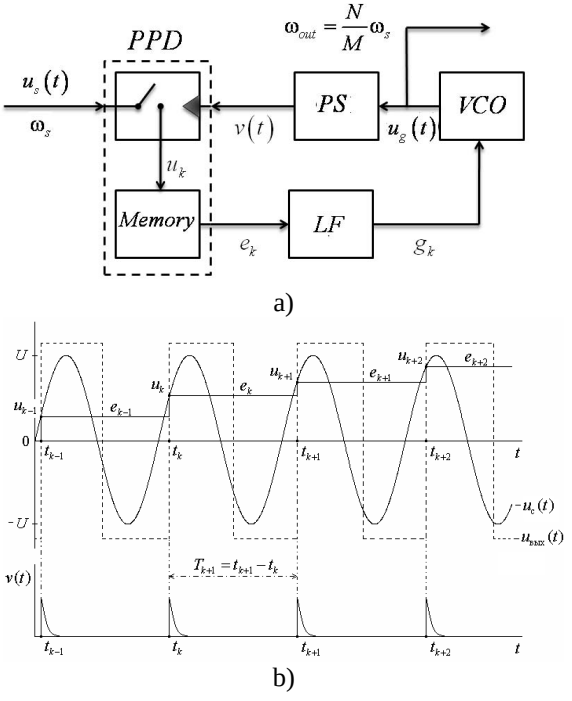


Fig. 3. Block diagram of PLL with samples (a) and formation of samples of input sinusoidal signal (b).

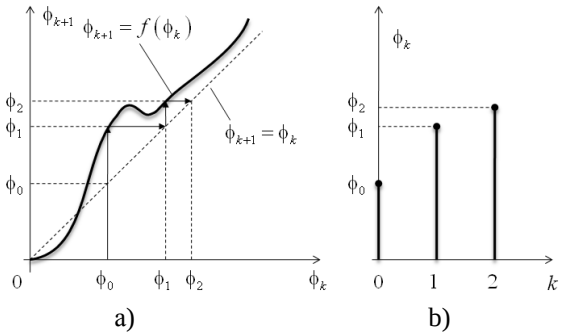


Fig. 4. Lamerej-Kenigs diagram (a) and temporary process (b).

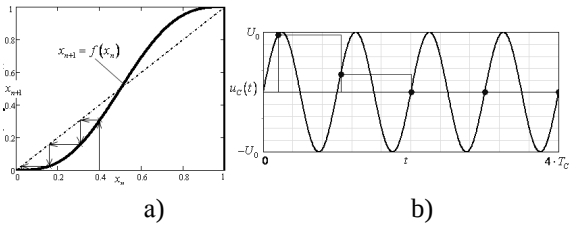


Fig. 5. Lamerej-Kenigs diagramm (a) and time process (b) of mapping (6) when $K = 1, B = 1, x_0 = 0,4$.

from the following expression:

$$\mu = \frac{\partial f\left(\widehat{x}, B, K\right)}{\partial \widehat{\phi}} = 1 - K \cdot \cos\left(2\pi \cdot \widehat{x}\right). \qquad (8)$$

From (8) it follows that for $K = 1$ multiplier equals to zero in two points $\widehat{x} = 0$ and $\widehat{x} = 1$. In the point $\widehat{x} = 0.5$ $\mu = 2$, hence it is not stable. When parameter B equals to 0,5 it is possible to discover the existence of 2T-cycle. In this case it is necessary to investigate fixed points of surface mapping $f\left(f(x, B, K), B, K\right)$. Lamerej-Kenigs diagram for the mapping of the circle when $B = 0,5$ is presented in Fig. 6. In this case generator's frequency equals to the doubled frequency of input signal.

Consideration of other types of dynamic can be performed analogically. Now we pass to the diagrams of dynamical modes observed in PLL with samples.

3.2. Physical Map of Dynamical Modes of PLL with Samples

Under the variation of parameters K и B over the wide range it is possible to discover the large number of different types of dynamics. Explicit maps of dynamical modes (synchronization zones) for the standard ($K \in [0,2]$) and modified ($K_\omega \in [0,1]$) mapping of circles when $B, B_\omega \in [0,1]$ are presented in Fig. 7a-b. In the area $K > 1$ near "Arnold tongues" can cross over. In this case in PLL with samples chaotic oscillations are observed. More detailed information on chaotic oscillations generation using PLL with samples can be found in [7].

It was discovered that in PLL with samples it is possible to realize the large number of synchronous modes of solid frequency multiplicity in corresponding synchronization zone ("Arnold tongue"). Despite of the attraction of such systems (possibility to realize the large number of synchronization zones) they have a considerable disadvantage. Before the consideration of mappings (6) and (7) dynamics in corresponding

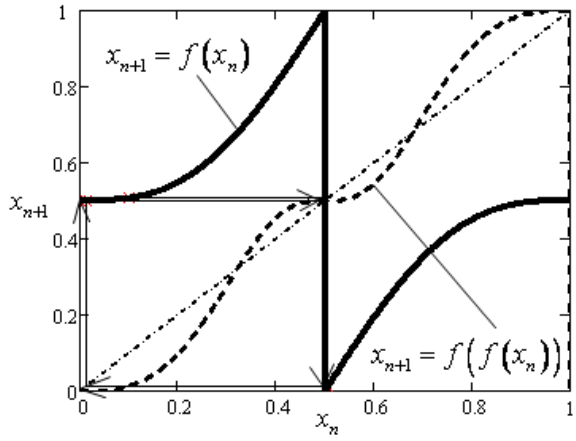


Fig. 6. Lamerej-Kenigs diagramm for the case $K = 1, B = 0,5$.

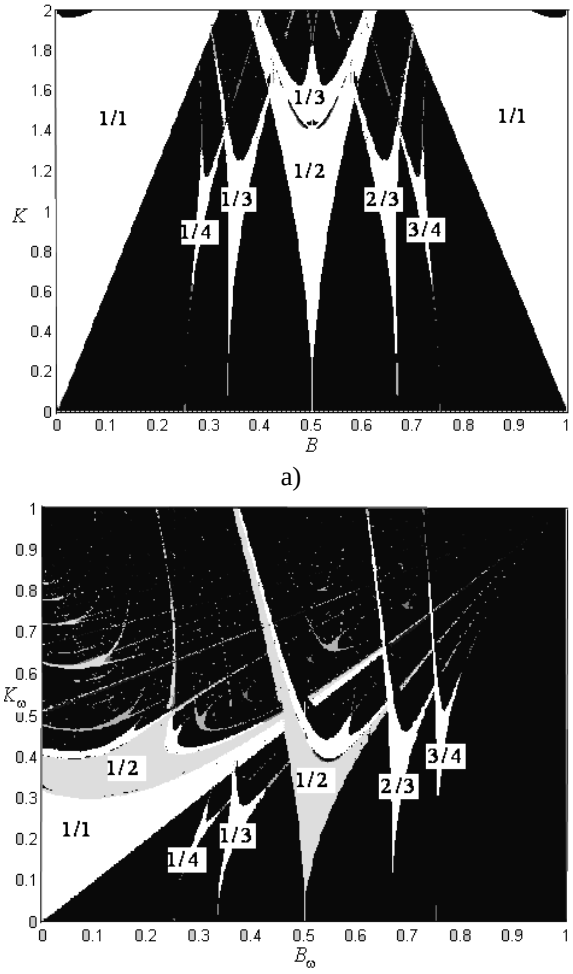


Fig. 7. Dynamical modes map in the case of VCO period control (a) and oscillation frequency control.

physical synchronization zones it is necessary to investigate the influence of input signal form on the map of synchronous modes. We take periodical oscillations constructed from AF as reference pilot. This can be explained (will be shown later) by the fact that synchronization zone modes of PLL with samples of fractional rate expand in the case of utilization of oscillations constructed from shifts of AF.

4. The Theory of AF and Methods of Formation of the Periodic Signals Constructed Based on AF

4.1. Operational Method of Decision of FDE of the Special Kind

According to [9-12] the AF are FDE decision of a following kind:

$$\sum_{i=1}^{n} a_i y^{(i)}\left(x\right) = \sum_{k=1}^{M} b_k y\left(ax - b_k\right), \qquad (8)$$

where $|a|>1$, $y^{(i)}(x)=d^i y(x)/dx^i$ and $y^{(0)}(x)=y(x)$. If $b_k\equiv 0\,(k=1,\ldots,M)$ then (8) passes in the ordinary differential equation. From shifts of the finite decisions of the equation (8) a homogeneous problem (without the right part). We consider an operational method of the decision of the equation (15). Let $d/dx\equiv p$. Then action of the operator p on function $y(x)$ is equivalent to its differentiation $py(x)=dy(x)/dx$, and n^{th} derivative on x from the function $y(x)$ we will write down so: $p^n y(x)=d^n y(x)/dx^n$. Expression $y(ax-b_k)$ in symbolical form looks like $y(ax-b_k)=y\left(a\left(x-\left[b_k/a\right]\right)\right)=e^{-\frac{b_k}{a}p}y(ax)$. We will write down FDE (8) in an operational form as follows:

$$\sum_{j=0}^{n}a_{n-j}p^j\left[y(x)\right]=\sum_{k=1}^{M}b_k e^{-\frac{b_k}{a}p}\left[y(ax)\right]. \qquad (9)$$

Here $[y(x)]$ denote the action of the operator $A(p)$ on function $y(x)$. Rewrite expression (9) in the kind connecting $y(x)$ and compressed function $y(ax)$

$$y(x)=K(p)\left[y(ax)\right], \qquad (10)$$

where $K(p)=\sum_{k=1}^{M}b_k e^{-\frac{b_k}{a}p}/\sum_{j=0}^{n}a_{n-j}p^j$. Let's assume that function $y(x)$ is finite. Will define its analytical representation by action of the operator $K(p)$ infinite number of times on δ-function. Then

$$y(x)=\prod_{i=0}^{\infty}K\left(\frac{p}{a^i}\right)\left[\delta(x)\right]. \qquad (11)$$

The operational method presented above allows to receive analytical FDE decisions of type (8) with variable coefficients if $a_i=a_i(x)$. Expression (11) can be interpreted as follows: finite AF $y(x)$ is reaction of the filter with transfer function $\prod_{i=0}^{\infty}K\left(\frac{p}{a^i}\right)$ on δ-function, i.e. is the pulse characteristic of this filter. Therefore for formation of the AF $y(x)$ is necessary to construction of the filter with transfer function $\prod_{i=0}^{\infty}K\left(\frac{p}{a^i}\right)$. It consists of cascade connection of inertional circuit $1/\sum_{j=0}^{n}a_{n-j}\left(\frac{p}{a^i}\right)^j, i=1,2,\ldots$ and delay lines $\sum_{k=1}^{M}b_k e^{-\frac{b_k}{a}\left(\frac{p}{a^i}\right)}, i=1,2,\ldots$. Will consider the other method of realization of the filter with operational factor of transfer $\Xi(p)=\prod_{i=0}^{\infty}K\left(\frac{p}{a^i}\right)$. As it is known [10,15] for finding of the frequency characteristic (FC) $\Xi(j\omega)$ of the filter with operational factor of transfer $\Xi(p)$, it is necessary to put $p=j\omega$. After the such replacement and receiving $\Xi(j\omega)$, it is possible to apply standard methods of filters synthesis on given FC, following Batterword or Chebyshev. The function $y(x)$ received from decision of FDE (8) is finite. Therefore an important point is consideration of a method of formation of the periodic signals made of its shifts. For the first time such problem has been put and solved in [12] for AF. Will consider the formation of the periodic signals constructed from AF.

4.2. The periodic Signals Constructed based on AF

The orthogonal periodic even system of functions has been named [12] $Kup(x)$ and odd one $\widehat{K}up(x)$. Will consider a technique of construction of these functions. So AF is finite decision of FDE of a kind

$$up'(x)=2\cdot\left(up(2x+1)-up(2x-1)\right). \qquad (12)$$

Operator $\Xi(p)$ of FDE (8) is written down so

$$\Xi(p)=\prod_{i=1}^{\infty}\frac{sh\left(p/2^i\right)}{p/2^i}. \qquad (13)$$

For obtain the FC of the filter with the pulse characteristic $up(x)$ it is enough to put in (13) $p=j\omega$. From (13) will receive

$$\Xi(j\omega)=\prod_{i=1}^{\infty}\frac{sh\left(j\omega/2^i\right)}{j\omega/2^i}=\prod_{i=1}^{\infty}\frac{\sin\left(\omega/2^i\right)}{\omega/2^i}. \qquad (14)$$

Thus, the evaluation method for function $up(x)$ is its representation in the form of return Fourier transform from (14). Even and odd system of periodic functions on interval $[-T,T]$ will write down as follows:

1. For the even functions $Kup(0,x)=1$,

$$Kup_1(x)=up\left(\frac{2}{T}x\right)-up\left(\frac{2}{T}(x-T)\right)-up\left(\frac{2}{T}(x+T)\right)$$
$$\ldots\quad\ldots\quad\ldots\quad\ldots\quad\ldots\quad\ldots\quad\ldots\quad\ldots\quad\ldots\quad.$$

2. For the odd functions $\widehat{K}up(0,x)=0$,

$$\widehat{K}up_1(x)=up\left(\frac{2}{T}\left(x-\frac{T}{2}\right)\right)-up\left(\frac{2}{T}\left(x+\frac{T}{2}\right)\right),$$
$$\ldots\quad\ldots\quad\ldots\quad\ldots\quad\ldots\quad\ldots\quad\ldots\quad\ldots\quad\ldots\quad.$$

Similar procedure of obtaining of periodic fluctuations «sewing» of elementary impulses can be applied for any finite decisions of FDE (8). For example for AF $fup_n\left(x\right)$ being decisions of following FDE:

$$fup_n'\left(x\right) = 2^{n-1}\sum_{k=0}^{n+2}\left(C_{n+1}^{k} - C_{n+1}^{k-1}\right)\times$$
$$\times fup_n\left(2^{n-1}x - \frac{2\left(k-1\right)-n}{2^{n+2}}\right)$$

which are defined in a kind

$$fup_n\left(x\right) = \frac{1}{2\pi}\int_{-\infty}^{\infty}\mathrm{sinc}^n\left(\frac{\omega}{2}\right)\prod_{i=1}^{\infty}\mathrm{sinc}\left(\frac{\omega}{2^i}\right)e^{i\omega x}d\omega.$$

Such system we will name $Kfup_n$ and $\widehat{K}fup_n\left(x\right)$ by analogy with $Kup\left(x\right)$ and $\widehat{K}up\left(x\right)$. Will consider as the physical map of dynamic modes of PLL with samples at use of periodic signals Kup and $Kfup_n$ will change.

4.3. Influence of the Form of the Input Signal on the Physical Map of Zones of Synchronous Modes of PLL With Samples

The important feature of PLL with samples is that the card of dynamic modes (zones of synchronous and asynchronous modes) for it essentially depends on the form of the input signal. Will copy the difference equation (6) taking into account any form of the input signal. Then

$$x_{k+1} = x_k + B - \left(K/2\pi\right)\cdot F\left[x_k\right]. \qquad (15)$$

Here $F[x]$ is 2π-periodic function. In expression (6) $F[x] = \sin\left(2\pi\cdot x\right)$. Will investigate as the form of the input signal (function kind in (15)) influences a physical map of zones of synchronous modes. We use following functions:

$$F_1[x] = Kup\left(2\pi\cdot x\right), \qquad (16)$$

$$F_2[x] = Kfup_3\left(2\pi\cdot x\right). \qquad (17)$$

Oscillograms of input signals, and also error signals in a mode of doubling of the frequency, corresponding to functions $F_{1,2}[x]$ are resulted on Fig. 8.

On Fig. 9 physical maps of zones of synchronous modes («Arnold's tongue») on a plane of operating parametres $\left(K,B\right)$ for input signals $F_{1,2}[x]$ at largely limits at $K<4$ are presented. From fig. 9 it is possible to make a conclusion that the form of an input signal essentially influences kinds of zones of synchronous and asynchronous zones depending on operating parametres. For example varying the form of an input signal it is possible to achieve expansion of a working range in a necessary interval of change of the basic physical parametres that is observed for signals Kup and $Kfup$. At $K>1$ the difficult physical picture of overlapping of zones of synchronous modes at use of atomic input signals unlike the signals $F_{1,2}[x]$.

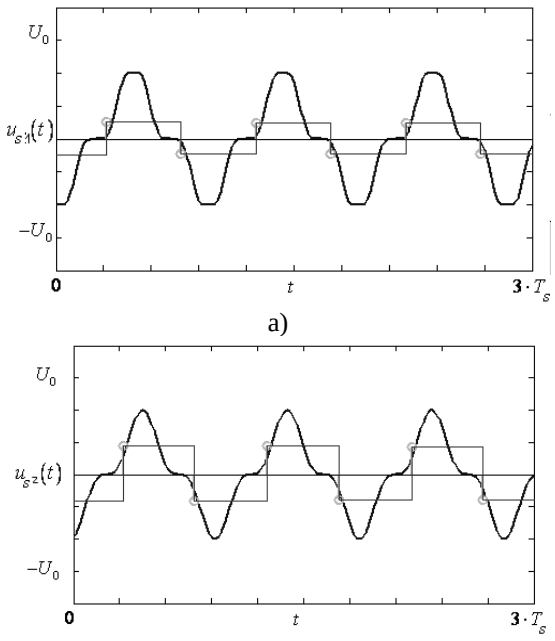


Fig. 8. Various forms of input signals $u_{s1,2}\left(t\right)$ (a)-(b) corresponding to various kinds of nonlinearity $F_{1,2}[x]$ in (15).

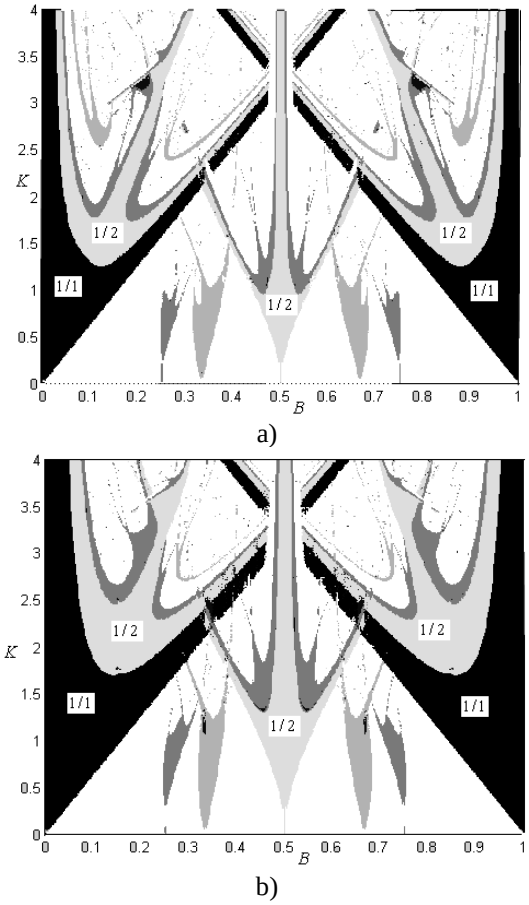


Fig. 9. Physical maps of zones of synchronous modes for various forms of input signals (a)-(b).

Presence of overlapping of physical zones on a card of operating parametres testifies to possibility of generating PLL of chaotic fluctuations. Thus, PLL with samples at use of signals Kup and $Kfup$ also it is possible to use as the generator of chaotic fluctuations. Let's pass to the analysis of dynamic processes in synchronism zones at the approach to their borders.

5. Influence of Non-Uniformity of Sample of the Input Signal on Structure of the Spectrum of Generated Fluctuations

Essential feature of PLL with samples is non-uniformity of arrangement of samples of input signal on an axis of time in synchronism zones. Will disassemble more in detail, in what physical zones this phenomenon and in what it results is shown. There is a question: whether non-uniformity of sample in a physical zone with frequency rate 1:1 will be shown? Earlier it has been shown that after transient there is a synchronisation of fluctuations VCO and the input signal and so that there comes a 1T-cycle (for one period of a signal 1 sample) and in this case (since some n) $x_n = x_{n+1} = x_{n+2} = \widehat{x}$. It turns out that the difference of co-ordinates $\Delta x = x_{n+1} - x_n$ equals to zero or that the same 2π. Thus there is an exact adjustment for frequency of an input signal (there is no heterogeneity). Hence heterogeneity is shown only in physical zones of the higher (more than 1) frequency rates.

Let's consider a mode of doubling of frequency when the operating conditions are chosen in a physical zone of synchronism of frequency rate 1/2. Oscillograms of input signals and generated fluctuations of PLL with samples at the approach to border of this physical zone are presented on Fig. 10a. In process of advancement to border of a physical zone of doubling of frequency non-uniformity of arrangement samples an input signal increases. The similar situation is observed and for physical zones of higher frequency rate. For example, on fig. 0б the behavior of input and target signals in a zone of trebling of frequency is presented. Here it is visible that three intervals T_1, T_2 and T_3 essentially differ from each other. The similar situation is observed and in physical zones of the higher frequency rate.

In what can result non-uniformity of sample of the input signal in physical zones of synchronous modes of fractional frequency rate of frequency? It is obvious that in this case the spectrum of generated fluctuations will contain parasitic spectral components on combinational frequencies. Using of PLL with samples in a synthesis mode high precision fluctuations inconveniently.

6. The Spectral Theory of the Analysis of Fluctuations of PLL with Samples

In the presence of a mismatch of frequencies of synchronizable fluctuations the spectrum of a target signal will be

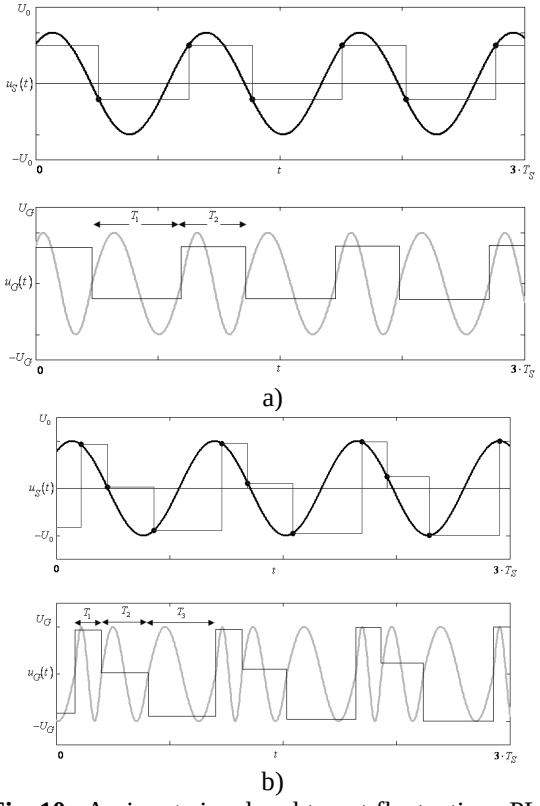


Fig. 10. An input signal and target fluctuations PLL with samples in case of the approach to border of a physical zone of synchronism of 1/2 and 1/3.

considerably deformed by parasitic components, and at enough strong mistuning the exit from a synchronous mode is possible. The spectrum of pure fluctuation (without parasitic a component) looks like $S(\omega) = S_0 \cdot \delta\left(\omega - \left(N/M\right)\omega_S\right)$, where the multipliers N and M are responsible for modes of multiplication and frequency division accordingly. That is there is one spectral a component on the necessary frequency, multiple frequency of an entrance signal. In zones of any frequency rate target signals (harmonious) are periodic with the period $T_S = 2\pi / \omega_S$. Their spectrum is discrete. Decomposition in a complex Fourier series looks like

$$s_{OUT}(t) = \sum_{n=-\infty}^{\infty} \dot{c}_n \cdot e^{jn\omega_S t},$$

where $\dot{c}_n = \frac{1}{T}\int_{-T}^{T} s_{OUT}(t) e^{-jn\omega_S t} dt$.

By consideration of a zone of synchronism of frequency rate 1.2 expression for the module $\dot{c}_n$ is (on positive frequencies) calculated

$$\left|\dot{c}_n\right| = \left|\frac{j}{2} e^{-jn\pi q}\left(q - \frac{(1-q)e^{-j2\pi q}}{1 + \frac{n}{1-nq}}\right)\right| \cdot \frac{\sin\left(\pi\left(1-nq\right)\right)}{\pi\left(1-nq\right)}. \quad (18)$$

Here, $q = T_1/T_S = \omega_S/\omega_1$. At $q = 0,5$ all parasitic spectral components are nulled, the spectrum is pure and represents the δ-function located on frequency $2\omega_S$. Expression (18) for a zone of doubling of frequency, or similar expressions for modes of division and multiplication of frequencies of any frequency rates allow to estimate quantitatively admissible level collateral a component in a spectrum of target signals of PLL with samples.

CONCLUSION

It is shown that in PLL with samples synchronization of fluctuations in physical zones of fractional frequency rate of frequency («Arnold's tongue ») is possible. Use of the periodic signals made from AF, essentially "enriches" a physical map of dynamic modes of system, leading to expansion of zones of synchronous modes of fractional frequency rate of frequency and possibility of generating of chaotic fluctuations. One of a lack which has been found out at research of dynamic processes in corresponding physical zones of synchronous modes, was non-uniformity of sample of an entrance signal, the leader to pollution of a spectrum of target fluctuations. Elements of the spectral theory of the analysis of target fluctuations of PLL with samples are given.

REFERENCES

1. "*Phase Locked Loops with Elements of Sampling*", 1989, edited by V.V. Shahgildyan, Radio and Communication, Moscow.
2. Lindsey, W. 1972, *Synchronization Systems in Communication and Control*, Prentice-Hall, Inc., Englewood Cliffs, New Jersey.
3. Leonov, G.A., Seledzhi, S.M. 2002, *Synchronization Systems in the Analog and Digital Circuitry*, Nevsky Dialect, St.Perersburg.
4. Manassevich, V. 1979, *Frequency Synthesizers. Theory and Design*, Communication, Moscow.
5. Belov, L.A. 2002, *Frequency and Signal Synthesizers*, Sains-Press, Moscow.
6. Kapranov, M.V. 2006, *Elements of the Theory of Phase Locked Loops*, MPEI Publ., Moscow.
7. Kapranov, M.V., Tomashevsky, A.I. 2009, *Regular and Chaotic Dynamics of Nonlinear Systems*, MPEI Publ., Moscow.
8. Kapranov, M.V., Safin, A.R. 2009, 'Oscillation spectrums in discrete synchronization system with nonuniform Sample', *Success in Modern Radio electronics*, **9**, 18-41.
9. Kravchenko, V.F. 2003, *Lectures on the Theory of Atomic Functions and Their Some Applications*, Publishing House Radio Engineering, Moscow.
10. Kravchenko, V.F., Perez-Meana, H.M., and Ponomaryov, V.I. 2009, *Adaptive Digital Processing of Multidimentional Signals with Applications*, Fizmatlit, Moscow.
11. Zelkin, E.G., Kravchenko, V.F., Gusevsky, V.I. 2005, *Constructive Methods of Approximation in Theory of Antennas*, Science-Press, Moscow.
12. Kravchenko, V.F., Safin, A.R. 2009, 'Generalized Kravchenko-Fourier transforms based on family of atomic functions', Proc. 11th Intl. Conf. Digital Signal Processing, Moscow, 135-170.

THE LIGHTNING RETURN-STROKE INITIATION POINT AS AN ULTRA-WIDEBAND SOURCE

Gardner R. L.

Consultant, Alexandria, VA
E-mail: Robert.L.Gardner@verizon.net

Abstract

Understanding the early growth of the lightning discharge is important because that part of the discharge evolution establishes the high-frequency transmissions from lightning. In this paper, we extend the work from ICEAA 2009 on quantitatively describing the radial charges, fields and currents from the relaxing environment between leader and return stroke events. The purpose of this work is to establish the initial conditions to be used later in detailed modeling of the return stroke initiation. The ICEAA 2009 work used a constant conductivity assumption. This paper will extend that work by describing the role of nonlinear conductivity, including a 3-spccies model, in the charge relaxation process. Finally, these currents are used in a simple field model.

Keywords: Lightning, Initiation, ultra-wideband.

1. INTRODUCTION

The beginning of the lightning return stroke is a very important time for understanding the generation of radio-frequency waves from lightning since most of the high-frequency content is from that time. In [1] and this paper, we examine the relaxation of the charge deposited from the leader processes before the return stroke. The purpose of these calculations is to find the initials conditions with which to begin calculation of the return-stroke current waveform. The process is as shown in Fig. 1 [2]. The open cylinders in Fig. 1 represent the region of calculation.

In [2], we examined this same problem with a simple constant gas conductivity model. Since the plasma here is rapidly evolving with the charge species and charge densities changing a nonlinear time-dependent model is more accurate, if less stable.

In this paper, we estimate the radial growth of the channel by modeling it as a spreading uniform cylinder. Initially, there is a cylinder of charge about a meter in diameter. One meter is about as small as the cylinder can be without a substantial current flowing. There is a continuing current of a few amps that flows throughout parts of this process and is used to determine an inner boundary condition. We then solve a series of rate equations, the continuity equation and Poisson's equation to show the relaxation of this part of the channel.

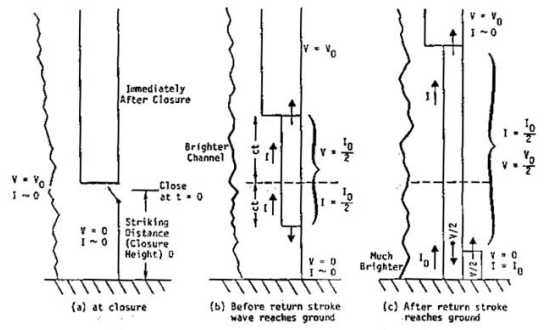


Fig. 1. Schematic of Return Stroke Initiation.

In short, we begin with an analytical model of the charge distribution from a cylinder of charge assuming that the leader processes have lowered negative charge into the channel and it remains there for a few milliseconds pending the beginning of the return stroke. We then allow the ions to move at a constant drift velocity. Finally, we consider the contribution to the changes in charge density from the 3-species rate equations describing ionized air.

2. LIGHTNING RETURN STROKE

A negative cloud-to-ground return stroke begins with the stepped leader [3]. The stepped leader lowers charge to ground in short bright steps. Each step is a few 10 s of meters long. For a 3 km return stroke this process takes about 20 ms to complete. After the stepped leader reaches a point about 10 m above the ground surface there is a joining of upward and downward traveling leaders that begins the return stroke [2]. The return stroke takes about 70 μs then there is a rest of about 40 ms before the dart leader begins. The dart leader takes about 2 ms to lower about 1 C into the 3 km channel. The second return stroke begins and takes about 60 μs. These numbers are only meant to support a rough order of magnitude-type calculation.

978-1-4244-7468-4/10/$26 ©2010 IEEE

Ref. [3] has provided estimates of the general parameters of the lightning return stroke process. From these, we can derive that the stepped leader lowers about 3 C/km of charge into a possibly 10 km long channel. The dart leader is somewhat less energetic and lowers about .3 C/km into the channel. Assuming uniform distribution along the channel allows easier estimates although the charge actually appears in complex clumps. If we examine a cross section of the channel, we find that the fields in the first meter are above breakdown and the self-fields of the electron distribution spread the electrons out through the volume very quickly. After about 1 m, the fields are below 1 MV/m and the electrons start to attach [4]. This attachment is fast compared to the ion drift velocity. The ion drift velocity is much lower than the electron drift velocity [4] so the growth of the channel is slowed substantially.

3. CONTENT

If we assume that the channel is uniformly filled with charge and concentrate on the parameters of the dart leader described above, we have a line charge of about 0.3 mC/m. The fields from this line source are simply calculated from equation (1).

$$E = \frac{\lambda}{2\pi\varepsilon_0 r}, \tag{1}$$

where λ is the charge per unit length and r is the radius to the observations point.

If we consider the charged region of the leader as a cylinder of charge whose outer radius is limited by a constant ion drift velocity then the fields are given by Equation (2) inside the channel and Eqn (1) outside,

$$E = \frac{\lambda r}{2\pi\varepsilon_0 R^2}, \tag{2}$$

where R is the outer radius of the cylinder and R is limited by the mobility of the ions or

$$R = \mu_i E t. \tag{3}$$

Eqns 2 and 3 form a transcendental equation for E that can be solved analytically to give

$$E \to \frac{\sqrt[3]{r\lambda}}{t^{2/3}\mu_i^{2/3}\sqrt[3]{2\pi\varepsilon_0}}. \tag{4}$$

If we apply the conditions of the dart leader to the model, we can find the distribution of the electric field in the system and that calculation is shown in Fig. 2.

A dart leader takes about 2 ms to develop allowing parts of the channel to expand over that time. Since much of the evolution is above the breakdown limit then the model is conservative in the predicting the spread of the channel. The channel radius is above 1 m so there is significant spreading of the charge. Equation 4 is our analytical model of the spreading.

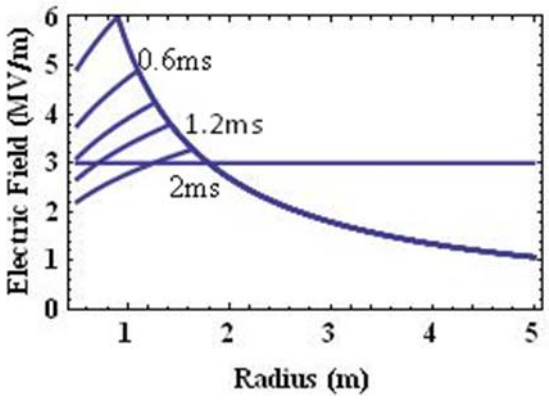


Fig. 2. Evolution of expanding channel.

4. NUMERICAL MODEL

Now, we add the motion of the ions directly to the calculation, but first we must determine the fields from the charges.

$$\nabla\bullet\vec{E} = \rho / \varepsilon_0 \tag{5}$$

where ρ is the total charge density. Equation (1) is a simple solution of (5), but (5) allows us to calculate the fields for more complex charge distributions. The equation of continuity allows the charge to update in response to the fields.

$$\nabla\bullet\vec{J} = -\frac{\partial\rho}{\partial t} \tag{6}$$

where

$$\vec{J} = \mu_i\rho\vec{E} = \mu_i n_i e\vec{E} \tag{7}$$

and ρ is the charge density, n_i is the ion number density and e is the electron charge. Equations (6) and (7) may be solved iteratively to calculate the relaxation of the charge column as function of time.

The charge density at a particular location changes as charge moves in and out of the region through equation (7) and there is a change due to the local air chemistry. In this work, we use the simple 3-species model common to EMP calculations [5]. The three charge densities that are important to this problem are: the electron density (N_e), positive ion density (N_-) and the positive ion density (N_+). The rate of production of these three species can be estimated by the three rate equations of equations (8).

$$\begin{aligned}
\frac{\partial N_e}{\partial t} &= g - k_1 N_e - k_2 N_e N_+, \\
\frac{\partial N_+}{\partial t} &= g - k_2 N_e - k_3 N_- N_+, \\
\frac{\partial N_-}{\partial t} &= k_1 N_e - k_3 N_- N_+.
\end{aligned} \tag{8}$$

In the region of field levels above 3 MV/m, avalanche, g, rapidly ionizes atoms and increases positive ion and electron densitie. The population of free electrons is reduced by attachment (k1) and dissociative recombination (k2) [3]. Attachment occurs on a 10^{-8}s time scale so is very quick compared to the other processes. Avalanche is a major source of electrons at high (> 3 MV/m) field strengths and occurs on an even faster time scale. Therefore, most of the charge carriers are singly charged ions of O2 and N2 molecules as assumed in the analytic model.

The ions move in a background plasma and so are slowed substantially to what is known as the drift velocity. The drift velocities of ions (μ_i) and of electrons (μ_e) are given by equation (2)

$$\mu_i = 2.5\times10^{-4},$$
$$\mu_e = 0.3\ \frac{\mathrm{m/s}}{\mathrm{V/m}}. \qquad (9)$$

Equations (9) show that the electrons move much faster in a given field than the ions. From that we can expect the electrons to quickly fill a channel out to about 3 MV/m and then attach quickly to molecules.

For the cylindrical case of the analytical model the fields relax as is shown in Fig. 3. For the same problem, the charge density relaxes as in Fig. 4. The initial charge column with one-meter radius is shown in red with subsequent relaxation shown, as well. While Figs. 2 and 3 only represent the constant drift velocity case, the 3-species air chemistry adds to little to this problem since the fields never exceed 3 MV/m and the equations become those shown. Other sets of initial conditions will be shown in the oral presentation.

5. RETURN STROKE INITIATION

The purpose of this calculation is to set up the initial conditions for use in a detailed calculation of the initiation. Originally the basis of the model was to be a nuclear lighting-like model [6] to get the high-frequency components of the return-stroke fields correct [7]. This model uses an outer boundary that specifies the current passing through the channel at the breakdown radius. The model tracks the various populations of charged species, the electric field, and heating. The propagation velocity of the tip is only 10^5 m/s, however, much lower than the observed velocity of the return stroke near the initiation point. The electromagnetic shock model of [8] provides some guidance for us in how to set up the propagation of the early return stroke and does give the correct velocity of propagation of near that of light. If we continue the thought process of the initiation model above with most of the net charge residing on ions, we can get to a physical model that also propagates near c. The ions will repel each other with the fields from the like charges. The bulk of the charge away from the center will also reside on ions that have limited mobility as described above. We treat the two regions separately even though they blend continuously.

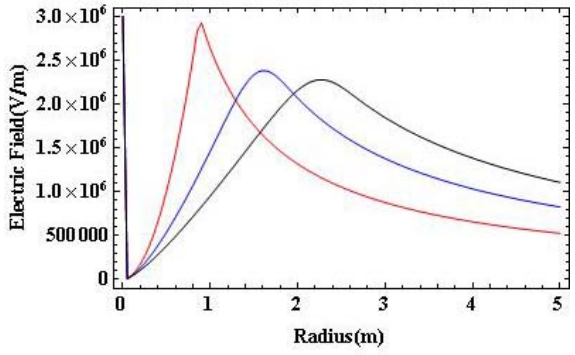


Fig. 3. Relaxation of the Electric Fields.

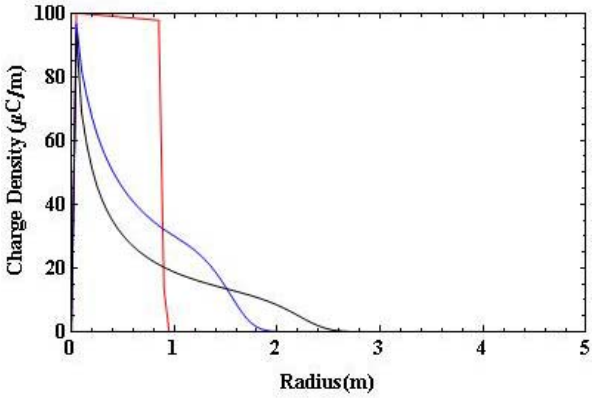


Fig. 4. Relaxation of the Charge Density.

When the leader channel reaches the upward propagating leader and communicates the ground potential to the high voltage of the channel the return stroke begins. When the first ion see the large field the ion will be stripped of its electron very quickly. Consider the first electron that sees the ground. That electron will begin moving toward the ground potential with the fields from the other ions and electrons pushing it away. That movement affects the other electrons through the charged species, thus beginning a wave up the center of the channel at a propagation speed near that of light. As the potential propagates up the channel it leaves a "lack of electrons" near the center of the channel raising the field levels near the center of the channel. As those field levels become near the breakdown levels ionization begins freeing more mobile electrons from the surrounding ions and feeding the channel with additional current from the surrounding cylindrical region collapsing in on the central channel current. This phenomenon approximates that of the electromagnetic shock of [8] but forms the basis of a model that will describe the currents as a function of position and time and can form a basis for the field calculation.

6. FIELDS

The fields from the currents above can be derived from a Green's function integration. In this case, we

will use a vertical electric dipole approximation of the fields. A more complex model [9] that includes the channel extent, horizontal fields and a simple ionosphere will be presented in the conference.

This field calculation begins with defining the Sommerfeld numerical distance, p, using the range r, the free space wave number k_0 and the ground and air impedances η_1 and η_0.

$$p = \frac{ik_0 r}{2}\left(\frac{\eta_1}{\eta_0}\right)^2. \qquad (10)$$

This definition allows the attenuation function $F(p)$ to be written

$$F(p) = 1 - i(\pi p)^{1/2} e^{-p} erfc(ip^{1/2}) \qquad (11)$$

And finally the vertical electric field is

$$E_z = \frac{i\omega\mu Ids}{2\pi\rho} e^{-ik\rho} F(p) \qquad (12)$$

where $\omega / 2\pi$ is the frequency and $I(\omega)ds$ is the dipole moment.

7. CONCLUSIONS

We have presented both analytical and numerical models for the relaxation of the charges in the channel left by the leader processes prior to the initiation of the return stoke. These calculations provide a set of initial conditions for a return stroke initiation model. Such a model must have a propagation velocity consistent with observation, that is, about that of light. Models that exclusively depend on the drift of charges in a plasma will not be adequate since they do not move at the high observed velocity. Finally, we have considered the broadband nature of the lightning fields at a distance.

REFERENCES

1. R. L. Gardner, “Leader derived initial conditions for a lightning return stroke”, Proceedings of the ICEAA, Turin, 2009.
2. R. L. Gardner, et al., “Comparison of published HEMP and natural lightning”, Lightning Electromagnetics, p. 504, Hemisphere, New York, 1990.
3. M. A. Uman, “The lightning discharge”, Academic Press, Orlando, 1987.
4. C. L. Longmire, et al., “Improvements in the treatment of Compton current and air conductivity in EMP problems”, NTIS AD-769-914, 1973.
5. K. S. H. Lee, ed., “EMP interaction: principles, techniques and reference data”, Hemisphere, Washington, 1986.
6. C. L. Longmire, et al., “A physical model of nuclear lightning”, Lightning Phenomenology Note 4, EMP Note Series, 1982.
7. R. L. Gardner, “Propagation along a cylindrical model of the lightning return stroke”, Proceedings of the ICEAA, Turin, 2007.
8. C. E. Baum and R. L. Gardner, “An introduction to leader tip modeling”, Lightning Electromagnetics, Hemisphere, New York, 1990.
9. R. L. Gardner, "Effect of the Propagation Path on Lightning Induced Transient Fields," *Radio Science, 16*, March-April 1981.

CELLULAR EFFECTS OF ULTRAWIDEBAND ULTRASHORT PULSED RADIATION AND MICROWAVE RADIATION EXPOSURE

Shckorbatov Y. G., Kolchigin N. N., Grabina V. A., Pasiuga V. N.

V.N. Karazin Kharkiv National University, Kharkiv, Ukraine
E-mail: Yury.G.Shckorbatov@univer.kharkov.ua

Abstract

The experimental data obtained since 2000 concerning cellular and molecular effects evoked in biological systems by exposure to ultrawideband ultrashort pulsed radiation and microwave radiation are discussed. The most significant cellular effects of electromagnetic fields exposure, such as: apoptosis, cell proliferation, genotoxic effects, and some underlining molecular processes are considered. Conclusion: the cell reaction to ultrawideband ultrashort pulsed radiation and microwave radiation is a multicomponent process that consists of specific and non-specific stress reactions and investigation of these reactions is essential in connection with the growing importance of electromagnetic factors as environmental components and their applications in medicine.

Keywords: Electromagnetic field, apoptosis, proliferation, genotoxic effect, micronuclei, DNA tbreaks, chromatin, heterochromatin, stress factors.

1. INTRODUCTION

The interest to the problems of reaction of biological systems – organisms and cells to electromagnetic radiation was growing in parallel with development of application of electromagnetic fields (EMF) in technique. At this time, in 1930-th appear works in which the biophysical mechanisms of biological action of EMF [1]. In the Kharkiv University the investigations of biological effects of microwaves began in 1970-th [2, 3]. Now the biological effects of ultrawideband an ultrashort pulsed radiation and microvawes are investigated at the Kharkov University at organism and cellular level [4-6]. In our other work presented at this symposium the recent data obtained on this theme at the Kharkiv University are analyzed in more details. In our opinion, the biological sense of molecular events that are induced by EMF in living organisms became clear at the level of living cell. The processes of apoptosis (programmed cell death), cell proliferation (cell propagation and cell populations renewal), and genotoxic effects (chromosome aberrations, micronuclei, DNA single strand and double strand brakes) are the biological 'outcome' of EMF exposure. The approach developed in Kharkiv National University is the study of chromatin microscopic structure (namely, euchromatin – heterochromatin transitions) in EMF-treated cells. The purpose of this work was to discuss some of the most significant, in our opinion, experimental data obtained since 2000 in the area of investigation of cellular biological effects of ultrawideband ultrashort pulsed radiation and microwave radiation.

2. CELLULAR EFFECTS OF ULTRAWIDEBAND ULTRASHORT PULSED RADIATION AND MICROWAVE RADIATION

2.1. APOPTOSIS

The problem of apoptosis and necrosis in cells exposed to microwaves and other EMFs in general attracts a considerable attention in relation with different medical problems such as cataract, and the role of microwaves in its induction, and the problems of anti-cancer therapy, where induction of apoptosis is a positive result. In dependence on cell type, wavelength, surface density of power, and regime of cell expose, the data obtained in different laboratories differ cardinally. The microwave-induced apoptosis is shown in the works of research group from the Zhejiang University (China). In the work [7] rabbits were exposed to microwave radiation (frequency of 2450 MHz) with a power density of 5 mW/cm^2 or 10 mW/cm^2. One eye of each rabbit was exposed to microwaves for 3 hours, while the contralateral eye served as a control, after exposure rabbits were slathered and the eye lens epithelial cells were obtained. To assess the degree of apoptosis cells were stained with standard method (annexin V + propidium iodie) and analyzed by the method of double staining flow cytometry. In a group of rabbits exposed to microwaves of

978-1-4244-7468-4/10/$26 ©2010 IEEE

5 mW/cm^2 power density the percentage of early apoptotic and necrotic cells significantly increased [7].

In the experimental research done in Lund University Hospital (Sweden) laboratory female Fischer 344 rats were exposed to microwaves (frequency 915 MHz) power densities of 0,24. 2,4, and 24 W/m^2, during 2 hours and slathered 50 days after microwave exposure. It was shown that in the brain of exposed animals occur damaged cells, named 'dark neurons', which were darkly stained with cresyl violet and often shrunken and characterized by loss of discernible internal cell structures. Authors do not exclude that the neuronal change described may represent apoptotic cell death [8].

Experiments in cultured neurons also indicate apoptosis induction under the influence of microwaves [9]. Rat primary neuronal cultures were exposed to a 900 MHz EMF with a specific absorption rate (SAR) of 2 W/kg for 24 h. Apoptosis was assessed by staining of nuclei with 4',6-diamino-2-phenylindole (DAPI) and fragmentation of DNA was assessed with TdT-mediated dUTP nick-end labeling (TUNEL) analyzed by flow cytometry. A statistically significant difference in the rate of apoptosis was found in the RF-field-exposed neurons. No increase in the caspase 3 activity was found, therefore the exposure of primary rat neurons to microwave fields may induce a caspase-independent pathway to apoptosis [9]. But at the less power density (0,25 W/kg) by the same research group in the same experimental model no apoptosis was observed [10].

In experiments of science group from Mitsubishi Chemical Safety Institute (Japan) [11] human glioblastoma A172 cells were exposed to 2.1425 GHz W-CDMA radiation at SARs of 80, 250, and 800 mW/kg, and continuous wave radiation at 80 mW/kg for 24 or 48 h. Human IMR-90 fibroblasts from fetal lungs were exposed to both modulated by code division multiple access (CDMA) and continuous wave (CW) radiation at a SAR of 80 mW/kg for 28 h. No significant differences in expression levels of phosphorylated p53 at serine 15 or total p53 were observed between the test groups and the negative controls Microarray hybridization and real-time RT-PCR analysis showed no noticeable differences in gene expression of the subsequent downstream targets of p53 signaling involved in apoptosis between the test groups and the negative controls. The Annexin V affinity assay revealed no significant differences in the percentage of apoptotic cells between the test groups of cells exposed to radio frequency (RF) signals and the sham-exposed negative controls. The data obtained confirm that exposure to low-level RF signals up to 800 mW/kg does not induce p53-dependent apoptosis, DNA damage, or other stress response in human cells [11].

EMF exposure at frequency 1.71 GHz (SAR value of 1.5 W/kg, exposure time 6 h) of mouse embryonic stem cells derived neural progenitor cells induced transiently affects the transcript level of genes related to apoptosis (bcl-2, bax), and cell cycle control (GADD45). However, these responses are not associated with detectable changes of cell physiology, no effects on mitochondrial function, nuclear apoptosis, cell proliferation, and chromosomal alterations were observed [12].

In the work [13] nonthermal effects of both a 900 MHz modulated into Global System for Mobile Communication (GSM) signal and a 900 MHz CW RF field at low SARs (70–76 mW/kg average) on human peripheral blood mononuclear cells (PBMCs) in vitro. The cycle phases, mitochondrial membrane potential, and susceptibility to apoptosis were found to be unaffected by the RF field. When cells were exposed to a CW RF field, no significant modifications were observed in comparison with sham-exposed cells.

Thus, as one can see, the question about possibility apoptosis induction by microwaves remains still unanswered but the existing experimental data indicating this possibility makes necessary further studies in this area which will determine the minimal power density of EMF that may induce apoptosis.

2.2. Cell Proliferation

The problem of the influence of EMF on cell proliferation may have medical applications in anti-cancer therapy and is connected with possible carcinogenic effect of EMF [14]. The experimental data are very different, and evidence about inhibition of proliferation and non-existence of such effect are numerous. As is done in the previous section, we begin with arguments 'pro'.

In the work [15] proliferation of cultured rabbit lens epithelial cells (RLEC) after the exposure to continuous microwave radiation at a frequency of 2,450 MHz and power densities of 0,10, 0,25, 0,50, 1,00, and 2,00 mW/cm2 for 8 h was studied. Cell morphologic changes were observed under a phase contrast microscope. Cell viability and the and cell cycle analysis were measured using flow cytometry. After exposure to 2.00 mW/cm^2 microwave radiation for 4, 6, and 8 h, the expression of cell cycle-regulatory proteins, P21WAF1 and P27Kip1, was examined using western blot analysis. The levels of P21WAF1 and P27Kip1 mRNA were analyzed by reverse transcription-polymerase chain reaction (RT-PCR). After 8 h of radiation treatment, cells treated with 0.50, 1.00, and 2.00 mW/cm^2 microwave radiation decreased cell viability, increased cell condensation and an inhibition of DNA synthesis. RLEC showed significant G0/G1 arrest. No obvious changes could be detected in the 0.10 and 0.25 mW/cm^2 microwave treatment groups. Protein expression of P27Kip1 was markedly increased after microwave radiation. However, the mRNA levels were unchanged. On the other hand, there were no detectable differences in P21WAF1 protein expression and mRNA levels between microwave treatment and control groups. These effects may account for the decline of lens epithelial proliferation after exposure to microwave radiation [15].

Microwave exposure may not only affect cell proliferation but can induce differentiation of cells. In the

work [16] is shown that millimeter range EMF treatment (wavelength range 7,5-10,0 mm) for 30 and 60 min at the power density of 4 mW/cm^2 successfully induced mesenchymal stem cells to differentiate as chondrocytes and the extent of differentiation increased with treatment duration.

However, in some works no microwave-induced stimulation of proliferation was registered. In the section 2.1 are cited works [12, 13] in which no EMF influence on cell proliferation was registered. In works [17, 18] the effects of microwave radiation on cell proliferation also was not detected. Exposure to a 1950 MHz RF field (exposure time 2 h, SAR was 1, 2, and 10 W/kg) has no effect on cell proliferation and expression of Hsp 27 and Hsp70, it may inhibit the phosphorylation of Hsp27 at Serine 78 in MO54 cells [17].

Exposure to electromagnetic fields with GSM frequency 900 MHz (SAR 1 W/kg and maximum duration 144 h) did not change viability/proliferation rate of the SN56 cholinergic cells or viability of cortical neurons [18].

Ultrawideband pulsed radiation effectively stimulate cell proliferation [19]. Electromagnetic ultrawideband pulses of 18 kV/m field intensity, 1 kHz repetition rate and 10 ns pulse width (exposure time of 0.25-3.0 h) had no effect on CL-S1 cell growth or viability during the subsequent 72-h culture period. However, exposure to similar nanopulses for prolonged periods of time (4-6 h) resulted in a significant increase in cell proliferation, as compared to untreated controls. Additional studies showed that nanopulse exposure enhanced CL-S1 cell growth when cells were maintained in media containing only epithelial growth factor (EGF) in concentration 10 ng/l, but had no effect on cells maintained in defined media that were mitogen-free or containing only insulin. Studies also showed that the growth-promoting effects of nanopulse exposure were associated with a relatively large increase in intracellular levels of phospho-MEK1 (active) and phospho-ERK1/2 (active) in these cells. These findings demonstrate that prolonged exposure to moderate levels of UWB enhanced EGF-dependent mitogenesis, and that this growth-promoting effect appears to be mediated by enhanced activation of the mitogen-activated protein kinase (MAPK) signalling pathway in pre-neoplastic CL-S1 mammary epithelial cells [19].

Summing up, the modern state of scientific literature does not enable to make clear decision about the action of microwave radiation on cell proliferation, whic may be connected with difference in applied experimental models, but probably, cell exposure to microwaves induces inhibition of proliferation. Exposure to ultrawideband ultrashort pulses, on the contrary, induces stimulation of cell proliferation.

2.3. Micronuclei, Comets, and Cell Nucleus Structure

The problem of ability of EMF to induce mutations disturbs scientists for many decades. [14]. Here are presented review of some relatively new data, appeared since 2000, obtained by the methods of micronuclei and comet assay. The micronuclei exist in cytoplasm in the period between cell divisions and are formed of the fragments of chromosomes and whole chromosomes, which are not able to participate in the normal mitosis. The number of micronuclei is a characteristics of mutation process. Comet assay chantries quantity of brakes in DNA molecules in one cell nucleus.

Adult male Wistar rats were exposed for 2h a day, 7 days a week for up to 30 days to continuous 2450MHz radiofrequency microwave radiation at a power density of 5-10mW/cm2. Sham-exposed rats were used as controls. Peripheral blood smears were examined for the extent of genotoxicity, as indicated by the presence of micronuclei in polychromatic erythrocytes (PCEs). The incidence of micronuclei/1000 PCEs in peripheral blood was significantly increased ($P<0.05$) in the subgroup exposed to microwave radiation after eight irradiation treatments of 2h each in comparison with the sham-exposed control group [20].

In the work [21] evaluated the induction of DNA and chromosomal damage in human blood leukocytes and lymphocytes, respectively. The signals were voice modulated 837 MHz produced by an analog signal generator or by a time division multiple access (TDMA) cellular telephone, 837 MHz generated by a code division multiple access (CDMA) cellular telephone (not voice modulated), and voice modulated 1909.8 MHz generated by a global system of mobile communication (GSM)-type personal communication systems (PCS) cellular telephone. DNA damage (strand breaks/alkali labile sites) was assessed in leukocytes using the alkaline (pH>13) single cell gel electrophoresis (SCG) assay. Chromosomal damage was evaluated in lymphocytes mitogenically stimulated to divide postexposure using the cytochalasin B-binucleate cell micronucleus assay. Cells were exposed at 37+/-1 degrees C, for 3 or 24 h at average specific absorption rates (SARs) of 1.0-10.0 W/kg. Exposure for either 3 or 24 h did not induce a significant increase in DNA damage in leukocytes, nor did exposure for 3 h induce a significant increase in micronucleated cells among lymphocytes. However, exposure to each of the four RF signal technologies for 24 h at an average SAR of 5.0 or 10.0 W/kg resulted in a significant and reproducible increase in the frequency of micronucleated lymphocytes. The magnitude of the response (approximately four fold) was independent of the technology, the presence or absence of voice modulation, and the frequency (837 vs. 1909.8 MHz). This research demonstrates that, under extended exposure conditions, RF signals at an average SAR of at least 5.0 W/kg are capable of inducing chromosomal damage in human lymphocytes [21].

In buccal epithelium cells of mobile phone users is reported a slight but statistically non significant increase of micronuclei number [22].

In the work [23] human blood cultures were exposed to a 1.9 GHz CW RF field for 2 h. Mean specific SARs of 0.0, 0.1, 0.26, 0.92, 2.4 and 10 W/kg were achieved, and the temperature within the cultures during a 2-h exposure was maintained at 37.00. No evidence of increased primary DNA damage was detected by any parameter for RF-field-exposed cultures at any SAR tested. The formation of micronuclei in the RF-field-exposed blood cell cultures was assessed using the cytokinesis-block micronucleus assay. There was no significant difference in the binucleated cell frequency, incidence of micronucleated binucleated cells, or total incidence of micronuclei between any of the RF-field-exposed cultures and the sham-exposed controls at any SAR tested [23].

No induction of micronuclei after microwave exposure was registered in the work [24]. DNA damage in human dermal fibroblasts from a healthy subject and from a subject affected by Turner's syndrome that were exposed for 24 h to RF radiation at 900 MHz. A signal similar to that emitted by GSM mobile phones was used at a specific absorption rate of 1 W/kg under strictly controlled conditions of temperature and dosimetry. To evaluate DNA damage after RF-radiation exposure, the alkaline comet assay and the cytokinesis-block micronucleus assay were used. The results revealed no genotoxic and cytotoxic effects from RF radiation alone in either cell line [24].

In numerous works is demonstrated the DNA brakes formation under the influence of microwaves. In [25] investigated DNA brakes induction in rat brain under the influence of low intensity microwaves (2.45 and 16.5 GHz, SAR 1.0 and 2.01 W/kg, respectively). Wistar rats (35 days old, male, six rats in each group) were selected for this study. These animals were exposed for 35 days at the above mentioned frequencies separately in two different exposure systems. After the exposure period, the rats were sacrificed and the whole brain tissue was dissected and used for study of single strand DNA breaks by micro gel electrophoresis (comet assay). Single strand DNA breaks were measured as tail length of comet. This study shows that the chronic exposure to these radiations cause statistically significant ($p < 0.001$) increase in DNA single strand breaks in brain cells of rat [25].

Cultured human diploid fibroblasts and cultured rat granulosa cells were exposed to intermittent and continuous RF EMF used in mobile phones, with different SAR and different mobile phone modulations [26]. DNA strand breaks were determined by means of the alkaline and neutral comet assay.RF-EMF exposure (1800 MHz; SAR 1.2 or 2 W/kg; different modulations; during 4, 16 and 24 h; intermittent 5 min on/10 min off or continuous wave) induced DNA single- and double-strand breaks. Effects occurred after 16 h exposure in both cell types and after different mobile-phone modulations. The intermittent exposure showed a stronger effect in the comet assay than continuous exposure. Authors conclude that the induced DNA damage cannot be based on thermal effects [26].

Human trophoblast HTR-8/SVneo cells were exposed for 4, 16 or 24h to 1,8 GHz CW and different GSM signals, namely GSM-217Hz and GSM-Talk (intermittent exposure: 5 min field on, 10 min field off) [27]. The alkaline comet assay was used to evaluate primary DNA damages and/or strand breaks due to uncompleted repair processes in HF-EMF exposed samples. The amplitude-modulated signals GSM-217Hz and GSM-Talk induced a significant increase in comet parameters in trophoblast cells after 16 and 24h of exposure, while the un-modulated CW was ineffective. However, alterations were rapidly recovered and the DNA integrity of HF-EMF exposed cells was similar to that of sham-exposed cells within 2h of recovery in the absence irradiation. The data suggest that HF-EMF with a carrier frequency and modulation scheme typical of the GSM signal may affect the DNA integrity [27].

In the works done in Kharkiv National University the changes induced in chromatin microscopic structure by microwave and ultrawideband ultrashort radiation are analyzed. In principlem reaction to both types uf EMF is the same – induction of transition euchromatin – heterochromatin, but the microwave radiation induces more pronounced effect than ultrawideband ultrashort radiation of thy same power density. In the work [4]. The effects of ultra wideband pulse radiation on human cells were investigated. The density of the flow of energy on the surface of irradiated object varied from 10-6 to 10-2 W/cm2 with exposure of 10 s. It was shown that heterochromatin granule quantity in cell nuclei increased under the influence of radiation from 10^{-4} to 10^{-2} W/cm^2. In some intervals, the effect increased with irradiation dose. At irradiation intensity 10^{-3} W/cm^{-2} the process of heterochromatin granule formation was fully reversible after 2 h of recovery; at intensity 10^{-2} W/cm^2 the reversion of irradiation effects was not full. The data obtained indicated the strong biological activity of ultrawideband ultrashort pulse radiation [4].

The biological effects of differently polarized microwave radiation on the chromatin state in human cells were estimated [5]. Isolated human buccal epithelium cells were irradiated by microwaves of frequency f.=35 GHz and surface power density 30 μW/cm^2. The state of chromatin in human cells was determined by methods of light and electron microscopy. The state of cell membranes was evaluated by the method of vital indigo carmine staining. The microwave-induced condensation of chromatin in human cells is revealed. Degree of microwave-induced condensation depends on the state of polarization of electromagnetic wave: In some cases left circularly polarized waves induce less effect than linearly polarized radiation. The linearly polarized electromagnetic waves induce cell membrane damage revealed by increase of cell staining. Thus, low-level microwave irradiation induces chromatin condensation in human cells and damages of cell membranes [5].

The data, presented in this section indicate that cell nucleus is deeply involved in the cell reaction to microwave and ultrawideband ultrashort pulsed radiation. Cell plasma membrane reactions to these factors are also of great significance.

3. CONCLUSION

Electromagnetic factors induce in cells stress reaction that consist of molecular, nuclear and membrane components. The general reactions to stress, such as oxidative stress [28], activation of heat-shock proteins [29] may play an important role in it. It was proposed that transcription of mRNA of heat-shock proteins and factors of transcription may be directly regulated by EMF [30]. In any case, the cytological components of reaction of living organism to electromagnetic factors that are considered in this paper have not only scientific interest, but may be used in diagnostics of degree of biological charge produced by EMF. The absence of uniformity in results obtained by different authors is very typical for such studies. In our opinion, it may be partly due to the differences in experimental objects and intensities of irradiation used in different laboratories.

REFERENCES

1. Rajewsky, B. 1938, 'The Biophysical Basis of Ultra-Short Wave Therapy', Radiology. **31** (6), 697-731.
2. Zalyubovskaya N.P., Chepel L.M., Shakhbazov V.G. 1970, 'Effect of millimeter, submillimeter wavelengths and the laser radiation on the development of *Drosophila melanogaster*'. *Vestn. Kharkov. Univ, Ser. biol. (Kharkov University Herald, Series Biology*. **39**(2), 42-4 (In Russian).
3. Zalyubovskaya N.P. 1973, 'The reaction of the living organisms to electromagnetic waves of millimeter range', *Uspekhy Fizicheskikh Nauk (Progress of the Physical Sciences)*. **110**(3), 462-4 (In Russian).
4. Shckorbatov Y.G., Pasiuga V.N., Kolchigin N.N., Batrakov D.O., Kazansky O.V., Kalashnkov V.V. 2009, 'Changes in the human nuclear chromatin induced by ultra wideband pulse irradiation'. *Cent. Europ. J. .Biol.* **4**(1), 97-106.
5. Shckorbatov Y.G., Pasiuga V.N., Kolchigin N.N., Grabina V.A., Batrakov D.O., Kalashnikov V.V., Ivanchenko D.D., Bykov V.N. 2009, 'The influence of differently polarized microwave radiation on chromatin in human cells'. *Int. J. Radiat. Biol.* **85** (4), 322-9.
6. Shckorbatov Y.G.,. Kolchigin N.N, Pasiuga V.N,, Kazansky O.V. 2008, 'Ultra short ultra wideband impulse irradiation effects on human cells'. *EUROEM Eropean Electromagnetics. Book of Abstracts, 21-25 July 2008 Swiss Federal Institute of Technology (EPFL), Lausanne, Switzerland* p. 123.
7. YE Juan, YAO Ke, LU Deqiang, WU Renyi, JIAN G Huai. 2001, 'Low power density microwave radiation induced early changes in rabbit lens epithelial cells'. *Chinese Medical Journal*, **114** (12), 1290-4.
8. Salford L.G., Brun A.E., Eberhardt J.L., Malmgren L., Persson B.R.R. 2003, 'Nerve Cell Damage in Mammalian Brain after Exposure to Microwaves from GSM Mobile Phones'. *Env. Health Persp.*, **111**(7), 881-3.
9. Joubert V., Bourthoumieu S., Leveque P., Yardin C. 2008, 'Apoptosis is induced by radiofrequency fields through the caspase-independent mitochondrial pathway in cortical neurons' Radiat Res. 69(1), 38-45.
10. Joubert V., Leveque P., Cueille M., Bourthoumieu S., Yardin C. 2007. 'No apoptosis is induced in rat cortical neurons exposed to GSM phone fields'. *Bioelectromagnetics*. **28**(2), 115-21.
11. Hirose H., Sakuma N., Kaji N., Suhara T., Sekijima M., Nojima T., Miyakoshi J. 2006, 'Phosphorylation and gene expression of p53 are not affected in human cells exposed to 2.1425 GHz band CW or W-CDMA modulated radiation allocated to mobile radio base stations'. *Bioelectromagnetics.* **27**(6), 494-504.
12. Nikolova T., Czyz J., Rolletschek A., Blyszczuk P., Fuchs J., Jovtchev G., Schuderer J., Kuster N., Wobus A. M. 2005, 'Electromagnetic fields affect transcript levels of apoptosisrelated genes in embryonic stem cell-derived neural progenitor cells'. *FASEB J.* **19**, 1686-8.
13. Capri M., Scarcella E., Fumelli C., Bianchi E., Salvioli S., Mesirca P., Agostini C., Antolini A., Schiavoni A., Castellani G., Bersanib F., Franceschia C. 2004, 'In vitro exposure of human lymphocytes to 900 MHz CW and GSM modulated radiofrequency: Studies of proliferation, apoptosis and mitochondrial membrane potential'.*Radiat. Res*. **162**, 211–8.
14. Lacy-Hulbert A, Metcalfe J. C. Hesketh R. 1998 'Biological responses to electromagnetic fields'. *The FASEB Journal*. **12**, 395-420.
15. Ke Yao, Kai Jun Wang, Zhao Hui Sun, Jian Tan, Wen Xu, Li Jun Zhu, De Qiang Lu. 2004 , 'Low power microwave radiation inhibits the proliferation of rabbit lens epithelial cells by upregulating P27Kip1 expression'. *Molecular Vision.* **10**, 138-43.
16. Guang-Wen Wu, Xian-Xiang Liu, Ming-Xia Wu, Jin-Yan Zhao, Wen-Lie Chen, Ru-Hui Lin, Jiu-Mao Lin. 2009, 'Experimental study of millimeter wave-induced differentiation of bone marrow mesenchymal stem cells into chondrocytes'. *Int. Journ. Mol. Med*. **23**, 461-7.
17. Miyakoshi, K.Takemasa Y., Takashima G.-R., Ding H., Hirose H., Koyama S. 2005, 'Effects of Exposure to a 1950 MHz Radio Frequency Field on Expression of Hsp70 and Hsp27 in Human Glioma Cells'. *Bioelectromagnetics.* **26**, 251-7.
18. Del Vecchio G, Giuliani A, Fernandez M, Mesirca P, Bersani F, Pinto R, Ardoino L, Lovisolo GA, Giardino L, Calzà L. 2009, 'Effect of radiofrequency electromagnetic field exposure on in vitro

models of neurodegenerative disease'. *Bioelectromagnetics*. **30**(7), 564-72.
19. Sylvester P.W., Shah S.J., Haynie D.T., Briski K.P. 2005, 'Effects of ultra-wideband electromagnetic pulses on pre-neoplastic mammary epithelial cell proliferation'. *Cell Prolif*. **38**(3), 153-63.
20. Trosic I., Busljeta I., Kasuba V., Rozgaj R. 2002, 'Micronucleus induction after whole-body microwave irradiation of rats'. *Mutat. Res.* **521**(1-2),73-9,
21. Tice R.R., Hook G.G., Donner M., McRee D.I., Guy A.W. 2002, 'Genotoxicity of radiofrequency signals. I. Investigation of DNA damage and micronuclei induction in cultured human blood cells'. *Bioelectromagnetics*. **23**(2), 113-26.
22. Yadav A.S., Sharma M.K. 'Increased frequency of micronucleated exfoliated cells among humans exposed in vivo to mobile telephone radiations'. *Mutat. Res.* **650**(2), 175-80.
23. McNamee J.P., Bellier P.V., Gajda G.B., Miller S.M., Lemay E.P., Lavallee B.F., Marro L/, Thansandote A. 2002, 'DNA Damage and Micronucleus Induction in Human Leukocytes after Acute In Vitro Exposure to a 1.9 GHz CW RF'. *Radiat. Res.* **158**(4):523-533,
24. Sannin A., Di Costanz G., Bresci F., Sarti M., Zeni O., Juutilainen J., Scarfì M. R. 2009, 'Human fibroblasts and 900 MHz radiofrequency radiation: evaluation of DNA damage after exposure and Co-exposure to 3-Chloro-4-(dichloromethyl)-5-Hydroxy-2(5h)-furanone (MX)'. *Radiation Research*. **171**(6),743-751.
25. Paulraj R., Behari J. 2006, 'Single strand DNA breaks in rat brain cells exposed to microwave radiation'. *Mutat. Res.* **596**, 76–80.
26. Diema E., Schwarz C., Adlkofer F., Jahn O., Rudiger H. 2005, Non-thermal DNA breakage by mobile-phone radiation (1800 MHz) in human fibroblasts and in transformed GFSH-R17 rat granulosa cells in vitro'. *Mutat. Res*. **583**, 178–183.
27. Franzellitti S, Valbonesi P, Ciancaglini N, Biondi C, Contin A, Bersani F, Fabbri E. 'Transient DNA damage induced by high-frequency electromagnetic fields (GSM 1.8GHz) in the human trophoblast HTR-8/SVneo cell line evaluated with the alkaline comet assay'. *Mutat. Res.* **683**(1-2), 35-42.
28. Desai N.R., Kesari K.K., Agarwal A. 2009, 'Pathophysiology of cell phone radiation: oxidative stress and carcinogenesis with focus on male reproductive system'. *Reproduct. Biol. Endocrinol*. **7**:114 doi:10.1186/1477-7827-7-114.
29. Sun Lixia, Yao Kea, Wang Kaijun, Lu Deqiang, Hu Huajun, Gao Xiangwei, Wang Baohong, Zheng Wei, Lou Jianling, Wu Wei. 2006, 'Effects of 1.8 GHz radiofrequency field on DNA damage and expression of heat shock protein 70 in human lens epithelial cells'. *Mutat. Res*. **602**, 135–142.
30. Lin H., Blank M., Rossol-Haseroth K., Goodman R. 2001, 'Regulating genes with electromagnetic response elements'. *Jour. Cell. Biochem*. **81**,143-8.

RADIATION AND RECEPTION OF THE SHORT SIGNALS BY THE LONG ANTENNAS

Immoreev I. Ya.

Moscow Aviation Institute, Moscow, Russia
E-mail: immoreev@aha.ru

Abstract

Features of formation of an antenna pattern and change of the signal's form are considered for cases when spatial duration of a signal becomes commensurable or less than physical sizes of the radiating or/and reception antennas. Results are received by modeling in MathCAD.

Keywords: UWB signal, antenna pattern, short signal, long antenna, reciprocity principle, matched.

1. INTRODUCTION

When spatial duration of a signal $c\tau$ (c – speed of light) becomes less than linear size L of the antenna, new important property arises in system: *the form of a signal essentially changes during his radiation and reception*. Change of the signal's form leads to change of the antenna patterns' structure, which is not peculiar to classical narrow-band antennas. Features of formation of antenna patterns on radiation and reception in those cases are considered below, when there are conditions: $c\tau < L$ or $c\tau << L$. The signals satisfying these conditions, further in the text refer to the simply short signals.

2. RADIATION OF SHORT SIGNALS

We use known a method which allows to divide the antenna into elementary radiators - dipoles Hertza which have the sizes allowing to assume uniform distribution of a current on length. Then the field of the radiating antenna can be received as the sum of fields which are radiated by these dipoles.

For use of this method it is necessary to define dependence of a field of the Hertz's dipole $E(\theta,t)$ from the law of a stimulating current's changes $i(t)$. In the majority of references this dependence is defined for the harmonious law of the current's change. To find parameters of a field at $c\tau << L$, it is necessary to define dependence of this field when a stimulating current has any change in time. Such dependence is described by expression:

$$E\left(\theta,t\right)=\frac{Z_0\sin\theta}{4\pi cr}\cdot\frac{d}{dt}\left[i\left(t-\frac{r}{c}\right)\right]\Delta L\,. \qquad (1)$$

Here: Z_0 – wave resistance of free space; θ – a corner between an axis of a dipole and a direction on a point of supervision; ΔL - length of a dipole; r - distance up to a point of supervision.

We use expression (1) and shall consider a field of the simple antenna as a linear radiator with length L which is actuated from one end by a pulse source of a current (Fig. 1).

We shall divide this antenna into elementary radiators in length ΔL. At figure are indicated: ΔL_j - j-th an elementary radiator; L_j - his coordinate. The pulse of a current $i(t)$ arises in a point O, is distributed along the antenna and consistently raises elementary radiators.

At occurrence of a pulse of a current in a point 0 there will be an excitation of the first elementary radiator and in a far zone there will be a field:

$$E_1(t,\theta)=\frac{Z_0\sin\theta}{4\pi cr}\cdot\frac{d}{dt}\left[i\left(t-\frac{L_1}{c_0}-\frac{r-L_1\cos\theta}{c}\right)\right]\cdot\Delta L_1$$

The same fields will arise at excitation of the following elementary radiators. The sum of fields of all radiators looks like:

$$E_\Sigma(t,\theta)=\frac{Z_0\sin\theta}{4\pi cr}\sum_{j=1}^{N}\frac{d}{dt}\left[i\left(t-\frac{L_j}{c}-\frac{r-L_j\cos\theta}{c}\right)\right]\cdot\Delta L_j$$

After all transformations this field looks like:

$$E_\Sigma(t,\theta)=\frac{Z_0\sin\theta}{4\pi r}\times$$
$$\times\frac{1}{\cos\Theta-1}\left[i\left(t-\frac{L}{c}-\frac{r-L\cos\Theta}{c}\right)-i\left(t-\frac{r}{c}\right)\right].$$

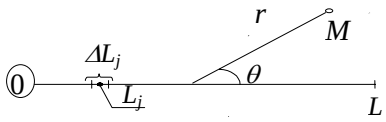


Fig. 1.

978-1-4244-7468-4/10/$26 ©2010 IEEE

This field of a radiator will consist of two parts, positive and negative, each of which repeats of the stimulating current's form. One part of this field is formed at the moment when a pulse of a current enter to a radiator, and another − at the moment when this pulse achieve by the end of a radiator. This process can be presented also, as radiation from a point of excitation and from the end of the antenna.

The form of a total field depends on a relationship between length of antenna L and duration of a pulse $c\tau$. At $L >> c\tau$ time of a delay of a signal considerably exceeds duration of a pulse. In result between two parts of a field the interval is formed, and the field will divide on two parts. On Fig. 2 the example of a total field of the radiator observable under a corner $\theta = 60°$, at $L = 10c\tau$ is resulted.

The received formulas allow to construct antenna patterns for electromagnetic field for the considered radiators. On Fig. 3 we see the antenna pattern for field for an example shown on Fig. 2. When $L >> c\tau$ the dependence of this field antenna pattern from time t is appear**.** Antenna pattern changes the form and position in space while the pulse of a current runs along a radiator (on Fig. 3 the antenna pattern by field is shown at the moments of time t_1, t_2, t_3 …).

Time-varying of the antenna pattern for field does its unsuitable for calculation of parameters of radiosystems as does not allow defining such parameters of the antenna as factor of the directed action, width of a beam, etc. Convenient for practical use is antenna pattern for energy $W(\theta)$ which finds as averaged power, radiated in each angular direction, while the pulse of a current runs along a radiator. $W(\theta)$ describes distribution of energy-flux density in space depending on a angle Θ:

$$W_T(\theta) = \frac{1}{Z_0}\int_{-\infty}^{+\infty} E_\Sigma^2(\theta, t)\, dt\,.$$

On Fig. 4 normalized power antenna patterns for various values of attitude $L / c\tau$ are showed. When $c\tau >> L$ antenna patterns for energy coincides with antenna patterns of the half-wave vibrator for field. When attitude $L / c\tau$ is increasing, the maximum of the antenna patterns for energy deviates from the normal and when $c\tau << L$ radiation of the antenna occurs along the aperture. At that the maximal value of the antenna patterns for energy grows, and its width is decreasing.

3. Reception of Short Signals

Let's consider antenna pattern for reception when $c\tau << L$. Fig. 2 shows the pulse's form of the field falling on the reception antenna, which will vary depending on a angle under which it is located concerning the transmitting antenna. In result the form of a pulse of the current caused by this field in the reception antenna, and the form of a voltage's pulse in its loading, caused by this current, will depend on an arrangement of antennas. Consequently antenna pattern of the reception antenna will depend on a mutual positioning of antennas.

On Fig. 5 the arrangement of the transmitting and reception antennas representing symmetric vibrators in length L_T and L_R is shown. The reception antenna is on distance r from the transmitting antenna in its distant

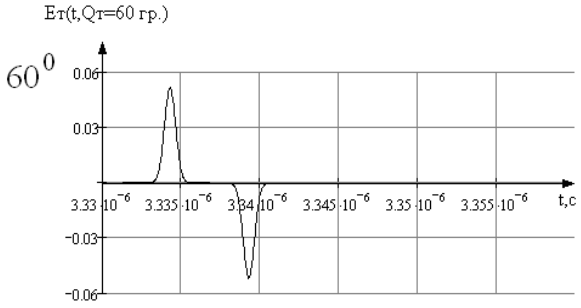


Fig. 2.

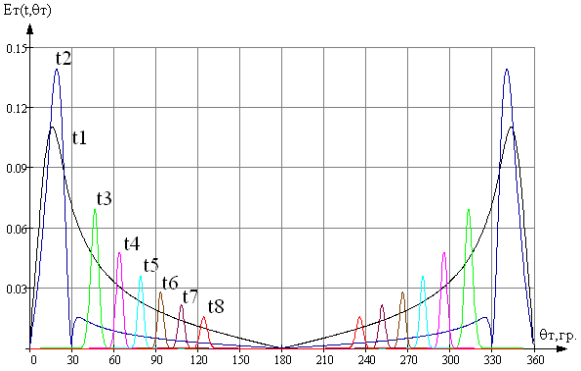


Fig. 3.

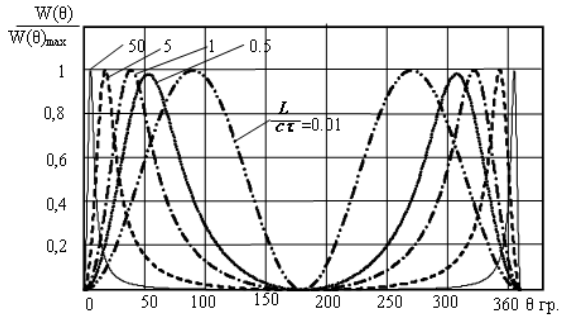


Fig. 4.

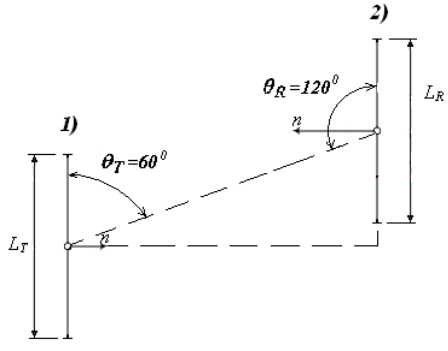


Fig. 5.

zone. Loading and the ends of vibrators are coordinated in a strip of frequencies of a signal and do not reflect energy. On Fig. 6 the example of the form of a pulse of a voltage in loading of the reception antenna $U(t,\theta)$, when angle $\theta_R = 60^\circ$ is shown.

On Fig. 6 is visible, that the voltage at loading of the reception antenna is the sum of two pulses, each of which repeats the form of the falling field's pulse. Change of the form of a pulse of a voltage at loading of the reception antenna at change of a angle of falling on it of a pulse of a field occurs as well as change of the form of a pulse of a field of the radiating antenna at change of a angle of observation. Therefore for the reception antenna it is necessary to use antenna pattern for energy which finds as averaged power accepted from each angular direction, while the pulse of a field runs along the aperture of the antenna. Antenna pattern for energy describes distribution of energy-flux density in space accepted by the antenna depending on a angle Θ:

$$W_R(\theta) = \frac{1}{Z_R}\int_{-\infty}^{+\infty} U_\Sigma^2(t,\theta)\,dt\,.$$

On Fig. 7 are shown normalized antenna pattern for energy at various values of a angle θ_T between the aperture of the transmitting antenna and its direction to the reception antenna. From Fig. 7 essential dependence of the form of reception antenna pattern for energy from a direction to transmitting antenna is visible.

4. Principle of Reciprocity and Reception Antenna Pattern

As indicated above, voltage $UH(\theta)$ depends not only on delays of a signal in antennas L_T and L_R, but also from a mutual positioning of these antennas, i.e. from angles θ_T and θ_R. It means, forms of the currents, which arise in radiation antennas and reception antennas, will be generally various. Hence, will have the different form and antenna pattern on radiation and reception.

On fig. 8, as an example, give two antenna patterns for energy: for transmitting $W_T(\theta)$ and for reception $W_R(\theta)$ when $L_T = L_R = 10c\tau$. On Fig. 8,a are shown antenna patterns when the antenna #1 radiates a short signal at a angle of observation $\theta_T = 60^\circ$, and the antenna #2 accepts this signal at the angle of observation $\theta_R = 120^\circ$. Antenna pattern on Fig. 8,b are shown for a case when the antenna #2 radiates a short signal at the angle of observation $\theta_T = 120^\circ$, and the antenna #1 accepts this signal at the angle of observation $\theta_R = 60^\circ$. We see, that according to a principle of reciprocity, in the same mode the form of the antenna pattern remains constant, irrespective of number and an placement of the antenna. At the same time antenna patterns essentially differ at transition of the antenna from one mode in another. It is feature of radiation and reception of the short UWB signals: When $c\tau << L$, antenna pattern in the mode of reception differs from antenna pattern in the mode of radiation as it is accepted in the classical theory of the antennas for narrow-band signals when $c\tau >> L$.

5. Radiation and Reception of Short Signals with Complex Structure

Above we considered radiation and reception by long antennas of simple short signals. In a some of practical cases there is a necessity of radiation and reception of short signals which have complex modulation inside a pulse, for example, linear frequency modulation or phase-code modulation. This condition can arise in practice:

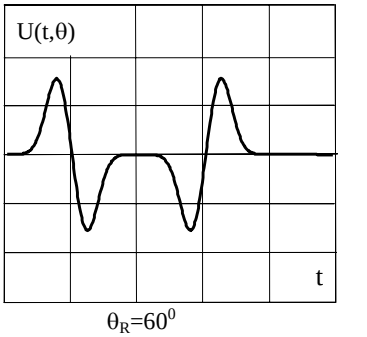


Fig. 6.

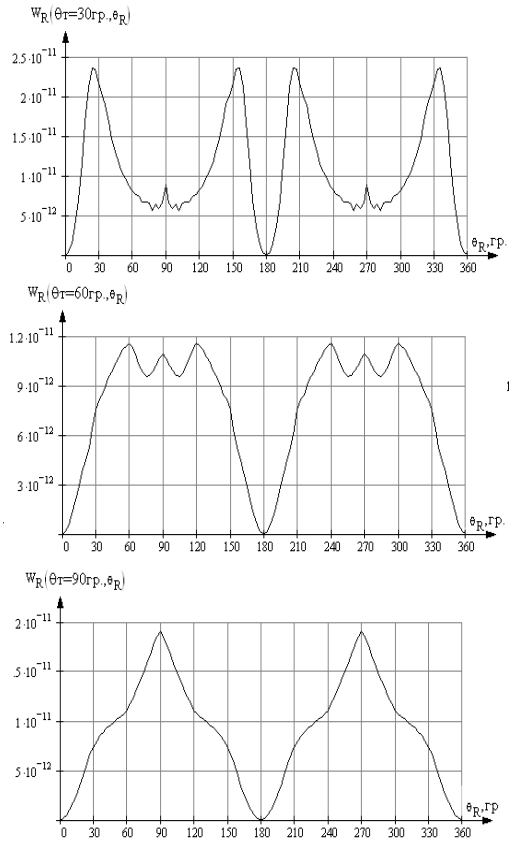


Fig. 7.

- in radars for recognition such as the target; such radars should have high resolution on range and on angular coordinates;
- in systems of a communication for silent transfers of the information into a range of frequencies and into space; such systems of a radio communication should work by short signals by narrow beams of the antenna.

Processing of complex signals is made in the matched filter on an output of the reception antenna. However the structure of such signals can be destroyed in time of radiation, that does not allow to execute their coordinated processing.

On Fig. 9 a field in a far zone is shown when the long antenna ($L_R = L_T = 10c\tau$) radiated a pulse with linear frequency modulation, duration $\tau = 11$ ns and factor of compression $B = 11$:

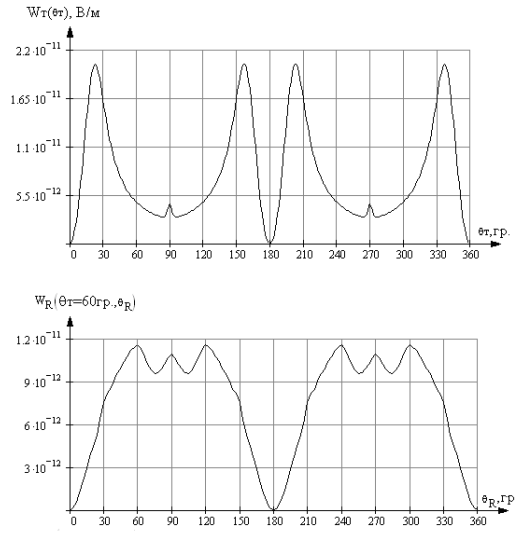


Fig. 8. a.

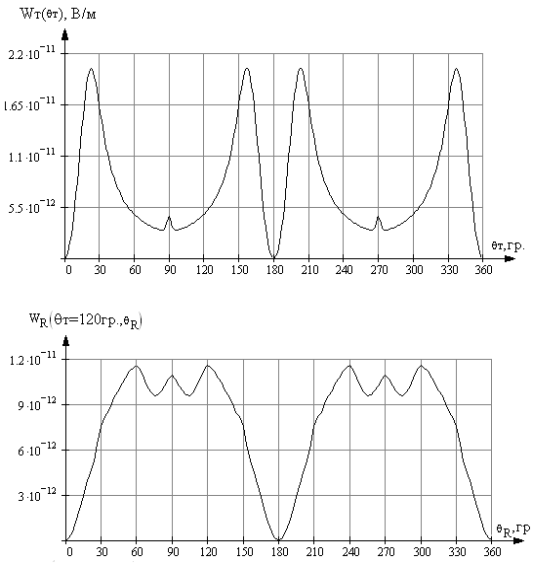


Fig. 8. b.

$$i(t) = \sin\left(2\pi f_0 t + \frac{\pi B t^2}{\tau^2}\right),$$

On Fig. 10 this signal on an output of the matched filter is shown at traditional processing. On a Fig. 11 the same signal on an output of the matched filter is shown after reception of the field shown in a Fig. 9 .

We see that the signal has completely "destruction".

The reason of a signal's change is the delay of a current's pulse in the transmitting antenna for a interval of the time, necessary for its run along the antenna $\Delta t = L / c$.

$$E_{\Sigma}(t,\theta) = \frac{Z_0 \sin\theta}{4\pi r} \cdot \frac{1}{\cos\Theta - 1} \times$$
$$\times \left[i\left(t - \frac{L}{c} - \frac{r - L\cos\Theta}{c}\right) - i\left(t - \frac{r}{c}\right) \right].$$

If to remove member L / c from the formula for a field $E_{\Sigma}(t,\theta)$, we shall receive on an output of the matched filter the signal similar to a Fig. 10. In that case the antenna patterns of the transmitting and reception antennas become identical.

6. CONCLUSION

When the signal has the spatial extension much less, than the length of the antenna:

- the form of the directivity diagram of antenna for

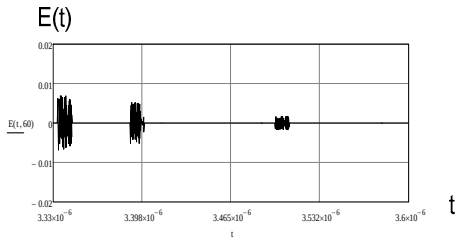


Fig. 9.

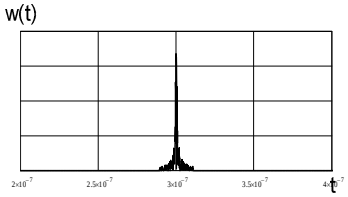


Fig. 10.

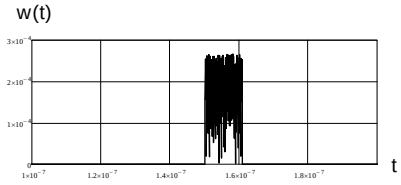


Fig. 11.

radiation does not coincide with the form of the directivity diagram of this antenna for reception;

- the form of a signal at loading of the reception antenna does not coincide with the form of a signal on an input of the transmitting antenna.

REFERENCES

1. Immoreev I. Ya. Ultrawideband Radars: Features and Capabilities. Journal of Communications Technology and Electronics, 2009, Vol. 54, No. 1, pp. 1–26.
2. Immoreev I. Ya., Siniavin A.N. Radiation of ultrawideband signals. The Annual «Antennas». 2001. Issue. 1.
3. Goldstein L.D. and Zernov N.V., Electromagnetic fields and waves. Soviet radio, 1971.
4. Zaiping N.: Radiation characteristics of travelling-wave antennas excited by nonsinusoidal currents. IEEE Electromagnetic Compatibility Transaction on… EMC-25, №1, 1983.
5. Smith G. S.: On the interpretation for radiation from simple current distribution. IEEE Antennas and Propagation Magazine. Vol. 40, No. 3, June 1998.
6. Zaizev A.V. Research of electromagnetic fields in time area. The Annual «Antennas». 2001, №6.
7. Baum C.E. Time domain Characterization of Antennas with TEM feeds. October 1998
8. Baum C.E. Transient Gain of Antennas Related to the Traditional Continuos Wave (CW). Definition of Gain Sensor and Simulation Notes. July 1997.
9. Lisitsyn V.P., Perunova V.S. Calculation of non-stationary radiation of dipole antennas with the help of the integrated equation in time domane. // Journal of Communications Technology and Electronics, 1985, V. 30, N 1, pp. 72-75.

IMPROVEMENT OF CHARACTERISTICS OF UWB DOUBLE RIDGED HORN ANTENNAS

Dubrovka F. F. and Sushko A. Ju.

National Technical University of Ukraine "Kyiv Polytechnic Institute",
Kyiv, Ukraine
E-mail: fedor.dubrovka@gmail.com, eyler@ua.fm

Abstract

Results of numerical optimization of electrical characteristics and geometry of ultra wideband double ridged horn antennas are presented. End-fire radiation patterns with side lobe level less than −10 dB and VSWR<2.0 over the frequency range 1−20 GHz at the compact prototype of the optimized antenna manufactured have been obtained.

Keywords: Double ridged horn antenna, ultra wideband antenna, ultra wideband horn antenna feeding.

1. INTRODUCTION

Ordinary horn antennas are widely used for transmission and reception of microwave signals due to simple design, high effectiveness and simple feeding. Measuring antennas and feeds for reflector antennas are two main applications of these horn antennas. Limited operating frequency range is the main drawback of them. That is why the antennas cannot be used in wideband (UWB) radio systems with required frequency bandwidths 2:1 and more.

For such applications a ridged horn antenna (RHA) was proposed by J. K. Shimizu [1] in 1961. But only in 2003 RHA was accurately analyzed numerically (including coaxial feeding) by C. Bruns [2] using full-wave method of moments. Operating frequency range of the RHA presented was 1 – 18 GHz. The author [2] pointed out the main drawback of this type of antennas, namely distortion of radiation pattern at frequencies higher than 12 GHz. In the mentioned frequency range radiation pattern has very high side lobes in diagonal planes and even exceed end-fire radiation. The same degradation of directional characteristic was observed in 4 prototypes of RHA of different manufactures [2]. New construction of RHA without side walls was presented by V. Rodriges [3]. But gain reduction and VSWR > 2.0 still take place for this modification. A modified RHA with dielectric material between ridges and absorbing structure in the feeding section has been introduced by A. Teggatz [4] for GPR applications. But at lower frequencies return loss increases up to –5 dB and at frequencies higher than 12 GHz radiation pattern is strongly distorted. Detailed investigation of radiation pattern degradation was described by D. Baumann [5]. Method FVTD and measurements in anechoic chamber was used to analyze the problem mentioned.

Analyzing electromagnetic characteristics of world famous manufacturers of UWB RHA (Rohde&Schwarz, Q-par Angus, Sunol Sciences, A. H. Systems, ETS Lindgren etc.) we find out that almost all antennas have some drawbacks. Mainly, antennas have gain drop in end-fire direction at higher frequencies (this also means high side lobe level and degradation of radiation pattern) and VSWR<2.0 not in the entire operating frequency range.

Thus, it is challenging problem to develop simple and compact UWB RHA that provides VSWR<2.0, end-fire radiation patterns, side lobe level < –10 dB in the frequency range 1 – 20 GHz.

2. PROPOSED MODIFICATIONS

Antenna characteristics calculation and its optimization were carried out using CST Microwave studio software, based on FDTD method. With the help of mentioned software it is possible to model the antenna structure together with coaxial feeding in detail.

Ridges (Fig. 1) are used to increase operating frequency range of the common HA construction. In our construction we choose ridge with exponential profile to match the impedance of coaxial feeding and free space. Ultra wide band operation is achieved due to special transition from the coaxial line to the ridged waveguide. Exactly this unit together with cavity back and position of ridges define bandwidth of antenna matching to coaxial feeding line. Computational analysis and practice show that appropriate construction of this transition can provide required return loss in the frequency range 20:1.

For the common design of RHA (Fig. 1) with solid side walls radiation pattern begins to split, so that end-fire maximum cannot be observed at frequencies higher 12 GHz. Such radiation pattern is qualified as lobed pattern and it is fundamentally not suitable for environment monitoring systems.

978-1-4244-7468-4/10/$26 ©2010 IEEE

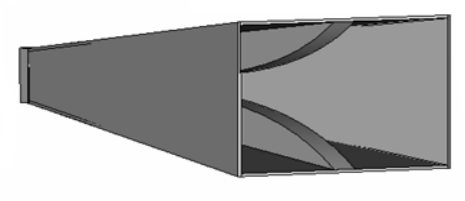


Fig. 1. Ridged horn antenna.

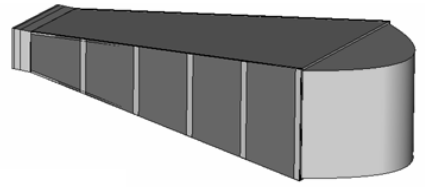


Fig. 2. Modified UWB RHA.

Next modifications are proposed to obtain one main beam and low side lobe level:

1. Solid side walls are replaced by dielectric walls with special 5 mm wide metallic strips (Fig. 2). These strips maintain currents and support the propagation of main H-wave. Dielectric side walls serve for construction capsulation and decreasing of the side lobe level in H-plane;
2. Dielectric lenses in E- and H-plane are used. They focus the radiation along the horn axis. Also lenses have definite matching function;
3. Antenna dimensions are reduced. It allows to improve radiation pattern in the higher end of the frequency range but with negligible reducing of gain in lower end. Also due to this modification we obtain lower side lobe level and smooth frequency dependence of gain.

Generally high antenna gain is achieved due to two factors: utilizing of lenses and increasing of the horn length to the optimal value.

Frequency dependence of the antenna gain is GHz. Additional gain, obtained using lenses, increases from 1 to 4,5 dB in the operating frequency range.

3. Optimization Results

Geometry optimization of the modified RHA for obtaining necessary electromagnetic characteristic is performed by varying the slot width between ridges, sizes and shape of cavity back and horn length.

It is established that width of the slot between ridges is an influential parameter for antenna return loss. The impedance around 50 Ohm in the feeding point for entire frequency range can be achieved by varying this parameter. Frequency dependence of VSWR for different slot width *d* is introduced on Fig. 3. The best values of VSWR is achieved for slot width 1,5 mm. For this value VSWR <2.0 in the frequency range 1 – 20 GHz.

The shape of the cavity back is chosen to provide simple construction, lower VSWR and the best influence on radiation patterns in the entire bandwidth. Simple flat plate turned out to be optimal for this application. This plate is situated on the optimized distance from feeding point that provide the best matching of the antenna.

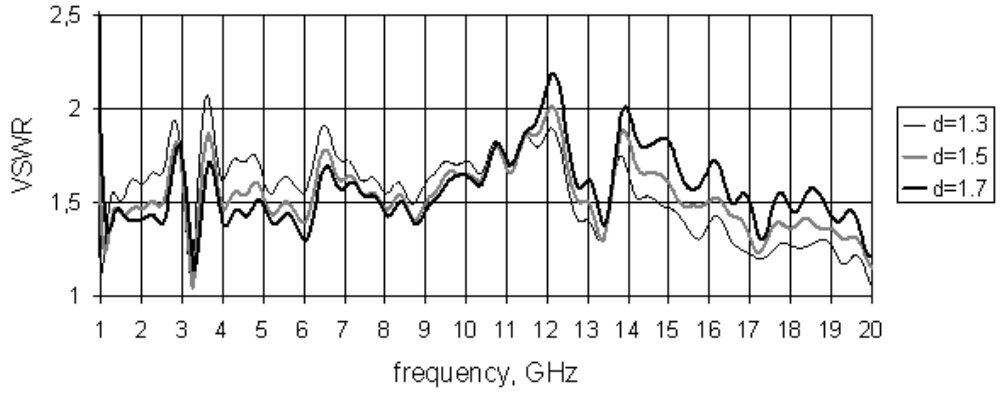


Fig. 3. Frequency dependence of VSWR for different slot width.

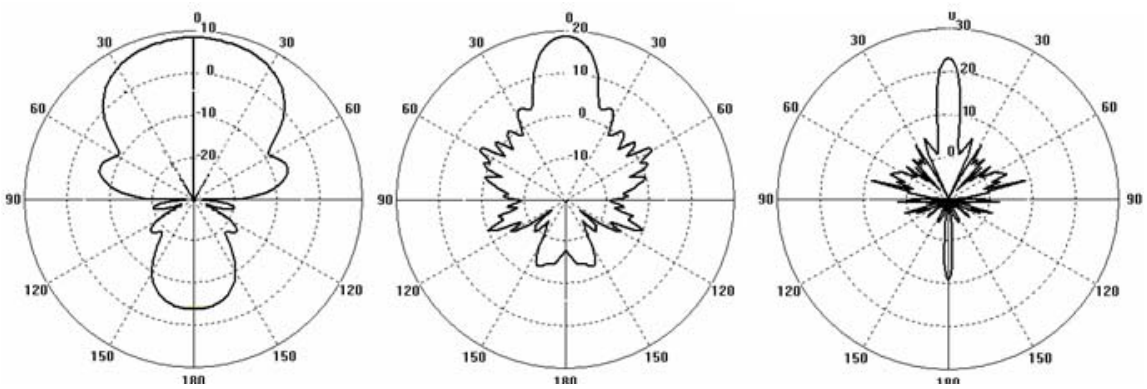


Fig. 4. Typical radiation patterns of UWB RHA for 2, 10 and 20 GHz.

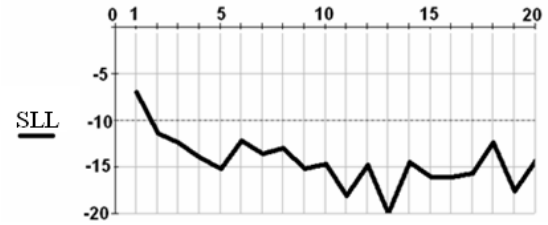


Fig. 5. Frequency dependence of SLL smooth enough in the entire frequency range 1 – 20.

It's obvious that maximum axis gain of RHA is reached during increasing of RHA length to definite optimal value. For optimal horn lens (around 250 mm) gain smoothly increases from 0 to 24 dB in the frequency range 1 – 20 GHz.

Radiation patterns of the optimized RHA for frequencies 2, 10 and 20 GHz are presented on Fig. 4. We can observe single end-fire main beam. Frequency dependence of the side lobe level maximum value is illustrated on Fig. 5 (maximum level is chosen in E-, H- and diagonal planes). Typical value of side lobe level does not exceed –15 dB.

4. Experimental Results

Real prototype of the modified and optimized UWB RHA was manufactured. Experimental and computed VSWR is presented on Fig. 6. Generally both experimental and calculated VSWR is less than 2.0. It can be seen that there is very good agreement between theoretical and measured results. These results prove the adequacy of proposed model, and also reality of the other obtained results.

5. Conclusions

The UWB RHA manufactured prototype meets all the specifications desired. In the frequency range 1 – 20 GHz side lobe level and gain of the proposed antenna are better than the state-of-the-art world analogues. Thus, the antenna developed can be recommended for manufacturing and application in antenna measuring systems, UWB radio system for environment monitoring and for other purposes, where frequency range up to 20:1 and end-fire radiation pattern with low side lobe level is required.

References

1. Shimizu J. K. Octave-Bandwidth Feed Horn for Paraboloid // *IRE Trans. Antennas and Propagation*. – 1961. – Vol. AP-9. – №2. – pp. 223-224.
2. Christian Bruns. Analysis and Simulation of a 1-18 GHz Broadband Double-Ridged Horn Antenna // *IEEE Trans. on EC*. – 2003. – Vol. 45. – №1.
3. Vicente R. New broadband EMC double-ridge guide horn antenna, 2004.
4. Teggatz A., Jostingmeier A., Omar A. A New TEM Double-Ridged Horn Antenna for Ground Penetrating Radar Applications, 2005.
5. Dirk Baumann, Christophe Fumeaux, Pascal Leuchtmann and Rudiger Vahldieck. Finite-Volume Time-Domain (FVTD) Modelling of a Broadband Double-Ridged Horn Antenna // *International journal of numerical modelling: electronic networks, devices and fields* Int. J. Numer. – 2004. – Vol. 17. – pp. 285-298.

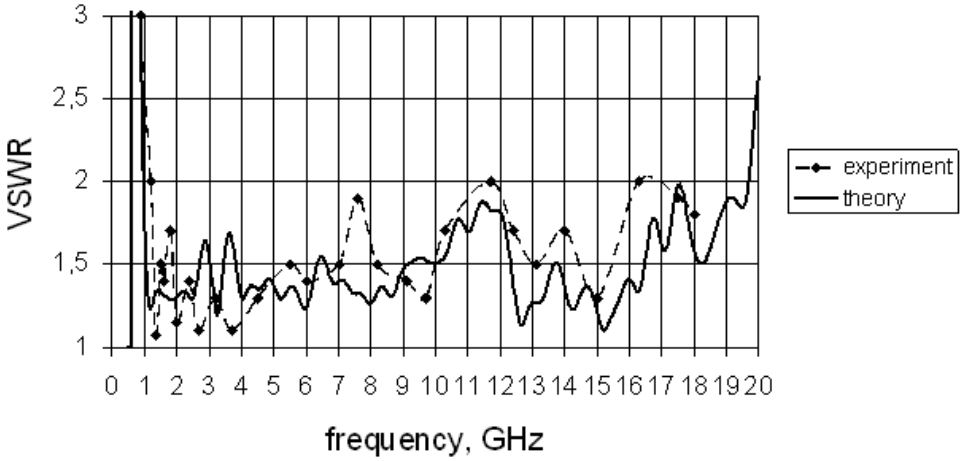


Fig. 6. Frequency dependence of theoretical and experimental VSWR.

UWB NOISE ACOUSTIC ATMOSPHERIC RADAR

Sinitsyn R. B. and Yanovsky F. J.

National Aviation University, Kieiv, Ukraine
E-mail: yanovsky@i.com.ua; comandor@i.com.ua

Abstract

In this paper we discuss a new approach to create the acoustic atmospheric radar (sodar) which is based on noise sounding waveform. Such sounding waveform fits all formal requirements to UWB signals and has remarkable characteristics including extremely high range and speed resolution. It is important to remember that all these good properties exist only in the case when we have independent samples. The noise signal forms the independent samples because of its nature.

The prototype of the radar is described and investigated theoretically, using computer simulation, and in natural conditions. Non-parametrical signal processing algorithm is developed based on statistical approach and digital signal processing. It has wonderful properties of invariance to the group of the noise and signal transforms and stable level of the false alarm probability can be applied for both acoustic and microwave UWB noise radars. The use of the FFT algorithm increases the speed of calculations and gives us the possibility of constructing digital random signal radars.

The results of this project confirm that the random signal radar is one of the most interesting types of radar. It combines properties of UWB radar with some additional features, based on random nature of the sounding waveform. These new properties allow us to simplify signal detection algorithms and measure a distance, an azimuth and a target velocity simultaneously with high resolution and accuracy.

978-1-4244-7468-4/10/$26 ©2010 IEEE

MODE EXPANSIONS IN TIME DOMAIN

Butrym A. Yu.

Karazin Kharkiv National University, Kharkiv, Ukraine
E-mail: *AButrym@ya.ru*

Abstract

The paper considers history of development and current state of the art of calculation techniques in time domain that are based on presenting sought fields in the form of mode expansion. Some peculiarities of the modes in case of transverse inhomogeneous dielectric filling are considered. Similarities and differences with the frequency domain modes are discussed. Directions of further development of the method are given.

Keywords: Mode Basis Method, Time Domain, evolutionary waveguide equations.

1. INTRODUCTION

When I started preparing this paper I realized that it can't be fitted into these Proceedings as a full paper since it would require more than 20 pages. That's why I present here only a sketch of the presentation while the complete paper will be published elsewhere later.

The subject of discussion is transient field in regular and/or closed structures. It includes cavities, cylindrical waveguides, free space, etc. The first publication on this subject as far as I know is dated back to 1949 [1]. Since then this method was reinvented in the papers by Tretyakov (1986, 1989 [2,3]), Borisov (1983, 1991 [4,5]), recently it was re-derived by Geyi (2006,2008 [6,7]). I work on advancing this method on the case of transverse inhomogeneous waveguides since 2002 [9] and other more complex cases. Brief review of the achieved results is the subject of this presentation.

2. MODES

The modes are known in radiophysics as some transverse configurations of the fields in a waveguide or cavity that doesn't change their shape in time or with propagation. They propagate independently and coupling may occur only at some irregularities. Considering propagation of transient fields in transverse inhomogeneous waveguides it was established that there is no such transverse field configuration that would propagate without changing its shape. Meanwhile it was possible to introduce "modes" as a complete set (basis) of transverse functions that are obtained from some eigenvalue boundary problem and can be used for expanding the sought fields.

3. FREQUENCY DOMAIN VS TIME DOMAIN

In the frequency domain any part of the phase front of a mode has the same propagation constant and thus it moves as a whole. In contrast in the time domain each part of the transient wave front moves with speed of light in a particular medium that's why the front should change its form. It results in mode coupling at propagation and thus makes questionable introduction of any modes as such. In the frequency domain it leads to frequency dependence of the mode configuration.

4. CAVITY

Strict consideration of transient fields in a cavity [2] has allowed not to lose any part of solution as it happens in the frequency domain where the divergence equations are silently omitted. It leads to introduction besides commonly known solenoidal modes that describes oscillating fields another class of solutions — irrotational modes that describe transient Coulomb and Ampere fields directly coupled with varying charges and irrotational currents that may exist in the cavity.

5. HOLLOW CYLINDRICAL WAVEGUIDE

Mode expansion of the fields in a hollow waveguide is exactly the same in FD and TD. The well-known cut-off waveguide dispersion relation $\beta^2 = k_0^2 - \kappa_n^2$ turns into Klein-Gordon propagation equation $(\partial_t^2 - \partial_z^2 + \kappa_n^2) f(z,t) = 0$, a solution to which can be easily presented with a convolution propagation operator given in terms of Bessel functions.

6. FREE SPACE

FS can be considered as a regular structure in two ways:

6.1. FREE SPACE AS A CYLINDRICAL WAVEGUIDE

In this case the fields are not restricted in the transverse direction by any boundary conditions except for

978-1-4244-7468-4/10/$26 ©2010 IEEE

the radiating ones and it leads to continual mode spectrum and using integrals instead of series in mode expansion. The modes in this case exist in the form of uncoupled "Bessel modes". Such consideration is most appropriate for considering wave beams and aperture (broadside radiating) antennas.

6.2. Free Space as a Conical Waveguide

FS can also be considered as a regular in r structure, at this the mode spectrum is discrete due to periodicity conditions on angle coordinates. Such consideration leads to spherical harmonics presentation [8] with mode amplitudes being governed by Klein-Gordon-Fock equation $(\partial_t^2 - \partial_r^2 + (\kappa_n/r)^2) f(r,t) = 0$. As one can see it is very similar to the KG equation with the difference that the cut-off frequency now depends on radius. It can be considered as a nonregular waveguide, at this the fields at the center (caustic) behaves as in evanescent waveguide section.

7. Regular Waveguide with Transverse Inhomogeneous Filling

As it was already discussed earlier in such waveguide mode coupling essentially occurs if speed of light varies in cross-section. At that instead of simple KG-equation we obtained KG-equation with matrix coefficients $(\mathbf{L}\partial_t^2 - \mathbf{K}\partial_z^2 + \mathbf{P}^2)\mathbf{f}(z,t) = 0$. The developed mode approach is based on using for field expansion such modes that diagonalize the matrix of cut-off frequencies $\mathbf{P}^2$. At that it was demonstrated that such a presentation converges very rapidly, so that only a finite number of modes is sufficient (with exponentially small residual errors) for presenting propagation of a band-limited signal [10]. Also such modes are not hybrid but pure E-, H- or T-waves.

8. Open Dielectric Waveguide

This problem is currently under study. It has both peculiarities discussed in sections 6.1 and 7. As a result we will be able to analyze excitation and propagation of ultrashort pulses in a fiber, and radiation from the end of a dielectric waveguide (rod antenna). Interesting feature is that in some cases there may exist both discrete and continuum spectrum in such a structure.

9. Moving Back to FD

The introduced modes are frequency independent and can be easily enumerated by cut-off frequencies and mode type (E-, H-, or T-mode). Substituting harmonic space-time dependence into the matrix KG equation leads to a simple presentation of the FD dispersion relation: $\det(\mathbf{L}k^2 - \mathbf{K}\beta^2 - \mathbf{P}^2) = 0$, which is an implicit polynomial by structure. It enables effective calculation and classification of the FD modes.

10. Cavity with Dispersive Medium

In case of a cavity filled with a dispersive medium there emerges a complex oscillating system with several coupled resonances originated from medium resonances and the volume (reverberation) resonance. As a result a single uncoupled mode has complex frequency response with several resonances. The method allows presenting the transient solution in a closed form.

11. Diffraction

Diffraction of a transient wave at some obstacle can be described by a convolution type operator. In case of simple boundary of media in a waveguide there is no mode conversion and the diffraction operator can be described by a function-kernel of the convolution. Some interesting effects have been found in this problem like excitation of a charge wave by E-mode in a conductive medium, transverse wave resonance at the boundary.

Another interesting time domain calculation technique for waveguide diffraction problem has been designed by uniting 1D FDTD schemes for independent mode channels with mode matching technique for coupling at the obstacle (like iris or junction) [11].

This approach also enabled us to consider radiation by TEM-horn like antennas (like biconical) as diffraction at junction of conical line with free space [11].

12. Further Development

Further development of the METD method will be aimed on considering propagation in waveguides with dispersive dielectric filling. The results will be also applicable to the problem of wave beam propagation in a layered dispersive medium (e.g. for GPR modeling).

Another challenging problem is consideration of non-regular waveguides where the modes depend on longitudinal coordinates that leads to additional mode coupling. It will enable analysis of such a problems as radiation of TEM-like antennas with inhomogeneous profile that in optimal way transforms TEM-wave in the antenna into radiated E-wave (such as Volcano antenna, ridge horn, non-regular ridge feeder for parabolic-reflector antenna etc.)

Conclusions

From the calculation point of view the mode approach allows to reduce the 4D problem in coordinates and time to two 2D problems: an elliptic type eigenvalue problem in transverse coordinates and a hyperbolic type propagation problem in longitudinal coordinate and time. It allows one to apply different approaches to each part of the problem and significantly decrease complexity of the problem.

The mode approach also makes possible a physical insight on the transient propagation process, determining some common properties of such phenomena.

Surely the references list below is far from completeness because of limited space; more references can be found in the latest papers by the author [10-12].

REFERENCES

1. *Kisunko G. V.*, Electrodynamics of hollow systems, VKAS, Leningrad, USSR, 1949.
2. *Tretyakov O. A.*, Mode basis method, Radiotekhika i electronika, Vol. 31, No 6, P. 1071-1082, 1986.
3. *O.A. Tretyakov*, "Waveguide evolutionary equations," Radiotechnics and electronics, Vol. 34, No 5, p. 917-926, 1989.
4. *Borisov, V.V.* Transients in waveguides. Publishing House of Leningrad State University, Leningrad, 1991, 156 p.
5. Borisov V.V. Nonperiodic electromagnetic fields in a sectoral horn // Radiotekhnika i Elektronika, vol.28, Mar.1983, p. 450-460.
6. *W. Geyi*, Time-domain theory of metal cavity resonator, Progress In Electromagnetics Research, PIER 78, P. 219-253, 2008.
7. *W. Geyi*, Time-domain theory of waveguide, Progress in Electromagnetics Research, PIER 59, 267-297, 2006.
8. *A. Shlivinski and E. Heyman*, Time-domain near-field analysis of short-pulse antennas – Part I: Spherical wave (multipole) expansion // IEEE Trans. Antennas and Propagation, vol. AP-47, no. 2, P. 271-279, February 1999.
9. *Butrym A. Yu., Tretyakov O. A.* "Modification of the method of evolutionary waveguide equations for the case of transverse inhomogeneous waveguides," Bulletin of Karazin Kharkiv National University, No. 544, 2002, Iss. 1, p. 71-74.
10. *Butrym, A. Y. and B. A. Kochetov*, "Time domain mode basis method for a waveguide with transverse inhomogeneous multi-connected cross-section. 2. Example of numerical implementation of the method," Radio Physics and Radio Astronomy, Vol. 14, No. 3, 266-277, 2009.
11. *M. N. Legenkiy and A. Y. Butrym* "Method of mode matching in time domain," PIER B, Vol. 22, p. 257-283, 2010.
12. *A. Y. Butrym and B. A. Kochetov* "Mode expansion in time domain for conical lines with angular medium inhomogeneity," PIER B, Vol. 19, p. 151-176, 2010.

NEW HYBRID METHODS

NEW KRAVCHENKO TRANSFORMS AND DIGITAL UWB SIGNAL PROCESSING

Kravchenko V. F. and Churikov D. V.

Kotel'nikov Institute of Radio Engineering and Electronics RAS, Moscow, Russia
E-mail: kravchenko_vf@fromru.com, mpio_nice@mail.ru

Abstract

In this report the new Kravchenko transforms based on atomic distributions [1-7] for digital UWB radar signal processing is proposed and proved. This approach have some advantages in comparison with Gabor transform for parameter estimation in radar.

Keywords: atomic functions, weight functions, radar, ultrawideband signals, DSP.

1. INTRODUCTION

To improve the quality of research and signal processing for improved methods of analysis and synthesis. Theory of atomic functions (AF) [1-7] allows to obtain new combined transformations. The advantage of the new atomic transforms is that they are based on a common mathematical apparatus. This provides flexibility, reliability as well as good physical characteristics.

2. NEW KRAVCHENKO TRANSFORMS

Consider the modified Fourier transform (FT) [1] with the following Kravchenko integral kernel [1-5]:

$$g_{u,\xi}\left(x\right)=\frac{1}{b}g\left(qx-u\right)\exp\left(i\xi x\right). \qquad (1)$$

In this expression $g\left(x\right)$ is the atomic function, u is the time shift, ξ is the frequency shift, q and b are scaling parameters. The energy of the kernel $g_{u,\xi}\left(x\right)$ is concentrated in the neighborhood of u on the interval σ_x measured by standard deviation $\left|g\left(x\right)\right|^2$. The spectrum of this function is $\widehat{g}\left(\omega\right)$ shifted to ξ, i.e. $\widehat{g}_{u,\xi}\left(\omega\right)=\widehat{g}\left(\omega-\xi\right)$. The energy of $\widehat{g}_{u,\xi}\left(\omega\right)$ is localized near the frequency ξ on the interval σ_ω. Thus the modified Kravchenko atomic transform (AT) has the following form:

$$\begin{aligned}y\left(u,\xi\right)&=\int_{-\infty}^{\infty}y\left(x\right)g^{*}_{u,\xi}\left(x\right)dt=\\&=\frac{1}{b}\int_{-\infty}^{\infty}y\left(x\right)g\left(qx-u\right)\exp\left(-i\xi x\right)dx.\end{aligned} \qquad (2)$$

Fig. 1 illustrates the field of time-frequency localization of function $g_{u,\xi}\left(x\right)$ for two sets of values u, ξ, q and b.

According to the principle of uncertainty [3,9-11] the product $\Delta=\sigma_\omega\sigma_x$ is constant and does not depend on the choice of parameter values u, ξ, q and b.

2.1. MODELS OF UWB SIGNALS

We shall consider models of the following UWB signals [3]:

$$y_1\left(t\right)=\mathrm{step}\left(\frac{t-0,5}{\tau}\right)-\mathrm{step}\left(\frac{t+0,5}{\tau}\right)\mathrm{sign}\left(t\right); \qquad (3)$$

$$\begin{aligned}y_2\left(t\right)=\left(-1\right)^n\sin\left(\frac{\pi n t}{\tau}\right)\exp\left(-\left|\frac{t}{\tau}\right|\right)\times\\\times\left(\mathrm{step}\left(\frac{t}{\tau}+1\right)-\mathrm{step}\left(\frac{t}{\tau}-1\right)\right);\end{aligned} \qquad (4)$$

$$y_3\left(t\right)=-\frac{2t}{\tau^2}\cdot\exp\left(-\left(\frac{t}{\tau}\right)^2\right); \qquad (5)$$

$$y_4\left(t\right)=-\frac{2}{\tau^2}\left(1-\frac{2t^2}{\tau^2}\right)\cdot\exp\left(-\left(\frac{t}{\tau}\right)^2\right); \qquad (6)$$

$$y_5\left(t\right)=\exp\left(-\left(\frac{t}{2\tau}\right)^2\right)n!\sum_{k=0}^{[n/2]}\left(-\frac{1}{2}\right)^k\frac{\left(t/\tau\right)^{n-2k}}{\left(n-2k\right)!k!};$$

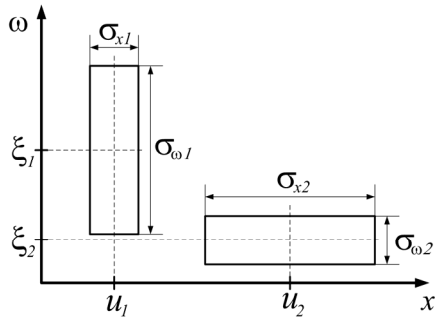


Fig. 1. Time-frequency localization of function $g_{u,\xi}\left(x\right)$.

978-1-4244-7468-4/10/$26 ©2010 IEEE

where $\mathrm{step}(t) = \begin{cases} 0, & t < 0; \\ 1, & t \geq 0. \end{cases}$ is Heaviside function, and $\mathrm{sign}(t)$ is the sign function of argument $\left(\mathrm{sing}(t) = 2\left(\mathrm{step}(t) - 0,5\right)\right)$. Their plots with results of Kravchenko atomic transformation are submitted on Figures 2-6, and physical characteristics are resulted in Table 1.

2.2. PHYSICAL CHARACTERISTICS OF UWB SIGNALS

To examine wavelet-functions and analyzed model UWB signals we shall use the following [3] modified physical characteristics: broadbandness parameter μ; minimal and maximal frequencies of spectral density function (SDF) $f_{\min}$, $f_{\max}$; the central frequency of SDF f_0; relative position of a maximum of SDF γ_1; relative position of the first zero of SDF γ_2; relative width of SDF on a level –3 dB γ_3; relative width of SDF on a level –6 dB γ_4; information losses (dB), observed at rejection a component with frequencies $f \notin [0, \nu]$ from SDF γ_5; information losses (dB) observed at rejection from SDF a component with frequencies $f \notin [f_{\min}, f_{\max}]$ γ_6; coherent amplification γ_7; equivalent noise band γ_8; maximum side-lobe level (dB) γ_9; parasitic amplitude modulation γ_{10}; the maximum conversion loss γ_{11}.

UWB signal is understood as a signal which parameter μ satisfies to the condition $1 \leq \mu < 2$.

As appears from table at a choice of different parametres modelling time signals can be considered as narrow-band, broadband or ultra-wideband. Kravchenko atomic transform allows to improve the time and frequency permission at the analysis.

3. CONCLUSION

New constructions of Kravchenko transform based on atomic functions (AF) are offered and proofed. The physical analysis of characteristics of the new Kravchenko transforms is carried out. It is shown that time and frequency properties of the new transform are good. Numerical experiment and the physical analysis of results confirm efficiency of new Kravchenko transforms in problems of UWB signal processing.

Table 1. Model UWB signals and their physical characteristics.

No. of realizations	Model UWB signals	μ	γ_1	γ_2	γ_3	γ_4	γ_5	γ_6	γ_7	γ_8	γ_9
1	$y_1(t)$, τ =1 s.	1,54	0,91	1,04	0,85	1,11	-1,58	-1,41	10,01	10,01	-5,29
2	$y_1(t)$, τ =1,5 s.	1,50	0,92	1,00	0,83	1,11	-1,49	-1,34	6,67	6,67	-5,28
3	$y_2(t)$, n=1	1,46	0,91	1,06	0,81	1,13	-11,47	-7,81	8,06	6,28	-12,99
4	$y_2(t)$, n=2	0,79	0,98	0,94	0,88	1,18	-10,18	-6,32	9,84	6,57	-8,19
5	$y_2(t)$, n=3	0,52	1,02	0,88	0,82	1,18	-9,53	-5,53	10,60	6,63	-8,60
6	$y_3(t)$, τ =0,3 s.	1,59	0,87	2,26	0,81	1,13	-37,58	-9,17	14,30	10,44	-49,15
7	$y_3(t)$, τ =0,5 s.	1,48	0,87	1,82	0,88	1,18	-8,80	-5,88	8,74	6,49	-18,87
8	$y_4(t)$, τ =0,3 s.	1,22	0,90	2,19	0,84	1,16	-32,05	-8,43	19,43	10,65	-43,44
9	$y_4(t)$, τ =0,5 s.	1,20	1,00	1,11	0,83	1,17	-6,20	-4,60	12,18	6,93	-14,08
10	$y_5(t)$, n=1, τ =0,15 s.	1,59	0,87	2,26	0,81	1,13	-37,58	-9,17	14,30	10,44	-49,15
11	$y_5(t)$, n=3, τ =0,15 s.	1,77	0,85	1,39	0,89	1,09	-25,77	-10,44	11,50	8,12	-34,63
12	$y_5(t)$, n=5, τ =0,15 s.	1,81	0,84	1,08	0,93	1,07	-17,01	-10,40	10,20	6,98	-26,63
13	$y_5(t)$, n=1, τ =0,1 s.	1,59	0,86	3,28	0,85	1,15	-96,77	-8,86	21,44	15,67	-108,30
14	$y_5(t)$, n=3, τ =0,1 s.	1,75	0,82	2,21	0,90	1,10	-81,50	-10,37	17,25	12,17	-92,79
15	$y_5(t)$, n=5, τ =0,1 s.	1,83	0,85	1,69	0,93	1,06	-68,61	-11,34	15,27	10,43	-77,97
16	$y_5(t)$, n=7, τ =0,1 s.	1,85	0,87	1,42	0,95	1,06	-57,50	-11,65	14,02	9,32	-67,70

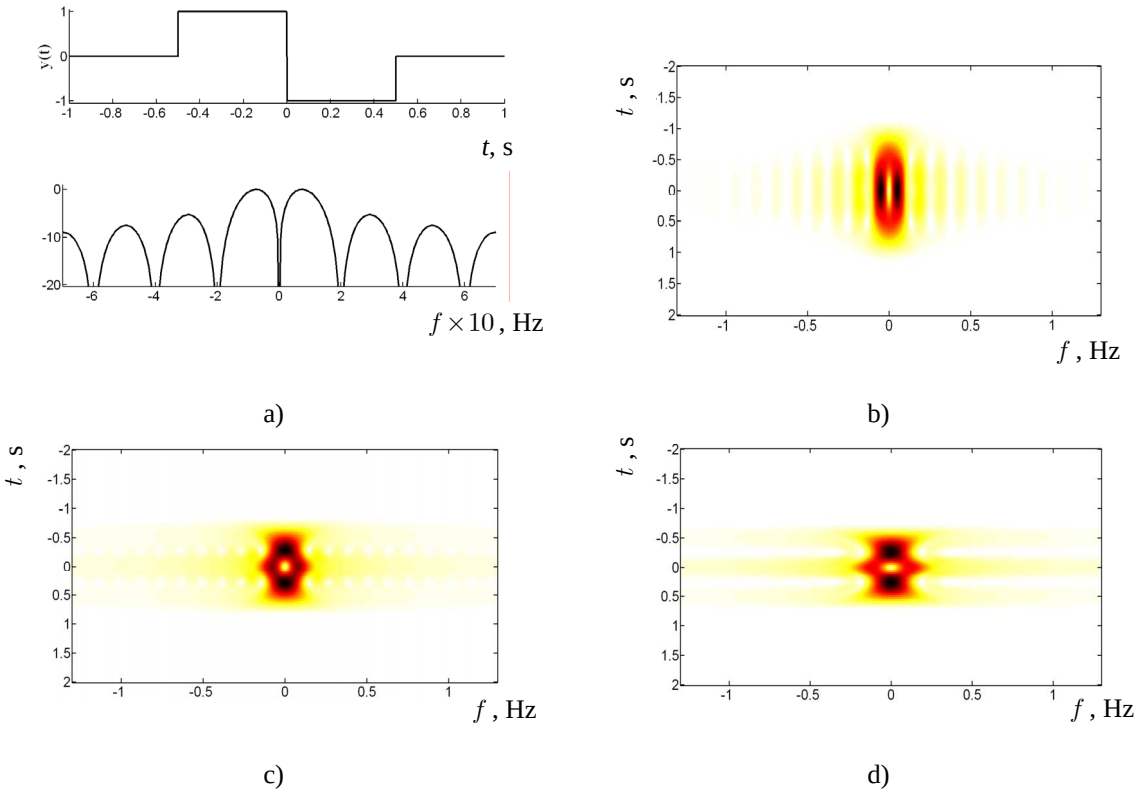


Fig. 2. Model signal $y_1(t)$, τ =1, their LACH (a), atomic transform for $q = 1,\ 2,\ 3$ (b, c, d).

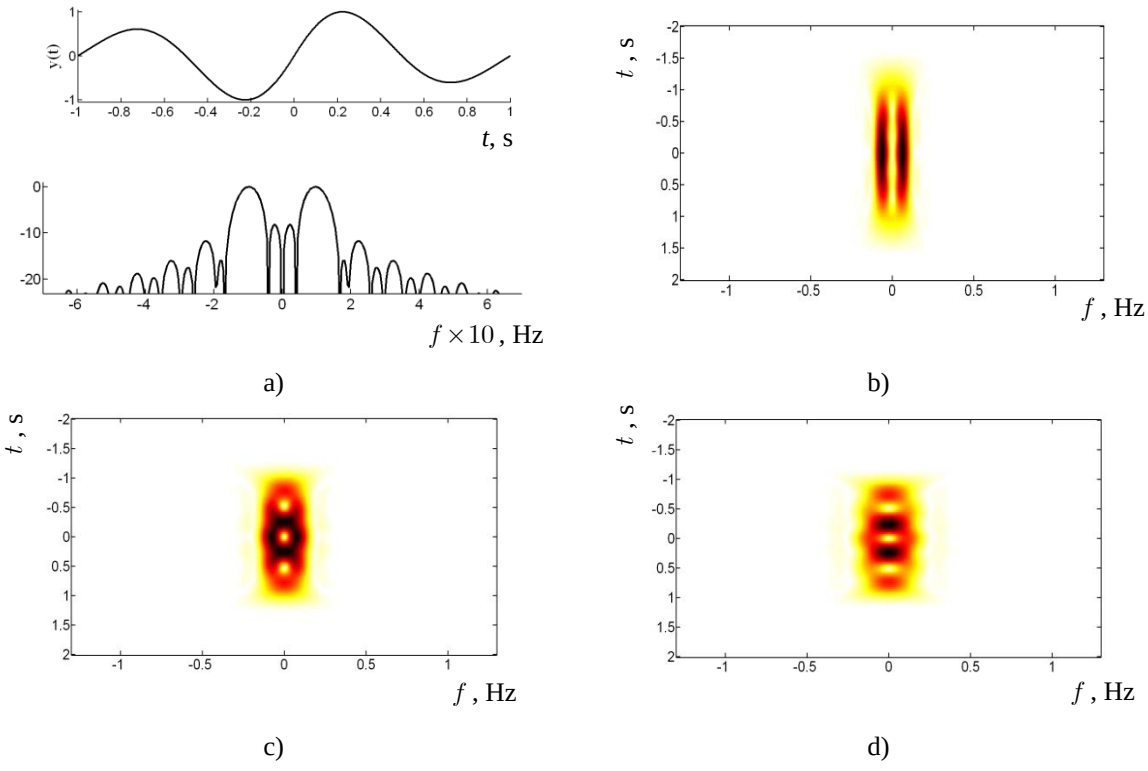


Fig. 3. Model signal $y_2(t)$, τ =1, their LACH (a), atomic transform for $q = 1,\ 2,\ 3$ (b, c, d).

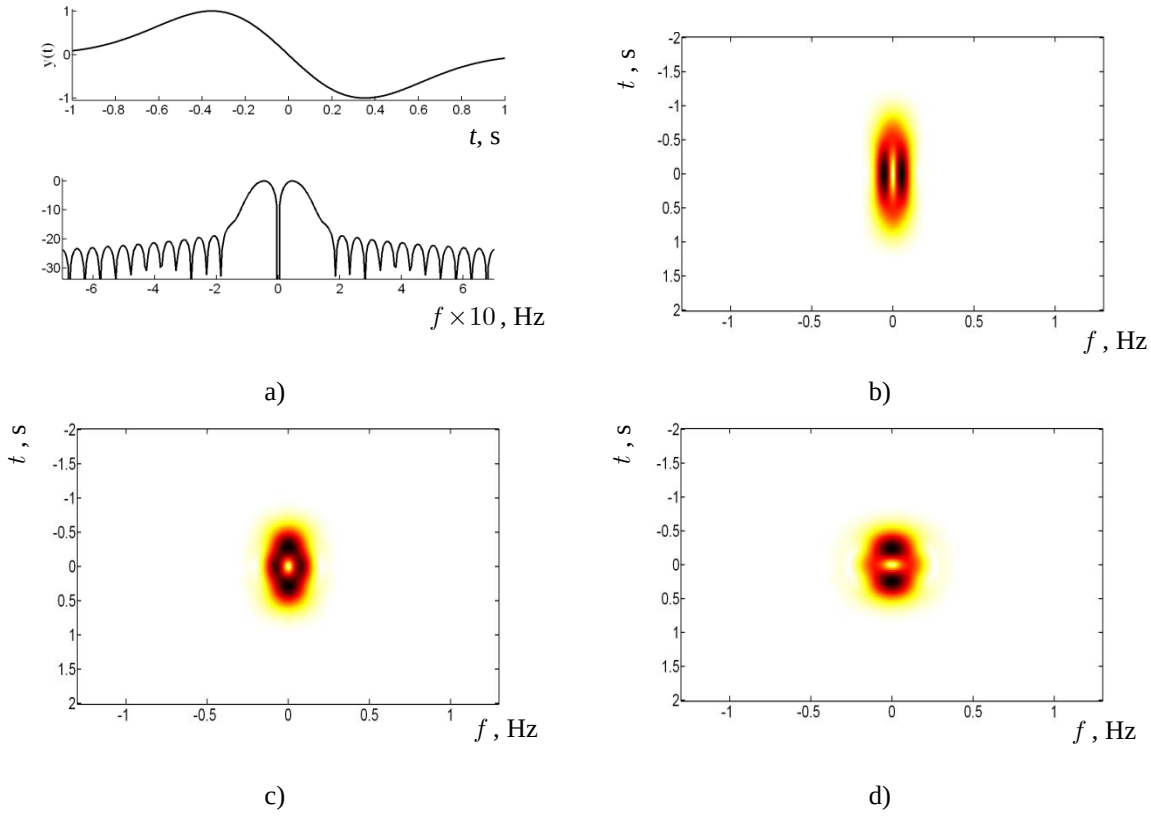


Fig. 4. Model signal $y_3(t)$, τ =1, their LACH (a), atomic transform for $q = 1,\ 2,\ 3$ (b, c, d).

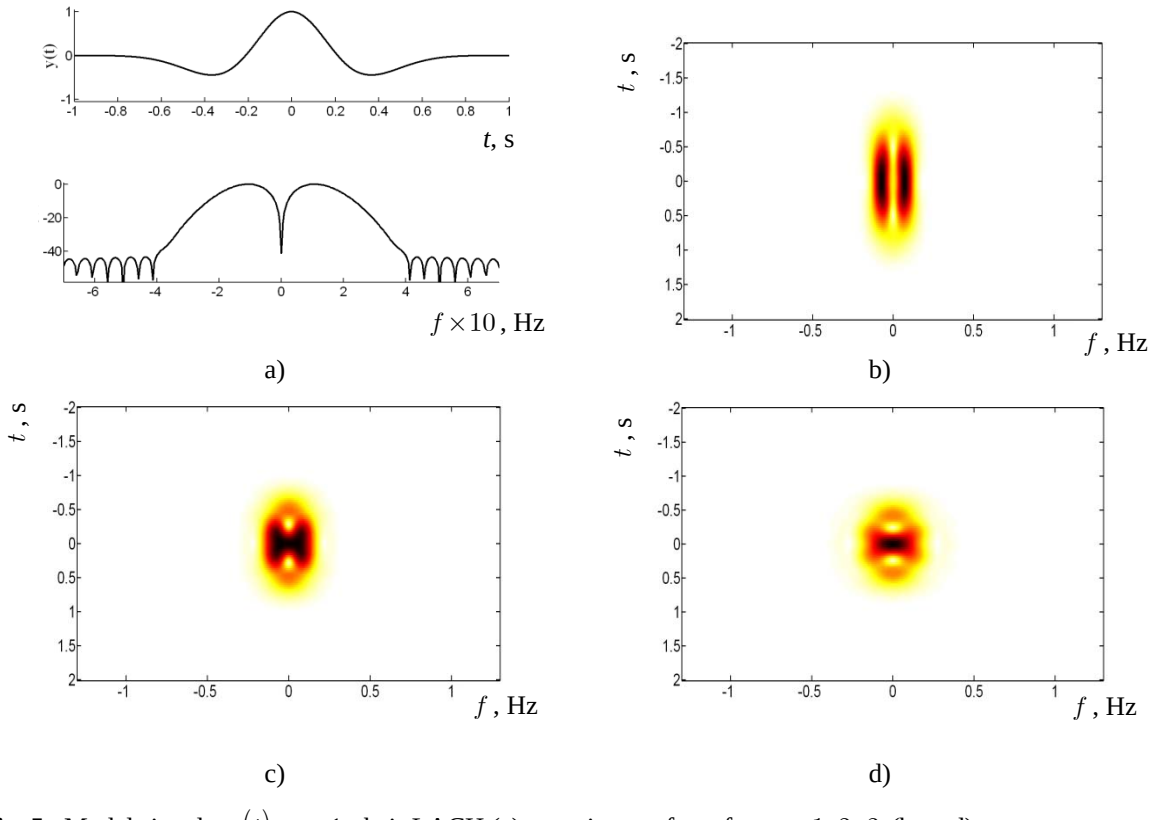


Fig. 5. Model signal $y_4(t)$, τ =1, their LACH (a), atomic transform for $q = 1,\ 2,\ 3$ (b, c, d).

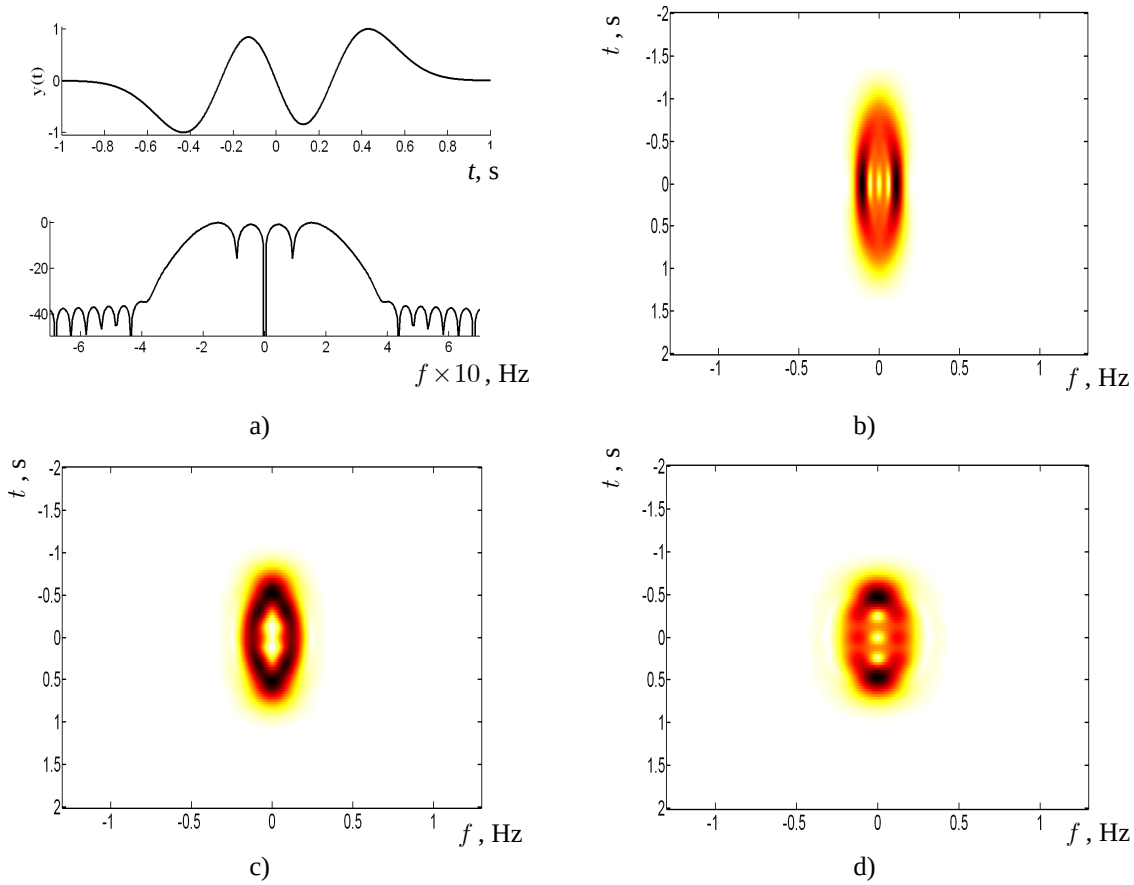


Fig. 6. Model signal $y_5(t)$, τ =1, their LACH (a), atomic transform for $q = 1, 2, 3$ (b, c, d).

REFERENCES

1. Kravchenko V.F. 2003, *Lectures on the Theory of Atomic Functions and their some Applications*, Moscow, Publishing House Radio Engineering.
2. Kravchenko V.F., Rvachev V.L. 2006, *Boolean Algebra, Atomic Functions and Wavelets in Physical Applications*. Moscow, Fizmatlit.
3. *Digital Signal and Image Processing in Radio Physical Applications*, Edited by V.F. Kravchenko, Moscow, Fizmatlit, 2007.
4. Volosyuk V.K., Kravchenko V.F. 2008, *Statistical Theory of Radio Technical Systems of Remote Sensing and Radar*. Moscow, Fizmatlit.
5. Kravchenko V.F., Perez-Meana H.M. & Ponomaryov V.I. 2009, *Adaptive Digital Processing of Multidimentional Signals with Applications*, Moscow, Fizmatlit.
6. Kravchenko V.F. 'Atomic and R-functions in Radiophysical Applications. Review'. *Proc. International Conference on Antenna Theory and Techniques*, Lviv, Ukraine, 3-12
7. Kravchenko V.F., Churikov D.V. 2008, 'Spectral Estimation and Digital UWB Signal Processing by Atomic Functions and Wavelets', *Proc. The Fourth International Conference on Ultrawideband and Ultrashort Impulse Signals*, Sevastopol, Ukraine, 27-33.

ATOMIC DISTRIBUTIONS IN SAR PROBLEMS

Kravchenko V. F. and Churikov D. V.

Kotel'nikov Institute of Radio Engineering and Electronics RAS, Moscow, Russia
E-mail: kravchenko_vf@fromru.com, mpio_nice@mail.ru

Abstract

In this report the new WA-systems Kravchenko-Rvachev functions based on atomic distributions [1-7] for SAR problems are proposed. New functions have the following main properties: compact support, smoothness and ultrawidebandness. This WA-systems Kravchenko-Rvachev functions are effective for UWB signal processing.

Keywords: atomic functions, ultrawideband signals, SAR, DSP.

1. INTRODUCTION

For the ultra-wideband (UWB) signal processing requires appropriate methods. They must have suitable characteristics, as well as their variation. These are the atomic distribution, which are constructed on basis of the Kravchenko-Rvachev functions with reference to problems of digital UWB signal processing are proposed.

2. ATOMIC DISTRIBUTIONS

Let's consider the following probability distributions in a kind weight functions (WF):

1. Kravchenko-Koshi

$$w_1(x) = \frac{b}{c\pi\left(b^2 + x^2\right)} h_a\left(\frac{x}{a-1}\right), \qquad (1)$$

$$a, b, c \in \mathbb{R},\ N = 2, 3, 4, \ldots .$$

2. Kravchenko-Gauss

$$w_2(x) = \frac{1}{\sqrt{2\pi}c} \exp\left(-\frac{x^2}{2b^2}\right) h_a\left(\frac{x}{a-1}\right), \qquad (2)$$

$$a, b, c \in \mathbb{R},\ N = 2, 3, 4, \ldots .$$

3. Kravchenko- Poisson

$$w_3(x) = \frac{1}{c} \exp\left(-\frac{x}{b}\right) h_a\left(\frac{x}{a-1}\right), \qquad (3)$$

$$b, c \in \mathbb{R},\ N = 2, 3, 4, \ldots .$$

4. Kravchenko- Rayleigh:

$$w_4(x) = \frac{x}{c} \exp\left(-\frac{x^2}{2 \cdot b^2}\right) h_a\left(\frac{x}{a-1}\right), \qquad (4)$$

$$b, c \in \mathbb{R},\ N = 2, 3, 4, \ldots .$$

Weight function $h_3\left(x/2\right)$ and its spectra are shown on Fig. 1. View of those functions are presented on Fig. 2, 3. It is known that mathematical models of radio signals and a radio noise are probability processes. Therefore stochastic distributions appear are convenient for UWB signal processing.

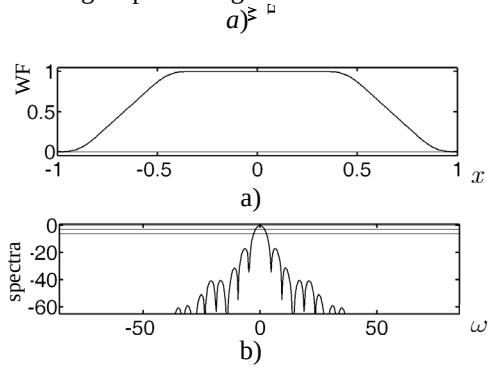


Fig. 1. WF $h_3\left(x/2\right)$ and its spectra.

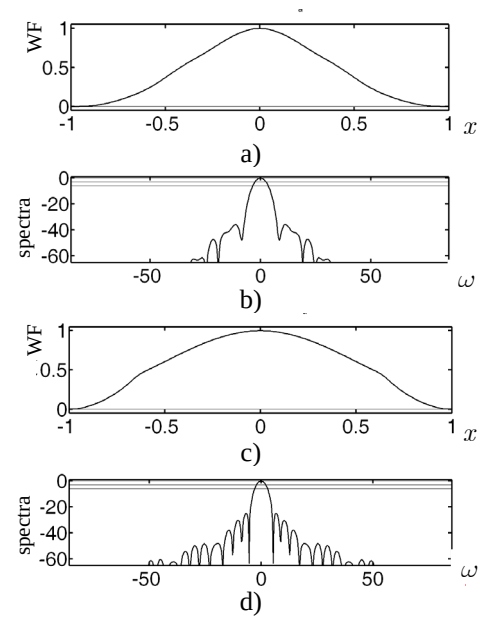


Fig. 2. View of $w_1\left(x;5,0.5\right)$ (a), $w_2\left(x;5,0.5\right)$ (c) and spectra (b), (d).

978-1-4244-7468-4/10/$26 ©2010 IEEE

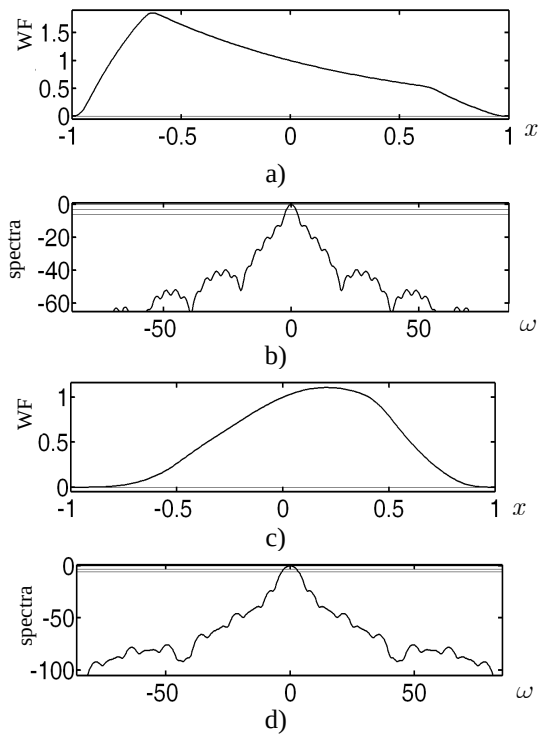


Fig. 3. View of $w_3\left(x;5,0.5\right)$ (a), $w_4\left(x;5,0.5\right)$ (c) and spectra (b), (d).

2.1. Physical Characteristics

To examine weight functions and analyzed model UWB signals we shall use the following [3] modified physical characteristics: broadbandness parameter μ (UWB signal is understood as a signal which parameter μ satisfies to the condition $1 \le \mu < 2$); minimal and maximal frequencies of spectral density function (SDF) $f_{\min}$, $f_{\max}$; the central frequency of SDF f_0; relative position of a maximum of SDF γ_1; relative position of the first zero of SDF γ_2; relative width of SDF on a level –3 dB γ_3; relative width of SDF on a level -6 dB γ_4; information losses (dB), observed at rejection a component with frequencies $f \notin \left[0,\nu\right]$ from SDF γ_5; information losses (dB) observed at rejection from SDF a component with frequencies $f \notin \left[f_{\min}, f_{\max}\right]$ γ_6; coherent amplification γ_7; equivalent noise band γ_8; maximum side-lobe level (dB) γ_9; parasitic amplitude modulation γ_{10}; the maximum conversion loss γ_{11}; And uncertainty constants on time and hour-tote which are defined so

$$x_f^* = \frac{1}{\left\|f\left(x\right)\right\|^2}\int\limits_{-\infty}^{\infty} x\left|f\left(x\right)\right|^2 dx\,,$$

$$\Delta_x = \frac{1}{\left\|f\left(x\right)\right\|}\left(\int\limits_{-\infty}^{\infty}\left(x-x_f^*\right)^2\left|f\left(x\right)\right|^2 dx\right)^{1/2},$$

$$\omega_{\hat f}^* = \frac{1}{\left\|\widehat f\left(\omega\right)\right\|^2}\int\limits_{-\infty}^{\infty}\omega\left|\widehat f\left(\omega\right)\right|^2 d\omega\,,$$

$$\Delta_\omega = \frac{1}{\left\|\widehat f\left(\omega\right)\right\|}\left(\int\limits_{-\infty}^{\infty}\left(\omega-\omega_{\hat f}^*\right)^2\left|\widehat f\left(\omega\right)\right|^2 d\omega\right)^{1/2}.$$

Time-frequency localization is characterized by product $\Delta = \Delta_x\Delta_\omega$.

2.2. Constructing of Orthogonal Kravchenko Wavelets

Orthogonal Kravchenko wavelets on base of atomic distributions (1)-(4) have smooth Fourier transform are proposed. Their construction [6-10] is carried out by means of the quadrature mirror filters $\widehat m_0\left(\omega\right)$. For maintenance of orthogonality performance, the following conditions in transitive area are necessary:

$$\left|\widehat m_0\left(\omega\right)\right|^2 + \left|\widehat m_0\left(\omega-2\pi\right)\right|^2 = 2\,.$$

Fourier transform of scaling function [4, 7] is defined from the equation

$$\widehat\varphi\left(\omega\right) = \prod_{k=1}^{\infty}\frac{1}{\sqrt2}\widehat m_0\left(\frac{\omega}{2^k}\right). \qquad (5)$$

Fourier transform of wavelet function can be written as

$$\widehat\psi\left(\omega\right) = \frac{1}{\sqrt2}\widehat g\left(\frac{\omega}{2}\right)\widehat\varphi\left(\frac{\omega}{2}\right), \qquad (6)$$

where $\widehat g\left(\omega\right) = \mathrm{e}^{-i\omega}\widehat m_0\left(\omega+\pi\right)$.

In Table 1 physical characteristics of new orthogonal wavelets on basis of $w_1\left(x\right)$ and $w_2\left(x\right)$ for different values of scaling of argument M in comparison with Meyer wavelet for the support [–6; 6] are resulted.

2.3. Quality Functional of Wavelet-Basis Choice for Analysis of UWB Signals

It is proposed to apply the quality functional in the analysis of the UWB signals allowing optimal choice of basic wavelets functions in such a form:

$$J\left(\psi,y\right) = \sum_{k=0}^{N}\left|\frac{\gamma_k^\psi - \gamma_k^y}{\gamma_k^y}\right|^2, \qquad (7)$$

where $\psi(t)$ is wavelet function, $y(t)$ is analyzed signal, γ_k^ψ and γ_k^y are their physical characteristics, and N is quantity of compared parameters. Here,

Table 1. Physical characteristics of Kravchenko-Koshi and Kravchenko-Gauss wavelet in comparison with Meyer wavelet for the support [-6;6].

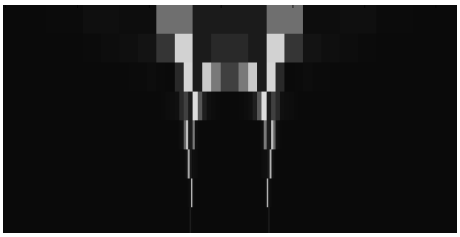
M	γ_2	γ_3	γ_4	γ_8	γ_9	γ_{10}	Δ_x	Δ_ω
Meyer wavelet								
–	4,118	3,126	3,295	4,148	–42,184	0,403	1,127	3,653
Kravchenko-Koshi wavelet								
0,8	4,305	3,107	3,407	4,660	–50,510	0,231	0,910	2,955
0,9	4,174	3,107	3,369	4,308	–47,468	0,272	0,960	3,118
1,0	4,062	3,126	3,351	4,024	–44,151	0,308	1,008	3,273
1,1	3,987	3,126	3,332	3,788	–42,226	0,343	1,053	3,421
1,2	3,912	3,126	3,313	3,584	–41,112	0,380	1,096	3,562
Kravchenko-Gauss wavelet								
0,8	4,305	3,107	3,426	4,689	–49,653	0,235	0,905	2,938
0,9	4,174	3,107	3,388	4,336	–46,744	0,276	0,955	3,100
1	4,062	3,126	3,351	4,052	–43,402	0,311	1,001	3,253
1,1	3,987	3,126	3,332	3,817	–41,411	0,344	1,046	3,398
1,2	3,912	3,126	3,313	3,615	–40,279	0,378	1,088	3,538

$\gamma_0 = \mu$ and $N = 4$. We shall consider models of the following UWB signals [3]:

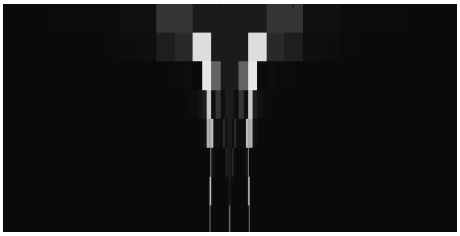
$$y_1(t) = H\left(\frac{t-0,5}{\tau}\right) - H\left(\frac{t+0,5}{\tau}\right)\mathrm{sign}(t); \quad (8)$$

$$y_2(t) = -\frac{2t}{\tau^2}\cdot\exp\left(-\left(\frac{t}{\tau}\right)^2\right). \quad (9)$$

Here $\mathrm{H}(t) = \begin{cases} 0, & t < 0; \\ 1, & t \geq 0. \end{cases}$ is Heaviside function, and $\mathrm{sign}(t)$ is the sign function of argument $\left(\mathrm{sing}(t) = 2\mathrm{H}(t) - 1\right)$. Their plots with results of Kravchenko atomic transformation are submitted on Fig. 4.



a)



b)

Fig. 4. Discrete wavelet coefficients of $y_1(t)$ (a), and $y_2(t)$ (b) for the Kravchenko-Koshi wavelet.

3. CONCLUSION

New constructions of Kravchenko transform based on atomic functions (AF) are offered and proofed. The physical analysis of characteristics of the new Kravchenko transforms is carried out. It is shown that time and frequency properties of the new transform are good. Numerical experiment and the physical analysis of results confirm efficiency of new Kravchenko transforms in problems of UWB signal processing.

REFERENCES

1. Kravchenko V.F. 2003, *Lectures on the Theory of Atomic Functions and their some Applications*, Moscow, Publishing House Radio Engineering.
2. Kravchenko V.F., Rvachev V.L. 2006, *Boolean Algebra, Atomic Functions and Wavelets in Physical Applications*. Moscow, Fizmatlit.
3. *Digital Signal and Image Processing in Radio Physical Applications*, Edited by V.F. Kravchenko, Moscow, Fizmatlit, 2007.
4. Volosyuk V.K., Kravchenko V.F. 2008, *Statistical Theory of Radio Technical Systems of Remote Sensing and Radar*. Moscow, Fizmatlit.
5. Kravchenko, V.F., Perez-Meana, H.M., and Ponomaryov, V.I. 2009, *Adaptive Digital Processing of Multidimentional Signals with Applications*, Moscow, Fizmatlit.
6. Kravchenko, V.F., Kravchenko, O.V., and Safin, A.R. 2009, 'Atomic Functions in Probability Theory and Stochastic Processes', *Publishing House Successes of Modern Radio Electronics*, Moscow, **5**, 23-39.
7. Kravchenko, V.F., Kravchenko, O.V., Safin, A.R., and Churikov, D.V., 2009, 'New Class of Probability Weight Functions in Digital Signal and Image Processing', *An International Journal Electromagnetic Waves and Electronic Systems*, Moscow, 14, **9**, 31-44.

NEW ANALITYCAL KRAVCHENKO WAVELETS IN SPECTRAL ESTIMATION OF UWB SIGNALS

Churikov D. V.

Kotel'nikov Institute of Radio Engineering and Electronics RAS, Moscow, Russia
E-mail: mpio_nice@mail.ru

Abstract

In this report the new analytical Kravchenko wavelet based on atomic functions [1-7] for spectral estimation of UWB are proposed. The constructed wavelets have a compact support and they are infinitely differentiable. It is shown that the proposed wavelets significantly improves the quality of UWB signal spectral estimations.

Keywords: atomic functions, wavelets, ultrawideband signals, DSP.

1. INTRODUCTION

Signals can be set in the form of some linear combination of elementary functions [3-5]

$$s\left(x\right)=\sum_{k=0}^{N-1}C\left(k\right)\varphi\left(k,x\right), \qquad (1)$$

where $\varphi\left(k,x\right)$ is an elementary function of number *k*, and *N* is quantity of the functions used in the decomposition. At approximation the generalized Fourier transformation of a kind

$$C\left(k\right)=\int_{0}^{T}s\left(x\right)\varphi\left(k,x\right)dt \qquad (2)$$

provides the minimum value of mean-square error. Thus, there is signal decomposition on some basis, which in many problems of digital signal processing cannot be orthogonal. In this report the new class of analytical WA-systems of Kravchenko functions on the basis of the theory of atomic functions (AF) [1-9] are constructed and proof. The all wavelet conditions [5-7] are satisfied exact.

2. WA-SYSTEMS OF KRAVCHENKO FUNCTIONS

2.1. PROPERTIES OF WAVELETS

It is known [2,6] that main properties of wavelets are localisation, a zero average and automodeling basis.
1. Condition of a zero average:

$$\int_{-\infty}^{\infty}\psi(t)dt=0\,. \qquad (3)$$

2. A limitation condition in time and in frequency areas:

$$\int\left|\psi(t)\right|^{2}dt<\infty\,,\ \int\left|\widehat{\psi}(\omega)\right|^{2}d\omega<\infty\,. \qquad (4)$$

3. Self-similarity of basis. A characteristic sign of basis of wavelet-transform is its self-similarity as all basic functions are received by means of scale transformations and shifts from same initial wavelet.

2.2. WAVELET TRANSFORM

Direct continuous transformation of one-dimensional signal [2-6] looks like

$$Wf(a,b)=\left|a\right|^{-1/2}\int_{-\infty}^{\infty}f(t)\tilde{\psi}\left(\frac{t-b}{a}\right)dt\,, \qquad (5)$$

where symbol "~" is designates complex conjugation, $\psi(t)$ is wavelet-function, a is scaling parameter, b is shift parameter. If function $\psi(t)$ is real then the wavelet-spectrum $Wf(a,b)$ is real too. If function $\psi(t)$ is analytical and complex valued then such wavelet is called analytical, and corresponding continuous transformation is analytical wavelet transform. Function $\psi(t)$ is called analytical [3,6] if its Fourier transform equals zero for negative frequencies $\widehat{\psi}(\omega)=0$ at $\omega<0$. As the wavelet-spectrum $Wf(a,b)$ for an analytical WT represents complex-valued function then peak $\left|Wf(a,b)\right|$ and phase $\arg Wf(a,b)$ characteristics are considered separately.

Presence of an imaginary part is the basic advantage of an analytical WT against the usual transformation as the phase characteristic takes into account the additional information about signal under consideration.

2.3. ANALYTICAL KRAVCHENKO WAVELETS

The expression for the wavelet function has the following form:

$$\psi\left(x\right)=\frac{1}{c}w\left(qx\right)\left\{\exp\left(i\eta x\right)-\frac{1}{q}A\left(\frac{\eta}{q}\right)\right\}, \qquad (6)$$

$$\psi_{a,b}\left(t\right)=\frac{1}{\sqrt{|\,\alpha\,|}}\psi\left(\frac{t-b}{\alpha}\right), \qquad (7)$$

where $w\left(t\right)$ is AF [1-4], $A\left(\eta\right)=\widehat{w}\left(\eta\right)\big/\widehat{w}\left(0\right)$, c and q are scaling parameters, α is the dilatation variable and b is represents time shift.

978-1-4244-7468-4/10/$26 ©2010 IEEE

For example, for the AF $h_a(t)$ we have

$$A(\eta)=\prod_{k=1}^{\infty}\operatorname{sinc}\left(\frac{\eta}{a^k}\right), \quad (8)$$

and

$$\psi_h(t)=h_a(t)\left\{\exp(i\eta t)-\prod_{k=1}^{\infty}\operatorname{sinc}\left(\frac{\eta}{a^k}\right)\right\}. \quad (9)$$

At numerical experiments we will be limited to a small number of multipliers of infinite product. It follows from fast convergence of function

$$A_M^*(\eta)=\prod_{k=1}^{M}\operatorname{sinc}\left(\frac{\eta}{a^k}\right),\ A(\eta)=\lim_{M\to\infty}A_M^*(\eta). \quad (10)$$

Let's define a relative error of calculations so

$$E(M)=100\%\frac{\left\|A(\eta)-A_M^*(\eta)\right\|_{L_2}}{\left\|A(\eta)\right\|_{L_2}}= \\ =100\%\frac{\sqrt{\int_{-\infty}^{\infty}\left(\prod_{k=1}^{\infty}\operatorname{sinc}\left(\frac{x}{a^k}\right)-\prod_{k=1}^{M}\operatorname{sinc}\left(\frac{x}{a^k}\right)\right)^2 dx}}{\sqrt{\int_{-\infty}^{\infty}\left(\prod_{k=1}^{\infty}\operatorname{sinc}\left(\frac{x}{a^k}\right)\right)^2 dx}}. \quad (11)$$

In table 1 values $E(M)$ for $a=2,\ 4$ are presented.

Table 1. Values of relative error norm for increasing of M.

M	1	2	3	4	5	6	7
$E(M)$, % (a=2)	32,345	3,706	0,726	0,175	0,044	0,011	0,003
$E(M)$, % (a=4)	17,437	0,410	0,017	0,001	-	-	-

2.4. Physical Characteristics of UWB Signals

To examine wavelet-functions and analyzed model UWB signals we shall use the following [3] modified physical characteristics: broadbandness parameter μ; minimal and maximal frequencies of spectral density function (SDF) $f_{\min}$, $f_{\max}$; the central frequency of SDF f_0; relative position of a maximum of SDF γ_1; relative position of the first zero of SDF γ_2; relative width of SDF on a level –3 dB γ_3; relative width of SDF on a level –6 dB γ_4; information losses (dB), observed at rejection a component with frequencies $f\notin[0,\nu]$ from SDF γ_5; information losses (dB) observed at rejection from SDF a component with frequencies $f\notin[f_{\min},f_{\max}]$ γ_6; coherent amplification γ_7; equivalent noise band γ_8; maximum side-lobe level (dB) γ_9; parasitic amplitude modulation γ_{10}; the maximum conversion loss γ_{11}.

The important physical parameters of wavelets are uncertainty constants on time and frequency which are defined so

$$x_f^*=\frac{1}{\left\|f(x)\right\|^2}\int_{-\infty}^{\infty}x\left|f(x)\right|^2dx, \quad (12)$$

$$\Delta_x=\frac{1}{\left\|f(x)\right\|}\left(\int_{-\infty}^{\infty}\left(x-x_f^*\right)^2\left|f(x)\right|^2dx\right)^{1/2}, \quad (13)$$

$$\omega_{\hat f}^*=\frac{1}{\left\|\hat f(\omega)\right\|^2}\int_{-\infty}^{\infty}\omega\left|\hat f(\omega)\right|^2d\omega, \quad (14)$$

$$\Delta_\omega=\frac{1}{\left\|\hat f(\omega)\right\|}\left(\int_{-\infty}^{\infty}\left(\omega-\omega_{\hat f}^*\right)^2\left|\hat f(\omega)\right|^2d\omega\right)^{1/2}. \quad (15)$$

Time-and-frequency localization is characterized by product $\Delta=\Delta_x\Delta_\omega$.

In table 2 the physical characteristics of Kravchenko wavelets are resulted. The real and imaginary parts of new wavelets and their spectra are presented on Fig. 1-4.

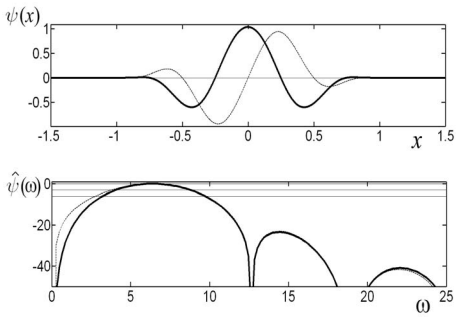


Fig. 1. (a): Function $\psi_h(t)$, (b): its spectra for $a=2,\ \eta=2\pi$ (solid line is real part, dashed line is imaginary one).

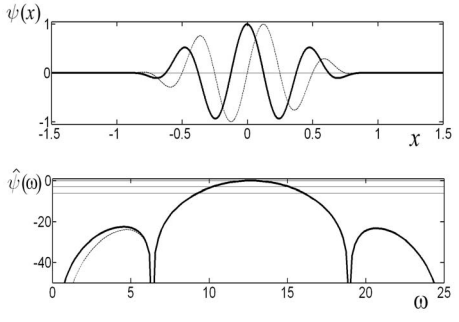


Fig. 2. (a): Function $\psi_h(t)$, (b): its spectra for $a=2,\ \eta=4\pi$ (solid line is real part, dashed line is imaginary one).

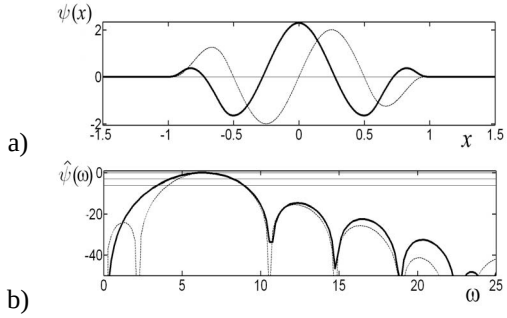


Fig. 3. (a): Function $\psi_h(t)$, (b): its spectra for $a = 4$, $\eta = 2\pi$ (solid line is real part, dashed line is imaginary one).

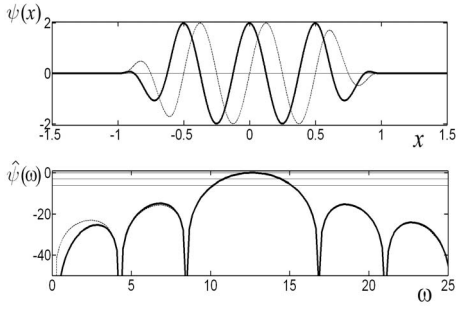


Fig. 4. (a): Function $\psi_h(t)$, (b): its spectra for $a = 4$, $\eta = 4\pi$ (solid line is real part, dashed line is imaginary one).

3. CONCLUSION

Advantage of complex WA-systems of Kravchenko functions in comparison with Morle wavelet is exact performance of a condition of a zero average for any value of modulation parametre. As parent AF is finit than at scaling of argument the kind of $A(\eta)$ does not change. If to put $\eta = \nu_i$, $i = 1,2,3,...$ where ν_i is zeros of $A(\eta)$ then (6) becomes simpler. The constructed wavelets have a compact support and they are infinitely differentiable. On their basis the 2D and orthogonal wavelets are constructed.

REFERENCES

1. Kravchenko V.F. 2003, Lectures on the Theory of Atomic Functions and their some Applications, Moscow, Publishing House Radio Engineering.
2. Kravchenko V.F., Rvachev V.L. 2006, Boolean Algebra, Atomic Functions and Wavelets in Physical Applications. Moscow, Fizmatlit.
3. Digital Signal and Image Processing in Radio Physical Applications, Edited by V.F. Kravchenko, Moscow, Fizmatlit, 2007.
4. Volosyuk V.K., Kravchenko V.F. 2008, Statistical Theory of Radio Technical Systems of Remote Sensing and Radar. Moscow, Fizmatlit.
5. Kravchenko, V.F., Perez-Meana, H.M., and Ponomaryov, V.I. 2009, Adaptive Digital Processing of Multidimentional Signals with Applications, Moscow, Fizmatlit.
6. Kravchenko, V.F., Churikov, D.V., 2008, 'Digital Processing and Spectral Estimation of Ultra-wideband Signals by Atomic Functions and Wavelets', *The Successes of Modern Radio Electronics*, **8**, 39-46.
7. Kravchenko, V.F., Churikov, D.V., 2009, A New Class of Orthogonal Kravchenko WA-system Functions $\left\{\widetilde{h_a(t)}\right\}$, Telecommunications and Radio Engineering, 68, **8**, 649-666.

Table 2. Physical characteristics of the real (*Re*) and imaginary (*Im*) parts of Kravchenko wavelets.

η	a		μ	γ_1	γ_2	γ_4	γ_7	γ_8	γ_9	γ_{10}	γ_{11}	Δ
π	*Re*	2	1,162	0,852	0,923	0,992	0,328	2,373	-18,421	0,820	4,572	0,023
	Im	2	1,556	0,587	1,275	0,857	0,318	2,521	-24,209	0,741	4,756	0,023
	Re	3	1,156	0,865	0,854	1,000	0,727	2,077	-14,011	1,083	4,257	0,019
	Im	3	1,536	0,604	1,154	0,858	0,695	2,275	-17,582	0,994	4,564	0,019
	Re	4	1,153	0,878	0,833	1,000	1,104	1,992	-12,353	1,220	4,213	0,017
	Im	4	1,508	0,612	1,123	0,878	1,060	2,161	-15,869	1,135	4,482	0,017
	Re	5	1,122	0,891	0,840	1,022	1,457	1,960	-11,413	1,311	4,233	0,016
	Im	5	1,548	0,604	1,114	0,854	1,412	2,087	-15,586	1,223	4,418	0,016
	Re	6	1,150	0,870	0,810	0,989	1,796	1,944	-10,890	1,377	4,263	0,015
	Im	6	1,533	0,609	1,118	0,870	1,755	2,036	-15,711	1,282	4,368	0,016
2π	*Re*	2	1,187	0,829	0,992	0,987	0,331	2,883	-23,537	0,556	5,154	0,019
	Im	2	1,350	0,759	0,947	0,946	0,318	3,108	-23,063	0,509	5,434	0,018
	Re	3	1,115	0,912	0,817	1,022	0,607	2,601	-16,801	0,701	4,854	0,017
	Im	3	1,008	1,016	0,786	1,079	0,632	2,402	-16,978	0,822	4,627	0,017
	Re	4	1,041	0,984	0,759	1,071	0,903	2,405	-14,642	0,837	4,648	0,016
	Im	4	0,844	1,185	0,745	1,167	0,955	2,149	-15,528	1,023	4,345	0,016
	Re	5	1,008	1,033	0,719	1,090	1,238	2,259	-13,968	0,941	4,480	0,015
	Im	5	0,791	1,255	0,704	1,196	1,296	2,061	-14,484	1,160	4,301	0,015
	Re	6	0,959	1,085	0,684	1,110	1,588	2,163	-13,501	1,020	4,370	0,014
	Im	6	0,750	1,333	0,679	1,229	1,641	2,026	-13,991	1,256	4,322	0,015

ULTRAWIDEBAND SIGNALS CONSTRUCTED FROM GENERALIZED WEYL-HEISENBERG BASES

Petrov D. A.

Lomonosov Moscow State University, Moscow, Russia
E-mail: dapetroff@gmail.com

Abstract

One type of UWB modulation is multiband-based and is accomplished by using multicarrier or OFDM. In the media with time-frequency dispersion well-localized bases ensure the best signal reconstruction. Generalized Weyl-Heisenberg bases structure, construction and optimization are considered. Presented modeling results confirm good localization characteristics for optimal parameters. This article presents the research work related to the development of enhanced modulation technique with Orthogonal Time-Frequency Division Multiplexing (OFTDM).

Keywords: OFDM, OFTDM, Weyl-Heisneberg basis, interchannel interference, digital modulation, broadband communication systems.

1. INTRODUCTION

Essentially, ultrawideband (UWB) communications come in one of two types – single-band and multiband. Impulse radio is a single-band UWB system. In impulse radio, the signal that represents a symbol consists of serial pulses with a very low duty cycle. The pulse width is very narrow, typically in nanoseconds. This small pulse width gives rise to a large bandwidth and a better resolution of multipath in UWB channels [1].

The other type of UWB modulation is multiband-based and is accomplished by using multicarrier or orthogonal frequency division multiplexing (OFDM). With OFDM-based modulation, systems can effectively deal with delay spread or frequency selectivity of UWB channels.

Transition over wireless channels is exposed to time-dispersion and frequency-dispersion. OFDM systems possess high spectral efficiency and robustness against multipath fading and impulse noise. Incorporation of cyclic prefix (CP) eliminates the influence of time-dispersion but reduces spectral and energy efficiency. In addition CP does not provide protection against frequency-dispersion caused by Doppler spread. In classical OFDM systems square pulse shaping functions are used [1]. In frequency domain they have the form of $\mathrm{sinc}\left(f\right)$ (or $\sin\left(f\right)\big/f$) function which has rather flat tails and is not localized well enough. Frequency-dispersion causes loss of orthogonality between subcarriers and result in errors, which depends critically on the frequency-localization of the transmitter pulse shaping function.

In the media with time-frequency dispersion well-localized bases ensure the best signal reconstruction [2, 3]. Utilization of such bases makes it possible to construct dens signal packages in time and frequency domain. In addition reduced number of guard intervals (or CPs) can be used to achieve better spectral and power efficiency. Thus, such extended modulation can be named OFTDM (Orthogonal Frequency-Time Division Multiplexing).

2. GENERALIZED WEYL-HEISENBERG BASES

2.1. DESCRIPTION

Generalized Weyl-Heizenberg bases are constructed by uniform shifts of one or several initializing (prototype) functions in time and frequency. Such bases are used for construction or model description of complex broadband signals. In general the set of these signals is defined as the linear shell over Weyl-Heizenberg basis functions.

It is well known that in digital communication systems based on OFDM transition principal to achieve maximal spectral efficiency is possible by using offset QAM [2-4]. Consistent with this type of modulation orthogonal Weyl-Heisenberg basis $\mathcal{B}\left[J_N\right]$ and transmitted OFTDM signal $s\left(t\right)$ in discrete time can be equivalently presented in the following form:

$$s\left[n\right]=\sum_{k=0}^{M-1}\left(\sum_{l=0}^{L-1}c_{k,l}^{R}\psi_{k,l}^{R}\left[n\right]+\right.$$
$$\left.+\sum_{l=0}^{L-1}c_{k,l}^{I}\psi_{k,l}^{I}\left[n\right]\right),\ n\in J_N, \tag{1}$$

$$\psi_{k,l}^{R}\left[n\right]=g\left[\left(n-lM\right)_{\mathrm{mod}\,N}\right]\cdot$$
$$\cdot\exp\left(j\frac{2\pi}{M}k\left(n-\alpha/2\right)\right), \tag{2}$$

978-1-4244-7468-4/10/$26 ©2010 IEEE

$$\psi_{k,l}^{I}\left[n\right] = -jg\left[\left(n + M\,/\,2 - lM\right)_{\mathrm{mod}\,N}\right]\cdot \cdot\exp\left(j\frac{2\pi}{M}k\left(n-\alpha/2\right)\right), \quad (3)$$

$$\mathcal{B}\left[J_N\right] \triangleq \left\{\psi_{k,l}^{R}\left[n\right], \psi_{k,l}^{I}\left[n\right]\right\}, \quad (4)$$

where sampling period $\Lambda = 1/MK\sigma_f$, σ_f is dispersion of the initializing function $g\left[n\right] = g\left[\Lambda n\right]$ in frequency domain, K is discretization parameter; $c_{k,l}^{R} = \mathrm{Re}(a_{k,l})$ and $c_{k,l}^{I} = \mathrm{Im}(a_{k,l})$ are real and imaginary parts of ordinary complex information QAM symbols $a_{k,l}$; $s\left[n\right] = s\left(nT/M\right)$; $J_N = \left\{0,1,...,N-1\right\}$, $N = L\cdot M$, $M \geq 2$ is even number of subcarriers, $L \neq 0$ is natural number; α is a phase parameter.

The system of basic functions $\mathcal{B}\left[J_N\right]$ is orthogonal in terms of real scalar product defined on the Hilbert space of discrete functions on J_N

$$\left\langle x\left[n\right], y\left[n\right]\right\rangle_R = \mathrm{Re}\sum_{n=0}^{N-1} x\left[n\right]\cdot y^{*}\left[n\right],$$

where * is the sign of complex conjugation.

Equation (1) describes the modulation algorithm of OFTDM signal in discrete time. Appropriate demodulation algorithm has the form

$$c_{k,l}^{R} = \left\langle s\left[n\right], \psi_{k,l}^{R}\left[n\right]\right\rangle_R,\ c_{k,l}^{I} = \left\langle s\left[n\right], \psi_{k,l}^{I}\left[n\right]\right\rangle_R.$$

2.2. SYNTHESIS

It is well known that time-frequency localization is limited by Heisenberg uncertainty relation

$$\sigma_\omega\sigma_\tau \geq 1/2, \quad (5)$$

where $\sigma_\omega = 2\pi\sigma_f$ and σ_τ corresponds to function's dispersion in frequency and time domain respectively. Expression (5) becomes an equality only for a Gaussian function

$$g_G\left(t\right) = \left(2\sigma_o\right)^{1/4}\exp\left(-\pi\sigma_o t^2\right),$$

where σ_o is localization governing parameter. In isotropic case $\sigma_\tau = \sigma_f = 1/\sqrt{4\pi}$ and

$$g_G^{isot}\left[n\right] = 2^{1/4}\exp\left(-\left(\frac{2\pi n}{MK}\right)^2\right). \quad (6)$$

Unfortunately WH-basis constructed from (6) (Gabor basis) will not be orthogonal. Thus, the following problem [5] should be solved:

Problem 1. On the subset $\mathfrak{A}$ of complex matrixes of size $N\times 2N$, which satisfy orthogonality condition

$$\mathrm{Re}(\mathbf{U}^{*}\mathbf{U}) = \mathbf{I}_{2N},\ \mathbf{U}\in\mathfrak{A}$$

it is necessary to find an optimal matrix $\mathbf{U}_{opt}$ which minimizes the following functional:

$$\mathbf{U}_{opt} : \min_{\mathbf{U}\in\mathfrak{A}}\left\|\mathbf{G}-\mathbf{U}\right\|_E^2, \quad (7)$$

where $\mathbf{G}$ is the Gabor basis matrix, $\left\|\mathbf{A}\right\|_E^2 = \mathrm{tr}(\mathbf{A}\mathbf{A}^{*})$ is the Frobenius norm and $\mathbf{U} = \left(\mathbf{U}_R, \mathbf{U}_I\right)$ is a $N\times 2N$ block matrix of basis $\mathcal{B}\left[J_N\right]$ with blocks $\mathbf{U}_R$, $\mathbf{U}_I$ - square $N\times N$ matrixes constructed from columns of basic functions (2), (3) for all indexes $k = 0,...,M-1$, $l = 0,...,L-1$.

2.3. OPTIMIZATION

Phase parameter α is included in the problem (7) as the parameter. It is possible to enhance the basis localization by solving the following extremal problem:

Problem 2. It is necessary to find such α_{opt} that minimizes the following functional:

$$a_{opt}:\ \min_{\alpha\in\mathbb{R}}\left(\left\|\mathbf{G}\left(\alpha\right)-\mathbf{U}_{opt}\right\|_E^2\right). \quad (8)$$

This problem can be analytically solved if forming function $g\left[n\right]$ is conjugate N-symmetrical $g\left[n\right] = g^{*}\left[\left(-n\right)_{\mathrm{mod}\,N}\right]$. In this case $\alpha_{opt} = M/2-1$.

It was also found that the quality of localization is strongly influenced by the choice of discretisation parameter K.

Problem 3. It is necessary to find such K_{opt} that minimizes the following functional:

$$K_{opt}:\ \min_{K\in\mathbb{R}}\left(\left\|\mathbf{G}\left(K\right)-\mathbf{U}_{opt}\right\|_E^2\right). \quad (9)$$

This problem was solved numerically for isotropic case.

3. MODELING RESULTS

Any shifts of phase parameter from the optimal value leads to loss of symmetry of basic functions. In addition side lobes increase (Fig. 2). For $\alpha > \alpha_{opt} = M/2-1$ lobes increase from the left and for $\alpha < \alpha_{opt}$ - from the right.

In isotropic case $K_{opt}\approx 2.5$. It is important that this value doesn't depend on basis parameters M and L. Any shifts from the optimal value also leads to the loss of localisation in time $K > K_{otp}$ or frequency $K < K_{opt}$ domain (Fig. 1).

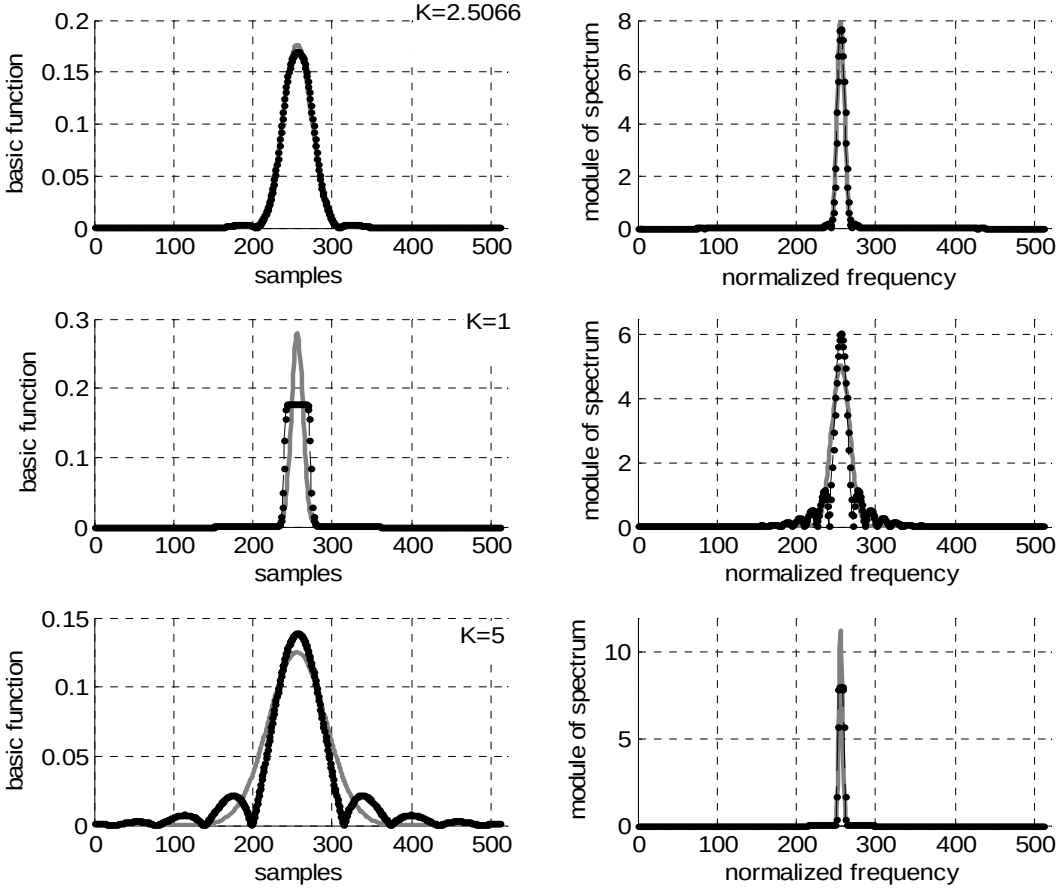


Fig. 1. Time (from the left) – frequency (from the right) localization of WH-basis initializing function (black dots) for several values of discretization parameter K. Gaussian function – grey curves.

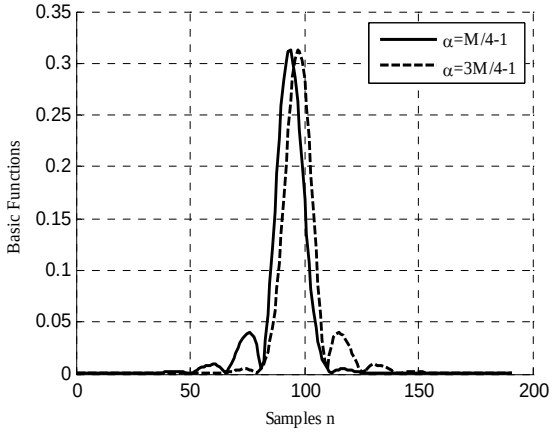


Fig. 2. Optimal basic function for $\alpha \neq \alpha_{opt}$.

4. CONCLUSION

Received results present the practical way of well-localized WH-bases utilization for UWB communications.

REFERENCES

1. Shen, X., Guisani, M., Qui, R.C., and Le-Ngoc, T. 2006, *Ultra-wideband Wireless Communications and Network*, John Wiley & Sons, Ltd.
2. Volchkov, V.P., Petrov, D.A. 2009, 'Orthogonal Well-Localized Weyl-Heisenberg Basis Construction and Optimization for Multicarrier Digital Communication Systems' *Proc. ICUMT 2009*. St. Petersburg, ISBN: 978-1-4244-3941-6, IEEE Catalog Number: CFP0963G-CDR.
3. Le Floch, B. 1995, 'Coded Orthogonal Frequency Division Multiplex'. *Proc. of the IEEE*, vol. 83, 6, 982-986.
4. Petrov D.A. 2009, 'Efficient Algorithm of Well-Localized Bases Construction for OFTDM systems.' In: *Proc. of 6th seminar FRUCT*, Helsinki, Finland, 2009, 106-113
5. Petrov D.A. 2010, 'Well-localized Bases Construction and optimization', *Matem. Mod. (Mathematical Modeling)*, **22**:3, 45–54.

THE ANALYSES OF PROCESS OF GENERATION AND RESONANCE SCATTERING OF WAVES ON CUBICALLY POLARISABLE LAYERED STRUCTURE

[1] Angermann L., [2] Yatsyk V. V. and [3] Yatsyk M. V.

[1] Institut für Mathematik, Technische Universität Clausthal, Germany
E-mail: lutz.angermann@tu-clausthal.de
[2] Usikov Institute of Radiophysics and Electronics NASU, Kharkov, Ukraine
E-mail: yatsyk@vk.kharkov.ua; vasyl.yatsyk@rambler.ru
[3] Kharkov National University of Radio Electronics, Kharkov, Ukraine
E-mail: kolya.yatsyk@rambler.ru

Abstract

The analysis of the scattering problem and the generation of the third harmonic by excitation by a plane wave passing a non-linear, isotropic, cubically polarisable, non-magnetic, linearly polarised (E polarisation), layered dielectric structure is carried out. Results of the numerical investigation of both the values of the non-linear dielectric constants corresponding to given amplitude of the incident field and of the scattered and generated fields are presented.

Keywords: Resonance scattering, cubic polarisability, generation of waves.

1. THE SCATTERING PROBLEM AND THE GENERATION OF THE THIRD HARMONIC

Consider the scattering problem and the generation of the third harmonic by excitation by a plane stationary electromagnetic wave on a nonmagnetic, isotropic, transversely inhomogeneous, and linearly polarized $\mathbf{E}=\left(E_x,0,0\right)$, $\mathbf{H}=\left(0,H_y,H_z\right)$ (E-polarization) the time dependence is $\exp\left(-in\omega t\right)$, with vector of cubically polarization $\mathbf{P}^{(\mathrm{NL})}=\left(P_x^{(\mathrm{NL})},0,0\right)$ nonlinearity layered dielectric structure, see Fig. 1.

The analysis of the diffraction problem of the plane wave $E_x^{\mathrm{inc}}\left(\kappa;y,z\right)=a_\kappa^{\mathrm{inc}}\exp\left(i\left[\Phi_\kappa y-\Gamma_\kappa\left(z-2\pi\delta\right)\right]\right)$ on the nonlinear structure with the Kleinman relation [1, 2] $\chi^{(3)}_{xxxx}\left(1\kappa\right)=\chi^{(3)}_{xxxx}\left(2\kappa\right)=\chi^{(3)}_{xxxx}\left(3\kappa\right)\equiv\chi^{(3)}_{xxxx}$ use is reduced to system of boundary problems [3-5]

$$\begin{cases}\left[\nabla^2+\kappa^2\varepsilon_\kappa\left(z,\alpha\left(z\right),E_x\left(\kappa;y,z\right),E_x\left(\kappa;y,z\right)\right)\right]\times\\ \qquad\times E_x\left(\kappa;y,z\right)=0,\\ \left[\nabla^2+\left(3\kappa\right)^2\varepsilon_{3\kappa}\left(z,\alpha\left(z\right),E_x\left(3\kappa;y,z\right),E_x\left(3\kappa;y,z\right)\right)\right]\times\\ \qquad\times E_x\left(3\kappa;y,z\right)=-\frac{1}{3}\alpha\left(z\right)\left(3\kappa\right)^2{E_x}^3\left(\kappa;y,z\right),\end{cases}\tag{1}$$

with generalized boundary to conditions for the complex Fourier amplitudes of the full fields of scattering and generation $E_x\left(n\kappa;y,z\right)=\delta_n^1E_x^{\mathrm{inc}}\left(n\kappa;y,z\right)+E_x^{\mathrm{scat}}\left(n\kappa;y,z\right)$ (where δ_n^m Kronecker delta):

$E_{\mathrm{tg}}\left(n\kappa;y,z\right)$ and $H_{\mathrm{tg}}\left(n\kappa;y,z\right)$ continuous on bonders of layers of nonlinear structure $\varepsilon_{n\kappa}$;

condition of spatial inhomogeneity on y, i.e. $E_x\left(n\kappa;y,z\right)=U\left(n\kappa;z\right)\exp\left(i\Phi_{n\kappa}y\right)$;

condition of phase synchronism of waves $\Phi_{n\kappa}=n\cdot\Phi_\kappa$, $n=1,3$, where $\Phi_{n\kappa}=n\kappa\sin\phi_{n\kappa}$;

and radiation conditions for the scattered and generation field

$$E_x^{scat}\left(n\kappa;y,z\right)=\\ =\begin{Bmatrix}a_{n\kappa}^{scat}\\ b_{n\kappa}^{scat}\end{Bmatrix}\exp\left(i\cdot\left(\Phi_{n\kappa}y\pm\Gamma_{n\kappa}\cdot\left(z\mp2\pi\delta\right)\right)\right),\ z\gtrless\pm2\pi\delta,$$

here $\Gamma_{n\kappa}=\sqrt{\left(n\kappa\right)^2-\Phi_{n\kappa}^2}>0,\quad n=1,3.$

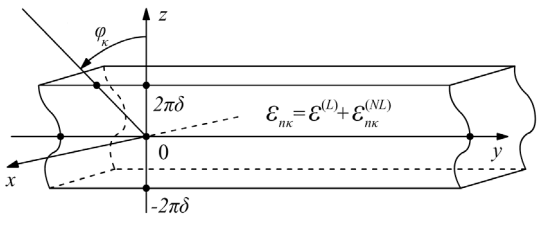


Fig. 1. The nonlinear dielectric layered structure.

978-1-4244-7468-4/10/$26 ©2010 IEEE

From the conditions of spatial inhomogeneity fields and homogeneity structure on y follows the condition of phase synchronism of waves $\Phi_{n\kappa} = n \cdot \Phi_{\kappa}$, $n = 1, 3$. This condition allows defining also corners of waves leaving from a layer $\phi_{n\kappa}^{\text{scat}} = -\phi_{n\kappa}$ in a reflection zone $z > 2\pi\delta$ and $\phi_{n\kappa}^{\text{scat}} = \pi + \phi_{n\kappa}$ in a zone of passage of a nonlinear structure at $z < -2\pi\delta$. From it the condition $\phi_{n\kappa} = \phi_{\kappa}$ also follows.

We look for the solution to problem in the form:

$$E_x\left(n\kappa; y, z\right) = U\left(n\kappa; z\right)\mathrm{e}^{i\Phi_{n\kappa}y} = \begin{cases} \delta_n^1 a_{n\kappa}^{\text{inc}}\, e^{i\left[\Phi_{n\kappa}\, y - \Gamma_{n\kappa}\cdot\left(z-2\pi\delta\right)\right]} + \\ +a_{n\kappa}^{\text{scat}} e^{i\left[\Phi_{n\kappa}y + \Gamma_{n\kappa}\cdot\left(z-2\pi\delta\right)\right]}, & z > 2\pi\delta, \\ U\left(n\kappa; z\right)\mathrm{e}^{i\Phi_{n\kappa}y}, & \left|z\right| \le 2\pi\delta, \\ b_{n\kappa}^{\text{scat}}\, \mathrm{e}^{i\left[\Phi_{n\kappa}y - \Gamma_{n\kappa}\cdot\left(z+2\pi\delta\right)\right]}, & z < -2\pi\delta. \end{cases} \quad (2)$$

Where: $U\left(n\kappa; 2\pi\delta\right) = \delta_n^1 a_{n\kappa}^{\text{inc}} + a_{n\kappa}^{\text{scat}}$, $U\left(n\kappa; -2\pi\delta\right) = b_{n\kappa}^{\text{scat}}$, $n = 1, 3$.

Here $\nabla^2 = \partial^2/\partial y^2 + \partial^2/\partial z^2$; $\omega = \kappa c$ is the dimensionless circular frequency; $\kappa = \omega/c \equiv 2\pi/\lambda$ is the dimensionless frequency parameter such that $h/l = 2\kappa\delta$, where λ is the free-space wavelength; c is the dimensionless quantity equal to the speed of light in the medium containing the layered structure; E_{tg} и H_{tg} - are tangential fields components on the layer boundary; $\Phi_{\kappa} = \kappa \cdot \sin\phi_{\kappa}$, ϕ_{κ} - is the angle of incidence of the plane wave on frequency κ, $|\phi_{\kappa}| < \pi/2$.

Dielectric permeability problem is $\varepsilon_{n\kappa} = \varepsilon^{(\text{L})} + \varepsilon_{n\kappa}^{(NL)}$, at $|z| \le 2\pi\delta$ and $\varepsilon_{n\kappa} = 1$, at $|z| > 2\pi\delta$; for the nonlinear layer at $|z| \le 2\pi\delta$ is [3]

$$\varepsilon_{n\kappa}\left(z, \alpha\left(z\right), E_x\left(\kappa; y, z\right), E_x\left(3\kappa; y, z\right)\right) \equiv \equiv \varepsilon_{n\kappa}\left(z, \alpha\left(z\right), U\left(\kappa; z\right), U\left(3\kappa; z\right)\right) = \varepsilon^{(\text{L})}\left(z\right) + +\alpha\left(z\right)\left(\left|U\left(\kappa; z\right)\right|^2 + \left|U\left(3\kappa; z\right)\right|^2 + \delta_n^1 \left|U\left(\kappa; z\right)\right| \times \times \left|U\left(3\kappa; z\right)\right| \exp\left\{ i\left[-3\arg U\left(\kappa; z\right) + \arg U\left(3\kappa; z\right)\right]\right\}\right), \quad \varepsilon^{(\text{L})}\left(z\right) = 1 + 4\pi\chi_{xx}^{(1)}\left(z\right), \; \alpha\left(z\right) = 3\pi\chi_{xxxx}^{(3)}\left(z\right). \quad (3)$$

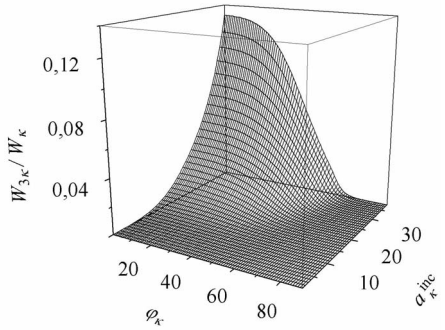


Fig. 2. Relative part of energy generated in the third harmonic.

To similarly results [3-6] we solve problem (1) by reducing it to a one-dimensional system nonlinear integral equations with respect to the scattered field components $U\left(n\kappa; z\right)$ (see (2)) in a nonlinear layer

$$U\left(n\kappa; z\right) + \frac{i\left(n\kappa\right)^2}{2\Gamma_{n\kappa}} \int_{-2\pi\delta}^{2\pi\delta} \exp\left(i\Gamma_{n\kappa}\left|z - z_0\right|\right) \times \times\left[1 - \varepsilon_{n\kappa}\left(z_0, \alpha\left(z_0\right), U\left(\kappa; z_0\right), U\left(3\kappa; z_0\right)\right)\right] \times \times U\left(n\kappa; z_0\right) dz_0 = \delta_n^1 U^{inc}\left(\kappa; z\right) + +\delta_n^3 \frac{i\left(3\kappa\right)^2}{6\Gamma_{3\kappa}} \int_{-2\pi\delta}^{2\pi\delta} \exp\left(i\Gamma_{3\kappa}\left|z - z_0\right|\right) \times \times\alpha\left(z_0\right)\left[U\left(\kappa; z_0\right)\right]^3 dz_0, \quad \left|z\right| \le 2\pi\delta, \; n = 1, 3. \quad (4)$$

System (4) and the problem (1) (just as in [3]) are reduced to system of nonlinear boundary problems of Sturm-Liouville type

$$\left\{ d^2/dz^2 + \Gamma_{n\kappa}^2 - \left(n\kappa\right)^2 \times \times\left[1 - \varepsilon_{n\kappa}\left(z, \alpha\left(z\right), U\left(\kappa; z\right), U\left(3\kappa; z\right)\right)\right]\right\} \times \times U\left(n\kappa; z\right) = -\delta_n^3 \frac{\left(3\kappa\right)^2}{3} \alpha\left(z\right)\left[U\left(\kappa; z\right)\right]^3, \quad \left|z\right| \le 2\pi\delta \quad (5)$$

$$\left(i\Gamma_{n\kappa} - d/dz\right)U\left(n\kappa; 2\pi\delta\right) = \delta_n^1 2i\Gamma_{\kappa} U^{inc}\left(\kappa; 2\pi\delta\right),$$
$$\left(i\Gamma_{n\kappa} + d/dz\right)U\left(n\kappa; -2\pi\delta\right) = 0; \; n = 1, 3.$$

On the basis of outcomes reduced in [3], the solution (5) can be received a finite element method.

2. THE NUMERICAL ANALYSES OF SCATTERING AND GENERATION

The numerical analysis of resonant scattering and generation of the third harmonic is presented further. Let's consider nonlinear dielectric layered structure $\varepsilon_{n\kappa}\left(z, \alpha\left(z\right), U\left(\kappa; z\right), U\left(3\kappa; z\right)\right) = \varepsilon^{(\text{L})} + \varepsilon_{n\kappa}^{(\text{NL})}$ (see (3)), with $\left\{\varepsilon^{(\text{L})}\left(z\right), \alpha\left(z\right)\right\} =$

$$= \begin{Bmatrix} \left\{\varepsilon^{(\text{L})} = 16, \alpha = \alpha_1\right\}, & z \in \left[-2\pi\delta, \; -2\pi\delta/3\right) \\ \left\{\varepsilon^{(\text{L})} = 64, \alpha = \alpha_2\right\}, & z \in \left[-2\pi\delta/3, \; 2\pi\delta/3\right] \\ \left\{\varepsilon^{(L)} = 16, \alpha = \alpha_3\right\}, & z \in \left(2\pi\delta/3, \; 2\pi\delta\right] \end{Bmatrix}$$

Parameters of considered structure: $\alpha_1 = \alpha_3 = 0.01$, $\alpha_2 = -0.01$; $\delta = 0.5$. The frequency of incident field of the plane wave is $\kappa = 0.25$.

Let's designate $W_{n\kappa} = \left|a_{n\kappa}^{\text{scat}}\right|^2 + \left|b_{n\kappa}^{\text{scat}}\right|^2$ full energy of scattering field on frequency $n\kappa$, $n = 1, 3$. So W_{κ} the full energy scattered on frequency κ, $W_{3\kappa}$ the full energy generated on frequency 3κ. The ration $W_{3\kappa}/W_{\kappa}$ characterizes relative part of energy generated in the third harmonic at the value a_{κ}^{inc}, see Fig. 2.

In particular, $W_{3\kappa} / W_{\kappa} = 0.132$ at $a_{\kappa}^{\text{inc}} = 38$, i.e. $W_{3\kappa}$ energy generated in the third harmonic makes 13.2% of energy W_{κ}.

Presented on a Fig. 3 (curve 5) and Fig. 4 function $\text{Im}(\varepsilon_{\kappa})$ characterizes energy losses in the nonlinear layer (on frequency κ of excitation) left on generation of an electromagnetic field of the third harmonic (on frequency 3κ). Let's notice, that on frequency 3κ nonlinear dielectric permeability $\varepsilon_{3\kappa}$ is real, see Fig. 3 (curves 6, 7) and (3).

Scattering (on frequency κ) and generating (on frequency 3κ) properties of nonlinear structure are resulted in Fig. 5. Here coefficients reflection at $n = 1$ (or generation at $n = 3$) $R_{n\kappa} = \left|a_{n\kappa}^{\text{scat}}\right|^2 \Big/ \left|a_{\kappa}^{\text{inc}}\right|^2$ in zone $z > 2\pi\delta$ and transient for $n = 1$ (or generation for $n = 3$) $T_{n\kappa} = \left|b_{n\kappa}^{\text{scat}}\right|^2 \Big/ \left|a_{\kappa}^{\text{inc}}\right|^2$ in zone $z < -2\pi\delta$.

The results of the numerical analysis are received with use of the iterative scheme for (4) on a basis of Simpson's quadrature, see [3]. Systems of the equations considered at dimension of the algebraic equations of the 501 order, the relative error of calculations did not surpass value 10^{-7}.

4. CONCLUSION

The dependence characterizing the portions of generated energy in the third harmonic on the value of the amplitude of the excitation field of the non-linear structure is investigated. Within the framework of the closed system under consideration it is shown that the imaginary part of the dielectric constant, determined by the value of the non-linear part of the polarization at the excitation frequency, characterizes the loss of energy in the non-linear medium (at the frequency of the incident field) due to the generation of the electromagnetic field of the third harmonic (at the triple frequency).

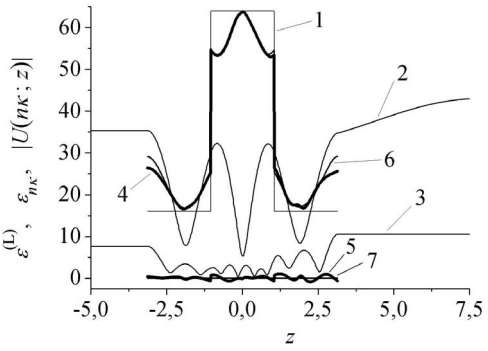


Fig. 3. Curves at $a_{\kappa}^{\text{inc}} = 38$ and $\phi_{\kappa} = 0^0$: $1 - \varepsilon^{(\text{L})}$, $2 - \left|U\left(\kappa; z\right)\right|$, $3 - \left|U\left(3\kappa; z\right)\right|$, $4 - \text{Re}\left(\varepsilon_{\kappa}\right)$, $5 - \text{Im}\left(\varepsilon_{\kappa}\right)$, $6 - \text{Re}\left(\varepsilon_{3\kappa}\right)$, $7 - \text{Im}\left(\varepsilon_{3\kappa}\right) \equiv 0$.

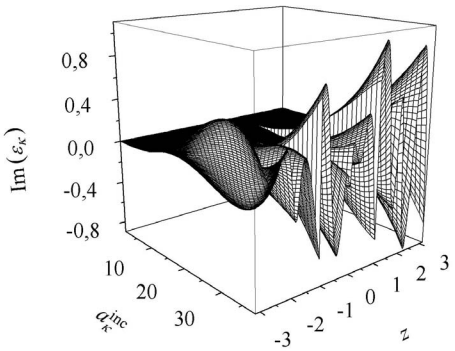


Fig. 4. Surface values $\text{Im}\left(\varepsilon_{\kappa}\left[a_{\kappa}^{\text{inc}}, z\right]\right)$ at $\phi_{\kappa} = 0^0$.

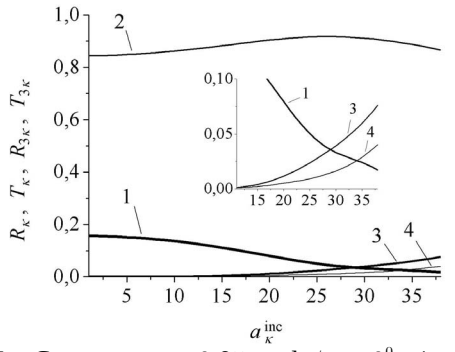


Fig. 5. Curves at $\kappa = 0.25$ and $\phi_{\kappa} = 0^0$: $1 - R_{\kappa}$, $2 - T_{\kappa}$, $3 - R_{3\kappa}$, $4 - T_{3\kappa}$

REFERENCES

1. D.A. Kleinman, “Nonlinear Dielectric Polarization in Optical Media”, Phys. Rev., Vol. 126, pp. 1977-1979, 1962.
2. B.K. Miloslavckiy, “Nonlinear Optics”, V.N. Karazin KSU, Kharkov, 2008.
3. Angermann L. and Yatsyk V.V. 2010, ‘Mathematical models of the analysis of processes of resonance scattering and generation of the third harmonic by the diffraction of a plane wave through a layered, cubically polarisable structure’, *J. Electromagnetic Waves and Electronic Systems*, **15**, no. 1, 36-49.
4. Shestopalov Yu.V. and Yatsyk V.V. 2007, ‘Resonance Scattering of Electromagnetic Waves by a Kerr Nonlinear Dielectric Layer’, *Radiotekhnika and Elektronika (J. Communications Technology and Electronics)*. **52**, no. 11, 1285-1300.
5. Kravchenko V.F. and Yatsyk V.V. 2007, ‘Effects of Resonant Scattering of Waves by Layered Dielectric Structure with Kerr-Type Nonlinearity’, *J. Electromagnetic Waves and Electronic Systems*, **12**, no. 12, 17-40.
6. Shestopalov V.P., Sirenko Yu.K. 1989, *Dynamic Theory of Gratings*, Naukova Dumka, Kiev.

TRANSIENT WAVE PROPAGATION IN RADIALLY INHOMOGENEOUS BICONICAL LINE

Kochetov B. A. and Butrym A. Yu.

Karazin Kharkov National University, Kharkov, Ukraine
E-mail: bkochetov@bk.ru

Abstract

Propagation of a transient wave in a radially inhomogeneous biconical line is considered in the time domain using mode basis method. The line is excited by impulse waveform current in a ring. Dependence of cutoff frequencies on the line geometry and dielectric filling are studied. The possibility to increase the radiating signal amplitude via introduction of radial layered dielectric filling is shown.

Keywords: Biconical line, impulse signal, time domain, spherical harmonics.

1. INTRODUCTION

Antennas based on biconical lines are traditionally used for receiving and radiating transient signals. It is explained by the fact that the TEM wave has no dispersion in this line. In biconical lines TE and TM waves can also exist. In the paper non-stationary TE-wave propagation in a regular radially inhomogeneous biconical line is considered.

2. PROBLEM STATEMENT

There is an unsymmetrical biconical line with radially inhomogeneous filling. Two circular cones with the common vertex form this line. The space between them is filled with radially inhomogeneous magneto-dielectric medium. On the surface of the cones are imposed boundary conditions that correspond to perfect electric conductor (PEC). In the spherical coordinate system, the circular cone is the coordinate surface. The first and second cones are defined via the equations $\theta = \theta_1$ and $\theta = \theta_2$, respectively. The geometry of the problem is shown in Fig. 1. The line is excited by the transient ring current of the following form:

$$\vec{J}\left(\vec{r},t\right) = \vec{\varphi}_0 \delta\left(r - R\right)\delta\left(\theta - \pi/2\right) f\left(t\right). \quad (1)$$

Here $\vec{\varphi}_0$ is the azimuth ort of spherical coordinate system, $\delta(\cdot)$ is Dirac delta-function, R is the ring radius, $f(t)$ is some arbitrary function dependent on temporal variable. For numerical calculation Laguerre impulse is used

$$f\left(t\right) = \left(t/T\right)^2 \left(1 - t/3T\right)\exp\left(-t/T\right), \quad (2)$$

where T is the scale factor.

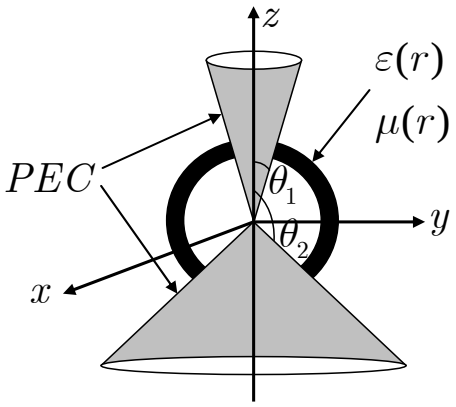


Fig. 1. An unsymmetrical radially inhomogeneous biconical line.

3. PROBLEM SOLUTION

In order to solve the problem under consideration the Mode Basis Method is used in spherical coordinate system [1, 2]. Within the framework of the method, the sought electric field in the line can be presented as follow:

$$\vec{E}\left(r,\theta,t\right) = -\frac{\vec{\varphi}_0}{\varepsilon_0^{1/2} r}\sum_{m=1}^{\infty}\frac{e_m\left(r,t\right)}{\sqrt{\nu_m\left(\nu_m+1\right)}}\frac{d\Phi_m\left(\theta\right)}{d\theta}. \quad (3)$$

Solution (3) is obtained in the form of expansion over spherical harmonics depending on the angular variable only. Functions $e_m(r,t)$, which are dependent on the radial coordinate and time, are so-called mode amplitudes. Basis functions (spherical harmonics) are determined as follow:

$$\Phi_m\left(\theta\right) = C_m\left[P_{\nu_m}\left(\cos\left(\theta\right)\right) - B_m Q_{\nu_m}\left(\cos\left(\theta\right)\right)\right]. \quad (4)$$

Here $P_{\nu_m}(\cdot)$ and $Q_{\nu_m}(\cdot)$ are the associated Legendre functions of first and second kind respectively, and

978-1-4244-7468-4/10/$26 ©2010 IEEE

constants C_m are found from the normalization condition $\frac{1}{2}\int_{\theta_1}^{\theta_2}\Phi_m(\theta)\Phi_n(\theta)\sin(\theta)d\theta = \delta_{mn}$ and

$$B_m = \left.\frac{dP_{\nu_m}\left(\cos\left(\theta\right)\right)}{d\theta}\right|_{\theta=\theta_1} \Bigg/ \left.\frac{dQ_{\nu_m}\left(\cos\left(\theta\right)\right)}{d\theta}\right|_{\theta=\theta_1} .$$

Real numbers ν_m are solutions of the following dispersion equation:

$$\begin{vmatrix} \left.\frac{dP_{\nu_m}\left(\cos\left(\theta\right)\right)}{d\theta}\right|_{\theta=\theta_1} & \left.\frac{dQ_{\nu_m}\left(\cos\left(\theta\right)\right)}{d\theta}\right|_{\theta=\theta_1} \\ \left.\frac{dP_{\nu_m}\left(\cos\left(\theta\right)\right)}{d\theta}\right|_{\theta=\theta_2} & \left.\frac{dQ_{\nu_m}\left(\cos\left(\theta\right)\right)}{d\theta}\right|_{\theta=\theta_2} \end{vmatrix} = 0 . \quad (5)$$

The expansion coefficients satisfy the following linear second order PDE with r-dependent coefficients $\varepsilon(r)$ and $\mu(r)$:

$$\begin{aligned} &\varepsilon\mu\frac{\partial^2 e_m}{\partial\tau^2} - \frac{\partial^2 e_m}{\partial r^2} + \frac{1}{\mu}\frac{d\mu}{dr}\frac{\partial e_m}{\partial r} + \mu\frac{p_m^2 e_m}{r^2} = \\ &= \frac{\sqrt{\mu_0}r\mu}{2\sqrt{\nu_m\left(\nu_m+1\right)}}\int_{\theta_1}^{\theta_2}\left(\vec{\varphi}_0\cdot\frac{\partial\vec{J}}{\partial\tau}\right)\frac{d\Phi_m^H}{d\theta}\sin(\theta)d\theta \end{aligned} \quad (6)$$

Where $\tau = ct$, c is the light velocity in vacuum.

This equation is solved by the finite difference method. At the first step, the continuous function is replaced by its discrete analogue:

$$e_m\left(r,\tau\right) \to e_m\big|_i^j = e_m\left(i\Delta r, j\Delta\tau\right) \quad (7)$$

Next, on the same grid, the finite difference approximation is used to define derivatives:

$$\begin{aligned} \left.\frac{\partial u}{\partial r}\right|_i^j &\approx \frac{u\big|_{i+1}^j - u\big|_{i-1}^j}{2\Delta r} \\ \left.\frac{\partial^2 u}{\partial r^2}\right|_i^j &\approx \frac{u\big|_{i+1}^j - 2\,u\big|_i^j + u\big|_{i-1}^j}{\Delta r^2} \\ \left.\frac{\partial^2 u}{\partial \tau^2}\right|_i^j &\approx \frac{u\big|_i^{j+1} - 2\,u\big|_i^j + u\big|_i^{j-1}}{\Delta \tau^2} \end{aligned} \quad (8)$$

Substituting (7) and (8) into equation (6) leads to the following explicit finite-difference scheme:

$$\begin{aligned} e_m^H\big|_i^{j+1} = {} & a_1\big|_i\, e_m^H\big|_i^j + a_2\big|_i\, e_m^H\big|_{i+1}^j + \\ & + a_3\big|_i\, e_m^H\big|_{i-1}^j - e_m^H\big|_i^{j-1} + F\big|_i^j \end{aligned} \quad (9)$$

Where $a_1\big|_i = 2 - \left(\Delta\tau^2\big/\varepsilon\big|_i\,\mu\big|_i\,\Delta r^2\right)\left(2 + p_m^2\big/i^2\right)$,

$a_2\big|_i = \left(\Delta\tau^2\big/\Delta r\,\varepsilon\big|_i\,\mu\big|_i\right)\left(1\big/\Delta r - \mu'\big|_i\big/2\mu\big|_i\right)$,

$a_3\big|_i = \left(\Delta\tau^2\big/\Delta r\,\varepsilon\big|_i\,\mu\big|_i\right)\left(1\big/\Delta r + \mu'\big|_i\big/2\,\mu\big|_i\right)$,

$$F\left(r,\tau\right) = -\frac{\Delta\tau^2}{\varepsilon\left(r\right)}\frac{\sqrt{\mu_0}r}{4\pi}\int_S\left[\vec{r}_0\times\frac{\partial\vec{J}}{\partial\tau}\right]\cdot\vec{H}_m^H dS ,$$

$\mu' = d\mu\big/dr$.

4. NUMERICAL RESULTS

Using formula (3) the electric field strength in the biconical line with arbitrary radially inhomogeneous magnetodielectric filling can be founded in any space point and time instant. In order to calculate the electric field in the infinite sum it is necessary taking into consideration the finite number of propagating modes only. Really, for each wavenumber k and for each sphere fixed radius R_0 only finite number of propagating modes is existed inside this sphere. The residuary modes are exponentially evanescent modes. Therefore, the influence of such modes can be neglected.

In all presented numerical results only initial ten terms in formula (3) are taken into consideration. In accordance with the results of the paper [3] it is more than enough to calculate fields with error less than 1%.

In Fig. 2 the temporal dependencies of the electric field strength in both homogeneous and radially inhomogeneous biconical line are presented. This dependences was calculated in space point $\left\{11R, \pi\big/2, \varphi\right\}$. The transmission-line parameters are $\theta_1 = \pi\big/4$, $\theta_2 = 3\pi\big/4$. In the calculations the problem parameters are chosen as follows: ring radius is $R = 1$, temporal scale factor is $T = R\big/c$. The homogeneous line is filled with vacuum. The radially inhomogeneous biconical line is filled with nonmagnetic medium with piecewise-constant permittivity. In other words, both the vertex of the cones and the ring current are shielded with a spherical dielectric layer. Impulse wave propagation in such line reminds radiation from dielectric cavity.

It follows from Fig. 2 that the amplitude of the first impulse in inhomogeneous line is greater than the impulse amplitude in homogeneous line with the same geometrical parameters. This is explained by the fact that the transient current source excites both propagating and evanescent modes. Evanescent modes decay in the pulse propagation thereby the initial pulse amplitude reduces. The cutoff frequencies decrease with increasing the radial coordinate also. In other words, the evanescent modes become propagating modes. In this case, all the excited modes are propagating in the line without filling in $R = 5$. The introduction of the dielectric filling nearly sources reduces the cutoff frequencies and leads to much less attenuation of the excited impulse. The electric field spectra are shown on Fig. 3. The dashed line corresponds to the first transmitted pulse. The field strength range is designed in the radial inhomogeneous line for the first-past

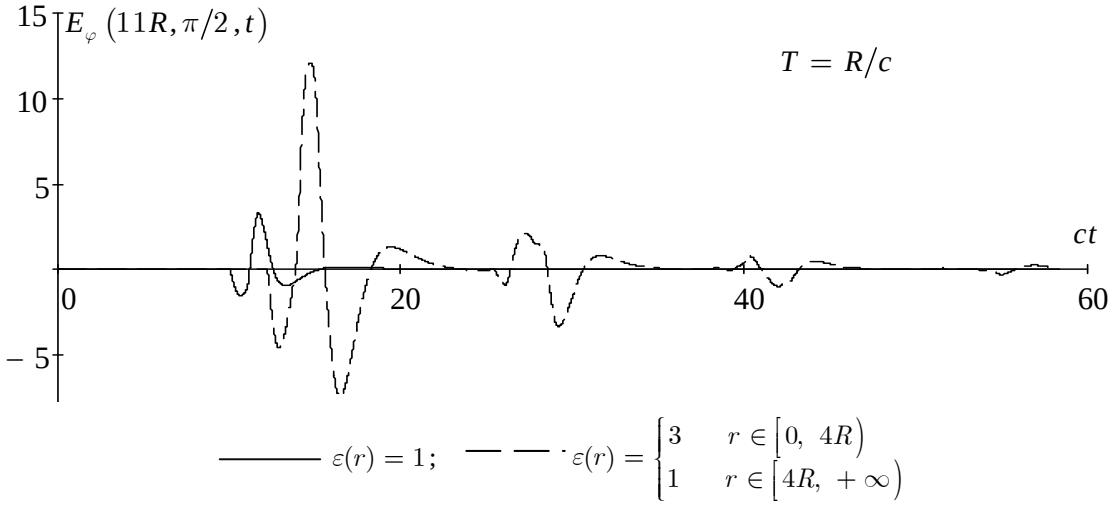


Fig. 2. The dependences of electric field strength on time are calculated in biconical in space point $\left\{11R, \pi/2, \varphi\right\}$; transmission-line parameters $\theta_1 = \pi/4$, $\theta_2 = 3\pi/4$.

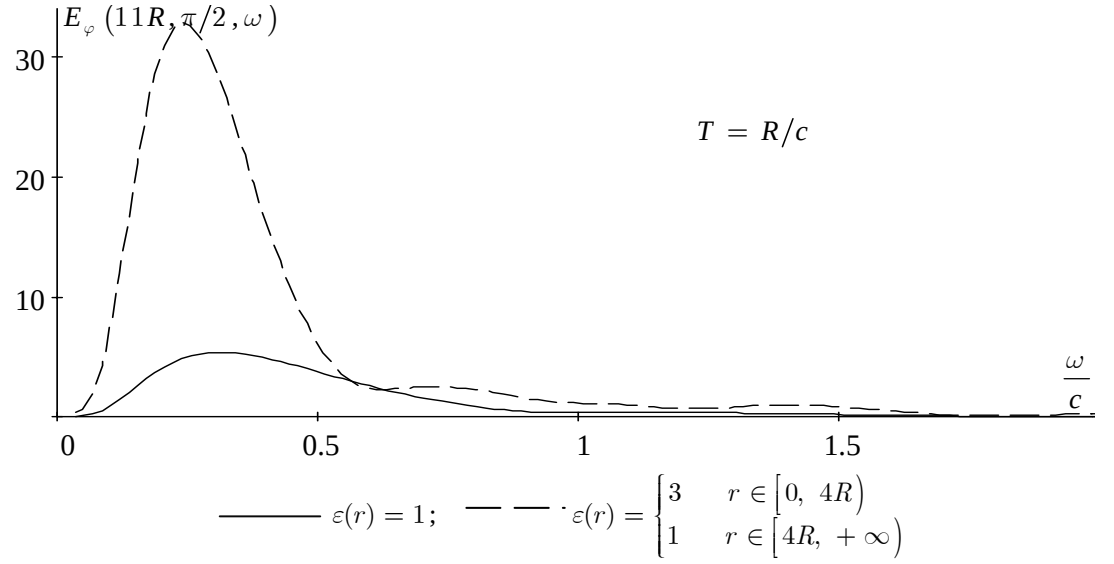


Fig. 3. The spectra of electric field strength are calculated in biconical lines in space point $\left\{11R, \pi/2, \varphi\right\}$; transmission-line parameters $\theta_1 = \pi/4$, $\theta_2 = 3\pi/4$.

momentum. The curves presented in Fig. 2 - Fig. 3 demonstrate the possibility of increasing the bandwidth of the transmission line by introducing an inhomogeneous filling.

5. CONCLUSIONS

The proposed new approach based on the mode basis method allows to calculate effectively the transient fields in conical transmission lines with inhomogeneous filling. In the framework of this method the fields in a homogeneous and radially inhomogeneous biconical transmission line is calculated. As a result, the possibility of increasing the broadband of the transmission line is shown via introducing partial filling without changing the geometrical dimensions.

REFERENCES

1. Tretyakov O., Dumin A., Dumina O., Katrich V. Modal basis method in radiation problems // *Proc. Int. Conf. on Math. Methods in Electromagnetic Theory* (MMET – 2004), Ukraine (Dnepropetrovsk), 2004. – P. 312-314.
2. Butrym A. Yu., Kochetov B. A. Mode expansion in time domain for conical lines with angular medium inhomogeneity // *PIER B.* – 2010. – Vol. 19. – P. 151-176.
3. B. A. Kochetov, A. Yu Butrym About convergence of the spherical mode expansions in time domain // *Bulletin of Kharkov national university No. 883, "Radiophysics and electronics"* – 2009. – Iss. 15. – P. 41-44. (in Russian)

OPTIMIZATION OF SIGNAL PROCESSING OF OWN RADIO-THERMAL RADIATION OF EXTENDED SOURCE IN WIDEBAND AND SUPER-WIDEBAND APERTURE SYNTHESIS SYSTEMS

Volosyuk V. K., Pavlikov V. V.

[1]National Aerospace University "Kharkiv Aviation Institute", Ukraine
[2]Air Force Center Scientific, Air Force University, Kharkov, Ukraine
E-mails: valeriy_volosyuk@mail.ru, pavlikov_kharkov@mail.ru

Abstract

The algorithm of optimum estimation the spatially-distributed parameters of fields of own radiation as functions of spatial coordinates is synthesized. This algorithm are received with reference to stationary multichannel radiometers with the arrays directed on investigated environments, and processing, which is characterized for systems of aperture synthesis. Feature of processing − application of transformations V_F and V_F^{-1} and reception of algorithms and structures of systems of broadband's and super-broadband's radiation processing, in situations when the condition space-time bandlimitedness is not carried out.

Keywords: Optimal wave fields processing, *V*-transformations, aperture synthesis.

1. INTRODUCTION

The report investigates possibilities of synthesis of algorithms optimum estimation the spatially-distributed parameters of fields of own radiation in the form of functions of spatial coordinates $\vec{\vartheta} = (\vec{\vartheta}_x, \vec{\vartheta}_y) = (\cos\vec{\theta}_x, \cos\vec{\theta}_y)$, i.e. $\vec{\lambda} = \vec{\lambda}(\vec{\vartheta})$, and, in particular, radio images of terrestrial covers in the form of spectral brightness $B(\vec{\vartheta})$ or radio-brightness temperatures $T_{Br}(\vec{\vartheta})$. This algorithm is received with reference to stationary multichannel radiometers with the arrays directed on investigated environments, and processing, characteristic for the systems of the aperture synthesis [1] which have gained the greatest distribution in radio astronomy. Is offered to use of transformations V_F and V_F^{-1} for reception of algorithms and structures of systems of processing of broadband and super-broadband radiation, in situations, when a condition space-time bandlimitedness (STB) is not carried out.

2. ALGORITHM SYNTHESIZING

2.1. INITIAL DATA

Watch equations for cases of reception of fields of own radiation of surfaces the spatially-distributed antenna systems look like:

$$\vec{\dot{u}}_{\Sigma}(t,\vec{r}') = \left\| \dot{u}_{k\Sigma}(t,\vec{r}') \right\| = \vec{\dot{u}}(t,\vec{r}',\vec{\lambda}) + \vec{\dot{n}}(t,\vec{r}'), \quad (1)$$

where $\vec{\dot{u}}(t,\vec{r}',\lambda) = \left\| \dot{u}_k(t,\vec{r}',\vec{\lambda}) \right\|$ − the registered process containing both useful making, and noise making (an external background, illumination with the sky, atmospheric noise) which cannot be separated on an input of registered system and participates further in optimum processing together with the useful; $\vec{\dot{n}}(t,\vec{r}') = \left\| \dot{n}_k(t,\vec{r}') \right\|$ − the space-time white noise playing a role of the regularizing additive (it is entered on exits of devices with frequency characteristics $\dot{K}(j2\pi f)$ in front of devices of optimum processing); $k = \overline{1,K}$ − quantity of registering elements of reception system (K should be more than number of estimated parameters $\vec{\lambda} = || \lambda_k ||$); $t \in (0,T)$ − observations time; $\vec{r}' = (x', y') \in D'$ − a vector characterizing position of elements of reception antenna system.

The spectral-angular density of complex amplitude $\dot{A}_k(\cdot)$ and spectral brightness $B_k(\cdot)$ taking into account $\dot{K}(j2\pi f)$ and directional pattern (DP) $\dot{F}_A(\vec{\vartheta} - \vec{\vartheta}_0, f)$ of the elementary aerials look like

$$\dot{A}_k(\vec{\vartheta}, f, \vec{\lambda}) = \dot{K}(j2\pi f)\dot{F}_A(\vec{\vartheta} - \vec{\vartheta}_0, f)\dot{A}_{ok}(\vec{\vartheta}, f, \vec{\lambda}), \quad (2)$$

$$B_k(\vec{\vartheta}, f, \vec{\lambda}) = \left|\dot{K}(j2\pi f)\right|^2 \left|\dot{F}_A(\vec{\vartheta} - \vec{\vartheta}_0, f)\right|^2 B_{ok}(\vec{\vartheta}, f, \vec{\lambda}), \quad (3)$$

where $\vec{\vartheta}_0$ − direction of the maximum of DP.

978-1-4244-7468-4/10/$26 ©2010 IEEE

Correlation function $R_k(\Delta r', \tau, \vec{\lambda})$ (mutual-coherence function $\dot{\Gamma}_k(\Delta r', \tau, \vec{\lambda})$) of the process $\vec{\dot{u}}(t, \vec{r}', \vec{\lambda})$ we will express through V_F - transformations [2-4]

$$\begin{aligned} R_k(\Delta r', \tau, \vec{\lambda}) &= < \dot{u}(t_1, \vec{r}_1', \vec{\lambda}) \dot{u}^*(t_2, \vec{r}_2', \vec{\lambda}) > \\ &= V_F^{-1}[B_k(\vec{\vartheta}, f, \vec{\lambda})] = \dot{\Gamma}_k(\Delta r', \tau, \vec{\lambda}). \end{aligned} \quad (4)$$

Spectral-angular density of complex amplitudes

$$\begin{aligned} \dot{A}_{ok}(\vec{\vartheta}, f, \vec{\lambda}) &= \dot{A}_{k\Sigma}(\vec{\vartheta}, f, \vec{\lambda}) = \\ &= \dot{A}_{kD}(\vec{\vartheta}, f, \vec{\lambda}) + \dot{A}_{kBg}(\vec{\vartheta}, f) \end{aligned} \quad (5)$$

and, accordingly, spectral brightness

$$\begin{aligned} B_{ok}(\vec{\vartheta}, f, \vec{\lambda}) &= B_{k\Sigma}(\vec{\vartheta}, f, \vec{\lambda}) = \\ &= B_{kD}(\vec{\vartheta}, f, \vec{\lambda}) + B_{kBg}(\vec{\vartheta}, f), \end{aligned} \quad (6)$$

contain such noises as an external background, noise of illumination by the sky, atmosphere, clouds and others, and also noise entrance registering devices which then are filtered on time and spatial frequencies by functions $\dot{K}(\cdot)$ and $\dot{F}(\cdot)$ together with useful signals of radiation. Background composed $B_{kBg}(\vec{\vartheta}, f)$ brings the basic contribution in a noise component of the accepted fluctuation. Illumination radiation usually include in useful components.

Correlation matrix of noises

$$\begin{aligned} &\left\| R_{nk}(t_1, t_2, \vec{r}_1', \vec{r}_2') \right\| = \\ &= diag\left\{ (N_{ok}/2)\, \delta(t_1 - t_2) \delta(\vec{r}_1' - \vec{r}_2') \right\}, \end{aligned} \quad (7)$$

where δ – delta function; $N_{ok}/2$ – spectral density of capacity of noises in k -th receiver.

Signal on an exit of a linear path k-th of receiver of radiometer $\dot{u}_k(t, \vec{\lambda})$ for distant Fraunhofer zone taking into account peak-phase distribution $\dot{I}_k(\vec{r}', f)$

$$\begin{aligned} \dot{u}_k(t, \lambda) &= \int_0^\infty \dot{K}(i2\pi f)\, \dot{u}_k(t, f, \vec{\lambda}) df = \\ &= \int_0^\infty \dot{K}(j2\pi f) \int_{D'} \dot{I}_k(\vec{r}', f) \int_\theta \dot{A}_{0k}(\vec{\vartheta}, f, \vec{\lambda}) \times \\ &\times \exp\left\{ j2\pi f (t - \vec{\vartheta}\vec{r}' c^{-1}) \right\} d\vec{\vartheta}\, d\vec{r}\, df. \end{aligned} \quad (8)$$

Then

$$R_{u_{k\Sigma}}(t_1, t_2, \vec{\lambda}) = R_k(t_1, t_2, \vec{\lambda}) + 0{,}5 N_{0k} \delta(t_1 - t_2), \quad (9)$$

where

$$R_k(t_1, t_2, \vec{\lambda}) = < \dot{u}_k(t_1, \vec{\lambda}) \dot{u}_k^*(t_2, \vec{\lambda}) > . \quad (10)$$

Substituting (9) in (10) and considering, that for not coherent sources

$$\begin{aligned} &< \dot{A}_{0k}(\vec{\vartheta}_1, f_1, \vec{\lambda}) \dot{A}_{0k}^*(\vec{\vartheta}_2, f_2, \vec{\lambda}) > = \\ &= B_{0k}(\vec{\vartheta}_1, f_1, \vec{\lambda}) \delta\left(f_1 - f_2\right) \delta\left(\vec{\vartheta}_1 - \vec{\vartheta}_2\right), \end{aligned}$$

and

$$| \dot{F}_A(\vec{\vartheta} - \vec{\vartheta}_0), f |^2 = | \int_{D'} \dot{I}_k(\vec{r}', f) \exp\{-i2\pi f \vec{\vartheta}\vec{r}' / c) d\vec{r}' \} |^2,$$

we receive the spectral representation of correlation function corresponding to Wiener-Khintchine theorem,

$$R_k(t_1, t_2, \vec{\lambda}) = F^{-1}\left[G_k(f, \vec{\lambda}) \right], \quad (11)$$

where a power spectrum (bilateral)

$$G_k(f, \vec{\lambda}) = \left| \dot{K}(j2\pi f) \right|^2 B_{Ak}(\vec{\vartheta}_0, f, \vec{\lambda}); \quad (12)$$

$$\begin{aligned} &B_{Ak}(\vec{\vartheta}_0, f, \vec{\lambda}) = \\ &= \int_\theta B_{0k}(\vec{\vartheta}, f, \vec{\lambda}) \left| \dot{F}_A(\vec{\vartheta} - \vec{\vartheta}_0, f) \right|^2 d\vec{\vartheta} \end{aligned} \quad (13)$$

– antenna spectral radio brightness; F^{-1} – inverse Fourier transformation.

According to Rayleigh-Jeans law connecting power brightness with temperatures of aerial T_{Ak} and radio-brightness $T_{Br\,k}$, we have

$$\begin{aligned} B_{Ak}(\vec{\vartheta}_o, f, \vec{\lambda}) &= 2k T_{Ak}(\vec{\vartheta}_0, f, \vec{\lambda})\, f^2 / c^2 = \\ &= \frac{1}{2} k f^2 c^{-2} \int_\theta T_{Br\,k}(\vec{\vartheta}, f, \vec{\lambda}) \left| \dot{F}_A(\vec{\vartheta} - \vec{\vartheta}_0), f \right|^2 d\vec{\vartheta}, \end{aligned} \quad (14)$$

where

$$\begin{aligned} &B_{0k}(\vec{\vartheta}, f, \vec{\lambda}) = B_{k\Sigma}(\vec{\vartheta}, f, \vec{\lambda}) = \\ &= B_{kD}(\vec{\vartheta}_0, f, \vec{\lambda}) + B_{kBg}; \\ &T_{Br\,k}(\vec{\vartheta}, f, \vec{\lambda}) = T_{Brk\Sigma}(\vec{\vartheta}, f, \vec{\lambda}) \\ &= T_{BrkD}(\vec{\vartheta}_0, f, \vec{\lambda}) + T_{BrkBg}. \end{aligned} \quad (15)$$

2.2. Algorithm Synthesizing

Let's receive algorithms of optimum estimation of the spatially-distributed parameters, equating to zero variation derivative of the likelihood functional's logarithm:

$$\delta \ln P\, [\vec{\dot{u}}_\Sigma(t, \vec{r}') / \vec{\lambda}(\vec{\vartheta})] / \delta \vec{\lambda}_j(\vec{\vartheta}) = 0\,.$$

Believing processes $\left\| \dot{u}_{k\Sigma}(t, \vec{r}') \right\|$ are Gaussian and independent among themselves, we will receive system of the likelihood's integrated equations of which can look like

$$\begin{aligned} &\sum_{k=1}^K \int \int_{-\infty}^\infty df_1 df_2 \frac{\partial B_{k\Sigma}[f_1, \vec{\vartheta}_1, \vec{\lambda}(\vec{\vartheta}_1)]}{\partial \lambda_j(\vec{\vartheta}_1)} \times \\ &\times \int_{-\infty}^\infty d\vec{\vartheta}_2 \frac{f_2^4}{c^4} \frac{\left| \dot{\Psi}(f_1 - f_2, f_2 \vec{\vartheta}_2 - f_1 \vec{\vartheta}_1) \right|^2}{B_{k\Sigma}[f_2, \vec{\vartheta}_2, \vec{\lambda}(\vec{\vartheta}_2)]} = \\ &= \sum_{k=1}^K \int_{-\infty}^\infty df_1 \frac{f_1^4}{c^4} \frac{\partial B_{k\Sigma}[f_1, \vec{\vartheta}_1, \vec{\lambda}(\vec{\vartheta}_1)] / \partial \lambda_j(\vec{\vartheta}_1)}{B^2{}_{k\Sigma}[f_1, \vec{\vartheta}_1, \vec{\lambda}(\vec{\vartheta}_1)]} \times \\ &\times \left| \dot{S}_{kTD'}(j2\pi f_1, \vec{\vartheta}_1) \right|^2, \end{aligned} \quad (16)$$

where $\partial B_{k\Sigma} / \partial \lambda_j$ – partial derivative;

$$\begin{aligned} &| \dot{S}_{kTD'}(j2\pi f, \vec{\vartheta}) |^2 = \\ &= | \int_T \int_{D'} \dot{u}_{k\Sigma}(t, \vec{r}') \exp\{-j2\pi f (t - \vec{\vartheta}\vec{r}' c^{-1})\} dt d\vec{r}' |^2 \end{aligned} \quad (17)$$

– V_F -periodogram, being generalization Fourier periodogram; $\dot{\Psi}(f_1 - f_2, f_1\vec{\vartheta}_1 - f_2\vec{\vartheta}_2)$ – ambiguity function of radiometric system on frequencies f and directions $\vec{\vartheta}$,

$$\left|\dot{\Psi}(\cdot)\right|^2 = \left|\int_T \int_{D'} \exp\left\{j2\pi[(f_1 - f_2)t - (f_1\vec{\vartheta}_1 - f_2\vec{\vartheta}_2)\frac{\vec{r}'}{c}]\right\} dt d\vec{r}'\right|^2 = \left|\dot{\Psi}_T(f_1 - f_2)\right|^2 \left|\dot{\Psi}_{D'}(f_1\vec{\vartheta}_1 - f_2\vec{\vartheta}_2)\right|^2.$$

At reception (16) following assumptions were accepted. Stochastic processes $u_{k\Sigma}(t,\vec{r}')$ in radio astronomy problems usually believe as ergodic and in Fraunhofer zone on variable $\vec{r}'$ statistically independent. Then correlation functions and complex mutual-coherence function these processes depend on a difference of arguments $t_1 - t_2 = \tau$ and $\Delta\vec{r}' = \vec{r}_1 - \vec{r}_2$. At performance of condition STB according to Van Zittert-Zernike theorem they are connected with spectral brightness of a extensive source of not coherent radiation with Fourier transformations.

Used below V_F -transformation allow to remove restriction on performance of this condition. Then

$$V_F[R_{k\Sigma}(\tau,\Delta\vec{r}')] = V_F[\dot{\Gamma}_{k\Sigma}(\tau,\Delta\vec{r}')] = c^2 f^{-2} B_k[f,\vec{\vartheta},\vec{\lambda}(\vec{\vartheta})] + 0,5N_{0k}, \quad (18)$$

$$B_{k\Sigma}[f,\vec{\vartheta},\vec{\lambda}(\vec{\vartheta})] = B_k[f,\vec{\vartheta},\vec{\lambda}(\vec{\vartheta})] + 0,5f^2c^{-2}N_{0k}.$$

Inverse correlation functions $W_{k\Sigma}$ is found from the integrated equation of the reversal. It is possible to show, that

$$W_{k\Sigma}[\tau,\Delta\vec{r}',\vec{\lambda}(\vec{\vartheta})] = V_F^{-1}\left\{B_{Wk}[f,\vec{\vartheta},\vec{\lambda}(\vec{\vartheta})]\right\};$$

$$B_{Wk}(\cdot) = f^4c^{-4}B_{k\Sigma}(\cdot).$$

The right parts of system (18) characterize the basic operations which are necessary for executing over the accepted field, and structure of radiometric system. Functional (mathematical) communications spectral brightness $B_{k\Sigma}$ with parameters $\vec{\lambda}$ rely known or from the decision of corresponding direct problems of dispersion for the chosen electrodynamic models, or are set in a kind the ratio regression, received experimental by. One of the most essential operations is formation V_F -periodogramm, being in itself insolvent estimation of spectral brightness $B_{k\Sigma}$ as functions of frequency f and directions $\vec{\vartheta}$.

Procedure of formation V_F -periodogram includes accepted processes separation on set of spectral components on time frequencies f, a phase delay of each of components on value $2\pi f\vec{\vartheta}\vec{r}'/c$ and inphase summation of the detained signals on all elements of array (to elements of an array), providing focusing of each component on direction $\vec{\vartheta}$ (formation of a fan of the beams covering set sector of the review and providing separate reception of signals from each direction $\vec{\vartheta}$). The multiplier before periodogram, containing size, inverse spectral brightness, sets structure of the inverse nonlinear filter in which it is carried out decorrelation of fluctuations $u_{k\Sigma}(t,\vec{r}')$. The width of a pass-band of this filter depends on intensity of noises $n_k(t,\vec{r}')$ set in (9) composed $0,5N_{0k}$ (at $N_{0k} = 0$ the pass-band is equal ∞ and the filter carries out full decorrelation of fluctuations). Averaging of the decorrelationed fluctuations at the expense of their integration on frequencies f provides a solvency of estimations of parameters $\vec{\lambda}(\vec{\vartheta})$. Decorrelation reduces radiuses of correlation of averaged processes both on frequencies f and to directions $\vec{\vartheta}$, and on time t and coordinates $\vec{r}'$, increasing number of independent readout of the received processes in spectral (on variables f and $\vec{\vartheta}$) and in spatially-time (on t and $\vec{r}'$) areas.

CONCLUSION

The algorithm optimum estimation the spatially-distributed parameters of fields of own radiation and, in particular, radio images of terrestrial covers in the form of spectral brightness $B(\vec{\vartheta})$ or radio-brightness temperatures $T_{Br}(\vec{\vartheta})$ is synthesized. These algorithms are received with reference to stationary multichannel radiometers with arrays and processing which is used in systems of aperture synthesis. It is shown, that application V_F - and V_F^{-1} -transformations allows to receive optimum algorithms of broadband's and super-broadband's radiation processing, in situations when condition STB is not carried out. The received algorithms are essentially more difficult in realization, than at performance of condition STB, however, can be shown to the last in a case when this condition is carried out.

REFERENCES

1. 'Image Formation From Coherence Functions in Astronomy' 1982. Ed. C. Van Shooneveld, Leiden Observatory, Leiden, The Netherlands.
2. Volosyuk V.K. 1993. 'Transforms of Fields and Their Correlation Functions into Spectral Characteristics of Extended Sources of Wideband Radiation [in Russian], *J. Izvestiya VUZ. Radioelektronika.* 27-30.
3. Volosyuk V.K. 1994. 'Spectral Transforms of Broadband and Their Correlation Characteristics. The Fresnel Approximation' [in Russian], *J. Izvestiya VUZ. Radioelektronika.* 58-66.
4. Volosyuk V.K. and Kravchenko V.F. 2008. 'Statistical theory of radiotechnikal systems of remote sensing and radar', Fizmatlit, Moscow.

SPACE-TIME SPECTRAL TRANSFORMATIONS OF WIDEBAND AND SUPER-WIDEBAND SIGNALS AND THEIR COHERENCE FUNCTIONS

Volosyuk V. K.

National Aerospace University "Kharkiv Aviation Institute", Kharkov, Ukraine
E-mail: valeriy_volosyuk@mail.ru

Abstract

The report proposes a new class of spectral V-transformations of wideband and super-wideband space-time signals and their modifications which are generalization of Fourier, Fresnel and Laplace transformations for analyzing and processing of wave fields. In the new V-transformations the restriction of space-time narrowity of band is removed. The Van Cittert-Zernike theorem is generalized.

Keywords: V-transformations, wave fields processing, generalization of Fourier, Fresnel, Laplace transformations and Van Cittert-Zernike theorem.

1. INTRODUCTION

At the solution of problems of mathematical physics in remote radio spectrometry [1], radio astronomy [2] and others there is a problem of applicability of Van Citterta-Zernike theorem, which connect cross-correlation function (CF) of a complex conjugate space-time processes (mutual-coherence function (CF)) with spectral brightness of a radiation's source, which coincide or like mathematical definition of the power spectral density (PSD), set by Khinchin theorem. Problem is in impossibility of division of the spatial and time component in the index of exponent. Only at performance quasi-monochromatic approximation (QMA) [2] (space-time bandlimitedness) the formulas corresponding to Van Cittert-Zernike theorem, may be analyzed as transformation (inverses) Fourier or Fresnel.

Below are proposed the transformations, which connect spacial-time processes (signals, fields), and them CF and FC with respective spectral characteristics in generally when QMA it is not carried out. These transformations are generalisation of transformations Fourier, Fresnel, Laplace for the spectral analysis of broadband and superbroadband wave fields [3-5].

2. V-TRANSFORMATIONS

2.1. INITIAL DATA

Physical and geometrical statement of a problem is illustrated on Fig. 1.

The radiation source is flat or conditionally led to a plane. Position of radiating elements are characterised or directional cosines $\vec{\vartheta} = (\vartheta_x = \cos\theta_x,\ \vartheta_y = \cos\theta_y)$, or coordinates $\vec{r} = (x, y) \in D$. Accordingly their radiating ability is characterising functions

$$\dot{A}\left(\vec{\vartheta}, f\right)\exp\left\{j2\pi ft\right\}df d\vec{\vartheta}\ ;\ \dot{A}\left(\vec{r}, f\right)\exp\left\{j2\pi ft\right\}df d\vec{r}\ ,$$

where $\dot{A}(\cdot)$ – spectrum-angular and spectrum-spatial density of complex amplitude.

The radiation field is registered by elements of plane D' through some time interval $t_3 = R(r, r')c^{-1}$ caused by delay of waves on distance R at their distribution with speed c from an element of radiation with co-ordinates $\vec{r}$ to the registering element with co-ordinates $\vec{r}' = (x', y') \in D'$.

If the area of registration of field D' is rather insignificant and is in **a Fraunghofer region**,

$$R\left[\vec{r}\left(\vec{\vartheta}\right), \vec{r}'\right] \approx R\left[\vec{r}\left(\vec{\vartheta}\right), O'\right] + \vec{\vartheta}\vec{r}'\ ;\quad \vec{\vartheta}\vec{r}' = \theta_x x' + \theta_y y'\ . \tag{1}$$

The total real field registered by an element of surface D' in point $\vec{r}'$:

$$u\left(\vec{r}', t\right) = \mathrm{Re}\int_{\vartheta}\int_{0}^{\infty}\dot{A}\left(\vec{\vartheta}, f\right) \times\exp\left\{j2\pi f\left[t - c^{-1}R\left(\vec{r}, O'\right) - c^{-1}\vec{\vartheta}\vec{r}'\right]\right\}df d\vec{\vartheta}, \tag{2}$$

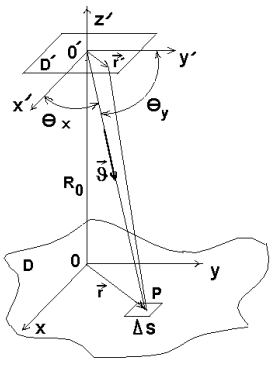


Fig. 1. Problem geometry.

978-1-4244-7468-4/10/$26 ©2010 IEEE

where $d\vec{\vartheta} = d\vartheta_x d\vartheta_y$.

Usually multiplier $\exp\{-j2\pi f c^{-1} R(\vec{r}, O')\}$ include in function $\dot{A}(\cdot)$. Entering нормированные coordinates $\vec{r}' = \vec{r}'/c$, we will write down expression for a registered field in Fraunghofer zone in a kind

$$u(\vec{r}',t) = \mathrm{Re}\int_{\vartheta}\int_{0}^{\infty} \dot{A}(\vec{\vartheta},f)\exp\left\{j2\pi f\left[t-\vec{\vartheta}\vec{r}'\right]\right\} df d\vec{\vartheta}\,. \tag{3}$$

For work in **a near-field zone** we will resolve

$$R(\vec{r},\vec{r}') = \sqrt{R(0,0')^2 + (x-x')^2 + (y-y')^2}$$

in Taylor series and we will abridge with the first members of decomposition (having entered $\left|\vec{r}-\vec{r}'\right|^2 = \left(x-x'\right)^2 + \left(y-y'\right)^2$)

$$R\left(\vec{r},\vec{r}'\right) \approx R\left(O,O'\right) + \left(\left|\vec{r}-\vec{r}'\right|^2\right)\Big/\left(2R\left(O,O'\right)\right),$$

$$u\left(\vec{r}',t\right) = \mathrm{Re}\int_{D}\int_{0}^{\infty} \dot{A}\left(\vec{\vartheta},f\right)\times$$

$$\times\exp\left\{j2\pi f\begin{bmatrix} t - c^{-1}R\left(O,O'\right) - \\ -0,5c^{-1}R^{-1}\left(O,O'\right)\left|\vec{r}-\vec{r}'\right|^2\end{bmatrix}\right\} df d\vec{r} =$$

$$= \mathrm{Re}\int_{D}\int_{0}^{\infty} \dot{A}\left(\vec{\vartheta},f\right)\exp\left\{j2\pi f\left[t-0,5\cdot\left|\vec{r}-\vec{r}'\right|^2\right]\right\} df d\vec{r}. \tag{4}$$

At performance QMA in infinite limits of integration expression (3) can be shown to three-dimensional transformation Fourier, and (4) - to transformation Fourier and Fresnel on variables f, t and $\vec{r},\vec{r}'$. However generally they cannot be considered as transformations Fourier and Fresnel [3, 4].

2.2. V_F, V_F^{-1}, V_{FL}, V_{FL}^{-1}, V_{n1}, V_{n1}^{-1}, V_{nL} AND V_{nL}^{-1} - TRANSFORMATIONS

Let's extend $\dot{A}(\vec{\vartheta},f)$ in negative area of variable f, $\dot{A}(\vec{\vartheta},f) = \dot{A}^*(\vec{\vartheta},-f)$ having reduced it in 2 times on absolute value. Considering also, that a range of definition of function $\dot{A}(\cdot)$ on variable $\vec{\vartheta}$ is circle $\vec{\vartheta}_x^2 + \vec{\vartheta}_y^2 \le 1$, will extend formally integration limits on $\pm\infty$, then

$$u\left(\vec{r}',t\right) = 0,5V_F^{-1}\left[\dot{A}\left(\vec{\vartheta},f\right)\right] = 0,5\int_{-\infty}^{\infty}\int_{-\infty}^{\infty} \dot{A}\left(\vec{\vartheta},f\right)\exp\left\{j2\pi f\left[t-\vec{\vartheta}\vec{r}'\right]\right\} df d\vec{\vartheta}\,. \tag{5}$$

Let's generalise this expression on a case when dimensions of vectors $\vec{\vartheta}$ and $\vec{r}'$ are equal *N* ($d\vec{\vartheta} = d\vartheta_1, d\vartheta_2, ..., d\vartheta_N$; $\vec{\vartheta}\vec{r} = \sum_{i=1}^{N} \vartheta_i x_i'$; *f* and *t* - scalar values).

Multiplying the left and right parts (5) on in a complex conjugate function $\exp\{-j2\pi f_1(t-\vec{\vartheta}_1\vec{r}')\}$ and integrating it on variables $\vec{r}' = \{x_i'\}$ and *t* in infinite limits it is resulted

$$0,5f^{-N}\dot{A}\left(\vec{\vartheta},f\right) = V_F\left[u\left(\vec{r}',t\right)\right] = \int\int_{-\infty}^{\infty} u\left(\vec{r}',t\right)\exp\left\{-j2\pi\left(t-\vec{\vartheta}\vec{r}'\right)\right\} dt d\vec{r}'; \tag{6}$$

$d\vec{r}' = dx_1' dx_2' ... dx_N'$.

These transformations are not Fourier transformations, as in the second composed under the sign of complex an exponent nonseparable variables *f* and $\vec{\vartheta}$ (time and spatial frequencies) and vectors, $\left\|f,\theta_1,\theta_2,...,\theta_N\right\|$ $\left\|t,x_1',x_2',...,x_N'\right\|$ do not make scalar product. However they can be considered as generalisation of transformations Fourier.

In **a condition of a near-field zone**

$$u(\vec{r}',t) = 0,5V_{n1}^{-1}\left[\dot{A}(\vec{r},f)\right] = 0,5\int_{-\infty}^{+\infty}\dot{A}(\vec{r},f)\exp\left\{j2\pi f(t-0,5\left|\vec{r}-\vec{r}'\right|^2)\right\} df d\vec{r} \tag{7}$$

$$0,5f^{-N}\dot{A}\left(\vec{r},f\right) = V_{\Phi 1}\left[u\left(\vec{r}',t\right)\right] = \int_{-}^{+}\int_{\infty}^{\infty} u\left(\vec{r}',t\right)\exp\left\{-j2\pi f\left(t-0,5\left|\vec{r}-\vec{r}'\right|^2\right)\right\} dt d\vec{r}'. \tag{8}$$

For complex analytical process $\dot{u}(\vec{r}',t) = u(\vec{r}',t) + ju_{\perp}(\vec{r}',t)$,

$$\dot{u}\left(\vec{r}',t\right) = V_{\Phi 1}^{-1}\left[\dot{A}\left(\vec{r},t\right)\right];\ f^{-N}\dot{A}\left(\vec{r},t\right) = V_{\Phi 1}\left[\dot{u}\left(\vec{r}',t\right)\right]. \tag{9}$$

Here $\dot{A}(\vec{r},f)$ – unilateral spectral density (it is equal to zero at $f<0$).

Let's pass formally in (5) and (6) from variable $j2\pi f$ to variable $p = \alpha + j2\pi f$ [4, 5]. And on variable t we will accept the bottom limit of integration equal to zero. Then we will receive

$$\dot{u}(\vec{r}',t) = 0,5\cdot V_{FL}^{-1}\left[\dot{A}(\vec{\vartheta},p)\right] = \frac{0,5}{2\pi j}\int_{-\infty}^{+\infty}\int_{\alpha-j\infty}^{\alpha+j\infty} \dot{A}(\vec{\vartheta},p)\exp\left\{p\left(t-\vec{\vartheta}\vec{r}'\right)\right\} dp d\vec{\vartheta}; \tag{10}$$

$$0,5\left(j2\pi\right)^N p^{-N}\dot{A}\left(\vec{\vartheta},p\right) = V_{FL}\left[u\left(\vec{r}',t\right)\right] = \int_{0}^{+\infty}\int_{-\infty}^{+\infty} u\left(\vec{r}',t\right)\exp\left\{-p\left(t-\vec{\vartheta}\vec{r}'\right)\right\} dt d\vec{r}; \tag{11}$$

As well as in the theory of Laplace transformations, for transformation convergence (11) on a variable it is necessary, that for all p from a range of definition of function $\dot{A}(\vec{\vartheta},p)$ the condition was satisfied:

$$\left|\int_{-\infty}^{\infty} u\left(\vec{r}',t\right)\exp\left\{p\vec{\vartheta}\vec{r}'\right\} d\vec{r}'\right| \le Me^{\gamma\cdot t}. \tag{12}$$

Valuable feature of V_{FL} and V_{FL}^{-1} transformations is that on a variable *t* they possess advantages of unilateral Laplace transformation. These transformations can be considered as generalisation of Laplace transformations, applicable for the analysis of multidimensional dynamic processes and wave fields in problems of mathematical physics.

For a **near-field zone**

$$u\left(\vec{r}',t\right)=0,5V_{\Phi L}^{-1}\left[\dot{A}\left(\vec{r},p\right)\right]$$
$$=\frac{0,5}{2\pi j}\int_{-\infty}^{+\infty}\int_{\alpha-j\infty}^{\alpha+j\infty}\dot{A}\left(\vec{r},p\right)\exp\left\{p\left(t-0,5\left|\vec{r}-\vec{r}'\right|^2\right)\right\}dpd\vec{r}; \quad (13)$$

$$0,5\left(j2\pi\right)^N p^{-N}\dot{A}\left(\vec{r},p\right)=V_{\Phi L}\left[u\left(\vec{r}',t\right)\right]$$
$$=\int_0^{+\infty}\int_{-\infty}^{+\infty}u\left(\vec{r}',t\right)\exp\left\{p\left(t-0,5\left|\vec{r}-\vec{r}'\right|^2\right)\right\}dtd\vec{r}'. \quad (14)$$

Here the same remarks are fair, as for V_{FL} и V_{FL}^{-1} transformations, i.e. also it is necessary, that the condition was satisfied

$$\left|\int_{-\infty}^{\infty}u\left(\vec{r}',t\right)\exp\left\{0,5p\left|\vec{r}-\vec{r}'\right|^2\right\}d\vec{r}'\right|\le Me^{\gamma t}.$$

2.3. SOME THEOREMS

As consequences of general Karunen theory about orthogonal decomposition of casual processes and in addition to spectral theorem Khintchine-Wiener can be considered following properties of the offered transformations.

Let casual spectral components $\dot{A}(\vec{\vartheta},f)$ and $\dot{A}(\vec{r},f)$ are uncorrelated at different values of variables θ, r and f i.e.

$$M\left[\dot{A}(\vec{\vartheta}_1,f_1)\dot{A}^*(\vec{\vartheta}_2,f_2)\right]=B\left(\vec{\vartheta}_1,f_1\right)\delta\left(\vec{\vartheta}_1-\vec{\vartheta}_2\right)\delta\left(f_1-f_2\right), \quad (15)$$

$$M\left[\dot{A}(\vec{r}_1,f_1)\dot{A}^*(\vec{r}_2,f_2)\right]=B\left(\vec{r}_1,f_1\right)\delta\left(\vec{r}_1-\vec{r}_2\right)\delta\left(f_1-f_2\right), \quad (16)$$

where $M[\cdot]$ - a population mean sign; $B[\cdot]$ - spectrum-angular and spectrum-spatial density of capacity of processes $u(\vec{r}',t)$.

Theorem 1. CF $R(\vec{\rho}',\tau)$, $\vec{\rho}'=\vec{r}_1'-\vec{r}_2',\tau=t_1-t_2$ of stationary and homogeneous process $u(\vec{r}',t)$ and its spektrum-angular density of capacity $B\left(\vec{\vartheta},f\right)$ are connected among themselves by pair V_F and V_F^{-1} transformations.

$$R(\vec{\rho}',\tau)=M\left[u(\vec{r}_1',f_1)u(\vec{r}_2',f_2)\right]=0,25V_F^{-1}\left[B\left(\vec{\vartheta},f\right)\right]; \quad (17)$$

$$0,25f^{-N}B\left(\vec{\vartheta},f\right)=V_F\left[R\left(\vec{\rho}',\tau\right)\right]. \quad (18)$$

Here PSD $B\left(\vec{\vartheta},f\right)$ is bilaterial and even function f.

Theorem 2. Mutual CF $\dot{n}(\vec{\rho}',\tau)$ in a complex conjugate analytical processes $\dot{u}(\vec{r}',t)$ and $\dot{u}^*(\vec{r}',t)$ (FC) and unilateral PSD $B(\vec{\theta},f)$ connecting among themselves in pair V_F and V_F^{-1} transformations.

$$\dot{\Gamma}\left(\vec{\rho}',\tau\right)=M\left[\dot{u}\left(\vec{r}_1',t_1\right)\dot{u}^*\left(\vec{r}_2',t_2\right)\right]=V_F^{-1}\left[B\left(\vec{\vartheta},f\right)\right], \quad (19)$$

$$f^{-N}\left[B\left(\vec{\vartheta},f\right)\right]=V_F\left[\dot{\Gamma}\left(\vec{\rho}',\tau\right)\right]. \quad (20)$$

Theorem 3. CF $R(\vec{r}_1,\vec{r}_2',\tau)$ of stationary (on a variable *t*) process (7) and PSD $B(\vec{r},f)$ (bilaterial even function f) are connected among themselves by pair transformations

$$R(\vec{r}_1,\vec{r}_2',\tau)=0,25V_{\Phi 2}^{-1}\left[B(\vec{r},f)\right]=$$
$$=0,25\int_{-}^{+}\int_{\infty}^{\infty}B(\vec{r},f)\times \quad (21)$$
$$\times\exp\left\{j2\pi f\left(\tau-0,5\left|\vec{r}_1'-\vec{r}\right|^2+0,5\left|\vec{r}_2'-\vec{r}\right|^2\right)\right\}dfd\vec{r};$$

$$0,25f^{-N}B(\vec{r},f)=V_{\Phi 2}\left[R(\vec{r}_1,\vec{r}_2',\tau)\right]=$$
$$=\int_{-}^{+}\int_{\infty}^{\infty}R(\vec{r}_1,\vec{r}_2',\tau)\times \quad (22)$$
$$\times\exp\left\{-j2\pi f\left(\tau-0,5\left|\vec{r}_1'-\vec{r}\right|^2+0,5\left|\vec{r}_2'-\vec{r}\right|^2\right)\right\}d\vec{r}_1'd\tau.$$

Theorem 4. Mutual CF in a complex conjugate analytical processes $\dot{u}(\vec{r}_1',t)$ and $\dot{u}^*(\vec{r}_2',t)$ (FC) and unilateral (equal to zero at $f<0$) spectral density $B(\vec{r},f)$ are connected among themselves by pair V_{n2} and $V^{-1}{}_{n2}$ transformations.

$$\dot{\Gamma}\left(\vec{r}_1',\vec{r}_2',\tau\right)=M\left[\dot{u}(\vec{r}_1',t_1)\dot{u}^*(\vec{r}_2',t_2)\right]=V_{\Phi 2}^{-1}\left[B\left(\vec{r},f\right)\right]; \quad (23)$$

$$f^{-N}B\left(\vec{r},f\right)=V_{\Phi 2}\left[\dot{\Gamma}\left(\vec{r}_1',\vec{r}_2',\tau\right)\right]. \quad (24)$$

CONCLUSION

Article results new transformations which establish one-to-one relation between spatial and spectral characteristics of widely - and super-broadband signals. It is shown, that these transformations are generalisation Fourier, Fresnel, Laplace transformation, and can be shown to them at performance of condition QMA. Some theorems establishing (on the basis of new transformations) communications between correlation functions (spatial coherence) and spectral brightness are resulted. The last, in particular, allow to solve radio astronomy problems when there are necessities of restoration of spatial spectral brightness of the spatially-distributed sources of own radio emission.

REFERENCES

1. Fal'kovich S.E., Ponomarev V.I. and Yu.V. Shkvarko 1989, 'Optimal Reception of Space-Time Signals in Radio Channels with Dispersion' [in Russian], Moscow, *Radio i Svyaz*.
2. 'Image Formation From Coherence Functions in Astronomy' 1982. Ed. C. Van Shooneveld, Leiden Observatory, Leiden, The Netherlands.
3. Volosyuk V.K. 1993. 'Transforms of Fields and Their Correlation Functions into Spectral Characteristics of Extended Sources of Wideband Radiation [in Russian], *J. Izvestiya VUZ. Radioelektronika.* 27-30.
4. Volosyuk V.K. 1994. 'Spectral Transforms of Broadband and Their Correlation Characteristics. The Fresnel Approximation' [in Russian], *J. Izvestiya VUZ. Radioelektronika.* 58-66.
5. Volosyuk V.K. and Kravchenko V.F. 2008. 'Statistical theory of radiotechnikal systems of remote sensing and radar', Fizmatlit, Moscow.

THEORETICAL INVESTIGATION, NUMERICAL SIMULATION. PROPAGATION AND SCATTERING IN NATURAL AND ARTIFICIAL MEDIA

MULTIELEMENT SYSTEMS OF DOUBLE SLOTS IN RECTANGULAR WAVEGUIDE WITH PARTIAL DIELECTRIC FILLING

Blinova N. K., Lyakhovsky A. A., Yatsuk L. P.

Karazin Kharkov National University, Kharkov, Ukraine
E-mail: Natalya.K.Blinova@univer.kharkov.ua

Abstract

Resonance characteristics of narrow transversal slots, energetic and directional characteristics of an antenna array (AA) with single transversal slots and double ones cut in a rectangular waveguide, partially filled with dielectric are investigated. In the case of the single transversal slots and double transversal slots a dielectric layer is parallel to broad walls of the waveguide. It was shown the possibility to construct an AA with double transversal slots the pattern without diffraction lobes and high level of radiation power in the frequency band.

Keywords: antenna array, double slots, horizontal polarization.

1. INTRODUCTION

Waveguide-slot antennas with transversal slots in a broad wall of a rectangular waveguide provide radiation having horizontal polarization. In resonance antennas transversal slots must be displaced from one to another at a distance of the waveguide wave length λ_g. In an empty waveguide this distance is greater than a wave length λ in a free space. Because of it the higher mode interference maxima appear in a radiating pattern. To prevent their appearance it is necessary to diminish the distance between the adjacent radiators. This can be achieved by means of using a down slowing system in a waveguide. For this purpose the dielectric layer parallel to the waveguide broad walls can be used. The layer width, its dielectric permittivity, a position in the cross-section of a waveguide, sizes of the slot can be used as arbitrary parameters controlling on the given frequency a phase of excitation of a slot and levels of a power, radiated and reflected by it. Such parameters are absent in a case of a hollow waveguide.

For increasing a transmission band of radiator frequencies and providing possibilities of a beam scanning of the linear waveguide-slot array in wider sector of angles sub-groups of slots are used. Such radiators are called as a group slot radiators. To them the so-called doubled slots belong. The papers [1], [2] are devoted to theoretical and experimental research of properties of the doubled longitudinal slots cut in a wide wall of a rectangular waveguide and systems of such slots as well. It was shown, that the increase of broadbandness of the doubled slot is possible only in a case when longitudinal slots are located close enough to a narrow wall of a waveguide. There are also broadband radiators as transverse double slots [3]. They are of interest from the point of view of research of possibilities of realization on their basis of aerials with wider transmission band, than aerials with single slots.

The aim of is paper is investigation of characteristics of the transverse slots systems cut in a rectangular waveguide partially filled with dielectric.

2. FOUNDATIONS OF THEORY AND METHOD OF SOLVING THE PROBLEM

The amplitude – phase distribution in multi-slot antenna can be found from the system of linear algebraic equations (SLAE) of the induced magnetomotive forces method (MF) [3] as well as the method of successive approximation which modification (MSA) was proposed in [4] for the taking into account the finite thickness of the waveguide wall and arbitrary loads. The MSA method is very useful because of the system of MF equations can be written only for one slot, that means that we need to solve only two equations instead $2N$, where N represents the number of antenna slots. Moreover, the using of MSA leads to independence of the eigen slot internal admittances from the edge load. These admittances were defined in [5]. Internal mutual slot admittances were not including into consideration with the MSA method. In the present work MSA method is applied.

It was necessary to find the conditions by which, firstly, the slot is resonance in one-mode operating band and, secondly, the wavelength in the waveguide at the resonance frequency is less than one in the free space. In order to define the one-mode operating band the cut off frequencies of higher order modes were

978-1-4244-7468-4/10/$26 ©2010 IEEE

found. The dispersion equation [7] for dominant LM-mode was solved for various t (layers thickness) and ε (permittivity). Besides the frequencies were found at which the condition $\lambda_g = \lambda$ is fulfilled. The energetic parameters of various length slots were calculated using the general theory of waveguide antennas elaborated in [3], excitation theory from [7] and formulas for the slots admittances obtained in [8]. The eigenvalues were found from the well known dispersion equations [6]. On the base of the results of [9] we came to the conclusion that the most interesting for practical applications is the case, when dielectric layer is situated tightly to the wall opposite to one where the slot is cut. In this case the resonance wavelength of the slot changes smoothly with t and ε unlike the case when dielectric is situated directly near the wall with the slot. In addition to it the slot is much better adjusted to the waveguide when the dielectric layer is apart from it.

The coefficients $\left|\dot{\Gamma}_1\right|^2$, $\left|\dot{\Gamma}_{12}\right|^2$ and $\left|S_\Sigma\right|^2$ (energetic characteristics) were calculated using general formulas from [3] in which the solution from [8] was used. The waveguide wall thickness was taken into account.

3. CALCULATION RESULTS

The calculations of energetic characteristics and directional characteristics were carried out for the systems shown in the Fig.1, when the dielectric layer is situated near wall opposite to the slot. It was supposed that $\varepsilon_1 = \varepsilon_2 = 1$, $\varepsilon_3 \neq 1$. Further we'll substitute t for b_3, where t is a thickness of the layer independently of its situation. The waveguide has cross section $a \times b = 23 \times 10\, mm$.

First of all, calculations were carried out for the slots $16\, mm$ long ($L = 16\, mm$) and $1.5\, mm$ wide ($d_1 = 1,5\, mm$). The slot was positioned symmetrically relative to the waveguide axis.

It is impotent to know on what distances $D = \lambda_g$ which is necessary to gash slots from each other in a resonant slot antenna.

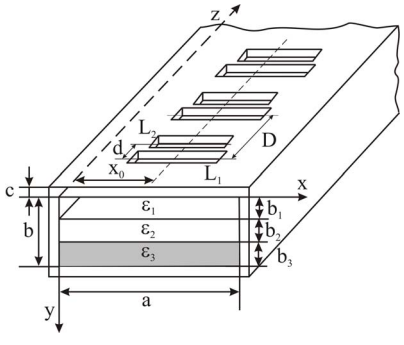


Fig. 1. Antenna array with double transverse slots in the waveguide with dielectric layer.

In order to define one-mode operating band of the waveguide considered the cut off wavelengths of higher modes were calculated [10] for the different values of t and ε. It was shown [10] that for every waveguide wavelength λ_g in the operating band $25 \le \lambda \le 45$ mm the combination of L and t can be found which provide the resonance radiation. For example, in the band $30 \le \lambda \le 38$ mm the lengths $15 \le L \le 18$ mm and 4 mm $> t >$ 3 mm are to be used.

The validity of the mathematical model constructed for one slot is confirmed to be true experimentally [10].

Calculation of power and directional performances of an array with 10 slots ($L = 16$ mm) in a hollow waveguide and in a wave guide, partly filled with dielectric was carried out. Values of t and ε were chosen: t=3.5 mm ε=7. In this case a slowness factor ξ was approximately 1,6 ($\xi = \lambda / \lambda_g$, λ – a free-space wavelength). Distance on different frequencies between adjacent radiators were $D = \lambda_g$ The calculation of these performances has been carried out for the lattice using doubled transverse slots. The dependencies of radiation coefficient and VSWR on a wave length are represented on the Fig. 2 and Fig. 3 accordingly. The curve 1 corresponds to the lattice of slots on a hollow waveguide; the curve 2 – to the lattice of single slots in a wave guide with the partial dielectric filling; the curve 3 – to the lattice of the doubled slots in a wave guide with the partial dielectric filling. For these cases the calculation of patterns were carried out on different frequencies. On the Fig.4 the pattern, calculated on λ_0=34 mm is represented.

In the lattice with doubled transverse slots the lengths L_1 of the first slots in each group were 16 mm, lengths of the second slots in each group L_2 were selected in such way to provide a maximum level of radiation, a minimum level of reflection of the lattice in the most wide range of lengths of waves. On Fig. 2-4 the dependences of radiation coefficient, VSWR on a wave length and patterns for the case of the doubled slots having length $L_1 = 16$ mm, $L_2 = 15$ mm are represented accordingly. It is visible, that occurrence of diffraction peaks in pattern is typical for the lattice of slots on a hollow waveguide (Fig. 4 curve – 1) that is intolerable. For lattices with the single and doubled slots in a wave guide with the partial dielectric filling diffraction peaks are absent (Fig.4 curves – 2,3). Radiation coefficient for single slots in a wave guide with the partial dielectric filling has high level in a narrow range of lengths of waves. For example, in the band of $\lambda = 34 - 36$ mm $\left|S\right|^2 = 0.8$ at low VSWR <1.25 (Fig. 2-3 curves – 2). Applying in the antenna array the doubled slots and selecting lengths of the second slot in each group it is

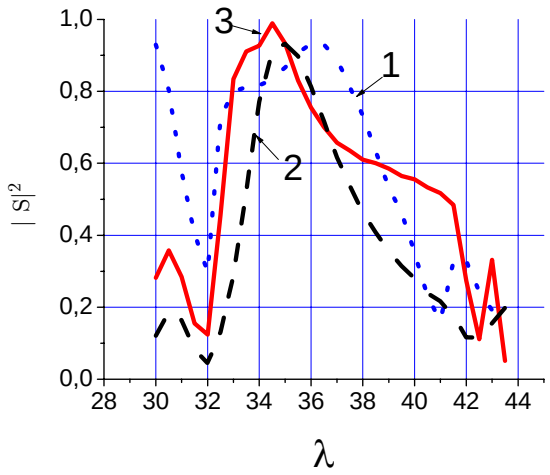


Fig. 2. Dependencies of radiation coefficient waveguide slot array.

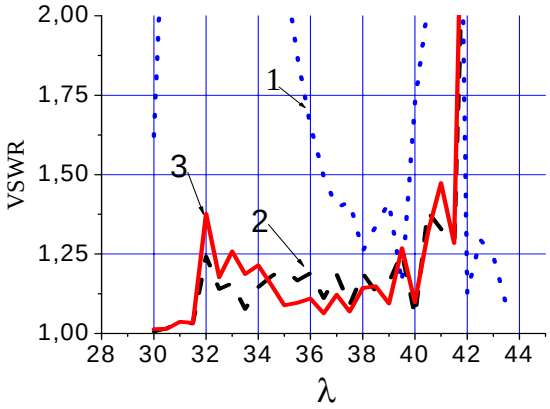


Fig. 3. Dependencies VSWR on a wave length in waveguide-slot array.

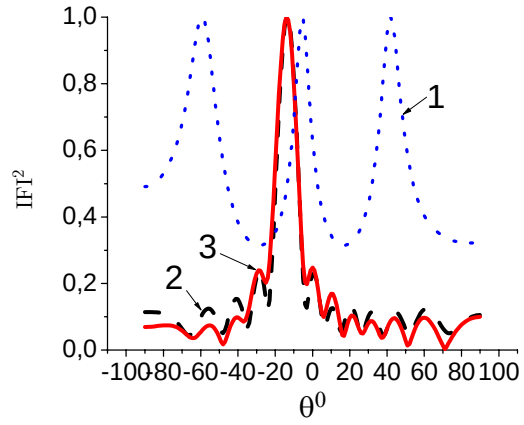


Fig. 4. The pattern of waveguide-slot array, calculated on $\lambda_0 = 34$ mm.

possible to receive wider transmission band at high $|S|^2$. For example, $|S|^2 = 0.8$ one can see in the range $33 \le \lambda \le 35.8mm$.

4. Conclusion

As a result of investigations carried out it was shown that it is possible to improve the pattern of resonance antenna with transversal slots using double slots in a waveguide, containing dielectric layer as a slowing down system. Such pattern has not diffraction lobes and works having high level of radiation in a more wide frequency band than a single slot array does.

References

1. Blinova N.K., Zhironkina A.V., Yatsuk L.P. 'Successive Approximation Method for the Linear System of Double Longitudinal Slots in a Rectangular Waveguide,' 2000, *Proc. International Conf. on Mathematical Methods in Electromagnetic theory*, Vol. 2, Kharkov, Ukraine, p. 485-487.
2. Yatsuk L.P., Blinova N.K. "Wide-band properties of the longitudinal double slot in the broad wall of rectangular waveguide" , 2001, *Radiotekhnika*, Moscow, Rassia , N. 6, p. 24-28.
3. Fel'd Ya. N. and Benenson L. S., 1959, *Antenna Feeder Devices*, Pt 2, Moscow, USSR: N.E. Zhukovsky Airforce Engineering Academy.
4. Yatsuk L.P., Blinova N.K., Zhironkina A.V. 'A mathematical model of a linear system of slots in a waveguide with an arbitrary reflecting load', 1992, *Telecommun. Radio Eng.* 2, *Radio eng.* (USA), vol. 47, no.7, p. 126-130.
5. Yatsuk L. P., 'Potential functions in the problem of exciting of the waveguide with three-layered dielectric by longitudinal magnetic current', *Radiophysics and electronics*, Kharkov, IRE NANU, N. 2-3, 212-217. 2001.
6. Egorov Y.V., 1967, *Partially filled waveguides*, Moscow, USSR: Sov. Radio.
7. Wainstein L.A., 1988, *Electromagnetic waves*, Moscow, USSR: Radio and svyaz'.
8. Yatsuk L.P., "Transverse Slots in a Rectangular Waveguide Filled With a Layered Dielectric", 1998, *Telecommunications and radioengineering*, vol. 52, 56-60.
9. Yatsuk L.P., "Physical properties of Transverse Slots in a Rectangular Waveguide Filled with a Layered Dielectric", 1998, *Telecommunications and radioengineering*, vol. 52, 61-65.
10. Blinova N.K., Lyakhovsky A.A., Yatsuk L.P. 'Slot Radiators in a Rectangular Waveguide Partly Filled with Dielectric' , 2008, *Conference Proceedings EuRAD*-2008, *European Radar Conference*. Amsterdam, Netherlands, p. 212-215.

DIFFRACTION PROBLEM BY A SYSTEM OF RECTANGULAR SLOTS IN A COMMON WALL OF RECTANGULAR WAVEGUIDES

Kaliberda M. E. and Pogarsky S. A.

Karazin Kharkov National University, Kharkov, Ukraine
E-mail: Sergey.A.Pogarsky@univer.kharkov.ua

Abstract

The diffraction problem by a system of rectangular slots in a common wall of two rectangular waveguides is considered. At first, using the mode-matching technique and the singular integral equations approach the diffraction problem by the gap of two semiinfinite regular rectangular waveguides and two semiinfinite rectangular waveguides with semiinfinite slots in a common wall is solved. Then, the solution of diffraction problem by one cell, containing slots, and by bounded system of cells is obtained using the operator approach.

Keywords: Rectangular waveguide, mode matching technique, singular integral equations.

1. INTRODUCTION

Waveguide couplers based on rectangular waveguides are widely used in microwave engineering since they have a variety of applications, such as filters, power dividers, directional couplers, etc. One can find enough investigations in which different approaches are used. For example the equivalent circuits approach, method of moments and others [1, 2].

In this report we consider the diffraction problem of the H-modes by the system of rectangular slots in the common wall of two rectangular waveguides (Fig. 1) using the operator approach [3]. We assume that the walls are infinitely conductive and are of zero thickness. We denote the transverse dimensions of waveguides as $a \times l$, $a \times (b-l)$. The time dependence is assumed to be $\exp(-i\omega t)$, k is a wave number.

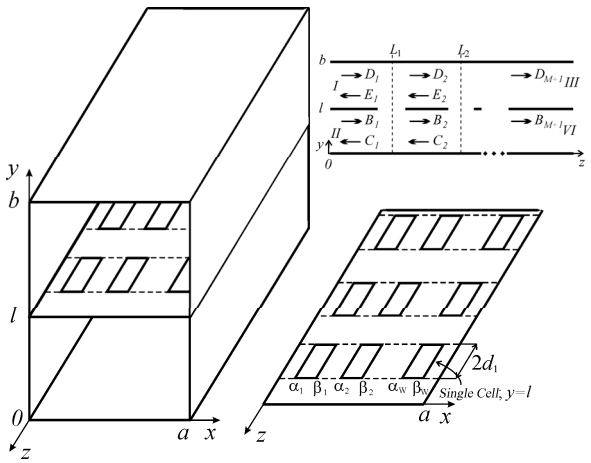


Fig. 1. Structure geometry and coordinate system.

2. SINGLE CELL

When we use the operator approach we need to solve the diffraction problem by a single cell. Then from the operator equations we can obtain properties of a finite number of cells. The scattering operators of a single cell we find in two stages. At first, using the mode matching technique, we solve the diffraction problem by the gap of a semi-infinite cell ($-\infty < z < 0$) and two rectangular waveguides with a common wall. Then, from operator equations, we obtain properties of a single cell.

We denote a single cell as the set $M_0 = \left\{(x;y;z), 0 < x < a, 0 < y < b, -d_1 < z < d_1\right\}$, where $2d_1$ is the slots length, and $P = \bigcup_{q=1}^{W} (\alpha_q;\beta_q) \subset (0;a)$ is a trace of slots set on the plane xOy.

The singular integral equation with additional conditions relatively unknown eigenwaves propagation constants γ_n^3, $\operatorname{Im}\gamma_n^3 < \operatorname{Im}\gamma_{n+1}^3$, $\operatorname{Re}\gamma_n^3 > \operatorname{Re}\gamma_{n+1}^3$, of the cell M_0 may be written in the form

$$\frac{1}{\pi}\int_P \frac{F(\zeta)}{\zeta-\phi}d\zeta + \frac{1}{\pi}\int_P K(\zeta;\phi)F(\zeta)d\zeta = 0,\ \ \phi \in P,$$

$$\frac{1}{\pi}\int_P Q(\zeta;\phi_q)F(\zeta)d\zeta = 0,$$

where function $F(\zeta)$ depends on the Fourier amplitudes of the field inside the cell, and the kernels $K(\zeta,\phi)$ and $Q(\zeta,\phi_q)$ depend on the unknown propagation constants.

978-1-4244-7468-4/10/$26 ©2010 IEEE

Let us represent the magnetic component H_z in the case of a semiinfimite cell in the form

$$H_z = \begin{cases} \sum_{m=0}^{\infty}\sum_{n=0}^{\infty} \cos\left(\frac{\pi m x}{a}\right)\cos\left(\frac{\pi n (y-b)}{l-b}\right)\times \\ \times\left[D^0_{m,n} e^{ik\gamma^1_{m,n}z} + D^1_{m,n}\, \mathrm{e}^{-ik\gamma^1_{m,n}z}\right], \text{in domain I}, \\ \sum_{m=0}^{\infty}\sum_{n=0}^{\infty} \cos\left(\frac{\pi m x}{a}\right)\cos\left(\frac{\pi n y}{l}\right)\times \\ \times\left[C^0_{m,n}\, \mathrm{e}^{ik\gamma^2_{m,n}z} + C^1_{m,n}\, \mathrm{e}^{-ik\gamma^2_{m,n}z}\right], \text{in domain II}, \\ \sum_{n=0}^{\infty}\sum_{m=0}^{\infty} \cos\left(\frac{\pi m x}{a}\right)\cos(\eta_{m,n} y)\times \\ \times\left[A^0_{m,n}\, \mathrm{e}^{-ik\gamma^3_n z} + A^1_{m,n}\, \mathrm{e}^{ik\gamma^3_n z}\right] + \\ +\sum_{m}\sum_{n} \cos\left(\frac{\pi m x}{a}\right)\cos\left(\frac{\pi n y}{b}\right)\times \\ \times\left[A^0_{m,n,0}\, \mathrm{e}^{-ik\gamma^4_{m,n}z} + A^1_{m,n,0}\, \mathrm{e}^{ik\gamma^4_{m,n}z}\right], \\ 0 < y < l, \ \text{in domain III} \end{cases}$$

where superscript 0 denotes the amplitude of incidence field. Using the continuity conditions of tangential components of electric and magnetic fields we obtain the following infinite system of linear algebraic equations, which can be solved using the reduction

$$bA^{1,1}_{m_0,0,0} = (b-l)D^{0,1}_{m_0,0} + lB^{0,1}_{m_0,0},$$

$$\gamma^1_0 D^{0,1}_{m_0,n_0} - \gamma^2_0 B^{0,1}_{m_0,n_0} = \sum_{q=0}^{\infty} C^3_{m_0,q} \frac{b\sin(\eta_{m_0,q})\eta_{m_0,q}}{2k^2 l(b-l)}\times$$
$$\times\left[\frac{A^{1,1}_{m_0,q}}{\gamma^3_q - \gamma^1_0} - \frac{A^{0,1}_{m_0,q}}{\gamma^3_q + \gamma^1_0}\right],$$

$$\gamma^1_p D^{0,1}_{m_p,n_p} = \sum_{q=0}^{\infty} C^2_{m_p,q} \frac{\sin(\eta_{m_p,q})\eta_{m_p,q}}{2k^2(b-l)}\left[\frac{A^{1,1}_{m_p,q}}{\gamma^3_q - \gamma^1_p} - \frac{A^{0,1}_{m_p,q}}{\gamma^3_q + \gamma^1_p}\right],$$

$$\gamma^2_p B^{0,1}_{m_p,n_p} = -\sum_{q=0}^{\infty} C^1_{m_p,q} \frac{\sin(\eta_{m_p,q})\eta_{m_p,q}}{2k^2 l}\times$$
$$\times\left[\frac{A^{1,1}_{m_p,q}}{\gamma^3_q - \gamma^2_p} - \frac{A^{0,1}_{m_p,q}}{\gamma^3_q + \gamma^2_p}\right],$$

where $p = 1,2,\ldots$, $\eta_{m,q}$ denotes the transverse wave numbers in domain III, $C^j_{m,q}$ are known constants.

Let us now consider a single cell M_0. The schematic representation of the structure and the directions of the eigenwaves propagation are shown in Fig. 2 We denote the vectors of the Fourier amplitudes of incident field as D^0 and C^0, and corresponding vectors of scattered field as D, C, E, and F. These vectors are related as follows:

$$E = e^- t_{31} e^+ A_1,$$
$$F = e^- t_{32} e^+ A_1,$$

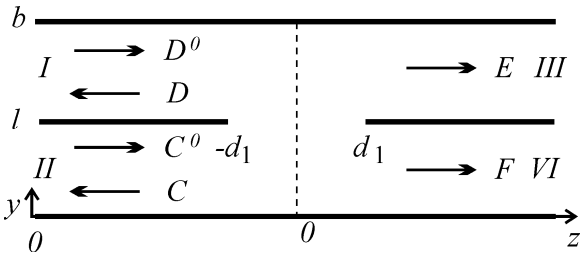


Fig. 2. Single cell.

$$D = e^- t_{31} e^+ A_2 + e^- t_{21} e^- C^0 + e^- t_{11} e^- D^0,$$
$$C = e^- t_{32} e^+ A_2 + e^- t_{22} e^- C^0 + e^- t_{12} e^- E^0,$$
$$A_1 = \left(\hat{I} - e^+ t_{33} e^+ e^+ t_{33} e^+\right)^{-1}\left(e^+ t_{13} e^- D^0 + e^+ t_{23} e^- C^0\right),$$
$$A_2 = e^+ t_{33} e^+ A_1,$$

where operators t_{ij} are the scattering operators of a semiinfinite cell, $e^{\pm}$ allow to determine the amplitudes variation of the field which occur when the coordinate system is shifted thou the distance d_1 in the positive or negative directions of the Oz axis.

3. FINITE SYSTEM OF CELLS

Let us now consider a system of M cells (Fig. 1). We denote the vectors of the Fourier amplitudes of incidence field as D_1 and B_1, and corresponding vectors of the field between the $(k-1)$ st and k th cells as B_k, C_k, D_k, and E_k. These vectors are connected as follows:

$$D_k = t_{13} e^+_{k-1} e^-_{k-2} D_{k-1} + t_{11} e^-_{k-1} e^+_k E_k + t_{21} e^-_{k-1} e^+_k C_k + t_{23} e^+_{k-1} e^-_{k-2} B_{k-1},$$

$$B_k = t_{14} e^+_{k-1} e^-_{k-2} D_{k-1} + t_{12} e^-_{k-1} e^+_k E_k + t_{22} e^-_{k-1} e^+_k C_k + t_{24} e^+_{k-1} e^-_{k-2} B_{k-1}, k = 2,\ldots,M+1,$$

$$E_k = t_{11} e^+_k e^-_{k-1} D_k + t_{13} e^-_k e^+_{k+1} E_{k+1} + t_{23} e^-_k e^+_{k+1} C_{k+1} + t_{21} e^+_k e^-_{k-1} B_k,$$

$$C_k = t_{12} e^+_k e^-_{k-1} D_k + t_{14} e^-_k e^+_{k+1} E_{k+1} + t_{24} e^-_k e^+_{k+1} C_{k+1} + t_{22} e^+_k e^-_{k-1} B_k, k = 1,\ldots,M$$

$$C_{M+1} = 0,\ E_{M+1} = 0,$$

where operators t_{ij} are the scattering operators of a single cell, $e^{\pm}_k$ allow to determine the amplitude variations of the field which occur when the coordinate system is shifted thou the distance L_k in the positive or negative directions of the Oz axis.

4. NUMERICAL RESULTS

Let us introduce the coefficient $|t_{14}|$ which is equal to the magnitude of the H_{10}-mode in the domain IV if the structure is excited by the H_{10}-mode from the domain I. Domains numbering is presented in fig. 1. Fig. 3 shows the dependence of the $|t_{14}|$ v.s. frequency f, GHz, for the structure consisting of one slot. The distance between the slot center and the center of a broad wall equals

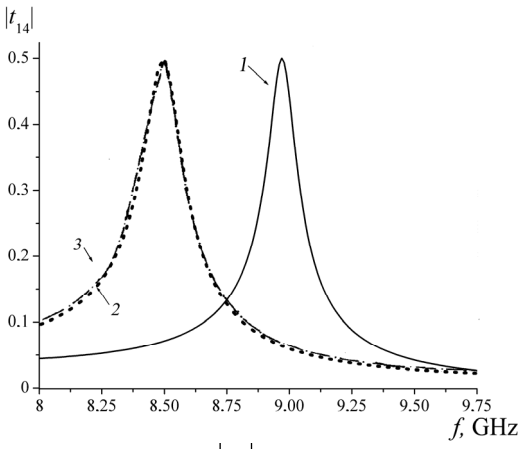


Fig. 3. Dependence of $|t_{14}|$ vs. f, GHz, for the structure consisting of a single slot, $h_0 = 0.3$ cm, $a = 2.286$ cm, $l = b - l = 1.016$ cm, $d = 0.1$ cm. Curve 1 – $d_1 = 0.746$ cm, curve 2 – $d_1 = 0.8$ cm, curve 3 – from [2], Fig. 3, curve 3.

$h_0 = 0.3$ cm, and $l = b - l = b/2$. The slot width $d = 0.1$. The results obtained using presented approach we compare with the results from [2], fig.3, curve 3.

Fig. 4. shows the dependence of the $|t_{14}|$ as a function of the slots length $2d_1$. Slots are placed symmetrically relatively the center of a broad wall, $x = a/2$. As one can see from the figure, when we shift the slots from the center of a broad wall, the interaction between waveguides increases.

Fig. 5 shows the dependence of the $|t_{14}|$ v.s. $L = L_2 - L_1$ for the structure containing four slots, $M = 2$. The variations of the parameter k result in shift of local maxima along the L/b axis. The dependencies are practically periodical with period $L/\lambda_g \approx 0.5$, where λ_g is the waveguide wavelength. Deviations from periodicity are caused by the influence of evanescent waveguide modes.

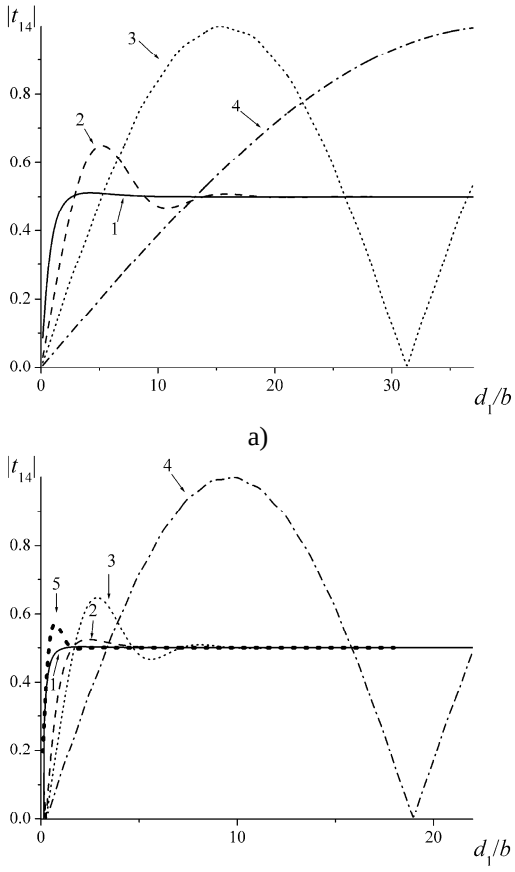


Fig. 4. Dependence of $|t_{14}|$ vs. d_1. a) One slot, $d/b = 0,3$. b) Two symmetrically placed slots, $d/b = 0.15$, $h/b = 0.3$. Curve 1 – $kb = 1.37$, curve 2 – $kb = 1.4$, curve 3 – $kb = 1.5$, curve 4 – $kb = 2$, curve 5 – $kb = 2$, $h/b = 1.8$

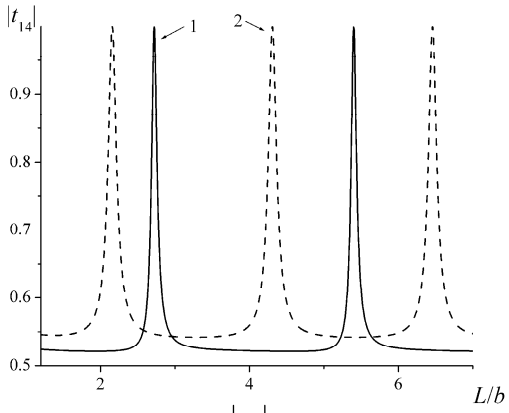


Fig. 5. Dependence of $|t_{14}|$ vs. L, for the structure consisting of two cells. Every cell contains two slots, $d/b = 0.15$, $h/b = 1.8$, $d_1/b = 0.5$, $a/b = 2.3$, $l/b = (b-l)/b$. Curve 1 – $kb = 1.8$, curve 2 – $kb = 2$.

5. CONCLUSIONS

In this report we considered the diffraction by an arbitrary set of rectangular slots in the common wall of two rectangular waveguides. The agreement between results obtained using the presented approach and the results given in [2], fig.3, is excellent. The presented approach can be used for solving of a number of problems.

REFERENCES

1. Bethe H. A. 1943, 'Theory of side windows in waveguides', Massachusetts Ins. of Tech., Cambridge, No. 43-27.
2. Datta A., Rajeek A. M., Chakrabarty A., Das B. N. 1995, 'S Matrix of a Broad Wall Coupler Between Dissimilar Rectangular Waveguides', *IEEE Trans. on MTT*. **43**, 56.
3. Litvinenko L. N., Reznik I. I., Litvinenko D. L. 1991, 'Wave Diffraction on the Semiinfinite Periodical Structures,' *Proc. of the Academy of Sciences of the Ukrainian SSR*. **6**, 62.

INVESTIGATION OF PHASE CODED SIGNALS BASED ON GENERALIZED FRANK CODES

Prudyus I. N., Sumyk M. M., Yankevych R. V.

National University "Lvivska Politechnika", Lviv, Ukraine
E-mail: roman.yankevych@gmail.com

Abstract

In this paper comparative analysis of spectral and correlation characteristics of phase coded signal based on Frank code is given.

Keywords: phase coded signal, specter, autocorrelation, crosscorrelation, ambiguity function, side lobes.

1. INTRODUCTION

Construction of the radio engineering systems with the use of adaptive algorithms of work requires to the search not only the laws of change of structure of the system and principles of its work but also choice of signal which in every concrete situation would allow (at all identical parameters of the system) to provide the receipt of more high-quality indexes of work.

2. RESEARCH DESCRIPTION

2.1. SIGNAL FORMING

As generalized Frank code we define a discrete complex signal which consists of the sequence of elementary signals, amplitude and phase of which we get according to the algorithm:

$$\theta_n = \theta_{pN+m} = pm\frac{2\pi}{N},\ 0 \le N-1,\ 0 \le m \le K-1,$$
$$A_n = \begin{cases} 1,\ 0 \le m \le L-1, \\ 0,\ L \le m \le K-1. \end{cases} \quad (1)$$

Where N is a number of phases levels in signal.

Generalized Frank code is formed as follows. A time domain equal to the duration of the signal T_S is divided in $M = NK$ temporal positions of duration $T_0 = T_S/M$. On each of these temporal positions radio signals with frequency f_0 are formed, rounding and initial phase if which are chosen according to the algorithm (1).

For this signals we have determined specific parameter P. P is parameter of the length of code taken, for example $P = 0.5$ means, that half of a code is taken. For investigation these parameters were $N = 11$, $M = 121$, $P = 0.3,\ 0.5,\ 0.7,\ 0.9,\ 1,\ 1.3,\ 1.5,\ 1.7,\ 2$.

For these signals specter, autocorrelation function, ambiguity function, ambiguity diagram were calculated and plotted. Additionally, side lobe levels mean value was calculated, which is useful for noise situation analysis.

2.2. RESULTS

Obtained results show us that signal, formed on the base of Frank code is wideband and has a good value of side lobes level.

Considering the named signal features it was suggested to research signals based on partial Frank

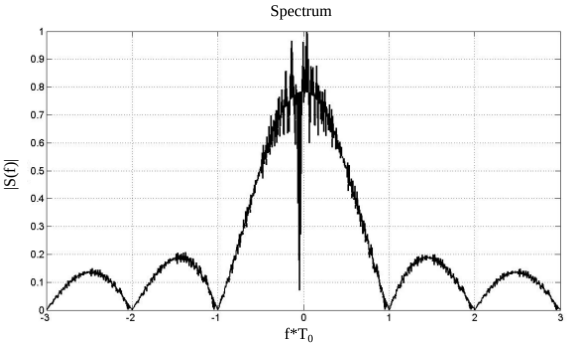


Fig. 1. Frank code based phasecoded signal spectrum ($P = 1$).

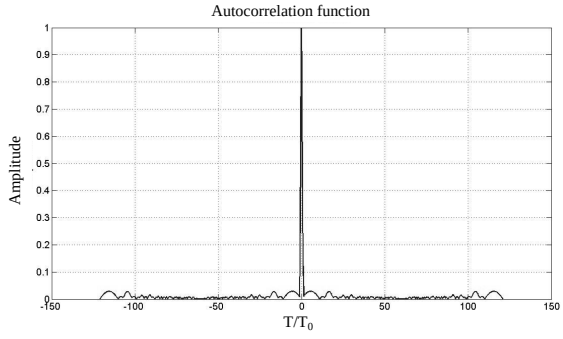


Fig. 2. Frank code based phasecoded signal autocorrelation function ($P = 1$).

978-1-4244-7468-4/10/$26 ©2010 IEEE

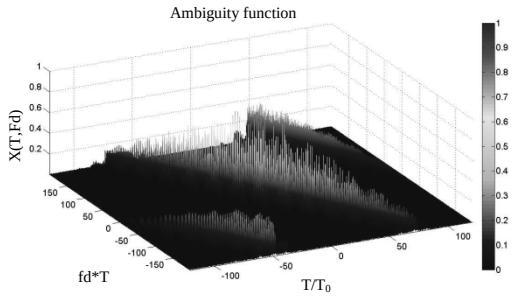


Fig. 3. Frank code based phasecoded signal ambiguity function ($P = 1$).

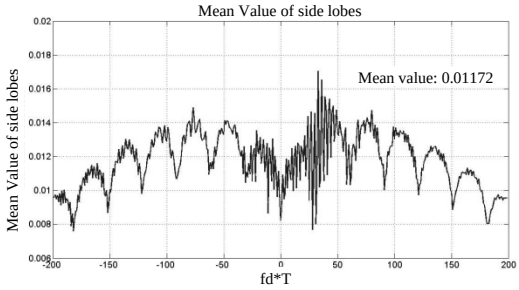


Fig. 4. Frank code based phasecoded signal side-lobes mean value ($P = 1$).

codes – Generalized Frank Codes. Obtained results on investigation of such signals are shown in Fig. 5-8.

3. CONCLUSIONS

The construction of the radio electronic systems with the use of adaptive algorithms of work requires some research not only into the laws of change of system structure and principles of its work but also into the selection of signal which, in a particular situation, would allow (at all identical parameters of the system) to provide higher indexes of its performance.

The results of the research work show us that polyphase signals based on Frank codes has good values of side lobes level, which is very important in radar systems.

The conducted investigations of particular Generalized Frank Code have shown that its specter has periodical minimums with constant width. Also their width depends on the parameter *P*, and it becomes narrower as parameter *P* comes closer to 1. So, such signals could be used for passive hindrances suppression in MTI systems.

REFERENCES

1. Sverdlyk M.B., Sumyk M.M., 'Research of multiphased codes', *NTS Radioelectronika I avtomatika*, Odesa, 1968. (In Russian)

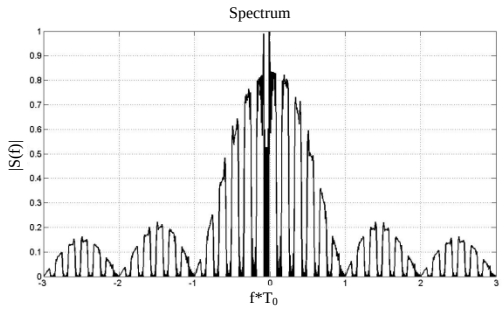


Fig. 5. Generalized Frank code based phasecoded signal spectrum ($P = 6 / 11$).

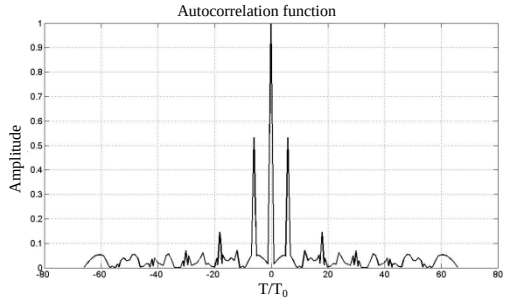


Fig. 6. Generalized Frank code based phasecoded signal autocorrelation function ($P = 6 / 11$)

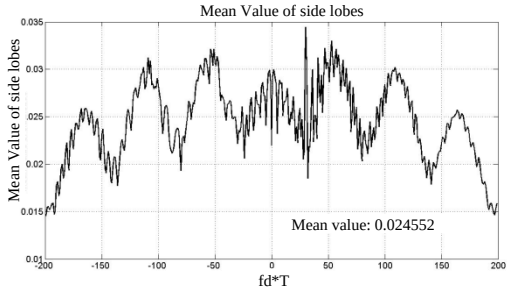


Fig. 7. Generalized Frank code based phasecoded signal side-lobes mean value ($P = 6 / 11$).

2. Sumyk M.M., *Theory basis of radiotechnical systems: Textbook*, 2005. Vydavnictvo Nacionalnogo Universiteta "Lvivska Politekhnica, Lviv, p. 240. (In Ukraine)
3. Bassem R. Mahafza, Ph.D., 'Radar Systems Analysis and Design Using MATLAB', COLSA Corporation, Huntsville, Alabama..
4. Nadav Levanon, Eli Mozeson, *Radar signals*, John Wiley & Sons, Inc., 2004.
5. Erkan Çankaya, *Use of the Ambiguity Function Technique for Target Detection in Phase Coded Continuous Wave Radars*, Middle East Techical University, Istambul, Decmber 2005.

DUAL REGULARIZATION IN ONE-DIMENSIONAL INVERSE SCATTERING PROBLEM

[1] Gaikovich K. P. , [1] Gaikovich P. K., [2] Galkin O. E., [2] Sumin M. I.

[1] Institute for Physics of Microstructures RAS, Nizhniy Novgorod, Russia
E-mail: gai@ipm.sci-nnov.ru
[2] Nizhniy Novgorod State University, Nizhniy Novgorod, Russia
E-mail: m.sumin@mm.unn.ru

Abstract

The considered inverse problem of electromagnetic scattering is widely applied in the subsurface profiling of media permittivity. In previous works, mainly the non-linear integral equation for the scattered field has been in use. It has been solved in the Born approximation or, sometimes, iteratively – beyond this approximation. However, the solution of this ill-posed problem at each step of iterations faced difficulties. To overcome these difficulties, we propose to use the new approach based on the Lagrange formalism applied to initial differential equations (Maxwell's equations). That gives a possibility to obtain the solution of one-dimensional inverse problems of scattering beyond the range of applicability of the perturbation theory. Based on the developed theory, the solution algorithm has been worked out and applied to the simplest one-dimensional problem of low frequency geomagnetic profiling of conductivity of the earth crust.

Keywords: Dual regularization, Maxwell's equations, inverse scattering problem, electromagnetic sounding, earth crust

1. INTRODUCTION

The problem of one-dimensional electromagnetic geomagnetic sounding has been formulated firstly by A.N.Tikhonov [1] for the ultra low-frequency sounding of earth crust and solved by him for a discrete multilayered distribution of media conductivity. The frequency dependence of the effective depth of the received signal formation (skin-depth) of measured fields was in use in this method, applied further in the magnetotelluric exploration. The depth of sounding achieves several kilometers at lowest frequencies.

For the case of a continuous conductivity profile, in frameworks of the one-dimensional electromagnetic perturbation theory, this problem has been reduced to the solution of the non-linear integral equation of the 1-st kind that has been solved iteratively using Tikhonov's method of generalized discrepancy in [2,3]. Here we develop the dual-regularization approach [4].

2. THEORY

2.1. ONE-DIMENSIONAL INVERSE PROBLEM OF SCATTERING

If the distribution of a probing electric field in the non-perturbed medium with the permittivity ε_0 is $\mathbf{E}_0(\mathbf{r})$, the total field $\mathbf{E}(\mathbf{r})$ for the same medium with inhomogeneities $\varepsilon_1(\mathbf{r}')$ can be expressed as a sum of probing and scattered fields and obtained iteratively from the Fredholm equation of the 2-nd kind [5,6]:

$$\mathbf{E}(\mathbf{r}) = \mathbf{E}_0(\mathbf{r}) + \mathbf{E}_1(\mathbf{r}) = \\ = \mathbf{E}_0(\mathbf{r}) - \frac{i\omega}{4\pi}\int_V \overleftrightarrow{\mathbf{G}}(\mathbf{r}',\mathbf{r})\varepsilon_1(\mathbf{r}')\mathbf{E}(\mathbf{r}')d\mathbf{r}' \quad (1)$$

beginning with the Born approximation

$$\mathbf{E}_1(\mathbf{r}) = -\frac{i\omega}{4\pi}\int_V \overleftrightarrow{\mathbf{G}}(\mathbf{r}',\mathbf{r})\varepsilon_1(\mathbf{r}')\mathbf{E}_0(\mathbf{r}')d\mathbf{r}', \quad (2)$$

where ω is the cyclic frequency. The Green tensor $\overleftrightarrow{\mathbf{G}}$ for homogeneous or multilayer media can be obtained using the input impedance formalism [5,6]. Equations (1,2) can also be used to solve the inverse scattering problem [6]. In the case of one-dimensional media, when plane waves are used as the probing field, the total field is expressed as $\mathbf{E}(\mathbf{r}) = \mathbf{E}(z)\exp(ik_x x + ik_y y)$ and the problem is much simplified and reduced to the equation

$$\mathbf{E}_1(z) = -\frac{i\omega}{4\pi}\int_{z'} \varepsilon_1(z')\overleftrightarrow{\mathbf{g}}(z',z)\mathbf{E}_0(z')dz'. \quad (3)$$

In the ultra low frequency band, the analysis can be simplified further. The approximation of Leontovich's boundary conditions is valid in this band, so the field in the medium can be considered as a plane wave with

978-1-4244-7468-4/10/$26 ©2010 IEEE

components E_x, H_y of electric and magnetic field respectively that propagates in the nadir direction relative the earth surface. Also, the permittivity at low frequencies is determined by the conductivity σ as $\varepsilon = \varepsilon' - i\varepsilon'' \approx -4\pi i\sigma / \omega$. Maxwell's equations for the complex amplitudes of electric and magnetic field are written as

$$\frac{d^2E}{dz^2} - i\frac{4\pi\sigma(z)\omega}{c^2}E = 0, \quad H = i\frac{c}{\omega}\frac{dE}{dz}, \qquad (4)$$

Fields are measured at the surface level in dependence on frequency:

$$E(z=0,\omega) = E_0(\omega),\ H(z=0,\omega) = H_0(\omega). \qquad (5)$$

These data can be compared to frequency dependences for the homogeneous medium with the conductivity $\sigma(z) = \sigma(0) = \sigma_0$:

$$E^0(\omega,z) = E_0^0(\omega)\exp\left(\frac{z}{\delta} + i\frac{z}{\delta}\right), \qquad (6)$$

$$H^0(\omega,z) = \frac{c(i-1)}{\omega\delta}E^0 = H_0^0(\omega)\exp\left(\frac{z}{\delta} + i\frac{z}{\delta}\right),$$

where $\delta = c / 2\pi\omega\sigma_0$ is the skin-depth. Using differences $\Delta H = H_0 - H^0$, $\Delta E = E_0 - E^0$ of these fields in the first guess at the solution of the nonlinear integral equation (3) or of the corresponding equation for the magnetic field, it is possible to solve the (3) iteratively, beginning with the Born approximation of perturbation theory. Results of the numerical study [3] have demonstrated serious limitations of such approach for large perturbations (typical in geology structures), when the Born approximation (first guess of iterative method) is inapplicable. To overcome these restrictions of perturbation theory, we develop here the new method, based on the theory [4,7], applied to initial Maxwell equations in its simplest version.

2.2. METHOD OF DUAL REGULARIZATION

Let us introduce new variables:

$$\mathrm{Re}\,E = x_1, \frac{d\,\mathrm{Re}\,E}{dz} = x_2, \mathrm{Im}\,E = x_3, \frac{d\,\mathrm{Im}\,E}{dz} = x_4.$$

Then the inverse problem for (4) in the range $z_0 \le z < 0$ lead to the equivalent problem of minimization

$$I_0(\xi,\sigma) \equiv \| \sigma \|^2 + | \xi |^2 \to \min,\ I_1(\xi,\sigma) = x_0(\omega), \qquad (7)$$

$$\sigma \in D \equiv \{\sigma \in L_2(z_0,0) : 0 \le \sigma(z) \le \sigma_0\} \subset L_2(z_0,0)$$

$$\frac{dx}{dz} = A(\sigma(z)\omega)x, \quad x(z_0) = \xi,$$

$$I_1(\xi,\sigma)(\omega) \equiv x[\xi,\sigma](0) \equiv x[\xi,\sigma\omega](0) \equiv x_0(\omega),$$

$$z_0 < 0,\ \omega \in [\omega_1,\omega_2],\ \xi \in R^4,$$

$$A(\sigma(z)\omega) = \begin{pmatrix} 0 & 1 & 0 & 0 \\ 0 & 0 & -a\sigma(z)\omega & 0 \\ 0 & 0 & 0 & 1 \\ a\sigma(z)\omega & 0 & 0 & 0 \end{pmatrix},$$

$$x_0(\omega) = \begin{pmatrix} 1 \\ H_{02}(\omega)\omega / c \\ 0 \\ H_{01}(\omega)\omega / c \end{pmatrix},$$

where $a = 4\pi / c^2$. It is possible to prove that this problem has a solution (there is no uniqueness). Denote the value of minimizing functional I_0 at this solution as I_0^*. In the considered nonlinear problem it is necessary to use the modified Lagrange function in the dual regularization of (7) [7]. It can be build as

$$\begin{aligned} &L_\mu(\xi,\sigma,\lambda) \equiv \| \sigma \|^2 + | \xi |^2 + \\ &+ \int_{\omega_1}^{\omega_2} (\lambda(\omega),\ x[\xi,\sigma](0,\omega) - x_0(\omega))d\omega + \\ &+ \mu\Big(\sqrt{\int_{\omega_1}^{\omega_2} | x[\xi,\sigma](0,\omega) - x_0(\omega) |^2\, d\omega} + \\ &+ \int_{\omega_1}^{\omega_2} | x[\xi,\sigma](0,\omega) - x_0(\omega) |^2\, d\omega\Big) \equiv \\ &\equiv \| \sigma \|^2 + | \xi |^2 + (\lambda, I_1(\xi,\sigma) - x_0(\omega)) + \\ &+ \mu(\| I_1(\xi,\sigma) - x_0(\omega) \| + \| I_1(\xi,\sigma) - x_0(\omega) \|^2). \end{aligned} \qquad (8)$$

The dual problem (Tikhonov regularization with the regularization parameter α) of maximizing the concave functional on the Hilbert space $L_2^4(\omega_1,\omega_2)$:

$$V_\mu(\lambda) - \alpha \| \lambda \|^2 \to \max,\ \| \lambda \| \le \mu, \qquad (9)$$

$$V_\mu(\lambda) \equiv \min_{\sigma \in D} L_\mu(\xi,\sigma,\lambda), \quad \lambda \in L_2^4(\omega_1,\omega_2),\ \mu > 0.$$

Details of the dual regularization algorithm are described in [4,7]. In this paper we present results of this problem solution based on a simplified approach – the minimization of the discrepancy functional $\| I_1(\sigma,\xi) - x_0(\omega) \|^2$ in (8) under the stipulation that $x \to 0$, when $z \to -\infty$.

3. NUMERICAL SIMULATION

In Figs. 1, 2 one results of the numerical simulation of the retrieval of conductivity profiles are shown. One can see in Fig. 1 a good retrieval of a very sharp inhomogeneity (layer with enhanced conductivity). The second example in Fig. 2 demonstrated the possibility of the developing approach to retrieve more complicated profiles of conductivity. Advantages of this approach as compared with the solution of integral equation [3] are quite obvious.

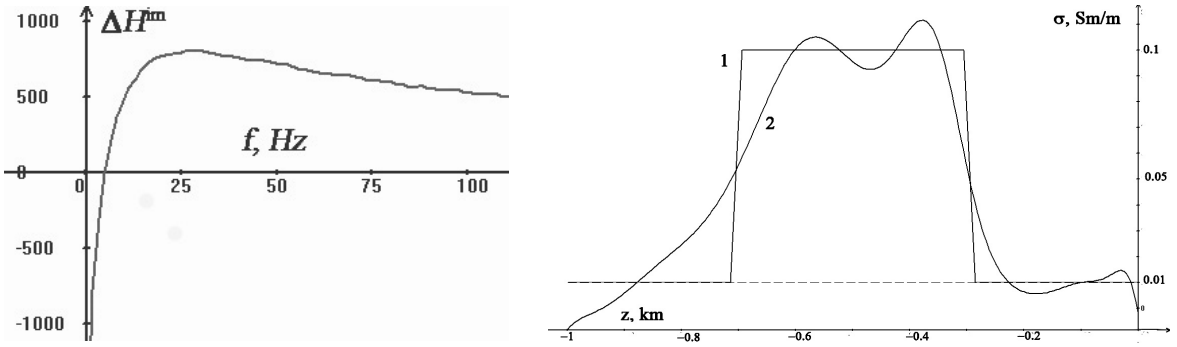


Fig. 1. Numerical modeling of the retrieval of the conductivity profile. Left, "measured data" ($\mathrm{Im}(\Delta H)$) in arbitrary units versus frequency $f = \omega/2\pi$ at the *rms* of the random error $\delta H_0 = 1\,\%$; right, 1 – initial profile, 2 – retrieval results.

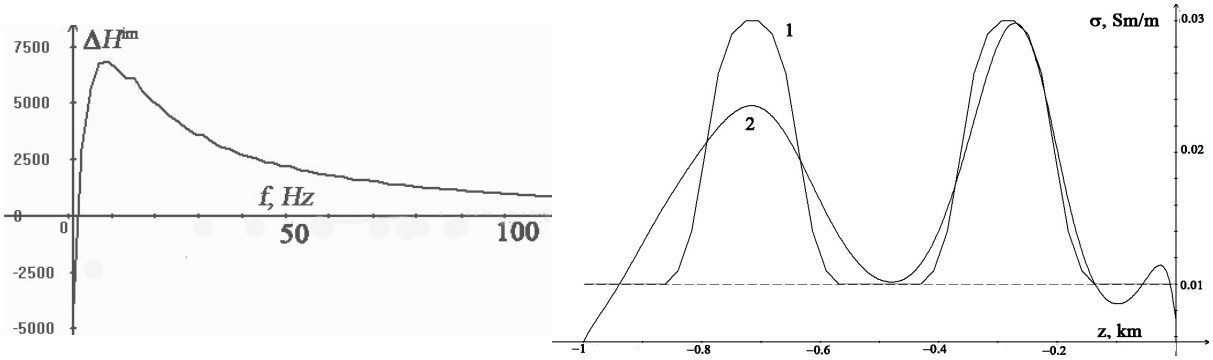


Fig. 2. The same, as in Fig. 1, but for the conductivity profile with two maxima.

4. PERMISSION TO PUBLISH

The authors are responsible for all material contained in the manuscript they submit.

ACKNOWLEDGMENTS

This work was supported by Russian Foundation for Basic Research grants *No*. 08-02-00117, 09-01-97019-r_povolzh'e and by the Program of the Russian Academy of Sciences.

REFERENCES

1. Tikhonov A. N. 1977, *Solution of ill-posed problems*, Winston, New York.
2. Gaikovich K. P. 2004, *Inverse Problems in Physical Diagnostics*, Nova Science Publishers Inc., New York.
3. Gaikovich K. P. 'Ultra low frequency sounding and tomography of earth crust', *Proc. 3d Int. Conf. "Ultrawideband and Ultrashort Impulse Signals"* , 2006, Sevastopol, Ukraine, 294-296.
4. Gaikovich K. P., Sumin M. I. 'Dual regularization in inverse problem of low frequency dielectric profiling', *Proc. 4th Int. Conf. "Ultrawideband and Ultrashort Impulse Signals"* , 2008, Sevastopol, Ukraine), 186-288.
5. Gaikovich K. P. 2007 'Subsurface near-field scanning tomography', *Physical Review Letters* **98**, p.183902.
6. Gaikovich K. P. , Gaikovich P. K. 2008 'Scanning coherent tomography of multilayered media with inhomogeneous region', *in Proc. ICTON 2008*, Athens, Greece, June 22-26, 2008, pp.246-249.
7. Sumin M. I. 2007, 'Regularized Dual Method for Nonlinear Mathematical Programming', *Comput. Math. Math. Phys.* **47**, 760-779.

EFFECTS OF UWB AND CHAOTIC SIGNALS ON SELECTED OSCILLATORS

[1] Ropiak C. A. and [2] Gardner R. L.

[1] Consultant, Naval Surface Warfare Center, Dahlgren Division, Q04
Email: Robert.L.Gardner@verizon.net
[2] Consultant, Naval Surface Warfare Center, Dahlgren Division, Q04
Email: Cynthia.Ropiak@SAQConsulting.com

Abstract

Engineers who work on survivability of complex infrastructure targets to high-power microwave illumination are careful to understand possible instabilities that can be forced by the threat illumination. Transition to chaos is one indicator of such instability. Engineers who design infrastructure systems are careful to consider the stability of the systems under normal operation, but do not normally consider external threats or stimulants that may contribute to the instability. Stoudt, Gardner, and Kohlberg [1-3] show examples of simple electronic systems that go unstable through a combination of pulsed field illumination and misdirected energy from a system power supply. In this paper, we will examine the effects on simple selected oscillators of multi-frequency (chaotic in that the center frequency jumps abruptly from frequency to frequency) and ultra wideband signals. The first case study is based on the Chua Circuit, which is very simple, but known to easily exhibit chaotic behavior. The Chua circuit can be described using only three nonlinear differential equations, so is near the minimum requirements for chaos. This study will use Mathematica© scripts to compare the Chua circuit results to that of a simple oscillator then add complexity to the target circuit so that it is clear where instabilities can be found and exploited.

Keywords: High-power microwave (HPM), high-power electromagnetic, susceptibility, infrastructure failure.

1. INTORDUCTION

Understanding the response of industrial control systems to various high-power microwave (HPM) waveforms is critical to insuring their survivability should a system ever be attacked. Insight into system response can be gained by studying the unstable nature of the driven Chua Circuit. To be specific, a driven Chua Circuit can have a stable solution for many potential drive waveforms. If we consider an HPM illumination of a system to be consistent with induction of a HPM wavefront on the circuit element we can study the response of the system thereby gaining insight into which type of waveforms induce instabilities vice others which merely perturb the system.

2. DRIVEN CHUA CIRCUIT

The Chua circuit is one of the simplest circuits that can show complex chaotic behavior and we use it here to represent an example of a failure mechanism caused by the injection of repeated pulses [4]. Fig. 1 shows a schematic of a Chua circuit.

Most of the circuit consists of an RLC oscillator, but the key component is the nonlinear element to the right of the diagram. Not only is that element nonlinear, it is also active, so when we inject a disturbing signal into the circuit, we will also attempt to draw energy from this source to help cause an instability in the system.

The three simultaneous equations of the driven Chua Circuit represent the current in the circuit and the voltages across the two capacitors in normalized form:

$$X'(t) = a\left\{Y(t) - \varphi[X(t)]\right\},$$
$$Y'(t) = -Y(t) + X(t) + Z(t) + ff(t)$$
$$Z'(t) = -b * Y(t)$$

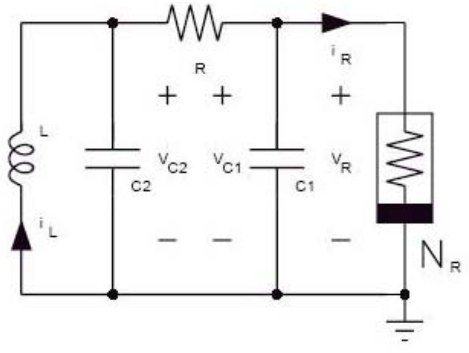


Fig. 1. Chua Circuit Schematic.

978-1-4244-7468-4/10/$26 ©2010 IEEE

$$X(t)=\frac{V_{C1}(t)}{RC1C2},\ Y(t)=\frac{V_{C2}(t)}{RC1C2},\ Z(t)=\frac{I_L(t)}{RC1C2}.$$

The constants are defined as: $a=\frac{C2}{b1}$, $b=\frac{R^2C2}{L}$. $ff(t)$ is the drive function and $\varphi(x)$ is the nonlinear characteristic of the Chua diode. In the following section we investigate the numerical solution to this set of equations for different representative HPM drive waveforms.

3. Stable Versus Unstable Drive Functions

As mentioned, the nonlinear impedance is represented by the function $\varphi(x)$, which for the purposes of our investigation is defined as:

$$\varphi(x)=\frac{2}{7}x-\frac{3}{14}\left[\frac{2}{Pi}ArcTan(10x+1)-\right.$$
$$\left.-\frac{2}{Pi}ArcTan(10x-1)\right].$$

Figure 2 contains a VI plot of the nonlinear impedance.

We begin by generating the numerical solution of the coupled differential equations with no external drive present; i.e. $ff(t)=0$. The solution is presented in Figure 3. Note that it is stable.

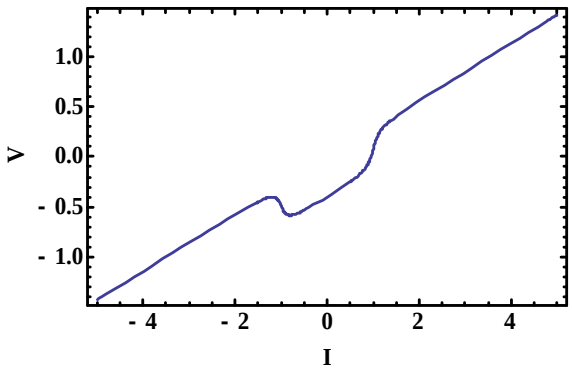


Fig. 2. VI Curve for Nonlinear Resistor.

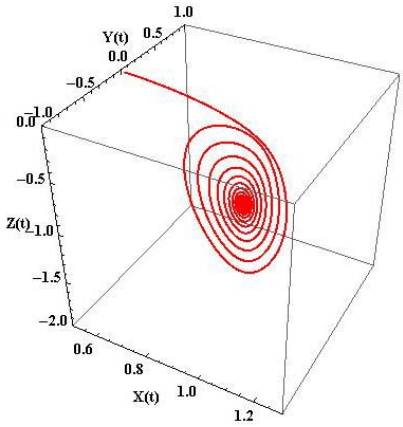


Fig. 3. Stable Solution using a Square Wave as a Drive Function.

Next we would like to investigate using a drive function that is representative of a multiple-pulse HPM wavefront incident on the system. Figure 4 contains a plot of such a multi-pulse drive function. Using this drive function in the coupled set of differential equations the numerical solution is generated and presented in Figure 5. We now see that the solution is no longer stable. To be specific, introduction of the multi-pulse drive waveform has changed the nature of the solution from that of a stable one to that of an unstable one.

For many HPM applications it is reasonable to expect a single pulse disturbance, so the stability of a single-pulse drive function is of interest. The numerical solution to the coupled differential equations for just such a single-pulse event is plotted in Figure 6.

We find that even a single pulse drive function is capable of inducing an unstable solution.

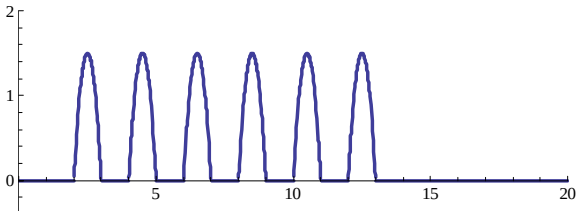


Fig. 4. Example multi-pulse HPM Drive Function.

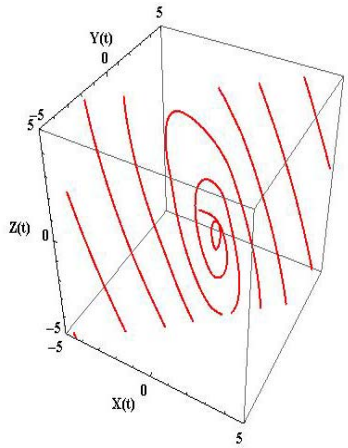


Fig. 5. Unstable Solution Using Multi-Pulse HPM as a Drive Function.

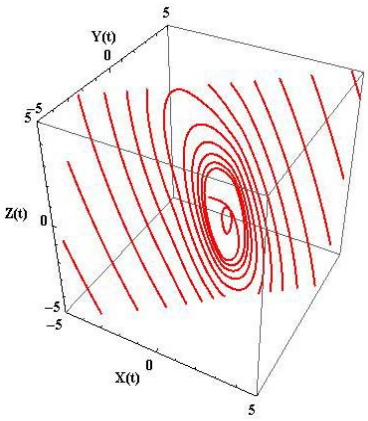


Fig. 6. Unstable Solution Using Single-Pulse HPM as a Drive Function.

Finally, we would like to investigate the case of an ultra-wideband drive function, which is equivalent to a much narrower pulse than previously investigated. The representative ultra-wideband drive function for this case is merely a shorter version of the previously studied waveform, making it more impulsive in nature. The numerical solution to the coupled differential equations using this shorter pulse drive waveform is presented in Figure 7.

Unlike the cases of single and multi-pulse HPM drive waveforms, we see that the narrow pulse, ultra-wideband drive function does not lead to an unstable solution.

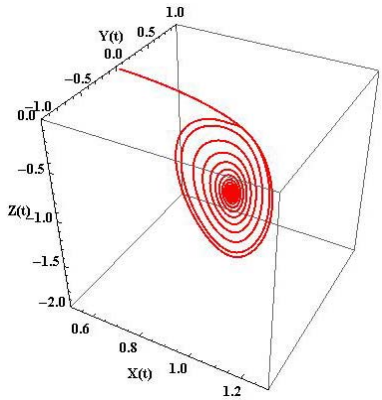


Fig. 7. Stable Solution Using Ultra-Wideband HPM as a Drive Function.

4. CONCLUSIONS

Understanding the instabilities of the driven Chua Circuit as they relate to HPM induced drive functions can give us insight into the potential system response of different types of HPM waveforms. In this paper we began a very basic investigation that ferreted out some critical system responses associated with traditional wideband HPM vice ultra-wideband drive functions.

REFERENCES

1. Matsumoto, T.: A chaotic attractor from Chua's circuit. IEEE Trans. CAS-31, no 12 (1984), 1055-1058
2. D. C. Stoudt, R. L. Gardner, and I Kohlberg, "The Role of Hybrid Models in Understanding Failure Mechanisms of Infrastructure Electronics Due to High-Power Microwave Illumination", *Proceedings of the International Conference on Electromagnetics in Advanced Applications*, Turin, September 2007.
3. I. Kohlberg and R. L. Gardner, "A Perspective of Electromagnetic Susceptibility of Discrete Event Dynamic Systems and Hybrid Systems", *Proceedings of the European Electromagnetics Symposium*, Lausanne, Switzerland, Jul. 2008.
4. S. Lynch, "Dynamical Systems with Applications using Mathematica", Springer, Boston, 2007.

THE INFLUENCE OF ILLUMINATING WAVE POLARIZATION STATE ON THE ELECTROMAGNETIC FIELD DISTRIBUTION INSIDE THE DIELECTRIC CYLINDER

Stasjuk N. N. and Gorobets N. N.

Karazin Kharkov National University, Kharkov, Ukraine
E-mail: saturnias@rambler.ru

Abstract

In this paper the results of theoretical analysis of the electromagnetic field distribution inside the dielectric cylinder for parallel and perpendicular incidence wave polarization state cases are presented. The computation has been performed for electric and magnetic field intensities in the circular cylinder cross section using geometrical optics. It has been shown that the electromagnetic field is focused in some region around the focal axis.

Keywords: Microwave, dielectric cylinder, plane wave, polarization, focus point.

1. INTRODACTION

With increasing the application field of a millimeter and submillimeter electromagnetic radiation the task of its influence identification on various objects becomes ever more pressing. For this purpose it is necessary to investigate the processes taken place inside and near the objects irradiated in detail.

2. PROBLEM FORMULATION

The electromagnetic field distribution inside an infinite dielectric cylinder which lateral surface is illuminated by the linear polarized plane wave is considered. The incident wave front is parallel to the cylinder axes in the selected coordinate system. At each point of a dielectric cylinder cross section the electric and magnetic field intensities are computed for the parallel and perpendicular polarized illuminating wave using geometrical optics. The parameters of the dielectric are not limited and the cylinder diameter is $D >> \lambda$.

Within the bounds of geometrical optics method the cylinder surface has been illuminated in the range of the wave sight angle $\varphi \in \left(-\frac{\pi}{2};\frac{\pi}{2}\right)$ relative to surface outer normal line.

An incident ray on a dielectric-air interface forms refracted and reflected rays. The passed rays which have been formed by the incident plane wave on the dielectric cylinder surface is focused in some area around the focal axis inside the cylinder or outside as second refraction of the rays (Fig. 1).

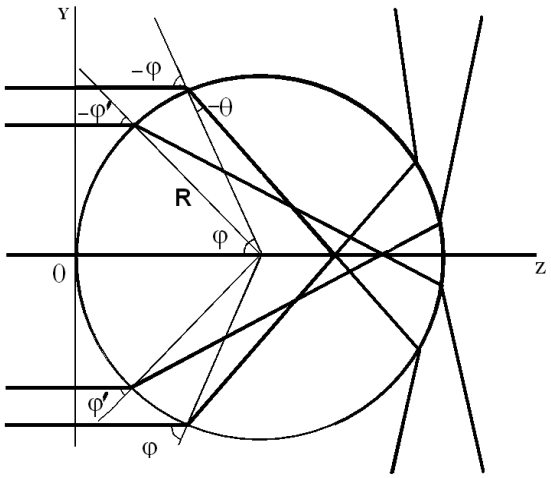


Fig. 1. The ray paths inside a dielectric cylinder.

In problem solving the ordinary approximations of geometrical optics are taken. The dielectric cylinder surface is considered as locally flat in point of ray incidence ($R >> \lambda$), therefore all geometrical optics lows hold true. The electrodynamics boundary conditions are correct in the form for a plane interface of two infinite medium with diverse electrophysical parameters.

The re-reflected ray amplitudes are accepted negligible inside the dielectric cylinder. The ray paths are determined in conformity with Snell's low.

To estimate the $\left|\dot{\vec{E}}\right|$ and $\left|\dot{\vec{H}}\right|$ field amplitudes at each point of a cylinder cross section it is necessary to define what rays can pass through the point. We solve the transcendental path equation for angle of incidence in given point for that

978-1-4244-7468-4/10/$26 ©2010 IEEE

$$y_n = R(1-\cos\varphi)\cdot tg(\varphi - \mathrm{Re}\,\theta(\varphi)) + \\ +R\sin\varphi - tg(\varphi - \mathrm{Re}(\theta))\cdot z_n \quad . \qquad (1)$$

The solution set φ_j for each pair (y_n, z_n) are substituted in expression for $\dot{\vec{E}}$ and $\dot{\vec{H}}$.

If the illuminating wave is the parallel polarized wave ($E \perp \vec{x}^0$) then

$$\vec{y}^0 \dot{E}_p(y_n, z_n) = \sum_j \dot{E}n_p(\varphi_j, y_n, z_n)\times \\ \times[k^2\sin^2\varphi_j - \cos\varphi_j\cdot(\mathrm{Re}(k_2\cos\theta(\varphi_j)) - i\alpha)] \quad , (2)$$

$$\vec{z}^0 \dot{E}_p(y_n, z_n) = \sum_j \dot{E}n_p(\varphi_j, y_n, z_n)\times \\ \times\sin\varphi_j[k\cos\varphi_j - (\mathrm{Re}(k_2\cos\theta(\varphi_j)) - i\alpha)] \quad , \qquad (3)$$

$$\dot{\vec{H}}_p(y_n, z_n) = \sum_j \left|\frac{E_0 D_p(\varphi_j)}{W}\right|\cdot e^{-\alpha(z_n - R(1-\cos\varphi_j))}\times \\ \times e^{i\cdot(\Omega(\varphi_j, y_n, z_n) + \arg k_2 - \arg W + \pi)} \quad , (4)$$

where $$\dot{E}n_p(\varphi_j, y_n, z_n) = \left|\frac{E_0 D_p(\varphi_j)}{k_2}\right|\times \\ \times e^{-\alpha(z_n - R(1-\cos\varphi_j))}\cdot e^{i\cdot\Omega(\varphi_j, y_n, z_n)},$$

$$\Omega(\varphi_j, y_n, z_n) = \arg D_p(\varphi_j) - y_n k\sin\varphi_j + kR\sin^2\varphi_j - \\ -\mathrm{Re}(k_2\cos\theta(\varphi_j))\cdot(z_n - R(1-\cos\varphi_j)) - \\ -kR(1-\cos\varphi_j),$$

α – medium absorptance , k – wave vector, W – wave resistance, D_s – refraction index in case of parallel polarized wave.

The sought result is absolute value of expression (4) and absolute value of vectors (2) and (3) complex sum.

If the illuminating wave is perpendicular polarized wave ($E \parallel \vec{x}^0$) then

$$\vec{y}^0 \dot{H}_s(y_n, z_n) = -\sum_j \frac{\dot{E}n_s(\varphi_j, y_n, z_n)}{W}\times \\ \times[k^2\sin^2\varphi_j - \cos\varphi_j\cdot(\mathrm{Re}(k_2\cos\theta(\varphi_j)) - i\alpha)] \quad , (5)$$

$$\vec{z}^0 \dot{H}_s(y_n, z_n) = -\sum_j \frac{\dot{E}n_s(\varphi_j, y_n, z_n)}{W}\times \\ \times\sin\varphi_j[k\cos\varphi_j - (\mathrm{Re}(k_2\cos\theta(\varphi_j)) - i\alpha)] \quad , \qquad (6)$$

$$\dot{\vec{E}}_s(y_n, z_n) = \vec{x}^0\sum_j \left|E_0 D_s(\varphi_j)\right|\cdot e^{-\alpha(z_n - R(1-\cos\varphi_j))}\times \\ \times e^{i\cdot(\Omega(\varphi_j, y_n, z_n) + \arg k_2)} \quad .(7)$$

where $$\dot{E}n_s(\varphi_j, y_n, z_n) = \left|\frac{E_0 D_s(\varphi_j)}{k_2}\right|\times \\ \times e^{-\alpha(z_n - R(1-\cos\varphi_j))}\cdot e^{i\cdot\Omega(\varphi_j, y_n, z_n)},$$

$$\Omega(\varphi_j, y_n, z_n) = \arg D_s(\varphi_j) - y_n k\sin\varphi_j + kR\sin^2\varphi_j - \\ -\mathrm{Re}(k_2\cos\theta(\varphi_j))\cdot(z_n - R(1-\cos\varphi_j)) - \\ -kR(1-\cos\varphi_j),$$

D_s – refraction index in case of perpendicular polarized wave.

The sought result is absolute value of expression (7) and absolute value of vectors (5) and (6) complex sum.

3. NUMERICAL RESULTS

The calculation has shown that the field inside dielectric cross section is distributed irregularly and it has multiple symmetric form relative to the focal axis. The electric and magnetic field intensities vary according to oscillating law on the focal axis of the dielectric cylinder cross section. This effect is the result of interference by three rays (central ray being spread on the cylinder focal axis and two symmetric rays being refracted at some angle to an incidence normal) which pass different optical distances (Fig. 1). An oscillations shape depends both on the cylinder parameters (radius, dielectric constant, dielectric loss tangent) and on the illuminating wave polarization state.

The obtained results have shown that the field local maxima and minima in the focus region depend on the radius of the cylinder and on its dielectric constant. The larger radius, the more field oscillations number per unit length without a value field maximum changing. In this region the field amplitude grows with increasing the distance from the cylinder cross section center in cases of both the parallel and perpendicular polarized illuminating wave. The behaviors and speeds of increasing the electric and magnetic field intensities differ from each other. The larger dielectric constant, the more the number of the field oscillations and focusing rays occur. The electric field intensity decreases and the magnetic field intensity grows with increasing the distance from the cylinder cross section center. The focus region moves to the cross section center and its extent reduces. In the case of small dielectric loss tangent ($tg\delta \ll 0.01$) the regions of equal amplitudes have the sector shapes widened from the focus region. The regions of the equal amplitudes have a difficult shape and decrease in the case of the larger dielectric loss tangent (Fig. 2 – 3).

4. CONCLUSION

The effect of focusing the electromagnetic waves of various polarization states by cylindrical, spherical and ellipsoidal dielectric objects can be some mechanism of an electromagnetic field influence on biologic objects, and a human in particular.

REFERENCES

1. Born M. and Wolf E. 1999, Principles of Optics: Electromagnetic Theory of Propagation, Interference and Diffraction of Light (7th ed.), Cambridge University Press.
2. Gorobets N.N. and Stasjuk N.N. 2008, 'The electromagnetic wave focusing inside a dielectric cylinder.' In: Herald of the Kharkov National University of V.N. Karazin Radiophysics and Electronics, Vol. 834, No. 13, 77-84, (in Russian).

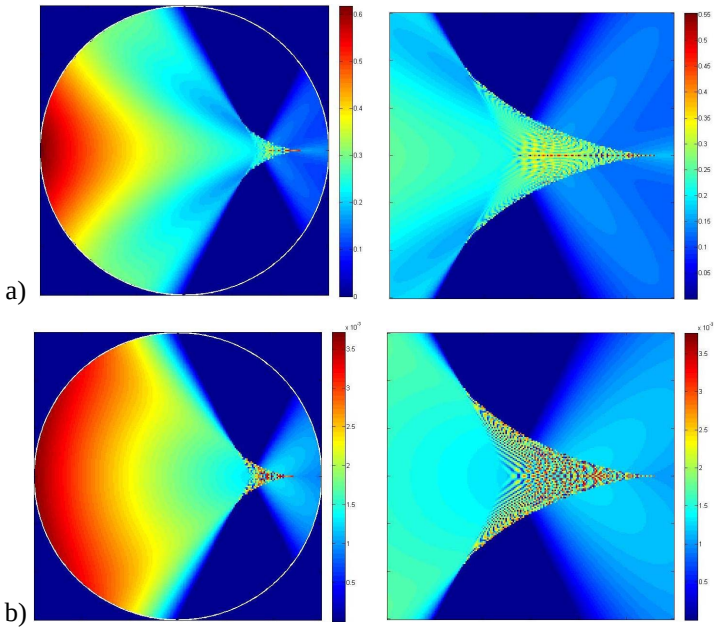


Fig. 2. $\left|E_p\right|$ (a) and $\left|H_p\right|$ (b) distributions inside dielectric cylinder cross section and same distributions in focus region in case of $\mathrm{R}{=}10\lambda$, $\varepsilon = 5$, $tg\delta = 0.01$ (parallel polarized wave).

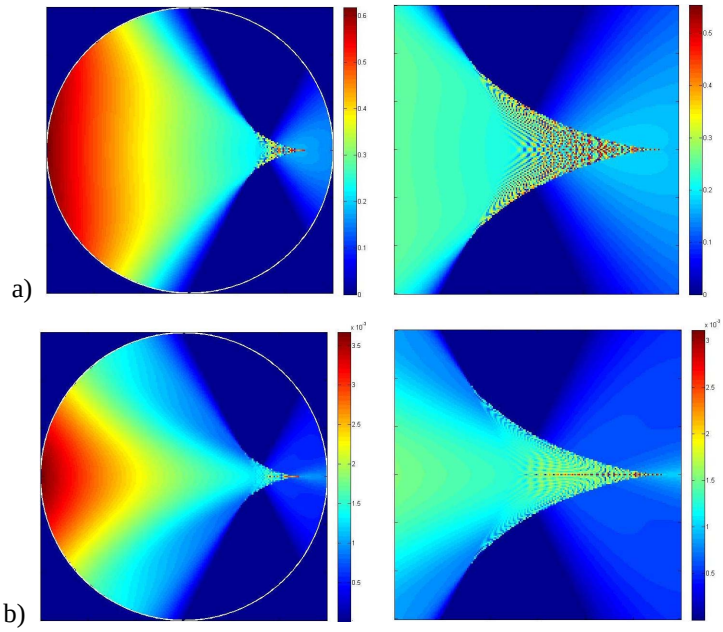


Fig. 3. $\left|E_s\right|$ (a) and $\left|H_s\right|$ (b) distributions inside dielectric cylinder cross section and same distributions in focus region in case of $\mathrm{R}{=}10\lambda$, $\varepsilon = 5$, $tg\delta = 0.01$ (perpendicular polarized wave).

EVOLUTIONARY EQUATIONS FOR ELECTROMAGNETIC FIELDS IN UNBOUNDED SPACE FILLED WITH LAYERED INHOMOGENEOUS NONLINEAR TRANSIENT MEDIUM WITH LOSSES

[1] Dumin O. M., [1] Tretyakov O.A., [1] Katrich V. A., [2] Dumina O. O., [1] Nesterenko M. V., [1] Kholodov V. I.

[1] Karazin Kharkiv National University, Kharkiv, Ukraine
E-mail: Alexander.N.Dumin@univer.kharkov.ua
[2] Ukrainian State Academy of Railway Transport, Kharkiv, Ukraine

Abstract

The transformation of Maxwell equations into the set of evolutionary equations is carried out for the case of arbitrary electrodynamic problem in unbounded space filled with layered inhomogeneous nonlinear transient medium with losses. The inhomogeneity of medium is permitted in longitudinal direction only. After elimination of longitudinal components of electromagnetic field the initial problem is converted into two matrix problems. It is proved that the matrix operators are self-adjoint. Eigen functions and eigen numbers of the operators are found. Using the operators to Maxwell equations is the projection of initial equation set into the modal basis in transversal plane. The completeness of the basis is proved by means of Weyl theorem about orthogonal splitting of Hilbert space. As a result, the evolutionary equation set is obtained. The procedure essentially simplifies the solving of the initial nonlinear transient problem because the three-dimensional problem is converted into the problem for one-dimensional evolutionary equations.

Keywords: Evolutionary equations, time domain, modal basis method, nonlinear transient inhomogeneous medium.

1. INTRODUCTION

The work presents the evolutionary approach to electromagnetics that is oriented to solve the problem in time domain directly. Utilization of the approach permits to solve transient problems in close and open electrodynamic structures filled with nonlinear inhomogeneous transient medium with losses in natural way, without Fourier transform application. Instead of Fourier transform that transfers the solution of the problem into the frequency domain where we lose the time variable only, the evolutionary approach converts three-dimensional problem into one-dimensional problem by means of modal basis constructed in transversal plane. The completeness of the basis is proved by means of Weyl theorem about orthogonal splitting of Hilbert space [1].

Originally the evolutionary approach was applied to the resonator problem [2]. It permitted to take into account dispersion of medium [3] and time dependence of permittivity [4] by natural course. Later the technique also known as modal basis method was used for problems in waveguides also filled with layered inhomogeneous nonlinear transient medium with losses [5]. An arbitrary electromagnetic field is expanded into series of four-dimensional eigen-vectors [6]. Weyl theorem about orthogonal splitting of Hilbert space [1] was used to prove completeness of the set of the eigen-vectors, and assisted to show clearly independence of TE-, TM-, and TEM-modes in a waveguide filled with homogeneous in transversal plane and linear medium. The case of inhomogeneous in transversal plane medium was considered as well [7].

The application of evolutionary approach to the radiation problem firstly was carried out in cylindrical coordinate system [8] but for the case of linear homogeneous medium only [9]. Nevertheless the problem of diffraction of transient wave on an open end of waveguide was solved in time domain directly by means of the evolutionary equation technique [10]. The approach, previously worked out by Tretyakov and Butrym, also described in [7], permitted to obtain the set of evolutionary equations for inhomogeneous in transversal plane medium [11].

Modal basis in spherical coordinate system was built in [12]. It was shown that the decreasing of dimension of the problem significantly decreases cal-

978-1-4244-7468-4/10/$26 ©2010 IEEE

culation time using analytical solution of problems and pure numerical solution as well [13]. Also it is possible to construct modal basis and solve the problems with angular inhomogeneity [14].

The purpose of the work is to obtain evolutionary equation set for the problem of propagation of transient electromagnetic waves in unbounded space filled with layered inhomogeneous nonlinear transient medium with losses.

2. THE STATEMENT OF THE PROBLEM

Transient electromagnetic fields is excited by given sources of field, electrical and magnetic charge and current connected by continuity equations

$$\operatorname{div}\vec{\mathcal{J}}_e+\frac{\partial}{\partial t}\rho_e=0,\ \operatorname{div}\vec{\mathcal{J}}_h+\frac{\partial}{\partial t}\rho_h=0$$

in unbounded space filled with nonlinear transient inhomogeneous in longitudinal direction medium specified by the constitutive relations of rather general kind like

$$\vec{\mathcal{D}}\left(\vec{\mathcal{E}}\right)=\varepsilon_0\vec{\mathcal{E}}+\vec{\mathcal{P}}\left(\vec{\mathcal{E}}\right);\ \vec{\mathcal{B}}\left(\vec{\mathcal{H}}\right)=\mu_0\left(\vec{\mathcal{H}}+\vec{\mathcal{M}}\left(\vec{\mathcal{H}}\right)\right);$$
$$\vec{\mathcal{J}}=\vec{\mathcal{J}}_\sigma\left(\vec{\mathcal{E}},\vec{\mathcal{H}}\right).$$

So, we state the problem for the Maxwell equation set

$$\operatorname{rot}\vec{\mathcal{H}}=\frac{\partial}{\partial t}\vec{\mathcal{D}}+\vec{\mathcal{J}}_\sigma+\vec{\mathcal{J}}_e;\ -\operatorname{rot}\vec{\mathcal{E}}=\frac{\partial}{\partial t}\vec{\mathcal{B}}+\vec{\mathcal{J}}_h;$$
$$\operatorname{div}\vec{\mathcal{D}}=\rho_\sigma+\rho_e;\quad \operatorname{div}\vec{\mathcal{B}}=\rho_h$$

with supplementary condition of field energy restriction

$$\int_{t_1}^{t_2}dt\int_{z_1}^{z_2}dz\int_0^{2\pi}d\varphi\int_0^{\infty}\rho d\rho\left(\varepsilon_0\vec{\mathcal{E}}\cdot\vec{\mathcal{E}}^*+\mu_0\vec{\mathcal{H}}\cdot\vec{\mathcal{H}}^*\right)<\infty$$

that is necessary for correct definition of norm in the modal basis later.

3. REORGANIZATION OF CONSTITUTIVE EQUATIONS

Let us allocate linear part in constitutive equations as follows

$$\vec{\mathcal{P}}\left(\vec{\mathcal{E}}\right)=\varepsilon_0\alpha\left(z,t\right)\vec{\mathcal{E}}+\vec{\mathcal{P}}'\left(\vec{\mathcal{E}}\right);$$
$$\vec{\mathcal{M}}\left(\vec{\mathcal{H}}\right)=\chi\left(z,t\right)\vec{\mathcal{H}}+\vec{\mathcal{M}}'\left(\vec{\mathcal{H}}\right);$$
$$\vec{\mathcal{D}}\left(\vec{\mathcal{E}}\right)=\varepsilon_0\varepsilon\left(z,t\right)\vec{\mathcal{E}}+\vec{\mathcal{P}}'\left(\vec{\mathcal{E}}\right);$$
$$\vec{\mathcal{B}}\left(\vec{\mathcal{H}}\right)=\mu_0\mu\left(z,t\right)\vec{\mathcal{H}}+\mu_0\vec{\mathcal{M}}'\left(\vec{\mathcal{H}}\right),$$

where $\varepsilon\left(z,t\right)=1+\alpha\left(z,t\right)$, $\mu\left(z,t\right)=1+\chi\left(z,t\right)$.

It permits to write out Maxwell equation set in more compact form

$$\operatorname{rot}\vec{\mathcal{H}}=\varepsilon_0\frac{\partial}{\partial t}\left\{\varepsilon\vec{\mathcal{E}}\right\}+\vec{\mathcal{J}};\ -\operatorname{rot}\vec{\mathcal{E}}=\mu_0\frac{\partial}{\partial t}\left\{\mu\vec{\mathcal{H}}\right\}+\vec{\mathcal{I}};$$
$$\varepsilon_0\operatorname{div}\left\{\varepsilon\vec{\mathcal{E}}\right\}=\varrho;\quad \mu_0\operatorname{div}\left\{\mu\vec{\mathcal{H}}\right\}=g,$$

where

$$\vec{\mathcal{J}}=\frac{\partial}{\partial t}\vec{\mathcal{P}}'\left(\vec{\mathcal{E}}\right)+\vec{\mathcal{J}}_\sigma\left(\vec{\mathcal{E}},\vec{\mathcal{H}}\right)+\vec{\mathcal{J}}_e;$$
$$\vec{\mathcal{I}}=\frac{\partial}{\partial t}\vec{\mathcal{M}}'\left(\vec{\mathcal{H}}\right)+\vec{\mathcal{J}}_h;$$
$$\varrho=-\operatorname{div}\vec{\mathcal{P}}'\left(\vec{\mathcal{E}}\right)+\rho_\sigma+\rho_e;\ g=-\operatorname{div}\vec{\mathcal{M}}'\left(\vec{\mathcal{H}}\right)+\rho_h.$$

4. MODAL BASIS CONSTRUCTION

Let's denote transversal vectors and its longitudinal component as follows

$$\vec{\mathcal{E}}=\vec{E}+\vec{z}_0E_z;\quad \vec{\mathcal{H}}=\vec{H}+\vec{z}_0H_z,$$
$$\vec{\mathcal{J}}=\vec{J}+\vec{z}_0J_z;\quad \vec{\mathcal{I}}=\vec{I}+\vec{z}_0I_z.$$

Projection of Maxwell equations into transversal plane and longitudinal axis gives us new equation set in which the longitudinal components of field can be eliminated:

$$W_H\vec{X}=\begin{pmatrix}\frac{1}{\mu}\frac{\partial}{\partial z}\mu\left\{\frac{\partial}{\partial t}\left(\varepsilon\vec{E}\right)+\frac{1}{\varepsilon_0}\frac{\partial}{\partial z}\left[\vec{H}\times\vec{z}_0\right]\right\}+\frac{1}{\varepsilon_0\mu}\left\{\frac{\partial}{\partial z}\mu\vec{J}+\frac{1}{\mu_0}\left[\vec{z}_0\times\nabla_\perp g\right]\right\}\\ -\frac{\partial}{\partial t}\mu\left\{\varepsilon_0\frac{\partial}{\partial t}\varepsilon\left[\vec{z}_0\times\vec{E}\right]+\frac{\partial}{\partial z}\vec{H}\right\}-\left\{\frac{\partial}{\partial t}\mu\left[\vec{z}_0\times\vec{J}\right]+\mu_0^{-1}\nabla_\perp I_z\right\}\end{pmatrix};$$

$$W_E\vec{X}=\begin{pmatrix}-\frac{\partial}{\partial t}\varepsilon\left\{\frac{\partial}{\partial z}\vec{E}+\mu_0\frac{\partial}{\partial t}\mu\left[\vec{H}\times\vec{z}_0\right]\right\}-\left\{\frac{\partial}{\partial t}\varepsilon\left[\vec{I}\times\vec{z}_0\right]+\varepsilon_0^{-1}\nabla_\perp J_z\right\}\\ \frac{1}{\varepsilon}\frac{\partial}{\partial z}\varepsilon\left\{\frac{1}{\mu_0}\frac{\partial}{\partial z}\left[\vec{z}_0\times\vec{E}\right]+\frac{\partial}{\partial t}\mu\vec{H}\right\}+\frac{1}{\varepsilon}\left\{\frac{1}{\mu_0}\frac{\partial}{\partial z}\varepsilon\vec{I}+\frac{1}{\varepsilon_0\mu_0}\left[\nabla_\perp\varrho\times\vec{z}_0\right]\right\}\end{pmatrix},$$

where

$$W_H\vec{X}=\begin{pmatrix}\mathcal{O} & \varepsilon_0^{-1}\left[\vec{z}_0\times\nabla_\perp\right]\nabla_\perp\cdot\\ \mu_0^{-1}\nabla_\perp\left[\vec{z}_0\times\nabla_\perp\right]\cdot & \mathcal{O}\end{pmatrix}\begin{pmatrix}\vec{E}\\ \vec{H}\end{pmatrix}=$$
$$\begin{pmatrix}\varepsilon_0^{-1}\left[\vec{z}_0\times\nabla_\perp\right]\nabla_\perp\cdot\vec{H}\\ \mu_0^{-1}\nabla_\perp\left[\vec{z}_0\times\nabla_\perp\right]\cdot\vec{E}\end{pmatrix};$$
$$W_E\vec{X}=\begin{pmatrix}\mathcal{O} & \varepsilon_0^{-1}\nabla_\perp\left[\nabla_\perp\times\vec{z}_0\right]\cdot\\ \mu_0^{-1}\left[\nabla_\perp\times\vec{z}_0\right]\nabla_\perp\cdot & \mathcal{O}\end{pmatrix}\begin{pmatrix}\vec{E}\\ \vec{H}\end{pmatrix}=$$
$$\begin{pmatrix}\varepsilon_0^{-1}\nabla_\perp\left[\nabla_\perp\times\vec{z}_0\right]\cdot\vec{H}\\ \mu_0^{-1}\left[\nabla_\perp\times\vec{z}_0\right]\nabla_\perp\cdot\vec{E}\end{pmatrix}.$$

Using Fourier-Bessel transform it is proved that operators W_H and W_E are self-adjoint ones. Their eigenvectors form basis in the Hilbert space L_2^4. The completeness of the basis is proved by Weyl theorem [1].

5. EVOLUTIONARY EQUATIONS

The projection of Maxwell equations on the modal basis gives us set of eight bounded evolutionary equations of first order on the amplitudes of field components. The set can be simplified and converted into

the two equations on amplitudes of longitudinal components

$$\left\{\varepsilon_0\mu_0\frac{\partial}{\partial t}\varepsilon\frac{\partial}{\partial t}\mu-\frac{\partial}{\partial z}\frac{1}{\mu}\frac{\partial}{\partial z}\mu+\chi^2\right\}A_m{}^H=$$

$$=-J_m+\varepsilon_0\frac{\partial}{\partial t}\varepsilon I_{zm}+\frac{1}{\mu_0}\frac{\partial}{\partial z}\frac{1}{\mu}g_m;$$

$$\left\{\varepsilon_0\mu_0\frac{\partial}{\partial t}\mu\frac{\partial}{\partial t}\varepsilon-\frac{\partial}{\partial z}\frac{1}{\varepsilon}\frac{\partial}{\partial z}\varepsilon+\xi^2\right\}A_n{}^E=$$

$$=-I_n+\mu_0\frac{\partial}{\partial t}\mu J_{zn}+\frac{1}{\varepsilon_0}\frac{\partial}{\partial z}\frac{1}{\varepsilon}\varrho_n,$$

where

$$H_z=-\sum_{m=0}^{\infty}\int_0^{\infty}d\chi\chi^2A_m{}^H(z,t;\chi)\psi_m;$$

$$E_z=-\sum_{n=0}^{\infty}\int_0^{\infty}d\xi\xi^2A_n{}^E(z,t;\xi)\phi_n;$$

$$\psi_m(\rho,\varphi;\chi)=\frac{J_m(\chi\rho)}{\sqrt{\chi}}e^{im\varphi};$$

$$\phi_n(\rho,\varphi;\xi)=\frac{J_n(\xi\rho)}{\sqrt{\xi}}e^{in\varphi}.$$

Other components of field can be easily obtained from longitudinal ones by Maxwell equations. Here sources of charges and currents, the influence of nonlinearity of medium and Ohm law in general case are included in right-hand sides of the equations

$$I_{zm}=\frac{1}{2\pi}\int_0^{2\pi}d\varphi\int_0^{\infty}\rho d\rho I_z\psi_m^*;$$

$$g_m=\frac{1}{2\pi}\int_0^{2\pi}d\varphi\int_0^{\infty}\rho d\rho g\psi_m^*;$$

$$J_{zn}=\frac{1}{2\pi}\int_0^{2\pi}d\varphi\int_0^{\infty}\rho d\rho J_z\phi_n^*;\ \varrho_n=\frac{1}{2\pi}\int_0^{2\pi}d\varphi\int_0^{\infty}\rho d\rho\varrho\phi_n^*;$$

$$J_m=\frac{1}{2\pi}\int_0^{2\pi}d\varphi\int_0^{\infty}\rho d\rho\vec{J}\cdot\left[\nabla\psi_m^*\times\vec{z}_0\right];$$

$$I_n=\frac{1}{2\pi}\int_0^{2\pi}d\varphi\int_0^{\infty}\rho d\rho\vec{I}\cdot\left[\vec{z}_0\times\nabla\phi_n^*\right].$$

So, the equations are indirectly bounded by their right-hand sides in general case.

6. CONCLUSION

The evolutionary equation set for the problem of propagation of transient electromagnetic waves in unbounded space filled with layered inhomogeneous nonlinear transient medium with losses is obtained.

REFERENCES

1. Weyl H. 1940, 'The method of orthogonal projection in potential theory', *Duke Math. J.* **7**, 411–444.
2. Tretyakov O.A. 1986, 'Modal basis method', *Radiotekhika i electronika.* **31**, No. 6, 1071-1082 (in Russian).
3. Antyufeyeva M. S., Butrym A. Yu. and Tretyakov O. A. 2009, 'Transient electromagnetic fields in cavity with dispersive double negative medium', *Progress In Electromagnetics Research M.* **8**, 51-65.
4. Antyufeyeva M. S. and Tretyakov O. A. 2010, 'Electromagnetic fields in a cavity filled with some nonstationary medium', *Progress In Electromagnetics Research B.* **19**, 177-203.
5. Tretyakov O. A. 1989 'Evolutionary waveguide equations', *Radiotekhika i electronika.* **34**, No. 5, 917-926 (in Russian).
6. Tretyakov O. 1993, 'Essentials of Non-stationary and Nonlinear Electromagnetic Field Theory. Analytical and Numerical Methods in Electromagnetic Wave Theory', Edited by M. Hashimoto, M. Idemen, and O.A. Tretyakov, Science House Co., Ltd, Tokio.
7. Butrym, A. Yu., Kochetov B. A. 2009, 'Time domain mode basis method for a waveguide with transverse inhomogeneous multi-connected cross-section. 1. The general theory of method', *Radio Physics and Radio Astronomy.* **14**, No. 2, 162-173 (in Russian).
8. Dumin A.N., Tretyakov O.A. 1996, 'Radiation of Arbitrary Signals by Plane Disk', *Proc. 6th Intl. Conf. Math. Methods in Electromagnetic Theory, (MMET'1996)* Lviv, 248-251.
9. Dumin A.N. 1999, 'Radiation of Transient Localized Waves from an Open-Ended coaxial waveguide with Infinite Flange', *Telecommunications and Radio Engineering.* **53**, No. 6, 30-34.
10. Dumin A.N., Katrich V.A., Pivnenko S.N., Tretyakov O.A. 2000, 'Comparative Analysis of Approximate and Exact Solutions of Transient Wave Radiation Problem', *Proc. 8th Intl. Conf. Math. Methods in Electromagnetic Theory (MMET'2000)*, Kharkov, 125-127.
11. Dumin A. N., Butrym A. Yu, Tretyakov O. A., Katrich V. A., and Dumina O. A. 2004, 'Transient electromagnetic fields in unbounded space with inhomogeneous medium', *Proceedings of the 2nd International Workshop on Ultrawideband and Ultrashort Impulse Signals (UWBUSIS'04)*, Sevastopol, 104-106.
12. Tretyakov O., Dumin A., Dumina O., Katrich V. 2004, 'Modal basis method in radiation problems', *Proc. Int. Conf. on Math. Methods in Electromagnetic Theory (MMET–2004)*, Dniepropetrovsk, 312–314.
13. Dumin O.M., Dumina O.O., Katrich V.A. 2010, 'Evolution of transient electromagnetic fields in radially inhomogeneous nonstationary medium', *Progress In Electromagnetics Research. PIER 103*. **103**, 403–418.
14. Butrym, A. Y., Kochetov B. A. 2010, 'Mode expansion in time domain for conical lines with angular medium inhomogeneity', *Progress In Electromagnetics Research B*, **19**, 151-176.

TIME-DOMAIN DESCRIPTOR MODELS FOR CIRCUITS WITH MULTICONDUCTOR TRANSMISSION LINES AND LUMPED ELEMENTS

[1] Rutkas A. G. and [2] Vlasenko L. A.

[1] Karazin Kharkiv National University, Kharkiv, Ukraine
E-mail: Anatoliy.G.Rutkas@univer.kharkov.ua
[2] Karazin Kharkiv National University, Kharkiv, Ukraine
E-mail: Larisa.A.Vlasenko@univer.kharkov.ua

Abstracts

We suggest a method to investigate impulse circuits with multiconductor transmission lines in time domain. The transmission lines are connected by a multi-port with linear and nonlinear lumped LCR-elements. In the general case, transient states in these circuits are described by degenerate or descriptor delay nonlinear integro-differential equations. We develop theory of such equations and numerical methods to find solutions.

Keywords: Multiconductor transmission line, lumped elements, loading multi-port, vector telegraph equations, delay integro-differential equation.

1. INTRODUCTION

Characteristics of transient states in circuits with multiconductor transmission lines are used to decompose non-monochromatic electromagnetic fields on mode components [1], to analyze and to construct electrical schemes of processors, microwave elements and subnetworks [2], distributed multiconductor interconnects and other microwave devices [3].

To investigate transient states in circuits with multiconductor transmission lines, we develop the method from [4,5] to decompose vector states of multiconductor transmission lines on mode components. The circuits under consideration can contain arbitrary number of lumped inductors and capacitors, linear and nonlinear resistors and conductors. Descriptor delay differential equations with integral addends arise in describing time-domain models of these circuits.

2. DYNAMIC EQUATIONS FOR CIRCUIT ELEMENTS

Voltage and current vectors $U(x,t), I(x,t) \in \boldsymbol{R}^n$ in a uniform transmission line with n coupled conductors satisfy the equations:

$$-\frac{\partial U}{\partial x} = L\frac{\partial I}{\partial t} + RI, \quad -\frac{\partial I}{\partial x} = C\frac{\partial U}{\partial t} + GU, \quad t \geq 0, \ \ 0 \leq x \leq l. \tag{1}$$

Here $L > 0, C > 0, R \geq 0, G \geq 0$ are real symmetric $n \times n$ matrices. The input $x = 0$ is perturbed by a vector voltage source $E(t)$ with internal matrix impedance $R_0 \geq 0$. It is equivalent to the non-homogeneous boundary condition at $x = 0$:

$$U(0,t) + R_0 I(0,t) = E(t). \tag{2}$$

The output of line $x = l$ is loaded by a $(n+1)$-port with arbitrary number of lumped elements. Oscillations of elementary one-ports with lumped elements are described by the non-linear differential equations

$$U_{L_i} = L_i \frac{dI_{L_i}}{dt} + r_i I_{L_i} + F_i(I_{L_i}),$$
$$I_{C_j} = C_j \frac{dU_{C_j}}{dt} + g_j U_{C_j} + W_j(U_{C_j}).$$

Then the boundary conditions at $x = l$ are a system of nonlinear differential algebraic equations with respect to $U_k(l,t), I_k(l,t), I_{L_i}(t), U_{C_j}(t)$.

3. THE CASE OF NON-DISPERSIVE LINE

If the matrices in (1) satisfy the condition $RC = LG$, then the line is non-dispersive. We suggest a new method to pass from the system of partial differential equations (1) with boundary conditions to a delay differential algebraic equation of the following vector form

$$\frac{d}{dt}(A_0 v(t)) + B_0 v(t) + \sum_{k,j=1}^{n} B_{kj} v(t - \frac{\omega_k + \omega_j}{2}) = f_0(t) + F_0(v), \tag{3}$$

where

$$v(t) = (I_k(l,t), U_k(l,t), I_{L_i}(t), U_{C_j}(t))^{tr}, \tag{4}$$

978-1-4244-7468-4/10/$26 ©2010 IEEE

$$\omega_k = 2l\sqrt{\lambda_k},\ \ \lambda_k \in \sigma(LC).$$

Values of $U(x,t), I(x,t)$ at arbitrary points (x,t) are expressed by values of $I_k(l,\tau), U_k(l,\tau)$ with the help of the damping factor and the D'Alembert principle.

Since $\det A_0 = 0$, equation (3) is *descriptor* or *degenerate*. For equation (3), we prove existence and uniqueness theorems, develop numerical methods to find solutions in the case of impulsive input signals $E(t)$. For this purpose we use mathematical and numerical methods from [8,9].

4. THE CASE OF DISPERSIVE LINE

In the case of dispersive multiconductor transmission line ($RC \neq LG$) we modify the method from [5] of integral representations of $I_k(x,t), U_k(x,t)$ by the source functions $\phi_k(t), \psi_k(t)$. The most simple time-domain model is obtained in the case of *normal symmetric line* when the matrices in (1) possess the properties:

$$\begin{aligned} C(\lambda L + R)G = G(\lambda L + R)C, \\ L(\lambda C + G)R = R(\lambda C + G)L. \end{aligned} \tag{5}$$

These properties are satisfied for single-wire transmission lines with scalar equations (1). Conditions (5) are also satisfied for many classes of multiconductor transmission lines, for example, [6,7].

We pass from the system of partial differential equations (1) with boundary conditions to the semi-linear delay integro-differential equation

$$\begin{aligned} \frac{d}{dt}(A_0 y(t)) + \sum_{k=0}^{n} B_k y(t-\omega_k) + \\ + \sum_{k=0}^{n} \int_0^{t-\omega_k} \Phi^k(t,s) y(s) ds = f(t) + F(y), \end{aligned} \tag{6}$$

where $y(t) = (\phi_k, \psi_k, I_{L_i}, U_{C_j})^{tr}(t)$, $\omega_0 = 0$, $\omega_k = l\sqrt{\lambda_k}$, Φ^k - matrix kernels whose elements contain scalar Bessel functions.

Since $\det A_0 = 0$, equations (6), as equation (3), are *descriptor* or *degenerate*. As in Section 3 for equations (3), we prove existence and uniqueness theorems for equations (6), develop numerical methods. In the case of cubic functions $F_i(x), W_j(x)$, there exists a unique global solution of initial value problem for equation (6).

5. EXAMPLE

Consider the three-conductor transmission line in Fig. 1 with input voltage source $E(t) = (E_1, E_2, E_3)^{tr}(t)$ and matrix input resistance R_0. The line output is loaded by a passive four-port, which contains 18 lumped elements such that 6 elements are nonlinear. The dimension of vector $y(t)$ in (6) is 12:

$$y(t) = (\phi_k(t), \psi_k(t), I_{L_i}(t), U_{C_j}(t))^{tr},\ \ k,i,j = 1,2,3.$$

The rank of A_0 (12×12) is equal to 5 ($\det A_0 = 0$), then equation (6) is descriptor or degenerate. The matrix B_0 has inverse B_0^{-1} and for this reason $\lambda A_0 + B_0$ is a regular matrix pencil.

We build a numerical solution $y(t)$ of equation (6), a numerical solution $U(x,t), I(x,t)$ of equation (1) and numerical values $I_{L_i}(t), U_{C_j}(t)$ under the following assumptions. The initial values are zero:

$$U(x,0) = 0,\ \ I(x,0) = 0,\ \ I_{L_i}(0) = 0,\ \ U_{C_j}(0) = 0.$$

The lumped parameters have the values:

$$\begin{aligned} L_1 = 0.5\cdot 10^{-9},\ \ L_2 = 10^{-9},\ \ L_3 = 2\cdot 10^{-9}\, H, \\ C_1 = 2,\ \ C_2 = 1,\ \ C_3 = 0{,}5\, pF, \\ g_1 = 0.1,\ \ g_2 = 0.2,\ \ g_3 = 0.3\,\Omega^{-1}, \\ r_1 = 0.01,\ \ r_2 = 0.02,\ \ r_3 = 0.03\,\Omega. \end{aligned}$$

The matrix parameters of transmission line are equal to

$$L = \begin{bmatrix} 15 & 7.5 & 10.5 \\ 7.5 & 30 & 9 \\ 10.5 & 9 & 30 \end{bmatrix} \cdot 10^{-12}\ \frac{H}{m},$$

$$C = \begin{bmatrix} 45 & 7.5 & 9 \\ 7.5 & 15 & 12 \\ 9 & 12 & 30 \end{bmatrix} \cdot 10^{-12}\ \frac{F}{m},$$

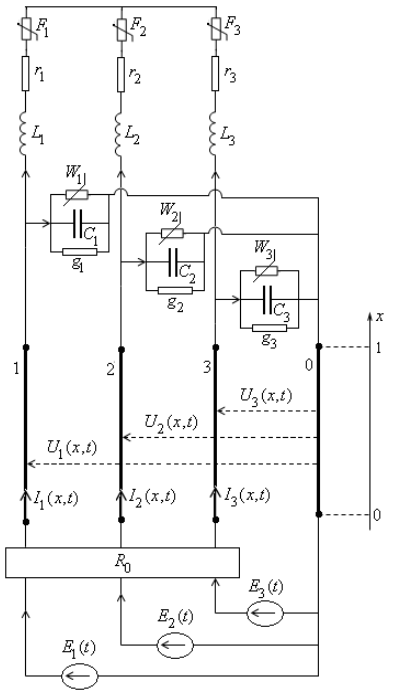


Fig. 1. The three-conductor transmission line.

$$R = \begin{bmatrix} 0.2 & 0.1423 & 0.1811 \\ 0.1423 & 0.3 & 0.2215 \\ 0.1811 & 0.2215 & 0.4 \end{bmatrix} \cdot 10^{-2} \ \frac{\Omega}{m},$$

$$G = \begin{bmatrix} 0.8 & 0.0606 & 0.0546 \\ 0.0606 & 0.3 & 0.1311 \\ 0.0546 & 0.1311 & 0.5 \end{bmatrix} \cdot 10^{-2} \ \frac{\Omega^{-1}}{m}.$$

We choose the nonlinear conductances $W_j(x) = b_j x^3$, $b_1 = 0.1, b_2 = 0.2, b_3 = 0.3$, the nonlinear resistances $F_i(x) = d_i x^3$, $d_1 = 1, d_2 = 2, d_3 = 3$, the input matrix resistance $R_0 = 0.1Rl\,\Omega$, the input voltage source $E(t)$ with the same components $E_k(t) = 2e^{-(t-\alpha)^2/2\sigma^2} v$, $\alpha = 21.4299\ ps$, $\sigma = 2.2163$. In Fig. 2-5, there are represented graphs of some components of $U(x,t), I(x,t), I_{L_i}(t), U_{C_j}(t)$.

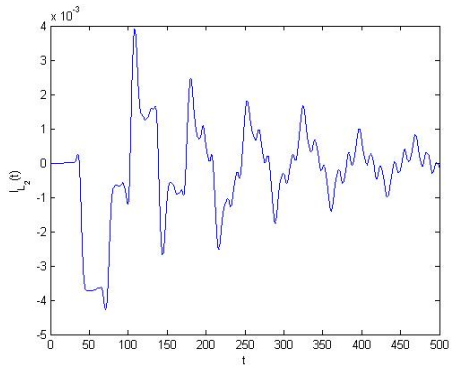


Fig. 2. The current $I_{L_2}(t)$.

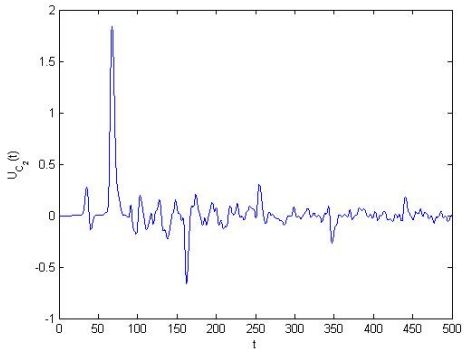


Fig. 3. The voltage $U_{C_2}(t)$.

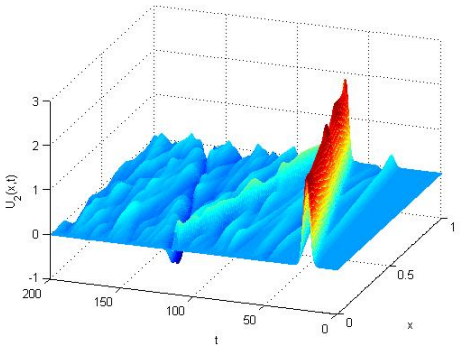


Fig. 4. The voltage $U_2(x,t)$.

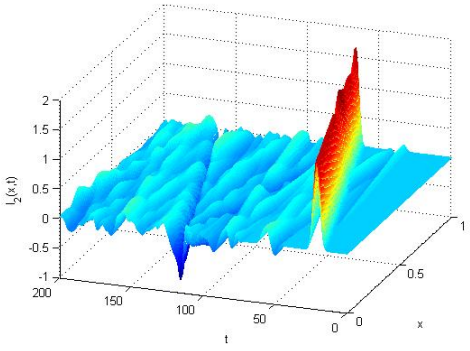


Fig. 5. The current $I_2(x,t)$.

REFERENCES

1. Shlivinski A., Heyman E. 1999, 'Time –Domain Near-Field Analysis of Short-Pulse Antennas-Part I: Spherical Wave (Multipole) Expansion', IEEE Trans. on Antennas and Propagation, **47**, N 2, 271-279.
2. Gunupudi P.K., Khazaka R., Nakhla M.S., Smy T., Celo D. 2003. 'Passive parameterized time-domain macromodels for high-speed transmission-line networks', IEEE Trans. on MTTV. **51**, N 12, 2347-2354.
3. Saraswat D., Achar R., Nakhla M.S. 2004, 'Passive Reduction Algorithm for RLC Interconnect Circuits With Embedded State-Space Systems', IEEE Trans. on MTT. **52**, N 9, 2215-2226.
4. Vlasenko L.A., Rutkas A.G. 2009, 'Transient states in a multiconductor transmission line with lumped elements on output. I. Non-dispersive line', *Radioelectronika i informatika*. N 1, 9-15.
5. Vlasenko L.A., Rutkas A.G. 2010, 'Transient states in a multiconductor transmission line with lumped elements on output. II. Dispersive line', *Radioelectronika i informatika*. N 1, 4-11.
6. Hayashi S. 1955, *Surges on transmission systems*, Denki-shoin, Inc., Kyoto, Japan.
7. Paul C.R. 1994, *Analysis of Multiconductor Transmission Lines*, John Wiley Sons. Inc., New York.
8. Rutkas A.G., Vlasenko L.A. 2003, 'Existence, uniqueness and continuous dependence for implicit semilinear functional differential equations', Nonlinear Analysis. TMA. **55**, 125-139.
9. Vlasenko L.A. 2006, *Evolutionary Models with Implicit and Degenerate Differential Equations*, Sistemnye Tekhnologii, Dniepropetrovsk.

ULTRAWIDEBAND SIGNALS AND PROCESSES

[1] Chernogor L. F. and [2] Lazorenko O. V.

[1] Karazin Kharkiv National University, Kharkiv, Ukraine
E-mail: Leonid.F.Chernogor@univer.kharkov.ua
[2] Kharkiv National University of Radio Electronics, Kharkiv, Ukraine
E-mail: Oleg-Lazorenko@yandex.ru

Abstract

Many processes in near-to-Earth space caused by effects of powerful non-stationary natural and artificial disturbance sources have been shown to be ultrawideband processes. Using a new signal analysis method called as the system spectral analysis, some parameters and peculiarities for that processes have been investigated and estimated.

Keywords: Ultrawideband signals and processes, near-to-Earth space, natural and artificial disturbance sources, system spectral analysis.

1. INTRODUCTION

Using experimental investigation results, many processes in the Earth – atmosphere – ionosphere – magnetosphere system were shown to be the ultrawideband (UWB) processes. Such processes can be caused by effects of powerful non-stationary natural and artificial disturbance sources such as, for example, powerful earthquakes, volcano explosions, industrial explosions, nuclear weapon tests, terminator passages and thunderbolts etc. Geomagnetic pulsations, rogue waves and other can be considered as UWB processes too [1 – 3].

For the analysis and processing of the UWB processes appears advisable to use the same methods which already were successfully used at research of the UWB signals. Actuality of this work is conditioned to these.

2. SYSTEM SPECTRAL ANALYSIS BASES

One of the most effective modern analysis methods, the system spectral analysis, is based on the simultaneous application of linear and non-linear integral transforms [4 – 6]. In first group there are the continuous wavelet transform (CWT), the analytical wavelet transform (AWT), the Gabor transform (GT), the adaptive Fourier transform (AFT) and the short-time Fourier transform (STFT). Second group includes the Fourier spectrogram (FS), the Wigner transform (WiT), the Choi-Williams transform (ChWT) and the Born-Jordan transform (BJT). In addition to the module of spectral density function (SDF), for every transform also skeletons, energograms, dispersions of the SDF module for linear transforms and standard deviations of the SDF module for non-linear transforms are used.

A basic idea of the system spectral analysis is compensation of lacks of one transforms due to advantages of other ones.

A quantity and set of integral transforms, used in the systems spectral analysis, can change in the future. In particular, below instead of Wigner transform the pseudo Wigner transform (PWiT) is used.

For the system spectral analysis performing the system of computer mathematics (SCM) MATLAB 7.X [7] including packages Wavelet Toolbox, Time-Frequency Toolbox [8], Wave Laboratory [9] and some original software for MATLAB created by authors was used.

3. SYSTEM SPECTRAL ANALYSIS OF THE UWB SIGNALS AND PROCESSES

Using the system spectral analysis, the set of UWB signals and processes were investigated in detail [6].

In particular, the natural electromagnetic UWB signal, obtained in the observatory of San-Diego (USA) in three days after the strong earthquake («Joshua Tree quake event» with magnitude $M = 6{,}1$), which took place on April, 22, 1992 in South California; the acoustic UWB pulse fixed during Bezymjanny volcano eruption (on March, 30, 1956); the temporal variations of full electronic content in an ionosphere, registered on the research stations in Goldstone, Yuma and Boulder (USA) during the explosion of the Sent-Hellens volcano (on May, 18, 1980); one of unique registrations of rogue wave by a height about 19 m in the North Sea, got in Norway and known as the «New Year wave» (on January, 1, 1995), temporal variations of terrestrial currents, related to the height nuclear explosion produced during operation "Argus II" (on August, 30, 1958); the variations of D- and H-components of the Earth's magnetic field induction, accompanying the «Proton» carrier launch from the Baykonur cosmodrome

978-1-4244-7468-4/10/$26 ©2010 IEEE

(Kazakhstan) on February, 12, 2000; acoustic pulse, generated at falling of the Tunguska body; and also variations of the Earth's magnetic field induction, caused by passing of terminator and by strongest x-ray solar eruption on December, 5, 2006 have been investigated. New information about the time-frequency structure of these signals and processes was obtained.

As an example applications of system spectral analysis let's consider results of investigations of temporal variations of full electronic content in an ionosphere, registered at the research station in Goldstone (USA) during the explosion of the Sent-Hellens volcano, which took place on May, 18, 1980 in 15.32 UT [10]. Duration of registration in time domain is $T_r = 420\,\mathrm{min}$, scope of process on the size of full electronic content is $\Delta \approx 1{,}2 \cdot 10^{17}\ \mathrm{m}^{-2}$, number of discrete data vector bins is $N_r = 861$. Counting out of time is conducted from a moment an explosion.

This UWB process has been found to be very complex (fig. 1, fig. 2). It contains the disturbances with three characteristic scales which are $T \sim 38\ \mathrm{min}$, $T \sim 75$ min and $T \sim 115\ \mathrm{min}$ (last it is possible to notice on a fig. 1, f, fig. 2, c, m, n) and have durations $\Delta t \sim 120$ min, $\Delta t \sim 100$ min and $\Delta t \sim 200$ min accordingly. The last values are indicated very approximately, as a time-frequency structure of process is complex enough practically for all used transforms.

Moreover, presumably, makes sense in general to talk about three different UWB processes with wideband indexes $\mu \approx 1{,}2$, $\mu \approx 0{,}7$ and $\mu \to 2$. Both the spectral functions of linear transforms and the SDF of nonlinear transforms talk in behalf on such interpretation of system spectral analysis results.

CONCLUSIONS

- The system spectral analysis as a new integrated signal analysis method based on the simultaneous application of linear and non-linear integral transforms got further development. Quantity and set of transforms applied can be increased in future.
- System approach first was successfully applied for the analysis of UWB signals and processes of different physical nature.
- It was shown, that the system spectral analysis allows to perform complex research of signal, compensating the lacks of one used integral transforms by advantages other ones, as every transform has the own unique set of properties.
- It was pointed that the simultaneous use of linear and non-linear transforms enables effective analysis of signals in presence both Gaussian (by linear transforms) and non-Gaussian noise (by non-linear transforms).
- The special data format for the representation of the system spectral analysis of signals was constructed.
- On the example of study of the real UWB signals and processes, having both artificial and natural character, efficiency of the system spectral analysis as a new integrated method of signal analysis was shown.

REFERENCES

1. Chernogor L. F., Rozumenko V. T. 2008, 'Earth – Atmosphere – Geospace as an Open Nonlinear Dynamical System', *Radio Physics and Radio Astronomy*, **13**, No. 2, 120-137.
2. Zalyubovsky I., Chernogor L., Rozumenko V. 2008, 'The Earth – Atmosphere – Geospace System: Main Properties, Processes and Phenomena', *Space Research in Ukraine. 2006 – 2008. The Report Prepared by the Space Research Institute of NASU-NSAU*, 19-29.
3. Chernogor L. F. 2008, *'About Nonlinearity in Nature and Science: Monograph'*, Kharkov: V. N. Karazin Kharkov National University (in Russian).
4. Lazorenko O. V., Chernogor L. F. 2007, 'System Spectral Analysis of Signals: Theoretical Bases and Practical Applications', *Radio Physics and Radio Astronomy*, **12**, No. 2, 162-181 (in Russian).
5. Chernogor L. F., Lazorenko O. V., 2008, 'System Spectral Analysis of the Ultrawideband Signals', *Proc. Ultrawideband and Ultrashort Impulse Signals, 15 – 19 September, 2008, Sevastopol, Ukraine*, 45-50.
6. Lazorenko O. V., Chernogor L. F. 2009, *'Ultrawideband Signals and Processes: Monograph'*, Kharkov: V. N. Karazin Kharkov National University (in Russian).
7. Manassah J. T. 2001, *Elementary Mathematical and Computational Tools for Electrical and Computer Engineers Using Matlab*, Boca Raton, CRC Press.
8. Auger F., Flandrin P., Goncalves P., Lemoine O. 2005, *Time-Frequency Toolbox Reference Guide*, Hewston, Rice University.
9. Mallat S. 1998, *A Wavelet Tour of Signal Processing*, Academic Press.
10. Roberts D. H., Klobuchar J. A., Fougere P. F., 1982, 'A Large-Amplitude Traveling Ionospheric Disturbance Produsedby the May 18, 1980, Explosion of Mount St. Hellens', *Journal of Geophysical Research*, **87**, No. A8, 6291-6301.

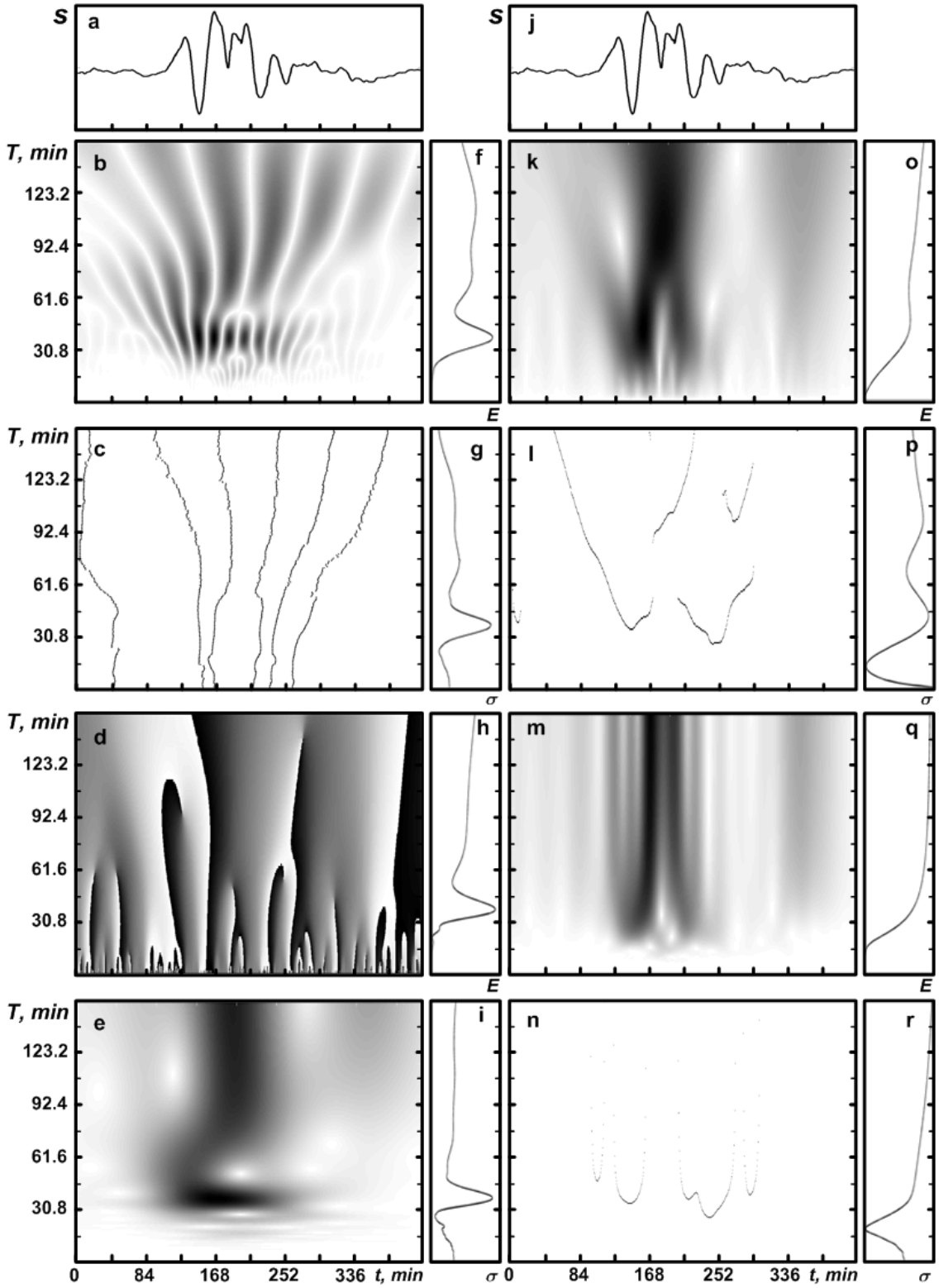


Fig. 1. The results of analysis of the temporal UWB variations of full electronic content in an ionosphere, registered on the research station in Goldstone (USA) during the explosion of the Sent-Hellens volcano (on May, 18, 1980): a, j – signal in time domain, b – CWT SDF with gaus1 wavelet, c – CWT SDF sceleton, d – phase of complex coefficients of AWT with cgau1 wavelet, e – GT SDF module, f – CWT SDF energogram, g – dispersion of CWT SDF coefficients, h – GT SDF energogram, i – dispersion of GT SDF module, k – AFT SDF module, l – AFT SDF sceleton, m – STFT SDF module, n – STFT SDF skeleton, o – AFT SDF energogram, p – dispersion of AFT SDF module, q – STFT SDF energogram, r – dispersion of AFT SDF module.

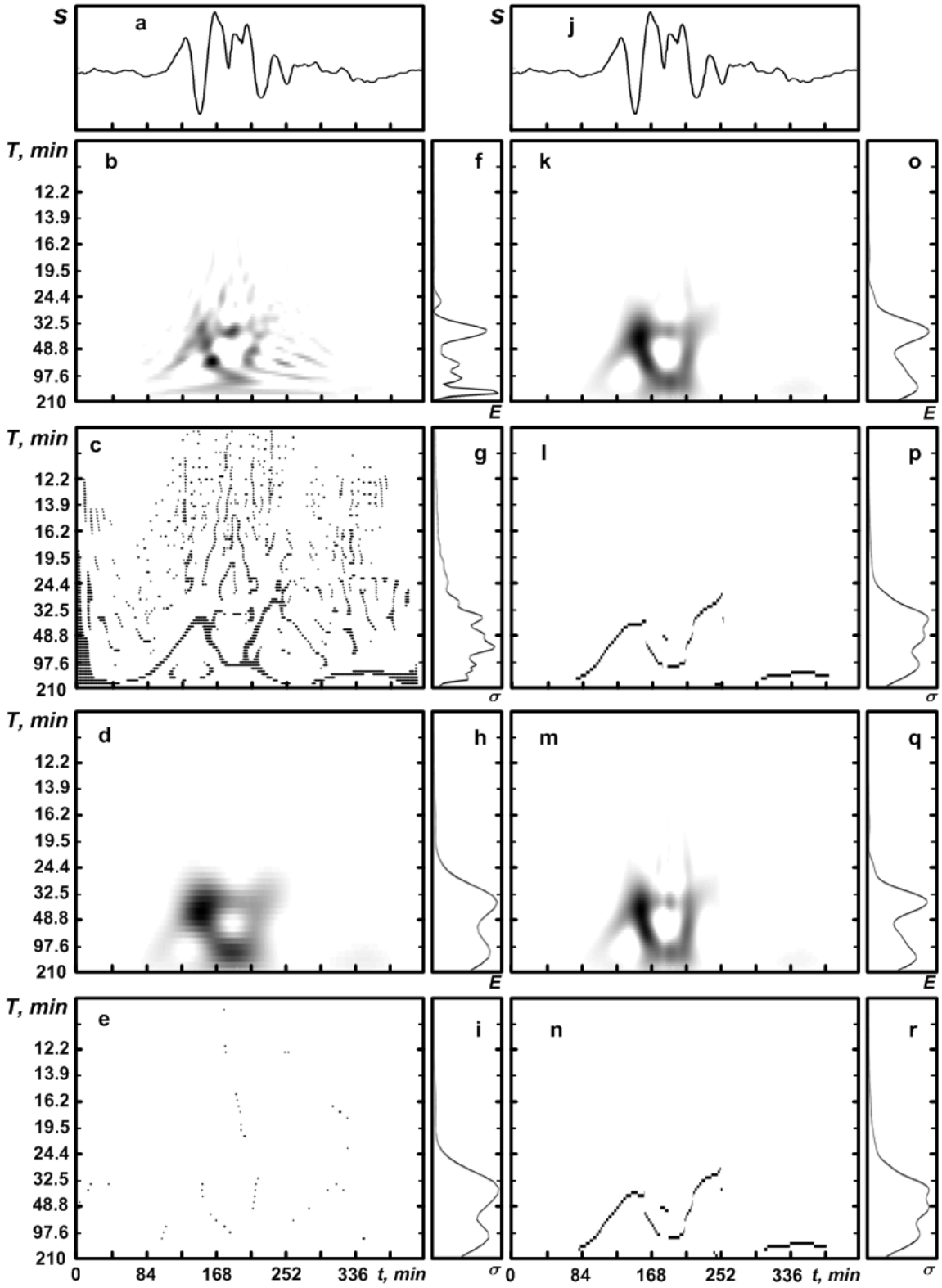


Fig. 2. The results of analysis of the temporal UWB variations of full electronic content in an ionosphere, registered on the research station in Goldstone (USA) during the explosion of the Sent-Hellens volcano (on May, 18, 1980): a, j – signal in time domain, b – PWiT SDF, c – PWiT SDF sceleton, d – FS SDF, e – FS SDF sceleton, f – PWiT SDF energogram, g – dispersion of PWiT SDF coefficients, h – FS SDF energogram, i – dispersion of FS SDF module, k – ChWT SDF module, l – ChWT SDF sceleton, m – BJT SDF module, n – BJT SDF skeleton, o – ChWT SDF energogram, p – dispersion of ChWT SDF module, q – BJT SDF energogram, r – dispersion of BJT SDF module.

ULTRA WIDEBAND SIGNALS SPECTRAL ANALYSIS

Syvozalizov N. A.

Karazin Kharkov National University, Kharkov, Ukraine
E-mail: jatsenkok@rambler.ru

Abstract

The representation and convergence problems of trigonometric and orthogonal Fourier theory are considered. The application peculiarities of classical spectral analysis to the case of ultra wideband signals and completed signals spectrum are discussed. Some conditions which restrict spectral methods application are pointed out.

Keywords: Ultra wideband signals, spectral analysis, Fourier series, convergent representation problem.

1. INTRODUCTION

Spectral analysis of signals (Fourier series and integral) is widely used in communication theory, information theory, theoretical radio engineering and other divisions of Fourier integral with integration limits at full interval of possible existence time of signal and for obtained of information about signal not infrequently statistical methods are used consisting in expansion it into a complete orthonormal system of functions, Fourier series or Fourier integral signal presentation.

Now impetuous progress of ultra wideband (UWB) technologies and investigations it in different areas of science and engineering is observed. The new kind of signals application which were appeared last fifteen years ago require both development and new mathematical methods usage for it analysis such us, system spectral analysis [1], different kind of wavelet analysis [2,3], and known transformation modification (for example, adaptive Fourier transformation[4]).

Nevertheless is spite of categorical opinion about proposes description of UWB signal: by spectral method, for frequency range determination which signal occupy, there is no another way, except Fourier series coefficients or Fourier transformation calculation. Therefore classical spectral analysis basis, convergence problem investigation, Fourier series and Fourier integral representation is case of UWB signal usage have certain interest. In considering given points we make use the theory of trigonometric and orthogonal series results [5,7].

2. REPRESENTATION OF UWB SIGNALS BY FOURIER SERIES PROBLEMS

The difficulties which arise in consequence of trigonometric Fourier series application for the complete signals presentations are pointed out in [6]. The problem about presentation possibility of any measurable function $f(x)$ by trigonometric series

$$\frac{a_0}{2}+\sum_{n=1}^{\infty}\left(a_n\cos nx+b_n\sin nx\right),$$

which converge (or summing up almost everywhere to $f(x)$) was formulated by N.N. Lusin at the beginning last century yet. Since that time N.N. Lusin problem they try to solve but it turn out very difficult and problem solution was unknown until the review [5] was write.

As concern the case, when function $f(x)$ is finite almost everywhere then in his direction fundamental result was obtained by D.E. Menshov who proved, than any no metric series, which almost everywhere converge to $f(x)$. D.E. Menshov theorem is valid and for series over Haar system.

The signal representation over Walsh system which was suggested by H.F. Harmuth at the beginning 1970 years [6] has practical importance, so far as on the basis of this presentation the different radio engineering systems were developed and exploited successfully.

3. CONVERGENCE OF FOURIER SERIES

The main problem of trigonometric and orthogonal series theory consist in convergence investigation of Fourier series of function $f(x)$ to it self or in reconstruction $f(x)$ by its Fourier series.

Kolmogorov-Selivestrov and Plevner established for trigonometric series that from condition

$$\sum_{n=0}^{\infty}\left(a_n^2+b_n^2\right)\log n<\infty$$

follows convergence almost everywhere on $[0,2\pi]$ series.

978-1-4244-7468-4/10/$26 ©2010 IEEE

$$\frac{a_0}{2}+\sum_{n=0}^{\infty}\left(a_n\cos nx+b_n\sin nx\right).$$

On the case of general orthogonal series completeness of system $\left\{\varphi_n\left(x\right)\right\}$ determines convergence of Fourier series. In order that the series

$$\sum_{n=0}^{\infty}a_n\varphi_n\left(x\right)$$

converges in $L^2(X,\mu)$ it is necessary and sufficient that equality

$$\sum_{n=1}^{\infty}\left|a_n\right|^2\left\|\varphi_n\right\|^2=\int_x\left|f\right|^2d\mu$$

holds true. However this convergence is not absolute. It is shown in [7] that any complete orthogonal system can be numerated in such order? That on it will exist divergent series from L^2.

4. FOURIER TRANSFORM

The concept about signal spectrum as Fourier integral applicable to complicated and wideband signals have been analyzed in [8] and it is shown incorrectness of spectrum calculation on infinite time interval and for signals description the instantaneous spectrum it is suggested to use.

Let point out conditions which in case of UWB signals spectral methods application restrict [9]. At first UWB signals transform essentially depend on middle frequency which like that it is impossible to exclude from consideration. Moreover the signal representation accuracy near its switching on point directly connected with spectral function representation accuracy in infinitely wide frequency range.

For UWB signals analysis in [4] it is suggested new kind of transformation-adaptive Fourier transform. The adaptability consists in adaptation of time internal processing to estimating period value of signal Fourier-component.

5. CONCLUSION

An appearance of a new, including "exotic" kind of signals, stimulates both development new methods for its analysis and boundary application search of classical spectral analysis and rigour standard increase of signal mathematical models.

REFERENCES

1. Lazorenko O.V., Chernogor L.F. 2007, 'The system spectral analysis: theoretical bases and practical applications', *Radiophysics and radio astronomy* 12, 162-181.
2. Lazorenko O.V., Lazorenko S.V., Chernogor L.F. 2007, 'The Wavelet-analysis of model signals with singularities 1. Continuous wavelet-transformation', *Radiophysics and radio astronomy* 12, 182-204.
3. Lazorenko O.V., Lazorenko S.V., Chernogor L.F. 2007, 'The Wavelet-analysis of model signals with singularities 2. Analytical and discrete wavelet transformation', *Radiophysics and radio astronomy* 12, 278-294.
4. Lazorenko O.V., Panasenko S.V., Chernogor L.F. 2005, 'Adaptive Fourier-transformation', *Electromagnetic waves and electronic systems* 10, 39-49.
5. Ulyanov P.L. 1964, 'Solved and unsolved problems of trigonometric and orthogonal series theory', *Uspekhi matem. nauk* 19, 3-69.
6. Harmuth H.F. 1985, *Nonsinusoidal waves in radar and radiocommunication*, Radio i svyaz, Moscow.
7. Olevskiy A.M. 1961, Divergent series from L^2 on complete systems, *Doklady akad.nauk SSSR.* 138, 545-548.
8. Bondarev B.N., Piza D.M. 2006.'Use of spectral presentations in radioenginering and communication', *Radioelect. ta telecom*, 14-18.
9. Astanin L.Y., Kostylev A.A. 1989, *Ultrawideband radar measurements*, Radio i svyaz, Moscow.

MATHEMATICAL MODELS OF RIGOROUS DIFFRACTION THEORY AND SIGNALS THEORY

Khoroshun V. V.

Karazin Kharkov National University, Kharkov, Ukraine
E-mail:khoroshun_vv@ukr.net

Abstract

In this paper it is pointed out that three from four summatory equations of mathematical diffraction theory of plane electromagnetic waves on planar periodical structures are entirely identical with mathematical model of unipolar impulses of different form. It is shown, that in geometrical optics approach the diffraction problem on gratings reduces to spectral characteristics of periodic sequence of rectangular form impulses determination

Keywords: Mathematical model, spectrum, signal, diffraction.

1. INTRODUCTION

Periodic sequence of different form impulses spectra in the case, when in the period one impulse contain, are investigated in detail [1-3]. Meanwhile the number of papers in which similar problem was solved for the case of presence in the period several impulses is considerably less [4], although practical interest to devices which work are based on summation on common load two or more reciprocally displaced in time videoimpulse sequences is rather high [5]. Moreover taking into consideration mathematical means similarity which is used for characteristics analysis both time-frequency and space spectra it is interesting application of results obtained by periodic impulses sequence (PIS) spectra analysis for problem solution of spectral characteristics optimization both simple [6] and multi-element gratings.

2. SOLUTION OF THE PROBLEM

Let us go into question in detail. Quite obviously that in Kirchhoff approach an electric field in grating plane is represented PIS of rectangular form, so far as uniform light of grating splits is suggested and field distortion near strip edges disregarded. In long wave resonance regions on electric field in gratings splits should be approximated in the basis of piece-sinusoidal (E-polarization) functions so far as such approximation allows representing electric field in splits as PIS of cosinusoidal form.

Let prove this statement. For this purpose we present the mathematical model of scattering plane E-polarized wave which obliquely falling on grating consisting of ideally conducting rods with rectangular cross-section [8].

$$\sum_n \begin{Bmatrix} a_n^{/} \\ b_n \end{Bmatrix} e^{ih_n x} = 0\,, \qquad \left(\frac{d}{2} < x < l - \frac{d}{2}\right)$$

$$\sum_n \begin{Bmatrix} a_n^{/} \\ b_n \end{Bmatrix} e^{ih_n x} = \sum_{m=1}^{\infty} \left(\begin{Bmatrix} c_m \\ \tilde{c}_m \end{Bmatrix} + \begin{Bmatrix} d_m \\ \tilde{d}_m \end{Bmatrix} \right) \varphi_m(x)\,, \quad |x| < \frac{d}{2}$$

$$\sum_n \begin{Bmatrix} a_n^{/} \\ b_n \end{Bmatrix} \gamma_n e^{ih_n x} - \gamma_0 =$$

$$= -\sum_{m=1}^{\infty} q_m \left(\begin{Bmatrix} c_m \\ \tilde{c}_m \end{Bmatrix} - \begin{Bmatrix} d_m \\ \tilde{d}_m \end{Bmatrix} \right) \varphi_m(x), \qquad |x| < \frac{d}{2},$$

where $\gamma_n = \frac{2\pi}{l}\sqrt{\kappa^2 - h_n^{\,2}}\,, \quad q_m = \sqrt{k_0^2 - \left(\frac{\pi m}{d}\right)^2}\,,$

$h_n = (2\pi/l)(n+\nu)\,, \qquad \nu = \kappa \sin(\zeta)\,, \qquad \kappa = l/\lambda\,,$

$\tilde{c}_m = c_m e^{iq_m h}\,,\ \tilde{d}_m = d_m e^{-iq_m h}\,,\ \varphi_m(x) = \sin\frac{\pi m}{d}\left(x + \frac{d}{2}\right),$

$a_n^{/} = a_n + \delta_{0n}\,,$ a_n and b_n – reflection and passage coefficients accordingly, δ_{0n} – Kroneker symbol, and rest of definitions correspond accepted in paper [8].

The discretization of mathematical model gives rise to direct and inverse connection formulas. In particular for passage coefficients b_n we have:

$$b_n = \frac{\theta}{2} \sum_{m=1}^{\infty} \left(c_m + d_m\right) K_m\left(\tau_n\right), \qquad (1)$$

where $K_m(\tau_n) = \frac{2}{\pi} m \frac{e^{i\frac{\pi}{2}\tau_n} - (-1)^m e^{-i\frac{\pi}{2}\tau_n}}{m^2 - \tau_n^{\,2}}\,,$

$\tau_n = 2\theta(n+\nu)$, at the same time for these functions the following summatory representation is valid:

978-1-4244-7468-4/10/$26 ©2010 IEEE

$$\sum_{n=-\infty}^{\infty} K_m(\tau_n) K_s(-\tau_n) = \begin{cases} 0, & m \neq s; \\ 2/\theta, & m = s, \ \mathrm{n} \in \mathrm{N} \end{cases}$$

The formula (1) was obtained in paper [4] in consideration of PIS spectra of cosinusoidal form and use of theorem about sum of function spectrum [1]. Below we consider PIS spectra of rectangular and cosinusoidal form in the case when in the period it is consisting of N impulses.

3. Optimization PIS Spectra of Different Form

Let in the period 2π of investigated PIS of different form it is consisting of N impulses, moreover every impulse has lengths τ_i and high U_i ($i = \overline{1,N}$). An original function $f(\alpha)$ is defined at the system of intervals $\{\alpha_i, \alpha_i + \tau_i\}$. Amplitude c_n and phase φ_n spectra are determined by Fourier series coefficients a_n and b_n in the following way:

$$c_0 = \frac{a_0}{2}, \quad \underset{n\neq 0}{c_n} = \sqrt{a_n^2 + b_n^2}, \quad \varphi_n = arctg(\frac{b_n}{a_n})$$

For the equilength impulses $\tau_i \equiv \tau$, arbitrary disposing in the period 2π, a_n and b_n present in the general form:

$$a_n = f_n(\tau)\sum_{i=1}^{N} U_i \cos((\pi\tau/2)(k_i+1)),$$
$$b_n = f_n(\tau)\sum_{i=1}^{N} U_i \sin((\pi\tau/2)(k_i+1)),$$

where $k_i = \frac{\alpha_i}{\theta_i}$, α_i - leading front phase of i-th impulse,

$$f_n(\tau) = \begin{cases} \frac{2}{\pi}\frac{\sin(n\tau/2)}{n} & (2) \\ \frac{\tau}{2}\frac{\cos(n\tau/2)}{\pi^2/4-(n\tau/2)^2} & (3), \end{cases}$$

and also (2) is for PIS rectangular form and (3) is for PIS of cosinusoidal form.

Let use obtained formula for optimization of binary sequence of rectangular form impulses spectral characteristics, since in the first place, namely this case is realized in frequency multipliers [5] and secondary for this case all the features of considered problem are shown and first of all interference nature of investigated phenomena. For amplitude spectrum c_n we have:

$$c_n = \frac{\tau}{n}\left|\frac{\sin(n\tau/2)}{n\tau/2}\right| \times$$
$$\times\sqrt{U_1^2 + U_2^2 + 2U_1U_2\cos(n(\alpha_2-\alpha_1))}.$$

This formula has cleanly interference nature that is c_n depends on impulses leading fronts phase difference.

4. Conclusion

In conclusion we use obtained results for spectral characteristics optimization of strip grating exited normally falling plane E-polarized wave. Taking into consideration evident analogies $\tau \Leftrightarrow d$, $2\pi \Leftrightarrow l$, condition for harmonics points translation (sliding), $l = \lambda \mid n \mid$, we obtain optimal value of grating gap width:

$$d = \frac{\lambda}{2}(2m+1), \quad m = \overline{0, n-1},$$

where λ – is wavelength of origin field.

The calculations show that main maximum for $|b_n|$ occur, if on grating gap greatest from possible for given n number of semi-wave is packed that is if the strip width is equal $\frac{\lambda}{2}$. An executed analysis may be generalized for multi element grating spectral characteristics optimization.

References

1. Kharkevich A.A. *Spectra and anaysis*. M., 1962.-257 c.
2. Gonorovskiy I.S. *Radioengineering circuits and signals*. M., Sov. radio, 1977.-608 p.
3. *Radioengineering circuits and signals* // Under ed. Samoylo K.A. M., 1982.-527 p.
4. Grubnik S.N., Nosich S.I., Khoroshun V.V. Optimization of spectral characteristics of periodic sequence of unipolar impulses of different form // *Bulletin Kharkov. Univ., Radiophysic and electronics*, №355, 1991.- P 84-89.
5. Kluchnik I.V., Kravchenko V.F., Khoroshun V.V. Optimization of spectral characteristics in balance frequency multipliers // *Proc. XIV Moscow scientific conference devoted Radio Day*. M., 1988.
6. Khoroshun V.V. Optimization of spectral characteristicsof strip like gratings // *Radiotechnika*. – 1990.– №2 .– P. 79–81.
7. Zholtkevych G.N., Khoroshun V.V., Khokholkov V.B. Computer simulation of electromagnetic waves diffraction on gratings consisting of ideally conducting rectangular bars (the case E-polarization) // *Bulletin Kharkiv National university. Mathematical and Informatics Technologies*, №527, 2008, P.121-133.

HILBERT TRANSFORM APPLICATION TO THE IMPULSE SIGNAL PROCESSING

[1] Batrakov D. O., [1] Golovin D. V., [1] Simachev A. A. and [2] Batrakova A. G.

[1] Karazin Kharkiv National University, Kharkiv, Ukraine
E-mail: Dmitry.O.Batrakov@univer.kharkov.ua
[2] Kharkiv National Auto-road University, Kharkiv, Ukraine

Abstract

Effective algorithm for processing impulse signals which are scattered by plane-layered media is discussed. The case, when effective thickness of layers is less than spatial size of an impulse is under consideration. Such problem of evaluating layers properties (thickness) is rather complicated for the implementation. Brief theoretical analysis of possibilities of various approaches for processing of signals is carried out. Computational algorithm and the corresponding software for evaluation not only a time delay, but also geometrical characteristics of the investigated structures are described. Both results of numerical modelling, experimental researches and sensitivity and resolution of different approaches are presented and discussed.

Keywords: Pulse signals, definition of a delay of signals, Hilbert transform, plane-layered media, thickness measurements.

1. INTRODUCTION

The development of the element base of modern radio-electronic devices on the one hand opens up new possibilities for their practical use, but on the other - dictates new requirements for the information processing techniques. This fully applies to the interpretation of georadar subsurface sounding data. The key feature of the video pulses processing is problem of pulse delay determination. This delay is basis for the determinination the physical and geometrical parameters of the objects. Previously proposed approaches to its solution [1,2], based on the application of the Hilbert transform and suitable for sensing dielectric layers with effective thickness greater than the spatial size of the probe pulse. On the other hand, in many practical applications (road construction, biomedicine), it is necessary to analyze the properties of multilayer structures consisting of thin layers (compared to the characteristic spatial size of the probe pulse). Direct application of the known methods of signal processing in this case is impossible. The aim of this work is to present methods and computational algorithms to interpret the data sensing multilayer objects with layers of small electrical thickness.

2. PROBLEM STATEMENT

As noted above, the solution of many practical problems need to receive data on the physical parameters (thickness, density, saturation) of inhomogeneous layered structures. Initial processing of experimental data in these problems are usually reduced to the problem of determining the temporal delay of the reflected pulse from the internal inhomogeneities. The main problem in this case is separation of overlapping signals and determining appropriate, such as primary, time points for each signal. Effective tool for solving such problems are algorithms that use the Hilbert transform. From the general signals theory it is known that the Hilbert transform for any arbitrary causal signal is an ideal broadband phase shifter, which provides rotation of the initial phases of all frequency components of the signal at an angle of 90º (shift to $\pi/2$). Direct Hilbert transform:

$$\tilde{x}(t) = TH\left[x(t)\right] = x(t) * (1/\pi t) = \frac{1}{\pi}\int_{-\infty}^{\infty}\frac{x(\tau)}{t-\tau}d\tau\,, \quad (1)$$

for the arbitrary function real $x(t)$, $-\infty < t < \infty$, could be given by convolution $x(t)$ with function $hb(t) = 1/(\pi t)$. Function $1/(t-\tau)$ called the kernel of the Hilbert transform. Integral of the transform has a singular point $a = t - \tau \Rightarrow 0$, in which one should use their Cauchy principal value: $\lim\limits_{a\to 0}\left[\int\limits_{-\infty}^{t-a}... + \int\limits_{t+a}^{\infty}...\right]$. In the literature on the theory of signals Hilbert transform for analog signals is proposed to perform not according to the formulas of the linear convolution operator $1/\pi t$, which leads to the ∞ at $t \Rightarrow 0$, but through a spectrum of the analytic function

978-1-4244-7468-4/10/$26 ©2010 IEEE

$$z(t) = x(t) + i\,\tilde{x}(t) \Leftrightarrow X(\nu) + i\,\tilde{X}(\nu) = Z(\nu); \quad i = \sqrt{-1}. \tag{2}$$

Substitute in (2) function $\tilde{X}(\nu) = -i\ sng(\nu)X(\nu)$, and obtain:

$$Z(\nu) = \left[1 + sng(\nu)\right]X(\nu), \tag{3}$$

where function $1 + sng(\nu)$ equals 0 at $\nu < 0$, equals 1 at $\nu = 0$ and 2 at $\nu > 0$, besides:

$$Z(\nu) = \begin{cases} 2X(\nu), & \nu > 0 \\ X(0), & \nu = 0 \\ 0, & \nu < 0 \end{cases} \tag{4}$$

i.e. the spectrum of the $z(t)$ function is one-side and could be obtained directly from the $x(t)$ function spectrum with $\nu \geq 0$. Inverse Fourier transform for $Z(\nu)$ function should lead one to a complex function $z(t)$, and from the (4) one can obtain:

$$x(t) = \mathrm{Re}\left[2\int_0^\infty X(\nu)\exp(i\,2\pi\,\nu\,t)\,d\nu\right], \tag{5}$$

$$\tilde{x}(t) = \mathrm{Im}\left[2\int_0^\infty X(\nu)\exp(i\,2\pi\,\nu t)\,d\nu\right]. \tag{6}$$

In discrete form, with a total N samples of the function $x(t)$ with time-step Δt and frequency step $\Delta\nu = 1/(N\Delta t)$:

$$X(n\Delta t) = \Delta t\sum_{k=0}^{N-1} x(k\Delta t)\exp(-i2\pi kn / N), \quad n = 0,1,\ldots,N/2, \tag{7}$$

$$x(k\Delta t) = \Delta f\,\mathrm{Re}\left[X_O + 2\sum_{n=1}^{N/2} X(n\Delta\nu)\exp(i2\pi kn / N)\right], \tag{8}$$

$$\tilde{x}(k\Delta t) = 2\Delta\nu\,\mathrm{Im}\left[\sum_{n=1}^{N/2} X(n\Delta\nu)\exp(i2\pi kn / N)\right]. \tag{9}$$

Based on the above properties of the Fourier and Hilbert transforms, the authors of [1] attempted to correct formulation of the concept of delay, calling the such delay the "Hilbert delay". The reason of this scheme application is based on the allocation of the total signal received by antenna, the so-called minimum phase part [3]. This allocation is carried out as follows: for the recorded signal $U(t)$ one can construct phase part of the spectral component with the formula:

$$\phi(\omega) = \frac{1}{\pi}\int_{-\infty}^{\infty} \frac{\ln|U(\theta)|}{\omega - \theta}d\theta. \tag{10}$$

where $|U(\theta)|$ - module of the Fourier spectrun of the initial signal $U(i\omega) = |U(\omega)|\cdot\exp[i\cdot\psi(\omega)]$. If this phase part express like: $\psi(\omega) = \phi(\omega) + \gamma(\omega)$, one can obtain following factorization for any signal:

$$V(i\omega) = |V(\omega)|\cdot\exp[i\cdot\phi(\omega)]\cdot\exp[i\cdot\gamma(\omega)] = V_{M\Phi}(i\omega)\cdot M(i\omega), \tag{11}$$

where $V_{M\Phi} = |V(\omega)|\cdot\exp[i\cdot\phi(\omega)]$ - Fourier spectrum of the minimal-phase signal part, $M(i\omega) = \exp[i\cdot\gamma(\omega)]$ - maximal-phase signal part spectrum $m(t)$. Module of the minimum-phase spectrum of the signal coincides with the modulus spectrum of the original signal, and the module of the spectrum maximum-phase part is equal to 1. As a function of uncertainty of the signal delay on Hilbert one should take the maximum-phase component $m(t)$ of the signal $U(t)$, i.e:

$$m(t) = \frac{1}{2}\pi\int_{-\infty}^{\infty} M(i\omega)\cdot\exp(i\omega t)d\omega. \tag{12}$$

Hilbert signal Delay relative to the time t = 0 is called the maximum of the delay ambiguity function. Analysis of the Hilbert transform properties shows that the maximum of its modulus will be in the points of signal smoothness violation, where the first derivative has discontinuity. These points are obviously the point of beginning of the signal, which makes such a determination delay intuitive. However, such approach has the drawback associated with the need to calculate the phase of the spectrum minimum phase components of the formula (10). Obviously, if harmonics with small amplitudes are present in the original signal spectrum, the modulus of the integrand $\ln|U(\theta)|$ increases strongly. And if any spectral amplitude is zero, this function generally tends to minus infinity. As shown by numerical simulation, this algorithm works well only for certain kinds of signals, whose shape is similar to the δ-function. This is understandable, since in the spectrum of δ-functions are present all the spectral components with equal amplitudes.

In another approach, proposed in [1] based algorithm for detecting UWB georadar signals and determination of their characteristics suggested to analize Hilbert transform module. More precisely, the modulus of the Hilbert transform will be the module of the function $\tilde{x}(t)$ defined by (1). But, in fact, authors propose to evaluate the integrated module of the analytic signal constructed from the original signal using Hilbert transform. Such a function is smooth and unipolar. It has only one maximum, so the detection signal on the time axis is reduced to finding the maxima of its modulus. The polarity of the pulse is determined by the values of the wave function at the time corresponding to the maximum of the module.

The transform function is usually represented in complex form $h(t) = x(t) + i\tilde{x}(t)$. In the theory of

analytic signals through its module $\left|h(t)\right|$ determines the pulse $A(t)$ envelope:

$$A(t) = \left|h(t)\right| = \sqrt{x^2(t) + \tilde{x}^2(t)} \qquad (13)$$

We propose the following scheme for determining the time delay of signals reflected from the inner boundary plane layered structures:

- With the transform of the original signal, represented by samples in the time domain according to (1) compute its Hilbert transform;
- Form the complex spectrum of the analitical signal;
- Synthesizing function of time distribution signal $A(t)$ module according to the formula (13);
- Search for peaks of this function;
- Determine the polarity of the reflected pulses on the basis of analysis of the sign of the function $x(t)$ at the appropriate time

3. NUMERICAL ALGORITHM

In order to perform numerical tests and for practical application of the proposed signals time delay determining scheme appropriate software has been developed.

With the help of this software a series of computational experiments were performed. Results of these experiments are shown at Fig. 1,2. As the probe was selected pulse of georadar "Odyag" used by the Department of research and design of roads Kharkov National Automobile and Highway University in the assessment of road surfaces and road pavements. The pulse duration is approximately 1 ns, repetition rate 20 kHz, amplitude - 200V.

As can be seen from the figure for the layer thickness of 1 cm used spectral Hilbert transform does not allow to determine the thickness, since the processed signal contains only one maximum (Fig. 3a). This same source signal processed using the integral of the Hilbert transform of the quadrature formula (1), has 2 peak, separated by a distance roughly corresponds to the thickness of the layer.

CONCLUSION

The main conclusions to be drawn from the results of numerical modeling is that the proposed algorithm and the developed software is an effective tool for monitoring of industrial sites and road construction. Proposed scheme of signals time delay calculating can be usefull for solution of the major georadar problems: subsurface structural and material inhomogeneities (of different nature) identification, different composition of the studied objects, especially structure and texture of investigated materials (porosity, layering).

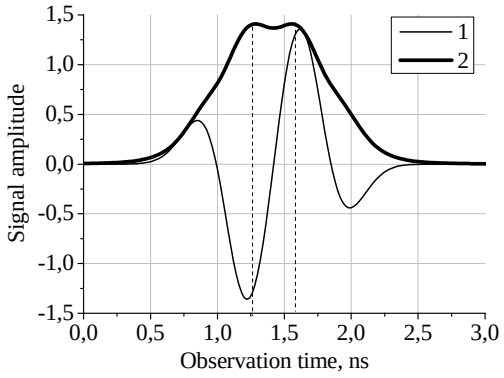


Fig. 1. (1) – georadar signal, (2) – transformed signal. Investigated structure is single layer with $\varepsilon = 3$ and height 1 cm.

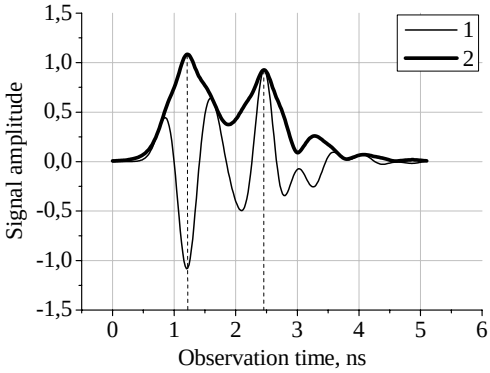


Fig. 2. (1) – georadar signal, (2) – transformed signal. Investigated structure is single layer with $\varepsilon = 3$ and height 8 cm.

In addition, the proposed pulse signals treatment algorithm can further be the basis for constructing of more complicated methods of determining the complex physical and geometrical characteristics of industrial structures and natural objects.

REFERENCES

1. Krylov V.V., Ponomarev D.M. 1980, 'Definition of the signal delay by Gilbert and methods of its measurement' Radiotehnika i Electronika, vol.25., #1, 204-206 (in Russian)
2. Oppengeim A.V., Shafer R.V., 1979, 'Digital Signal Processing', Moscow
3. Vasil'ev V.N., Gurov I.P., 1998, 'Computer processing of signals in the annex interferometer system', St. Petersburg (in Russian)
4. Khruslov E.Y., Shepelsky D. G., 1994, 'Inverse scattering method in electromagnetic sounding theory. Inverse problems', vol.10, #2, 1-37
5. Batrakov D.O., Tarasov M.M., 1999, 'An algorithm for solving inverse scattering problems based on the Pontryagin maximum principle' Radiotehnika i Electronika vol.44, #2, 137-142 (in Russian)

QUASI-RESONANCE ACCOUNTING IN REPRESENTATION OF WIDEBAND FREQUENCY RESPONSE OF TWO-DIMENSIONAL OPEN RESONANCE STRUCTURES

Andreev M. V. and Borulko V. F.

Dnepropetrovsk National University, Dnepropetrovsk, Ukraine
E-mail: microwave@mail.dsu.dp.ua, dsu-microwave@mail.ru

Abstract

The problem of selection of convenient model of wideband frequency response of open resonance structures was examined. Importance of influence of the quasi-resonance effects on formation of resonance curve is demonstrated. For quasi-resonance accounting the square root singularity was used.

Keywords: Pole model, quasi-resonance, open resonance structure.

1. INTRODUCTION

The complex resonance frequencies in wideband frequency response of a scatterer are important elements in target classification and identification. In the singularity expansion method [1] the response of reflection from metal objects is determined by a set of poles which are typical for these objects. But domination of these poles becomes apparent only in late-time part of the response. Early-time component is determined by the shape of exciting pulse and low-Q interaction of reflections from target scattering centers [2]. Usually in such models the effects forming non-pole singularities of the frequency response are left out of account. Consideration of such effects is of interest and for simplicity they were examined on example of open resonance structures of the simple shape.

The frequency response of the resonance structure is defined by resonance behavior of complex amplitudes of eigenmodes in decomposition of field [3]. Therefore traditionally for representation of the frequency response of the open resonance structures the sum of pole functions is used. But under the analyses in wide frequency band such model can give the significant deviation from the frequency response of the real structure under test. This deviation will be largest on the periphery of the resonance peaks for the frequency intervals remote from resonance frequencies.

The quasi-resonances of radiated and leaky waves which are manifested at prolonged transient process of transformation of exciting field in the resonator eigenmode can be the reason for such deviations. Under certain relations between resonator Q factor and parameters of exciting field the small number of large initial rereflections of unformed field can become apparent on background of large number of small reflections of the shaped field. Their total contribution forms the singularity of the frequency response with shape which strongly is differed from shape of the pole singularity.

In [4] these effects were considered on an example of three-dimensional open resonance structure formed by two spherical mirrors. Here they have been considered for two-dimensional open resonance structures.

2. BASIC CONCEPT

The two-dimensional open resonance structures formed by two mirrors placed in parallel along the *x* and on distance *l* along *z* (fig. 1) were considered. It was supposed that along *y* the structure was homogeneous and had infinite length.

If the structure is unlimited and homogeneous along the *x*, then under excitation by point source (endless current filament along the *y*) the field will be determined by expression [5]:

$$u_0(x,z)=\frac{j}{l}\sum_{n=1}^{\infty}\frac{\sin(\gamma_n z)\sin(\gamma_n \zeta)}{\chi_n}e^{-j\chi_n|x-\xi|}, \quad (1)$$

where $\chi_n=\sqrt{k^2-\gamma_n^2}$ and $\gamma_n=n\pi/l$ are longitudinal and transverse components of wave number *k*, (ξ,ζ) is location of the source. Accordingly, the fre-

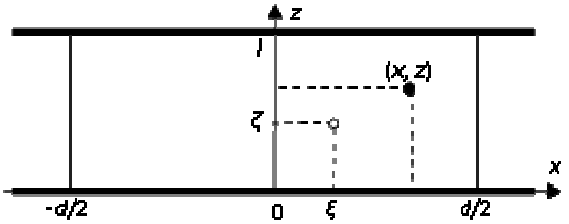


Fig. 1. The geometry of the resonance structure.

978-1-4244-7468-4/10/$26 ©2010 IEEE

quency response in the observation point for the case $x = \xi = 0$ will be determined by function

$$u_0(f) = \frac{jf_0}{\pi} \sum_{n=1}^{\infty} \frac{\sin(\gamma_n z)\sin(\gamma_n \zeta)}{\sqrt{f^2 - (nf_0)^2}}, \qquad (2)$$

where $f_0 = c/2l$ is beat frequency along *z*, *c* is light speed. This function will have square root singularity (quasi-resonance) on frequencies which are multiple of f_0. On the other hand at excitation of such structure by the eigenmode (plane wave which is unlimited along *x* and *y*) the frequency response on these frequencies will have pure pole singularity (resonance). Because of unboundedness of structure along *x* the transition process of transformation of field of the point source into the eigenmode is unlimited in time.

If the structure is bounded along the *x* by the open boundaries $x = \pm d/2$ with the reflection coefficient from them R_n, then the field of the point source in such structure can be represented as a sum of the field of the unlimited structure u_0 (the divergent traveling wave) and the resonance part u_r (standing wave):

$$u = u_0 + u_r = u_0 + \sum_{n=1}^{\infty} B_n(x) C_n(z) T_n(d), \qquad (3)$$

where

$$B_n(x) = \cos\chi_n(x+\xi) + R_n e^{-j\chi_n d}\cos\chi_n(x-\xi), \quad (4)$$

$$C_n(z) = j\sin(\gamma_n z)\sin(\gamma_n \zeta)/\chi_n l. \qquad (5)$$

$$T(d) = 2R_n e^{-j\chi_n d}/\left(1 - R_n^2 e^{-j2\chi_n d}\right). \qquad (6)$$

Dielectric layer with permeability ε which is filling area $-d/2 \le x \le d/2$, $0 \le z \le l$ in hollow parallel-plane waveguide can be an example of such open resonance structure. In this case, the reflection coefficient is given by

$$R_n = \frac{\chi_n - \chi_n^0}{\chi_n + \chi_n^0}, \qquad (7)$$

where $\chi_n = \sqrt{\varepsilon k^2 - \gamma_n^2}$ is longitudinal wave number for the part of parallel-plane waveguide filled by the dielectric, $\chi_n^0 = \sqrt{k^2 - \gamma_n^2}$ is longitudinal wave number for the unfilled parallel-plane waveguide.

For case $\varepsilon \to 1$ the small number of high-Q resonances will be located in the narrow frequency band $f_0/\sqrt{\varepsilon} < f < f_0$. Only one resonance will be in this band if $\varepsilon < 1 + (2l/d)^2$. In this case for very large *d* this resonance peak will be so close to quasi-resonance peak that they will merge in one peak.

Fig. 2 demonstrates the variation of form of frequency response under the increase of *d* for the layer with $\varepsilon = 1.002 + 0.001j$, $l/\lambda = 0.5$ ($x = \xi = 0$). For the examined example fig. 3 demonstrates the increase of relative contribution of quasi-resonance part $\|u_0\|^2/\|u\|^2$ and reduction of the contribution of resonance part $\|u_r\|^2/\|u\|^2$ under the increase of *d*. In fig. 4 for value $d/\lambda = 4$ the view of the frequency response of components of model (3) is presented. Fig. 4 demonstrates that the periphery of the frequency response is completely determined by quasi-resonance term u_0. In fig. 5 the view of time-domain response for the value $d/\lambda = 4$ is presented. It demonstrates that the start segment of this response entirely is determined by quasi-resonance term u_0, and only after its decrease the resonance term u_r begins to determine the form of the time-domain response.

The square root singularity of frequency response occurs also on frequency f_0 under fulfillment of condition $d = 2ml/\sqrt{\varepsilon - 1}$ for $m = 0,1,\ldots$. At $f \to f_0$ the approximation $R(f) \approx 1 - 2c_R\sqrt{f^2 - f_0^2}$ is valid, where c_R is the coefficient weakly dependent on frequency. Hence it follows that in neighborhood of f_0 it is possible to use the approximation $u(f) \approx c_u/\sqrt{f - f_0}$, where c_u is the coefficient weakly dependent on frequency. Therefore when the resonance peak is located on cutoff frequency of hollow waveguide its form will not be determined by pole, but square root singularity. If such peak will be approximated by the pole function, the approximation quality will be low.

For approximation of the frequency response of such and more complicated open resonance structures taking into account resonance and quasi-resonance components the model has been taken in next form

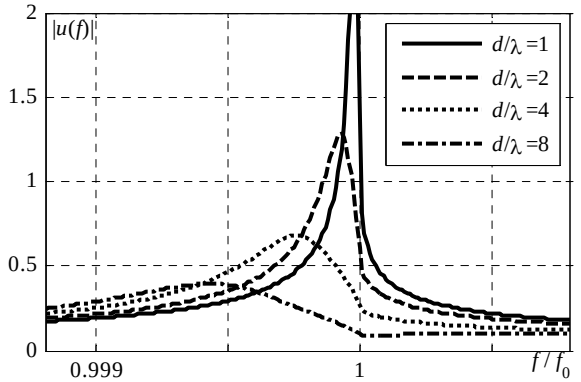


Fig. 2. The frequency response for different *d*.

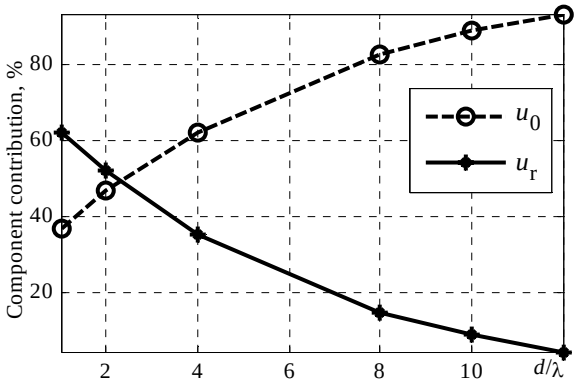


Fig. 3. Contribution of components of model (3).

$$u_M(f,\mathbf{p}) = \sum_{m=1}^{M} \frac{r_m}{f - f_m} + \sum_{n=1}^{N} \frac{q_n}{\sqrt{f^2 - (nf_q)^2}}, \quad (8)$$

where $\mathbf{p} = \{f_1, \ldots, f_M, f_q\}$ is vector of frequency parameters of the model. The algorithm of determination of model parameters on the basis of the concept of quasisolution searching has been developed.

3. Experimental Results

An efficiency of the considered model was analyzed on the example of approximation of frequency responses of resonance structures in the form of the dielectric layer in parallel-plane waveguide.

The result of approximation by pure pole for layer with d/λ = 4 is demonstrated in fig. 6. The error of approximation $\delta = \|u - u_M\|^2 / \|u\|^2$ for frequency band $\Delta f / f_0 = 0.2$ was 20 % and for frequency band $\Delta f / f_0 = 1$ was 32 % that corroborates an inefficiency of rational model, especially for approximation of the wideband response. The inadequacy of such model demonstrates the representation of these curves in the time domain (fig. 7): the decay rate of early-time components because of the influence of quasi-resonance greater than the decay rate of late-time components and that does not correspond to the model of exponential decay. Therefore the estimation of quality factor has the understated value $1.5 \cdot 10^3$.

The use in the model (8) of quasi-resonance term has allowed to reduce the approximation error to 0.1% (for both bands), that corresponds to the approximation with graphical accuracy (therefore there is no point in demonstrating the curves). The estimation of the quality factor has been increased to $3.8 \cdot 10^3$.

This research has shown inadequacy of pure pole model for representation of open resonator frequency response and necessity of quasi-resonance accounting.

References

1. Baum C.E., Rothwell E.J., Chen K.-M. & Nyquist D.P. 1991, 'The singularity expansion method and its application to target identification', *Proceedings of the IEEE*. **79**, 1481-1492.
2. Rothwell E.J., Chen K.-M., Nyquist D.P., Ilavarasan P., Ross J. E., Bebermeyer R. & Li Q. 1994, 'A general E-pulse scheme arising from the dual early-time/late-time behavior of radar scatterer', *IEEE Trans. Antennas Propagat*. **42**, 1336-1341.
3. Weinstein L. A. 1969, *Open Resonators and Open Waveguides*, The Golem Press, Colorado.
4. Andreev M.V., Borulko V.F., and Drobakhin O.O., 2008, 'Modification of pole model for wideband responses of distributed structures', *Proc. 4th Int. Conf. on Ultrawideband and Ultrashort Impulse Signals*, Sevastopol, 204-206.
5. Budak B.M., Samarsky A.A., Thichonov A.A. 1988, *A Collection of Problems in Mathematical Physics*, Dover Publication, New York.

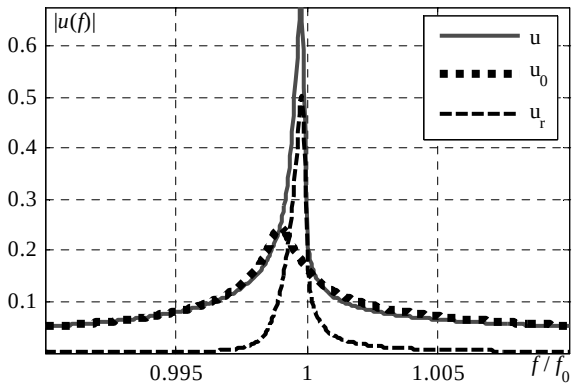


Fig. 4. The frequency response for d/λ = 4.

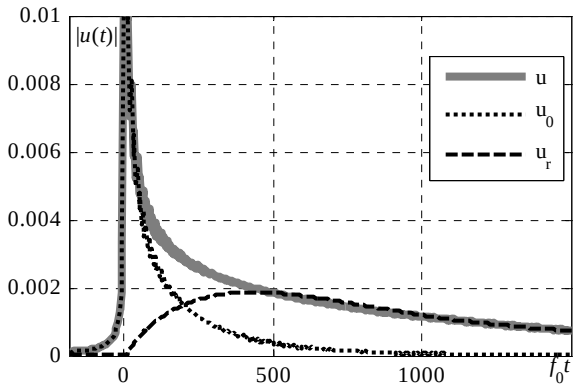


Fig. 5. The time-domain response for d/λ = 4.

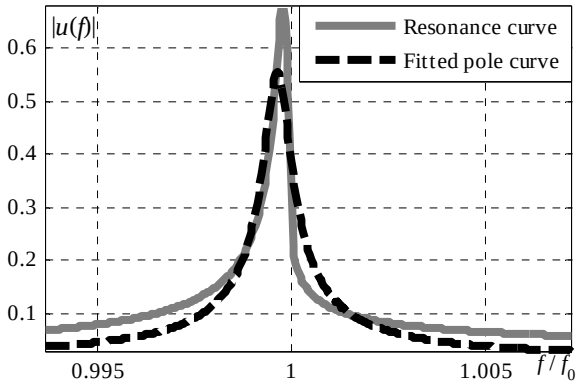


Fig. 6. The result of approximation by pure pole.

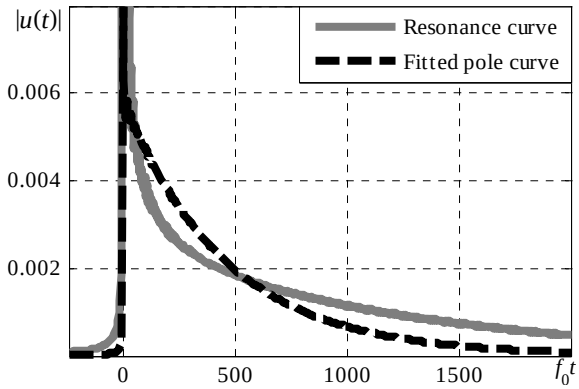


Fig. 7. The time-domain signal of approximation.

IMPULSE SIGNAL PROPAGATION IN OPEN DIELECTRIC CIRCULAR WAVEGUIDE

Legenkiy M. N. and Butrym A. Yu.

Karazin Kharkiv National University, Kharkiv, Ukraine
E-mail: mlegenkiy@ya.ru

Abstract

The paper considers generalization of Mode Basis Method for calculation of pulse signal propagation in a circular open dielectric waveguide. The mode functions are calculated by Integral Equations Method. It is shown that the circular dielectric waveguide possesses only continuous spectrum. Then an integral-differential System of Evolutionary Equations is obtained that describes mode amplitudes evolution in time with propagation. Its solution by the method of moments is proposed. Propagation of some pulse signal in a circular dielectric waveguide is calculated.

Keywords: Mode Basis Method, circular dielectric waveguide, Integral Equation Method, continuous spectrum, system of evolutionary equations, method of moments.

1. INTRODUCTION

A lot of electromagnetic problems that require application of Time Domain (TD) methods have appeared recently. Among such is the problem of pulse signals propagation in an open dielectric waveguide. This problem emerges in analysis of ultrashort pulse propagation in optic and photonic waveguides (fibers), pulse radiation by dielectric rod antennas.

The problem will be treated with Mode Basis Method (MBM) proposed by Prof. Tretyakov [1]. MBM is the method of incomplete separation of variables in Maxwell equations in TD. From the Maxwell equations some transversal coordinate derivative operators are derived. These operators can be proved to be self-adjoint ones. Therefore their eigenfunctions constitute a complete basis for expansion of the sought fields. Thus the solution in TD is presented in the form of mode expansion with coefficients (mode amplitudes) depending on longitudinal coordinate and time. The basis is found from the boundary eigenvalue problem for the obtained operators.

There are implementations of MBM for field analysis in a closed waveguide with inhomogeneous dielectric [2], and in the free space (mode spectrum being continuous in this case) [3]. For a closed waveguide the transverse coordinate boundary eigenvalue problem results in a discrete mode spectrum due to finiteness of the cross-section. In case of the free space the solution to the transverse boundary problem has to satisfy only Somerfield condition at infinity [4], hence in such a structure there is a continuous mode spectrum.

We are going to consider a pulse signal propagation in an open cylindrical waveguide by MBM. Mode basis construction for the case of open structures by Integral Equations Method was considered in [4]. In this paper we obtain the System of Evolutionary Equations; consider its solution with the help of the Method of Moments and FDTD technique; and present some numerical results.

2. SYSTEM OF EVOLUTIONARY EQUATIONS

In order to obtain the system of evolutionary equations describing the change of the fields during its propagation in the structure the sought fields can be expanded into integrals over the modes as

$$\begin{aligned}
&\sqrt{\mu_0}H_z(z,t,\vec{r}) = \int_p h(z,t;p)\,p\,\Phi^h(\vec{r};p)\,dp,\\
&\sqrt{\varepsilon_0}E_z(z,t,\vec{r}) = \int_p e(z,t,p)\,p\,\Phi^e(\vec{r},p)\,dp,\\
&\sqrt{\varepsilon_0}\vec{E}(z,t,\vec{r}) = \int_p \begin{pmatrix} v^h(z,t;p)\vec{E}^h(\vec{r};p) + \\ +v^e(z,t,p)\vec{E}^e(\vec{r},p) \end{pmatrix} dp,\\
&\sqrt{\mu_0}\vec{H}(z,t,\vec{r}) = \int_p \begin{pmatrix} i^h(z,t,p)\vec{H}^h(\vec{r},p) + \\ +i^e(z,t,p)\vec{H}^e(\vec{r},p) \end{pmatrix} dp.
\end{aligned} \tag{1}$$

Substituting expansions (1) into Maxwell equations and using orthogonal relations for mode functions [2] one can obtain the following evolutionary equations

$$\begin{aligned}
&\partial_\tau i^h(p) + \int L^{hh}(p',p)\,\partial_z v^h(p')\,dp' = -J^m_{Hh}(p),\\
&\int K^{hh}(p,p')\,\partial_\tau i^h(p')\,dp' + \partial_z v^h(p) = -J^m_{Eh}(p).
\end{aligned} \tag{2}$$

$$\begin{aligned}
&\partial_\tau v^e(p) + \int L^{ee}(p,p')\,\partial_z i^e(p')\,dp' = -J^e_{Ee}(p),\\
&\int K^{ee}(p',p)\,\partial_\tau v^e(p')\,dp' + \partial_z i^e(p) = -J^e_{He}(p).
\end{aligned} \tag{3}$$

978-1-4244-7468-4/10/$26 ©2010 IEEE

$$\begin{aligned}
&\int\left(L^{he}(p',p)\partial_z^2 v^h(p')+L^{ee}(p',p)\partial_z^2 v^e(p')\right)dp',\\
&\partial_{z\tau}^2 i^e(p)-\int p'^2 v^e(p')dp'=\rho_\Psi^e(p)-\partial_z J_{He}^m(p),\\
&\int\left(K^{eh}(p,p')\partial_\tau^2 i^h(p')+K^{ee}(p,p')\partial_\tau^2 i^e(p')\right)dp',\\
&\partial_{z\tau}^2 v^e(p)+\int p'^2 i^e(p')dp'=-J_\Phi^{ez}(p)-\partial_\tau J_{Ee}^m(p).
\end{aligned}\quad(4)$$

$$\begin{aligned}
&\int\left(L^{hh}(p,p')\partial_z^2 i^h(p')+L^{he}(p,p')\partial_z^2 i^e(p')\right)dp',\\
&\partial_{\tau z}^2 v^h(p)-\int p'^2 i^h(p')dp'=\rho_\Psi^m(p)-\partial_z J_{Eh}^e(p),\\
&\int\left(K^{hh}(p',p)\partial_\tau v^h(p')+K^{eh}(p',p)\partial_\tau v^e(p')\right)dp',\\
&+\partial_{\tau z}^2 i^h(p)+\int p'^2 v^h(p')dp'=-J_\Phi^{mz}(p)-\partial_\tau J_{Hh}^e(p).
\end{aligned}\quad(5)$$

$$\begin{aligned}
v^h(p)&=-\int K^{hh}(p,p')\partial_\tau h_z(p')dp'-J_\Phi^{mz}(p),\\
v^e(p)&=\partial_z e_z(p)-\rho_\Phi^e(p),\\
i^h(p)&=\partial_z h_z(p)-\rho_\Psi^m(p),\\
i^e(p)&=-\int K^{ee}(p',p)\partial_\tau e_z(p')dp'-J_\Phi^{ez}(p).
\end{aligned}\quad(6)$$

Here we use the following coupling functions

$$\begin{aligned}
L^{hh}(p,p')&=\int\vec{z}_0\cdot\left[\vec{E}^h(\vec{r},p)\times\vec{H}^h(\vec{r},p')\right]dS,\\
L^{ee}(p,p')&=\int\vec{z}_0\cdot\left[\vec{E}^e(\vec{r},p)\times\vec{H}^e(\vec{r},p')\right]dS,\\
L^{he}(p,p')&=\int\vec{z}_0\cdot\left[\vec{E}^h(\vec{r},p)\times\vec{H}^e(\vec{r},p')\right]dS.\\
K^{hh}(p,p')&=\int\varepsilon_\perp\vec{z}_0\cdot\left[\vec{E}^h(\vec{r},p)\times\vec{H}^h(\vec{r},p')\right]dS;\\
K^{ee}(p,p')&=\int\varepsilon_\perp\vec{z}_0\cdot\left[\vec{E}^e(\vec{r},p)\times\vec{H}^e(\vec{r},p')\right]dS;\\
K^{eh}(p,p')&=\int\varepsilon_\perp\vec{z}_0\cdot\left[\vec{E}^e(\vec{r},p)\times\vec{H}^h(\vec{r},p')\right]dS.
\end{aligned}$$

Expressions for these coupling functions were obtained in a closed form. In the right hand parts of equations (2) - (6) one can see source functions, defined as follows:

$$\begin{aligned}
J_{Eh}^e(p)&=\int\sqrt{\mu_0}\,\vec{J}(\vec{r})\cdot\vec{E}^h(\vec{r},p)\,dS,\\
J_{Ee}^e(p)&=\int\sqrt{\mu_0}\,\vec{J}(\vec{r})\cdot\vec{E}^e(\vec{r},p)\,dS,\\
J_{Hh}^e(p)&=\int\sqrt{\mu_0}\,\vec{J}(\vec{r})\cdot\left[\vec{H}^h(\vec{r},p)\times\vec{z}_0\right]dS,\\
J_{He}^e(p)&=\int\sqrt{\mu_0}\,\vec{J}(\vec{r})\cdot\left[\vec{H}^e(\vec{r},p)\times\vec{z}_0\right]dS,\\
J_{Eh}^m(p)&=\int\sqrt{\varepsilon_0}\vec{\hat{J}}(\vec{r})\cdot\varepsilon_\perp\left[\vec{z}_0\times\vec{E}^h(\vec{r},p)\right]dS,\\
J_{Ee}^m(p)&=\int\sqrt{\varepsilon_0}\vec{\hat{J}}(\vec{r})\cdot\varepsilon_\perp\left[\vec{z}_0\times\vec{E}^e(\vec{r},p)\right]dS,\\
J_{Hh}^m(p)&=\int\sqrt{\mu_0}\,\vec{\hat{J}}(\vec{r})\cdot\vec{H}^h(\vec{r},p)\,dS,\\
J_{He}^m(p)&=\int\sqrt{\mu_0}\,\vec{\hat{J}}(\vec{r})\cdot\vec{H}^e(\vec{r},p)\,dS.\\
J_\Phi^{ez}(p)&=p\int\sqrt{\mu_0}\,J_z(\vec{r})\Phi^e(\vec{r},p)\,dS,\\
J_\Psi^{ez}(p)&=p\int\sqrt{\mu_0}\,J_z(\vec{r})\Psi^e(\vec{r},p)\,dS,
\end{aligned}\quad(7)$$

$$\begin{aligned}
\rho_\Phi^e(p)&=p\int\sqrt{\varepsilon_0^{-1}}\rho(\vec{r})\Phi^e(\vec{r},p)dS,\\
\rho_\Psi^e(p)&=p\int\sqrt{\varepsilon_0^{-1}}\rho(\vec{r})\Psi^e(\vec{r},p)dS,\\
J_\Phi^{mz}(p)&=p\int\sqrt{\varepsilon_0}\,\hat{J}_z(\vec{r})\Phi^h(\vec{r},p)\,dS,\\
J_\Psi^{mz}(p)&=p\int\sqrt{\varepsilon_0}\,\hat{J}_z(\vec{r})\Psi^h(\vec{r},p)\,dS,\\
\rho_\Phi^m(p)&=p\int\sqrt{\mu_0^{-1}}\hat{\rho}(\vec{r})\Phi^h(\vec{r},p)\,dS,\\
\rho_\Psi^m(p)&=p\int\sqrt{\mu_0^{-1}}\hat{\rho}(\vec{r})\Psi^h(\vec{r},p)\,dS.
\end{aligned}\quad(8)$$

In formulae (2)-(6), (7)-(8) for brevity sake we omit the time and longitudinal coordinate dependences (z,t) for mode amplitudes and source functions.

3. PULSE PROPAGATION IN DIELECTRIC WAVEGUIDE

In order to verify the proposed approach we are going to consider pulse propagation in a circular dielectric waveguide and compare the obtained results with those of FDTD modeling. The fiber is excited by a ring of azimuthal magnetic currents [5]. In order to obtain the excitation function with limited mode and frequency spectrum we use the ring of $\vec{\varphi}_0$ -magnetic currents with gaussian waveform and radial shape $\hat{J}(\vec{r},z,t)=\cos(\varphi)\,\delta(z-z_0)\exp(-((r-r_0)/0.12a)^2)\times$ $\times\exp(-((t-t_0)/T)^2)$ where $a=1.1, r_0=0.5\,a,$ $T=a/(5c), t_0=5T$. The system of evolutionary equations with such source can be reduced to a pair of second order equations

$$\begin{cases}
\int\left(K^{hh}(p',p)\partial_\tau^2-L^{hh}(p',p)\partial_z^2\right)v_h(p')dp'+\\
\int\left(p'^2 v_h(p')+K^{eh}(p',p)\partial_\tau^2 v_e(p')\right)dp'=\partial_z J_{Hh}^m(p);\\
\int\left(K^{ee}(p',p)\partial_\tau^2-L^{ee}(p',p)\partial_z^2\right)v_e(p')dp'+\\
\int\left(p'^2 v_e(p')-L^{he}(p',p)\partial_z^2 v_h(p')\right)dp'=\partial_z J_{He}^m(p).
\end{cases}\quad(9)$$

Using Finite Element Method [6] we express the mode amplitude in the form of expansion over some orthogonal functions $v^{e,h}(p)=\sum V_j^{e,h}\psi_j(p)$ $\int_p\psi_j(p)\psi_i(p)dp=\delta_{i,j}$. So system of integro-differential equations (9) reduces to the system of matrix differential equations

$$\begin{cases}
\mathbf{K^{hh}}\cdot\partial_\tau^2\mathbf{V^h}-\mathbf{L^{hh}}\cdot\partial_z^2\mathbf{V^h}+\mathbf{P^2}\cdot\mathbf{V^h}+\mathbf{K^{eh}}\cdot\partial_\tau^2\mathbf{V^e}=\\
\qquad=\partial_z\mathbf{J_{Hh}^m};\\
\mathbf{K^{ee}}\cdot\partial_\tau^2\mathbf{V^e}-\mathbf{L^{ee}}\cdot\partial_z^2\mathbf{V^e}+\mathbf{P^2}\cdot\mathbf{V^e}-\mathbf{L^{he}}\cdot\partial_z^2\mathbf{V^h}=\\
\qquad=\partial_z\mathbf{J_{He}^m}.
\end{cases}\quad(10)$$

Where we introduced the following matrices

$$\mathbf{K}^{\mathbf{hh}}{}_{i,j}=\int\int K^{hh}(p',p)\psi_j(p')\psi_i(p)dp'dp,$$

$$\mathbf{L}^{\mathbf{hh}}{}_{i,j}=\int\int L^{hh}(p',p)\psi_j(p')\psi_i(p)dp'dp,$$

$$\mathbf{K}^{\mathbf{eh}}{}_{i,j}=\int\int K^{eh}(p',p)\psi_j(p')\psi_i(p)dp'dp,$$

$$\mathbf{P}^{\mathbf{2}}{}_{i,j}=\int\int p'^2\psi_j(p')\psi_i(p)dp'dp,$$

$$\mathbf{K}^{\mathbf{ee}}{}_{i,j}=\int\int K^{ee}(p',p)\psi_j(p')\psi_i(p)dp'dp,$$

$$\mathbf{L}^{\mathbf{ee}}{}_{i,j}=\int\int L^{ee}(p',p)\psi_j(p')\psi_i(p)dp'dp,$$

$$\mathbf{L}^{\mathbf{he}}{}_{i,j}=\int\int L^{he}(p',p)\psi_j(p')\psi_i(p)dp'dp,$$

$$\left(\mathbf{J}^{\mathbf{m}}_{\mathbf{Hh}}\right)_i=\int J^m_{Hh}(p)\psi_i(p)dp,\left(\mathbf{J}^{\mathbf{m}}_{\mathbf{He}}\right)_i=\int J^m_{He}(p)\psi_i(p)dp.$$

The obtained matrix system of differential equations can be solved numerically by FDTD-like method [7]. Introducing the following matrices $\mathbf{A}^{\mathbf{bb}}=2\mathbf{I}-2s^2\mathbf{L}^{\mathbf{bb}}\cdot(\mathbf{L}^{\mathbf{bb}})^T-dt^2\mathbf{L}^{\mathbf{bb}}\cdot\mathbf{P}^{\mathbf{2}}$, $\mathbf{B}^{\mathbf{bb}}=s^2\mathbf{L}^{\mathbf{bb}}\cdot(\mathbf{L}^{\mathbf{bb}})^T$, and $\mathbf{C}^{\mathbf{he}}=s^2\mathbf{L}^{\mathbf{ee}}\cdot(\mathbf{L}^{\mathbf{he}})^T$, $\mathbf{C}^{\mathbf{eh}}=\mathbf{L}^{\mathbf{hh}}\cdot(\mathbf{K}^{\mathbf{eh}})^T$. Where $b=e,h$, $\mathbf{I}$ is identity matrix, dt is the time step, $s=c_0\,dt/dz$ is the Courant number (c_0 is the speed of light). Then FDTD solution to (10) can be written as an explicit march-in-time formulae

$$\begin{aligned}&\mathbf{V}^{\mathbf{e}}\Big|_n^{k+1}=\mathbf{A}^{\mathbf{ee}}\cdot\mathbf{V}^{\mathbf{e}}\Big|_n^k+\mathbf{B}^{\mathbf{ee}}\cdot\left(\mathbf{V}^{\mathbf{e}}\Big|_{n+1}^k+\mathbf{V}^{\mathbf{e}}\Big|_{n-1}^k\right)\\&+\mathbf{C}^{\mathbf{he}}\cdot\left(\mathbf{V}^{\mathbf{h}}\Big|_{n+1}^k-2\,\mathbf{V}^{\mathbf{h}}\Big|_n^k+\mathbf{V}^{\mathbf{h}}\Big|_{n-1}^k\right)-\mathbf{V}^{\mathbf{e}}\Big|_n^{k-1};\\&\mathbf{V}^{\mathbf{h}}\Big|_n^{k+1}=\mathbf{A}^{\mathbf{hh}}\cdot\mathbf{V}^{\mathbf{h}}\Big|_n^k+\mathbf{B}^{\mathbf{hh}}\cdot\left(\mathbf{V}^{\mathbf{h}}\Big|_{n+1}^k+\mathbf{V}^{\mathbf{h}}\Big|_{n-1}^k\right)\\&-\mathbf{C}^{\mathbf{eh}}\cdot\left(\mathbf{V}^{\mathbf{e}}\Big|_n^{k+1}-2\,\mathbf{V}^{\mathbf{e}}\Big|_n^k+\mathbf{V}^{\mathbf{e}}\Big|_n^{k-1}\right)-\mathbf{V}^{\mathbf{h}}\Big|_n^{k-1};\end{aligned}\qquad(11)$$

$\mathbf{V}^{\mathbf{e}}$ and $\mathbf{V}^{\mathbf{h}}$ mode amplitudes are calculated in collocated time and space points. The superscript (subscript) in (11) designates the time (space) index. The excitation cross-section $z=z_0$ is placed at midway between space points n_0 and n_0+1. In order to excite the structure by magnetic current (11) after each time step we add the source function as follows:

$$\begin{aligned}&\mathbf{V}^{\mathbf{e}}\Big|_{n+1}^k+=\frac{1}{2}dz\,\mathbf{J}^{\mathbf{m}}_{\mathbf{He}}f(kdt),\ \mathbf{V}^{\mathbf{h}}\Big|_{n+1}^k+=\frac{1}{2}dz\,\mathbf{J}^{\mathbf{m}}_{\mathbf{Hh}}f(kdt),\\&\mathbf{V}^{\mathbf{e}}\Big|_n^k-=\frac{1}{2}dz\,\mathbf{J}^{\mathbf{m}}_{\mathbf{He}}f(kdt),\quad \mathbf{V}^{\mathbf{h}}\Big|_n^k-=\frac{1}{2}dz\,\mathbf{J}^{\mathbf{m}}_{\mathbf{Hh}}f(kdt).\end{aligned}\qquad(12)$$

The results of such modeling were compared with those of direct BOR FDTD [7].

In Fig. 1 one can see radial distribution of E_θ component in some cross-section (the shaded area shows the dielectric core with $\varepsilon=12$) calculated by both methods. A good agreement between the curves confirms validity of the proposed approach. In Fig. 2 the radial distribution of E_z component is presented in the same cross-section as in Fig. 1 at different time instants. One can see how the wave leaks from the waveguide.

CONCLUSIONS

Generalization of Mode Basis Method for an open dielectric waveguide is considered. The mode basis for the structure is constructed based on integral equations formulation. It is shown that circular dielectric waveguide possesses only continuous spectrum. The integro-differential System of Evolutionary Equations is obtained. This system is reduced to the system of matrix differential equations by method of moments. The solution of the obtained system by FDTD method is proposed. The propagation of pulse signal in circular dielectric waveguide is calculated. The results of the calculation by the proposed method match well with the results of BOR FDTD modeling that confirms validity of the approach.

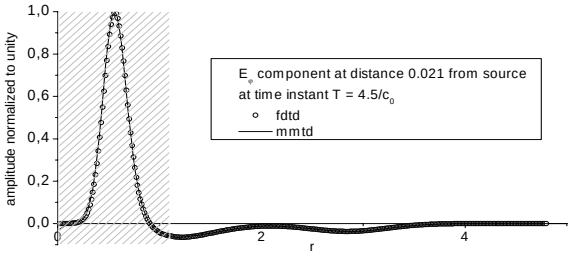


Fig. 1. Comparison of the radial field distributions obtained by different methods.

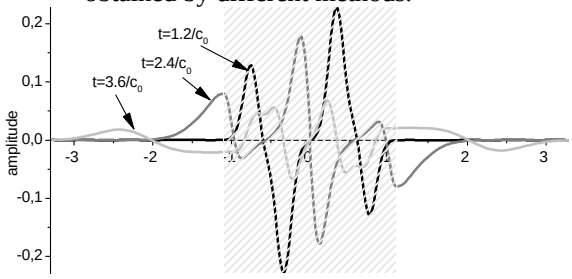


Fig. 2. Radial field distributions at different time instants.

REFERENCES

1. O.A. Tretyakov, "Waveguide evolutionary equations," Radiotechn. and electron., Vol. 34, No 5, p. 917-926, 1989.
2. A. Butrym, B. Kochetov, "Time domain mode basis method for a waveguide with transverse inhomogeneous multi- connected cross-section. 1. The general theory of method, " Radio Physics and Radio Astronomy, Vol. 14, No. 2, 162-173, 2009 (in Russian)
3. Butrym A. Yu., Zheng Yu, Dumin A. N., Tretyakov O. A. Transient wave beam diffraction by lossy dielectric half space // MMET'04, 2004. – P. 345-347.
4. M. Legenkiy, A. Butrym, "Mode basis construction for open dielectric structures by integral equations method", Bulletin of Karazin Kharkiv National University, No. 883, No. 15, 50-53, 2009 (in Russian).
5. S. Hanham, T. Bird, "High Efficiency Excitation of Dielectric Rods Using a Magnetic Ring Current", IEEE Trans. on Ant. and Prop., Vol. 56, No. 6, June 2006, 1805-1808.
6. D. Hutton, "Fundamentals of finite element analysis", 1 st ed. McGraw-Hill, 2004.
7. A. Taflove, "Computational Electrodynamics: The Finite Difference Time Domain Method," Norwood, 1995.

SPECTRUM CONTROL IN OPEN RESONATORS: TIME-DOMAIN SIMULATION

[1] Shafalyuk O. S., [2] Sirenko Y. K. and [2] Velychko L. G.

[1] Macquarie University, North Ryde, NSW, Australia
E-mail: oshafaly@maths.mq.edu.au
[2] Usikov Institute of Radiophysics and Electronics, Kharkov, Ukraine
E-mail: lgv@ire.kharkov.ua

Abstract

The efficiency of different ways for simulating the controlled changes of spectral characteristics of open electrodynamic resonant structures are studied and evaluated in the paper.

Keywords: Open resonator, free oscillations, eigenfrequency, spectrum sparseness.

1. INTRODUCTION

The need to change spectra of open resonators and to construct the resonators that are capable to sustain oscillations with a given field pattern and given Q-factor arise when solving many applied radiophysical problems. They are generally connected with the design of various devices such as solid-state generators, resonant antennas, power compressors, or radiators of short high-power radio pulses.

There exist many ways to attain a spectrum sparseness in resonators with simple dielectric or metal mirrors. For example, a low-sized scattering object can be placed in the antinode of some high-Q oscillation, and it will destroy this oscillation. The corresponding complex eigenfrequency vanishes from the spectrum. By changing mirror's curvature, one can control a degree of beams defocusing, and hence, the Q-factor of the corresponding oscillations. A similar result can be obtained by varying the mirror transmission or reflectivity. Through rotating the mirrors or replacing the flat mirrors by the mirrors of curved or broken shape, one can break the beam trajectory and force the beam to leave the resonator, thus changing its spectrum.

High-Q free oscillations decay very slowly; therefore to obtain reliable results in time-domain simulation of the processes of this kind, we should use those methods whose computational error is not high both for small and for large values of time. Rigorous time-domain approaches based on the standard finite-difference algorithms with the original exact absorbing conditions on the virtual boundaries truncating the domain of computation [1] meet this requirement. The technique of this kind allows one to obtain reliable results when investigating long-duration transient processes.

2. ANALYSIS AND SPECTRUM SPARSENESS OF THE RESONATORS OF CLASSICAL CONFIGURATION

In Fig. 1, one of the geometries, which have been computed, is shown. This is 2-D resonator with the mirrors whose specific conductivity was chosen to be the conductivity of copper. The structure is excited from a feeding waveguide. The area of computation is bounded by the dashed lines (the artificial boundary $\mathbf{L}$). An additional artificial boundary $\mathbf{L}_1$ is placed in the cross section of the feeding waveguide; the boundary condition posed on this boundary simulates the excitation of the structure by an eigen wave of a semi-infinite waveguide [1]. The resonator is excited by a pulsed H_{01}-wave with the time dependence

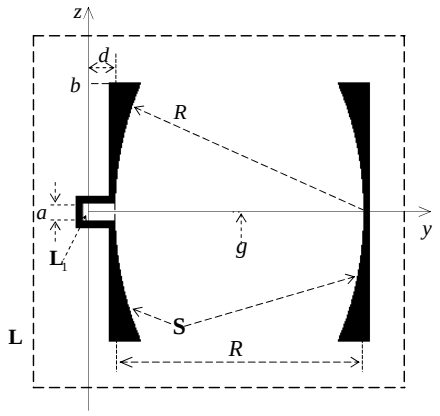


Fig. 1. A confocal resonator with a waveguide input ($R = 9.0$, $b = 4.0$, $a = 0.56$, $d = 1.2$). The point $g = \{5.7, 0.0\}$ is located at the center of the resonator.

978-1-4244-7468-4/10/$26 ©2010 IEEE

$$F_1(t) = \\ = 4\frac{\cos\left[\tilde{k}(t-25)\right]\sin\left[\Delta k(t-25)\right]}{t-25}\chi(100-t), \quad (1)$$
$$\tilde{k} = 8.0,\ \Delta k = 1.2$$

The SI system of units is used. The variable t is the product of the real time by the velocity of light in free space.

The resonator response on this excitation is presented in Fig. 2.

The next step is to excite the resonator by a quasi-monochromatic H_{01}-wave

$$F_2(t) = P(t)\cos\left[\tilde{k}(t-0.5)\right], \\ P(t):\ 0.1-5-75-80 \quad (2)$$

($P(t)$: $t_1 - t_2 - t_3 - t_4$ is a trapeziform envelope being equal to zero for $t < t_1$, $t > t_4$ and to unity for $t_2 \le t \le t_3$), whose central frequency $\tilde{k} = K_j$ ($j = 1,2,...,6$) coincides with the resonant frequencies determined previously (see Fig. 2). The results for $k = K_2 \approx 7.4$ are shown in Fig. 3.

We next replaced the right-hand mirror with a metal plane reflector

$$\chi[y-(R/2+d)]\,\chi[(R/2+d)+0.2-y]\,\chi[b-|z|]$$

located in the symmetry plane of the resonator. The resonant frequencies of the modified resonator are little different from those for the original resonator. The main distinction is that the oscillations, whose antinodes fell previously on the symmetry plane, disappear from the spectrum. The spectrum crowding is not observed any more in the neighborhood of the eigen frequencies. All oscillation modes sustained by this resonator are clearly defined when exciting the resonator by quasi-monochromatic signals with the corresponding central frequencies.

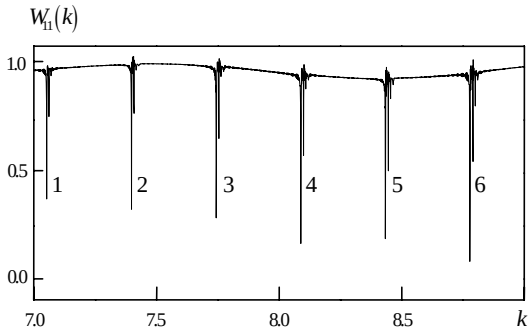


Fig. 2. Excitation of the resonator by the pulsed H_{01}-wave (1). Relative fraction of energy reflected back into the input waveguide; the resonant frequencies are: $K_1 \approx 7.05$, $K_2 \approx 7.4$, $K_3 \approx 7.74$, $K_4 \approx 8.09$, $K_5 \approx 8.43$, and $K_6 \approx 8.78$.

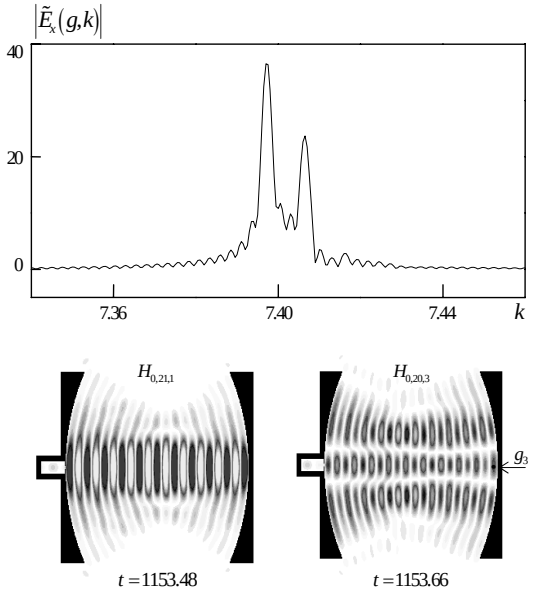


Fig. 3. The resonator's response on the quasi-monochromatic H_{01}-wave (2) with the central frequency $\tilde{k} = 7.4$. Spectral amplitudes of the E_x-component at the point $g = g_3$; spatial distribution of $E_x(g,t)$ at $t = 1153.48$ and $t = 1153.66$.

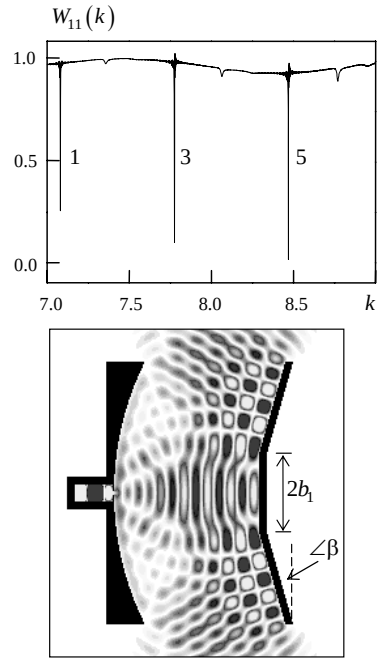


Fig. 4. The response of the modified resonator ($b_1 = 1.24$, $\beta = 16$) on the pulsed H_{01}-wave (1) and spatial distribution of $E_x(g,t)$ at $t = 32$.

The spectrum can be rarified significantly with abrupt decrease of Q-factors of the $H_{0,n,3}$-oscillations through modification of resonator's geometry as it shown in Fig. 4,b: the right-hand plane mirror is replaced by the

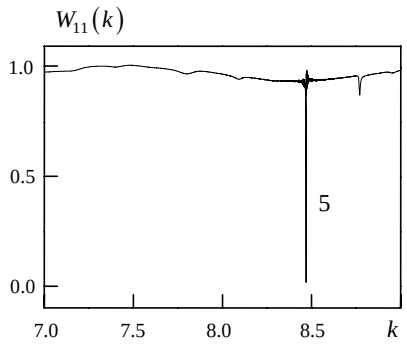


Fig. 5. A reduction in number of free oscillations in the resonator modified by placing a thin metal band inside. The response of the modified resonator on the pulsed H_{01}-wave (2).

piecewise-plane reflector whose central section is determined by the field spot dimensions for $H_{0,n,1}$-oscillations. The Q-factor of the $H_{0,n,3}$-oscillations, which are nominally present in the spectrum of the modified resonator, are governed by the angle β.

A drastic spectrum sparseness in the modified resonator (Fig. 5) is accomplished by the use of a thin (the thickness is $\overline{h} = 0.04$) metal band being placed along the line of antinodes of the $H_{0,12,1}$-oscillations. It does not distort the $H_{0,12,1}$-oscillations and, at the same time, breaks down the $H_{0,10,1}$- and $H_{0,11,1}$-oscillations (pure spectrum sparseness). The band width ($2b_2 = 0.28$) is much less than the field spot size of the longitudinal oscillations. Because of this, the band can not act as a mirror reducing resonator's volume and giving rise to oscillations with fewer field variations.

Similar results have been obtained for semi-transparent mirrors as right-hand reflectors, namely, a dielectric mirror with the permittivity $\varepsilon = 40$ and a grating mirror. The resonators of this kind are interesting as resonant antennas radiating through these semi-transparent mirrors and as the accumulators of energy in power compressors, from which the energy is radiated when the mirror becomes transparent. The imaginary parts of the complex eigenfrequencies $\overline{k}$ corresponding to the isolated oscillations are evaluated from a behavior of the freely oscillating (once the sources are switched off) field

$$U(g,t) = U(\tau) \approx A\exp(\tau \operatorname{Im}\overline{k})\cos(\tau \operatorname{Re}\overline{k} + B), \quad \tau = t - t_4 > 0 \tag{3}$$

generated by the quasi-monochromatic H_{01}-wave (2) with the central frequency $\tilde{k} = \operatorname{Re}\overline{k}$ [2,3]. The observation point g in (3) is located, as a rule, close to an oscillation antinode, while the minimal signal duration is dictated by the following requirement: within a frequency band occupied by the signal (2), there must be no values $\operatorname{Re}\overline{k}_m$ associated with other high-Q free oscillations.

REFERENCES

1. Sirenko, Y. K., Strom S., and Yashina N. P. 2007, *Modeling and Analysis of Transient Processes in Open Resonant Structures. New Methods and Techniques*, Springer, New York.
2. Sirenko Y. K., Velychko L. G. & Erden F. 2004, 'Time-domain and frequency-domain methods combined in the study of open resonance structures of complex geometry', *Progress Electromag. Res.* **44**, 57–79.
3. Velychko L. G., Sirenko Y. K. & Shafalyuk O. S. 2006, 'Time-domain analysis of open resonators. Analytical grounds', *Progress Electromag. Res*. **61**, 1–26.

POINTWISE RADIATOR IN FDTD METHOD

Varyanitza-Roshchupkina L. A.

A.Ya. Usikov Institute of Radio Physics and Electronics of NAS of Ukraine,
Kharkiv, Ukraine
E-mail: vla@ire.kharkov.ua

Abstract

The veracity of numerical FDTD simulation depends on a large extent on correct realization of the EM field source in the computation scheme. A survey of physical correspondence, simplicity of realization and convergence for several basic types of sources, being widespread in literature on FDTD simulation, is presented in the work.

Keywords: FDTD, source, simulation.

1. INTRODUCTION

The finite-difference time-domain method [1] is one of the most popular methods of computational electrodynamics problems solution. Because of its universality and simplicity of realization this method is widely used quite beyond problems of nonstationary electrodynamics, covering lately many more problems, including those ones been previously solved in traditional style by quite different methods, for example, integral methods or frequency-domain methods (as a rule, the time-domain solution is intermediate here and then it acts as a source of frequency-dependent characteristics).

The original classical Yee algorithm presents a central-difference approximation of rotor Maxwell equations [2]. The distinction of this scheme is arrangement of electric and magnetic field components that is defined by the so-called Yee cell (Fig. 1).

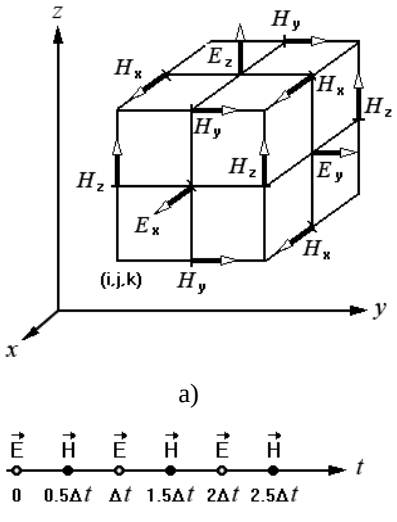


Fig. 1. The Yee arrangement algorithm for field components a) in space, b) in time.

The finite-difference analog of Maxwell equations derived as a result of changes and transformations is an explicit scheme, based on 6 expressions for field component calculation. The common view of them can be represented by the following compact form:

$$U_{i_1}^{W} = W_{i_1}\Big|_{0}^{+1/2} = C_a(r)W_{i_1}\Big|_{0}^{-1/2} + C_b(r)\left(\bar{W}_{i_2}\Big|_{+1/2}^{0} - \bar{W}_{i_2}\Big|_{-1/2}^{0}\right) + C_c(r)\left(\bar{W}_{i_3}\Big|_{-1/2}^{0} - \bar{W}_{i_3}\Big|_{+1/2}^{0}\right). \quad (1)$$

These are update equations. Here W_{i_1} – is one of the calculated field components,

$$W = (E \mid H) \leftrightarrow \bar{W} = (H \mid E),$$

$$\{i_1, i_2, i_3\} = = (\{x,y,z\} \mid \{y,x,z\} \mid \{z,x,y\}),$$

upper indexes after vertical bar represent the time shift (in discretization steps), inferior indexes represent the same in space; *C* are coefficients which depend on the discretization grid size Δ and material properties in the calculation point *r*.

The scheme (1) approximates the initial problem with the second order of accuracy. The algorithm stability is defined by the Courant condition (2):

$$\Delta t \le \left(c\sqrt{\frac{1}{\Delta x^2} + \frac{1}{\Delta y^2} + \frac{1}{\Delta z^2}} \right)^{-1}, \quad (2)$$

where c is the speed of light in the material being modeled.

The first problem which an investigator is confronted by while solving any problem by the finite-difference time-domain method is a problem of correct mathematical formulation of the EM wave source, its correct introduction into the scheme, as well the exact correspondence between the physical source and its numerical analog.

An incident plane wave is historically one of the first sources, the correct and compact realizations of which were studied in early works on FDTD simulation. However, despite the enormous number of works, devoted to this research area, there are some

978-1-4244-7468-4/10/$26 ©2010 IEEE

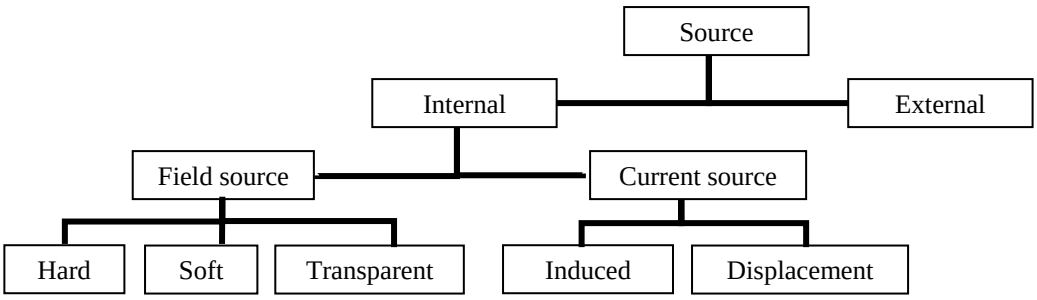


Fig. 2. Pointwise sources.

difficulties of its realization by now (for example, correct description of the oblique incidence case) [3].

The emergency of pointwise sources consideration has occurred rather lately in connection with a great increase of works, devoted to the analysis of the near-field of sources, the mathematical approximation of which can be a current filament (a pointwise source in two-dimensional space) or a point dipole (a point source in three-dimensional space). Difficulties and peculiarities related to realization of the last type of sources are considered in the work.

There are two basic approaches to the EM wave source introduction into a computational scheme. These are introduction of so-called external sources and internal sources (Fig. 2). The external source is a source, the field of which is precomputed analytically or by some numerical methods, and introduced into a scheme often by the total-field/scattered-field formulation or by a scattered-field approach [1]. It is used more particularly for analyzing stationery processes. The merit of this method is the controlled accuracy of the introduced external field. The essential shortcoming of this approach is an increase in storage capacity being necessary for data storage (especially in case of a scattered-field approach). Moreover for number of tasks such a field introduction is improbable at all. Therefore investigators and computer engineers widely use the second (internal) method of source introduction, where a source is embedded into a computational scheme. The advantage of the internal source is its compactness. It means that minimum grid points but not the whole computational domain are used to describe the source field. Thus, for example, a plane wave field can be set by defining of one of the field components on plane, a cylindrical wave field – by defining field on straight line; spherical wave field can be set by defining field component values at only one point.

Our further investigation is devoted to the analysis of the pointwise internal sources.

2. SOURCES

The description of an extraneous force action with EM field excitation is often consists in changing of the constitutive equation. One of the formalizations is following:

$$\vec{\mathbf{j}}^{W} = \sigma^{W}(\vec{\mathbf{W}} + \vec{\mathbf{W}}_{source}),\ \vec{\mathbf{j}}^{W} = \sigma^{W}\vec{\mathbf{W}} + \vec{\mathbf{j}}^{W}_{source}. \quad (3)$$

Thus, the EM field excitation can be described by two ways: by the extraneous currents $\vec{\mathbf{j}}^{W}_{source}$ or the extraneous fields $\vec{\mathbf{W}}_{source}$.

2.1. CURRENT SOURCES

2.1.1. Induced current source.

It's easy to introduce extraneous currents into the scheme (1) [1,4]:

$$W_{i_1\ source}\Big|_{0}^{+1/2} = U^{W}_{i_1} + C_d(r) j^{W}_{i_1\ source}\Big|_{0}^{0}. \quad (4)$$

Since as a rule the FDTD grid cell size is smaller than 1/10 of the radiated wavelength λ, such a source acts physically as a dipole antenna, co-directed with i_1, and with a size equaling to the cell size Δ. To calculate the field of the ideal infinitesimal dipole source it is necessary only to add the coefficient $1/\Delta$ before the second addend in the equation (4).

Such a method of source introduction differs by its simplicity of realization and high accuracy at fulfillment of the conditions 1) of stability (2); 2) $\lambda / \Delta \geq 20$ [1]; 3) the spectrum of signal describing the current time variation doesn't have a constant component.

The importance of the third condition is described below.

The EM field source, introduced into the scheme by means of extraneous currents (4), formally represents conduction currents, which exist only in a lossy medium. Nevertheless, such a source introduction is widespread even in cases, when the source is located in free space.

Any extraneous currents, introduced into the Maxwell equation, should accumulate an appropriate charge according to the continuity equation [5]. In case, when a source is in a lossy medium, this charge exists during only a limited amount of time (relaxation time), and then it disappears. In free space these charges, conditioned by the effect of the current source, can exist infinitely and lead to an appearance of dc-component in the solution.

All signals, time integrals of which have a nonzero value, have this «nonphysical» characteristic proper. It is possible to avoid this peculiarity by a few ways:

- by using bipolar symmetrical signal as a driving function;
- by using specially fitted «0-dc function» as a driving function [6,7];
- by expanding the driving function into Taylor series.

2.1.2. Displacement current source.

Since it's impossible to introduce conduction currents into free space correctly, it has been proposed to introduce the displacement currents as EM field sources [7]:

$$\vec{\mathbf{j}}^{W} = \sigma^{W}\vec{\mathbf{W}} + \vec{\mathbf{j}}^{W}_{source} = \sigma^{W}\vec{\mathbf{W}} - \frac{\partial \vec{\mathbf{W}}_{source}}{\partial t}. \quad (5)$$

Investigations carried out by authors of [7] have shown that

- this method of signal assignment has considerable fewer restrictions on the excitation signal waveform;
- field wave from this source holds the shape at propagation in space (in contrast to the induced current source).

Though the source introduced by (5) is described here as a current source, it is specified per se by the function describing the field change. Thus, this source can be added accordingly to those field sources, which are represented in the next part of this work.

2.2. FIELD SOURCES

The pointwise field source is usually realized in the FDTD grid as a hard source or a soft source. The advantage of the hard source is simplicity of its description because it consists only in setting a field component in one node of the FDTD grid [1]:

$$W_{i_1\ source}(t) = f(t). \quad (6)$$

The field radiated by the hard source physically corresponds to the field radiated by the voltage source [8].

This source type has one peculiarity, which can be considered both like its merit and its shortcoming, depending on the aim of simulation. It has the reflection power effect. As a rule, source point has the same material characteristics as adjacent points in the grid, and that's why it should not dissipate the energy. This prevents notable with investigation of stationary processes.

In certain literature [9, 10] this problem is solved by description of the field source as a sum of the driving function (6) and the value calculated by one of the basic equations (1):

$$W_{i_1\ source}(t) = U^{W}_{i_1} + f(t). \quad (7)$$

This is a so-called soft source.

Though this approach results in the source without scatter properties (and in this regard being transparent), its energy characteristics differ greatly from the energy of the hard source. Effect and realization of this source corresponds more to a source, specified by current sources. And that is why exactly the current source is meant sometimes by a soft source in FDTD literature [11].

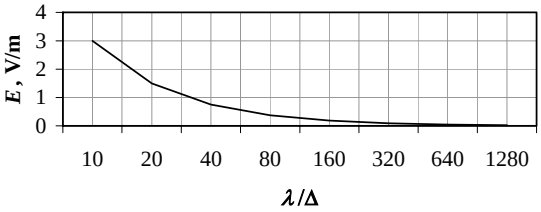


Fig. 3. Dependence of the field amplitude E on sizes of sampling interval (for field source).

The method considered in the work [12] describes the source which radiates the same amount of energy as the hard source, but the source isn't a scatterer at that. This is a so-called transparent source. But realization of such a source leads to extra complications of the computation scheme.

One general shortcoming for all sources, specified by means of field changes and introduced into a scheme with formulas (6)-(7), is that such sources don't fulfill one of basic requirements, established for any discretization scheme, - the convergence of received solutions. It means that at downsizing the grid the received solutions will not tend to the exact solution (Fig. 3). So, the source which is presented by formulas (6)-(7) properly describes time responses of the simulated field, but is absolutely unfit to analyze amplitude characteristics of simulated EM processes. It's possible to avoid this unpleasant peculiarity if to take into account the results of work [11], described below.

Though hard and soft sources greatly differ as for energy characteristics as for physical correspondence, it has turned out that when there are no reflectors in free space, it is possible to find a relation between these two source types. It was shown in work [11] that the field radiated by a hard source is identical to the field radiated by a soft source at condition:

$$E_{source}(t) = -\frac{1}{3\varepsilon_0(\Delta s)^2}\int_{-\infty}^{t} I_{source}(t)dt. \quad (8)$$

3. CONCLUSION. PROS AND CONS.

The review of point sources of the EM field used at FDTD simulation has shown that all considered source type has both merits and certain shortcomings.

When choosing a method of source introduction into the FDTD scheme for numerical simulation veracity it is necessary to take into account a variety of factors (Table 1):

- correspondence of a simulated physical source to its numerical analog;
- presence or absence of the source reflection properties;

Table 1. Main features of sources.

Source		Physical correspondence	Reflection property (y, S/m)	Convergence of solutions	Simplicity of realization
Current		Dipole	0	+	+
Field	Hard	Voltage source	∞	−	+
	Soft	Dipole	0	−	+
	Trans.	Voltage source	0	−	−

- requirement of exact time-amplitude characteristics (amplitude + form) or only time characteristics (form) of a simulated field;
- capability of simple realization and estimation of available computer resources.

Thus, for example, a hard source is well fitted to simulate the feed probe of a waveguide. A soft source (or current source) is more appropriate to simulate diffraction problems.

There are a lot of cases, when it is possible to ignore one of unwanted properties:

- In transient electromagnetics if a point hard source is located far from scatterers and the distance between them is sufficient for a propagated EM wave to be completely shaped, the source could be totally ejected from schemes together with its reflection characteristics.
- Another way is to use the method of subtraction of the function, corresponding to a signal, received in observation point at absence of objects, from a signal received in observation point at diffraction on the object. At that the reflection properties of the source stop to play any part on the stipulation that the source is located at a distance from an object preventing interaction between the source and the object. (This fact had been successfully used by the authors of works [13-14] on investigating the videopulse electromagnetic wave diffraction on subsurface objects).

REFERENCES

1. Taflove A. 1995, 'Computational electrodynamics. The Finite-Difference Time-Domain Method'. Artech House, Boston-London.
2. Yee K.S. 1966, 'Numerical solution of initial boundary value problems involving Maxwell's equations in isotropic media'. *IEEE Trans. Antennas and Propagation*, **14 -** 2, 302-307.
3. Mansourabadi M., and Pourkazemi A. 2008, 'FDTD hard source and soft source reviews and modifications'. *Progress In Electromagnetics Research C*, **3**, 143-160.
4. Sirenko Yu.K. 2003, 'Simulation and analysis of transient processes in open periodic, waveguide and compact resonators'. Edena, Kharkov.
5. Wagner C.L., and Schneider J.B. 1998, 'Divergent fields, charge, and capacitance in FDTD simulations'. *IEEE Trans. Microwave Theory and Techniques*, **46 -** 12, 2131-2136.
6. Mogghaddam M., Yannakakis E., Chew W.C., and Randall C. 1991 'Modelling of the subsurface interface radar'. *J. Electromagn. Wave Applic.*, **51**, 17-39.
7. Su T., Yu W., and Mittra R. 2005, 'A new look at FDTD Excitation sources'. *IEEE Microwave and optical technology letters*, **45** – 3, 203-207.
8. Brench C.E., and Ramahi O.M. 1998, 'Source selection criteria for FDTD'. *IEEE Trans. Antennas and Propagation*, **46 -** 8, 491-494.
9. Zhao A.P., Raisanen A.V., and Cvetkovic S.R. 1995, 'A fast and efficient FDTD algorithm for the analysis of planar microstrip discontinuities by using a simple source excitation scheme'. *IEEE Microwave Guided Wave Lett.*, **5 -** 10, 341–343.
10. Zhao A.P. and Raisanen A.V., 1996. 'Application of a simple and efficient source excitation technique to the FDTD analysis of waveguide and microstrip circuits'. *IEEE Trans. Microwave Theory Tech.,* **44** -9, 1535–1539.
11. Costen F., Вйrenger J.-P., and Brown A.K. 2009, 'Comparison of FDTD Hard Source With FDTD Soft Source and Accuracy Assessment in Debye Media'. *IEEE Trans. Antennas and Propagation*, **57 -** 7, 2014-2022.
12. Schneider J. B., Wagner C. L., and Ramahi O.M. 1998, 'Implementation of Transparent Sources in FDTD Simulations'. *IEEE Trans. Antennas and Propagation*, **46 -** 8, 1159-1168.
13. Varyanitza-Roshchupkina L.A., Pochanin G.P. 2004, 'Radar Images Of The Covered Trenches. FDTD Simulation'. *Proc. II-nd Int. Workshop "UWBUSIS"*, Sevastopol (Ukraine), 101-103.
14. Varyanitza-roshchupkina L.A., Pochanin G.P. 2006, 'Videopulse electromagnetic wave diffraction on subsurface objects'. *J. of Radio Phys. and Electr*. **11** - 2, 240–252.

MODELING THE ELECTROMAGNETIC IMPULSE INTERACTION WITH A HUMAN SKIN TAKING INTO ACCOUNT A DISPERSION

Simachova O. N.

Karazin Kharkov National University, Kharkov, Ukraine
E-mail: O.N.Simachova@mail.ru

Abstract

The problem of the plane electromagnetic impulse propagation through the dielectric layer with the human skin parameters is considered in this paper. The layer permittivity depends upon a frequency by the Debye model. The impulse with a Gauss temporal form falls with an arbitrary angle on the dielectric layer that lies on the half-infinite layer of a fat tissue. The temporal forms of reflected and transmitted impulses and their energy characteristics dispersion dependence are investigated.

Keywords: Electromagnetic impulse, dielectric layer, skin model, dispersion, reflection and transmission coefficients.

1. INTRODUCTION

The interest grew to the pulse signals lately. It is connected with the number of electromagnetic pulse fields' features in comparison with monochromatic fields. The stationary fields interaction with dielectric structures such as a flat layered medium, a sphere, a cylinder were studied in the number of papers [1-3], more difficult cases (a multilayered sphere, a multilayered cylinder) are considered as well [4-5]. But for pulse fields phenomena appeared are not studied well. That's why the video impulse interaction with the dielectric flat layered structure that models a human skin taking into account a dispersion by the Debye formula is considered in this paper. The results are calculated temporal reflected, absorbed and transmitted fields characteristics; also parts of reflected and transmitted energy are determined.

2. PROBLEM STATEMENT

The electromagnetic impulse with a flat front $F_{in}(\xi)$ falls from a free space with the angle θ on the flat layered structure consisted of the layer with the dielectric constants ε_1, μ_1 that lies on the dielectric half-space with ε_f, μ_f (Fig. 1).

The incident pulse temporal form is

$$F_{in}\left(\xi\right) = A_0 e^{-\frac{\xi^2}{2a^2}}, \qquad (1)$$

where $\xi = \dfrac{n_x x + n_y y + n_z z}{c} - t$, A_0 - an amplitude, $2a$ – a duration at the level $1/\sqrt{e}$.

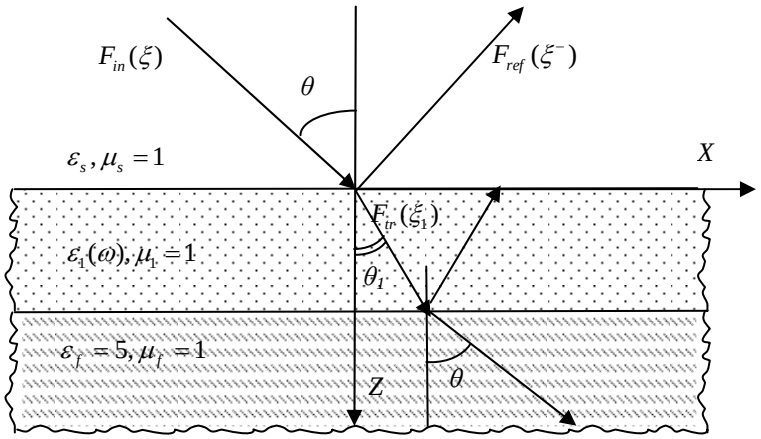


Fig. 1. Problem statement.

978-1-4244-7468-4/10/$26 ©2010 IEEE

We consider as $F_{in}(\xi)$ electric field E_y if E-polarization is and H_y if H-polarization is. Let the plane of incidence matches with a plane xOz. Then $n_x = \sin\theta$, $n_y = 0$, $n_z = \cos\theta$,

$$\xi = \frac{x\sin\theta + z\cos\theta}{c} - t\,.$$

We distribute the incident video impulse on the first boundary to the spectrum as partial plane waves by the direct Fourier translation:

$$F_{in}(\xi) = \int_{-\infty}^{\infty} F(\omega) e^{i\omega\xi} d\omega\,, \qquad (2)$$

where

$$F(\omega) = \frac{1}{2\pi}\int_{-\infty}^{\infty} F_{in}(\xi) e^{-i\omega\xi} d\xi = \frac{A_0}{\sqrt{2\pi}} a e^{-\frac{\omega^2 a^2}{2}}\,, \qquad (3)$$

$$F_{in}(\xi) = \frac{A_0 a}{\sqrt{2\pi}}\int_{-\infty}^{\infty} e^{-\frac{\omega^2 a^2}{2}} e^{i\omega\xi} d\omega \qquad (4)$$

We use Fresnel coefficients for amplitudes of reflected $V(\omega,\theta)$ and transmitted waves $R(\omega,\theta)$ because the boundary is smooth and media are isotropic [6].

Then a reflected signal is described by the expression:

$$F_{ref}(\xi^-) = \frac{A_0 a}{\sqrt{2\pi}}\int_{-\infty}^{\infty} V(\omega,\theta) e^{-\frac{\omega^2 a^2}{2}} e^{i\omega\xi^-} d\omega\,, \qquad (5)$$

where $$\xi^- = \frac{x\sin\theta - z\cos\theta}{c} - t\,, \qquad (6)$$

and a transmitted signal:

$$F_{tr}(\xi_1) = \frac{A_0 a}{\sqrt{2\pi}}\int_{-\infty}^{\infty} R(\omega,\theta) e^{-\frac{\omega^2 a^2}{2}} e^{i\omega\xi_1(\omega)} d\omega\,, \qquad (7)$$

where $$\xi_1(\omega) = \frac{x\sin\theta_1(\omega) + z\cos\theta_1(\omega)}{c} - t\,. \qquad (8)$$

A refraction angle θ_1 is dependent upon frequency and determined as:

$$\theta_1(\omega) = \arcsin(\sqrt{\varepsilon_s / \varepsilon_1(\omega)}\sin\theta)\,. \qquad (9)$$

We consider the impulse transmitting through the dielectric layer as a sequence of transmitting the impulse through two boundaries: air-dielectric, dielectric-layer.

The permittivity of the layer is complex and described by the Debye approximation, that is the most satisfied for biological media [7]:

$$\varepsilon = \varepsilon_\infty + \frac{\varepsilon_0 - \varepsilon_\infty}{1 + i\omega\tau}\,, \qquad (10)$$

where a relaxation time $\tau = \dfrac{\varepsilon_0 - \varepsilon_\infty}{\sigma_\infty - \sigma_0}$, (11)

ε_0 and ε_∞ - medium permittivities at frequencies on the range higher and lower than the characteristics frequency ω_c, that is equal to the reciprocal time of relaxation τ.

We consider the signal transmitted through the first boundary as the incident signal on the dielectric half-space with ε_f, μ_f.

$$F_{tr}(\xi_1(\omega)) = \frac{A_0 a}{\sqrt{2\pi}}\int_{-\infty}^{\infty} R(\omega,\theta) e^{-\frac{\omega^2 a^2}{2}} e^{i\omega\xi_1(\omega)} d\omega\,. \qquad (12)$$

We use the Fresnel coefficients for each incident partial plane wave in the Fourier- decomposition. In this case the incidence angle on the second boundary differs from the incidence angle on the first boundary. These angles are connected by the Snell equation.

Taking into consideration secondary reflections into the layer the result reflected field can be written as

$$F_{ref}^{(n)}\left(\xi^-\right) = \frac{A_0 a}{\sqrt{2\pi}}\int_{-\infty}^{\infty} e^{-\frac{\omega^2 a^2}{2}} e^{i\omega\xi^-}\left(V(\omega,\theta) + \right.$$
$$\left. + \sum_{n=2}^{\infty} R(\omega,\theta)\cdot R_-(\omega,\theta_1)\cdot V_-^{n-2}(\omega,\theta_1)\cdot V_1^{n-1}(\omega,\theta_1)\right) d\omega, \qquad (13)$$

and the transmitted field

$$F_{tr}^{(n)}\left(\xi_1\right) = \frac{A_0 a}{\sqrt{2\pi}}\int_{-\infty}^{\infty} e^{-\frac{\omega^2 a^2}{2}} e^{i\omega\xi_1(\omega)} \times$$
$$\sum_{n=2}^{\infty} R(\omega,\theta)\cdot R_1(\omega,\theta_1)\cdot V_-^{n-1}(\omega,\theta_1)\cdot V_1^{n-1}(\omega,\theta_1) d\omega. \qquad (14)$$

3. RESULTS

Let's consider the impulse incidence on the skin layer that lies on the fat tissue as an example for the modeling. Values ε_0, ε_∞ and τ for a skin are [7]: $\varepsilon_\infty = 361{,}67$, $\varepsilon_0 = 34{,}9$, $\tau = 8{,}8\cdot 10^{-12}$ c; a fat permittivity $\varepsilon_f = 5$.

The calculated temporal forms for reflected and transmitted pulses for different incident angles are illustrated on the Fig. 2 and 3.

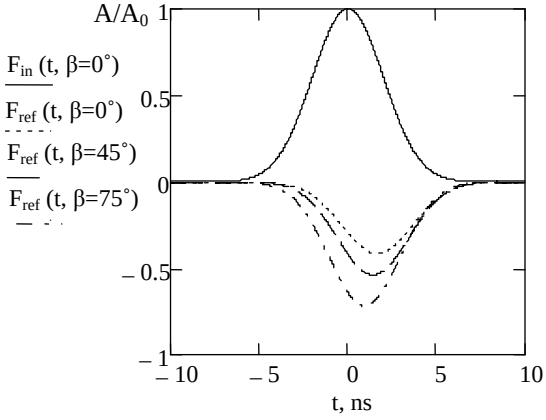


Fig. 2. The temporal dependence of reflected signals from the layer for different incidence angles.

The reflected impulse changed its polarity in comparison with the incident signal polarity because the Fresnel coefficient is negative, that is the pulse passes from a medium with a lower refractive index to a medium with

a higher refractive index. In this case reflected from the boundary signal experiences changing the phase on π in comparison with the incident signal. The reflected signals forms didn't change, that is they have Gauss forms. But the maximum displaced in time, and the lower incidence angle, the bigger displacement. When the incidence angle increases the reflected signal amplitude grows, and at the angles near the glancing angle almost all incident signal reflects from the boundary.

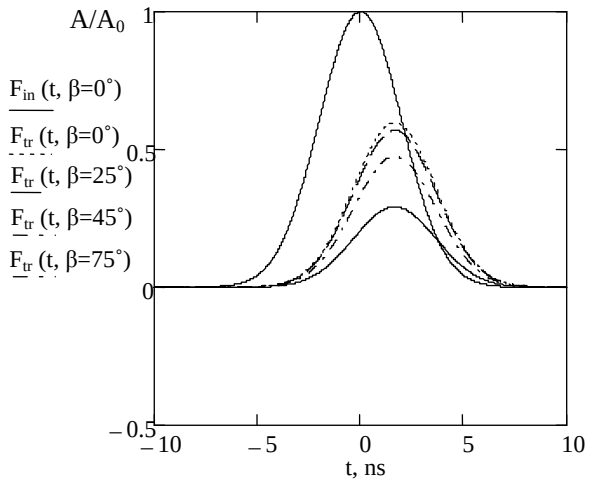


Fig. 3. The temporal dependence of transmitted signals for the layer for different incidence angles.

The transmitted signal doesn't change its polarity and form because one of media is not dispersive, but the transmitted signal maximum decreases very much when the incidence angle increases. The flow angle approaches to the normal angle, because the dielectric medium has greater refraction coefficient in comparison the air.

Let's see how the incidence impulse energy distributes between the reflected and refracted fields. The dependence of the reflected and transmitted fields' energy from the incidence angle is shown at the Fig. 4.

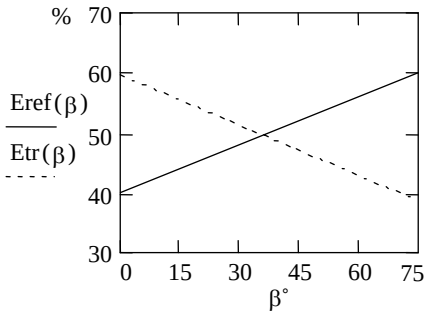


Fig. 4. The reflected and transmitted fields' energy dependence.

As we can see at the figures the energy of the reflected field is about 40% of the incidence field energy at the normal incidence angle. The greater incidence angle, the more energy reflects. The reflected energy maximum is at the limit angle of total reflection and at the angles $\theta > \arcsin\sqrt{\varepsilon_2 / \varepsilon_1} \approx 70^\circ$ the incident field energy doesn't transmit into the layer. The transmitted field energy depends upon the incidence angle inversely and is about 60 % at the normal incidence.

4. CONCLUSIONS

The program for the temporal distribution calculation of the transmitted and reflected signals for the dielectric layer taking into account the permittivity dispersion was created. The problem was solved in time domain for an arbitrary form and duration of the incident impulse signal. It was calculated that the reflected signal changes its polarity if the second medium permittivity greater than the first medium permittivity. The transmitted signal always has the same polarity as the incident signal has. This property put in the Fresnel coefficients. The reflected and transmitted plots confirmed these statements. The reflected field energy depends in direct proportion to the incidence angle, for the transmitted field inverse relation is observed. At the normal incidence angle about 60 % of the incidence energy transmits into the layer that says about good penetrability of the impulse signals.

REFERENCES

1. Sukharevsky O. I., Gorelyshev S. A., Riabokon E. A. Scattering pulse signal on layer-uniform half-space // *Proc. 2nd International Workshop on "Ultrawideband and ultrashort impulse signals"* (UWBUSIS-2004). Sevastopol (Ukraine). September 19-22, 2004. P.184-186.
2. Guzev M.A., Popov G.V. Reflection from layered dielectric structures with combined regular and random ingomogeneities // *Journal of telecommunications and information technology*, Vol. 1, No. 2, 2000. P. 80-82.
3. Nefedov E.I. *Electromagnetic waves diffraction on dielectric structures*. – M.: Nauka, 1979. – P. 272.
4. Li R., Han X. Debye series analysis of forward scattering by a multi-layered sphere // *PIERS (Progress In Electromagnetics Research Symposium) Online*, Vol. 3, No. 2, 2007. P. 209-212.
5. Wu Z.-S., Li H.-Y. Debye series of scattering by a multi-layered cylinder in an off-axis 2D Gaussian beam // *Chinese Physical Letters*, Vol. 25, No. 5, 2008. P. 1672-1675.
6. Landau L.D., Lifshic E.M. *Electrodinamics of continuous media*. – M.: Nauka, 1982. – P. 407.
7. Martinsen Ø.G., Grimnes S., Shwan H.P. Interface phenomena and dielectric properties of biological tissues // Encyclopedia of Surface and Colloid Science, 2002. P. 2643-2652.

PRESENTATION OF THE FIELD SURFACE WAVE GENERATED BY AN ANTENNA AT THE INTERFACE OF TWO HOMOGENEOUS MEDIA

[1,2] Rudenchik A. E., [1,2] Volkomirskaya L. B., [1,2] Reznikov A. E. and [3] Bezrukova E. G.

[1] Pushkov Institute of Terrestrial Magnetism, Ionosphere and Radio Wave Propagation, Troitsk, Moscow Region. 142190; mila@izmiran.ru
[2] JSC "Timer", ul. Lesnaya d.4B, Troitsk, Moscow Region., 142190
[3] Yaroslavl State Technical University, Moskovsky Prospect 88, Yaroslavl, 150023, Russia

Abstract

In circumstances where the dispersion of the permittivity can be neglected, the tangential component of the surface wave is expressed through the Laplace function of two complex arguments algebraically. This reduces the computation time of the surface wave at a given point to a few milliseconds, and to determine the current in the radiating antenna, as well as the dielectric constant of the underlying surface, for the time of the order of several seconds.

Obtain estimates of the surface wave field for the most typical parameters of soils. These calculations can be used to select regularizators inverse GPR for quantitative calculations of the parameters of the soil and for the qualitative interpretation of GPR data.

Keywords: GPR, data interpretation, GROT-12, underlying surface.

One of the problems that arise in the interpretation of GPR data an operational definition of the current in the antenna and the dielectric permittivity of the underlying surface from data on the surface wave. Measurements of the field at GPR studies are conducted, usually at short distances from the radiating antenna, which don't use of known representations of the far field [1]. In [2] proposed a mechanism for the calculation of near-field antenna and obtain expressions for the field of the antenna is a thin wire lying in the plane at the interface of two homogeneous environments. The electric field in the fault plane at any distance from the antenna can be represented as:

$$\begin{aligned}
&\mathbf{E}(t,\mathbf{s}) = \frac{1}{2i\pi}\int_C e^{pt}\mathbf{E}(p,\mathbf{s})dp,\\
&\mathbf{E}(p,\mathbf{s}) = \mathbf{E}^{(J)}(p,\mathbf{s}) + \mathbf{E}^{(C)}(p,\mathbf{s}),\\
&\mathbf{E}^{(J)}(p,\mathbf{s}) = -\frac{1}{\pi c}\int_B \mathbf{I}(p,b)G^{(J)}(p,|\,\mathbf{s}-\mathbf{s}_0\,|)db, \quad (1)\\
&E^{(C)}_{y,z}(p,\mathbf{s}) = \frac{1}{\pi c}\left[\left(m_{y,z}G'I_b\right)\Big|_2 - \left(m_{y,z}G'I_b\right)\Big|_1 - \right.\\
&\left. -\int_B m_{y,z}(\mathbf{s}-\mathbf{s}_0)G'(p,|\,\mathbf{s}-\mathbf{s}_0\,|)\frac{dI_b(p,b)}{db}db\right].
\end{aligned}$$

Here, b - distance along the contour of the antenna B, s_0 - the coordinate of a point on the circuit, and the indices 1,2 are the ends of the circuit $\mathbf{I}(p,b)$ - the current in the antenna $I_b(p,b)$ - the projection of power onto the unit vector tangent to the contour, which is up to the mark coincides with the current module . $\mathbf{m}(\mathbf{s}) = \mathbf{s}/s$ The function $G^{(J)}(p,s)$ is expressed through the standard features:

$$\begin{aligned}
&G^{(J)}(p,s) = G^{(J)}_b(p,s) - G^{(J)}_a(p,s),\\
&G^{(J)}_{a,b}(p,s) = \frac{\pi c}{s^3 p\varepsilon_-}e^{-ik_{a,b}s}(1+ik_{a,b}s), \quad ,\ (2)\\
&k_{a,b} \equiv k_{a,b}(p) = -i\frac{p}{c}\sqrt{\varepsilon_{a,b}(p)} = -i\frac{p}{c}n_{a,b}(p).
\end{aligned}$$

Here, $\varepsilon_a \equiv \varepsilon_a(p)$ and $\varepsilon_b \equiv \varepsilon_b(p)$ - above permittivity ($x<0$) and below ($x>0$) interface $\varepsilon_- = (\varepsilon_a - \varepsilon_b)/2$. The function $G'(p,s)$ can be represented as

$$\begin{aligned}
&G'(p,s) = \frac{\partial G(p,s)}{\partial s},\\
&G(p,s) = G^{(C)}(p,s) + W^{(0)}(p,s).
\end{aligned} \quad (3)$$

Here

$$G^{(C)}(p,s) = G^{(C)}_b(p,s) - G^{(C)}_a(p,s),$$

978-1-4244-7468-4/10/$26 ©2010 IEEE

$$G_{a,b}^{(C)}(p,s) = -\frac{\pi c}{sp\varepsilon_-}\frac{\varepsilon_{b,a}}{\varepsilon_a+\varepsilon_b}e^{-ik_{a,b}s},$$

$$W^{(0)}(p,s) = W_b^{(0)}(p,s) - W_a^{(0)}(p,s),$$

$$W_{a,b}^{(0)}(p,s) = i\frac{ck_c}{2p\varepsilon_-}\frac{\varepsilon_{a,b}}{\varepsilon_a+\varepsilon_b}W_{a,b}(p,s), \qquad (4)$$

$$W_{a,b}(p,s) = k_c\int k_{1,2}^{-1}(k_c^2-l^2)^{-1}e^{-ils}dl = \qquad (5)$$

$$= 2\pi k_c\int_0^\infty k_{1,2}^{-1}(k_c^2-l^2)^{-1}J_0(ls)ldl,$$

$$k_c \equiv k_c(p) = -i\frac{p}{c}\left(\frac{\varepsilon_a\varepsilon_b}{\varepsilon_a+\varepsilon_b}\right)^{1/2} = -i\frac{p}{c}n_c(p),$$

$$k_{1,2} \equiv k_{1,2}(p,l) = -i\left(\frac{p^2}{c^2}\varepsilon_{a,b}+l^2\right)^{1/2},$$

$J_0(...)$ is Bessel function.

Views similar to (1) - (4), were obtained by Sommerfeld in [3], but direct calculation of the improper, slowly converging integral in (4), followed by the Fourier transform is a cumbersome task even for modern computers. We set ourselves the task of developing an algorithm for rapid calculation of the functions and the study of analytic properties of these functions. Last necessary to ensure that the reverse Laplace transform of (1) to find the contours in the complex plane p, for which numerical integration is performed as quickly as possible. Inverse Laplace transform representation of the field and the surface wave as a function of time has made it possible to obtain expressions for the field components of the surface wave [4], whose calculation on serial computers with 3 GHz clock speed is about 0.1 ms when account is taken of dispersion, and about 5 s when the dispersion of the permittivity can be neglected. After calculating the current direct problem GPR - definition of the field reflected from the medium inhomogeneities signals is linear. Some results of calculations of the surface wave at different parameters are shown in Fig. 1. Parameters of the medium and the radiator are left in the window calculation of the field surface wave.

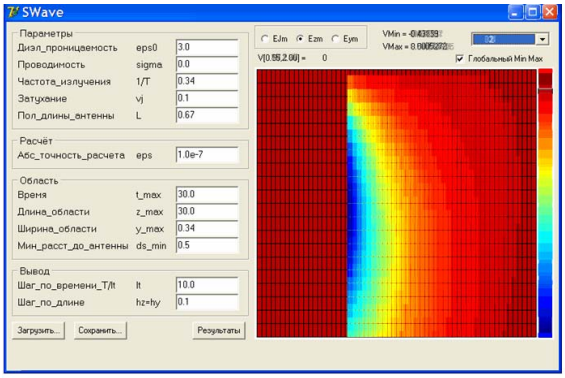


Fig. 1. A Windows program for calculating the components E_z field surface wave in the near field antenna.

The method of calculation of the surface waves is applicable to any frequency, any distance from the emitter and the arbitrary form of dispersion of dielectric constant. Therefore, it can be applied in solving a wide range of issues - from optics to electro sounding.

REFERENCES

1. Brekhovskikh L.M. *Waves in layered medium*, 1957, Izdatelstvo AN SSSR M. (In Russian)
2. Rudenchuk E. A., Volkomirskaya L. B., Reznikov A. E., Sakhterov V. I. Analytical presentation of 3D-field of radiation in medium with two layers and inverse problem of georadar sounding. *Uspekhi sovremennoj radioelectroniki*, 2009, № 1-2, pp. 29-38. (In Russian)
3. Sommerfeld A. Uber die Ausbreitung der Wellen in der drahtlosen Telegraphe. *Annalen der Physik* 1926, V81, pp. 1135-1153.
4. Rudenchik E.A., Volkomirskaya L.B. Reznikov A.E and Bezrukova E.G. Analitical Representation of the Surface Wave generated by an Antenna at the Interface between Two Homogeneous Media, ISSN 1541-308X, *Physics of Wave Phenomena*, 2010, Vol.18, No.2, pp. 1-9.

PULSE EXCITATION OF A CAVITY WITH DISPERSIVE MEDIUM THAT REFRACTIVE INDEX IS POSITIVE AND NEGATIVE

[1] M. S. Antyufeyeva, [2] O. A. Tretyakov

[1] Karazin Kharkov National University, Kharkov, Ukraine
e-mail: Maria.S.Antyufeyeva@univer.kharkov.ua
[2] Gebze Institute of Technology, Gebze, Turkey

Abstract

Excitation of electromagnetic fields by a wideband current pulse in a cavity filled with dispersive medium and bounded by a closed perfectly conducting surface is studied. Frequency dependence of the cavity filling is described by combination Lorentz poles for permittivity and permeability. Some features of such electromagnetic system and transient field evolution are presented.

Keywords: Cavity resonator, metamaterial, dispersion, double negative media, transient excitation, analytical approach in time domain.

1. INTRODUCTION

In recent years many theoretical and practical investigations is devoted to modeling and realization of medium with negative refractive index (NRI) and study properties of transmitted electromagnetic fields [1–4]. But usually this studying is realized in consideration one frequency or very short frequency interval of obtained dependence of effective parameters of composite structure that form medium with NRI. There are double problem – in one side it is obtained effective values of electromagnetic properties of the structure by finding characteristics of transmitted electromagnetic field, in another side it is studied some useful and interesting effects of transmission electromagnetic waves through such structure, and at this time it is considered its properties in one frequency. In addition, one of main problems is practical realization of three dimension medium with NRI with given properties and without undesired effects.

This paper considers properties of cavity with totally dispersive medium and properties of electromagnetic oscillation in this structure. Author's purpose is to avoid some of referred imperfection in this investigation in regard to medium with NRI. Firstly, for theoretical research of the problem effective electromagnetic parameters of the medium is used, but their frequency dependence is simulated by several Lorentz poles for permittivity and permeability in wide frequency interval. In Time Domain (TD) this formulation corresponds to the set of differential equations relating polarization and magnetization with electric and magnetic field strengths, p_e, p_m – poles number.

$$\partial_t^{\,2}\boldsymbol{\mathcal{P}} + \gamma_{p_e}\partial_t\boldsymbol{\mathcal{P}} + \omega_{p_e}^2\boldsymbol{\mathcal{P}} = \chi_{p_e}\omega_{p_e}^2\boldsymbol{\mathcal{E}}(\mathbf{r},t)\,, \qquad (1)$$

$$\partial_t^{\,2}\boldsymbol{\mathcal{M}} + \gamma_{p_m}\partial_t\boldsymbol{\mathcal{M}} + \omega_{p_m}^2\boldsymbol{\mathcal{M}} = \chi_{p_m}\omega_{p_m}^2\boldsymbol{\mathcal{H}}(\mathbf{r},t)\,. \qquad (2)$$

Secondly, idea of isotropic medium with NRI is based on some ideas and results of [4]. For validity of this presentation of the medium as homogeneous and isotropic and using effective parameters of medium properties we assume that the particles of composite structure are appreciably smaller than cavity sizes and used wavelength.

2. PROBLEM STATEMENT AND ANALYTICAL SOLUTIONS

We consider a cavity bounded with a PEC singly-connected closed surface. Within the frame of Evolutionary Approach to Electromagnetics in TD [5-8] the sought vectors of electric and magnetic fields strength, polarization and magnetization are expanded into a series of cavity modes. By this, total problem is separated on two individual problems: one of them is spatial problem of finding cavity modes for given geometry of the cavity, another is the problem of finding of time coefficients of the expansion (mode amplitudes). The cavity modes can be found as solutions to the Dirichlet or Neumann eigenvalue problems for Laplacian [1–3]; these are well known for various cavity geometries. Equations for finding mode amplitudes are the result of projecting Maxwell equations, constitutive relation, given impressed electric and magnetic currents and initial conditions onto the basis generated of the set of cavity modes. These evolutionary equations can be written in a matrix form

$$\frac{d}{dt}\mathbf{X}(t) + \mathbf{Q}_{sol}\cdot\mathbf{X}(t) = \mathbf{F}_{sol}(t),\ \ \mathbf{X}(t)\Big|_{t=0} = \mathbf{X}_0; \quad (3)$$

$$\begin{aligned}
&\frac{d}{dt}\mathbf{Y}^e(t) + \mathbf{Q}^e_{irr}\cdot\mathbf{Y}^e(t) = \mathbf{F}^e_{irr}(t),\ \ \mathbf{Y}^e(t)\Big|_{t=0} = \mathbf{Y}^e_0;\\
&\frac{d}{dt}\mathbf{Y}^h(t) + \mathbf{Q}^h_{irr}\cdot\mathbf{Y}^h(t) = \mathbf{F}^h_{irr}(t),\ \ \mathbf{Y}^h(t)\Big|_{t=0} = \mathbf{Y}^h_0,
\end{aligned} \quad (4)$$

978-1-4244-7468-4/10/$26 ©2010 IEEE

where matrices $\mathbf{Q}_{sol}$, $\mathbf{Q}^{e}_{irr}$, $\mathbf{Q}^{h}_{irr}$ contain parameters of permittivity and permeability model and information of cavity geometry – eigenfrequencies of empty cavity (eigenvalues of spatial boundary problem). Eigenvalues of the matrices gives us the inherent complex eigenfrequency of the filled cavity.

We consider excitation by electric current pulse without any magnetic sources, thus the mode amplitudes of magnetic currents $j^{h}_{n,\beta}(t)$ are zero, and this results in absence of magnetic irrotational part of the field. Solenoidal and irrotational mode amplitudes of the electric current expansion are specified by the same time dependence

$$j^{e}_{n,\alpha}(t) = A_{n,\alpha}\left(\tfrac{t}{T}\right)^{2}\left(1-\tfrac{t}{3T}\right)e^{-t/T}. \qquad (5)$$

The solution of the system (3) yields solenoidal mode amplitudes in the following form:

$$\mathbf{X}(t) = A_n\sum_{k=1}^{5}\mathbf{K}\left(\lambda_k^{sol}\right)I\left(\lambda_k^{sol},t\right)col\left(1,0,0,...,0\right), \qquad \mathbf{K}\left(\lambda_k^{sol}\right) = \prod_{s\neq k}^{s=1..5}\frac{\lambda_s^{sol}\mathbf{U}-\mathbf{Q}_{sol}}{\lambda_s^{sol}-\lambda_k^{sol}}. \qquad (6)$$

where λ_k^{sol} are eigenvalues of matrix $\mathbf{Q}_{sol}$, and the function $I(\lambda,t)$ is defined as

$$I(\lambda,t) = -\frac{2\lambda T\exp\left(-\lambda t\right)}{\left(\lambda T-1\right)^{4}} - \frac{\exp\left(-t/T\right)}{\lambda-1/T}\left\{\frac{1}{3}\left(\frac{t}{T}\right)^{3} - \frac{\lambda T\left(\frac{t}{T}\right)^{2}}{\lambda T-1} + \frac{2\lambda T\left(\frac{t}{T}\right)}{\left(\lambda T-1\right)^{2}} - \frac{2\lambda T}{\left(\lambda T-1\right)^{3}}\right\}.$$

Dimension of the matrix $\mathbf{Q}_{sol}$ is $2+2P_e+2P_m$, P_e, P_m are quantity of Lorentz poles of permittivity and permeability model. There is gives us the complex resonance system with P_e+P_m+1 eigen resonances.

3. RESULTS

Using presented approach we have possibility to obtain complex eigenfrequency of the cavity filled with dispersive medium. Frequency dependence of medium refractive index is taken into account in wide range of frequencies and has positive and negative values. Cavity with such dispersive medium represents the compound system with a few resonances. One of the resonances is conditioned by the re-reflection of the field between cavity walls (cavity resonance). Other resonances are conditioned by resonance properties of the medium (medium resonance). Figure 1 presents the frequency dependencies of real and imaginary part of refractive index of the medium, simulated by three Lorentz poles for permittivity and permeability. Frequency of one of medium resonances is decrease with decreasing cavity size and has values in the frame of interval ~9 – 20 GHz, where refractive index has negative values and $n'(f) > n''(f)$. Other frequencies of medium resonances are situated in the range of negative value of refractive index, but $n'(f) < n''(f)$. Between

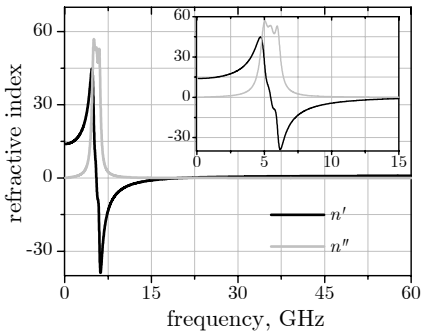


Fig. 1. Frequency dependence of medium refractive index modeled by three poles for permittivity and permeability.

frequencies of the system resonances is an available frequency ranges where oscillations cannot exist.

For the end it should be noted that the performance of excitation of the cavity by pulse current is depend on frequency of maximum of spectral density of excitation signal and obtained frequency responses of the cavity as function of cavity size. Resonances that have different nature are excited with different efficiency for some cavity sizes.

REFERENCES

1. Nader Engheta and Richard W. Ziolkowski, "A positive future for double-negative metamaterials," *IEEE Trans. Microwave Theor. Tech.* **53** (4), 1535-1556 (2005).
2. Bozza G., Oliveri G., Raffetto M. 'Anomalous TEM modes in guiding structures filled with double negative and double positive materials' *IEEE Microwave Wireless Comp. Lett.* **17**(1), 19–21, (2007)
3. Marcos P. and Soukoulis C.M. 'Transmission properties and effective electromagnetic parameters of double negative metamaterials' *Optic Express*, 11(7), 649–661(2003)
4. Vendik I., Vendik O., Kolmakov I. and Odit M. "Modelling of isotropic double negative media for microwave applications" *Opto-Electronics Review*. **14**, (3), 179–186, 2006.
5. Aksoy S., Antyufeyeva M., Basaran E., Ergin A.A., Tretyakov, O.A. "Time-domain cavity oscillations supported by a temporally dispersive dielectric"**.** *IEEE Trans. Microwave Theor. Tech.*, **53**, 2465 – 2471
6. Antyufeyeva M. S. "Electromagnetic field oscillations in a cavity with multipole Debye medium" *Proceedings of the 11th International Conf. on Mathematical Methods in Electromagnetic Theory*, 312 – 314, 2006.
7. Tretyakov O.A. 'The method of modal basis.', *Radiotechnika i Elektronika*, **31**, 1071–1082, 1986.
8. Tretyakov O. A. 'Essentials of nonstationary and nonlinear electromagnetic field theory'. *Analytical and Numerical Methods in the Electromagnetic Wave Theory*, in ed. by M. Hashimoto, M. Idemen, O. A. Tretyakov. Science House Co., Ltd., Tokyo, 1993.

APPLICATIONS (GPR, RADARS, COMUNICATION, MEDICINE)

A PROLATE-SPHEROIDAL IMPULSE-RADIATING ANTENNA SYSTEM TO LAUNCH AND FOCUS 100-PS PULSES FOR MELANOMA TREATMENT

Prashanth Kumar, Serhat Altunc, Carl E. Baum, C. Jerald Buchenauer, Christos G. Christodoulou and Edl Schamiloglu

Department of Electrical and Computer Engineering. University of New Mexico,
Albuquerque, NM, 87106, USA
E-mail: prash@unm.edu

Abstract

This paper briefly reviews the design of a prolate-spheroidal impulse-radiating antenna system, to launch and focus fast (100 ps) high-voltage (> 100 kV) pulses, as a non-invasive tool for melanoma (skin cancer) treatment. The experiments on a graded five-layer dielectric lens, designed to match the pulses into a biological target medium, are outlined. The design of a switch system to launch high-voltage spherical TEM pulses is also summarized.

Keywords: Impulse-radiating antenna, prolate-spheroidal reflector, focusing lens, picosecond pulses, switch, launching lens, melanoma.

1. INTRODUCTION

Impulse radiating antennas can radiate very fast electromagnetic pulses with high field amplitudes. Recent research shows that such pulses can be used to kill melanoma cells or aid in gene insertion [1]. At present, electric fields are invasively delivered to the tumor using implanted electrodes. A non-invasive technique to deliver these electric fields is practically more desirable. A Prolate-Spheroidal Impulse-Radiating Antenna (PSIRA) is one such device, in which a prolate-spheroidal reflector is used to focus electric fields in the near-field region, where the biological target (skin cancer cells) is located. A focusing lens is used to match the electric fields launched in air into the target medium.

2. THE PROLATE-SPHEROIDAL IMPULSE-RADIATING ANTENNA (PSIRA)

The Impulse Radiating Antenna (IRA) is a focused aperture hyperband antenna suited for radiating very fast, high-voltage (> 100 kV) pulses in a narrow beam. IRAs are composed of two main parts, a conical TEM transmission line, called the feed arms, and a focusing optic which is usually a reflector or a lens. To focus the electric fields reflected by the reflector, onto a target located in the near-field, a prolate-spheroidal reflector must be used [2].

The side view of a 60^0 four feed-arm PSIRA is shown in Fig 1. The 60^0 four feed-arm configuration is found to provide the largest electric fields compared to other feed-arm configurations. The dimensions of the feed-arms are determined by their 200 Ω pulse impedances [3].

The PSIRA system has two foci. An inhomogeneous spherical TEM wave launched on the guiding conical conductors from one focus ($-z_0$) is converted, by a double stereographic transformation, to a second (reflected) inhomogeneous spherical TEM wave propagating toward the second focus ($+z_0$) [2].

The reflector geometry, and position of the truncation plane, z_p, are optimized to maximize the electric fields concentrated at the second focal point. The following dimensions were found to be most suitable [3],

$$z_p = 0, \quad a = 0.625 \text{ m}, \quad b = \psi = 0.5 \text{ m}, \\ z_0 = 0.375 \text{ m}, \quad l = 1 \text{ m}, \tag{1}$$

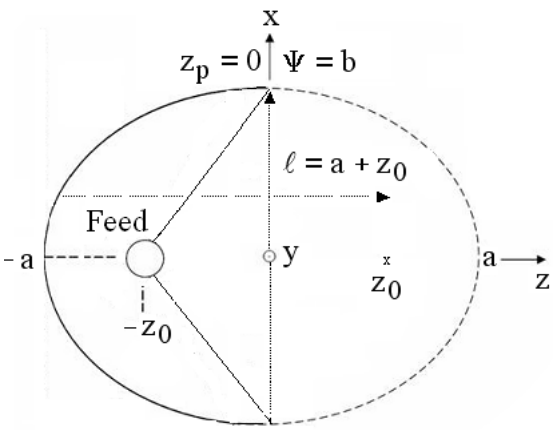


Fig. 1. Front view of a four-feed arm PSIRA [2].

978-1-4244-7468-4/10/$26 ©2010 IEEE

where, $z_p = z$ – coordinate of the truncation plane,

$a, b =$ radii of the prolate-spheroid,

$z_0 = \left(a^2 - b^2\right)^{1/2} =$ focal distance

$l = a + z_0 =$ distance used for normalization,

Ψ = radial coordinate.

The size of the reflector is optimized for an input pulse with a 100 ps rise time, as this yields practically reasonable dimensions.

CST Microwave Studio, a three dimensional, Finite Integral Time Domain (FITD), commercially available software, was used for our simulations. A 1 V, 100 ps ramp rising step was used as the input in all simulations.

3. FOCUSING LENS

One problem with placing the fields at the target concerns the dielectric properties of the target medium and its surroundings. If the wave incident on the target is in air, but the target medium has a large permittivity (say about 81 for water), there will be a significant reflection of the pulse leading to a smaller field in the target medium [4]. This mismatch can be reduced by using a graded dielectric lens. This lens is called the focusing lens. A schematic of the PSIRA and focusing lens system is shown in Fig. 2.

A 10 layer lens, $\varepsilon_{r\min} = 1$ to $\varepsilon_{r\max} = 81$, with a 15 cm radius was found to provide satisfactory electric enhancement. Besides reducing the reflection of the input pulse incident on the target, the focusing lens has two additional advantages: (1) the electric field at the second focal point is amplified by $\varepsilon_{r\max}^{1/4}$ and (2) the beam width (spot diameter) is reduced by $\varepsilon_{r\max}^{-1/2}$ [5].

As a proof of concept, a five-layer focusing lens, $\varepsilon_{r\min} = 1$ to $\varepsilon_{r\max} = 9$, was studied. The experimental "zoomed-in" impulse waveforms, at the second focal point, in air and inside the lens are compared in Fig. 3. The FWHM of the impulse in air is 100 ps while that inside the lens is 130 ps. The larger FWHM inside the lens is mostly due to losses in the lens materials. The

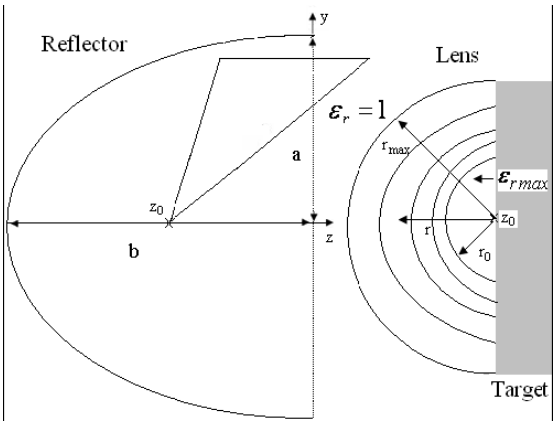


Fig. 2. PSIRA and focusing lens system [5].

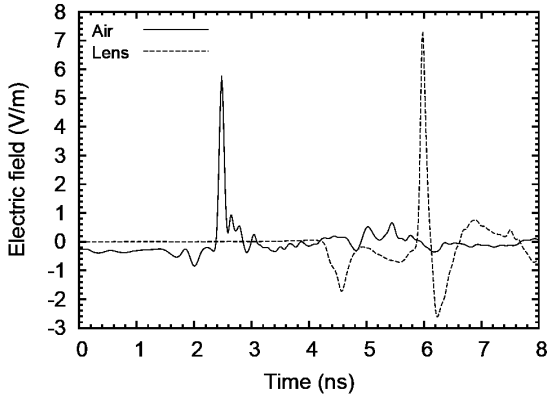


Fig. 3. Comparison of "zoomed-in" electric field impulse, at second focal point, in air and in lens [5].

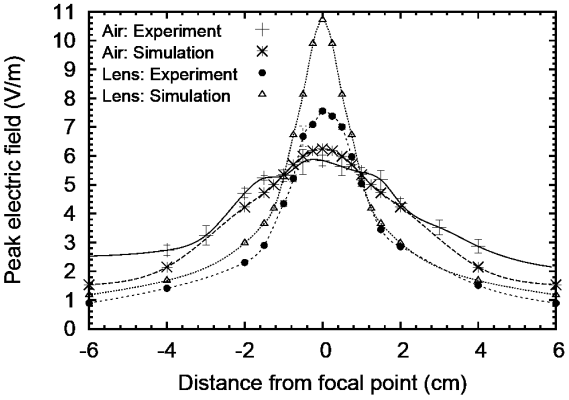


Fig. 4. Comparison of simulation and experiment results for beam width in air and inside lens [5].

electric enhancement is approximately 1.7 as expected from theory [5]. Fig. 4 compares the numerical simulation and experimental results for the beam width (spot diameter) in air and inside the lens. Again, the larger beam width in the lens, compared to the corresponding simulation results, is due to losses in the lens materials. In the experiments, the spot diameter is reduced by a factor of 2.5 while in the simulations it is reduced by a factor of 3.04. These results agree well with those obtained from analytical calculations.

4. DESIGN OF THE SWITCH SYSTEM

For input voltages of 100 kV or more, a switch system and "launching" lens are necessary to effectively launch a spherical TEM wave from the first focal point. The switch system consists of switch cones, a pressure vessel and a gas (typically hydrogen) chamber.

The geometrical center of the switch cones coincides with the first focal point. Various switch configurations were investigated in an effort to maximize the impulse amplitude at the second focal point with a minimum compromise in the spot size. The Truncated Four-Feed Arm with Switch Cones (T4FASC) design

was found to provide the most satisfactory results [6]. In this configuration, a 200 Ω bi-cone switch, of height 1.0 cm, centered at the first focal point, transitions to the conical feed-arms of the PSIRA. The feed arms are truncated; the length of the feed arms from the first focal point is approximately 19 cm.

The pressure vessel can be considered to serve as a (launching) lens. This considerably simplifies the design of the switch system. Two pressure vessel designs were investigated: (1) Spherical Pressure Vessel (SPV) with a Spherical Hydrogen Chamber (SHC) and (2) Cylindrical Pressure Vessel (CPV) with a Cylindrical Hydrogen Chamber (SHC). The SPVSHC design is the simplest as the shape of the pressure vessel conforms to the spherical wave-front originating from the source (first focal point). The dimensions of the CPV were determined using optical (high frequency) approximations.

The waveforms at the second focal point for the SPV and CPV configurations are compared in Fig. 5. One notes that the CPV configuration has a lower amplitude than the SPV design. This is because the optical approximations used in the CPV design are invalid at the lower frequencies in the input pulse. Experimentally however, the CPV design is attractive as it is easier to fabricate.

The dimensions of the pressure vessel and feed-arms for both configurations were optimized to maximize the peak focal impulse amplitude with minimum increase in the spot size.

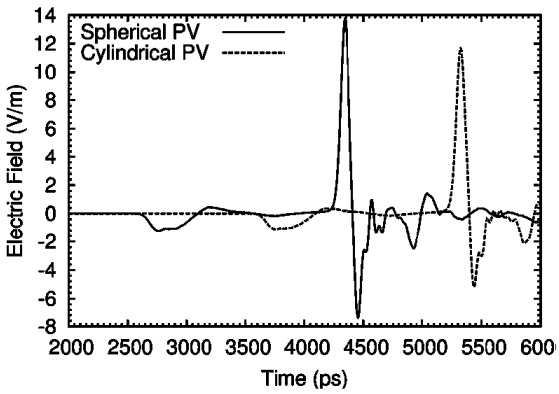


Fig. 5. Comparison of focal impulse waveforms for the spherical and cylindrical pressure vessel designs.

4. CONCLUDING REMARKS

This paper has presented the design of a PSIRA, focusing lens and switch system. The design is conceptually complete. Experimental results with a five-layer, dielectric focusing lens agree well those obtained from simulations and analytical approximations.

Future work involves finding better materials with less loss and dispersion for the focusing lens. The practical realization of the switch system and high-voltage experimental results will also be important in characterizing the efficacy of the full PSIRA system.

ACKNOWLEDGMENTS

The authors would like to thank their colleagues at the Old Dominion University for their valuable discussions and input.

REFERENCES

1. K. H. Schoenbach, B. Hargrave, R. P. Joshi, J. F. Kolb, C. Osgood, R. Nuccitelli, A. Pakhomov, R. J. Swanson, M. Stacey, J. A. White, S. Xiao, J. Zhang, S. J. Beebe, P. F. Blackmore, and E. S. Buescher. Bioelectric Effects of Intense Nanosecond Pulses. *IEEE Transactions on Dielectrics and Electrical Insulation*, 14(5):1088 – 1119, October 2007.
2. C. E. Baum. Focal waveform of a prolate-spheroidal impulse-radiating antenna. *Radio Sci.*, 42(RS6S27), 2007.
3. S. Altunc. Focal Waveform of a Prolate-Spheroidal Impulse-Radiating Antenna (IRA). PhD thesis, University of New Mexico, December 2007.
4. C. E. Baum. Addition of a Lens before the Second Focus of a Prolate-Spheroidal IRA. *Sensor and Simulation Note512*, April 2006.
5. P. Kumar, S. Altunc, C. E. Baum, C. G. Christodoulou, E. Schamiloglu, and C. J. Buchenauer. Radially Inhomogeneous Spherical Dielectric Lens for Matching 100 ps Pulses into Biological Targets. *Accepted for publication, IEEE Transactions Plasma Science, SpecialIssue - Nonthermal Medical/Biological Applications UsingIonized Gases and Electromagnetic Fields*, 2010.
6. P. Kumar, S. Altunc, C. E. Baum, C. G. Christodoulou and E. Schamiloglu, "Launching a Fast (100 ps), High-Voltage (> 100 kV) Pulse into a Biological Target", *International Conference on Electromagnetics in Advanced Applications (ICEAA)*, Sydney, Australia, September 2010.

DATA RATE IN IMPULSE ULTRA WIDEBAND RADIO NETWORKS

Bunin S. G.

National Polytechnic University "KPI", Kiev, Ukraine
E-mail: sgbunin@ukr.net

Abstract

The paper deals with one of principal issues of IR-UWB application – achievable date rates in multiple access radio networks.

It is shown that conventional representation of IR-UWB signals as very high rate carrier does not reflect real facts. Data rates in radio networks with multiple access and presentation of data by orthogonal impulse series are much less than those stated.

Frequency limitations of UWB spectrum especially its higher part are also decrease possible data rates.

Keywords: Impulse radio ultra wide band (IR-UWB), duty factor, impulse duration, orthogonal code, coherent reception.

1. INTRODUCTION

It is generally accepted, that impulse radio ultra wideband signals (IR-UWB) provide very high data rates and high of traffic density within an area unit [1]. Such assertion is usually based on Shannon formula, which shows that data transmission rate is proportional to the bandwidth occupied by a signal. Indeed, impulse signal of one nanosecond duration, for example, occupies frequencies from near zero to about ten gigahertz. However, if information is presented by one impulse, the impulse presents just one bit of information. Thus, «direct» application of Shannon formula for impulse signals is not correct.

2. MODULATION

For estimation of possible transmission rates it is reasonable to examine them in time domain. Maximally possible rate in a single channel communication system can be proportional to the amount of impulses, presenting the bits of information during a time unit. High data rate will be attained by the dense «packing» of impulses in time. And, obviously, the shorter impulses, the higher transmission rate.

However, a transmission by non modulated impulses will correspond to the binary information transfer «with a passive pause», when impulses represent either 0 or 1. For binary transmission (0 and 1) or multiple characters information transmission impulse modulation is needed to recognize the bit value. There are many types of impulse modulation proposed – amplitude, phase, time-hopping and code impulse series. All of them have one or another shortcoming, which complicate receivers (requirements of very fine synchronization, exactness of the matched filters elements making and other). Non-coherent methods of short impulsive signals reception allow simplifying receivers thanks to increased tolerance of above mentioned problems.

Shortening impulses duration reduces their energy. Indemnification of energy can be attained either due to the increase of impulse amplitudes or their amounts in the signal. The first is presently limited by the amplitude-frequency mask of FCC [2], second – accessible, but reduces the information rate. Nevertheless, presentation of informative bits by impulse code sequences is the best method of modulation because it allows to carry out addressing of signals to the concrete receivers tuned to the codes, and to use the passive matched filters, invariant in time and not requiring the signal synchronizations.

3. MULTIPLE ACCESS AND SIGNAL ORTHOGONALITY

In a narrow-band signals radio networks it is necessary to employ a Medium Access Control (MAC) protocols, which reduce transmission rate of each subscriber. If IR-UWB signals are used in a radio network, imposition of many subscriber's signals is possible if they are orthogonal and receivers have an ability to select necessary signals from a total stream. Impulse signals are orthogonal if they displaced in time in relation to each other, and the receiver has an ability to be synchronized with each of them (reception on the active correlator with synchronization). This condition requires minimum coincidence in time of impulses from different subscribers. Orthogonality is also provided by the choice of different temporal impulse positions of for each of signals. In this case it is possible usage of passive filters, matched with sig-

978-1-4244-7468-4/10/$26 ©2010 IEEE

nals, without the synchronization. Thus we have an equivalent of code division multiplexing.

The temporal bit encoding by number of impulses allows reducing energy of impulses at transmission side and compensating signal energy by adding up energy of many impulses at a reception side, providing a necessary signal-to-noise ratio on the decision making device of the receiver.

4. SIGNALS' TRANSPARENCY

In networks with IR-UWB signals MAC protocol with the code modulation can be removed, if the orthogonality of the code sequences provide 'mutual transparency', i.e. code sequences allow to place the impulses of users' in pauses between the impulses of each other signals. By other words, pauses between the impulses of each of subscribers' signal must suffice for placing in them impulses of signals of other subscribers. It is necessary to understand the 'mutual transparency' in majority sense: the possible mutual coincidences of impulses of different subscribers must be at minimum to keep the probability of erroneous reception of «stranger» code sequence at minimum – i.e. 'orthogonality' always means 'quasi orthogonality'.

Signal 'transparency' can be presented by mean duty cycle factor: $\overline{q} > T / n\tau = 1 / Vn\tau$, where T is duration of bit of signal, τ is pulse width, n is amount of impulses in the code sequence, $V = 1 / T$ is data transfer rate in the network. A total value of duty cycle in the network with N active subscribers $Q = T / \sum_{N} n\tau$ must be more than 1 to provide transmissions of all subscribers with minimum probability of impulse coincidence of their signals. Thus the total data rate in a radio network with code division is equal $V \le 1 / Qn\tau$.

Fig. 1 shows total data rates in a network with impulse durations at the mean duty cycle value equals 10.

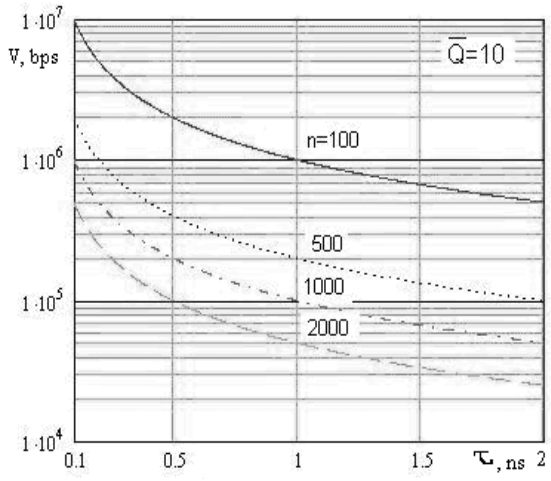


Fig. 1 Network data rates vs. signals impulse durations.

5. IMPULSE SPECTRUM LIMITATIONS

Data rate speed up is possible by reduction number of impulses *n* and impulse duration τ minimization. First undesirable, as diminishes the variety of codes and energy of signal, second – also diminishes signal energy, and in addition displaces the maximum signal spectrum toward more high-frequency region of radio spectrum.

Spectrum limitation of such ultra wideband signals is necessary, although it may be a temporal fact preventing interference from them to the existent communication systems. The FCC mask on power and spectrum limits communication possibilities - limits distance (up to 10 meters) and on data rate. The signal, which the best fits the mask, must have duration of 0,146 ns. This corresponds to the maximum of its spectrum in the middle of 3.1 – 10.6 GHz, i.e. 6.85 GHz. Accordingly to fig. 1, data rate in a network with signals consisting of 500 impulses per bit does not exceed 1 megabit per second.

It would seem that impulse duration shortening can be the mean for data rate speeding up.

Presently there are facilities and devices, generating impulses less than 10 picoseconds duration of enough power. However there is a problem to keep so small durations under frequency limitations of the impulse spectrums. Limitation of low frequency part of the spectrum (lower then its maximum) does not influence the impulse width, though changes its form (that can cause some problem for impulse coherent reception). But high frequency limitation with low pass filtering and especially band-pass filtering increase impulse duration. That contradicts to the purpose – increase of speed of transmission. It is the same possible to say at the key-in of impulses through полосовые filters.

Fig. 2 illustrates the result of 25 picoseconds monocycle spectrum limitation by 30 – 50 GHz bandpass filter: the initial Gaussian mono-impulse degenerates in 45 – 50 picoseconds duration radio-impulse.

If one passes such short impulse through a bandpass filter, fitted to the FCC mask, the result will be catastrophic (Fig. 3).

6. CONCLUSIONS

The code modulation of IR-UWB signals is the effective method to provide quasi orthogonality and addressing signals in radio networks, allowing providing multiple access to radio channel without MAC protocols. At the same time, it reduces data rate due to necessity of providing of «mutual transparency» of all signals.

Data rate speed up can be provided by shortening of impulse durations. Here however displacement of a spectrum maximum to more high-frequency band of radio spectrum takes place. It will be a reason to select new band for future IR-UWB communications in a comparatively less-used regions of radio spectrum higher 50 GHz.

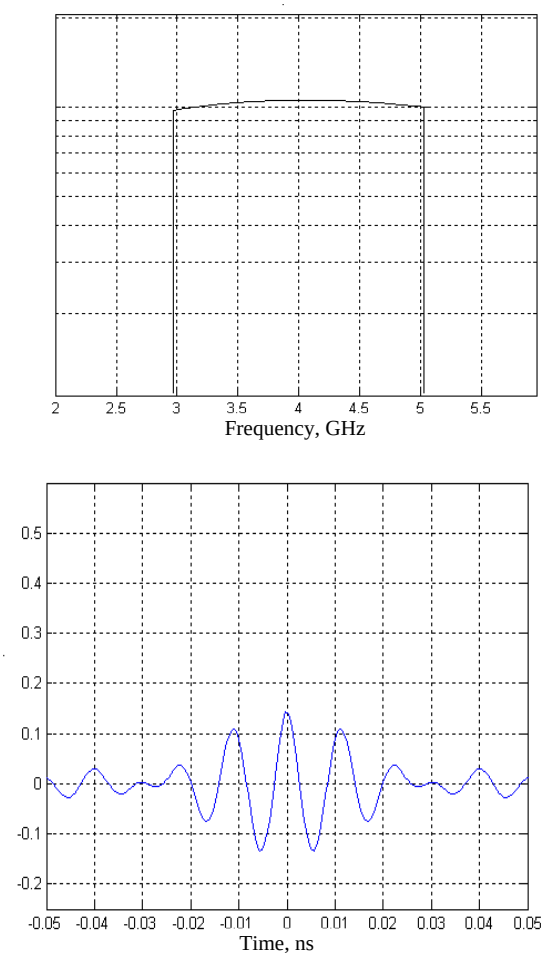


Fig. 2. 30 – 50 GHz band-pass filter and shape of 25 ps impulse after the filter.

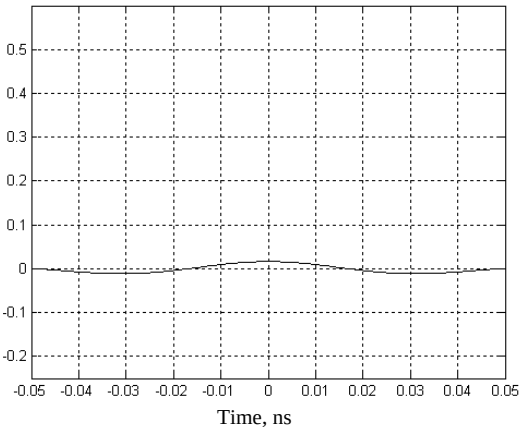


Fig. 3. Shape of 25 ps impulse after the FCC mask limitation.

However there should be no low-pass or strict band-pass impulse spectrum limitations which results in the impulse durations increase. High-pass spectrum limitations can be conceivable and desirable to prevent interference from and to radio systems using lower part of the spectrum.

REFERENCES

1. L. E. Miller. Why UWB? A Review of Ultrawideband Technology.// Report to NETEX Project Office, DARPA. Wireless Communication Technologies Group National Institute of Standards and Technology. Gaithersburg, Maryland. April 2003.
2. Federal Communications Commission (FCC) “First Report and Order in The Matter of Revision of Part 15 of the Commission’s Rules Regarding Ultrawideband Transmission Systems” ET-Docket 98-153, FCC 02-48, released April 22, 2002.

Ultrawideband and Ultrashort Impulse Signals, 6-10 September, 2010, Sevastopol, Ukraine pp. 144-146

USE OF THE ULTRAWIDEBAND FMCW SIGNAL FOR HF COMMUNICATION RADIOCHANNEL DIAGNOSTICS

Ilyin N. V., Khakhinov V. V. and Ponomarchuk S. N.

Institute of Solar-Terrestrial Physics
Russian Academy of Science, Siberian Branch, Irkutsk, Russia
E-mail: khakhin@iszf.irk.ru

Abstract

Ultrawideband frequency modulated continuous wave (FMCW) signals are using for ionospheric sounding by chirp sounders. We can use two techniques of digitizing. The first one is digitizing at intermediate frequency. The second one is digitizing at double maximum frequency of signal. Both of them use uniform sampling. In this paper we propose technique of non uniform sampling of FMCW signal.

We describe the usage of FMCW signal in backscatter ionosphere sounding (BS) regimes. The results of BS give us possibility for direct diagnostics of HF radiochannel. We also present results of modeling and interpretation of BS ionograms which were obtained on the base of Institute of Solar-Terrestrial Physics chirpsounder.

Keywords: FMCW signal; non-equidistant sampling; digital signal processing.

1. INTRODUCTION

The diagnostics of ionospheric radiochannel properties is important for fundamental research and for a wide range of practical problems which deal with radio communication provision. At present ionosphere sounding is carried out by chirpsounders which use ultrawideband FMCW signals. The chirpsounder can operates in vertical, oblique (OS) and BS ionosphere sounding regimes. The result of single work session is ionogram – the dependence of amplitude and group delay on frequency. The processing of FMCW chirpsounders signals in OS and BS regimes allows to carry out real-time direct radiochannel diagnostics. The sounding results give information on radio waves propagation conditions without restoration and correction of ionospheric parameters.

The theoretical investigation of the ultrawideband FMCW signal propagation through ionospheric radiochannel was used to propose an analysis technique of received signal form on intermediate frequency (IF) [1]. This technique allows us to obtain radio channel transfer function thus expanding the direct diagnostics techniques abilities.

The goal of this report is the investigation of direct diagnostics abilities for decameter communication channel under BS by continuous ultrawideband FMCW signal on the base of chirp signal propagation modeling and non-equidistant sampling and digital processing techniques of sounding signals.

2. USING OF THE FMCW SIGNAL FOR RADIOCHANNEL DIAGNOSTIC

The basic operation scheme of the chirp ionosonde is well known [2,3]. The chirp signal with duration of several minutes is radiated within the range of 1-30 MHz:

$$e_{tr}\left(t\right) = \sin \chi t^2, \tag{1}$$

where χ is the chirp rate.

Assuming that characteristics of the ionospheric radio channel are linear, the signal at the ionosonde receiver input may be written as a convolution $e(t)$ with the radiochannel pulse response $h\left(\tau\right)$:

$$e_{rec}\left(t\right) = \int_0^\infty h\left(\tau\right) e_{tr}\left(t-\tau\right) d\tau\,. \tag{2}$$

The received signal within the chirp ionosonde receiver is mixed with the reference oscillator signal. The mixing result runs through the low-pass filter in order to remove the HF component. Samples separated by the time window $w(t)$ at instants of time t_k are fed to the spectrum analyzer input. The sequence of output spectra is recorded (digitized) and is the result of one operation session of the chirp ionosonde. The sequence of output spectrum $S_k\left(F\right)$ involves two terms: the first is concentrated in the region of F positive values, and the second is in the region of negative ones. Since $S_k\left(F\right)$ is the Fourier transform of a real function, the following condi-

978-1-4244-7468-4/10/$26 ©2010 IEEE

tion is fulfilled: $S_k\left(-F\right)=S_k^*\left(F\right)$. We confine ourselves to considering $S_k^+\left(F\right)$ for F positive values:

$$S_k^+\left(F\right)=\frac{1}{4}e^{iFt_k}\int_0^\infty h(\tau)W(F-2\chi\tau)e^{i\left(\chi\tau^2-2\chi t_k\tau\right)}d\tau\,. \quad (3)$$

Here $W\left(F-2\chi\tau\right)$ is the window spectrum. The windows used in chirp sounders have a narrow band of about ten Hz, and the spectrum is localized close to zero of argument. Initial frequency of the analyzer's working range exceeds the window-spectrum bandwidth. Thus the lower limit of integration with respect to τ can be extended down to $-\infty$. If we change the integration variable τ for $y=F/2\chi-\tau$, introduce the function $b\left(y\right)=e^{i\chi y^2}W\left(2\chi y\right)$, and also express the pulse response in terms of the transfer function of the ionospheric radio channel $H(\omega)$ [2], the spectrum can be written as:

$$S_k^+(F)=\frac{\pi}{2}e^{i\frac{F^2}{4\chi}}\int_{-\infty}^\infty H(\omega)B(\omega+2\chi t_k-F)e^{-i\frac{\omega F}{2\chi}}d\omega\,. \quad (4)$$

Here $B(\omega+2\chi t_k-\Omega)$ is the Fourier transform of function $b(y)$.

3. DIGITIZING OF FMCW SIGNAL

In [1] it was shown that for reconstructing transfer function of the ionospheric radiochannel we can use digitizing FMCW signal at the IF. Usually technique for digitizing is based on the WKS (Whittaker, Kotelnikov, Shannon) equidistant sampling theorem. Modern devices execute sampling on doubled maximum frequency and following operations are executed in digital form. However, for FMCW signal which is used in ionosondes this sampling is redundant so far as the frequency is varied from 1 to 30 MHz.

Below we will show that it is possible to modify WKS theorem for FMCW signal. This technique allows to sample signal irregularly, but synchronously with FMCW frequency changing.

Signal $f(t)\in L_2$ lies on interval $t\in[0,T]$, and out of this interval signal is equal to 0. Let us make the substitution of variable $t=\tilde{g}(z)$ of the form $z(t)=(\omega_0+\chi t)\cdot t=g(t)t$, and which is monotonous on this interval. The execution of monotony substitution provides existing of simple inverse substitution. Let us notice that

$$f(t)=f(\tilde{g}(z))=\tilde{f}(z)=\tilde{f}(z(t))\,.$$

The signal obtained as a result of such substitution is $\tilde{f}(z)\in L_2$ on interval $z\in[0,Z]$, where $Z=z(T)$. Let us apply WKS theorem to new variable signal:

$$\tilde{f}(z)\approx\sum_{k=0}^{N_z}\tilde{f}\left(\frac{k\pi}{\Omega'}\right)\frac{\sin(\Omega' z-k\pi)}{\Omega' z-k\pi}, \quad (5)$$

where $N_z=Z\Omega'/\pi$, Ω' is chosen in accordance with essential accuracy.

If we will return to variable t by using inverse substitution $z(t)=g(t)\cdot t$, then signal $f(t)$ will be restored in the form of Kotelnikov series, but the samples for $f(t)$ will be non-equidistant.

$$f(t)\approx\sum_{k=0}^{N_z}f\left(t_k\right)\frac{\sin(\Omega' z(t)-k\pi)}{\Omega' z(t)-k\pi}=\sum_{k=0}^{N_z}f\left(\tilde{g}\left(\frac{k\pi}{\Omega'}\right)\right)\frac{\sin(\Omega' g(t)\cdot t-k\pi)}{\Omega' g(t)\cdot t-k\pi}\,. \quad (6)$$

where $t_k=\tilde{g}(z_k)=\tilde{g}\left(\frac{k\pi}{\Omega'}\right)$

Obviously, under substitution of variable the Fourier spectrum will be different. But we have formulae for transformation of one spectra to another and after inverse substitution the spectrum will be restored.

Thus we use synchronous detection of frequency modulated signal. The multiplication by reference oscillator signal is the particular case of synchronous detection. Another particular case is uniform sampling. Further transformations are executed by ordinary digital technique as it is described in [1].

4. USING ULTRAWIDEBAND FMCW FOR DIRECT DIAGNOSTICS OF HF COMMUNICATION RADIOCHANNEL

One of techniques that give the most potential possibilities in HF channel is the BS [4]. By using BS we can diagnose medium in large spatial regions within several thousands kilometers. The registration of BS signal allows us to control ionosphere conditions and investigate scattering properties of ground surface.

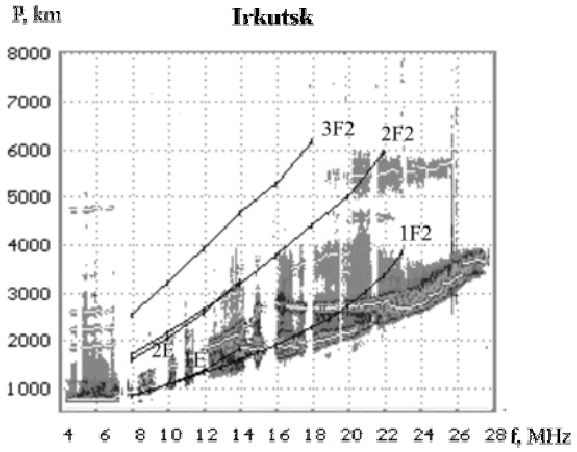
The modeling of FMCW signals characteristics under BS in the framework of waveguide approach [5] is carried out on the base of incoherent scatter approximation in which scattered field characteristics are expressed through incidence field characteristics (incidence angle and amplitude) and local scatter diagram or scatter coefficients.

By modeling of BS signal characteristics and experimental data analysis we have revealed weakly changed ratio (under ionosphere parameters variations) of group path P_m, which corresponds to leading edge of BS signal and distance to illuminated zone border D_m (P_m / D_m). Given adiabatic relation allow us to determine maximal usable frequency (MUF) of propagation mode on given radio path with a help of BS data. For ionosphere parameters forecast we can calculate range-frequency characteristics $P_m(f)$ and $D_m(f)$. Also, for given range D we can calculate ratio $\eta=P_m/D$ and after that on real range-frequency characteristic of BS by leading edge we can determine the frequency for which

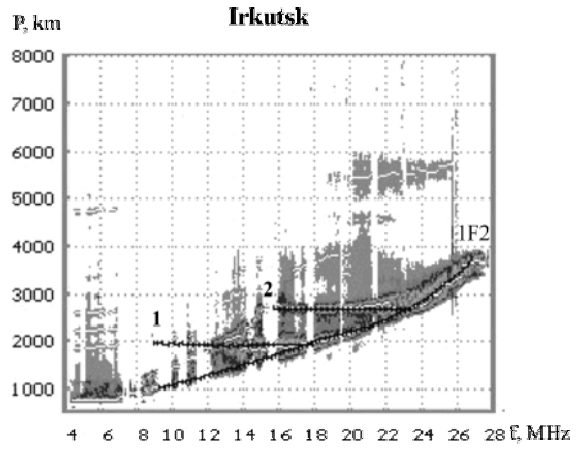
group path is equal to value $P = \eta D$. The calculated frequency will be real f_m for given D .

The approbation of proposed technique for BS signals characteristics calculation is carried out by means of experimental data obtained by ISTP chirpsounder (Irkutsk). As an example on Fig.1 we present BS ionograms obtained on 29 February 1996, 4:49 UT under sounding in Asia-pacific ocean region direction with modeling results of range-frequency characteristics of BS signal by leading edge, processing by amplitude relief (1a) and interpretation (1b).

For BS signals interpretation we use reconstruction technique for range-frequency characteristics of BS signal by current BS data on the base of invariant P_m / D_m. The results of one-hop mode 1F2 reconstruction are presented on Fig.1b. The processing of amplitude relief has shown the presence of horizontal tracks with nearly constant delay. For interpretation of these signals we used reconstruction technique for range-frequency characteristics of BS signal by current BS data. Using the results of BS signals modeling by leading edge and marked tracks of one-hop signals



a)



b)

Fig. 1. The BS ionograms, modeling results (a) and interpretations (b). 29 February 1996, 4:49 UT.

we can calculate MUF for OS f_m^r on fixed ranges grid. On the base of calculation results we can obtain ranges for which group path P_m approximately complies with horizontal track delay. Using the long-term forecast of range-frequency characteristics for oblique sounding on chosen ranges in relative frequency grid $\beta = f / f_m^p$, where f_m^p is prognosis value of MUF propagation mode, we can carry out the interpretation of horizontal "tracks" by means of recalculation of model oblique sounding range-frequency characteristics on real frequency grid βf_m^r. The calculation results of range-frequency OS characteristics for propagation mode 1F2 on ranges 1800 km and 2500 km are shown on Fig.1b by lines with numbers 1 and 2. The determination of scattering objects positions by receiving points coordinates of OS signals on chosen distances from transmitter shows that appearance of horizontal bands on BS ionograms in our experiment can be connected with scattering on transition border between sea and land.

CONCLUSION

The suggested technique of non-equidistant sampling for ultrawideband FMCW signal, synchronized with changing signal frequency allows to restore signal with a help of formulae (6). In fact, it is generalization of WKS theorem for the case of special signals such as FMCW signals.

Further analysis of both in-phase and quadrature components of the FMCW signal is carried out by standard processing. As a result we obtain the dependence of group delay on frequency - ionogram of ionosonder. The application of BS techniques allows to conduct direct diagnostics of HF communication radiochannel.

REFERENCES

1. Ilyin N.V. and Khakhinov V.V. 2006, 'The theoretical investigation of the ultrawideband FMCW signal propagation through ionospheric radiochannel.' *Proc. Fifth Int. Conf. Ultrawideband and Ultrashort Impulse Signals, Sevastopol,344-346*.
2. Ilyin N.V., Khakhinov V.V., et. al. 1996, 'The theory of chirp-signal ionospheric sounding.' *Proc. Int. Symp. Anten.&Prop.*, Chiba, 3.
3. Ivanov V.A., Kurkin V.I., et. al 2003. `Chirp ionosonde and its application in the ionospheric researches` *Radioph.&Quantum Electr.* **46**, 821-851.
4. Ponomarchuk S.N., Kurkin V.I., Oinats A.V. 2009, 'The diagfnostics of ionosphere and earth ground surface by backscatter sounding data', *Proc. Int. Conf. Progress in Electromagnetics Research Symposium,* Moscow, 1245-1248.
5. Kurkin V.I., Orlov I.I., and Popov V.N. 1981, *Normal wave technique in HF radio communication problem*. Nauka, Moscow.

Ultrawideband and Ultrashort Impulse Signals, 6-10 September, 2010, Sevastopol, Ukraine pp. 147-149

MEASUREMENT OF COORDINATES OF THE TARGETS PLACED BEHIND OF RADIO-TRANSPARENT BARRIER WITH MULTI-STATIC ULTRA-WIDE BAND RADAR

Myakinkov A. V. and Smirnova D. M.

State Technical University of Nizhny Novgorod, Russia
E-mail: redvillage@mail.ru, smirnovadarya@gmail.com

Abstract

High accuracy measurement of coordinates of the targets placed behind of radio-transparent barrier (inside of closed room) using ultra-wide band (UWB) radar seems to be the perspective field of the investigation. The results of these investigations could be useful when solving problems concerned with combating terrorism, security etc.

Keywords: Multi-static ultra-wide band radar, measurement of coordinates, identification of measurements, mathematical modeling.

1. INTRODUCTION

The abilities of UWB radars in respect to the coordinate measurement are different and depend upon the radar configuration [1-4]. One of possible ways to provide high accuracy of coordinate measurement is using of several space-distributed UWB sensors. These sensors could be placed, for example, along the outside wall of the room.

Antennas, used in UWB radars, usually possess slightly-directional properties [4]. Thus, using short-pulse probing signal, every sensor (position) of the system can provide measurement of only range of the target [3]. Using measurements of the range of the same target obtained in different positions, one can compute target coordinates by different methods.

When several targets are placed simultaneously in radar cover, the problem of identification of range measurements arises due to arising of false measurements. This is caused by the crossing of position lines corresponding to different targets. The quantity of false measurements rises sharply with rising of the quantity of targets. The possible ways to exclude false measurements are increasing the quantity of positions or, in another case, target coordinate measurement with the same positions, but using different methods.

2. MODEL OF OBSERVATION PROCESS

2.1. SYSTEM CONFIGURATION

The paper deals with analysis of the system consisting of three UWB sensors placed along the same wall of the room, outside of the room. Data containing measurements of primary parameters (target ranges) are passed to the computer for the secondary processing.

When developing algorithms of target coordinate measurement, it is worthwhile to use the maximally simplified geometrical model of the radar cover. We assume that radiation pattern of antenna of each sensor presents the angular sector with width $\Delta\theta = 90^\circ$. Target detection is not provided outside of this sector. Thus, the maximal cover of the radar is obtained with the minimal distance between the antennas and practically coincides with the cover of the central sensor.

2.2 MODEL OF DISTRIBUTED TARGET

Since the linear size of a target (human) could be sufficiently more than wavelength ($\lambda = 0.15$ m) in dependence upon the target position, we should consider a model of space distributed target.

We consider a model of target consisting of a set of flash points. For the case of a human target, these flash points could be placed along the ellipse. Taking into account the typical size of the chest cross section of a standing human, we assume the half ellipses to be equal $a_{tg} \approx 0.25$ m, $b_{tg} \approx 0.125$ m. Considered model of a distributed target is illustrated by Fig. 1. In Fig. 1 ε is target foreshortening, α_{norm} is angle between the direction to the point and normal to the line concatenating two adjacent points, $\vec{r}_{tg} = \left(x_{tg}, y_{tg}\right)$ is radius vector of the target center.

In Fig. 1, the filled circles present the illuminated points, while light circles present the shadowed points. The approximation of geometrical optics was used.

The radiobrightness of each flash point could be approximated with a function depending upon the angle α_{norm}:

$$A_{fp} = F\left(\alpha_{\text{norm}}\right) \quad (1)$$

978-1-4244-7468-4/10/$26 ©2010 IEEE

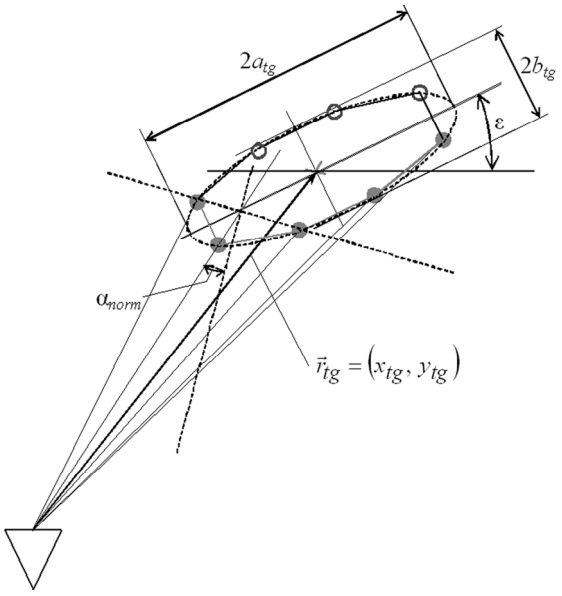


Fig. 1. Geometrical model of distributed target.

Obviously, that function (1) has a maximum when $\alpha_{\text{norm}} = 0$. Target reflected signal presents a superposition of the signals reflected from different illuminated flash points with different radiobrightness. Thus, we consider the following model of the estimation of target range:

$$r_i = \frac{\sum_{k=1}^{N_{vis}} r_k A_{rp,k}}{\sum_{k=1}^{N_{vis}} A_{rp,k}} + \Delta r_{Gauss} \qquad (2)$$

where N_{vis} is the quantity of illuminated points, r_k is range of *k*-th point, Δr_{Gauss} is the random error of range measurement.

The error of a single target range measurement is assumed to be equal

$$\Delta r_1 = \left|\vec{r}_{tg}\right| - r_i, \qquad (3)$$

3. Algorithm of Coordinate Measurement

The simplest approach of coordinate measurement is the following. Assume that several targets are placed inside of the room. Firstly, we obtain the group of cross points of the position lines (circles) corresponding to the side sensors. Then, we select those points from this group, which are placed near the position line corresponding to range measured from the central sensor.

The disadvantage of this approach is that several targets could be detected in each channel on the practically the same range. In this case, false target blips will be shown on the indicator. The matter of the problem is the following. In presence of random errors of target range measurement, we have not exactly cross points of position lines, but ambiguity areas with a size depending upon the range measurement accuracy. The increasing of the quantity of the targets leads to the arising of false blips caused by the crossing of different ambiguity areas.

We propose an algorithm of target coordinate measurement developed to minimize the probability of arising of false blips. This algorithm consists of identification of points belonged to different two groups. The first group contains measurements obtained as cross points of position lines built using range measurements (circles) from two side sensors. The second group contains points obtained using measurements of differential range from two side positions and range from the central position.

In multi-target situation, each group of points contains correct target blips as well as false blips. We denote two analyzed groups as vectors

$$\vec{G}_1 = \begin{bmatrix} \vec{r}_1^{(1)} \\ \vec{r}_2^{(1)} \\ \cdots \\ \vec{r}_{N1}^{(1)} \end{bmatrix} = \begin{bmatrix} x_1^{(1)} & y_1^{(1)} \\ x_2^{(1)} & y_2^{(1)} \\ \cdots \\ x_{N1}^{(1)} & y_{N1}^{(1)} \end{bmatrix}, \vec{G}_2 = \begin{bmatrix} \vec{r}_1^{(2)} \\ \vec{r}_2^{(2)} \\ \cdots \\ \vec{r}_{N2}^{(2)} \end{bmatrix} = \begin{bmatrix} x_1^{(2)} & y_1^{(2)} \\ x_2^{(2)} & y_2^{(2)} \\ \cdots \\ x_{N2}^{(2)} & y_{N2}^{(2)} \end{bmatrix}. \qquad (4)$$

Only points satisfying the condition $d_{ij} < R_{ij}$ should be selected, where d_{ij} is Euclidean distance between the points, i is the number of point from the first group, j is the number of point from the second group, R_{ij} is radius of ambiguity area depending upon the values of the errors of range measurements. The values of d_{ij} and R_{ij} are defined by the following:

$$d_{ij} = D\left(\vec{r}_i^{(1)}, \vec{r}_j^{(2)}\right) = \sqrt{\left(x_i^{(1)} - x_j^{(2)}\right)^2 + \left(y_i^{(1)} - y_j^{(2)}\right)^2}, \qquad (5)$$

$$R_{ij} = k\sqrt{\sigma_x^2\left(\vec{r}_i^{(1)}, \vec{r}_j^{(2)}\right) + \sigma_y^2\left(\vec{r}_i^{(1)}, \vec{r}_j^{(2)}\right)}, \qquad (6)$$

where k is selected from the conditions of appropriate value of the probability of false measurement, σ_x^2, σ_y^2 are variances of the errors of target coordinate measurement in the area of supposed target location.

To improve the accuracy of target coordinate measurement, the algorithm of inter-observe identification is used. This algorithm combines the ideas of inter-period integration widely used in pulse radars and algorithm of gating target blips usually used at the stage of secondary processing.

Fig. 2 illustrates the matter of inter-observe identification algorithm. The vector delay line organized as a table is shown. Each cell of the table contains two values: scalar attribute of target blip presence and vector $\vec{r} = \left(x_{ij}, y_{ij}\right)$. The number of strings in the table, N_1, corresponds to the maximally blips per one observation. The number of columns, N_2, corresponds to the number of analyzed observations.

Each Column of the table contains blips and measurements had been identified in the corresponding ob-

servation. During the next observation, shift of the delay line is performed, new measurement is written into the first column, and algorithm of sorting is applied to new data. If new measurement arises inside of the gate formed using averaged data in *i*-th string, new measurement is replaced into corresponding string. As a result, every string contains measurements corresponding to the same target. In Fig. 2 data associated with the same target are shown by the same form inside of the cells.

When the quantity of target blips and corresponding measurements in any string exceeds the threshold, decision about target detection is accepted. The averaged via the whole string measurement is accepted as eventual estimation of target coordinate vector.

The size of the gate used for the sorting of measurements is defined by the a-priory data concerning target size. Also, two-level gating approach is possible. First time, fixed gate is used. Its size is defined be the target size. Then, adaptive gate, defined by information about target coordinate measurement accuracy, is applied.

3. RESULTS OF MATHEMATICAL MODELING

The performance of proposed target coordinate measurement algorithms had been explored using mathematical modeling. To estimate the probability of correct identification, 1000 independent experiments with a model had been made. Target blip and corresponding coordinate measurement were accepted to be correctly identified only in the case, when distance between this blip and exact target position did not exceed the size of ambiguity area. The size of ambiguity area is defined by coordinate measurement accuracy. This accuracy had been calculated beforehand for each area inside of the radar cover.

The graphs of dependence of correct target identification probability, P_{corr}, upon the root mean square errors of range measurement, σ_r, are shown in Fig.3. In Fig. 3 curves 1 correspond to the situation when only one target is placed inside of the room. Curves 2 correspond to the case of three targets. Solid lines and dashed lines are for the case when array pitch $d = 1$ m, dotted and dashed-dotted lines are for the case when $d = 3$ m. The estimation of the correct identification probability had been obtained as a ratio of the blips inside of the area of exact target placement, to the general quantity of the targets inside of the radar cover.

It is clear from the analysis of graphs in Fig.3, that the probability of correct target identification raises with increasing of distance between the sensors.

4. CONCLUSION

The analysis of considered algorithms shows that the use of mentioned algorithms of measurement identification, excluding of false measurement and inter-observe identification provide correct target coordinate estimation with the probability close to unit. The

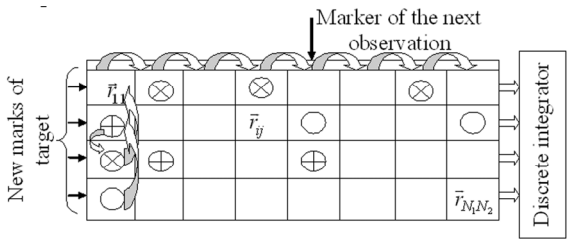


Fig. 2. Algorithm of inter-observe identification.

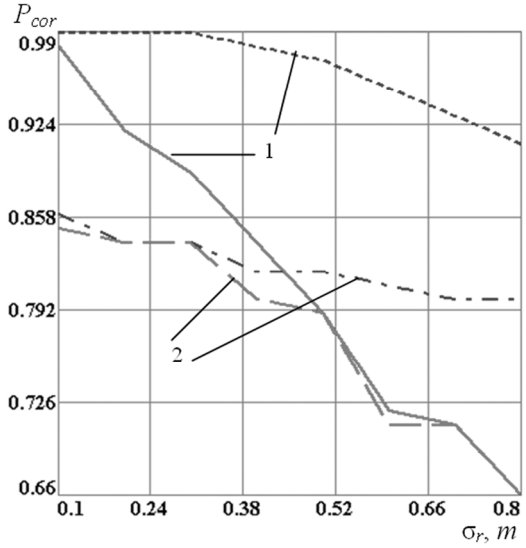


Fig. 3. Probability of correct target identification.

same time, the accuracy of coordinate measurement is appropriate when rms errors of range measurements do not exceed the values of about 0.3 m. The size of the monitored room is about 10x10 m.

REFERENCES

1. Immoreev I. Ya. Ultra-wide band radars. Features and opportunities // Radiotehnika i electronika. 2009. Vol. 54. №1. 5-31.
2. Problems o subsurface radiolocation. Collective monography / edited by PhD A. Yu. Grinev. Moscow, Russia: Radio engineering, 2005. 416.
3. Andriyanov A.V., Dombek M.G. Systems for investigation of objects in space and transmission lines by using UWB signals // Proc. Int. conf. on UWB technologies. IWUWBT2005. 8-10 Dec. 2005, Japan. 105-109.
4. Andriyanov A.V. Generators, Antennas and Registrator For UWB Radar Application // Proc. 3rd IEEE Conference on Ultra-wide band Systems and Technologies, 18-21 May. 2004, Kyoto. Japan. 145-150.

DETECTION AND COORDINATE MEASUREMENT OF TARGETS BY ULTRA-WIDE BAND RADAR WITH ANTENNA ARRAY

Myakinkov A. V. and Smirnova D. M.

State Technical University of Nizhny Novgorod, Russia
E-mail: redvillage@mail.ru

Abstract

Algorithms of digital signal processing are widely used in modern ultra-wide band (UWB) radars to solve problems of target detection and coordinate measurement. The paper deals with general algorithms of signal processing in ultra-wide band short-pulse radar with antenna array. The radar is developed for the monitoring of moving objects placed behind of radio-transparent barriers. The results of mathematical modeling are presented.

Keywords: Ultra-wide band short-pulse radar, antenna array, digital signal processing, beam forming, target detection, coordinate measurement.

1. INTRODUCTION

Algorithms of digital signal processing are widely used in modern ultra-wide band (UWB) radars to solve problems of target detection and coordinate measurement [1]. The stroboscopic transformation is used for registration of UWB signals. Using a sequence of time-shifted probing signals, an array of samples could be obtained. Every element of this array is defined by the value of UWB signal reflected from corresponding range resolution element.

In UWB radar, an antenna array could be used to measure the angle coordinate of moving object. The use of UWB short-pulse signals in radars with antenna array has several specific features concerning the signal processing algorithms. The paper deals with the analysis of these features. General algorithms of signal processing in ultra-wide band short-pulse radar developed for the monitoring of moving objects placed behind of radio-transparent barrier are considered. The results of mathematical modeling are presented.

2. ALGORITHM OF SPACE-TIME SIGNAL PROCESSING

In accordance with recommendations of international standards, a waveform with carrier $f_0 = 6$ GHz and duration $T_{\text{CH}} = 200$ ps of the level of half amplitude should be used in radar of considered type. The bandwidth of the signal is about 5 GHz. The mathematical model of such a signal could be approximately described as following:

$$s_{\text{tr}}(t) = \exp\left\{-a\left(t - T_{CH}/2\right)^2\right\} \times \cos\left[2\pi b\left(t - T_{CH}/2\right) + \phi_0\right], \quad (1)$$

where a and b are signal parameters defining its bandwidth and carrier, φ_0 is random phase.

The reflecting properties of the target could be described with a set of flash points. Thus, we will consider the model of space-distributed target as a linear discrete filter with a pulse response describe by the following:

$$h(t) = \sum_{n=0}^{N-1} A_n e^{j\phi_n} \delta(t - t_n), \quad (2)$$

where N is the number of target flash points, A_n and φ_n present amplitude and phase of reflection coefficient of *n*-th flash point, $t_n = \frac{2r_n}{c}$, r_n is range of *n*-th flash point, $\delta(x)$ is delta-function.

Taking into account the accepted models of probing signal and distributed target, the reflected signal $s_{\text{tg}}(t)$ could be written as following:

$$s_{\text{tg}}(t) = s_{\text{tr}}(t) \otimes h(t) = \sum_{n=0}^{N-1} A_n e^{j\phi_n} s_{\text{tr}}(t - t_n). \quad (3)$$

The graph of probing signal is shown in Fig. 1,a, while Fig. 1,b shows a signal reflected from a multi-point target. Both signals are presented in discrete time, *n*.

In general case, the optimal processing of UWB signal reflected from the space-distributed target should be considered in terms of detection of stochastic signal with unknown waveform, delay and amplitude [2-4]. However, as results of experimental investigations show, the target usually has one dominant flash point. In this case, we can ignore the varying of the waveform and use a classic matched filtering of the signal with unknown phase and amplitude.

978-1-4244-7468-4/10/$26 ©2010 IEEE

The functional diagram of space-time processing based on UWB antenna array is shown in Fig. 2.

In Fig. 2 Re_i is receiving part of *i*-th element of antenna array, ADC_i is analog to digital converter, MF_i is complex matched filter, SF_i is space filter, TH is threshold unit.

In linear approximation of wave front, target returned signals in receiving channels of adjacent array elements are mutually delayed with time interval $\Delta t = d \sin \alpha$, where d is distance between the array elements (array pitch), α is angle of arrival of the target returned signal in respect to the normal of the array. The optimal space processing consists of coherent integration of the signals received by different array elements. For this purpose, a set of space filters is used. Every filter consists of delay line and summation unit with weighting coefficients. To provide forming of beam in required direction, the optimal set of delays and weighting coefficients is calculated.

The threshold units provide detection of target returns. The adaptive threshold is calculated with a corresponding unit to provide false alarm rate stabilization.

3. Directional Properties of UWB Antenna Array

In general case, the radiation pattern of UWB antenna should be obtained for a set of different frequencies inside of the band of waveform in use. But we would like to estimate the integrated directivity characteristic, which could be used in the whole probing signal band. To solve the mentioned problem, let us consider two-dimensional space-time pulse response defined by the following:

$$\Phi(\alpha, t) = \sum_{i=0}^{N-1} S_i\left(t - i\frac{d \sin \alpha}{c}\right), \qquad (4)$$

where $S_i(t)$ is UWB signal reflected from one-point target and received in the channel of *i*-th element of the array. This signal is described with a model (1).

Two-dimensional space-time pulse characteristic of UWB array which consists of $N = 4$ elements is shown in Fig. 3,a.

For the convenience of the analysis, it is worthwhile to use one-dimensional (plane) function which defines the dependence of array gain upon the direction to the one-point target. To obtain this function, we should find the maximal value of signal (4) in time dimension for every value of azimuth. We will dedicate this function as $\Phi_1(\alpha)$. Curves 1, 2 and 3 in Fig. 3,b are correspondingly directivity characteristics of antenna array consisting of omni-directional elements, directivity characteristic of single array element and multiplication of these two functions.

Fig. 4 illustrates the mutual location of azimuth beams when array pitch $d = \lambda / 2 = 0,075$ m. Curve 1 shows the central beam, curve 2 corresponds to the first side beam, curve 3 is for 7-th beam. With the parameters of array under consideration, the beams

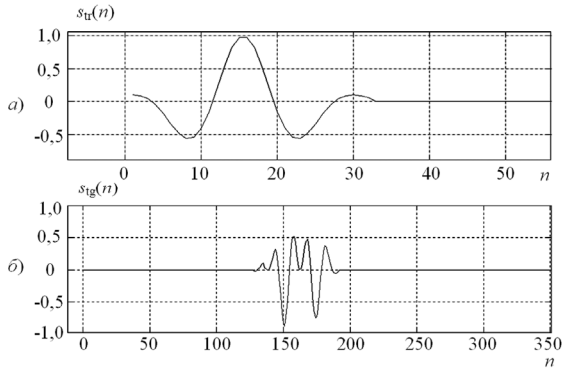


Fig. 1. Probing and reflected signals.

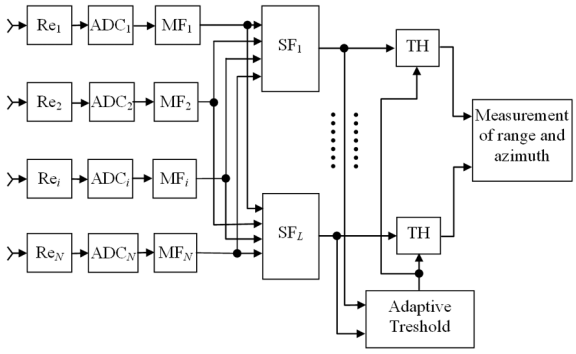
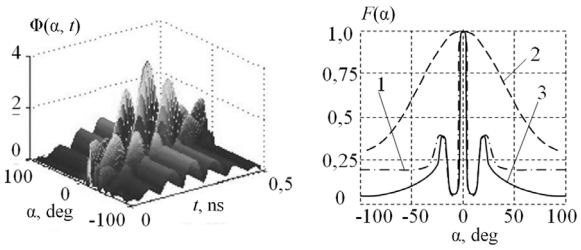


Fig. 2. Functional Diagram of STP.



a) b)

Fig. 3. Two-dimensional space-time pulse response of the array and azimuth beams

numerated from 1 to 7 cover the azimuth sector from zero to about 55 deg. The adjacent beams overlap on the level of about 0.4.

One of the major problems to be solved providing detection and unambiguous coordinate measurement of the target, is arising of false target blips caused by target detection by side lobes of antenna array beams. High level of side lobes is caused by small quantity of antenna array elements N ($N = 4$).

To exclude these false blips, maximum selection in an appropriate range area could be used. The size of this area corresponds to duration of UWB signal.

4. Algorithms of Coordinate Measurement

The result of space-time signal processing is presented as a two-dimensional array of samples in dimensions of range and azimuth. This array contains maximums cor-

responding to the placement of targets. The graph of mentioned two-dimensional array is shown in Fig. 5.

Assume, that the maximum takes place in space filter with the number of $n_{sp,\max}$. It is not difficult to show that in this case the estimation of target azimuth could be obtained as the following:

$$\widehat{\alpha} = \arcsin\left\{\frac{0.15\left[N_{SC}/2 - n_{sp,\max}\right]T_{CH}}{\left(N_{CH}-1\right)d}\right\}, \quad (5)$$

where N_{SC} is the number of space filters, N_{CH} is number of samples per pulse.

Then, we obtain estimations of target Cartesian coordinates:

$$\begin{aligned}\widehat{x} &= \frac{N_R R_{\max}}{N_0}\sin\widehat{\alpha},\\ \widehat{y} &= \frac{N_R R_{\max}}{N_0}\cos\widehat{\alpha},\end{aligned} \quad (6)$$

where N_R is the number of range cell corresponding to the maximum.

The work of considered algorithm had been investigated by the mathematical modeling. Fig. 6 shows the dependence of root mean square errors of target coordinate estimation upon the target placement inside of the room. When modeling, the following system parameters were accepted: wavelength $\lambda = 0.15$ m, duration of the probing pulse signal $T_{\text{CH}} = 0.2$ ns, array pitch $d = 0.5\lambda$, the number of array elements $N = 4$, the number of samples per one pulse $N_{CH} = 16$.

When target range is small, the spherical form of the wave front leads to the rising of errors. The central part of the room is optimal area from point of view of the coordinate measurement accuracy. Further increasing of target range is followed by the increasing of coordinate measurement errors. This is caused by the increasing of angular resolution distance.

5. Conclusion

The proposed algorithms of signal processing in UWB radar with antenna array in the most cases provide correct indication of moving objects. The indicated placement of targets (human) differs from the exact placement less then with 0.5 m. The same time, required resolution in range and azimuth is provided.

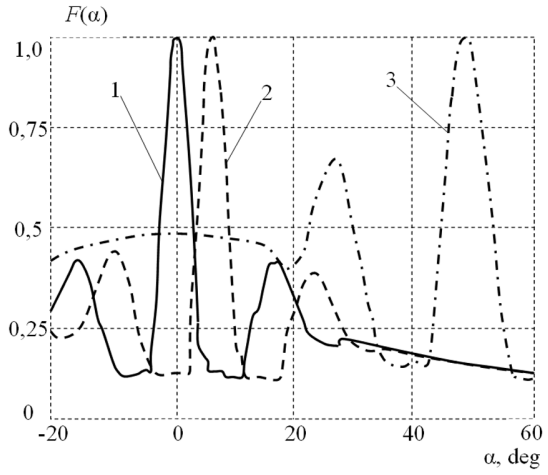


Fig. 4. Azimuth beams of UWB antenna array.

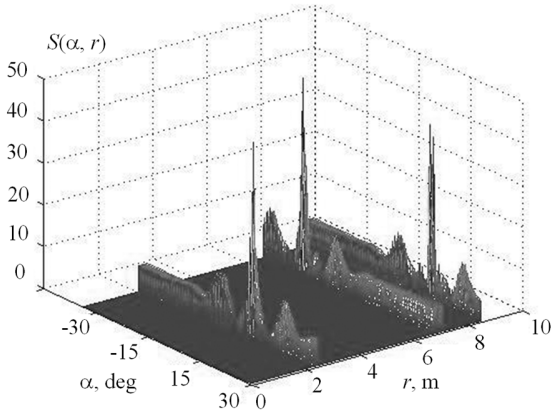


Fig. 5. Results of space-time processing.

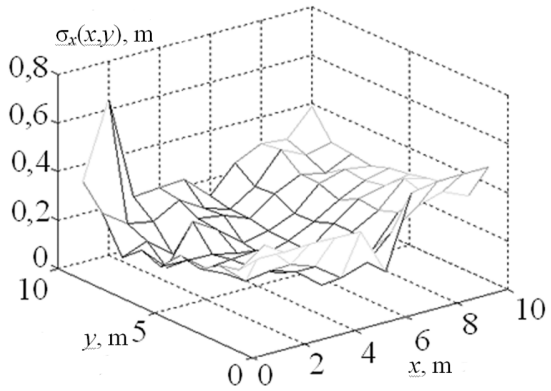


Fig. 6. Root mean square errors of coordinate estimation.

References

1. Andriyanov A.V. Generators, Antennas and Registrator For UWB Radar Application // *Proc. 3rd IEEE Conference on Ultrawideband Systems and Technologies*, 18-21 May. 2004, Kyoto. Japan. 145-150.
2. Immoreev I. Ya. Ultrawideband radars. Features and opportunities // *Radio engineering and electronics*. 2009. Vol. 54. №1. 5-31.
3. *Problems o subsurface radiolocation*. Collective monography / edited by PhD A. Yu. Grinev. Moscow, Russia: Radio engineering, 2005. 416.
4. Andriyanov A.V., Dombek M.G. Systems for investigation of objects in space and transmission lines by using UWB signals // *Proc. Int. conf. on UWB technologies. IWUWBT'2005*. 8-10 Dec. 2005, Japan. 105-109.

SEARCH ALGORITHM FOR LOCAL OBJECTS IN GPR IMAGE

Shkvyrya Y.

National Academy of Sciences of Ukraine
Usikov Institute of Radiophysics and Electronics, Kharkiv, Ukraine
E-mail: y_shkvirya@ire.kharkov.ua

Abstract

An automatic search algorithm for local objects in GPR profile has been considered in the work. The algorithm is based on the Hough transform. The proper software tool has been developed in order to analyze the accuracy of the permittivity of ground as well as coordinates of the local object in a GPR profile. The algorithm efficiency with simulated data has been shown. The influence of the sampling-step at sounding on the algorithm accuracy has been considered.

Keywords: Ground penetrating radar (GPR), dielectric permittivity, Hough transform, collecting element, defocusing.

1. INTRODUCTION

A lot of algorithms and methods of data processing for ground penetrating radar (GPR) have been developed at present time [1, 2, 3, 4]. They allow improving the signal-noise ratio and present the results of subsurface survey in convenient for the operator form.

The automatic search algorithm for local objects using the Hough transform is of great attention in this article [5].

The Hough transform is effective for searching for and identification of objects which can be defined analytically, for example: straight lines, circles, ellipses, hyperbolas, etc. in monochrome image. A monochrome image is the image consisting of points of two types which are background points and points of interest.

In the considered problem the Hough transform is aimed for searching for the local objects being displayed in hyperbolic form in GPR profile.

2. HOUGH TRANSFORM

Let's consider the Hough transform method adapted for searching the hyperbolic curves. The equation of the hyperbola which is the image of local objects located at points with coordinates (x0, y0), has the form [4]:

$$y_0\left(x_0\right) = \sqrt{\varepsilon\left(x - x_0\right)^2 + y^2} \qquad (1)$$

where x and y – are coordinates of the current profile, ε is the dielectric constant of ground.

Since the hyperbola shape is uniquely defined by such parameters as the object location and permittivity of ground, and the Hough transform allows to find hyperboles just with a given set of parameters, the problem of searching for a local object in profile can be solved uniquely.

When searching with the Hough transform the Hough space is created which breaks up into fixed-size pixels denoted as collecting elements. The initial value of collecting elements in the Hough space is zero. If the point of interest of the analyzed image after the Hough transform enters in a collecting element, the value of this collecting element is incremented by one. After the data processing there is the field of collecting elements generates in the Hough space. Maximum values of collecting elements indicate coordinates of local objects, and the dielectric constants at which the largest values of collecting elements are obtained, correspond to the dielectric permittivity of ground in detected object areas.

A detailed description of the process of searching for hyperbolic curves using the Hough transform is presented in [5].

The possibility of automatic detection of the hyperbolic response by local objects was shown in the known works [5, 6]. However, the error of determination of their coordinates and the permittivity of ground was not above a few percents even for a geometrically exact hyperbolas corresponding to the absence of such interfering factors as noise, interference, availability of layered and other inhomogeneities in ground. So, the problem is what has an influence on the accuracy of objects location measurements.

3. SOFTWARE

The software tool that implements the automatic search algorithm based on the Hough transform has been developed for the investigation.

The window of the program is as follows (Fig. 1):

978-1-4244-7468-4/10/$26 ©2010 IEEE

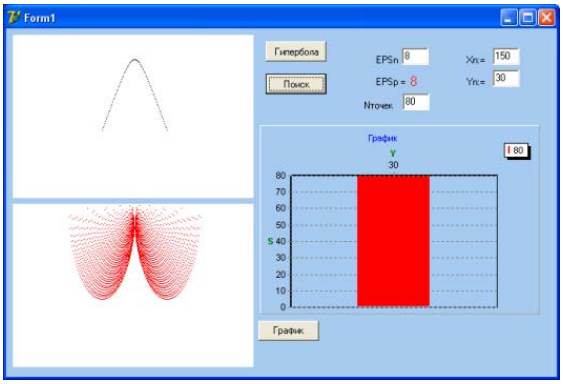


Fig. 1. The image of the window.

The program allows simulating the hyperbola (the image of the local object in profile). For simulating the hyperbole it is necessary to set-up the following parameters:

- the dielectric permittivity of medium;
- coordinates of vertices of the hyperbola;
- the number of points of interest of the created hyperbole.

In order to find the local object in the GPR image and to determine the depth of the local object it is necessary to know the following parameters:

- the length of the sounding route;
- the observation time interval.

The program determines the hyperbola location, the permittivity of medium and calculates the depth of occurrence of the local object in automatic mode.

4. Example of Automatic Search for the Local Object

Let the coordinates of the hyperbola vertex in the profile are (100, 50), the number of points of the hyperbola (points of interest) be equal to 100. And let the permittivity of the medium be equal to 8. As a result the image is presented in Fig. 2.

Then the automatic search algorithm for local objects is applied to the simulated profile. During the data processing the medium permittivity is determined and the Hough parameter space with collecting elements is created (Fig. 3).

Coordinates of the collecting element of the maximum magnitude correspond to the hyperbola vertices with accuracy of the size of collecting elements (Fig. 4).

If permittivities, taken for simulation and calculated at data processing, coincide, then after searching the value of the collecting element at a point with object coordinates will equal to the number of points of the hyperbola, given at hyperbola simulation. As a result, we obtain coordinates of the hyperbola vertices and the medium permittivity. They correspond to values preassigned at hyperbola simulation.

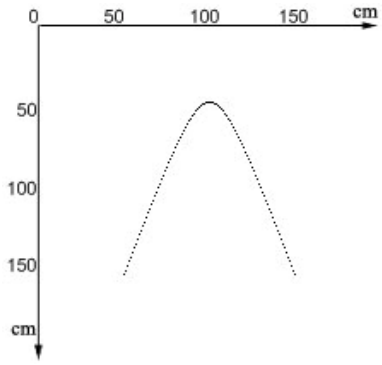


Fig. 2. Image of the local object.

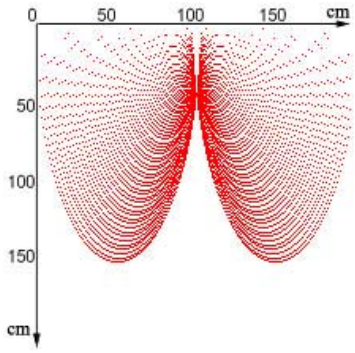


Fig. 3. Hough parameter spaces.

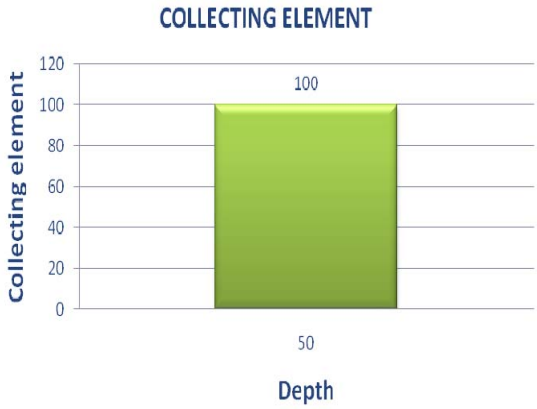


Fig. 4. Collecting element.

5. Precision Characteristics

Using the developed software we have analyzed the dependence of values of the collecting element and the positional accuracy of the hyperbola vertex, which corresponds to position of the local object, on values of the dielectric permittivity of medium, on the depth of occurrence of the object and on the sampling step along the route.

It was observed that at shallow depths the value of the collecting element decreases. A number of points in the hyperbole do not get into the collecting element located at the vertex of the hyperbola, but get into the collecting elements in the vicinity of the hyperbola vertex. There is a "defocusing" of the collecting element.

The following is the diagram of defocusing of the collecting element with a number of points of the original hyperbola equal to 100, for different values of dielectric permittivity of medium and the depth of occurrence of the local object (Fig. 5).

It is well seen in Fig. 5 that at shallow depths (less then 10 cm) from 40% to 10% of points of the hyperbole do not get into the collecting element located at the vertex of the hyperbola while at depths greater than 10 cm all points of interest of the hyperbole get into correct collecting element independently of values of dielectric constant of ground.

Reduced accuracy of calculation of coordinates of the hyperbola vertex at low depth is caused by discrete representation of the hyperbola in the image. The coordinates of the hyperbola in the simulation could be as integer as real. However, points representing the hyperbola in the profile have only integer coordinates. Therefore, due to a rounding of real numbers we obtain the displacement of points of interest belonging to a hyperbola along the axes of coordinates. As a result some of points in the Hough space get into the collecting elements located in the vicinity of the proper collecting element.

Improvement of accuracy of the algorithm could be achieved by reducing of the sampling step. The smaller the sampling interval, the more precisely could be defined parameters of the hyperbola, and hence the permittivity of the ground and the depth of the local object. But with decreasing in the sampling step the processing time increases.

The developed program allows to analyze the accuracy of the search algorithm relative to any necessary set of parameters consisting of the permittivity of the ground, coordinates of a local object, the sampling step at measurement, and to optimize the amount of necessary georadar measurements and volume of necessary data providing the desired accuracy of measurement of the object's coordinates.

CONCLUSIONS

Thus, the software tool has been developed to investigate the accuracy of the automatic search algorithm.

The accuracy of the algorithm has been analyzed at different values of the permittivity of medium, the depth of the local object occurrence and sampling steps.

A "defocusing" of the collecting element has been noted at the vertex of the hyperbola, when the local object is located at a shallow depth (of 10 cm) even when permittivity of the medium is known correctly. Solution of this problem is decreasing of the sampling step.

The developed program allows optimizing the process GPR measurements by a preliminary assessment of the required set of sounding which provides the required accuracy.

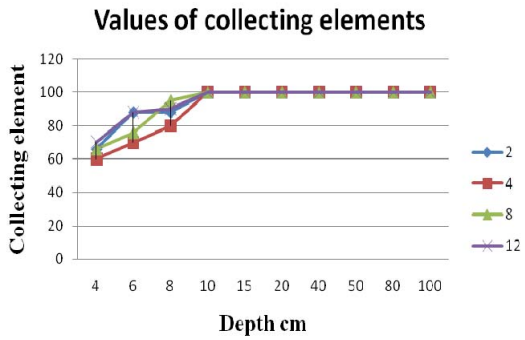


Fig. 5. Values of collecting elements.

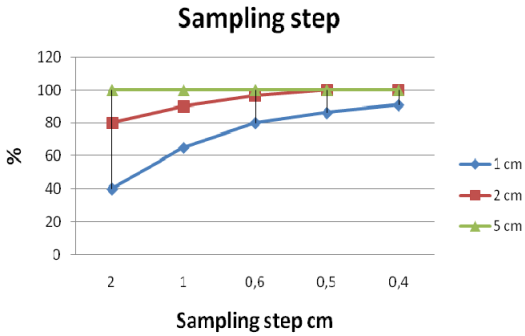


Fig. 6. Sampling step.

REFERENCES

1. Ballard D. H. 1981, *Generalizing the Hough Transform to Detect Arbitrary Shapes.*
2. Heather and Yang May 2005,Spatial Decomposition of The Hough Transform, *IEEE computer Society*.
3. Fitton N.C., Cox S.J.D. 1998, Optimising the application of the Hough Transform for automatic feature extraction from geoscientific images. *Computers & Geosciences*, vol. 24, № 10, PP. 933-951
4. Zelenkov A., Zelenkov S. 2004, The Choice of the Migration Method for Subsurface Radiolocation Signals Processing, *Electronics and Electrical Engineering. Kaunas: Technologija*, No. 3(52). PP. 41-46.
5. Golovko M.M. and Pochanin G.P. 2004, 'Application of the Hough transform for automatic detection of objects in georadar profiles,' *Electromagnetic waves and electronics systems*, vol. 9, no. 9-10, PP. 22-30.
6. Soldovieri F., Persico R., Golovko M.M., Pochanin G.P. 2009, 'Two Strategies for the Determination of Soil Permittivity by GPR Data', *The success of modern electronics*. №5. PP. 60-73.

Ultrawideband and Ultrashort Impulse Signals, 6-10 September, 2010, Sevastopol, Ukraine pp. 156-158

MULTIFREQUENCY MICROWAVE TOMOGRAPHY OF ABSORBING INHOMOGENEITIES

[1] Gaikovich K. P., [1] Gaikovich P. K., [2] Maksimovitch Ye. S., [2] Badeev V. A.

[1] Institute for Physics of Microstructures RAS,
GSP-105, Nizhniy Novgorod, Russia
E-mail: gai@ipm.sci-nnov.ru
[2] Institute of Applied Physics National Academy of Sciences of Belarus,
Minsk, Belarus
E-mail: makhel@iaph.bas-net.by

Abstract

A method of the near-field scanning coherent tomography has been developed for the microwave diagnostics of the 3D subsurface structure of the complex permittivity. This method uses data of 2D scanning over lateral co-ordinates above the ground surface with the dipole emitter-receiver system. Multifrequency measurements provide the depth sensitivity. The regularization algorithm based on the Tikhonov's method of generalized discrepancy has been developed for Fredholm integral equations of the 1-st kind with complex-valued functions and applied for the solution of the corresponding inverse scattering problem. Results are presented for the tomography of 3D complex permittivity distribution originated by the melting ice sample buried in the sand.

Keywords: Microwave subsurface sounding, near-field scanning tomography, inverse scattering problem, complex permittivity.

1. INTRODUCTION

Methods of active and passive electromagnetic subsurface sounding are widely in use to determine the inner structure of permittivity or temperature distribution inside various media [1]. Tomography methods (retrieval of 3D structures) lead to the most complicated inverse problems. In the active electromagnetic tomography, the 3D permittivity distribution of subsurface inhomogeneities should be obtained by measurements of the scattered field. To obtain the necessary data set, the 2D transversal distribution of the scattered field should be measured by the 2D scanning along the media interface in dependence on a third (depth-sensitive) parameter, such as frequency. The corresponding inverse scattering problem is based on the solution of the 3D nonlinear integral equation of the 1-st kind with the 6D kernel [2]. It is clear that straightforward methods of solution lead to hard restrictions on achievable resolution. For far-field measurements there is also the known Rayleigh limitation of resolution.

In the considered here method of coherent microwave near-field tomography of the subsurface permittivity, above-mentioned difficulties are surmounted. We use here the general approach to the near-field scanning tomography [2] and its application to the near-field electromagnetic scattering [3-4] based on 2D lateral plane wave decomposition of corresponding Green functions that reduces the initial 3D integral equation to the one-dimensional Fredholm integral equation of the 1st kind relative to the depth profile of the lateral spectrum of permittivity. This approach overcomes problems of the solution of 3D integral equations and leads to a high-performance and mathematically consistent algorithm based on the method of generalized discrepancy [5].

First experimental results of this method of tomography has been presented in [6]. Measurements of the scattered signal for an ice target buried in the sand have been carried out using experimental set-up including vector network analyzer Agilent E5071B, two identical bow-tie antennas in bi-static configuration, operating in the frequency range of 1.7 to 7.0 GHz and the sandbox. The frequency serves here as the depth- sensitivity parameter. In order to form the necessary 3D data set, C-scan has to be obtained. This is achieved by collecting a series of A-scans (801 points over the frequency range) on a horizontal survey lines (11×15 measuring points through 2 cm) over the sandbox surface.

The theory of this tomography method, developed in [2-3], involves in the integral equation the distribution of the complex permittivity, but, in the beginning of our experiments, algorithms were available for only real-value integral equations. Because of this reason, the theory has been modified in [6] for the tomography of real-value targets, and the known algorithm of Tikhonov's method of generalized discrepancy has

978-1-4244-7468-4/10/$26 ©2010 IEEE

been applied to retrieve the 3D distribution of the real part of permittivity.

However, permittivity perturbations related to the melting ice include also the absorbing range related to the water diffusion around the target, and it was the reason to develop necessary algorithms for complex-value integral equations and to use them in analysis. These algorithms have been developed in [5] and studied in the numerical simulation [7] for conditions of this experiment.

2. THEORY

Let us the scattering range is embedded in a medium with the complex permittivity ε_0, so, its total 3D distribution can be expressed as $\varepsilon(\mathbf{r}) = \varepsilon_0 + \varepsilon_1(\mathbf{r})$. The total field is a sum of the unperturbed field of the source and the scattered component $\mathbf{E}(x,y,\omega) = \mathbf{E}_0(x,y,\omega) + \mathbf{E}_1(x,y,\omega)$. Variations of the received signal *s* are proportional to the convolution of the instrument function *F* of the receiver and the scattered field $\mathbf{E}_1(x,y,\omega)$. In frameworks of the Born approximation, for the proposed in [3-4] scheme of measurements with the fixed the source-receiver vector $\boldsymbol{\delta}\mathbf{r}$, when the structure of sounding field is invariable relative to the receiver position, it is possible to express the transversal spectrum (2D inverse Fourier transform over *x* and *y*) of measured signal variations as:

$$
\begin{aligned}
s(k_x,k_y,\omega) &= F_i(k_x,k_y,\omega)E_{1i}(k_x,k_y,\omega) = \\
&= \int_{z'} \varepsilon_1(k_x,k_y,z') \times \\
\times i\pi\omega\, F_i(k_x,k_y,\omega) &\int_{-\infty}^{\infty}\int_{-\infty}^{\infty} e^{i(k_x+\kappa_x)\delta x + i(k_y+\kappa_y)\delta y} d\kappa_x d\kappa_y \times \\
\times \{ \int_{z''} & [j_i(-k_x-\kappa_x,-k_y-\kappa_y,z''-z-\delta z)\times \\
\times g_{ij}^{12}(k_x+\kappa_x,k_y+\kappa_y,z',z'')] & g_{ji}^{21}(\kappa_x,\kappa_y,z,z')dz''\} dz',
\end{aligned}
\tag{1}
$$

where g_{ji}^{lk} are *k*-space components of the Green tensor above and below the air-ground interface; j_i is the source current distribution. To obtain the transversal spectrum of a source, the surface current distribution on antennas has been calculated using CST Microwave Studio. We assume that the receiver has the same transfer function as the source ($F_i(k_x,k_y,\omega) = j_i(k_x,k_y,\omega)$). To solve the Fredholm integral equation (1) for each pair of spectral components, the algorithm based on the generalized discrepancy method in the complex Hilbert space W_2^1 has been worked out in [6] and applied here to solve the tomography problem for inhomogeneities with the complex-value distribution of permittivity. Finally, the desired 3D structure of permittivity is obtained by the 2D inverse Fourier transform:

$$
\varepsilon_1(x,y,z) = \iint \varepsilon_1(\kappa_x,\kappa_y,z) e^{i\kappa_x x + i\kappa_y y} d\kappa_x d\kappa_y . \tag{2}
$$

The depth sensitivity for multifrequency measurements is related to the frequency dependence both of the medium absorption and of the extinction depth of evanescent components of the probing field. For the targets in the near-field zone of electrically-small antennas, it is possible to achieve a subwavelength resolution of the proposed tomography.

3. RESULTS OF THE MICROWAVE TOMOGRAPHY

Applying the described approach for the experimental results [5], we have obtained tomography images for the studied inhomogeneities of the complex permittivity. Multifrequency measurements based on the 2D lateral scanning of the complex signal $s(x,y,f)$ for six chosen frequencies: 1.7, 2.76, 3.82, 4.88, 5.94, 7.0 GHz have been used in analysis. The source-receiver system include two identical bow-tie transmitting and receiving antennas with the length of arms 3.8 cm and the width of 5.4 cm, placed in the *y*-direction; the fixed distance between centers of antennas was $\delta x = 7.5$ cm. They were scanning together in the rectangle *x*-*y* area above the range of the subsurface ice target with sizes 10×10×4 cm that has been buried in the sand at the depth $z = -9$ cm.

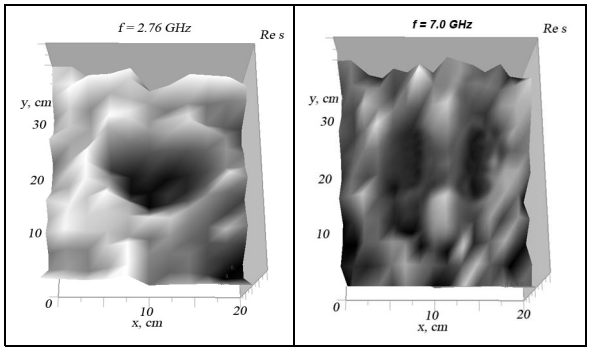


Fig. 1. Measured distributions of the received signal over the studied region at two frequencies. Left, $\mathrm{Re}\, s(x,y,f = 2.76\ GHz)$; right, $\mathrm{Re}\, s(x,y,f = 7.0\ GHz)$.

In Fig. 1 one can see the microwave image of the buried ice target at two frequencies $f_2 = 2.76$ GHz (wavelength 10.83 cm) and $f_2 = 7.0$ GHz (4.3 cm). This result shows the sensitivity of measurements to the subsurface inhomogeneous region. Also, it is possible to see that the relative level of measurement errors was high enough (about 0.2). But there is a possibility to reduce errors, involving in analysis data, averaged over frequency bands around reasonable chosen frequencies – using measurements at all avail-

able 800 frequencies. It makes possible to reduce the level of random errors by an order.

In this study, results of 2D scanning at 6 frequencies have been used to solve the integral equation (1) relative to the depth profile of the lateral spectrum of permittivity perturbation $\varepsilon_1(k_x, k_y, z)$ for each pair of spectral components. Then, from (2), we have obtained the desired 3D structure (tomogram) of the complex permittivity $\varepsilon_1(x, y, z)$ of the studied inhomogeneity. In Fig. 2 the vertical section of the retrieved 3D permittivity (tomogram) is presented; in Fig. 3 – the tomogram in the horizontal section at the depth of the ice target.

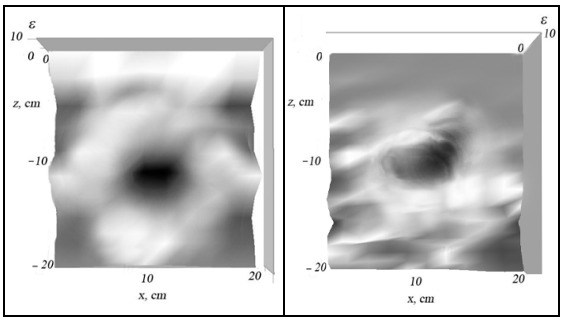


Fig. 2. Vertical section of the retrieved 3D permittivity (tomogram) at $y = 16$ cm. Left, $\mathrm{Re}\,\varepsilon_1(x, z)$; right, $\mathrm{Im}\,\varepsilon_1(x, z)$.

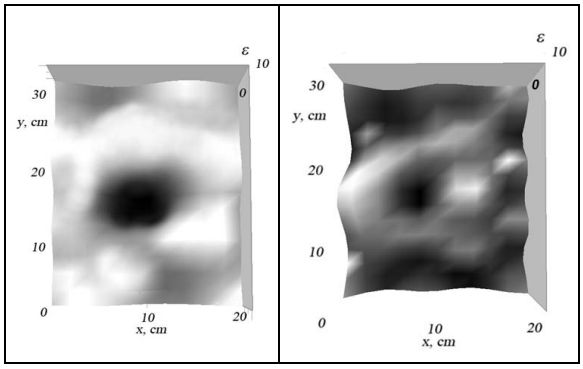


Fig. 3. Horizontal section of the retrieved 3D permittivity (tomogram) at $z = -9$ cm. Left, $\mathrm{Re}\,\varepsilon_1(x, y)$; right, $\mathrm{Im}\,\varepsilon_1(x, y)$.

Results, taking into account a high enough level of errors, are in a reasonable correspondence with the expected distribution of the real and imaginary parts of permittivity, related to the buried melting ice. One can see regions of low values both for real and imaginary parts of permittivity approximately at the position of the ice target. There are also regions of enhanced values of these permittivity parameters around the ice location that could be expected because the influence of the enhanced water content related to diffusion of water because of melting.

4. Conclusion

We have applied a new method of near-field multifrequency coherent tomography in the microwave range to retrieve the subsurface 3D structure of complex permittivity. Our first results show the feasibility of this method for tomography of absorbing inhomogeneities. Further study should determine possible regions of this tomography application.

5. Permission to Publish

The authors are responsible for all material contained in the manuscript they submit.

Acknowledgments

This work was supported by the Russian Foundation for Basic Research (grant *No*. 08-02-00117) and by the Program of the Russian Academy of Sciences.

References

1. Gaikovich K. P. 2004, *Inverse Problems in Physical Diagnostics*, Nova Science Publishers Inc., New York.
2. Gaikovich K. P. 2007, 'Subsurface near-field scanning tomography', *Phys. Rev. Lett*. **98**, 183902)**;** *Phys. Rev. Lett*. **98**, 269902.
3. Gaikovich K. P. , Gaikovich P. K. 2008, 'Scanning coherent tomography of multilayered media with inhomogeneous region', 2008, *Proc. ICTON 2008, Greece, June 22-26*, Athens, 246-9.
4. Gaikovich P. K. 2008 'Scanning coherent tomography of multilayered media with inhomogeneous region', *Proc. 4th International Conference "Ultrawideband and Ultrashort Impulse Signals" (15-19 September, Sevastopol, Ukraine)*, Sevastopol, pp. 189-191.
5. Gaikovich K. P. 2010, 'Inverse scattering problem in Hilbert space' (invited), *Proc. ICTON 2010, 27 June – 1 July 2010*, Munich.
6. Gaikovich K. P., Gaikovich P. K., Maksimovitch Ye. S., Badeev V. A., Mikhnev V. A. 'Near-field microwave tomography', *Proc. of 7th International Conference on Antenna Theory and Technique (6-9 October, 2009 Lviv, Ukraine)*, Lviv, 262-4.
7. Gaikovich K. P., Gaikovich P. K., Maksimovitch Ye. S., Badeev V. A. 'Study of scanning microwave tomography of subsurface targets', 2010, *Proc. of CriMico 2010, 13-17. Sept. 2010*, Sevastopol.

UWB BABY MONITOR

[1] Ziganshin E. G., [2] Numerov M. A., [3] Vygolov S. A.

[1] NanoPulse, Inc., Moscow, Russia
E-mail: zig@nanopulse.ru
[2] NanoPulse, Inc., Moscow, Russia
E-mail: mikenum@nanopulse.ru
[3] NanoPulse, Inc., Moscow, Russia
E-mail: vigolov@nanopulse.ru

Abstract

A successful case for UWB technology application to Vital Signs Monitoring Systems created by authors is presented in this paper. Baby Monitor for remote contactless monitoring of respiratory and heart rate is designed both for consumer and medical infant monitoring applications.

Unlike conventional sound- and video-based baby monitors, which do not provide any useful information at infant sleep time (no sounds or static picture) the devices allow permanent parental control and effectively prevent Sudden Infant Death Syndrome (SIDS) from occurring. SIDS is reported to be leading death cause of healthy infants after one month age.

Keywords: Ultra-Wide Band; Medical Radar; Monitoring; Newborn; Respiration; Sleep apnea syndrome; Sudden infant death syndrome; Infant incubator.

1. INTRODUCTION

This article considers high tech UWB solutions for one of the most important up-to-date challenges – opportune diagnostics of obstructive sleep disorders also known as sleep apnea, primarily for babies, which often cause sudden infant death syndrome (SIDS) to occur. Sleep apnea is a sleep disorder characterized by pauses in breathing during sleep. The standard definition of any apneic event includes a minimum 10 second interval between breaths.

Babies often display violation of their respiratory rhythm, which can be irregular, shallow, fast or slow, even respiratory arrest may happen.

If apnea is suspected or diagnosed, parents or medical personnel may install a baby monitor until the condition is outgrown. However not every baby monitor is able to detect apnea. The choice must be done in favor of devices capable to perform continuous vital signs monitoring including motion activity, respiration and heart-beating and give timely alarm in case of abnormal condition occurs.

2. BABY MONITORING

The importance of constant control over infant's activity, especially during sleeptime is hard to overestimate.

At present a typical baby monitor is a radio system used to remotely hear (and optionally watch) the infant. The transmitter is placed near to the child and the receiver is placed near to the person caring for the infant.

However conventional baby monitors are not able to detect sleep apnea and prevent SIDS. This is caused by nature of the systems, which react on sound meaning that the baby is alive or display image of sleeping baby with no confirmation whether it breathes or not. Thus many doctors believe conventional baby monitors provide a false sense of security.

There are several solutions though aiming SIDS prevention by looking at infant's respiration.

- Placing piezo-sensor pad below cot mattress which detects even the slightest movements. Such systems are limited to the sensor pad area and heavy for transportation for away use. Moreover, the sensor pad requires prevention maintenance activities in order to avoid high humidity level at the sensor location.
- Motion sensor located in flexible rubber tip which is attached the diaper. The sensor detects even the slightest movements. Drawback of such systems is that the sensor tip must always be in contact with the skin which may disturb and irritate the baby.
- Radar solutions prove to be contactless as well as sensitive enough while due to their RF nature they are dependent on reflected signal quality and signal to noise ratio. Next chapter will be focused on UWB radars which we find optimal to become the basis for next generation baby monitors.

978-1-4244-7468-4/10/$26 ©2010 IEEE

3. UWB BABY MONITORS

3.1. NANOPULSE BABY SLEEPGUARD

NanoPulse Baby SleepGuard (BSG) shown on Fig. 1 is a composite device which enables contactless monitoring of newborns. Unlike conventional sound and video based baby monitors, which react on natural activity of the infants and do not provide any useful information at their sleep time BSG constantly looks over the babies and controls their respiration and heart-beating rates as well as general body motion while they are asleep. BSG is also equipped with temperature sensor and microphone.

The device informs supervisor about baby's condition and alarms when it observes dangerous abnormal parameter value preventing from SIDS occurring.

BSG consists of the sensor unit (SU) and the parent unit (PU).

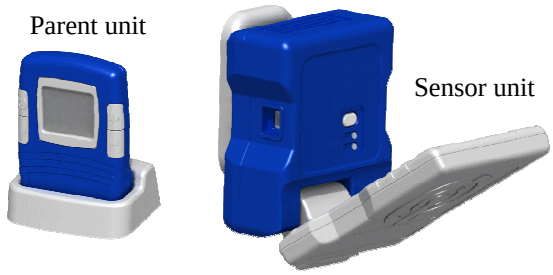


Fig. 1. NanoPulse Baby SleepGuard.

Essence of the device is its original SU construction which contains UWB radar with two independent spaced receiving channels with internal coherence relative to sounding short impulse radio signal which enables achieving improved reliability in human body motion registration. Reliability is improved due to the following factors:

- low probability of reflected signal phases fitting the low sensitivity area of phase detectors simultaneously for both channels;
- significant decrease of probability for simultaneous dramatic drop of reflected signal level in both channels (because of interference).

The device detects the following baby's conditions:

- Sleep – the baby sleeps with no motion, the device counts its respiration frequency and, in favorable conditions, pulse rate. Case of any slight movements supervisor will be informed by a message.
- Awake – the condition is characterized by long term movements of high amplitude.
- Alarm – respiratory arrest is detected or respiration frequency is abnormally low.

SU comes along with digital signal processing module and performs the following functions: measuring vital sign parameter values of the baby; transmitting measured values to the PU; continuous recording measured values into built-in or attached nonvolatile memory.

PU performs the following functions: signaling about measured vital sign values with display, buzzer and vibrator; setting up SU and PU parameters via a user menu; running continuous self-check on both SU and PU operation (battery charge level, radio link quality).

Data communication between SU and PU is implemented via digital radio protocol in ISM frequency band.

3.2. NANOPULSE INFANT INCUBATOR MONITOR

Infant Incubator Monitor is designed for continuous contactless monitoring of premature or ill baby's vital signs such as motion, respiration and heart-beating when the baby is placed in infant incubator. The device is also capable to check environmental parameters such as temperature, humidity, atmosphere conditions in the incubator.

Presently probes must be attached to the baby in order to perform described above monitoring. Such actions can hurt the baby. NanoPulse Infant Incubator Monitor is contactless and trauma-free. The device informs supervisor about baby's condition and alarms when it observes dangerous abnormal parameter value preventing SIDS.

There are two variants of the device implementation: autonomous device and embedded OEM module. First one has its own primary and backup power unit, LCD indicator, control module and alarm system. The device is implemented as a monoblock and is mounted on the top cover of the incubator. OEM-version has to be integrated in power, control and indication systems of the whole incubator. The device can be mounted inside the incubator body.

4. TESTING NANOPULSE UWB SOLUTIONS

4.1. LABORATORY TESTS

The baby is simulated by an oscillating subwoofer controlled by a PC via DAC.

Test strategy starts from testing reaction on single frequency oscillations simulating typical infant's respiration frequencies which lay between 30 and 60 breathes per minute. Next, respiration frequency is modulated by heart beats having 1/10 of the respiration amplitude and frequency between 80 and 210 oscillations per minute. Finally, the test program simulates apnea conditions alternated with fast and slow respiration frequencies, sometimes interfered by motion (a simple handshake of the test engineer).

Generally, test results show high reliability of the device and reaction on dangerous infant's states no later than 20 seconds after the event occurs. In all "good" cases baby monitor behaves silently as expected.

4.2. REAL LIFE TESTS

There is a challenge for getting official permission for running clinical tests which requires passing SSP

(State Standard Specification) certification. Therefore we rely on volunteering parents at present, not involving medical labs.

After getting permission from a spouse couple for running the tests on their baby we executed a series of hours-long sleep tests on 6 months-old girl placing SU at 50–70 cm above the cot. Data was recorded and transferred on PC for further analysis with UltraScope application software. The results show themselves to be very interesting:

- 86% of the time respiration was clearly seen in 20–40 breaths per minute range, 14% of the time respiration was masked by motion.
- 83% of the time heart-beating was clearly seen in 90–120 beats per minute range, 17% of the time heart-beating was masked by motion.
- There are many breath-holding incidents even though the baby is considered healthy. Most of the pauses have their length ~3–5 seconds, however there are several events which can be classified as sleep apnea when pause between two sequential breathes exceeds 10 seconds.

Baby's respiration and heart-beating charts for normal and apnea respiration and pulse rates are shown on Fig. 2 and Fig. 3 respectively. For the second graph the pause between two sequential breathes reaches 11 seconds.

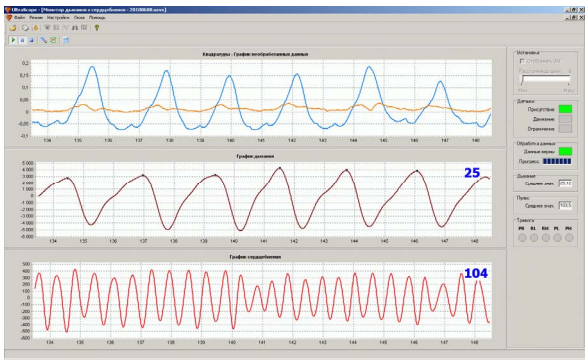


Fig. 2. Incoming signals, infant's respiration and heart-beating charts – normal condition.

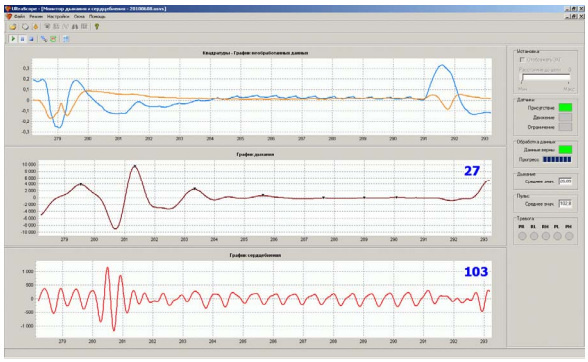


Fig. 3. Incoming signals, infant's respiration and heart-beating charts – sleep apnea condition.

Obviously the amount of tests in real conditions is very limited as of today and we do not have valid statistical data for making final conclusion about proper devices operation. Nevertheless we still consider NanoPulse UWB solutions for baby monitoring and SIDS prevention have significant potential which is 100% proven by the tests conducted so far.

5. Conclusions

Described NanoPulse Baby SleepGuard and Infant Incubator Monitor UWB solutions improve quality of service and awareness of the patients at homes, in hospitals and medical centers especially in terms of opportune apnea detection and SIDS prevention. However, in order to see these UWB solutions in the market more tests and clinical trials must be conducted and completed in real environment for making highly reliable and safe end user products.

References

1. Caples SM, Gami AS, Somers VK (February 2005). "Obstructive sleep apnea". Annals of Internal Medicine 142 (3): 187–97. doi:10.1001/archinte.142.1.187. PMID 15684207.
2. Enrico M. Staderini, "UWB radars in medicine," IEEE Aerospace and Electronic Systems Magazine, Vol. 17, Issue 1, Page:13-18, 2002.
3. Immoreev I. Y., Samkov S. V. "Ultra-Wideband (UWB) Radar For Remote Measuring Main Parameters of Patien's Activity". UWBUSIS'02, Kharkov National University, Kharkov, Ukraine, October 1, 2002.
4. Pavlov S. N., Samkov S. V., Solodov E. V. "UWB radars in the field of bio-medicine application." UWBST, 4-7 July, 2006, Russia.

Appendix A – NanoPulse UWB Baby Monitor Technical Parameters

- Center frequency: 7 GHz.
- Signal bandwidth (-10dB): 510 MHz.
- Pulse duration (half-height): 2.5 ns.
- Pulse power: 1 mW.
- Average radiated power: 10 uW.
- Operational range: 20–80 cm.
- Antennas beam width: 60°.
- Max. power flux density: 0.01uW/cm^2.
- Minimal respiration rate: 5 ppm.
- Maximal heart rate: 300 ppm.
- SU Battery life: 1 day continuously.
- PU Battery life: 2–4 weeks.
- SU-PU link distance: 30m indoor.

PROPOSALS TO BUILD A PROMISING ULTRA-WIDEBAND WIRELESS COMMUNICATIONS

Shostko I. S., Almakadma T.

Kharkov National University of Radio Electronics, Kharkov, Ukraine
E-mail: igor-shostko@yandex.ru

Abstract

The variants of constructing promising ultra-wideband wireless communications systems based on the new standard. This standard specifies an ultra wideband (UWB) physical layer for a wireless personal area network (PAN), utilizing the unlicensed 3100 - 10600 MHz frequency band, supporting data rates of 53.3, 80, 106.7, 160, 200, 320, 400, 480, 640, 800, 960 and 1024 Mb/s.

This standard specifies a Multi Band Orthogonal Frequency Division Modulation (MBOFDM) scheme to transmit information. A total of 110 sub-carriers (100 data carriers and 10 guard carriers) are used per band to transmit the information. Frequency-domain spreading, time-domain spreading, modulation and forward error correction (FEC) coding are used to vary the data rates.

Keywords: Ultra-wideband wireless communications systems, Multi Band Orthogonal Frequency Division Modulation.

1. INTRODUCTION

Intensive development of information society requires the development and introduction of newer information and communication technologies, deeper exploitation of the network, natural and physical resources, more productive information processing systems. Besides, our society is on the verge of avalanche increase of the number of consumers and producers of information, acting under the brand name "smart home". The variety of technologies of information exchange: Wired Ethernet (100 Mbps, 100Base-T), PNA, PLC, fiber-optic (100Base-FX, 1000Base-LX, 1000Base-SX), wireless (Bluetooth, WiFi, WiMAX), cellular (G2-G5), as well as all network technologies on the one hand pointing to the need to provide cooperation of their work, and on the other hand requires use of a variety of terminal equipment.

EMC limitations and biological safety of users overlap the problems of increased demand in quantity and quality of information. However, lack of frequency bands, their workload, the mutual influence require new system solutions. Under these conditions, an increase of the number of technologies and equipment are unlikely to meet the needs of the coming growth in traffic.

There is a need to focus on those technologies that meet the maximum requirements with guaranteed quality. In our view, the core problem of present time and future is the problem of providing services at the level of access. It is that level, which is the most costly, most multitechnological and here it is necessary to provide maximum convenience for the user to simplify access with a single module, reliability, biological safety and high quality transmission of content.

2. PROPOSALS FOR THE CONSTRUCTION OF ACCESS NETWORKS

The multiple nature of access networks, especially those located in high-rise buildings, EMC and biological safety, the ability to integrate different technologies are the basic requirements to which this network must satisfy in each premises of a subscriber. Obviously, the network subscriber and the information system of "smart home" must be integrated and provide a unified structure. The concept of "smart home" provides the organization of interaction of all elements on a single management interface. It is necessary to ensure the exchange of information in the subscriber network (CPN) and the Internet. The main pressure on the exchange of information should be provided by wireless technologies. As the advantages of these technologies can be noted the simplicity of expansion and mobility of managed system elements. But it should be taken into account that the premises of a subscriber are used as elements requiring low capacity to control (lighting, heating systems) and as terminals for multimedia services (plasma display panels, video phones, etc.). In addition, there are terminals of mobile telecommunications services, which must also operate in the premises of the subscriber. In this connection it is possible to organize the

978-1-4244-7468-4/10/$26 ©2010 IEEE

interaction of all elements in the "smart home", including terminal services of public communication based on wireless communication. This will allow to:

- provide a standardized stack management and transmission of multimedia information;
- reduce dramatically the resources used by wireless communications systems;
- improve the EMC characteristics and biological safety in the "smart home".

All external information flows will be directed through a gateway at the network level in the room number. In this case, the gateway to the subscriber premises can also commute the internal information sharing elements of "smart home". Thus, it is necessary to consider the possibility of using the existing access network and subscriber network in the room, from the standpoint of their using in the concept of "smart home".

As the basis of wireless technology it is necessary to choose such technology which would ensure the above-mentioned requirements. An example of this may be a standard Wireless USB [1]. Standard Wireless USB is based on the concept of platform UWB (Ultra Wideband, UWB) wireless technology for data transmission over short - up to 10 meters distance, high bandwidth (up to 1024 Mbps) and low power consumption. UWB platform is a solution for wireless transmission of high quality multimedia content such as videos, between consumer electronics and PC peripherals. During data transferring over short distances UWB technology seems more superior in comparison to competing standards. It is especially well-observed in the measurement of such a thing as "the maximum possible density of data rate. If you are using 802.11b-compatible equipment, it is about 1 kbit/s/m^2, Bluetooth-compatible - about 30 kbit/s/m^2, and 802.11a-compliant - about 83 kbit/s/m^2, then the use of UWB technology the value of this figure reaches 1 Mbit/s/m^2. One of the key advantages of UWB technology is that it does not interfere with other wireless technologies used today, such as Wi-Fi, WiMAX and cellular. Recommended spectral density of radiation does not exceed the level of -41.3 dBm/MHz. As a result of this, there two useful practical conclusions emerged: absence of influence on the work of other means of communication and miserly power consumption. Schematically, the Wireless USB standard interface involves the use of two main "layers" for data exchange - transport and physical layer. The transport layer is based on the above mentioned ultra wideband (UWB) technology, the physical level is the level of environmental data formation, where, in spite of the WUSB, W1394 (Wireless FireWire), Bluetooth can easily figure, and other protocols, which are not invented and not creatd yet. Wireless USB standard is the first UWB-interface, driven to commercial status.

Standard transport layer Multi Band OFDM for Wireless USB regulates spectral plot of width 7.5 GHz, which is divided into five channels and several individual sub-bands at 528 MHz for each channel. As a result 14 sub-bands, each of width 528 MHz, grouped in 5 frequency plots, with each of the 14 sub-bands, applied to standard Wireless USB has the ability to support data speeds 53.3, 80, 106,7, 160, 200, 320, 400, 480, 640, 800, 960 and 1024 Mbps. The difference in the rates is determined by rate of convolutional coding and modulation type. With an increase in the number of frequency bands involved speeds will increase. The flexibility of the new wireless standard means that in different countries could allow to use not all subranges, but it does not influence the final performance. At the subscriber premises, you can choose the minimum data rate to control appliances and systems (lighting, heating, etc.) and high-speed multimedia services to terminals (plasma display panels, video phones, etc.)

As for the topology of Wireless USB, here viewed analogy with wired USB - device has its own address, obtained during connection or transfer. In this topology, the host controller initiates all data exchange between connected devices, allocating time slots and bandwidth to each connected device. This group is called a cluster. The host controller can support up to 127 devices in the cluster group. Clusters coexist in an overlapping spatial environment with minimum interference, which allows to operate multiple WUSB-clusters within the overall range.

Thus, the organization of interaction of all elements in the "smart home", including terminal services, public communications, a forward-standard wireless WUSB allows to:

- provide standardized stack management and transmission of multimedia information;
- reduce dramatically the resources used in wireless communication systems;
- improve the EMC characteristics and the biosecurity in the "smart home".

All external information flows will be channeled through a gateway at the network level in the room number. In this case, the gateway to the subscriber premises can commute and internal information sharing elements of "smart home". Consider the typical structure of the access network according to the concept MUSE [2] (Fig. 1).

Network indoor subscriber (CPN) is connected through Access Gateway (RGW) and further to the access node (AN) network access provider (NAP). NAP is connected to the SBC ISP-level applications (ASP) through the boundary node (EN). One key element of access is subscriber gateway (Residentional Gateway, RGW). RGW is a multifunctional element that performs many functions in spite of the standard data transmission between the subscriber network and the Internet. In particular, it is necessary to ensure interaction of network elements of fixed and mobile subsystems, authentication, support for a given level of Q_oS for multimedia flows in the direction of terminals of different services in CPN. Thus, ad-

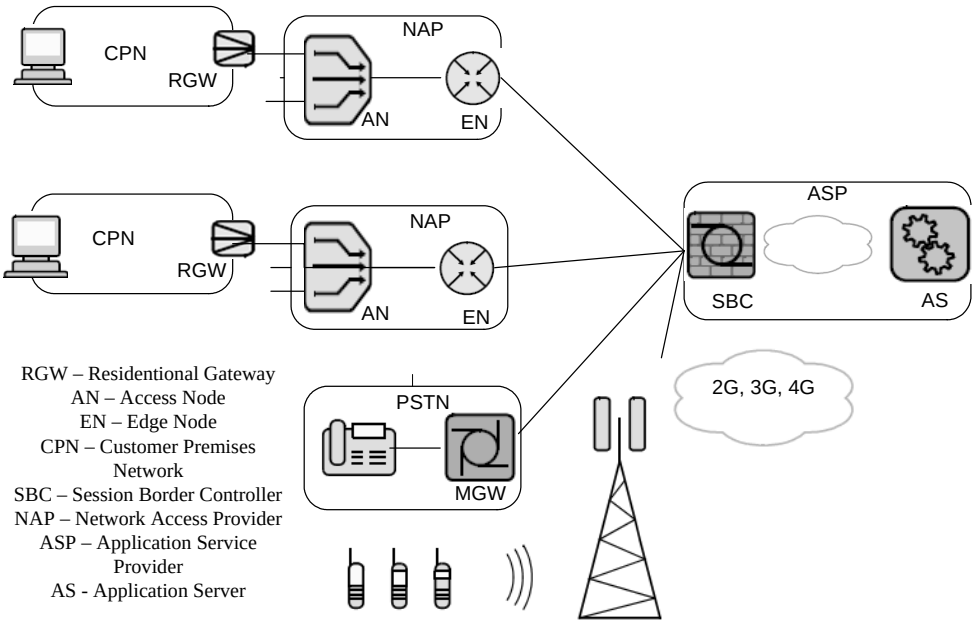


Fig. 1. Structure of the access network according to the concept MUSE.

vanced RGW is switching center network in the premises of the subscriber.

Functional modern RGW has an open architecture, according to Fig. 2, which shows the general structure of the standard (Triple Play) and forward (Multiple Play) RGW.

As it is evident, advanced RGW contains several groups of interfaces: to connect to the access network operator (xDSL, optical), to connect the terminal services in the premises of the subscriber (ETH, WiFi), and also to connect additional devices. Functionally gateway contains network termination NT1 and NT2. In addition, advanced RGW includes set-top boxes (STB) and the FXS port for connecting analog telephones. Advanced RGW contains several interfaces to provide such additional functions as the general office of personal video recording, printing and multifunction office interface for connecting multiple devices, such as via USB2.This feature can be used in various applications for (photo, video, etc.) storage device.

Thus, the use of the premises of the subscriber gateway RGW, able to integrate external and internal information flows, with the addition of its interfaces WUSB should ensure the integration of all the terminals in a single system.

The decisions of a number of tasks:

- analysis of the impact on bandwidth gateway RGW interface WUSB - choose the location of the UWB transceiver devices inside the premises;
- construction and justification of the mathematical model of elements of radio and SSHPS used in the TCS;
- determining of requirements for the design and metrological characteristics of transceiver channels SSHPS;
- developing of methods for correcting the shape and the signal spectrum for different elements of radio with the requirements of speed, providing multiple access, synchronization accuracy, longer range radio communications and to ensure electromagnetic compatibility overlapping frequency bands.

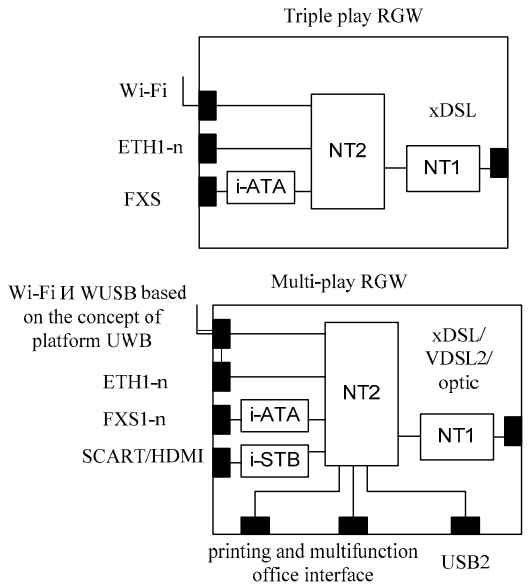


Fig. 2. Modern RGW.

REFERENCES

1. Wireless universal serial bus specification.
2. Muse deliverable tf3.3 - specification of an advanced, flexible, multi-service residential gateway.

WIRELESS SECURE COMMUNICATIONS USING UWB NOISE WAVEFORMS WITH CODE SPECTRUM MODULATION

Kalinin V. I.

Kotel'nikov Institute of Radio Engineering and Electronics of RAS, Fryazino branch, Russia
E-mail: val.kalinin@mail.ru

Abstract

The results of experimental investigation and numerical simulation of wireless covert noise communications with code spectral modulation are discussed. Transmit covertness of UWB wireless communications is evaluated by the signal-to-noise ratio and bit-error rate performances.

Keywords: Wireless communications, ultra wideband noise waveforms, spectrum modulation, covertness.

1. INTRODUCTION

The security of wireless multiple access communications and their resistance to interference become some of the more important system features when many wireless devices simultaneously operate in the same vicinity [1-3]. Direct sequence communication systems such as CDMA/OFDMA systems based on spread spectrum technology are characterized by the beautiful performances of signal-to-noise ratio (SNR) and bit-error rate (BER). But outside observers using repeatable properties of pseudorandom spreading sequences can detect or intercept noise-like signals radiated by these systems. Ultra wideband (UWB) noise continuously waveforms provide secure wireless communications because they cannot be detected by means of traditional receivers based on statistical signal processing [1-5].

In the present paper we discuss the results of experimental investigation and numerical analysis of detection performances for wireless covert noise communications with code spectral modulation.

2. DESCRIPTION AND ANALYSIS OF COMMUNICATION SYSTEM

The proposed wireless noise communication system consists of a transmitter with code spectral modulation and a noise-correlating receiver with correlation or double spectrum processing. The data transmission is performed by continuous noise carriers [3-5]. This noise carrier waveform $n(t)$ is generated by a noise source, which provides a zero-mean white Gaussian signal with low power spectral density in the 3.1-4.1 GHz frequency range [4-5].

Generated UWB noise waveform $n(t)$ with the uniform power spectrum in the frequency bandwidth $\Delta f = 1000$ MHz is split into two in-phase components with equal level. One of these components is used as the reference signal. The other part of the $n(t)$ waveform is delayed in a two-section delay line for different times $T_0 = 10$ ns or $T_1 = 20$ ns according to the informative bits flow "0" or "1". Code-time commutation of delay sections T_0, T_1 is performed with the transmission rate $C = 1 / T_b$ of informative bits. After that the message noise signal delayed at the different times T_0, T_1 is linearly summed with the reference noise signal.

The sum noise signal

$$z_{0,1}(t) = n(t) + H_{0,1} n(t - T_{0,1}) \qquad (1)$$

is sent at the input of transmit antenna. Let the transmission coefficients $H_{1,0} = h_{1,0} \exp(i\theta_{1,0})$ and the delay times $T_{1,0}$ in both delay channels are independent of a frequency *f* in the frequency bandwidth Δf.

The interference of perfect incoherent noise waveforms occurs when the delay times $T_{0,1}$ between the delayed waveforms $H_{0,1} n(t - T_{0,1})$ and the reference $n(t)$ substantially exceed coherence time $\tau_c = 1 / \Delta f = 1$ ns for these noise waveforms:

$$T_{0,1} >> \tau_c, \qquad T_{0,1} \Delta f >> 1. \qquad (2)$$

The power spectrum of the sum signal (1) is estimated over the symbol duration T_b in the form:

$$S_z(f) = S_n(f)[1 + h_{0,1}^2 + 2h_{0,1} \cos(2\pi f T_{0,1} + \theta_{0,1})], \qquad (3)$$

where $S_n(f)$ is the power spectrum of the initial noise waveform $n(t)$.

978-1-4244-7468-4/10/$26 ©2010 IEEE

The power spectral density (3) has the periodic modulation as a result of the interference of perfect incoherent reference and delayed waveform. The spectrum modulation period $F_0 = 1/T_0$ or $F_1 = 1/T_1$ is defined by the delay time T_0 or T_1 according to the informative bits flow "0" or "1".

The sum noise waveforms $z_0(t)$ and $z_1(t)$ with code spectral modulation (3) are radiated by a transmit antenna to a communication link.

The experimental power spectrum $S_z(f)$ of the first sum waveform is shown in Fig. 1a. The frequency period $F_0 = 1/T_0 = 100.0$ MHz of the spectral modulation is inversely proportional to the first channel delay time $T_0 = 10$ ns.

The transmit noise waveforms both $z_1(t)$ and $z_0(t)$ have the same 3.1-4.1 GHz frequency band and the same coherence time $\tau_c = 1/\Delta f = 1$ ns. The large frequency bandwidth $\Delta f = 1000$ MHz of used noise continuous waveforms is the necessary condition (2) for the realization of the offered communication [3-5]. For the case of UWB waveforms, the condition (2) can be written as

$$\Delta f >> F_0; F_1. \qquad (4)$$

In consequence of the interference of perfect incoherent reference and delayed waveforms we observe many interference periods in the power spectrum shown in Fig. 1a.

Two-channel correlation receiver accomplishes the optimal processing of noise waveforms [1-2, 5]. Double spectral processing is another method of correlation measurements [3-4].

A block diagram of the communication receiver with double spectral processing is shown in Fig. 2.

The signal $r(t)$ at the output of receive antenna (RA) contents the useful signals $z_{0,1}(t)$ and noise interference $v(t)$. The power spectrum $S_r(f)$ of received noise signal $r(t)$ is estimated by means of spectrum analyzer SA during the symbol time length T_b.

$$S_r(f) = K(f)S_n(f)\left[1 + h_{0,1}^2 + \right.$$
$$\left. + 2h_{0,1}\cos(2\pi f T_{0,1} + \theta_{0,1})\right] + S_v(f), \qquad (5)$$

where $K(f)$ is the total transmission coefficient of the useful signals $z_{0,1}(t)$, and $S_v(f)$ is the power spectrum of the noise interference $v(t)$.

The spectrum modulation depth of the received signal is defined by a behavior of the coefficient $K(f)$ and is not uniform function of frequency argument f, as shown in Fig. 1. This performance is the result of dispersion distortion of wideband waveforms in the transmitter and propagation channels. Frequency and dispersive distortions in channels reduce correlation receiver output. Code spectral modulation method allows decreasing distortion affects because both message noise signal and noise reference are propagate in the same channel over the same frequency band.

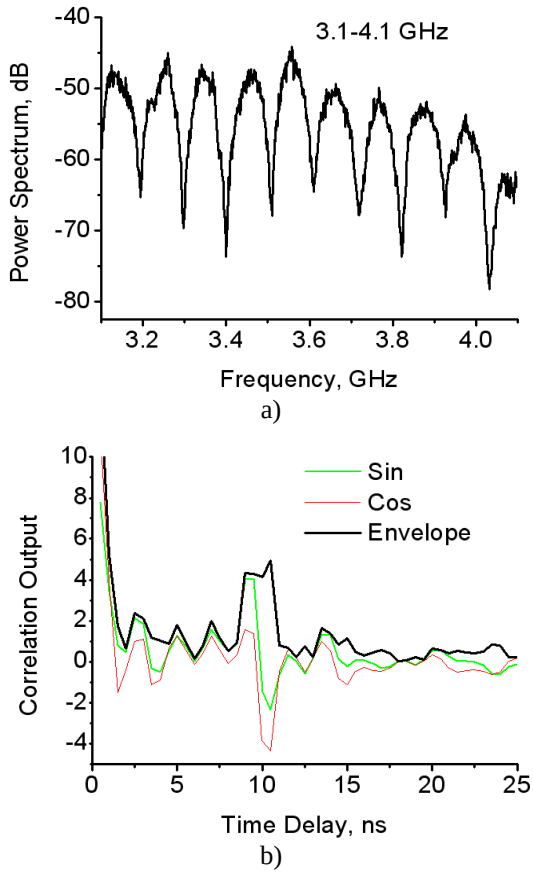


Fig. 1. Power spectrum a) and autocorrelation function b) of received UWB noise signal with frequency bandwidth W = 1000 MHz.



Fig. 2. Block diagram of the communication receiver with double spectrum processing.

Auto-correlation functions of both received noise waveforms $z_1(t)$; $z_0(t)$ can be defined in result of Fast Fourier Transform (FFT) of noise power spectral density (5). Let the total transmit coefficient be constant $K(f) = k$ in the frequency bandwidth Δf. The correlation function of the received waveform $r(t)$ can be expressed as

$$R_r(\tau) = 4\pi k^2\left[R_n(\tau) + R_n(\tau - T_{1,0}) + \right.$$
$$\left. + R_n(\tau + T_{1,0})\right] + R_v(\tau), \qquad (6)$$

where $R_n(\tau)$ and $R_v(\tau)$ are consequently correlation functions of noise continuous waveform $n(t)$, and noise interference $v(t)$. The relation (6) is derived in the case $h_0 = h_1 = 1$.

Auto-correlation function (6) contents the information correlation peaks at T_0 or T_1 time shifts when "0" or "1" inform symbols are consequently received.

Auto-correlation function (6) shown in Fig. 1b is calculated for transmit symbol "0" using quadrature components.

The peak detector (PD) analyzes digital correlation output of the Fast Fourier Transform (FFT). The peak search function is used to position the marker at the peak of the digital correlation response. The peak detector can find the information correlation peaks at time shifts T_0 or T_1 when "0" or "1" information symbols are consequently received. In this way transmit data (0;1) are unequivocal reconstructed in result of double spectral processing of received noise waveforms (1).

3. SYSTEM PERFORMANCE

BER performance analysis of proposed communications is performed for a link with additive zero-mean band-pass Gaussian noise interference uncorrelated with the transmitted signals. Noise continuously waveforms $z_{0,1}(t)$ contented digital information and noise continuously interference $v(t)$ have the same rectangular shape of power spectrums in the same frequency bandwidth Δf. In this case the channel signal-to-noise ratio (SNR) is defined at the receive antenna output as relation

$$q = \sigma_z^2 / \sigma_v^2 = N_z / N_v \qquad (7)$$

where σ_z^2, σ_v^2 are respectively the mean-square intensities of transmit signals $z_{0,1}(t)$ and noise interference $v(t)$, and N_z, N_v are their constant power spectral density. The expression of channel SNR (7) can be written as

$$q = 2\sigma_n^2 / \sigma_v^2 = 2N_n / N_v, \qquad (8)$$

because $n(t)$ and $n(t - T_{0,1})$ are the perfect incoherent noise waveforms.

Now let us define the system gain $B = \Delta f T_b$ as the product of the transmit bandwidth Δf with the bit duration T_b. The data rate $C = 1 / T_b$ is inversely proportional to the bit duration T_b. Therefore the system gain B can be written as

$$B = \Delta f T_b = \Delta f / C. \qquad (9)$$

The proposed UWB wireless communication system is characterized by high values of the system gain $B = \Delta f / C >> 1$ varying from 50 to 1000.

The relationship between the channel SNR (q) and the usually used baseband SNR (q_0) can be expressed as

$$q_0 = Bq = \left(\Delta f / C\right) q \qquad (10)$$

From (10) we can note that the system gain $B = \Delta f / C$ determines the SNR improvement from the receive antenna output to the FFT output shown in Fig. 2.

The wireless data transmission is performed on the base of noise continuously signals with a low power spectral density of 7.0×10^{-5} mBt/MHz in the 3.1-4.1 GHz frequency range.

Simulation results for the probability of error show that we can achieve BER values of $10^{-4} - 10^{-5}$ for a channel SNR value from – 6 dB to – 4 dB. Wireless data transmission is performed with the rate $C = 1.0$ Mb/s in a channel with a strong noise interference. The data transmit distance is evaluated as $R = 54$ meters.

UWB wireless noise system carries out a covert data transmission and can operates when the channel SNR is negative.

4. CONCLUSIONS

Digital secure wireless communication system based on UWB noise continuous waveforms with code spectral modulation in a transmitter and double spectrum processing in a receiver is proposed for short-range data transmission with the rate 1.0 Mb/s. BER performance achieves values of $10^{-4} - 10^{-5}$ at the channel SNR from – 6 dB to – 4 dB. UWB wireless communication system can operates under the enemy receiver's thermal noise floor when noise continuously waveforms with low power spectral density are radiated in the 3.1-4.1 GHz frequency range. This feature provides low probability of detection and low probability of intercept (LPD/LPI) wireless data transmission.

ACKNOWLEDGMENTS

The author would like to thank Dr. V.V. Chapursky, Bauman Moscow State Technical University, for his continued support and numerical analysis.

This work has been supported by the Russian Foundation for Basic Research.

REFERENCES

1. Rushforth, C.K., Transmitted-reference techniques for random or unknown channels, *IEEE Trans. Inf. Theory*, vol. 10, no 1, pp.39-42, January 1964.
2. R.M. Narayanan and J. Chuang, Covert communications using heterodyne correlation random noise signals, *Electronics Letters*, vol.43, no. 22, pp.1211-1212, 2007.
3. V.I. Kalinin, Spectral Modulation of Wideband Noise Signals, *J. of Communications Technology and Electronics*, vol.41, no.5, pp.452-457, 1996.
4. V.I. Kalinin, Ultra-Wideband Data Transmission with Double Spectral Processing of Noise Signals, *Technical Physics Letters*, Vol. 31, No. 11, pp. 929-931, 2005.
5. Chapursky V.V., and Kalinin V.I., UWB Wireless Communications with Signal Correlation Processing, *CriMiCo'2008, Conf. Proceedings*, Sevastopol: Weber Publishing Co., Vol.1, p. 283-284.

WIRELESS FIELD BUS COMMUNICATION WITH SOFTWARE DEFINED IR-UWB IN A MANUFACTURING ENVIRONMENT

Masini M.[#*1], Alpert T.[#2], Lang F.[#3], Grözing M.[#4] and Berroth M.[#5]

[#] Institute of Electrical and Optical Communications Engineering, Universität Stuttgart, Germany
*GSaME- Graduate School advanced Manufacturing Engineering, Universität Stuttgart, Germany
[1]m.masini@ieee.org
[2]thomas.alpert@int.uni-stuttgart.de
[3]felix.lang@int.uni-stuttgart.de
[4]m.groezing@int.uni-stuttgart.de
[5]berroth@int.uni-stuttgart.de

Abstract

This paper elaborates a concept for a wireless field bus communication with software defined ultra wide band with impulse radio modulation (IR-UWB) in manufacturing environments. A wireless field bus offers an important improvement to the smart factory due to increasing requirements for connectivity, adaptability and flexibility. Former analysis showed the benefit of using UWB technology for the wireless field bus transmission in manufacturing environment.

In order to determine the best type of IR-UWB modulation a software defined radio system with direct sequence synthesizers is convenient. For this purpose on the transmitter side a digital-analog-converter (DAC) with 25 GS/s controlled by FPGA feeds directly the UWB antenna. On the receiver side the received signal is amplified by a low noise amplifier (LNA) and converted to a digital signal by an analog-digital-converter with as well 25 GS/s. The digital signal is further processed with a FPGA. This enables the adaptation of transmission parameters during operation. Thereby the transmission parameter, channels, antennas and RF components can be investigated.

Keywords: UWB, software defined, modular testing platform, FPGA, DAC, ADC.

1. INTRODUCTION

1.1. SMART FACTORY

In the meantime many manufacturing companies achieve a high level of technology. In the business model "Stuttgarter Unternehmensmodell" [1] is shown that transformability in all layer of companies is a crucial factor to survive in a turbulent environment. In order to reach a high flexibility and transformability in the whole company the shop floor level has to be incremented in flexibility in the same way. For a smart factory it is also an important point to have a highly flexible information system. Therefore one of the central goals is to develop variable and reusable hardware modules. With a wireless field bus such modules can be realized very flexible, plug-and-play capable and easy to reconfigure.

1.2. APPROACH

In order to develop a wireless field bus at first the requirements have to be elicited and analyzed. These can be compared with the properties of the possible communication technologies so one can be chosen. For the selected wireless transmission standard, the architecture for the wireless field bus can now be designed. In order to evaluate the transmission a platform with replaceable modules has to be developed. However, this platform should be able to generate the IR-UWB signal in direct sequencing mode and digitize the received signal without down sampling of the signal. With this platform the wireless field bus can be evaluated and measured in the manufacturing environment.

1.3 RELATED WORK

Willig et al. [2] discuss the problem of meeting the requirements of industrial environments, the usage of existing wireless technologies for field applications and their combination with wired systems. Therefore, the authors compare Bluetooth, WPAN (IEEE 802.15.4) and WLAN (IEEE 802.11a/b/g). They additionally show that a wireless field bus is beneficial for industrial applications. They do not involve UWB in this comparison but see the UWB as a future opportunity.

978-1-4244-7468-4/10/$26 ©2010 IEEE

Furthermore Willig presents a wireless extension for PROFIBUS [3]. In this approach, he develop a device to couple the wired part of the field bus with a wireless virtual ring extension.

Körber presents a concept of a modular wireless real-time sensor and actuator network for factory automation applications [4], but he doesn't consider crucial requirements of robustness and security and hereby communication dependability in industrial environments. However, he doesn't include the UWB technology in the comparison.

Katja Schwieger [5] analyzes the energy efficiency of different wireless networks with low data rate. Different wireless technologies in the ISM-band are compared. She shows that UWB allows very energy efficient transceivers.

2. Requirements Engineering and Comparison of Possible Wireless Communication Technologies

In order to develop a wireless field bus communication the requirements have to be chosen very careful. In a earlier work the requirements have been elicited and analyzed [6]. The most important requirement detected is the dependability. Reliable data transmission for control and production data acquisition in a plant is a crucial issue. The main advantage of a field bus is the real time capability which relies on the dependability of the transmission. Therefore the wireless transmission has to be very robust against interference, strong attenuation and multipath propagation. Similar important is the requirement of energy efficiency. Consequently a very good energy efficiency can render possible completely autonomous sensor with small batteries or even an energy harvesting module [7].

Table 1. Decision Matrix.

Requirement	WLAN	ZigBee	Bluetooth	UWB	wired
Robustness	+	-	+	++	++
Energy Eff.	-	o	-	++	+
Real-Time	-	o	o	+	++
Flexibility	++	+	+	+	--
Total	o	o	o	++	

With the result of this decision matrix in Table 1 the wireless technologies WLAN, ZigBee, Bluetooth and UWB have been compared. UWB with impulse radio modulation has been selected for the implementation of the wireless field bus. UWB for low data rate transmission is defined in the IEEE 802.15.4a.

3. Concept

In order to develop the wireless field bus with UWB it is convenient to use an evaluation platform with different modules which can be replaced and reconfigured. So the optimum for modulation, coding and power efficiency can be elaborated. Furthermore the configuration of the evaluation platform is to be assigned with the field bus. Without loss of generality in this concept the field bus PROFIBUS (PROcess FIeld BUS) is used. PROFIBUS is a widely-used field bus in the automation technology.

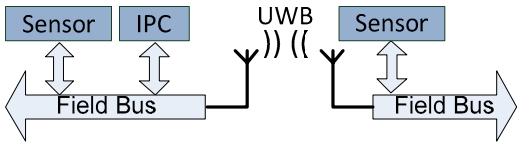


Fig. 1. An Example of a wireless field bus bridge with UWB

The intention of this wireless field bus realization is not the complete replacement of field bus wires, but the supplement of wireless field bus bridge (e.g. for a single movable sensor like it is shown in figure 1).

3.1. Architecture

The architecture of the testing platform provides a transparent wireless field bus bridge. The field bus interface receives the Profibus signal and passes the information with the shifted voltage levels to the FPGA. In the FPGA there are mainly two modules, first the modulator implemented with a DSP (Digital Signal Processor) and second the configuration module. The configuration module is connected to the Profibus as slave and can be addressed over the Profibus.

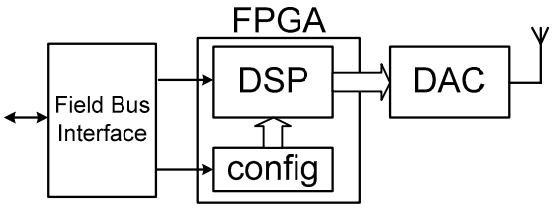


Fig. 2. Architecture of the Transmitter

This means a received bit of the field bus is coded into an impulse radio signal sequence by the DSP. The type of impulse can be selected by the configuration module as well as the destination address and the pre-distortion in order to equalize the distortions caused by the channel as well as the antennas. The DSP generates the digital stream for the DAC (Digital-to-Analog Converter) which converts it to the analog impulse for the UWB-antenna (Fig. 2).

On the receiver side, an LNA amplifies the received signal for the acquisition by the ADC (Analog-to-Digital Converter) avoiding analog components except the LNA and a band pass (BP) filter on the receiver side. The demodulation of the received signal can be conducted using a real-time implementation on an FPGA again (Fig. 3). Intending both the transmitter and the receiver as direct sequencing converter the

DAC and the ADC has to cope with the high UWB frequency up to 10 GHz. According to the Nyquist-Shannon sampling theorem the converters need at least a sampling rate of 20 GS/s.

3.3. DAC

The DAC of Alpert presented in [8] which is suitable for the proposed concept can achieve sampling rates up to 25 GSs^{-1}. With this DAC direct sampling in the first Nyquist band can be achieved for the whole UWB frequency range. In Fig. 4 the ENOB (Effective Number of Bits) are plotted from 0-12 GHz. The output of the DAC can directly feed the UWB antenna given the low power emission in the UWB.

3.4. ADC

The 6 bit ADC developed by Lang [9], with sampling rates of up to 25 GS/s and an ENOB of more than 3 bit for an analog input signal with 10 GHz (Fig. 5), can be used for direct sampling of the received and amplified signal.

4. CONCLUSION

The main benefit of the presented testing platform is the possibility to test in real time different implementation possibilities due to the fast DAC and ADC with a direct sequencing. The presented solution for the software defined IR-UWB transmission offers the possibility to detect the most efficient transmission. With the easy to use interface in the configurator connected with Profibus the modulation scheme can be adapted on the running system. Subsequently a energy efficient and easy to use single chip solution for the wireless field bus can be designed with the results of this testing platform.

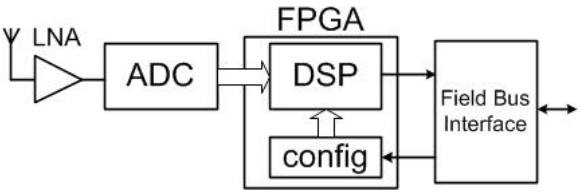


Fig. 3. Architecture of the Receiver.

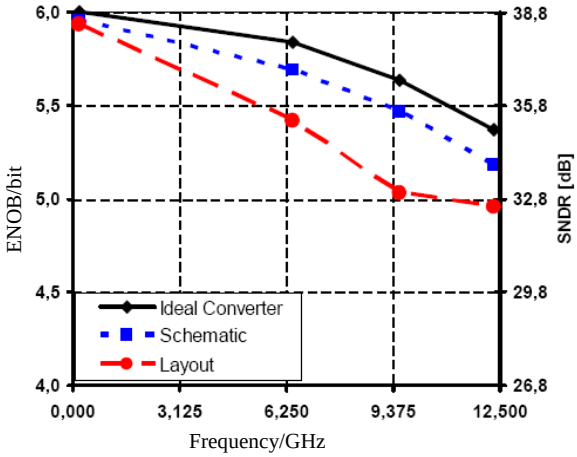


Fig. 4. ENOB of the DAC [9].

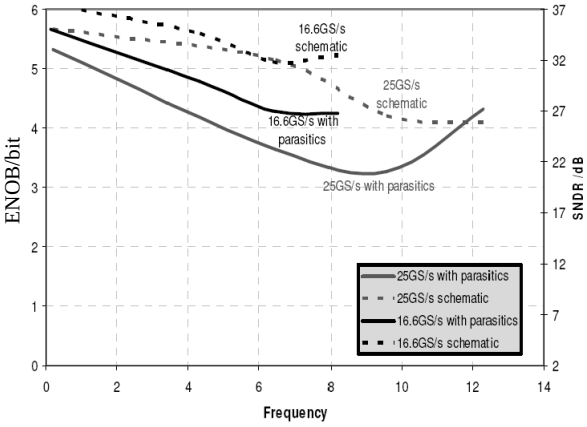


Fig. 5. ENOB of the ADC [10].

4. REFERENCES

1. E. Westkämper, E. Zahn, Wandlungsfähige Produktionsunternehmen: Das Stuttgarter Unternehmensmodell. Berlin: Springer, 2009.
2. A. Willig, K. Matheus, and A. Wolisz, "Wireless Technology in Industrial Networks", in *Proceedings of the IEEE*, 2005, pp. 1130-1151.
3. A. Willig, "An architecture for wireless extension of PROFIBUS: Industrial Electronics Society, 2003. IECON '03", vol. 3, pp. 2369-2375 Vol.3.
4. H.-J. Körber, "Konzeptstudie zur Implementierung eines modularen echtzeitfähigen drahtlosen Sensor-/Aktornetzes für die Fertigungsautomatisierung", Dissertation, Helmut Schmidt Universität Hamburg, 2007
5. K. Schwieger, *Betrachtungen zur Energieeffizienz in Funknetzwerken mit geringer Datenrate*. Dresden: Vogt, 2006.
6. M. Masini, et al., "Wireless Field Bus Communication with UWB for Manufacturing Environments". Vienna, ICMS, 2010
7. S. Roundy, et al. "Power Sources for Wireless Sensor Networks", in *Wireless Sensor Networks*, 2004, pp. 1–17.
8. T. Alpert, et al, "25 GS/s 6-bit Pseudo Segmented Current Steering DAC in 90 nm CMOS", *ESSCIRC*, Fringe, Athens, 2009.
9. F. Lang, et al. "Design of a 25 GS/s 6-bit Flash-ADC in 90 nm CMOS technology", *ESSCIRC*, Fringe, Athens, 2009.

PRACTICAL APPLICATION OF UWB GEORADAR TECHNIQUE FOR INVESTIGATIONS OF CULTURAL HERITAGE OBJECTS

Yastrebov Yu. V., Kostyleva V. V., Nikolaev V. A., and Barilko M. S.

Radioavionika Corporation, P.O.B. 111, St-Petersburg, 198103, Russia
Phone: (812) 251 2743, E-mail: vanagas@bk.ru

Abstract

The UWB GPR technique is applied for investigation of covered structure of cultural heritage objects without affect their construction integrity. The obtained information is important for restorers since the most part of it is not available for conventional diagnostic methods and technical documentation is often lost. Some examples of cultural heritage objects investigations are performed.

Keywords: GPR, cultural heritage objects.

1. INTRODUCTION

The nondestructive check technique using the UWB is widely applied in different areas including the diagnostics of cultural heritage objects. The conventional diagnostic methods not satisfy the present-day requirements of restorers in the field of data acquisition about technical state of historical sites for decision on restoration program. UWB GPR technique allows investigating the covered structure of cultural heritage objects without affect the construction integrity and significant decorative elements. The obtained information is important because of the most part of it is not available for other conventional methods and technical documentation is often lost.

Using the UWB GPR technique for diagnostic and monitoring of cultural heritage objects allows solving the following problems:

- Determination of structure layers thickness;
- Estimation of homogeneity (continuity) of materials of structural units and elements;
- Search and following of engineering services including non-metallic ones;
- Location and depth determination of structural anomalies (foreign inclusions and objects) in structural units and elements.

2. GPR DIAGNOSTIC OF CULTURAL HERITAGE OBJECTS

The using of georadar technique for investigation of cultural heritage object is very interesting and complicated problem. In this case the whole spectrum of georadar available possibilities is needed. Restores are interested in as well ultra-thin layers such as stucco as the construction of massive pedestal with thickness of several meters.

Let us give some examples of practical works concerned with diagnostic of cultural heritage object.

The goal of investigation of the mosaic floor of the Concert Pavilion in Pushkin was to define bridging structure, location of humidity zones and metal fastener elements. The example of georadar image of the scan trace over the mosaic blocks and marble slabs is shown in Fig. 1. The thickness of mosaic is near 2 cm. The humidity zone is indicated by circle. It is located above the vertex of the brick arch indicated by dotted curves. The structure of the arch bridging was confirmed by investigations with low-frequency antennas.

The investigation of the pedestal of the monument to Nicolas I was a complicated problem. The multitier pedestal is constructed from 118 blocks of red and dark-gray granite, red quartzite and white marble. The pedestal is decorated by four female figures, four high relieves and armours of bronze. As the result of investigations the estimation of stone blocks thickness had

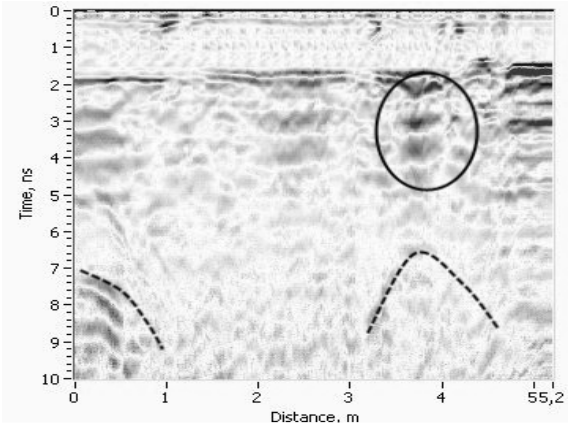


Fig. 1. Georadar image of trace over mosaic floor.

978-1-4244-7468-4/10/$26 ©2010 IEEE

been received, the places of destruction of binding material and the location of the humidity zones had become clear. Two vertical metal pillars passing through the whole pedestal were revealed. They serve for attachment of the statue to the base. The georadar image of the trace in the upper part of the pedestal is shown in Fig. 2 where the pillar is observed at the depth of near 1.3 m (in dotted circle).

In Fig. 3 the georadar image of the trace over the quartzite blocks is performed where anyone can see the characteristic hyperbolas from metal dowels indicated by arrows. The same hyperbolas from upper fasteners of high relief are observed in Fig.4 where the georadar image of the above the high relief trace is shown.

In our opinion the integration of different methods is very important for the diagnostic of cultural heritage objects. During the investigation of the monument to Nicolas I the using of video endoscope allowed to determine the power of corrosion of high relief and sculpture fasteners. Endoscope images confirm the destruction of the binding material detected by GPR researches. The area of the anchor corrosion is indicated by arrow in Fig. 5.

During the investigation of atlantes of the portico of the New Hermitage the complex of methods was used: georadar, metal detector, video endoscope, ultrasonic flaw detector. The goals were to determine the construction of atlantes fastening to the upper beam and the base pedestal and the fastening of the pedestal to the granite stylobate of portico.

As the result of investigation the location and the dimensions of dowels were established. The example of the georadar image of trace over the pedestal is shown in Fig. 6 where the dowel is observed in the center. The using of the metal detector allowed to determine the material of the dowel: it is bronze but not iron.

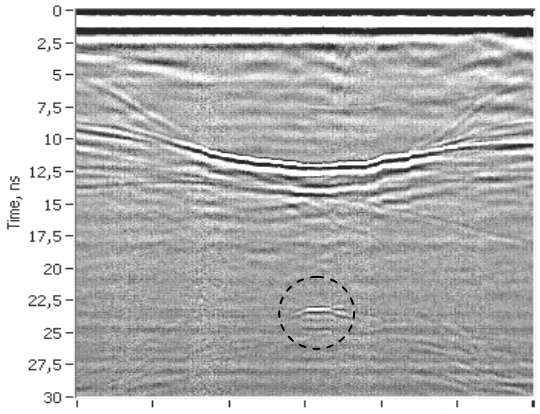


Fig. 2. Georadar image of trace over the upper part of pedestal.

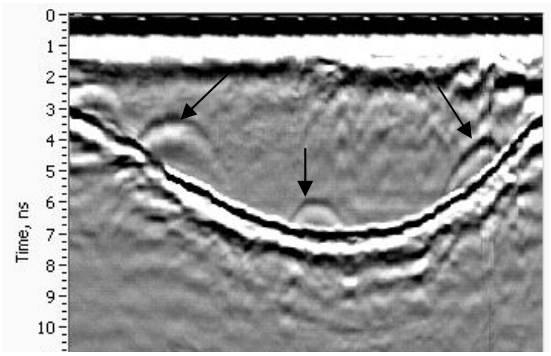


Fig. 3. Georadar image of trace over the lower part of pedestal.

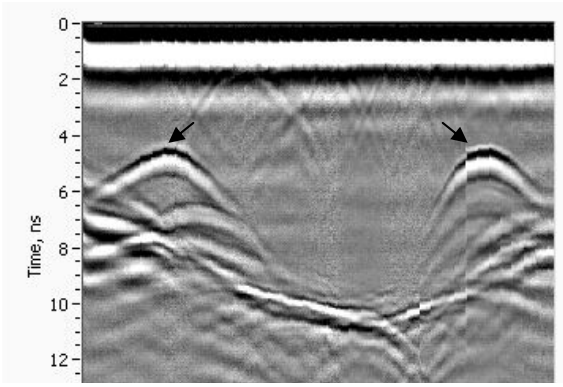


Fig. 4. Georadar image of trace over quartzite blocks above high relief.

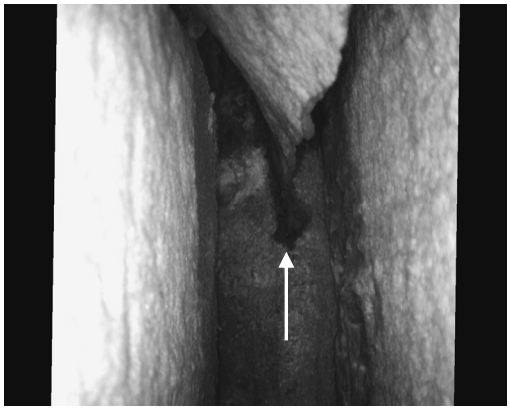


Fig. 5. Video endoscope image of anchor corrosion.

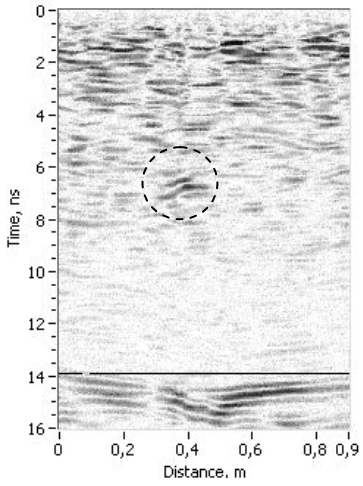


Fig. 6. Georadar image of trace over the bottom of granite pedestal.

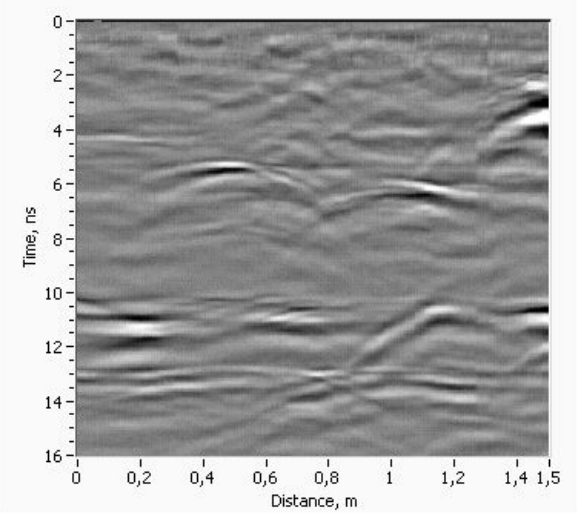


Fig. 7. Georadar image of trace over horizontal beam above sculpture

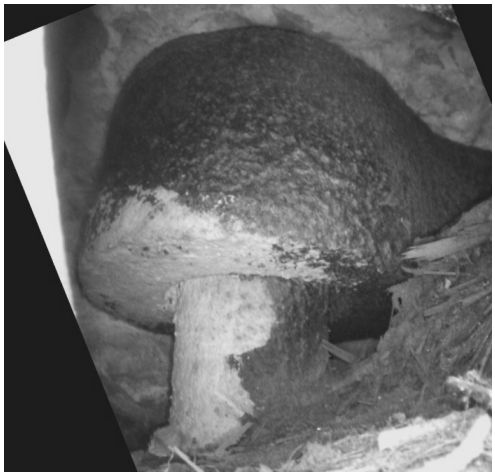


Fig. 8. Video endoscope image of wrought iron anchor and vertical dowel

The investigation of the atlantes upper fasteners from the front size of portico through the horizontal beam was carried out with GPR (the example of the radar image is shown in Fig.7), but from the of atlantes' heads the video endoscope was used (Fig.8). Thus the construction of upper fasteners was revealed and slight differences were discovered for several sculptures.

3. CONCLUSION

The integration of methods (georadar, metal detector, video endoscope, ultrasonic detector) provides the comprehensive information about objects for the specialists of restoration. We think that the list of methods in use should be expanded.

In St-Petersburg and other regions of Russia we have investigated more than twenty cultural heritage objects. In “Radioavionica Corporation” based on acquired experience “The technique of investigation of architectural monuments and city sculpture using the ultrawideband .radiolocation sounding” was worked out which was authorized by Government of St-Petersburg.

It is essential to acquaint restorers and constructors with the georadar technique possibilities and to increase the number of the investigated objects because all of them demand unique approach and give unique experience.

ESTIMATION OF DIELECTRIC PERMITTIVITY OF MEDIUM BY ANALYSIS OF UWB RADIOLOCATION SIGNALS FROM LOCAL OBJECT

Yastrebov Yu. V., Kostyleva V. V. and Nikolaev V. A.

Radioavionika Corporation, P.O.B. 111, St-Petersburg, 198103, Russia
Phone: (812) 251 2743, E-mail: vanagas@bk.ru

Abstract

The method of accuracy enhancement of medium permittivity estimation based on measurements of time delays of UWB signals reflected from local object and received in different points of radar scanning trace is suggested. The mathematical relations have been obtained for estimation of investigated medium permittivity and measurement errors and evaluation of algorithm accuracy gain in comparison with common methods has been made.

Keywords: GPR, permittivity.

1. INTRODUCTION

The determination of electrophysical properties (conductivity and dielectric permittivity) of medium using UWB GPR data is the ill-conditioned inverse problem.

The solution of such problem is possible within the certain limits and essentially depended on the method of acquisition of initial information. In the case in question the time delays of UWB signals reflected from local object over scanning with steady speed or in step manner as shown in Fig. 1 are used as initial information.

Transmitting and receiving antennas are sequentially placed in i point of trace ($i = 0;\pm1;\pm2;...;\pm M/2$). During antennas move along the scanning trace the local object is observed not only in the one point just above it but in several points up to maximum distance $\pm L/2$ depended on antenna pattern width, signal attenuation in medium, etc. As a result the reflected from local object signals form the hyperbola which shape depends on permittivity ε of investigated medium and local object depth R_0 (Fig. 2).

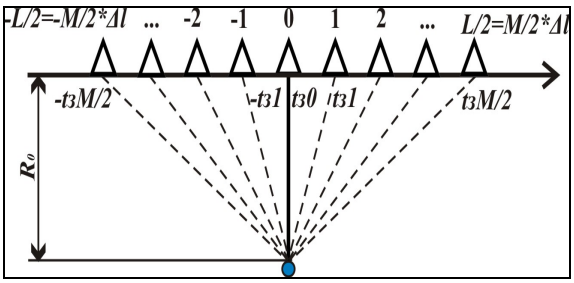


Fig. 1. Radar scanning trace.

Fig. 3 gives an example of the real radar image from two local objects placed at different depths

The method of estimation and local object depth evaluation is known [1]. The corresponding values may be found from equations:

$$\varepsilon = \frac{t_0^2 \cdot c^2}{4 \cdot R_0^2}\ , \qquad (1)$$

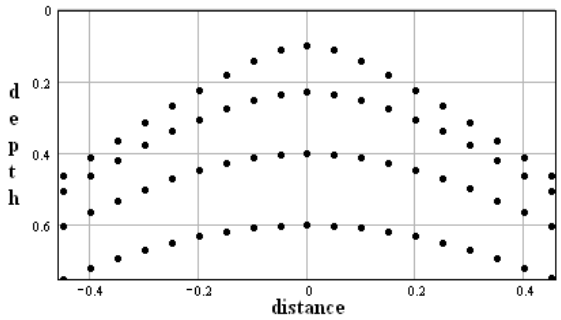


Fig. 2. An example of calculated responses from local objects placed at different depths.

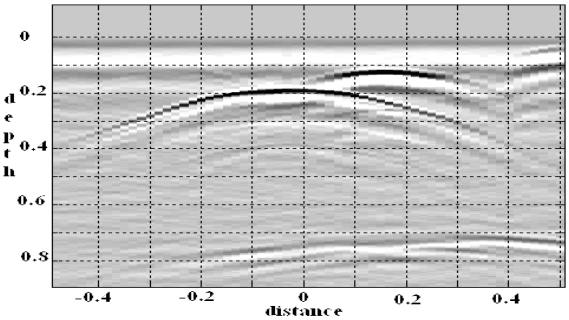


Fig. 3. An example of the real radar image.

978-1-4244-7468-4/10/$26 ©2010 IEEE

$$R_0 = \sqrt{\frac{t_0^2 \cdot i^2 \cdot \Delta l^2}{t_i^2 - t_0^2}} \qquad (2)$$

where R_0 is local object depth; ε is medium permittivity; c is electromagnetic constant; t_0 is time delay of signal in the vertex of hyperbola, when antenna system places in point $i = 0$; t_i is time delay of signal.

From equations (1) and (2) it is clear that for evaluation of permittivity and local object depth it is necessary to measure time delay of signal at least in two points of trace, for example t_0 and t_i.

The accuracy of permittivity evaluation is specified mainly by errors of time delay measurements and distance between points measurement:

Potential for accuracy enhancement of permittivity estimation using time delay measurements in only two points of radar trace is limited as the information from other points of radar trace is ignored. In this connection the method of accuracy enhancement of permittivity estimation is suggested based on weighting averaging of time delay measurements in several points along radar trace.

The problem solution is considered under the following limitations:

- Let us assume that geometric optics laws are applicable for radiolocation signals;
- The object is local and its responses form the characteristic hyperbola on radar image;
- The medium under investigation is homogeneous;
- The distribution law of time delay fluctuations of reflected from local object signals is assume to be normal;
- The antenna pattern is rather wide and the attenuation in medium is low that allows to receive local object response at a considerable distance from it.

2. Problem Statement and Principles of Solution

In order to obtain the optimal estimation for permittivity of medium with local object in it let us use maximum likelihood criterion and logarithm of likelihood ratio as decision function [2].

Let GPR antenna system move discretely with Δl step over medium interface above the local object situated at the depth of R_0. The distance $R(i)$ from local object to arbitrary point of radar trace is described by equation:

$$R(i) = \sqrt{i^2 \cdot \Delta l^2 + \left(t_0 \frac{c}{2 \cdot \varepsilon}\right)^2}.$$

The propagation time of signal from local object to antenna system placed at point i is:

$$t(i) = \frac{2 \cdot R \cdot \varepsilon}{c} = \sqrt{\frac{4 \cdot \varepsilon}{c^2} \cdot \left(i^2 \cdot \Delta l^2 + t_0^{\,2}\right)}.$$

The equation for $t(i)$ expand into Maclaurin series:

$$t(i) = t_0 + 2 \cdot \varepsilon \cdot i^2 \cdot \frac{\Delta l^2}{t_0 \cdot c^2} - $$
$$-2 \cdot \varepsilon^2 \cdot i^4 \cdot \frac{\Delta l^4}{t_0^3 \cdot c^4} + 4 \cdot \varepsilon^3 \cdot i^6 \cdot \frac{\Delta l^6}{t_0^5 \cdot c^6} \cdots$$

Using series terms up to second order we obtain the following expression for time delay:

$$t(i) = t_0 + 2 \cdot \varepsilon \cdot i^2 \cdot \frac{\Delta l^2}{t_0 \cdot c^2} + n(i),$$

where $n(i)$ is random fluctuations of time delay of signal at point i caused by internal noise, time instability of sweep etc.

Let us consider the realization of time delay of radar signals relative to t_0 depending on antenna system position as the input realization for permittivity evaluation:

$$y(i, \varepsilon) = G \cdot \varepsilon \cdot i^2 \cdot \Delta l^2 + n(i),$$

where the following designation is used for accommodation:

$$G = \frac{2}{c^2 \cdot t_0}.$$

Let us represent the input realization in vector form:

$$\overline{Y}(\varepsilon) = \overline{x}(\varepsilon) + \overline{n},$$

where $\overline{x}(\varepsilon)$ is the vector of predicted realization of time delay of radar signals.

Suppose that the distribution law of random time fluctuations $\overline{n}$ is normal and using the maximum likelihood ratio for estimation of signal with fully known parameters with the exception of estimated one we obtain:

$$\ln l\left[\overline{Y}(\varepsilon)\right] = \xi(\varepsilon) - 0.5 \cdot q^2(\varepsilon) =$$
$$= \overline{Y}^T(\varepsilon) \cdot \overline{r}(\varepsilon) - 0.5 \cdot \overline{x}^T(\varepsilon) \cdot \overline{r}(\varepsilon),$$

where $\overline{r}(\varepsilon) = \Phi^{-1} \cdot \overline{x}(\varepsilon)$, Φ^{-1} is inverse correlation matrix of time delay fluctuations of radar signal.

Maximum likelihood estimation $\hat{\varepsilon}$ is described by equation:

$$\hat{\varepsilon} = \frac{\overline{Y}^T(\varepsilon) \cdot \overline{R}}{\overline{X}^T \cdot \overline{R}} \qquad (3)$$

where $\overline{X}^T \cdot \overline{R}$ is $\overline{x}(\varepsilon) \cdot \overline{r}(\varepsilon)$ normalized by ε.

The error variance of estimation has the form:

$$\sigma_{\varepsilon}^2 = \frac{1}{\overline{X}^T \cdot \overline{R}} \qquad (4)$$

In assumption that time delay fluctuations are uncorrelated the correlation matrix of phase fluctuation is described by equation:

$$\Phi = \left|\sigma_t^2\right| \cdot \left|\delta_{ij}\right|$$

where σ_t^2 is time fluctuation variance; δ_{ij} is Kronecker symbol.

In that case a weight vector is equal to predicted realization normalized by variance:

$$\overline{X}^T = G \cdot L^2 \big/ M^2 \times$$
$$\times \left\| -\left(M/2\right)^2 \quad \cdots \quad -1 \quad 0 \quad 1 \quad \cdots \quad \left(M/2\right)^2 \right\|,$$

where $G = \dfrac{2}{c^2 \cdot t_0}$.

Taking into account of $\overline{X}^T \cdot \overline{X}$ may be substituted by common sum [3] the equation for permittivity evaluation and measurement error variance would have the form:

$$\widehat{\varepsilon} = \frac{15 \cdot M \cdot \sum_{i=1}^{M/2} i^2 (y_i - y_i)}{G \cdot L^2 \left(\frac{M}{2}+1\right) \cdot \left(M+1\right) \cdot \left[3 \cdot \left(\frac{M}{2}\right)^2 + 3\left(\frac{M}{2}\right) - 1\right]}.$$

$$\sigma_{\varepsilon}^2 = \frac{15\sigma_t^2 \cdot M^4}{G^2 L^4 \left(\frac{M}{2}\right)\left(\frac{M}{2}+1\right)\left(M+1\right)\left[3 \cdot \left(\frac{M}{2}\right)^2 + 3 \cdot \left(\frac{M}{2}\right) - 1\right]}. \qquad (5)$$

When time delay measurements realize in two points of radar trace (without averaging along the trace) the measurement error variance σ_{ε}^2 ($M = 2$) is calculated using the formula:

$$\sigma_{\varepsilon}^2 = \frac{8 \cdot \sigma_t^2}{G^2 \cdot L^4}. \qquad (6)$$

The ratio of variances (5) and (6) permits to estimate the gain of suggested method of permittivity estimation against the common case with measurements in two points of radar trace. The accuracy gain depends on the number of points along the radar trace where measurements of time delay take place and is described by equation:

$$B\left(M\right) = \frac{8 \cdot \left(\frac{M}{2}+1\right) \cdot \left(M+1\right) \cdot \left[3 \cdot \left(\frac{M}{2}\right)^2 + 3 \cdot \left(\frac{M}{2}\right) - 1\right]}{20 \cdot M^3}.$$

The dependence of accuracy gain on the number of measurement points is shown in Fig. 4.

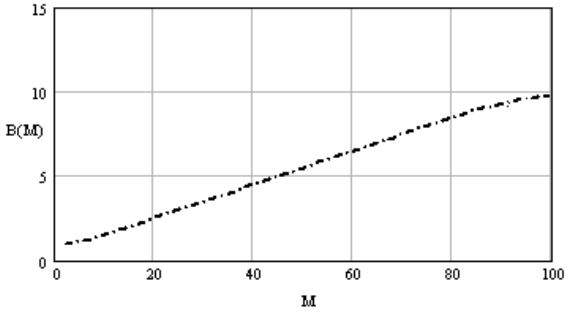


Fig. 4. Accuracy gain dependence on the number of measurement points.

It is clear from the plot that increasing the number of points along the trace where the measurements of time delay of signals reflected from local object take place causes the improving of accuracy gain for permittivity evaluation. Thus for $M = 20$ the accuracy gain is 2.5 times more, for $M = 50$ – 5.5 times more.

3. CONCLUSION

Thus the method of accuracy enhancement of medium permittivity evaluation is suggested. Math equations for evaluation of medium permittivity and measurement errors are performed. The accuracy gain of suggested algorithm versus common method is estimate.

REFERENCES

1. Finkelshtein M., Karpuhin V., Kutev V., Metelkin V. '*Subsurface radiolocation*'. Ed. Finkelshtein M. Moscow: Radio i Svyaz, 1994.
2. Shirman Ya., Manzhos V. '*Theory and technique of processing of radiolocation information against background clutter*', Moscow: Radio i Svyaz, 1981.
3. Prudnikov A., Brychkov Yu., Marichev O. '*Integrals and series*'. Moscow: Nauka, 1981.

RECONSTRUCTION OF PERMITTIVITY PROFILE OF STRATIFIED STRUCTURES WITH LOSSES ON BASIS OF DIVERGENT BEAM PROBING USING MULTIFREQUENCY DATA IN WIDE FREQUENCY BAND

[1] Alexin S. G. and [2] Drobakhin O. O.

Dniepropetrovsk National University, Dniepropetrovsk, Ukraine
[1] E-mail: AlexinSergey@ua.fm
[2] E-mail: drobakhino@mail.ru

Abstract

Three well-known methods of layered structure permittivity profile reconstruction on the basis of microwave probing are under consideration. The methods are discrete analog of Gel'fand-Levitan integral equation method supposing Goupillaud model, the method of dynamic deconvolution and the method based on Newton-Kantorovich iterative scheme implementation to Riccati differential equation. The methods are discussed with assumptions of probing beam divergence and heat losses in material.

Keywords: Permittivity profile, stratified structure, reflection coefficient, nondestructive testing, divergent-wave probing, reflectors localization.

1. INTRODUCTION

The problem of 1-D permittivity profile (PP) $q(x) = \varepsilon(x)\left(1 - j\,\mathrm{tg}\delta(x)\right)$ reconstruction on basis of reflection coefficient in frequency domain (RCFD) concerned with medical tomography, geoexploration, nondestructive testing of industrial items etc. Simultaneous accounting both heat losses in material and divergence of probing beam provides taking into consideration essential effects having place in real experiment and thus allows achieving more accurate reconstruction of PP. In the case of single reflector consideration the first effect leads to reducing of inserted reflection coefficient versus distance relatively intrinsic RC of the reflector by exponential low, while the second effect leads to the reducing by hyperbolic low. Despite the lows similarity correct reconstruction of PP can be performed if experiment provides high accuracy of measured data.

Three well-known methods of layered structure PP reconstruction on the basis of microwave probing are under consideration. The methods are discrete analog of Gel'fand-Levitan integral equation method (DAGLM) supposing Goupillaud model [1], the method of dynamic deconvolution (MDD) [2] and the method based on Newton-Kantorovich iterative scheme (NKIS) implementation to Riccati differential equation [3]. The first two methods are similar one to another in an idea of layer-by-layer reconstruction in consecutive order as opposed to the third one providing simultaneous estimation of all the layers.

2. MODELS OF RCFD IN THE CASES OF PLANE-WAVE AND DIVERGENT-WAVE PROBING

If plane model is considered for normal-falling probing wave, RCFD of stratified structure having N layers with complex permittivity q_k and thickness d_k ($k = 1,2,\ldots,N$) can be synthesized using well-known iterative scheme [4] supposing consecutive layers introducing:

$$R^{(k)}\left(\omega_n\right) = \frac{r_{N-k} + R^{(k-1)}\left(\omega_n\right) e^{-j\omega_n 2d_{N-k+1}\sqrt{q_{N-k+1}}/C}}{1 + r_{N-k} R^{(k-1)}\left(\omega_n\right) e^{-j\omega_n 2d_{N-k+1}\sqrt{q_{N-k+1}}/C}}, \quad (1)$$

with k being iteration number. The scheme is started from $R^{(0)}\left(\omega_n\right) = r_N$ and provides $R^{(N)}\left(\omega_n\right)$ being desired RCFD of the structure. $r_m = \dfrac{\sqrt{q_m} - \sqrt{q_{m+1}}}{\sqrt{q_m} + \sqrt{q_{m+1}}}$ is RC of interface $m = 0,1,\ldots,N$, $q_0 = q_{-\infty}$ and $q_{N+1} = q_{\infty}$ are permittivity of front and back half-spaces respectively, C is light speed.

If the sample and a transceiver horn aren't placed enough remotely, RCFD can by synthesized using approach [5] supposing 3 stages: synthesizing of plane-front impulse response of reflection (PFIRR) on interval bringing considerable part of reflected energy; correction

978-1-4244-7468-4/10/$26 ©2010 IEEE

of impulse magnitudes; transformation of IRR to frequency domain. The approach was developed on the paraxial optic approximation and takes into consideration electromagnetic beam focusing-defocusing properties of interfaces between layers with different materials. Let's use notation $R_{(n_1,n_2,\ldots,n_N)}$ for magnitude of PFIRR impulse formed after n_1 passing of layer 1, n_2 passing of layer 2, …, n_N passing of layer N (one passing includes forward and backward propagation). Then magnitude of corresponding impulse of divergent-front IRR can be obtained through following correction:

$$R_{(n_1,n_2,\ldots,n_N)} \to R_{(n_1,n_2,\ldots,n_N)} \frac{2z-x}{2z-x+2\sum_{k=1}^{N}\frac{n_k d_k}{\operatorname{Re}\sqrt{q_k}}}, \quad (2)$$

with z being distance between horn aperture and front interface of sample and x being distance from aperture to phase center of beam.

3. The Method of Dynamic Deconvolution

MDD was originally developed [2] on inversion of (1) by the way of successive layers removing. The parameters of next removed layer are estimated on the basis of parametrical spectral analysis (PSA) results: magnitude of the first impulse $R_0^{(k)}$ and delay of the second one $\tau_1^{(k)}$. RCFD after next layer removal is obtained as:

$$R^{(k-1)}\left(\omega_n\right) = \frac{R^{(k)}\left(\omega_n\right) - R_0^{(k)}}{1 - R_0^{(k)} R^{(k)}\left(\omega_n\right)} e^{j\omega_n \tau_1^{(k)}}$$

with $k = N, N-1, \ldots, 1$.

Generalization of MDD to the case of divergent probing wave model consideration is complicated because absence of analog of equation (1) for RCFD of N-layered structure. But structure having only 1 layer provides fully correct equation including Lerch transcendent function $\Phi(\xi, s, a) = \sum_{n=0}^{\infty} \xi^n / (a+n)^s$ with $s = 1$ what makes possible development of MDD modification that approximately take into account beam divergence. Corresponding iterative scheme:

$$R^{(k-1)}\left(\omega_n\right) = \frac{-1}{R_0^{(k)}} \Phi^{-1,\xi}\left(\frac{1 - R_0^{(k)} R^{(k)}\left(\omega_n\right)}{a^{(k)}\left(1 - \left(R_0^{(k)}\right)^2\right)}\right) e^{j\omega_n \tau_1^{(k)}}, \quad (3)$$

with $a^{(k)} = \dfrac{2z^{(k)} - x}{2d_{N-k+1} / \operatorname{Re}\sqrt{q_{N-k+1}}}$,

$$z^{(k)} = \begin{cases} z, & \text{if } k = N, \\ z^{(k+1)} + \dfrac{d_{N-k}}{\operatorname{Re}\sqrt{q_{N-k}}}, & \text{if } N-1 \geq k \geq 1. \end{cases}$$

$\Phi^{-1,\xi}\left(\ldots\right)$ is used for notation of function inverting Lerch transcendent $\Phi(\xi, 1, a^{(k)})$ relatively variable ξ.

Despite the divergence accounting isn't absolutely correct, the modification proposed can provide fully-accurate reconstruction. The reason is that transformation (3) correctly compensates divergence effect for magnitudes of main impulses (that are impulses corresponding to first reflection from interfaces).

4. Discrete Analog of Gel'fand-Levitan Method

DAGLM allows reconstructing of real part of PP on the basis of known IRR which can be found from measured RCFD by the way of PSA. The equidistant sampling of IRR is demanded in this method. On iteration $k = 1, 2, 3, \ldots$ the iterative scheme brings parameters of next partial layer ε_k and d_k considering solving of SLAE that includes values of sampled IRR $R_0, R_1, \ldots, R_k$ [1]. The method can be accelerated using the block matrix inversion application for the purpose of the SLAE solving [6].

Despite the method was developed in supposition of plane-front model for probing impulse, simple modification makes DAGLM appropriate for reconstruction in the case of divergent-front impulse probing. In this case every iteration of DAGLM must be supplemented with the stage of the treated impulse magnitude correction. The impulse with magnitude R_k that appears in [6, Eq.1] on iteration k should be amplified as following:

$$R_k \to R_k \frac{2z - x + 2\sum_{m=1}^{k}\frac{d_m}{\sqrt{\varepsilon_m}}}{2z - x}.$$

The sum in numerator is given by all the layers having been reconstructed previously; the parameter $2z - x$ must be known. The correcting transformation doesn't absolutely conform with IRR model (2), but it becomes more and more correct when layers permittivity contrast is decreasing. The cause is that transformation is absolutely valid for the main impulses as opposed to echo ones. But numerical experiment has shown that approach can also be effective for layered structures with relatively high contrast of ε.

Note that development of fully-valued discrete analog of the method based on Gel'fand-Levitan integral equation [1] providing complex permittivity profile reconstruction demands cancellation of Goupillaud media model that essentially complicates the method.

5. Newton-Kantorovich Iterative Scheme

NKIS [3, 8] provides reconstruction of PP through numerical solving of the Riccati differential equation connecting PP function $q(\omega, x)$ and spatial distribution of reflection coefficient $r(\omega, x)$:

$$\frac{dr(\omega,x)}{dx}=2j\frac{\omega}{C}\sqrt{q(\omega,x)}r(\omega,x)+\frac{1-r^2(\omega,x)}{4q(\omega,x)}\frac{dq(\omega,x)}{dx}. \quad (4)$$

The initial data for reconstruction is the reflection coefficient before structure $r(\omega_n,-0)$ measured on some grid of frequencies ω_n ($n=1,2,...,M$). If permittivity is considered to be complex-valued but non-dispersive in frequency band of measurements, equation (4) provides high accuracy and stability of NKIS being treated in coordinate $\zeta(x)=\int_0^x\sqrt{q(x')}dx'$ [8]. The scheme implies choosing electrical depth of reconstruction $\zeta_{\max}$, some initial distribution $q^{(0)}(\zeta)$ for $\zeta\in\left(0,\zeta_{\max}\right]$ and iterative correction of PP using sequence of corrections $\Delta q^{(k)}(\zeta)$. The corrections are expanded on some system of N basic functions ($N\le M$). On iteration $k=1,2,3,...$ PP is given by:

$$q^{(k)}(\zeta)=q^{(k-1)}(\zeta)+\sum_{n=1}^{N}P_n^{(k)}\phi_n(\zeta)$$

with $P_n^{(k)}$ being k^{th} iteration correction of coefficient corresponding to n^{th} basic function $\phi_n(\zeta)$. Unknown coefficients are obtained as solution of the SLAE (with coefficients matrix of size $M\times N$) having to be solved at every iteration. Discrete bases choosing ensures adequate PP reconstruction if structure is known to be stratified. Good results are provided by the basis containing Π-shape functions [8] every of which equals 1 inside its own layer and 0 outside.

It must be noted that taking into consideration probing beam divergence implies corresponding generalization of Riccati equation (4) being the base for NKIS development. The problem provides an essential obstacle.

6. The Problem of Interfaces Localization

If discrete basis is used for the purpose of PP representation, the reconstruction process can be divided into two stages. Firstly, electrical coordinates of interfaces ζ_n must be obtained and, secondly, NKIS must be launched for layers permittivity matching. The problem of reflecting interfaces localization is usually solved with use of PSA methods but this approach doesn't distinguish main impulses and echo ones.

The disadvantage is suppressed in the method [3] implying preliminary approximate PP reconstruction using NKIS with exponential basis and subsequent interfaces identification as points where spatial distribution of modulus of permittivity derivative reaches local maxima. The imperfection of the second method is low accuracy of ζ_n. Two methods can be used in couple producing hybrid approach [7] that provides strong points combination.

Another method [8] based on PSA results interpretation utilizes information containing in delays of echo impulses for more precise estimation of main impulses delays. The indices of some spectral component $R_{(n_1,n_2,...,n_N)}$ are determined by the way of matching of probability distribution functions of spectral component expectation and spectral component disposition.

7. Comparison of the Methods of PP Reconstruction

At the end let's compare possibilities and demands of three methods described above (Table 1). Column 'Demands' shows whether method of reconstruction supposes PSA performing or interfaces localization (IL). In the second case echo spectral components is considered to be excluded from the list obtained by PSA.

Table 1. Comparison of the methods of PP reconstruction.

Method of PP reconstruction	Divergence accounting	Losses accounting	Demands
MDD	yes	yes	PSA / IL
DAGLM	yes	no	PSA
NKIS	no	yes	IL

References

1. K. Aki and P. G. Richards 1980, *Quantitative Seismology. Theory and methods*, W. H. Freeman and Company.
2. E. A. Robinson 1982, 'Spectral Approach to Geophysical Inversion by Lorentz, Fourier and Radon Transforms', *Proc. IEEE*. **70**, 1039-1054.
3. V. Mikhnev and P.-V. Vainikainen 2000, 'Iterative Step-Like Reconstruction of Stratified Dielectric Media from Multifrequency Reflected-Field Data', *Subsurface Sensing Technologies and Applications*. **1**, 65-78.
4. Brekhovskih L. M. 1957, *Waves in Stratified Media*, Moscow, AS USSR.
5. Drobakhin O. O. 1994, 'Determination of Reflected Impulse Amplitude Dependence in the Method of Radio Pulse Envelope Synthesizing', *Russian Journal of Nondestructive Testing*. **8**, 48-55.
6. Alexin S. G., Antropov O. S., and Drobakhin O. O. 2008, 'Reconstruction of Permittivity Profile by Gel'fand-Levitan Method using Reflectometry Data Extrapolation', *Proc. UWBUSIS'08*, Sevastopol, 201-203.
7. Alexin S. G., Drobakhin O. O. 2009, 'Inverse Problem Solving for Layered Dielectric Structure using Newton-Kantorovich Iterative Scheme with Increased Accuracy', *Proc. DIPED'09*, Lvov, 227-231.
8. Alexin S. G., Drobakhin O. O. 2010, 'Reconstruction of Permittivity Profile of Stratified Lossy Dielectric using Newton-Kantorovich Iterative Scheme', *Telecommunications and Radio Engineering*. **69(9)**, 817-840.

ESTIMATION POWER AND SPATIAL CHARACTERISTICS OF ULTRAWIDEBAND RADAR FOR STATEMENT OF PROTECTING HANDICAPS

Vlasik S. N., Yermakov G. V., Zima I. I.

[2] Kozshedub Air Force Kharkiv University, Kharkiv, Ukraine
E-mail: YermakovGV@ukr.net

Abstract

Considered the factors that determine the conditions of radiotechnic suppress radiolines control explosive devices, an analysis of experimental studies and an estimate of parameters suppressed radiolines that allows us to determine energetically and spatial characteristics of the antenna system. On the basis of tactical considerations location ultrawideband RTS combat formations moving columns, select a maximal range of producer interference, 20 m and the spectral composition of the signal handicaps of 100 ... 3000 MHz.

Keywords: Radiotechnic suppress, radiolines control explosive devices, ultrawideband signal, handicaps.

Statistics indicate that today radio-controlled explosive devices (RCED) are being increasingly used in carrying out terrorist acts. The preferential use of RCED properties determined primarily by the relative security, wich determing the distance between the position of the explosion-ments and the place of detonation. Most RCED used in an attack on the transport military columns - cars, armored vehicles, etc.

Canal transmission of information RCED can be characterized by the following parameters [1].

1. Frequency. There is a high probability of use in RCED equipment produced for industry of the various models remote control. Distribution of the radiofrequencies allocated in different countries according to the radio "radio reglament", covers parts of the frequency range from 20 to 500 MHz. Mobile radio station general application, paging system, howling and cellular work in some areas up to 2000 MHz frequency, which is isolated as for scientific, industrial and community-based health goals. We are currently mastered frequency band 2300-2400 MHz. The most probable frequency range for RCED are mastered a range of up to 1000 MHz, it is also likely to present the application of expansion range up to 2000 MHz, in the long run we should expect improvement in the range RCED to 3000 MHz.

2. Distance range of RCED depends of the energy potential of the transmitter and the receiver sensitivity. The energy potential is the product of the power output amplifier of the transmitter and the gain of the radiating antenna.

Effective gain of the transmitting and receiving antennas depends on the design and the allowable size. Most antennas used in RCED are antennas bayonets type and executed in the form telescopic antenna or pigtail. Analysis of the literature shows that non-optimality of the antennas size leads to the fact that their effective gain is less than – 6 dB.

3. Losses on the road. Loss of power signal on the road can be divided into polarization and distance. Polarization losses due to non-optimal arrangement of radiation and receiving antennas relative to each other, to meet the requirements for concealed of their placement. In this case increased losses can be estimated as 3 dB [1].

Due to the proximity of the propagation path radiosignals RCED to the earth's surface power input signal decreases in proportion to 4-th degree instead of the 2-nd for the propagation in free space [2].

In real terms remove the terrorist to place a bookmark is unknown and may vary within wide limits. The paper proposes used an indicator of the efficiency of protection in the form of the relative ratio, defined as [2]:

$$K = D_p / R_{T\max},$$

where $R_{T\max}$ – the maximum distance between the terrorist from transferring part RCED and place a bookmark receiving part RCED for this magnitude ranks D_p, which still provided failure receiver RCED.

The coefficient K is a function of the transmitter noise parameters and RUVU and does not depend on their mutual arrangement. For broadband noise, and receiver and transmitter antennas interference near the ground surface, indicator of the protection is defined as [2]:

$$K = \left(\frac{P_h G_h D f_r g}{PG D f_h} \right)^{1/4}, \qquad (1)$$

where PG - energy potential transmitter RCED; $P_h G_h$ - energy potential handicaps transmitters Chica

978-1-4244-7468-4/10/$26 ©2010 IEEE

interference Δf_r - effective band pass of the receiver RUVU linear part; Δf_h - the width of the spectrum of the handicap signal; γ - polarization coefficient.

The above analysis of the radiolines control explosive devices parameters makes it possible to make the following main conclusions.

The urgency of the problem makes the search and analyze the different ways opposition radio-controlled means of terrorism, including electronic methods. To counter RCED can be used methods radioblocking and functional defeat (FD). Functional defeat of RCED defeat by powerful single pulse yourself or sequences that cause destruction of the receiver input circuits.

To the FD RCED can be used sighting or barrage handicaps. Sighting handicaps has a significant energy gain compared with the barrage, but its implementation requires information on value of the frequencies at which the works repressed radio electronics. With broadband barrage handicap power output throughout a given range of frequencies. Carrier frequency used by terrorists, and the type of its equip-do in this case is not taken into account.

As broadband barrage handicap may use ultrawideband (UWB) videopulse signals of nanosecond duration. At present, theoretical research and created UWB radio system (RTS) for various purposes.

The energy potential of the director interference depends on the power of interference and antenna gain, determined by the width of its pattern. The use of alldirectional antennas line type leads to a decrease energy potential of RTS suppression RCED. In this for the FR radioexplosive expedient is the use of sectoral RTS with sharp-direct of the antennas.

The analysis of experimental studies and numerical parameters RCED avoided the exclusion to determine the energy and spatial characteristics of the antenna systems for blocking radiolines explosive devices.

Table. 1 shows typical values of the intensity electric field, may be necessary for the FD input channels radioexplosive for different operating frequencies f, the gain D, sensitivity U_{min} and dynamic range of the receiver 60 dB.

Table 1. The magnitude of the electric field, ensuring the normal operation RCED.

f, MHz	L, m	D	U_{min}, μkV	E_{min}, mV/m	E_{max}, V/m
50	0,6	0,2	5	0,367	0,367
100	0,3	0,2	5	0,183	0,183
500	0,3	1	5	0,016	0,016
1000	0,15	1	2	0,003	0,003
2000	0,15	2	2	0,001	0,001
3000	0,1	2	2	0,0007	0,0007

The energy threshold for achieving effective prefect degradation of electronic elements is determined by the thermal relaxation time of the processes, which for semiconductor devices and integrated circuits is $\tau_r \geq 10$ ... 100 ns. When the condition $\tau_p \leq \tau_r$ for amplifycation the thermal effect, causing the degradation of radio-elements, require periodic follow-sequence UWB signals. The expression for the evaluation of the required input power semiconductor device, leading to its degradation has the form:

$$P_{degr} = \frac{K_{П} S_{p\text{-}n}}{\sqrt{\tau_{\Sigma}}}, \qquad (2)$$

where K - constant damage, depending on the type of semiconductor device and has the dimension [kW/(ms)1/2 cm–2]; τ_{Σ} - total time of exposure to the stricken RTS periodically a sequence of pulses; $S_{p\text{-}n}$ – p-n square junction in cm2.

Equation (2) to determine summary power required for degradation of the elements under the action of a pulses periodic sequence at inband impact:

$$P_{degr}^{int} = P_{degr} P_{П}.$$

Table 2 shows the evaluation values of power inband to be applied P_{degr}^{int}, sufficient for the degradation radioelectronic-governmental elements under the influence of ultrashort pulses pack $\tau_{\Sigma} = 100$ ms.

Table 2. Evaluation power P_{degr}^{int}, mW.

Instrument SC type	$K_{П}$	$S_{p\text{-}n}$, cm²	τ_{Σ}, ms	P_{degr}^{int}	
				$K_{СП} = 10$	$K_{СП} = 15$
Diodes SC and transistors	0,1	$10^{-3} – 5\cdot10^{-2}$	10^2	$3 – 2\cdot10^2$	$10 – 5\cdot10^2$
Diodes UHF	0,01	$10^{-3} – 5\cdot10^{-2}$	10^2	0,3 - 20	1 - 50
IC and LIC	0,1	$10^{-4} – 2\cdot10^{-3}$	10^2	0,3 - 6	1 - 20

SC - semiconductor; IC – integrated circuits; LIC - large integrated circuits.

As seen from Table 2, the maximum power for FD inband exposure, necessary for the degradation of semiconductor diodes and transistors amounts to 500 mW. Using data from Table 1, can be calculated signal power required for a normal work of an explosive device:

$$P_{nw} = S \cdot A_{eff},$$

where $S = E_{max}^2 / Z_v$ – density of the flow powerfully received signal; $Z_v = 120\pi$ – impedance of free space; $A_{eff} = G\frac{\lambda^2}{4\pi}$ – effective antenna square.

To achieve maximum power of 500 mW (Table 2), providing the degradation of diodes and transistors,

the intensities of the electric field will have value: for 50 MHz – E = 18 V/m, for 100 MHz – E = 37 V/m, for 500 MHz - E = 82 V/m, for 1000 MHz – E = 165 V/m, for 2000 MHz - E = 217 V/m, for 3000 MHz – E = 308 V/m

Table 3. Signal power, sufficient to undermine radio-controlled explosive device

f, MHz	L, m	D	P_{nw}^{max}, Вт
50	0,6	0,2	$1,98 \cdot 10^{-4}$
100	0,3	0,2	$1,24 \cdot 10^{-6}$
500	0,3	1	$1,86 \cdot 10^{-8}$
1000	0,15	1	$1,63 \cdot 10^{-10}$
2000	0,15	2	$9,1 \cdot 10^{-12}$
3000	0,1	2	$1,98 \cdot 10^{-12}$

On the basis of tactical considerations, the decay of location UWB RTS for FD RCED in combat formations moving column, select the maximum distance of choreographer interference R_{hand} = 20 m.

To estimate the geometric dimensions of the antenna system as a reference we take the average medium frequency spectrum of UWB signal f_0 = 1,5 GHz, for which we define Ehand (f_0) = 180 V/(m Hz). In accordance with the formula for an ideal radiocommunication for the direction of maximum antenna system [3]:

$$E_{hand} = \frac{\sqrt{60 P_{\Sigma} D_{hand}}}{R_{hand}},$$

where P_{Σ} - peak power of the transmitter (on frequency 1,5 GHz); D_{hand} - maximum gain antenna Of UWB RTS, get that $P_{\Sigma} D_{ПОМ} \approx 216\ kW$. Fig. 1 shows the relationship between gain antenna system and the forward power for the given values of the electric field and distance.

Note that in order to reduce losses in polarization, it is desirable to use an antenna with circular polarization of the radiated field. As this antenna is proposed to use the paraboloid of rotation with the irradiator in the form of a conical spiral antenna excited to occur UWB signal videopulse type nanosecond.

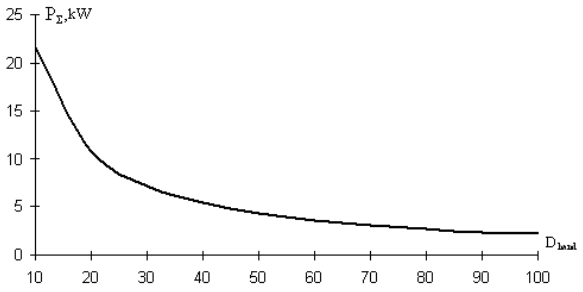


Fig. 1. The relation between gain antenna system and the forward power.

Assume that the gain antenna system $D_{max} = 100$. The gain depends on the electrical characteristics of the antenna feeder system. Using the known the relation [3]:

$$D_{max} = \frac{25000 \div 30000}{2\Theta^0_{0,5P} 2\phi^0_{0,5P}},$$

where $2\Theta^0_{0,5P}, 2\phi^0_{0,5P}$ - the width of pattern, in degrees, we find that for axisymmetric antenna lead-rank beamwidth is 15,80.

Given that the width of pattern can be estimated with formula:

$$2\Theta^0_{0,5P} = \frac{(65 \div 70)\lambda}{d},$$

where λ - wavelength; d – aperture diameter, we find that the aperture size is $d = 0,875$ m.

To increase the radiation resistance should increase the electrical size of the antenna system, as well as the fact that the lowest frequency range $f_{ter} = 100$ MHz ($\lambda = 3$ m), final but we choose a reflector antenna diameter $d = 1,5$ m.

In accordance with the data in Fig. 1 for gain antenna $D = 100$ power UWB RTS will be the value $P_{\Sigma} = 2,2$ kW, taking into account path loss for propagation along the surface of the Earth (30 dB at 50 m).

CONCLUSIONS

Considered the factors that determine the conditions of radiotechnic suppress radiolines control explosive devices, an analysis of experimental studies and an estimate of parameters suppressed radiolines that allows us to determine energetically and spatial characteristics of the antenna system. On the basis of tactical considerations location ultrawideband RTS combat formations moving columns, select a maximal range of producer interference, 20 m and the spectral composition of the signal handicaps of 100 ... 3000 MHz

When the above data, we can consider the coefficient of protection (1). Under the assumption that $P = 1$ W, $G_h = 2$, $\Delta f_r = 20$ kHz, $P_{\Sigma} G_h = 2,16$ kW, $\Delta f_h = 3$ GHz, we find that $K = 0,4$. This value is valid if you delete a bookmark from the site of the terrorist bombing of 50 m.

REFERENCES

1. Khabarov V. B., 'Once again on the prospects of radio controlled explosives devices and methods to combat with them,' *Special equipment*. 2004. № 1. PP. 16-24.
2. Iskhakov B., Kargashin B., Yudin, L. 'Problems of combat radio-controlled explosive device properties', *Special equipment*. 2000. № 2. PP. 8-14.
3. Shifrin Ya. S. *Antennas*. Proc. Allowance. Kh.: VIRTA, 1976. -407 p.

THE USAGE OF EXTREMAL COHERENT INTEGRATION IN THE ALGORITHMS OF PROCESSING OF REFLECTED SYGNALS

Mitrofanov D. G.

[1] Antiaircraft defense Academy, Smolensk, Russian Federation
E-mail: mdgvapvo@yandex.ru

Abstract

The advantages of digital algorithms when processing of radar data are indicated. The directions of coherent combining usage of returned signals in radar systems are shown. The range of new digital algorithms of the movement of air objects estimate parameters (including signals with carrier frequency tuning from impulse to impulse) is described and it is based on the list of degree of taking realizations coherence. The requirement for sound signals parameters, providing single retrieval of information, are determined.

Keywords: Coherent integration, signal processing, signals rebuilding frequency, velocity measurement, turbo propeller effect (TPE), air object (AO), scattering centre (SC), two-dimensional radar tracking image (TDRTI), trajectory instability (TI), range portrait (RP).

In the radar engineering using analogue processing of accepted signals, coherent integration was realized only on the bound intervals in which limits of radiowaves reflection objects were considered as the motionless. Digital processing has allowed to spend necessary transformations with a delay which affected however the quality of accepted decisions. The size of this delay is so small that the radar station personnel (RS) does not notice its presence, and it is considered to be that necessary decisions are developed in real time. Thus quality of the received information is essentially improved that allows passing from statistical approaches to deterministic when making a decision.

For example, at the digital correlation analysis of accepted realizations the estimation of angular behavioral activity of air objects (AO) is possible to conduct [1]. It allows to organize longer coherent addition (accumulation) of signals on intervals of Air Objects fading and to organize more effective averaging of signs on intervals with maximum slew rate of AO. Besides, digital processing has opened a way to coherent addition of signals with frequency tuning (FT) [2].

The tendency of gradual transition from manned to unmanned aviation of streamline forms and small sizes will by all means lead to the decrease of range in typical RS. It grounds the search of ways of artificial increase in working relationship of signal-noise. One of such ways is the increase in duration of coherent accumulation and restoration of coherence, lost in view of trajectory instability (TI) of the flight of AO and influence of other destabilized factors. The new method of formation of two-dimensional radar-tracking images (TDRTI) of AO is based on such principle, its essence is shown in [1,2]. And the specified method assumes the formation of range portrait (RP) objects from reflected FT signals by means of operation of discrete Fourier transformation which as a matter of fact provides the coherent addition of different frequency signals. The range portrait formed by a method of integration (coherent addition of elements) frequency characteristic of AO, represents a set of temporal echoes of such kind as $\mathrm{sinc}(\chi)$. The amplitude of the response of disseminating centre (DC) is proportional to a range frequencies tuning F and the effective area of dispersion (EAD) of a given disperser, and the location of echoes is defined by radial removal from a point of basic range (from RS). The range portrait is the pulse characteristic (PC) of the object, in which the location of each echoes is proportional to the removal of corresponding DC from RS. The possibility of coherent addition of signals at PC reception is analytically proved in [2].

By the construction of RP from the point of view of securing the best coherence the right choice of correlation between the quantity of frequencies N, the period of repetition by impulses T_i and a range of reorganization F is of great importance. This choice should be made on a base of requirement: the width of the narrowest petal of the reflective characteristic AO should prevail over change of the angular position AO during multifrequency dispatch NT_i. Simultaneously it is necessary to provide a condition of a correct choice of a frequency pitch $F / N < c / L_0$, where

978-1-4244-7468-4/10/$26 ©2010 IEEE

L_0 – is a radial size of the object, c – is a speed of distribution of radio-waves. Under insisting of these demands range portrait of AO will have high characteristics, and during a multifrequency dispatch the fluctuations connected with snaking of a glider AO will not take negative.

For strengthening of coherent properties of the frequency characteristic (FC) it is required to eliminate negative phases influence connected with radial movement AO. The method of elimination such phase incursion and the measurement of speed AO in a mode of reorganization of frequency is offered in [3]. The algorithm of measurement in [3] is based on maximization of the coherent sum of components FC. The variations of a method [3] are already received. One of them instead of entropy of vector RP uses dispersion production for the third central moment [4]. Another opens a possibility of measurement of radial speed AO at the limited number of working frequencies in patch of signal building frequency (SBF). At large variety of methods and approaches to processing of the reflected signals all of them are united by a generality of a plan which assumes maximization of coherent properties of accepted reflexions. Corresponding algorithms lead to the hypothetical fading in space of moving AO where upon the reflected signals become sinfaz (quasi in-phase when using SBF).

The using together with a method of inverse synthesizing of the aperture allows forming TDRTRI AO in which SC coordinates are distributed in two mutually perpendicular directions: on longitudinal and cross-section range. The physical base for definition of separate SC on cross-section co-ordinate is a changing of an angle accompanied AO. An algorithmic base of permission SC is coherent addition of the reflected signals in spectral area. The angle changing can be a consequence of rectilinear flight AO and its casual angular moving at TI, shown at snacking of glider in turbulent atmosphere. Distribution of responses SC in TDRTRI depends on their geometric arrangements concerning the centre of support of object (CSO) and parameters of moving AO. The form of responses is defined by a $\mathrm{sinc}(\chi)$ function in two mutually perpendicular directions. The location of each SC in a cross-section direction (spectrum) is defined its secondary Doppler frequency Fm, and the radial arrangement answers the structure of RP.

For correct reproduction in TDRTI an azimuthal portrait AO it is necessary to fulfill the following conditions: the width of a spectrum must be smaller the return frequency of digitization of a signal in time. That is for the maximum frequency of secondary spectrum $F_{\max}$ should inequality $F_{\max} < 1/(NT_i)$ be fulfilled. Simultaneously the step of reorganization of frequency $\Delta f = F/(N-1)$ defines a time interval of unequivocal reproduction of IC object of $T_u = 1/\Delta f$. The quantity T_u should provide qualitative supervision of RP of the largest AO in a distance window $cT_u/2$, where c – a velocity of light. So, the fulfillment of the condition $cT_u/2 > L_{0\max}$, where $L_{0\max}$ – is the maximum radial extent of object is necessary.

As a result of presence of errors of measurement of range R and radial speed V_r, and also in a kind of vibrations of the case of a glider and deviations of the centre of weights AO from a rectilinear trajectory during construction TDRTI phase focusing of adjacent RP is necessary. The algorithm of focusing consists in restoration of coherence, lost in view of errors measurement of distance and input its amendments on base of the measured radial speed.

As alarm signs of recognition in the form of TDRTRI and RP represent the coherent sums of the reflected signals there is a possibility to spend a classification of AO at lower entrance relations a signal/noise.

Coherent addition of signals can effectively be used and in algorithms movement parameters measurement AO. The method of detection AO and measurements since their speeds in RS the circular review of a metric range [5] is developed, for example. The problem of this method is to provide RS the circular review for short term (commensurable with the period of one turn of the aerial on an azimuth) authentic detection AO and measurement of parameters of their movement in pre-affairs of all surrounding air space, and irrespective of type of impellent installations and a movement direction AO. The method uses a principle of compensation of phase races in the reflected signals caused by movement AO, a way of the multiplication the accepted signals on the special phase multiplier also considering possibility of presence at object of radial and tangential components of speed. At the correct selection of a phase multiplier the reflected signals become in-phase, and the vector of their coherent addition is maximized. Upon the maximization of a vector of the coherent sum of the reflected signals true values radial and tangential since speed of movement of object are established. The problem of the compensation of negative influence of high-frequency turbo-propeller peak-phase modulation [6] is solving. The method is intended for the realization in survey RS the metric and decimeter range, used for the control of air space in radar-tracking systems of double appointment, i.e. carrying out of a problem of detection and measurement in interests of the various ministries and departments. Similar radars of the review have the special importance in control systems of air traffic and in landing radar-tracking complexes of air field services of the ministry of civil aircraft.

The advantages of coherent integration are expedient for using in algorithms identification signs AO, caused by display of turbo-propeller effect (TPE). It is especially important in presence of noise and interfering influences when position of turbo-propeller reflex-

ions in a spectrum is shown vaguely. The plan of abstraction of the first turbo-propeller components F_1 is based on that the remaining components arise on multiple frequencies nF_1 where $n = 1,2,\ldots$. The gain-phase parameters of multiple turbo-propeller components are connected among themselves by a generality of the nature of their occurrence. So, the harmonic facts can be put with the account of phase attacks, i.e. to spend their complex addition by a method of return transformation of Fourier. Sequentially touching prospective frequency positions of harmonics TPE in regard to a glider component (at exact indemnification primary Doppler making a glider component in a spectrum occupies zero position on an axis of frequencies), upon maximization the response in the pulse characteristic of the turbo-propeller nature it is possible unequivocally to determine size F_1 used as a sign of identification AO.

Thus, coherent integration is actively used now in digital algorithms of processing of the radar-tracking information. The account of advantages coherent integration allows not only to raise resulting relation a signal-noise, but also to create new methods of allocation of parameters of movement of air objects.

REFERENCES

1. D. G. Mitrofanov, 'The method of building radar images of aerodynamical aircrafts', *Flying*. 2006. № 11. pp. 52–60.
2. D. G. Mitrofanov, 'The integrated adaptive method of building radar images in the systems of twofold purpose direction,' *The theory and control systems*. 2006. № 1. pp. 101–118.
3. D. A. Majorov, V. A. Sevostjanov, D. G. Mitrofanov, 'The measurement of radial velocity of air objects in a mode of rebuilding frequency,' *The measurement technique*, 2008. № 2. pp. 43–47.
4. D. G. Mitrofanov, N. V. Silaev, D. A. Majorov and others, 'The method of measurement of radial velocity of an air object in a mode of reorganization of frequency from an impulse to an impulse at the lowered relation a signal-noise'. G01S 13/58. The demand for the invention № 2008148789.
5. D. G. Mitrofanov, V. P. Lihachev, A. G. Prohorkin, D. A. Majorov, O. S. Trofimov. 'The method of definition of parameters of movement of air objects in survey radars for the account of using the coherent properties of the reflected signals.' G01S 13/42. The demand for the invention № 2009140564.
6. D. G. Mitrofanov, A. G. Prohorkin, 'The methods of indemnification of influence of components of turbine effect at construction of images of air objects,' *Radio engineering*, 2007. № 2. pp. 3–9.

Ultrawideband and Ultrashort Impulse Signals, 6-10 September, 2010, Sevastopol, Ukraine pp. 186-188

SPREADING SEQUENCE SELECTION SCHEME FOR NBI SUPPRESSION IN DS-UWB SYSTEMS

Wang C., Ying R., Wei Y. and Yang Y.

Department of Electronic Engineering, Shanghai Jiao Tong University, P. R. China
E-mail: chengwang.china@gmail.com

Abstract

Interference suppression is important for the ultra-wideband (UWB) systems to operate over spectrum occupied by pre-existing narrowband systems. In this paper, a spreading sequence selection scheme is proposed for code-aided interference suppression in direct-sequence UWB (DS-UWB) systems. Compared with a randomly selected spreading sequence, the presented scheme can ensure the system achieves suboptimal performance. Compared with our recently proposed eigenvector sign (EVS) spreading sequence, an equalizer can be avoided for high speed application by using the selected spreading sequence, which reduces the complexity of system implementation.

Keywords: Ultra-wideband (UWB), narrowband interference (NBI) suppression.

1. INTRODUCTION

Since ultra-wideband (UWB) systems are planned to coexist with other legacy narrowband systems, the transmission power of the UWB devices is strictly limited by the FCC so that the pre-existing narrowband systems will be affected by the UWB signals only at a negligible level. However, these narrowband systems may cause severe interference to the UWB system which may jam the UWB receiver completely [1-3]. Hence, interference suppression is very crucial to UWB systems.

It is well known that the direct sequence (DS) systems have inherent interference suppression capabilities. However, when the spreading gain is restricted and the interfering signal is very strong, the spreading gain cannot provide sufficient degree of interference suppression capability. In this case, some signal processing techniques must be employed to further improve the system performance. The early narrowband interference (NBI) suppression techniques were mainly based on linear predictors or interpolators. Further performance enhancement was obtained by using nonlinear filters. Another important method of NBI suppression is the code-aided technique developed in [4]. It was shown that the code-aided technique significantly outperforms all other linear or nonlinear methods of NBI suppression. Compared with traditional wideband systems, NBI suppression in UWB systems is a more challenging problem due to the restricted transmission power of UWB devices. The authors of [1] investigated NBI suppression in time-hopping UWB based on linear interpolators. The nonlinear prediction filter was applied to a single user DS-UWB system in [2]. In [3], we extended the code-aided interference suppression technique to DS-UWB systems and introduced a new type of spreading sequence named eigenvector sign (EVS) sequence, which significantly improves the NBI suppression capability of the code-aided technique. Due to the lack of sharply peaked autocorrelation for the EVS spreading sequence, some type of inter-chip-interference (ICI) mitigation such as equalizer is required for very high data rate applications, which increases the complexity of the receiver [3]. In this paper, we propose a scheme for finding a spreading sequence that can provide suboptimal performance while also has good autocorrelation properties, thus, an equalizer can be saved which reduces the complexity of the receiver.

2. OUR PREVIOUS WORK

In [3], we extended the code-aided interference suppression technique to DS-UWB systems. The output signal-to-interference-plus-noise ratio (SINR) of the code-aided detector is given by

$$\mathrm{SINR} = P\,[\boldsymbol{s}^T(\boldsymbol{R}_i + \sigma_n^2\boldsymbol{I})^{-1}\boldsymbol{s}], \qquad (1)$$

where P is the power of the received DS-UWB signal, $\boldsymbol{s}$ is the spreading sequence vector, $\boldsymbol{R}_i$ and $\sigma_n^2\boldsymbol{I}$ are the covariance matrices of the NBI vector and noise vector, respectively. From (1), it is clear that the output SINR is a quadratic form. Thus, for a given P, the SINR is dependent on the spreading sequence vector $\boldsymbol{s}$ and the covariance matrices of $\boldsymbol{i}$ and $\boldsymbol{n}$.

Consider a quadratic form $\boldsymbol{x}^T\boldsymbol{A}\boldsymbol{x}$ where $\boldsymbol{A}$ is a real symmetric matrix, it is known that when $\boldsymbol{x}$ takes the eigenvector corresponding to the largest eigenvalue of $\boldsymbol{A}$, the quadratic form $\boldsymbol{x}^T\boldsymbol{A}\boldsymbol{x}$ can be maximized to the value equal to the largest eigenvalue of $\boldsymbol{A}$ [3]. That is, if we use the eigenvector corresponding to the largest eigenvalue of $(\boldsymbol{R}_i + \sigma_n^2\boldsymbol{I})^{-1}$ as $\boldsymbol{s}$, the maximum SINR (i.e., the maximum value of the quadratic form in (1)) could be obtained which equals to the largest eigenva-

978-1-4244-7468-4/10/$26 ©2010 IEEE

lue of $(\boldsymbol{R}_i + \sigma_n^2 \boldsymbol{I})^{-1}$. However, the eigenvector could not be used directly as a spreading sequence because the spreading sequence can only take values of ±1. The underlying idea in [3] is that if we could find a sequence taking values ±1 which is very close, in terms of angle between two vectors, to the eigenvector corresponding to the largest eigenvalue of $(\boldsymbol{R}_i + \sigma_n^2 \boldsymbol{I})^{-1}$, a larger SINR can be obtained which is close to the largest eigenvalue of $(\boldsymbol{R}_i + \sigma_n^2 \boldsymbol{I})^{-1}$. According to [3], the desired spreading sequence $\boldsymbol{s}$ is

$$\boldsymbol{s} = \mathrm{sgn}(\boldsymbol{x}_{\max}) \tag{2}$$

where $\boldsymbol{x}_{\max}$ is the eigenvector corresponding to the largest eigenvalue of $(\boldsymbol{R}_i + \sigma_n^2 \boldsymbol{I})^{-1}$. We name $\boldsymbol{s}$ as the eigenvector sign (EVS) sequence. It has been shown that the EVS sequence can provide a near-optimum SINR performance. The conditions under which the EVS sequence can potentially be used as spreading sequence are discussed in detail in [3].

3. A SPREADING SEQUENCE SELECTION SCHEME

Due to the lack of sharply peaked autocorrelation for the EVS sequence, some type of ICI mitigation such as equalizer might be required for very high rate implementations [3, 5], which increases the complexity of the receiver. In this work, we propose a scheme for finding a spreading sequence that can provide suboptimum output SINR while also has good autocorrelation properties. Thus, an equalizer can be avoided for high speed application by using the selected spreading sequence, which reduces the complexity of the receiver. Base on the idea that if the selected spreading sequence $\boldsymbol{s}$ is very close, in terms of angle between two vectors, to the eigenvector corresponding to the largest eigenvalue of $(\boldsymbol{R}_i + \sigma_n^2 \boldsymbol{I})^{-1}$, a larger SINR can be achieved which is close to the largest eigenvalue of $(\boldsymbol{R}_i + \sigma_n^2 \boldsymbol{I})^{-1}$, we propose a scheme as follows.

- Step 1) Construct a set of *m*-sequences { $\boldsymbol{s}_j$, $j = 1,2,...,n$ }.
- Step 2) Obtain the largest eigenvalue $\lambda_{\max}$ and the corresponding eigenvector $\boldsymbol{x}_{\max}$ of $(\boldsymbol{R}_i + \sigma_n^2 \boldsymbol{I})^{-1}$.
- Step 3) Compute the angle θ_j between sequence vector $\boldsymbol{s}_j$ and eigenvector $\boldsymbol{x}_{\max}$, θ_j is given by

$$\theta_j = \cos^{-1}\left(\frac{|\,\boldsymbol{s}_j^T \boldsymbol{x}_{\max}\,|}{\|\,\boldsymbol{s}_j\,\| \cdot \|\,\boldsymbol{x}_{\max}\,\|}\right), \quad j = 1,2,...,n, \tag{3}$$

where $\boldsymbol{s}_j^T \boldsymbol{x}_{\max}$ is the inner product of $\boldsymbol{s}_j$ and $\boldsymbol{x}_{\max}$, $\|\boldsymbol{s}_j\|$ and $\|\boldsymbol{x}_{\max}\|$ are the norms of $\boldsymbol{s}_j$ and $\boldsymbol{x}_{\max}$, respectively.

- Step 4) Select $\boldsymbol{s}_k$ as the desired spreading sequence where $\theta_k = \min\{\theta_j,\ j = 1,2,...,n\}$, i.e., $\boldsymbol{s}_k$ is the closest sequence vector to the vector $\boldsymbol{x}_{\max}$ in the set.

Note that for the sequence vector $\boldsymbol{s}_j$ of length n, $\|\boldsymbol{s}_j\|$ is $\sqrt{n}$. For a given $(\boldsymbol{R}_i + \sigma_n^2 \boldsymbol{I})$, $\|\boldsymbol{x}_{\max}\|$ is fixed. Consequently, in Step 3) and 4), computing θ_j, $j = 1,2,...,n$ and finding the spreading sequence $\boldsymbol{s}_k$ that yields the smallest angle θ_k is equivalent to computing the inner product $\boldsymbol{s}_j^T \boldsymbol{x}_{\max}$ ($j = 1,2,...,n$) and finding the sequence $\boldsymbol{s}_k$ that provides the largest $|\,\boldsymbol{s}_k^T \boldsymbol{x}_{\max}\,|$, thus, the computation of θ_j is unnecessary, we only need to calculate $\boldsymbol{s}_j^T \boldsymbol{x}_{\max}$ which reduces the computational complexity in step 3).

4. COMPUTATIONAL COMPLEXITY ANALYSIS

As pointed out in [3], it is an NP-hard problem to find the spreading sequence that maximizes the SINR in (1). Our proposal provides a less complex approach to obtain a spreading code that yields a sub-optimum SINR. Suppose one primitive polynomial of degree r is used to construct a set of *m*-sequences of length n, where $n = 2^r - 1$. Hence, there are n *m*-sequences in the set that consists of an *m*-sequence and $n-1$ circular-shifted versions of itself. The computation of the proposed scheme mainly involves two operations. One is the computation of the largest eigenvalue and the corresponding eigenvector of $(\boldsymbol{R}_i + \sigma_n^2 \boldsymbol{I})^{-1}$ at a cost of $O(n^2)$ [3]. Another is the computation of n inner products with complexity $O(n^2)$. Consequently, the computation complexity of the proposed scheme is also $O(n^2)$. An alternative solution to find the *m*-sequence that yields the maximum SINR is by using exhaustive search, which needs to calculate n quadratic forms and involves $O(n^3)$ operations. It is more complex than the proposed scheme.

5. NUMERICAL RESULTS

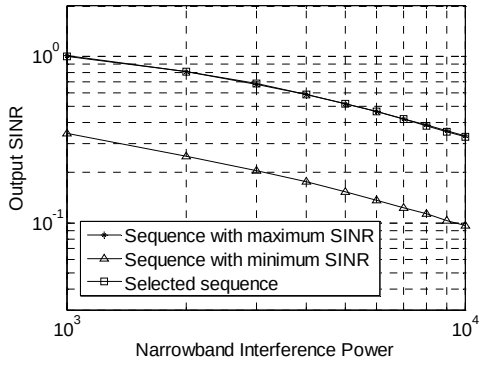
Length 15 and 31 *m*-sequence sets are evaluated[1]. The NBI signal is modeled as a passband Gaussian process [1, 3] with carrier frequency $f_c = 5.8$ G and bandwidth $B = 54$ M, the chip rate is 220 M. Simulations are conducted using the CM1 IEEE 802.15.3a channel models [5]. Partial-Rake (PRake) is evaluated which combines the $L_p = 5$ first arriving paths and maximal ratio combining (MRC) is applied to the outputs of code-aided detectors of the L_p fingers. Without loss

[1] Length 12 and 24 ternary spreading codes are adopted by the 802.15.3a DS-UWB proposal. It has been shown in [6] that *m*-sequences are more effective for mitigating the ICI than ternary spreading codes if BPSK modulation is employed.

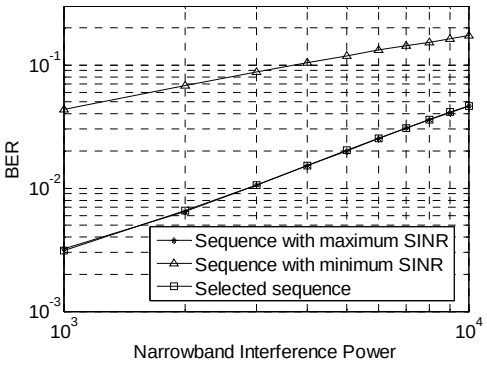
of generality, we assume the total received UWB signal power of the L_p paths is 1 μW, that is

$$\sum_{l=1}^{L_p} P_l = 1 \ \mu\text{W}, \tag{4}$$

where P_l is the received UWB signal power of the l th path. The noise power is held constant at 0.01 μW, while the interference power varies from 10^3 to 10^4 μW. In Fig. 1 (a) and Fig. 2 (a), for a given interference power, the *m*-sequences providing the maximum and minimum SINR's are obtained by an exhaustive search over the entire set for the purpose of performance comparison. The curve of SINR performance of a randomly selected spreading sequence will fall into an area between the curves of maximum SINR and minimum SINR. The BER is obtained by sending 10^6 data symbols for each given NBI power value. The results shown in Fig. 1 and Fig. 2 are averages of 100 channel realizations. Compared with a randomly selected spreading sequence, the selected *m*-sequence obtained by the proposed scheme can ensure the system achieves suboptimal performance. Note that in Fig. 1, the maximum SINR curve and the SINR performance curve of the selected sequence almost coincide with each other.

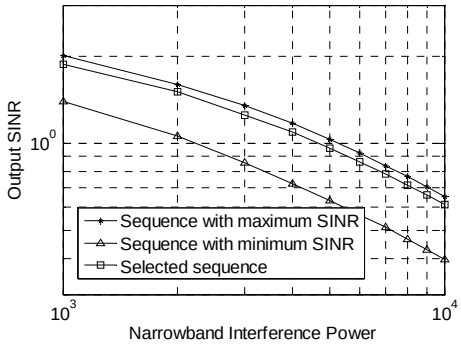


(a) SINR

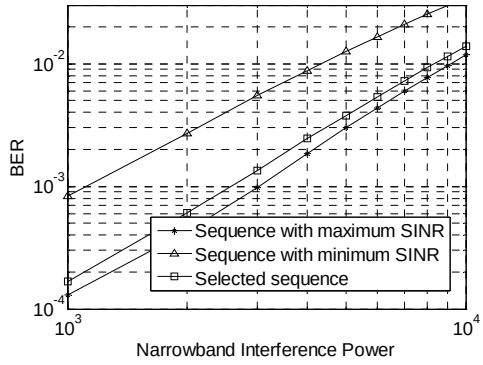


(b) BER

Fig. 1. Performance against NBI using selected spreading sequence of length 15.



(a) SINR



(b) BER

Fig. 2. Performance against NBI using selected spreading sequence of length 31.

6. CONCLUSION

Base on the fact that the output SINR of the code-aided NBI suppression technique depends on the statistical characteristic of the interference and the spreading sequence, we propose a spreading sequence selection scheme. Numerical results show that the code-aided technique can achieve a suboptimal SINR by employing the properly selected spreading sequence. Compared with our recently proposed EVS spreading sequence, the selected spreading sequence has good autocorrelation properties, which help to combat the ICI for very high data rate applications and reduce the system complexity at the receiver.

REFERENCES

1. Wang J., Tung W. T. 2006, 'Narrowband interference suppression in time-hopping impulse radio ultra-wideband communications', *IEEE Trans. Commun.*, 54, 6, 1057-1067.
2. Gaffney B., Fagan A. D. 2006, 'Adaptive nonlinear narrow band interference rejection in ternary DS-UWB," *Proc. IEEE ICC*, 3146-3150.
3. Wang C., Ma M., Ying R., and Yang Y. 2010, 'Narrowband interference mitigation in DS-UWB systems," *IEEE Signal Processing Letters*, 17, 5, 429-432.
4. Poor H. V., Wang X. 1997, 'Code-aided interference suppression for DS/CDMA communications-Part 1: Interference suppression capability', *IEEE Trans. Commun.*, 45, 9, 1101–1111.
5. Molisch A. F., Foerster J. R., Pendergrass M.,2003, 'Channel models for ultrawideband personal area networks', *IEEE Wireless Commun.*, 10, 6, 14-21.
6. Pagani P. 2008, 'Evaluation of the DS-UWB system performance using innovative spreading codes', *Proc. 14th European Wireless Conf.*, 1-5.

WAY OF AN ESTIMATION TRAJECTORY INSTABILITY OF FLIGHT OF THE AIR TARGETS

Prohorkin A. G.

Antiaircraft defense Academy, Smolensk, Russian Federation
E-mail: prohorkin@yandex.ru

Abstract

In article necessity of measurement and the account for systems of construction of radar-tracking images of parameters trajectory instability flight is proved. The method of an estimation of the law of change of angular speed of turn of the air target on sequence range profiles is offered. The estimation of reliability of the received information is made at decrease in the relation a signal/noise.

Keywords: Range profiles, trajectory instability flight.

One of perspective directions in radiolocation is construction and the analysis of radar images. Thus the two-dimensional images reflecting an arrangement of brilliant points on a surface of the aircraft on coordinates of inclined and cross range are considered as the most informative. The allowing along a sighting line is provided due to use of superbroadband signals or signals with reorganization of a carrier frequency. In a direction, perpendicular sighting lines of the purpose, the allowing of brilliant points is provided with the help of a method of inverse synthetic aperture radar imaging. Thus the greatest complexity is represented with the due to of agency trajectory instability (TI) flight for angular speed of change of a foreshortening of the purpose. Now a series of ways of an estimation of parameters TI flight of the purpose with the help correlation characteristics (CC) [1] and characteristics speeds of change of the diagram of backscattering (CSCDB) [2] sequences of the signals reflected from the target is developed. Deficiency of the specified ways is that their implementation is possible only at tall relations signal/noise as machining of the reflected signals does not assume their accumulation with the help of direct addition or engaging of algorithms of Fourier transform. Besides use of these ways at construction of radar images demands addition in signals with reorganization of frequency of monofrequent pulses.

At change of a target aspect ratio for due to trajectory instability distances up to separate brilliant points change unequally. Owing to an interference of the signals reflected from separate brilliant points in limits its range of an element, the amplitude and a phase making range profiles (RP) eventually will change. The more angular speed of change target aspect ratio, the will be more significant a difference between the same elements contiguous RP. Thus, for an estimation of angular speed of turn of the target it is necessary to analyze speed of change of complex amplitude of the same elements of sequence RP. The most expedient is the finding of magnitude of changes sinus and cosines quadrature components contiguous RP as they contain the information, both on amplitude and on a phase of the given element of range.

In this case formation trajectory characteristics (TC) will be will be defined by the following expression

$$u_n = \frac{1}{K}\sum_{k=1}^{K}\left\{\left|\dot{H}_{kn}\right|\cos\phi_{kn} - \left|\dot{H}_{k,n+1}\right|\cos\phi_{k,n+1} + \left|\dot{H}_{kn}\right|\sin\phi_{kn} - \left|\dot{H}_{k,n+1}\right|\sin\phi_{k,n+1}\right\}, \quad (1)$$

where $\left|\dot{H}_{kn}\right|\cos\phi_{kn}$ and $\left|\dot{H}_{kn}\right|\sin\phi_{kn}$ – accordingly sinus and cosines quadrature components RP; K – quantity of elements in RP; k – element number in RP; $n = 1,\ldots,N-1$ – serial number of RP.

In interests of decrease of agency of noise on form TC for machining it is necessary to use only those elements RP in which there are reflections from scattering centre of the sail plane of the target. For this purpose in first RP numbers of elements k are defined, the amplitude of a signal in which exceeds the established threshold level determined by an average level of noise which can be calculated as arithmetic-mean amplitudes of all elements RP. Formation TC is expedient for carrying out by comparison of complex amplitudes only in these elements RP.

Formed TC reflects only character of change of angular speed target aspect ratio, instead of its absolute value. Therefore received with the help of expression (1) characteristic is necessary for normalizing.

For check of serviceability and efficiency of an offered way imitating modeling reflection from the plane such as B-52, making flight with the following parameters was used: range of 30 km, height of 1000 m, an initial aspect ratio 33º, speed of 100 m/s. Thus rovings a

978-1-4244-7468-4/10/$26 ©2010 IEEE

glider of the plane for the due to TI flight with amplitude 2º and angular speed 1,5 º/sec were modeled. For construction of everyone RP reflections of 128 signals with reorganization of frequency in a range of 150 MHz and the period of following 30 мкс were used.

In Fig. 1 it is present TC, generated by results of the described imitating modeling with the help of expression (1). For an opportunity of an estimation of the received results in Fig. 1 dashed line present true law of change of angular speed of rotation of the purpose.

Originally formed TC has very bluffy, and for convenience of search of locals extremums carry out its smoothing. That at smoothing to not lose the information on position of groups of the reflected signals corresponding to various angular speed of rotation of the target, duration of the individual sample T_{is} used for smoothing TC, should not exceed a quarter of minimal period TI T_{TI}. The amount of readout TC N_c used for its smoothing, in this case should not exceed the relation of a quarter of period TH to time of formation of one RP T_{RP} $N_c \le T_{TI} / 4T_{RT}$. That is, time of accumulation N_c of readout for smoothing TC should not exceed $T_{TI} / 4$. In view of it expression for calculation of values smoothed TC can be presented as

$$u_{sm\ n} = \frac{1}{N_c} \sum_{m=1}^{N_c} u_{n+m-N_c/2} \ . \qquad (2)$$

Fivefold smoothing generated TC a method sliding average (at $N_c = 100$) transforms TC to a kind shown in Fig. 2.

Smoothed TX almost authentically displays the law of change of angular speed of turn of the target. It is necessary to take into account, that formation TC was made at absence of noise. It is obvious, that the given destabilizing factor will render negative influence on selfdescriptiveness as TC, and developed before ways.

At high relation signal/noise ($q = 40$ dB and more) all estimated characteristics precisely enough reflect the law of change of angular speed of turn of the target. At reduction of the relation signal/noise in estimated characteristics the distortions shown in change of their form and essential reduction of depth of modulation start to arise. For increase in depth of modulation of estimated characteristics and their preservation selfdescriptiveness it is offered to carry out them normalization in limits from 0 up to 1. The result of use of the given procedure at formation of estimated characteristics for the relation $q = 5$ dB is resulted in Fig. 3.

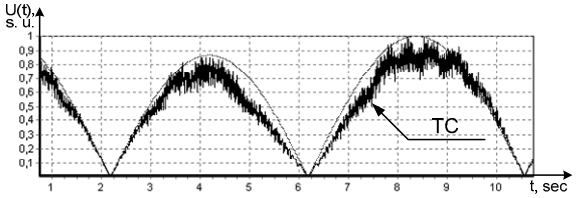


Fig. 1. Trajectory characteristic of the plane B-52.

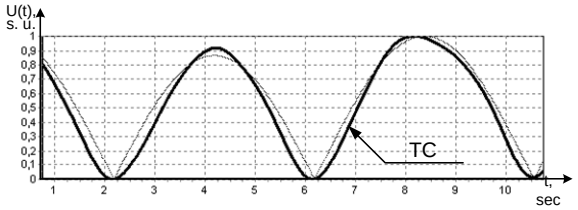


Fig. 2. Trajectory characteristic of plane B-52 after smoothing.

Normalization in limits from 0 up to 1 gives more visual mapping estimated characteristics and allows to compare them to true legitimacy of change of an angular velocity of turn of the target. Effect of noise results to that at $q = 5$ dB the CSCDB undergoes rather significant deformation and does not represent the true law of an angular velocity of twirl of the purpose. The CC in part saves the selfdescriptiveness, but in it the additional undershootings essentially worsening possibility of its practical usage start to appear. Trajectory characteristic of noticeable deformation does not undergo. It is stipulated by that for its forming signals after conducting the Fourier transforms having at the expense of storage much the higher ratio signal/noise use. Thus antijamming ability TC that will be higher, than a lot of frequencies uses in signals with modification of frequency for forming RP.

For quantitative matching efficiency and stability of the offered way with earlier known ways in conditions of the increased level of noise it is offered to use estimations Z_j under the least squares method [3], calculated for everyone j th relation signal/noise

$$Z_j = \sum_{n=1}^{N-1} \left(u_{sm\ n} - u_{TI\ n} \right)^2 , \qquad (3)$$

where $u_{sm\ n}$ – value of the estimated characteristic normalized from 0 up to 1, $u_{TI\ n}$ is true legitimacy of change of an angular speed of turn of the target normalized from 0 up to 1.

In Fig. 4 results of a quantitative estimation of correspondence of the surveyed estimated characteristics to the real law of change of an angular speed of turn of aspect ratio of the target are instanced at q from –7 up to 25 dB. In interests of rise of visualization of schedules smoothing the obtained results was made.

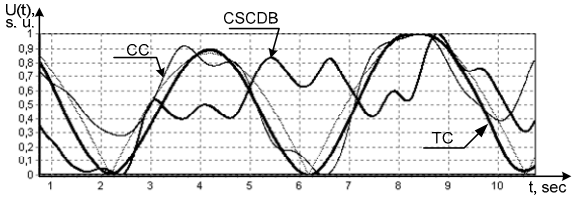


Fig. 3. Estimated characteristics generated at the relation $q = 5$ dB and use normalization from 0 up to 1.

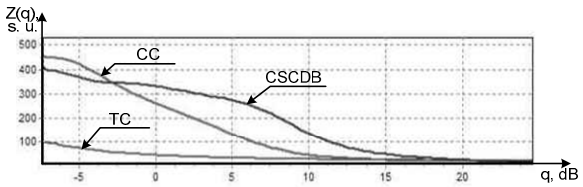


Fig. 4. Quantitative estimation of selfdescriptiveness estimated characteristics at various relation signal/noise.

The estimation under the least squares method shows, that at the relation $q = 20$ dB and more estimated characteristics of essential differences have no signal / noise ($Z = 21...25$). At lowering up to $q = 10$ dB the increase in estimations Z describing errors of forming, for CC $Z = 50$, for CSCDB $Z = 140$, while similar deformation in TC start to originate only at $q = -1$ dB ($Z = 49$) is observed. It allows to make a conclusions on applicability TC for analysis TI of flight at much lower relation signal/noise, in comparison with known ways.

Thus, the offered way allows to form reliable estimations of the law of change of an angular speed of turn of the target at considerably lower relation signal/noise, in comparison with known ways. The way can be recommended for usage in systems of construction of radar images for their adapting to agency TI of flight.

REFERENCES

1. Mitrofanov D. G. 'Method of reconstruction of radiolocation images for aerodynamic aircraft,' M.: *Polet*, 2006. № 11. P. 52–60. (In Russian)
2. Prokhorkin A. G., Mitrofanov D. G., Nefedov S. I., Fomin E. A., 'Research of Doppler images of aircraft to account of its transverse,' M.: Radiopromyshlenostj, 2009. # 1. (In Russian)
3. Ventcelj E.S., *Probability theory*, M. Vyshaya shkola, 2001. 575 p. (In Russian)

BIOLOGICAL EFFECTS OF ULTRAWIDEBAND RADIATION

[1] Shckorbatov Y. G., [2] Kolchigin N. N., [1] Pasiuga V. N., [2] Kazansky O. V.

[1] V.N. Karazin Kharkiv National University, Institute of Biology, Kharkiv, Ukraine
E-mail: shckor@univer.kharkov.ua
[2] V.N. Karazin Kharkiv National University, Department of Theoretical Radiophysics, Kharkiv, Ukraine
E-mail: Nikolay.N.Kolchigin@univer.kharkov.ua

Abstract

Research works on biological effects of ultrawideband pulsed radiation which were realized in the Kharkiv National University are summarized. Investigations were done on different biological objects: human cells, *Artemia sp.*, *Drosophila melanogaster*. Biological effects of ultrawideband pulsed radiation were observed in a range from 10^{-6} to 10^{-2} W/cm^2. Different experimental models revealed different sensitivity to low-level radiation. The most sensitive to low-level radiation was the *Artemia sp.* hatching percentage (10^{-6} Wcm^2). Human cells were less sensitive to radiation (10^{-4} W/cm^2). Irradiation of more power (10^{-3} W/cm^2) induced dominant lethal mutations (DLM) in *Drosophila*. In our opinion, the most appropriate method for assessment of biological effects of irradiation is evaluation of heterochromatin granules quantity (HGQ) in human cells.

Keywords: Buccal epithelium cells, *Drosophila melanogaster*, *Artemia sp.*, heterochromatin granules quantity, dominant lethal mutations.

1. INTRODUCTION

Ultrawideband radiation is widely applied in technique but its biological effects are not enough investigated. In the work [1] the effects of ultrawideband irradiation on the rate of biochemical reactions and cell membrane properties are demonstrated. Series of works were realized in the Kharkiv National University demonstrate biological effects of ultrawideband pulsed irradiation on human cells [2], mutation rate in *Drosophila* [3], *Artemia sp.* hatching and chromatin structure [4], but comparative analysis of this effects was not done before.

2. MATERIALS AND METHODS

2.1. BIOLOGICAL OBJECTS

In our investigations we used different biological objects.

Human buccal epithelium cells were obtained from donors of different age (from 17 to 53). Cells were obtained from the inner surface of cheek by sterile spatula and placed in buffer solution of the following composition: 2.89 mM calcium chloride, and 3.03 mM phosphate buffer, pH = 7.0. Irradiation of cells was realized in a drop of cell suspension (10 μl) placed on the glass slide. Immediately or after a definite period of time after irradiation cells were stained by 2% orcein solution in 45% acetic acid. In stained cells heterochromatin granules quantity (HGQ) was counted. In each variant of experiment the 30 nuclei were analyzed. The mean HGQ and standard error of the mean was calculated.

We used *Drosophila melanogaster* (stock Canton-S) in our experiments. *Drosophila* was cultivated in standard conditions (25°C, on yeast medium). The viability of *Drosophila melanogaster* after irradiation was evaluated by the quantity of adult insects developed from the irradiated eggs of one synchronic laying. Eggs were hatched during 3 hours by 30 *Drosophila* females of 7 day age. The frequency of dominant lethal mutations (DLM) was determined by the standard method [5]. We counted quantity of eggs in hatchings made by 10 previously irradiated *Drosophila* females during 8 hours. The frequency of eggs stopped their development 9 hours after laying was used as a early dominant lethal development mutations frequency. The frequency of eggs stopped their development later than 9 hours after laying was used as a late dominant lethal development mutations frequency. The frequency of mutations in non-irradiated *Drosophila* females was used as a control.

We also used *Artemia sp.* as model object in our investigations. Crustacean of the order *Anostraca* (class *Branchiopoda*) *Artemia sp.* lives in salt water lakes throw ought the world. In our experiments we used air dry cists of *Artemia* stored before experiment at a room temperature for 3 years. The viability of *Artemia* cists was assessed by hatching percentage. Cists hatched in salt water (35‰) for 48 hours. After irradiation before hatching cists were stored for 20 days. In nauplia (larvae) we estimated the number of HGQ.

978-1-4244-7468-4/10/$26 ©2010 IEEE

In all experiments we used "blind" method and sham operated control. All data were processed by t-Student method and ANOVA test.

2.2. EXPOSURE OF SAMPLES

We used original experimental setup developed at the Department of Theoretical Radiophysics. The short pulse generator formed the sequence of pulses with amplitude 25 V and a pulse duration 500 ps at the half of pulse height. Pulses were emitted at series with iteration frequency 1 MHz. The surface power of irradiation was in the range from 10^{-6} to 10^{-2} W/cm^2. The temporal and frequency characteristics of impulse are presented in Fig. 1. Exposure time in all experiments was 10 s.

3. RESULTS AND DISCUSSION

The data obtained on *Artemia* revealed the hatching stimulation even at the lowest of tested of pulse ultrawideband irradiation intensity (10^{-6} W/cm^2) (Fig. 2).

As one can see effect of hatching stimulation is of trigger type – increase of irradiation power does not result in increase of biological effect.

Ultrawideband pulsed irradiation induced an increase of the HGQ in new-born *Artemia* nauplia (Fig. 3).

As a test object we also used the cells of human buccal epithelium. Pulse irradiation induced chromatin condensation in this type of cells, but the sensitivity of cells of different donors to irradiation was different. The power of 10^{-4} W/cm^2 induced an increase of HGQ in cells of all donors (Fig. 4)

The phenomenon of chromatin condensation under the influence of low-level pulse irradiation is reversible.

For irradiation of power 10^{-3} W/cm^2 the cell recovery was observed after 2 hours, but for 10^{-2} W/cm^2 it was not observed at all [2].

Drosophila melanogaster fecundity proved to be stable to low-level pulsed irradiation: exposure of *Drosophila* eggs to irradiation in the range of 10^{-5} – 10^{-2} W/cm^2 do not influenced the number of adult insects developed from the synchronized leis (Fig. 5).

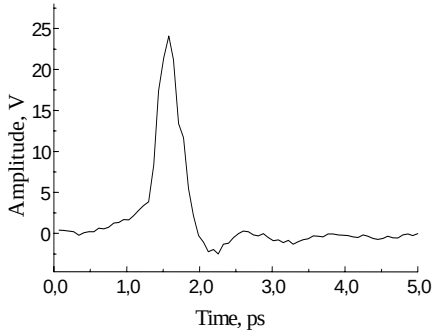


Fig. 1. Time characteristics of test impulse.

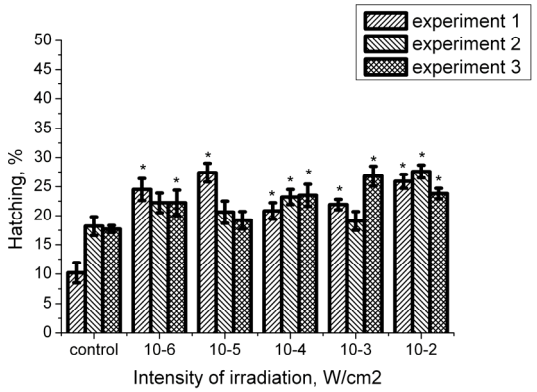


Fig. 2. Influence of ultrawideband pulsed irradiation on hatching % of *Artremia*, from [4], with changes

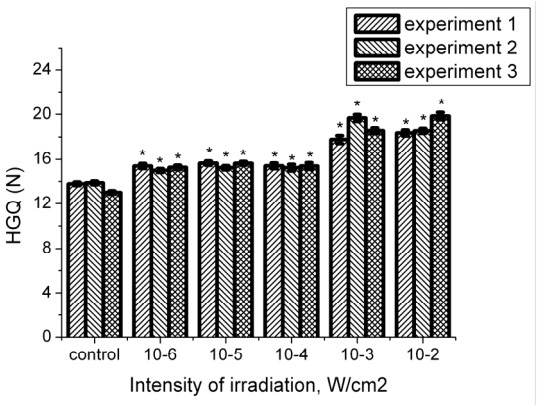


Fig. 3. Influence of ultrawideband pulse irradiation on the state of chromatin in Artemia cell nuclei, from [4], with changes.

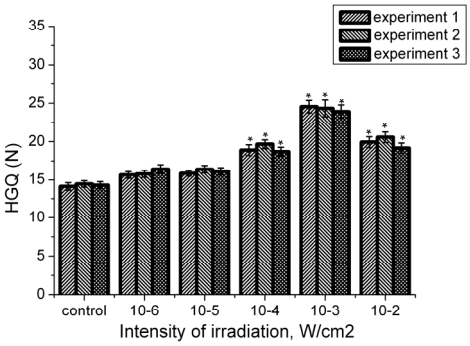


Fig. 4. Influence of ultrawideband pulse irradiation on the state of chromatin in buccal epithelium cell, from [2].

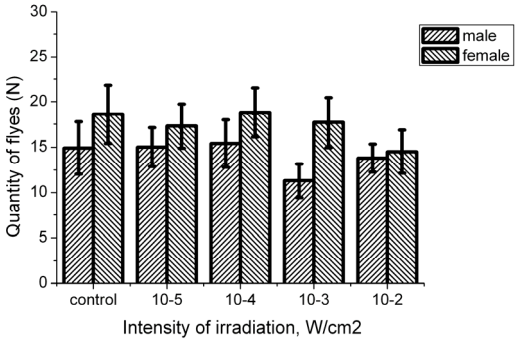


Fig. 5. The number of flies developed from synchronous hatches irradiated by ultrawideband pulse irradiation, from [3].

On the other hand, pulsed irradiation induced dominant lethal mutations (DLM) as it was revealed by the egg test [5] (Fig. 6).

The effect of DLM induction depends on the irradiation power. The effects were observed at the irradiation power of 10^{-4}-10^{-2} W/cm^2.

Comparing the results obtained applying different experimental model systems one can conclude that the lowest power threshold for sensitivity of different biological systems to the ultrawideband pulsed radiation is 10^{-4} W/cm^2. Human cells are, to our opinion, the object that most accurately reflects the sensitivity of the human organism to external effects. Therefore, we proposed to evaluate the biological impact of ultrawideband radiation by the effect of chromatin condensation in human buccal epithelium cells [6}.

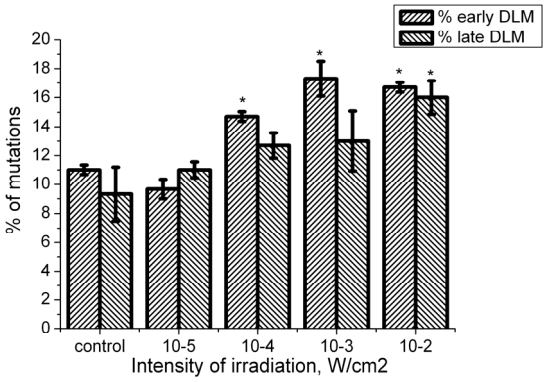


Fig. 6. The number of DLM in the progeny of flies subjected to ultra wideband pulse irradiation at the egg stage, from [3], with changes.

4. CONCLUSION

Ultrawideband pulsed irradiation reveals great biological activity. Even at a short exposure time (10 s) the significant changes in nuclear chromatin condensation within the range of power of 10^{-6} – 10^{-2} W/cm^2 (*Artemia*) and 10^{-4} – 10^{-2} Wcm^2 (human cells) are induced.

On the organism level the ultrawideband pulsed irradiation induces increase of Artemia hatching (10-6 – 10-2 W/cm2) and DLM induction in Drosophila (10-4 – 10-2 W/cm2), but not induces changes in fecundity of Drosophila.

Summing up, all tested biological objects reveal the close sensitivity to ultrawideband pulsed radiation, the minimal power density that induces biological effect at exposure time 10 s in different experimental models (except *Artemia*) is about 10^{-4} W/cm^2. Human buccal epithelium cells are the most adequate object for investigations of human-related biological effects of ultrawideband pulsed radiation and may be recommended for laboratory test assay of biological effects of low-level ultrawideband pulsed radiation.

REFERENCES

1. Albanese, R., Blashak, J., Medina, R., Penn, J. 1994, Ultrashort electromagnetic signals: biophysical questions, safety issues, and medical opportunities. *Aviation, Space, and Environmental Medicine*, v.65, N5, p.A116-A120.
2. Shckorbatov, Y. G., Pasiuga, V. N., Kolchigin, N. N., Batrakov, D. O., Kazansky, O. V., Kalashnkov, V. V. 2009, Changes in the human nuclear chromatin induced by ultra wideband pulse irradiation, *Central European Journal of Biology*, V.4., P. 97-106.
3. Shckorbatov, Y., Pasiuga, V., Shakina, L., Grabina, V., Kolchigin, N., Ivanchenko, D., Kazansky, O., Bykov, V. 2007, *Drosophila melanogaster* viability and mutability under the influence of low energy microwave monochromatic and ultra wideband impulse field, *6th International Conference on Antenna Theory and Techniques*, Sevastopol, 2007, P. 289-291.
4. Shckorbatov, Y. G., Rudneva, I. I., Pasiuga, V. N., Kolchigin, N. N., Ivanchenko, D. D., Kazanskiy, O. V., Shaida, V. G. 2009, hatching of eggs of artemia and change of the state of chromatin under the influence of electromagnetic fields, *CriMiCo 2009*, Sevastopol, P. 360-362.
5. Landa, V., Sula, J., Marec, F., Matha, V., Soldan, T. 1991, Methods for Assessing Exposure of Insects. In: Methods for assessing exposure of human and non-human biota, Edited by Tardiff R. G., Goldstein B., Published by John Wiley & Sons Lid.
6. Shckorbatov, Y.G., Kolchigin, M.M., Pasiuga V.N., Kazansky O.V. Method of determination of the biological effect of a ultrawideband pulsed radiation. Patent for useful model number 35375. Registered in the State Register of Patents of Ukraine for 10.09.2008. Bul. Number 17 (in Ukrainian).

THE DEVICE FOR REMOTE MONITORING OF HUMAN'S HEARTBEAT

Shirokov I. B., Slesareva A. V., Korepanov A. L.

Sevastopol National Technical Universithy (SNTU), Sevastopol, Ukraine
E-mail: shirokov@ieee.org

Abstract

This article describes creating principles of the device intended for round-the-clock human breath and heart rate monitoring. This device can be used in intensive care unit's and burns departments, maternity hospitals and also by EMERCOM employees. Heart rate detection is possible because of the Doppler effect. The Doppler frequency selection is based on the homodyne method of signal conversion.

Keywords: Heart rhythm, homodyne method, radar, Doppler effect.

1. INTRODUCTION

In the medicine of the critical states the problem of the clinical observation takes a special place because the patient's current condition tracking can have essential importance. Physician getting the information which describes the control processes of the main vital signs by monitoring the patient's heart rate. Utilization of this information is the perspective human body's state control method. Currently, medical equipment intended for round-the-clock patient state monitoring is bulky and has a direct contact with patient's body. This equipment's sensors are connected with external recording equipment by tubes and wires. For the critical patients in intensive care units and burn departments such contact creates discomfort condition. In addition, it is undesirable to use on the patients with heavy skin wounds. The last statement is also refers to the newly-born babies state controlling, especially to the prematurely born children state controlling. The real need in physiological parameters remote detection exists.

2. MAIN PART

The developed device pointed to solve the problem of the heart rate and breath's parameters non-contact monitoring. This can be achieved by applying the method for diagnosing the human's vascular system quality using a pulse wave velocity narrowband measuring device. The device is based on the method of probing the human body by electromagnetic waves. The radar probing main advantage is the ability of electromagnetic waves to spread in a variety of dielectric media with a high degree of heterogeneity and, besides, it is possible "sensing reflection", i. e. when transmitter and receiver located at the same side of the object. The study of complex environments with one-sided approach is the main area of the radar probing application. Radio locators, used in these cases, known as subsurface in the literature [1-3].

In human's bodies, objects which have more or less periodic fluctuations are the reduction of the heart muscle (the frequencies range (0.8...3) Hz) and fluctuations in ore cell in the respiration process (the frequency range (0.1…0.5) Hz). The particular frequency determines by physical activity and body condition of the subject. When probing the human body, electromagnetic waves reflect from the media interfaces with different inductive capacity whose value primarily depends on the blood percentage in a given organ of the body. The strongest reflections are possible from the interfaces air – chest, the chest – the lungs, as well as from the interface the body tissue – blood. The latter is especially contrasted to the heart and to large vessels.

Consider the principle of the suggested device (Fig. 1). The device consists of microwave oscillator (MWO), microwave amplifier (MWA), directional coupler (DC), two antennas (A1) and (A2), mixer (MIX), low-frequency amplifiers (LFA), low-pass filter (LPF), microcontroller system (MC), and personal computer (PC).

Antenna A1 is a transmitter's one, antenna A2 is a receiver's one. The amplified with high-frequency

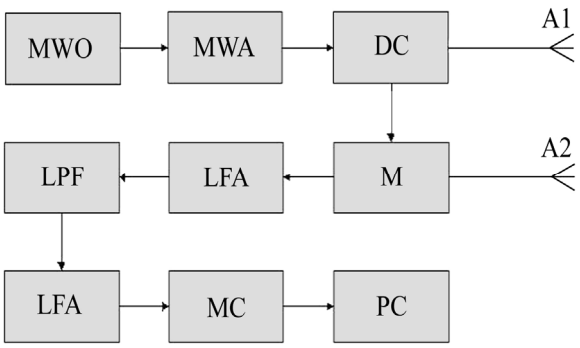


Fig. 1. The device functional scheme.

978-1-4244-7468-4/10/$26 ©2010 IEEE

amplifier HFA signal from the high frequency generator HFG feeds antenna A1.

The irradiation of the human organism with a harmonic signal with a frequency of about 1,5 GHz forms the reflected from the human body wave. Due to the blood movement through the vessels, the reflected from the human body wave has an extended spectrum. Highlighting the Doppler frequency shift by comparing the incident and reflected from the human body waves, we can determine the heart rate.

The part of falling microwave power (through directional coupler) and the reflected from the human body microwave power (through the antennas A1 and A2) both arrives at the mixer M and the mixer's output signal with a difference frequency is formed. This scheme is called homodyne, and upon very high frequency of the fundamental signal it allows to highlight the frequency of the Doppler shift, which in our case will be the only units Hertz.

We use the single-frequency operation matter as we don't need in distance determination, as it was described in previous researches. The demands on antenna design are not rigid in this case.

The reflected microwave signal is very weak and it presences on a basis of noise. Low frequency signal, cleaned from noise and amplified (through low-pass filter and two-stage low-frequency amplifier), enters for further processing into the analog-digital converter of the microcontroller.

In any case, the signal which is presented on an input of microcontroller system is not regular. This signal consists from several spectral components and the result signal is the sum of these components. These components are caused by human's breath, human's heartbeat, human's movement, and movement of personnel and other things in nearby proximity to person under the test. So, we can not use the simplest signal processing procedure to discriminate each of these signals, at least two of them: signal which corresponds to human's breath and signal which corresponds to human's heartbeat.

Microcontroller carries out the spectral analysis of this composite signal. Certain requirements are maintained to the microcontroller as the spectral analysis must be carried out in real time. Microcontroller must have essential memory's volume and essential speed. We used microcontroller of Microchip PIC32 family in presented application. The number of digits in 32 lets us to implement needed speed of signal processing in real time.

Microcontroller System consists of proper microcontroller, LCD display and interface to PC. We implemented USB interface in order to communicate to PC. Mentioned interface was more complicated than ordinary RS232 one, but last interface usually is not supported in modern laptops.

The appearance of the prototype device is shown in Fig. 2.

The device measures heart rate and breathing of the patient remotely and without contact at a distance of

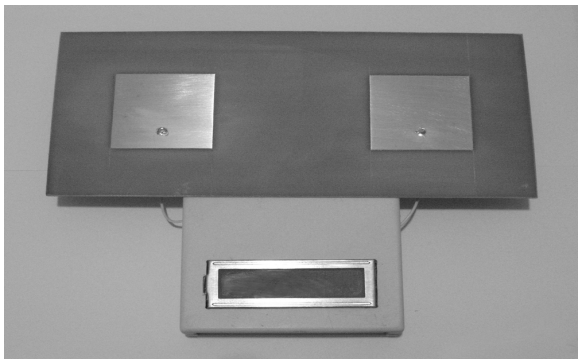


Fig. 2. Appearance of the prototype device.

30 cm to 2 m. Output information in the form of numerical values of respiration and heart rate after fixed time interval (1 minute, for example) is shown on the device's LCD and is transmitted to PC by the communication channel. PC lets us to save the history of controlled parameters, which is essentially useful for medical observations and diagnosis. Described device can operate as stand alone unit as well.

Also, the device calculates the important for clinicians indices of heart rate variability, namely, mode, mode amplitude, variation swing and tension index (a method of variation pulsometry).

3. CONCLUSION

The main feature of the proposed device is the implementation of reading information by non-contact way, through clothing, and there are no adverse effects on human. There is availability and adjustment possibility to change the data-acquisition process (duration of a deposition, sensitivity, etc.) via computer interface; there is the possibility of data long-term recording for subsequent treatment.

The developed device for remote monitoring of human's pulse and breath allows quickly, easily and effectively carry out registration of human's physiological parameters in medicine of critical states. Also, the device can be used by the Rescue Service and EMERCOM to quickly diagnose victims directly on the event place.

Further, described approach can be useful in mining industry for monitoring of health state of mine's workers [2].

REFERENCES

1. Vasiliev I.A., Ivashov S.I. and Makarenkov V.I. "RF Band High Resolution Sounding of Building Structures and Works" *Proc. of the 7th Int. Conf. on GPR'98*, University of Kansas, Lawrence, Kansas, USA, 1998, vol. 2, pp. 707-710.
2. Shirokov I.B., 'The Way of Search of Obstruction Victim and Remote Control of His Heartbeat,' *Patent Ukraine*, № 89933, Op. v B. № 5 from 10.03.2010. (In Russian)

SUSCEPTIBILITY ANALYSIS OF COMPLEX INFRASTRUCTURE TARGETS

[1] Gardner R. L. and [2] Stoudt D. C.

[1] Consultant, Naval Surface Warfare Center, Dahlgren Division, Q04
E-mail: Robert.L.Gardner@verizon.net
[2] US Navy Distinguished Engineer for Directed Energy, Naval Surface Warfare Center, Dahlgren Division E-mail: DLGR_NSWC_Q04_DE@navy.mil

Abstract

Previously, the authors explored the use of hybrid functional models to find failure modes of simple infrastructure models. Pulsed excitation was shown to be effective in causing failures in simple oscillators and related simple models, using the energy of the circuit to bring about the failure. A simple SCADA system was used as a practical example of these failure models in infrastructure systems. In this paper, we extend this technique to clusters of SCADAs (as might be used in real systems). The first demonstration shows that unwanted excitation of odd functional resonance modes can cause failure of one of these clusters. Finally, functional failures in complex interconnects between the SCADA units can cause system failure.

Keywords: High-power microwave, high-power electromagnetics, susceptibility, infrastructure failure.

1. INTRODUCTION

High-power microwave (HPM) tests have shown that extended illumination of some complex targets has shown lower thresholds than short-pulse illumination [1,6]. The extended illumination can consist of hundreds of microseconds or longer pulses. The short-pulse illuminations typically are single shot or few-pulse illuminations of around 100 nanoseconds duration. This variation in sensitivity leads us to believe that more complex systems can be caused to fail from repeated but relatively weak insult. We have used an analysis tool called SCICOS [7,10] that is particularly designed to model the functional behavior of complex systems.

Hybrid Models [8] predict the behavior of systems with multiple states. A car with a manual transmission would be an example of such a system. In each gear, the car has a certain characteristic RPM versus speed curve. If the transmission is shifted into the lowest gear at the highest speed failure can occur. If the gear shift occurs too quickly then failure also is likely. Hybrid system failures often occur when there is an unwanted or abrupt transition between discrete states.

To introduce the application of the hybrid technique, we use the well-known Chua circuit [9]. The Chua circuit is an oscillator that can be stable or unstable depending on the parameters. In this case, we use a stable configuration but shown the transition into instability from an unwanted, repeated transient, as described above.

In [7] the authors described various failure mechanisms of a SCADA system that is designed to maintain a water level in a tank. This SCADA trainer is used because there is an apparatus available for testing of our models in Dahlgren [2]. The NSWC test facility is used to test SCADAs and other related equipment against electromagnetic insult. The main part of this paper considers the extension of the model to include three SCADA trainers with complex interactions and unwanted drive to show failure through excitation of odd modes of fluid movement between the tanks.

2. DRIVEN CHUA CIRCUIT

The Chua circuit is one of the simplest circuits that can show complex chaotic behavior and we use it here to represent an example of a failure mechanism caused by the injection of repeated pulses [9]. Fig. 1 shows a schematic of a Chua circuit.

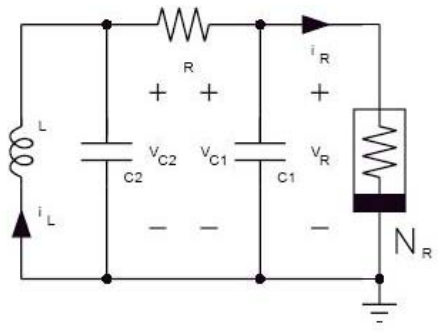


Fig. 1: Chua Circuit Schematic.

978-1-4244-7468-4/10/$26 ©2010 IEEE

Most of the circuit consists of an RLC oscillator, but the key component is the nonlinear element to the right of the diagram. Not only is that element nonlinear, it is also active, so when we inject a disturbing signal into the circuit, we will also attempt to draw energy from this source to help cause an instability in the system. We have solved the three coupled nonlinear differential equations represented by the circuit with the freely available code ScicosLab [10]. ScicosLab is a system that is designed to help solve hybrid models [7]. Fig. 2 shows the solution diagram for the three differential equations.

Note the injection of a field-induced voltage onto one of the capacitors. Repeated injection causes the originally stable to system to run away as shown in Fig. 3.

The 3 axes of the diagram are the current through the resistor and the voltages across the two capacitors. The excitation is from a repeated square wave and the impact on that drive on the circuit behavior is apparent near the center, but not as it runs away.

3. SCADA SYSTEM

The Directed Energy Technology Office uses a large open air test facility to test the effects of electromagnetic waves on complex systems. The building has a number of electronic systems installed to provide realistic testing of those systems [9]. Figure 3 shows a photograph of one of the SCADA systems used.

There are two SCADA system trainers at NSWC. One of those systems has a tank with a level controller. The level of the tank is controlled by the pump and the release valve for the drain as shown in Fig. 4. This layout is a combination of the two test facility SCADAs.

The tank has a level sensor that is used to control the level in the tank and the level of the liquid in the tank represents the independent variable in the differential equation describing the system. There is a gravity drain proportional to the square root of the level, so that the equation is nonlinear. The SCICOS solution is shown in [7]. In the following section three of these SCADA trainer models are used to demonstrate a more complex failure mode.

4. COMBINED SCADA MODEL

Fig. 5 shows an initial simple version of the combined system. The square wave generator represents the flow into the system, where the -2 amplifier forces flow from both of the outer SCADAs through the center SCADA, representing an odd mode. This representation is unrealistic and forced and is used for illustration of this mode only.

Fluid depths for this configuration as a function of time are shown in Fig. 6. The two outer tank levels evolve as they are designed. That is, the levels drain through gravity until they reach the 10% level then the tanks begin to fill. Since a larger amount of fluid is forced into the center tank, it overflows as shown by the green line exceeding the 90% limit and continuing to rise.

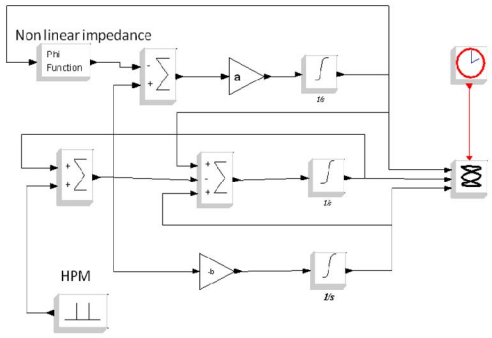


Fig. 2: Solution for Chua circuit.

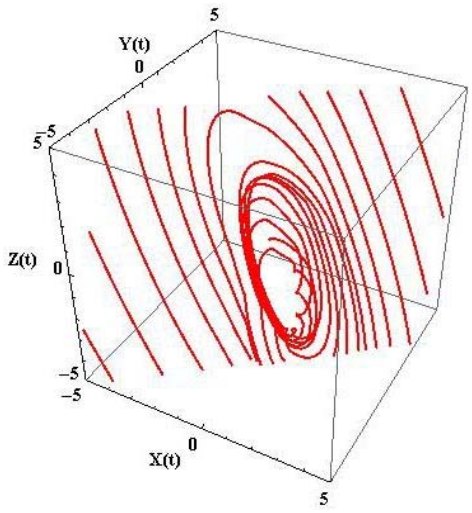


Fig. 3: "Runaway" of currents and voltages for the driven Chua circuit.

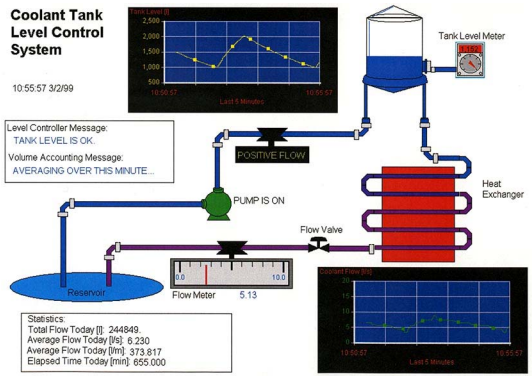


Fig. 4: NSWC SCADA Trainer.

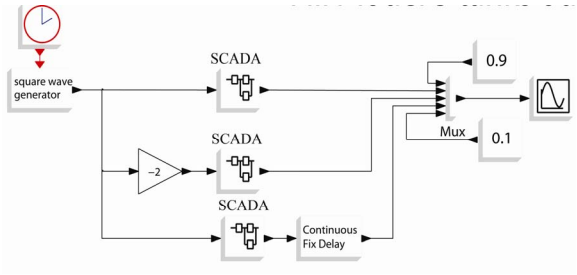


Fig. 5: "Runaway" of currents and voltages for the driven Chua circuit.

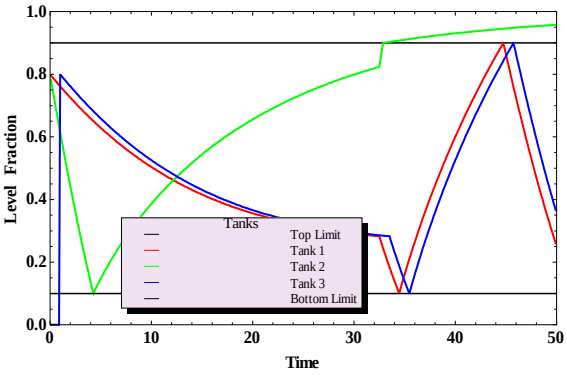


Fig. 6: Level Evolution for Simple Case.

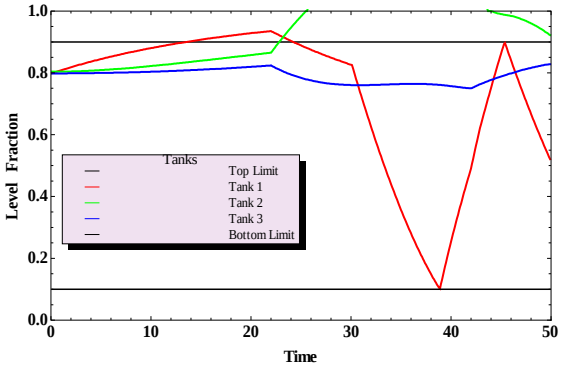


Fig. 3: Level Evolution of the Complex Case.

Finally, we consider the complex case in Fig. 7. That system also has 3 SCADAs, but the interconnection is much more complex. The gravity drains from each of SCADAs 1 and 2 flow into the succeeding tank. Further, each pair of tanks has a pump connecting them. The tank interconnects have cross controllers that examine the tank levels and trigger if the tank imbalance is larger than 40%. They also react to an HPM induced current in the system by reversing the direction of the 2-3 controller forcing extra liquid into the center system, as before.

Fig. 8 shows the evolution of the liquid height for this case.

As before, the center tank overflows. The top tank only reacts to the liquid flowing into the system but the other two tanks respond to the gravity feed from the previous tanks.

This model is relatively simple but its purpose is to show the development of a tool that can show functional failures resulting from many-pulse or continuous-wave illumination. In the future, applications with complex failure modes can be demonstrated. These types of control system models represent many coupled nonlinear differential equations. Their solution can demonstrate many failure modes including chaos.

5. STABILITY

The designers of all real systems expect that the systems they design will be stable when all of the control systems operate. Our purpose is to determine how a repeated "nudge" at a system resonance can bring a system down. This type of failure occurred in an oil pipe line whose pump added to the pressure in the pipe

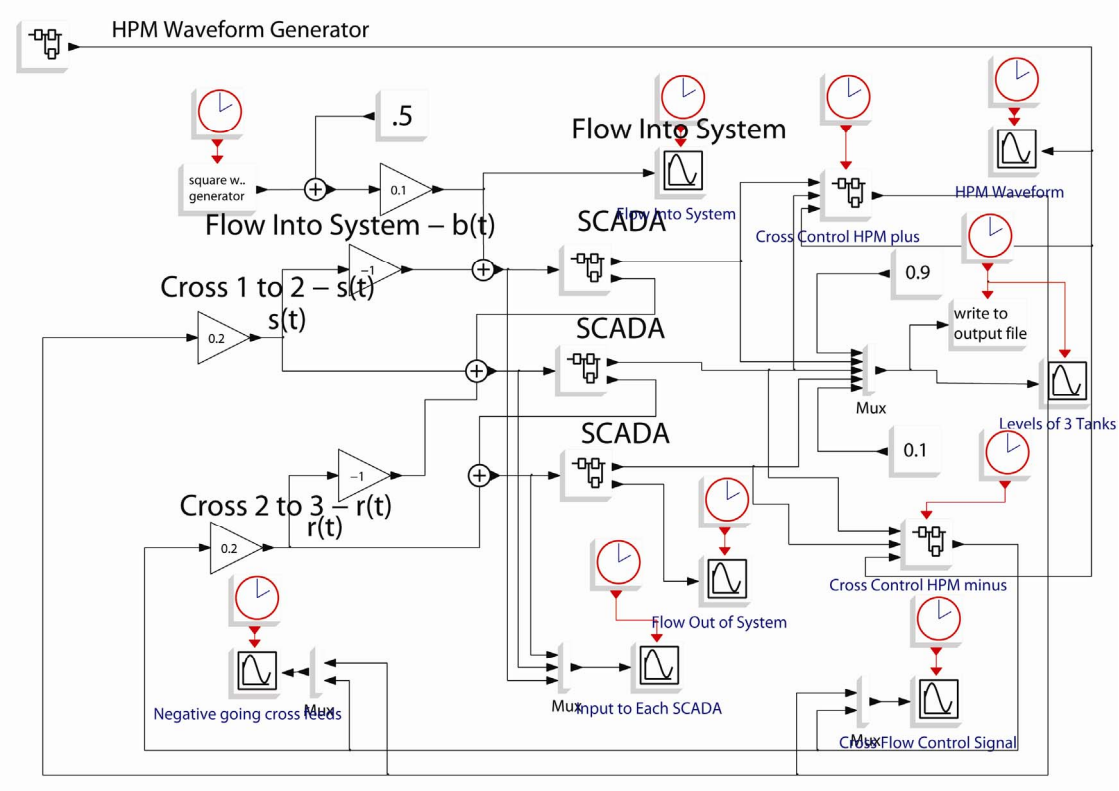


Fig. 2: Complex SCADA System With Interconnects.

at the peak pressure point of pressure waves traveling through the pipe – eventually causing the pressure waves to increase beyond the capacity of the pipe.

Stability of complex nonlinear hybrid systems is difficult to determine [10]. Usually, the approach to showing stability is to find a bounding function that does not grow at late times (Lyapunov function). For hybrid systems, overall bounding functions are difficult to find and one must make do with bounding functions for individual states. When insult is included in the model, whose purpose is to destabilize the system, establishing stability becomes even more difficult.

6. CONCLUSIONS

We have started with the SCADA trainer of [7] as a building block of more complex systems. Three systems is the minimum needed to demonstrate odd-mode characteristics. While odd-mode failures can be demonstrated with simple interconnects, we have gone on to show similar failure mechanisms for complex interconnects. This more complex system further develops the techniques for functionally modeling potential failure modes for complex infrastructure targets.

REFERENCES

1. J. LoVetri, A. TM. Wilbers, A.P.M. Zwamborn. "Microwave Interaction with a Personal Computer: Experiment and Modeling", *Proc. of 13th Int. Zurich Symposium on EMC.* Zurich, Switzerland, 1999, p.203-206.
2. Stoudt, D. C., "Building the Capability to Perform Electromagnetics Effects Tests on Complex Systems", *Proceedings of the European Electromagnetics Symposium*, Lausanne, Switzerland, Jul 2008.
3. R. L. Gardner and D. C. Stoudt, "Review of Susceptibility Data and Analysis Techniques in High-Power Electromagnetics", *Proceedings of the USNC/URSI Meeting*, Boulder, CO, Jan 2009.
4. I. Kohlberg, R. L. Gardner, R. Boling and C. Ropiak, "Theoretical Considerations Regarding Assessment of HEMP and IEMI Upset of Digital Systems", *Proceedings of the 28th General Assembly of the International Union of Radio Science*, Delhi, India, October 2005.
5. I. Kohlberg and R. L. Gardner, "Functional and Communications Theory Models in Susceptibility Analysis", *Proceedings of the North American Radio Science Meeting*, Columbus OH, June 2003.
6. I. Kohlberg, R. L. Gardner, and C. Ropiak, "Techniques Relevant to the Analysis of Electromagnetic Interference Effects on Electronic Systems", *Proceedings of the International Conference on Electromagnetics in Advanced Applications*, Turin, September 2005.
7. D. C. Stoudt, R. L. Gardner, and I Kohlberg, "The Role of Hybrid Models in Understanding Failure Mechanisms of Infrastructure Electronics Due to High-Power Microwave Illumination", *Proceedings of the International Conference on Electromagnetics in Advanced Applications*, Turin, September 2007.
8. I. Kohlberg and R. L. Gardner, "A Perspective of Electromagnetic Susceptibility of Discrete Event Dynamic Systems and Hybrid Systems", *Proceedings of the European Electromagnetics Symposium* , Lausanne, Switzerland, Jul. 2008.
9. S. Lynch, "Dynamical Systems with Applications using Mathematica", Springer, Boston, 2007.
10. S. L. Campbell, J. P. Chancellor and R. Nikoukhah, Modeling and Simulation in Scilab/Scicos, Springer, New York 2006.
11. W. M. Haddad and V. Chellaboina, *Nonlinear Dynamical Systems and Control*, Princeton University Press, Princeton, NJ, 2008.

THE MOTION TRAJECTORY RESTORING FOR RADAR OBSERVATION OF LIVING OBJECTS

Ochotnikov D. A.

Russia, Moscow Aviation Institute, junior research fellow, postgraduate student,
E-mail: denisoffice@mail.ru

Abstract

Some technologies of medical radars design are discussed in the report. Radars are intended to obtain the mechanical moving trajectory of living organism chest.

Peculiarities of radar detection of targets performing seesaw motion are considered. Data obtaining and processing problems are investigated, methods of initial object motion trajectory restoring are examined by means of two quadratures use, constant component elimination and arctan-demodulation. Methods of received signal processing and computing are proposed.

1. PAGE FORMAT

Radar systems for living organism observation, the so-called bioradiolocation systems find a wide application at present. The peculiarity of bioradiolocation is that observed objects perform as a rule not rectilinear movements but seesaw motion (the chest and heart of human). Tracking is performed against the background of radar signals reflected from immovable, fixed objects, this complicates obtaining true observation results and human organs monitoring. Processing of signals reflected from living objects movable and immovable against the background of greet number of preventing reflections is discussed in this report.

The immovable, fixed human body contains two sources of independent time variant seesaw motions: chest and heart. The body observation comes to these motions characteristics definition: the amplitude, the frequency and obtaining of body displacement trajectory in time.

Radar information from biological object can be obtained by means of well-known method of phase detecting which allows to select signals reflected from moving object against the background of signals reflected from immovable, fixed objects on the basis of Doppler increment of signal frequency.

The method is based on the use of phase detector, output voltage of which depends on the phase difference between received and reference signals. To avoid ambiguity two quadrature outputs are used when their reference signals are shifted at 90 degrees. To detect the object motion one quadrature is sufficient. But to define motion characteristics or to restore the object trajectory two quadratures are necessary to use because of the nonlinearity of phase detector characteristic.

In this work the new analytic method of the object motion trajectory restoring from two quadratures of phase receiver is proposed which works efficiently in presence of multiple local objects.

2. CHARACTERISTICS OF THE OBSERVED OBJECT MOTION

In [1, 2] the possibility of motion registration of living organisms surfaces including human organs was shown. The type of chest motion of human in quiescent state can be described by quasiperiodic function (Fig. 1). The target wich is on the distance R_1 from radar performs seesaw motion in the direction of the normal line to radar. Target approaches to radar at the minimum distance R_{MIN} and moves away from radar at the maximum distance R_{MAX} (Fig. 2). For the purpose of simplicity the case of periodic motion in one plane with constant frequency is considered.

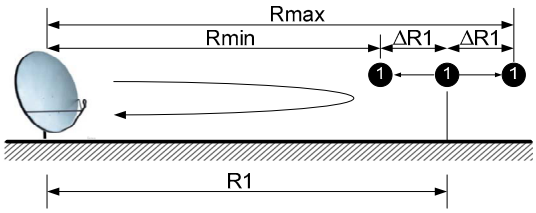


Fig. 1. One-point target which moves in seesaw mode with amplitude ΔR_1 and frequency F.

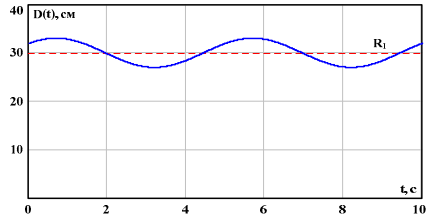


Fig. 2. Distance changes between radar and target.

978-1-4244-7468-4/10/$26 ©2010 IEEE

In the phase detecting method phase is the signal parameter which define target position in the space. Since the transfer function of phase detector which describes the dependence of output voltage from phase difference between received and reference signals, is cosine function, the reflected signal from the target is described by following formula [3]:

$$u = \frac{E_0 E_1}{2} n T_0 \cos\left[2\omega_0 \left(\frac{R_1 + \Delta R_1 \sin\left(\Omega_1 t + \theta\right)}{c}\right)\right], \quad (1)$$

where T_0 – period of sounding signal cycling oscillations; n – integer number of periods participating in integration process; $\omega_0 = 2\pi f_0$ - circular frequency of radiated signal; $\Delta R_1 = \left|R_{MAX} - R_{MIN}\right| / 2$ –amplitude of target motion; $\Omega_1 = 2\pi F_1$ – circular frequency of target motion; θ – initial value of target motion phase; E_0, E_1 – amplitudes of received and reference signals; R_1 – target distance; c – the speed of light; u – output voltage of the phase detector.

Formula (1) shows dependency of voltage on the correlator output from the observed object distance. The model formed on the basis of formula (1) allows to consider the correlator output signal at different motion parameters. Figures 3,4 present output signal FD for various cases of relationship between wave length λ_0 and target seesaw motion amplitude ΔR_1 at the frequency value of 3 Hz.

These figures show that when the amplitude of the motion grows the output signal form starts to change. In the output signal additional harmonics with multiple frequencies appear. This complicates direct measurement of target motion frequency at some values of motion amplitude. It can be shown that signal change takes place when target distance fulfils condition $R_1 = n\lambda_0 / 8 \ (n = 1,3,5,\ldots)$, in this case the signal acquires constant component. The radar distance $R_1 = n\lambda_0 / 4 \ (n = 1,2,3,\ldots)$, on which motion trajectory of the oscillating body is transmittedin the output signal of the receiver practically without changes, is named optimal distance. If the radar is used in presence of multiple local objects [4, 5, 6], their reflections get also in the receiver. Because of interference of signals reflected from several objects the position of objects, from which signals have been reflected, is not identified (Fig. 5,6).

Signal, roused by the reflections from several targets, give rise to the voltage in the receiver, which (is changed) varieties as sinusoidal with the frequency of sounding signal when the phase and the amplitude depend of targets distances and their RCS (Radar cross section).

On the basis of the model considered one can make following resume:

1) The linear dependence of the output receiver voltage alteration from the chest shift exists only near $R_1 = n\lambda_0 / 4 \ (n = 1,2,3,\ldots)$ under the stipulation that the shift ΔR_1 is small enough as compared with the wave length λ_0;

2) The output receiver voltage acquires additional harmonics with multiple frequencies in the case when $\Delta R_1 \geq \lambda_0$;

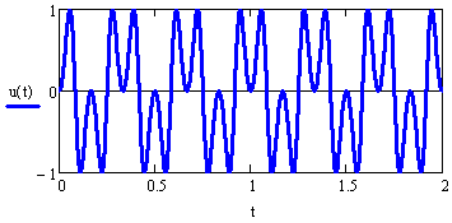


Fig. 3. Time diagram of correlator output signal when observed target oscillates on the distance $n\lambda_0 / 4 \ (n = 1,2,3,\ldots)$ from radar, $\Delta R_1 / \lambda_0 = 1/2$.

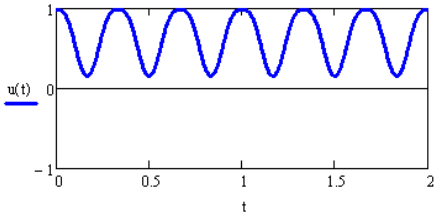


Fig. 4. Time diagram of correlator output signal when observed target oscillates on the distance $n\lambda_0 / 8 \ (n = 1,3,5,\ldots)$ from radar, $\Delta R_1 / \lambda_0 = 1/5$.

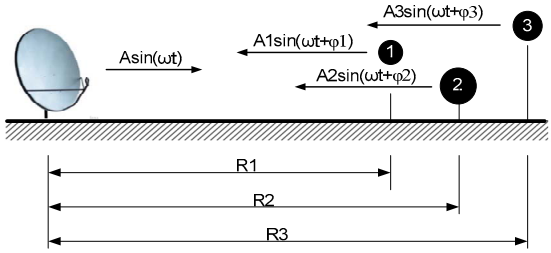


Fig. 5. The reflection of the monochromatic wave from several targets.

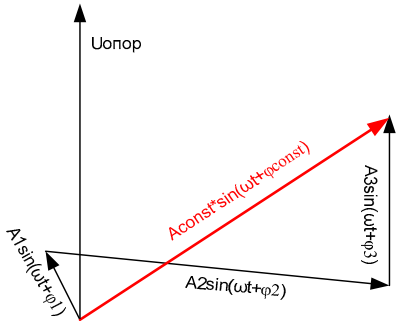


Fig. 6. Composition of reflections from local objects.

3) Besides signal frequency changes the constant component appear ("useful constant component"), when the object distance deviates from the optimal one;

4) The presence of reflections from local objects results in the greet constant component appearance in the signal, which cannot be apparently distinguished from the useful constant component.

3. THE MOTION, MOVEMENT TRAJECTORY ESTIMATION BY USING TWO QUADRATURES

The method of object surveillance by use of one quadrature was considered above. To estimate the target motion trajectory it is necessary to use two quadratures. In this case the radar sensitivity to target position can be overcome.

Since two quadratures allow to represent the signal in vector form, the phase-time relationship can be expressed by formula (2) [3,7]. But in the presence of reflections from local objects the output quadratures voltages have the great constant component, and this doesn't allow to use this formula, what has been presented in the first section.

$$\phi(t) = \mathrm{arcTg}\left\{\frac{\sin(\phi(t))}{\cos(\phi(t))}\right\}. \qquad (2)$$

The constant component can be removed from the signal by means of the filter. But there is a useful constant component in this signal, which must be separated from the constant component, roused by reflections from local objects. Including arctangent demodulation allow to save information about the motion roused by the heart- breathing activity and insensibility to the target position. Some results of modelling such system were obtained.

REFERENCE

1. Greneker E.F. Radar Sensing of Heartbeat and Respiration at a Distance with Application at the Technology. IEE Conference RADAR-97, 14-16 October 1997, Conf. Publication Number 449, P 150-154.
2. Microwave Life-Detection System for Searching Human Subjects Under Earthquake Rubble or Behind Barrier./Kun-Mu Chen, Yong Huang, Jianping Zhang, A. Norman. // IEEE Transactions on Biomedical Engineering, vol. 27, No 1, January 2000, pp 105-114.
3. Immoreev, S. Ivashov. Remote monitoring of human cardio-respiratory system parameters by radar and its applications, Ultrawideband and Ultrashort Impulse Signals, Sevastopol, Ukraine, 15-19 September, 2008.
4. Immoreev I.J., Samkov S.V., 'Ultra Wideband (UWB) Radar for the Remote Measuring of Main Parameters of Patient's Vital Activity,' *Radio Physics and Radio Astronomy* (Ukraine), 2002, V. 7, No. 4, PP. 404-407.
5. Immoreev I.J., Fedotov D.V., 'Detection of ultra wideband radar signals scattered from complex targets,' *Radio Physics and Radio Astronomy* (Ukraine), 2002, V.7, No. 4, PP. 408-412.
6. Bugaev A.S., Vasilyev I.A., Ivashov S.I. et all 'Detection and remote diagnostics of people behind obstacle with radar,' *Radiotecnica*. 2003. №7. PP. 42-47.
7. Olga Boric-Lubecke "Arctangent Demodulation With DC Offset Compensation in Quadrature Doppler Radar Receiver Systems", *Ieee Transactions on Microwave Theory and Techniques*, Vol. 55, No. 5, May 2007.
8. Immoreev I., Samkov S., Teh-Ho Tao, 'Short - Distance Ultra-Wideband Radars,' *Theory and Designing, International Conference on Radar Systems* (RADAR 2004). 18-23 October 2004. Toulouse, France.
9. Immoreev I., Samkov S., Teh-Ho Tao, 'Short – Distance Ultrawideband Radars,' *IEEE Aerospace and Electronic Systems Magazine*. V. 20, № 6, 2005, PP. 9-14.
10. Immoreev I., Teh-Ho Tao, 'UWB Radar for Patient Monitoring,' *IEEE Aerospace and Electronic Systems Magazine*. V. 23, № 11, 2008, PP. 11-18.

GENERATION, RADIATION, RECEIVING

PULSE EXCITATION OF ACOUSTIC OSCILLATIONS OF A CELL

Harlanov A. V.

Volgograd State Technical University, Volgograd, Russia
E-mail: harlanov_av@mail.ru

Abstract

At excitation of the oscillations depending not only from time, but also from co-ordinates will matter not only frequency of exciting force, but also distribution of this force in space. The particular interest represents excitation of acoustic oscillations of a biological cell under the influence of an external electromagnetic wave.

Owing to equivalence of co-ordinates was the one-dimensional model – a string rigidly fixed from both parties is taken

It has been received that the greatest amplitude of oscillations arises provided that frequency of external force is equal to own frequency of fluctuations of a string, and the length of a string is less than half of length of a wave. However at equality of frequencies of acoustic and electromagnetic fluctuations of length of waves of electromagnetic fluctuations will accept very much great values.

Pulse influence was offered high-frequency signal is included on short time with the period equal to the period of own acoustic fluctuations of a string. The amplitude of fluctuations thus increases.

Keywords: Acoustic oscillations, electromagnetic wave, amplitude, resonance, biological cell.

1. INTRODUCTION

At excitation of the oscillations depending not only from time, but also from coordinates (for example, excitation of mechanical oscillations of a membrane by external force), arises a question: whether the resonance will have only time character (that is to depend on frequency of compelling force), or the spatial factor (force distribution on coordinates) will matter also. The Particular interest represents excitation of acoustic oscillations of a cell under the influence of an external electromagnetic wave [1]. We will consider this question more in detail.

2. STATEMENT OF A PROBLEM

As coordinates are independent, oscillations of three- two- and one-dimensional objects will essentially not differ. Therefore, for simplicity, we will consider an one-dimensional case – a string, length l, fixed with two parties, being in the viscous environment and capable to make the compelled oscillations under the influence of external force (figure 1) [2].

Dynamics equation will register in a kind:

$$T\frac{\partial^2\xi}{\partial x^2}dx + f_в\left(x,t\right)dx + f_c dx = \rho dx\frac{\partial^2\xi}{\partial t^2},$$

where $f_в\left(x,t\right)$ – the compelling force operating on unit of length of a string, $f_c = -r\dfrac{\partial\xi}{\partial t}$ – the force of viscous resistance operating on unit of length of a string, $\rho = m/l$ – linear density of a string. After transformations:

$$\rho\frac{\partial^2\xi}{\partial t^2} + r\frac{\partial\xi}{\partial t} - T\frac{\partial^2\xi}{\partial x^2} = f_в\left(x,t\right)$$

Thus, it is necessary to find the decision of the non-uniform linear differential equation of the second order in private derivatives for various kinds of function.

2.1. KINDS OF COMPELLING FORCE

Compelling force we will represent in a kind $f_в\left(x,t\right) = f_1\left(x\right)f_2\left(t\right)$, where $f_1\left(x\right) = A\sin\left(kx\right)$.

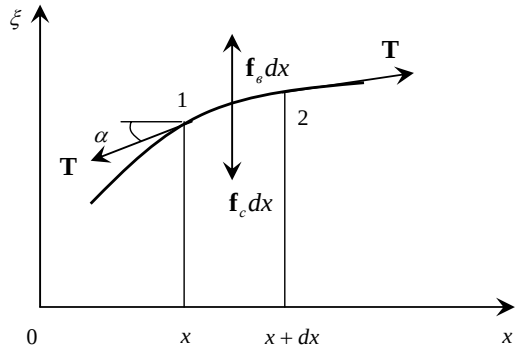


Fig. 1. The Forces operating on an element of a string *dx* ($\mathbf{f}_в dx$ – compelling force, $\mathbf{f}_c$dx – force of viscous resistance, **T** – force of a tension).

978-1-4244-7468-4/10/$26 ©2010 IEEE

As functions we take functions of a following kind:

$$f_2(t) = \sin(\omega_1 t), \quad (1)$$

$$f_2(t) = \begin{cases} \sin(\omega_1 t), \text{if } m\mathrm{T} \le t < mT + n\dfrac{\pi}{\omega_1}, \\ 0, \text{ if } m\mathrm{T} + n\dfrac{\pi}{\omega_1} \le t < (m+1)T + n\dfrac{\pi}{\omega_1}, \end{cases} \quad (2)$$

3. PARAMETERS OF SYSTEM

As us excitation of acoustic oscillations of a cell under the influence of an electromagnetic field we will pick up corresponding parameters of our system interests. An electromagnetic wave, falling on a cell, raises in it electromagnetic oscillations. At intensity of a wave I = 10 mWcm^{-2} the amplitude of intensity of electromagnetic oscillations can reach values 10^6 Vm^{-1}. We will cut out in a membrane a thin strip in length of $5\cdot10^{-5}$ m and width 1 nanometer (a thickness of a membrane too an order of 1 nanometer). Considering that membrane density ~ 10^4 kgm^{-3} [3], a membrane tension on unit of length ~ 1 Nm^{-1} [4], and a membrane charge ~ 10^{-13} C [5], we will receive the following parameters necessary for calculations (table 1).

Table 1. System parameters.

Parameter	Value
Density (ρ), kgm^{-1}	10^{-14}
Resistance factor (*r*), kgs^{-1}	10^{-7}
String tension (*T*), N	10^{-9}
Length of a string (*l*), m	$5\cdot10^{-6}$
Amplitude of force (*A*), Nm^{-1}	10^{-5}

4. RESULTS

As coordinate *x* and time *t* – independent variables the initial equation will register in a kind:

$$\rho y \frac{d^2 z}{dt^2} + ry\frac{dz}{dt} - T\frac{d^2 y}{dx^2} z = f_в(x,t), \quad (3)$$

where $\xi(x,t) = y(x)z(t)$. At each moment of time the equation $-T\dfrac{d^2 y}{dx^2} = f_в(x)$ then found *y* it is substituted in the equation (3) which is reduced to the differential equation of one unknown person of the second order which dares methods of Newmark and Wilson dares [6]. Comparison of the received decisions among themselves and with known results has shown good convergence of methods.

4.1. HARMONIOUS SIGNAL

Let's consider at first influence (1) ($f_в(x,t) = A_1 \sin(kx)\sin(\omega_1 t)$) – (see Fig. 2).

Apparently from Fig. 2, the maximum value of a deviation of oscillations of a string is reached, when frequency of external force is equal to frequency of own oscillations of system, and along a string half of length of a wave keeps within. The particular interest represents a spatial resonance. The maximum value of a deviation of a string exceeds value of a deviation of a string at the big lengths of waves no more than on 25 %. But at reduction of length of a wave there is a sharp reduction of a deviation of a string – for example, in a case when along a string 4 half waves a string deviation keep within makes 0,4 % from the maximum. Also it is necessary to notice that resonant increase of amplitude is not observed in cases when frequency of compelling force is not equal to own frequency of oscillations of a string and also when along length of a string the integer of half waves (in these points keeps within local minima) are observed.

4.2. PULSE SIGNAL

Let's consider kind influence (2). Dependence of compelling force on time is presented in Fig. 3. The greatest deviations of a string arise for a case $n = 1$.

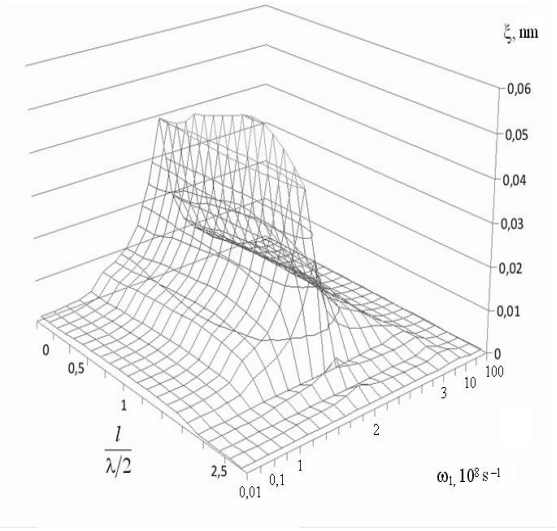


Fig. 2. Spatially-temporarily resonance.

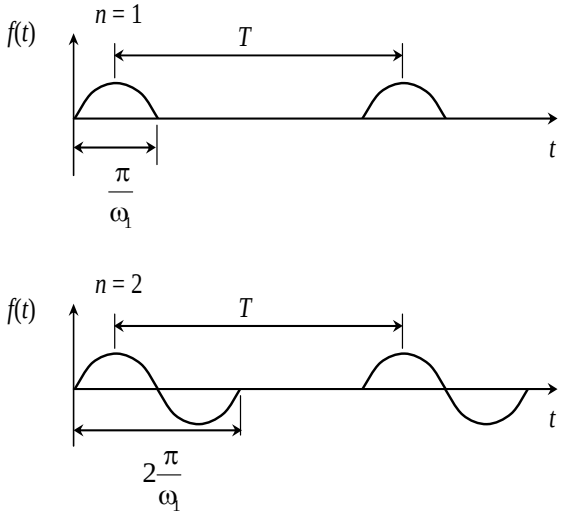


Fig. 3. The schedule of function (2).

At frequency ω_1 increase 10 times (that is reduction of width of an impulse) the amplitude of oscillations of a string decreases too 10 times. Therefore all further calculations are presented for a case $\omega_1 = 10^{10}$ s^{-1}.

The spatial resonance (Fig. 4) again arises under a condition $\left(\frac{l}{\lambda/2} = 1\right)$ and more strongly pronounced concerning small lengths of waves, than big.

In Fig. 5 dependence of amplitude of oscillations of a string on the period of a pulse signal is presented. The main resonance is observed at $T = T_0$, other resonances arise at $T = 2T_0$, $T = 3T_0$, etc. The schedule is received provided that $\frac{l}{\lambda/2} = 1$.

4. CONCLUSIONS

All above-stated can explain influence of electromagnetic waves on bioobjects, in particular on a cell. At an irradiation of a cell the electromagnetic oscillations which electric component can represent itself as compelling force of acoustic oscillations of a membrane arise an electromagnetic wave, in it (Acoustic oscillations of a cell are important for its functioning). We will consider a case of influence of a kind (1). At equality of lengths of waves of acoustic and electromagnetic oscillations of a cell of frequency will differ strongly, hence, a resonance it will not be observed. At equality of frequencies two cases are possible: 1) the length of a wave of electromagnetic oscillations is proportional to diameter of a cell then the length of a wave of acoustic oscillations is much less the than sizes of a cell, hence, amplitude of such acoustic oscillations is very small; 2) the length of a wave of acoustic oscillations is proportional to diameter of a cell, however length of a wave of electromagnetic oscillations in this case will be much more sizes of a cell, that is such electromagnetic oscillations are simply impossible. In other words, it is impossible kind signal (1) to excite acoustic oscillations of a cell. At kind influence (2) (the pulse signal) turns out other result – the high-frequency compelling signal (frequency corresponds to own frequency of electromagnetic oscillations of a cell) is sent by impulses (the impulse period corresponds to the period of acoustic oscillations) – the spatially-temporarily resonance as a result should be shown. Thus, pulse influence appears more effective, than usual harmonious influence. Also it is necessary to notice that in the given one-dimensional case two frequencies – one for occurrence of a spatial resonance, another – for time are necessary. In a two-dimensional case the signal with three frequencies can appear more effective.

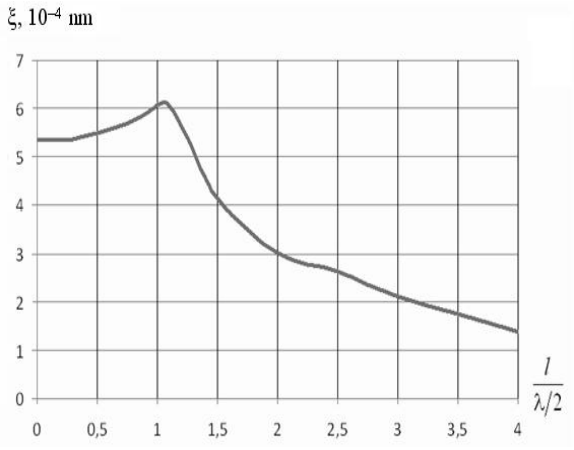


Fig. 4. Spatial resonance.

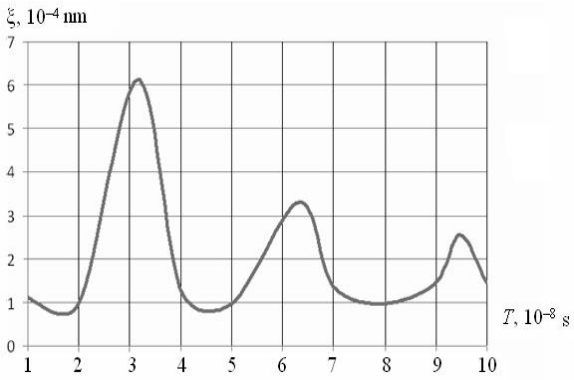


Fig. 5. Time resonance.

REFERENCES

1. Harlanov A. V. Spatially - temporarily resonance. (Russian). Biomedical radioelectronics. 2008, No 4, 24 – 30.
2. F. M. Mors and G. Feshbah, Methods of theoretical physics, v. 1. (Traslated into Russian) Izdat. Inostr, Literaturi, Moscow, 1960.
3. Shein A. G., Harlanov A. V., Nikulin R. N. Account of acoustic oscillations of a cell. (Russian). Biomedical radioelectronics. 2005, No 3, 18 – 25.
4. Golant M. B. Acousto-electric waves in cell membranes of living organisms - a key problem for understanding of mm-waves interaction with living. Collection of works "Effects of low-intensity mm-waves influence on living organisms". Publishers: IRE RAS, Moscow, 1993.
5. Betskii O.V., Lebedeva N. N. Modern representations about mechanisms of influence of low intensive mm-waves on biological objects. Mm-waves in biology and medicine. 2001, No 3, 5–19.
6. K. – J. Bathe, E. L. Wilson, Numerical methods in finite element analysis, Prentice-Hall, Inc., 1976.

HIGH SPEED AND EFFICIENT SELECTIVELY SENSITIVE PHOTODETECTORS

[1] St. Collin, [1] F. Pardo, [2] S. V. Averin, [1] N. Bardou and [1] J. L. Pelouard

[1] Laboratoire de Photonique et de Nanostructures CNRS,
Route de Nozay, 91460 Marcoussis, France
[2] Fryazino branch of the Institution of Russian academy of sciences,
Kotel'nikov Institute of Radio Engineering and Electronics of RAS,
square acad. Vvedensky 1, 141190, Fryazino, Moscow region, Russia.
E-mail: sva278@ire216.msk.su

Abstract

We report on the resonance cavity MSM-photodiode structures based on nanoscale metallic gratings which are used both as a tool for efficient light confinement and the photocarriers collection. The finger spacing of these detectors is less than the wavelength of incident light. Short collection path along with low diode capacitance (8 fF) allows theoretical cut-off frequencies as high as 500 GHz. Detector has record quantum efficiency of 46% and high selectivity (FWHM=17 nm) at wavelength 790 nm.

Keywords: MSM-photodetector, metallic grating, quantum efficiency, Bragg reflector, reflection coefficient, resonance cavity, high-speed response.

1. INTRODUCTION

High-speed and efficient photodetectors have received much attention in the recent years. These detectors are the key components in high bit rate optical communication, terahertz generation by photomixing and in scientific instrumentation. Metal-semicon-ductor-metal photodetectors (MSM-PD) have become an important device in modern optoelectronics [1-3]. Based on the interdigitated Schottky contact structure the MSM-PD has simple device technology, fast response, small capacitance and ease of integration with electronic circuitries. For identical transit times and device area MSM-PD has four times lower capacitance and thus higher cut-off frequency obtained as compared with PIN-PD [1]. The highest response speed measured to date (FWHM = 0.58 ps) has been achieved in LT-MSM detector with 100 nm finger spacing but with very low quantum efficiency of 2% due to the opacity of detector metallic contacts and low-temperature-grown GaAs active layer [2]. Another approach for considerable shortening detector response time (FWHM = 0.63 ps) was in use of MSM-heterobarrier diode structure [3] and again has resulted in poor quantum efficiency of ~8 %. In order to increase the cut-off frequency of the MSM-PD the thickness of absorption layer has to be reduced and becomes smaller than the absorption depth resulting in a decrease of detector efficiency. The achievement of quantum efficiencies greater than ~50 % with cut-off frequencies above 300 GHz requires new solutions to confine effectively the absorption of light in nanoscale, low capacitance structures.

2. RESULTS AND DISCUSSION

2.1. DESCRIPTION OF THE RCE SMSM-PD

We report on the resonance cavity enhanced sub-wavelength MSM-photodiode structure (RCE SMSM-PD) based on nanoscale (feature dimensions smaller than $\lambda/8$) metallic gratings which are used both as a tool for efficient light confinement and rapid photocarriers collection. Fig. 1 shows the schematic cross-section of detector structure. The bottom mirror is a quarter wave stack multilayer Bragg reflector. The resonance cavity is made of a thin absorbing layer (GaAs) on top of optically transparent "spacing" layer. The thickness of the absorbing layer can be only a few tens of nanometers and the thickness of the spacing layer is adjusted to satisfy the Fabry-Perot condition.

The RCE SMSM-PD has been realized on a semi-insulating GaAs substrate. The semiconductor layer

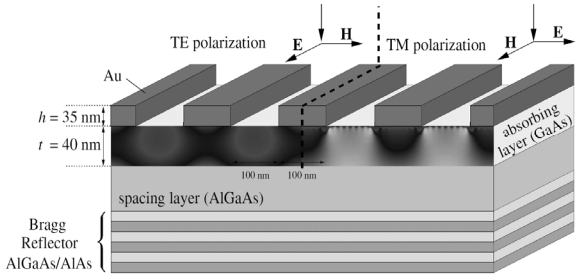


Fig. 1. Structure of RCE SMSM-PD and spatial distribution of the electric filed intensity in the absorbing layer for TE (left) and TM (right) polarization.

978-1-4244-7468-4/10/$26 ©2010 IEEE

structure was grown by molecular beam epitaxy. The multilayer Bragg reflector is composed of 24 periods of quarter waves AlAs/$Al_{0.2}Ga_{0.8}As$ layers. The GaAs absorption layer thickness is 40 nm. For the resonance at ~800 nm wavelength in the center of the stop band of the Bragg mirror the $Al_{0.35}Ga_{0.65}As$ spacing layer thickness was chosen to be 30 nm. We have fabricated these RCE SMSM-PD on GaAs substrates with Ti/Au gratings and 100 nm finger width and spacing. The grating was defined by electron-beam assisted evaporation and lifted off in trichloroethylene. The 5 nm thick titanium layer has been used to improve the metal adhesion to the GaAs active layer. The measured reflectivity of fabricated devices 3x3, 5x5, 10x10 μm^2 in size for TE and TM polarization matched well with theory confirming the efficient resonance transmission.

2.2. Optical Transparency of the MSM-Diode Metallic Gratings

The light interaction with metallic gratings of MSM-PD are commonly explained by geometrical consideration: light is reflected on metallic contacts and transmitted in between the contacts [1]. That explanation does not make sense in subwavelength metallic gratings. Recently Ebbesen et al, while exploring the optical properties of submicrometre cylindrical cavities in metallic films, have found that arrays of such holes display highly unusual transmission at wavelengths as large as ten times the diameter of the cylinders [4]. These unusual optical properties of two-dimensional periodic structures with feature dimensions up to ten times smaller than a wavelength of incoming light are due to coupling of light with plasmons–electronic excitations–on the surface of the periodically patterned metal film [4]. Excitation of horizontal surface-plasmon resonances leads to a strong enhancement of the field intensity on the horizontal surfaces of the metallic film, which results in efficient transmission through subwavelength holes by tunneling [5]. Strong confinement and transmission of light in periodical subwavelength apertures of metallic films have initiated a number of theoretical studies [5,6] and have brought about to a possibility of elaboration of new photonic devices. In particular, this mechanism has already been applied in emissive devices [7] and tunable filters [8]. The interdigitated electrodes of the MSM-PD basically form a grating. For the first time we used the effective transmission of light through metallic gratings with a feature dimensions much smaller than a wavelength of incoming optical signal for efficient light confinement in the active volume of the MSM-PD. A modal method and S-matrix formalism [5,6] have been applied for the electromagnetic calculations of the total diode structure. Fig. 2 shows experimental and theoretical reflection/absorption spectra of 40 nm-height Au (35 nm)/Ti (5 nm) grating and 100 nm finger spacing and finger width in TE polarization of incoming light. Both calculation and experimental data demonstrate that, in spite of the metal interdigital contacts of the MSM-PD, only small part of incoming light is reflected from the detector surface, whereas 50% of light penetrates into the diode structure and assimilates in active GaAs producing electron-hole pairs.

2.3. I-V Characteristics

I-V characteristics of the diodes have been examined with Agilent 4156C analyzer of semiconductor structures. The RCE SMSM-diodes have nearly symmetrical I-V curves (Fig. 3) with typical dc dark current of 8 pA at 1V and 30 pA at 2 V bias voltage for the 5x5 μm^2 device with 100 nm finger gap and width. I-V curves were examining by taking into account the barrier height dependence on the electric field and tunneling through the barrier [9]. Following this analysis we have extracted the Schottky barrier height Φ=0.6 eV and diode ideality coefficient n=1.05 for our RCE SMSM-PD. These parameters indicate high quality of Schottky contacts and the absence of intermediate oxide layer at the Ti-GaAs interface. Low level of dark current density (1 пА/ мкм^2) allows to realize high sensitive detectors of optical radiation on these structures.

2.4. Detector Spectral Sensitivity and Quantum Efficiency

The spectral dependence of the RCE SMSM-detector responsivity has been measured using tunable laser source and high resolution Jvon-Yobin spectrometer. The spectrometer was calibrated with Ar-lamp as a

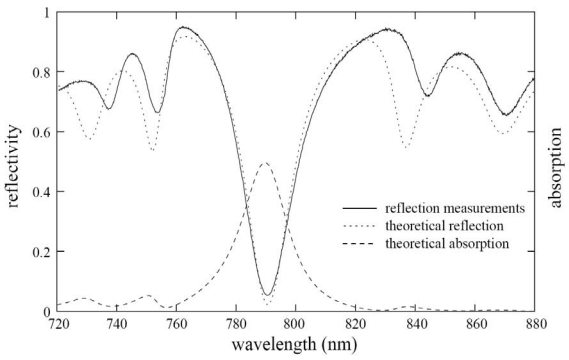


Fig. 2. Reflection and absorption spectra in TE-polarization of light.

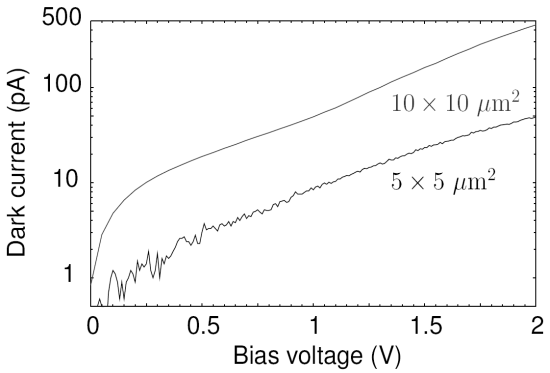


Fig. 3. I-V curves of RCE SMSM-PD.

reference. The spectral dependence of the laser power and all optical components was evaluated using calibrated detector Newport 818-ST. A laser spot diameter smaller than the MSM-diode area has been focused on RCE SMSM-PD with an objective and traced on the screen with CCD camera. Subsequent measurements of the RCE SMSM-PD and reference Newport detector against the Newport 818-ST calibration detector yielded absolute detector responsivity at a particular laser wavelength. The final RCE SMSM-PD spectral responsivity curve was then obtained using this calibration points, Fig. 4. These measurements have demonstrated detector resonance behavior with good agreement with calculations.

Our devices have reached an experimental external efficiency of 46 % at 790 nm for low level of optical excitation in TE polarization, Fig. 4. This is efficiency improvement by more than order of magnitude in comparison with conventional MSM photodetector with a similar geometry of 100 nm finger spacing [2]. The efficient collection of photocarriers through a high and homogeneous electric field in RCE SMSM-PD with only 50 nm mean carrier collection path along with low diode capacitance (8 fF) should allow theoretical cut-off frequencies as high as 500 GHz. Response time measurements are now in progress. Our RCE SMSM-PD is relatively narrow-band detector. At the wavelength of maximum sensitivity (790 nm) FWHM=17 nm. Spectral location of detector resonant wavelength can be selected with the period of the gratings and the height of the interdigitated slits. These selectively sensitive photodetectors will be efficient for spectral bandwidth filtering useful in WDM applications.

3. CONCLUSION

Design principles and technology of high-speed and efficient MSM-photodetectors based on nanoscale metallic gratings which are used both as a tool for efficient light confinement and the photocarriers collection have been developed. The measurements of quantum efficiency and reflection coefficients are in accordance with theoretical estimates. Short collection path of the photogenerated carriers along with low diode capacitance (8 fF) should allow theoretical cut-off frequencies as high as 500 GHz. Detector has record quantum efficiency of 46% and high selectivity (FWHM=17 nm) at λ=790 nm. Low level of dark current density (j=1 pA/μm^2) allows to realize high speed and selectively sensitive photodetectors of optical radiation.

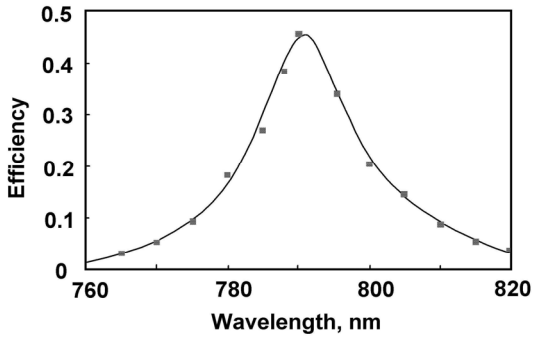


Fig. 4. QE of RCE SMSM-PD.

REFERENCES

1. Soole, J.B.D. and Schumacher, H. 1991, 'InGaAs metal-semiconductor-metal photodetectors for long wavelength optical communications', *IEEE J. Quantum Electron.* **27**, 737-52.
2. Chou, S.Y. Liu, Y., Khalil, W., Hsiang, T.Y., and Alexandrou, S. 1992, 'Ultrafast nanoscale metal-semiconductor-metal photodiodes on bulk and low-temperature grown GaAs', *Appl.Phys.Lett.*, **61,** 819-21.
3. Stein von Kaminski, E., Roskos, H.G., Averin, S.V., Geelen, H.G., Kohl, A., Spangenberg, B., and Kurz, H. 1993,'Ultrafast heterobarrier metal-semiconductor-metal photodiodes', *OSA Proceedings*, **14,** 33-6.
4. Ebbesen, T.W., Lezec, H.J., Ghaemi, H.F., Thio, T., and Wolff, P.A. 1998, 'Extraordinary optical transmission through sub-wavelength hole arrays', *Nature*, **391,** 667- 9.
5. Martin-Moreno, L., Garsia-Vidal, F.J., Lezec, H.J., Pellerin, K.M, Thio, T., Pendry, J.B., and Ebbesen, T.W., 2001,'Theory of Extraordinary Optical Transmission through Subwavelength Hole Arrays', *Phys.Rev.Lett.*, **86,** 1114-7.
6. Porto, J.A., Garca-Vidal, F.J., Pendry, J.B. 1999, 'Transmission resonances on metallic gratings with very narrow slits' *Phys.Rev.Lett.*, **83,** 2845-8.
7. Worthing, P.T., Barnes, W.L. 2001, 'Efficient coupling of surface plasmon polaritons to radiation using bi-grating', *Appl.Phys.Lett.*,**79,** 3035-7.
8. Kim, T.J., Thio, T., Ebbesen, T.W., Grupp, D.E., and Lezec, H.J. 1999,' Control of Optical Transmission Through Metals Perforated with Subwavelength Hole Arrays', *Opt. Lett,* **24,** 256-8.
9. Averin, S.V., Chan, Y.C., and Lam, Y.L. 2000, 'Evaluation of Schottky contact parameters in metal-semiconductor-metal photodiode structure', *Appl.Phys.Lett.*, **77,** 274-6.

ELECTROMAGNETIC WAVES RADIATION BY THIN VIBRATORS WITH ASYMMETRICAL SURFACE IMPEDANCE

[1] Nesterenko M. V., [2] Dakhov V. M., [3] Katrich V. A., [4] Berdnik S. L. and [5] Pshenichnaya S. V.

V. N. Karazin Kharkov National University, Kharkov, Ukraine
E-mail: [1]Mikhail.V.Nesterenko@gmail.com; [2]Dakhov@univer.kharkov.ua;
[3,5]vkatrich@univer.kharkov.ua; [4]Sergey.L.Berdnik@univer.kharkov.ua

Abstract

The problem about radiation of electromagnetic waves by the thin vibrator with the symmetrical and antisymmetrical components of the surface impedance relative to its centre, where the point source of excitation is located, has been solved by the generalized method of induced electromotive forces. The analytical expressions, obtained in a closed form, allow to obtain the current distribution along the vibrator length and to calculate its electrodynamic characteristics. The calculations of the vibrators input parameters of different electrical length, dependent of the values of both symmetrical and antisymmetrical components of the vibrator surface impedance, have been made.

Keywords: Radiation of electromagnetic waves, a thin vibrator, surface impedance, the method of induced EMF.

1. INTRODUCTION

At present thin vibrators are applied as different resonant elements of antenna-waveguide devices widely. The variety of available vibrator structures and also the creation of new constructions on their basis stipulate constant interest of investigators to the problems of their analysis and synthesis. So, for example, location of different active and passive elements in definite points along the vibrator antenna and also the vibrator excitation in the point apart from the centre create additional possibilities to form the set electrodynamic characteristics of vibrator radiators. The availability of the surface impedance in such vibrators, which is constant along their length, gives additional possibilities to design radiating systems with the set electrodynamic characteristics both at central [1] and shifted [2] locations of the point of excitation.

The solution of the problem about radiation of electromagnetic waves by thin vibrators with symmetrical excitation and asymmetrical distributed surface impedance along their length by the generalized method of induced electromotive forces (EMF) is represented in this paper.

2. THEORY

The integral-differential equation concerning the electrical current for the vibrators, representing themselves the thin rectilinear impedance cylinder of the radius r and the length $2L$ ($r/(2L)<<1$), located in free space and excited by the set field of the impressed sources, has the following form [3]:

$$\left(\frac{\mathrm{d}^2}{\mathrm{d}s^2}+k^2\right)\int_{-L}^{L} J(s')G_s(s,s')\,\mathrm{d}s' = -i\omega E_{0s}(s) + i\omega z_i(s)J(s) \quad . \qquad (1)$$

Here $z_i(s)$ is the complex internal impedance per unit length of the vibrator, Ohm/m; $E_{0s}(s)$ is the component of the electrical field of the impressed sources along the vibrator axis; $G_s(s,s') = \dfrac{e^{-ik\sqrt{(s-s')^2+r^2}}}{\sqrt{(s-s')^2+r^2}}$; $k=2\pi/\lambda$, λ is the wavelength in free space ($r/\lambda<<1$); ω is the circular frequency; $s(s')$ is the longitudinal coordinate, coupled with the axis (the surface) of the vibrator; $J(s)$ is the searched current, suitable for the boundary conditions: $J(\pm L)=0$.

Both the field of impressed sources and the internal impedance of the vibrator can be represented by the sum of two components – symmetrical (the index "*s*") and antisymmetrical (the index "*a*") relative to its geometrical centre: $E_{0s}(s)=E^s_{0s}(s)+E^a_{0s}(s)$, $z_i(s)=z^s_i(s)+z^a_i(s)$ in a more general case. Naturally, at this the current in the vibrator will also consist of two parts – $J(s)=J^s(s)+J^a(s)$, which can be represented in the form of the product of the unknown

978-1-4244-7468-4/10/$26 ©2010 IEEE

amplitudes $J_0^{s,a}$ on the set functions of distributions $f^{s,a}(s)$: $J^{s,a}(s) = J_0^{s,a} f^{s,a}(s)$. Let us use the generalized method of induced electromotive forces (EMF) in order to solve the equation (1), reliability of application of which is shown in [3] for vibrators with the variable impedance.

Then (1) is transformed into the system of the algebraic equations of the second order:

$$\begin{cases} J_0^s(Z^s + F_{zs}^{s2}) + J_0^a F_{za}^{sa} = -(i\omega / 2k)E^s, \\ J_0^a(Z^a + F_{zs}^{a2}) + J_0^s F_{za}^{sa} = -(i\omega / 2k)E^a. \end{cases} \quad (2)$$

The following symbols are accepted in (2):

$$Z^{s,a} = \frac{1}{2k}\int_{-L}^{L} f^{s,a}(s)\left[\left(\frac{\mathrm{d}^2}{\mathrm{d}s^2} + k^2\right)\int_{-L}^{L} f^{s,a}(s')G_s(s,s')\mathrm{d}s'\right]\mathrm{d}s,$$

$$F_{zs}^{s2,a2} = -\frac{i\omega}{2k}\int_{-L}^{L}[f^{s,a}(s)]^2 z_i^s(s)\mathrm{d}s,$$

$$F_{za}^{s,a} = -\frac{i\omega}{2k}\int_{-L}^{L} f^s(s)f^a(s)z_i^a(s)\mathrm{d}s,$$

$$E^{s,a} = \int_{-L}^{L} f^{s,a}(s)E_{0s}^{s,a}(s)\mathrm{d}s. \quad (3)$$

The solution of the equations system (2) at the vibrator symmetrical excitation ($E_{0s}^a(s) = 0$) and the asymmetrical surface impedance ($z_i^a(s) \neq 0$) has the following form:

$$J(s) = -\frac{i\omega}{2k}E^s\left[\frac{(Z^a + F_{zs}^{a2})f^s(s) - F_{za}^{sa}f^a(s)}{(Z^s + F_{zs}^{s2})(Z^a + F_{zs}^{a2}) - (F_{za}^{sa})^2}\right]. \quad (4)$$

Let the vibrator be excited by the hypothetical generator of the voltage V_0: $E_{0s}^s(s) = V_0\delta(s)$ in the centre ($s = 0$). Then the current symmetrical component can be approximated by the following function [3] rather precisely: $f^s(s) = \sin\tilde{k}(L - |s|)$, where $\tilde{k} = k - \frac{i2\pi z_i^{cp}}{Z_0\Omega}$, $z_i^{cp} = \frac{1}{2L}\int_{-L}^{L} z_i(s)\mathrm{d}s$ is the mean value of the internal impedance along the vibrator length, $Z_0 = 120\pi$ Ohm, $\Omega = 2\ln(2L / r)$. Let us use the following expression for the current antisymmetrical component [3]: $f^a(s) = \sin 2ks - 2\sin ks\cos kL$.

Let us represent the functions $z_i^{s,a}(s)$ in the form $z_i^{s,a}(s) = z_i^{s,a}\varphi^{s,a}(s)$ and also take into account the following ratio $2\pi r z_i^{s,a} / Z_0 = \overline{Z}_S^{s,a} = \overline{R}_S^{s,a} + i\overline{X}_S^{s,a}$, where $\overline{Z}_S^{s,a}$ is the normalized surface impedance of the vibrator [4].

We shall consider the following functions of the impedance distribution (which are realized rather easily in practice): $\varphi^s(s) = 1$ – the constant distribution along the vibrator; $\varphi^a(s) = \mathrm{sign}\, s = (|s|/s)$ – the stepped alternating distribution. At this the components of the surface impedance along the vibrator are defined by the ratios $\overline{Z}_S^{s,a} = (\overline{Z}_{S1} \pm \overline{Z}_{S2}) / 2$, where $\overline{Z}_{S1,2}$ are the surface impedances of the first and the second arms of the vibrator, correspondingly.

Knowledge of the real distribution of the current permits to calculate all suitable electrodynamic characteristics of the impedance vibrator. So, we obtain the following expression for the input impedance in the feeding points $Z_{in} = R_{in} + X_{in}$, Ohm:

$$Z_{in} = \frac{60i[(Z^s + F_{zs}^{s2}) - (F_{za}^{sa})^2(Z^a + F_{zs}^{a2})]}{\sin^2\tilde{k}L}, \quad (5)$$

and the coefficient of reflection S_{11} into the feeding line with the wave resistance W equals:

$$S_{11} = \frac{Z_{in} - \mathrm{W}}{Z_{in} + \mathrm{W}}. \quad (6)$$

3. NUMERICAL RESULTS

One of the main factors, defining the range of the use of symmetrical vibrators in antenna practice, is the possibility of matching of its input impedance with the wave resistance of the feeding feeder line. The suitable matching can be made for any ratio $2L / \lambda$ at the use of additional elements of tuning at the operation on the fixed wave length. The surface impedance, distributed on the vibrator arms in one or another way, can be used as such an "additional element of tuning" successfully. Let us show this possibility with the help of the results of the numerical calculations of the thin vibrators electrodynamic characteristics, having symmetrical excitation and asymmetrical distribution of purely imaginary surface impedance.

Fig. 1 represents the dependences of the module of the coefficient of reflection $|S_{11}|$ from $\overline{X}_S^a$ at $\overline{X}_S^s = const$ for the vibrators of different electrical length $2L / \lambda_0$ (it is accepted here and further, that $\mathrm{W} = 50$ Ohm, the operating frequency $f_0 = 3$ GHz, λ_0 =10.0 cm, correspondingly, $r = L / 75$). As it is seen, there is a combination of the values $\overline{X}_S^s$ and $\overline{X}_S^a$ for each value $2L / \lambda_0$, at which the coefficient of reflection is minimal; that is, the vibrator is tuned into resonance.

The current amplitude distributions along the vibrators with the electrical length $2L = 0.25\lambda_0$ and $2L = 0.4\lambda_0$ and also the dependences $|S_{11}|$ in the band of frequencies (Figs. 2,3) have been calculated

in order to ground reliability of the obtained approximate analytical expression for the current (4).

Fig. 2,3 also represent the calculated data, obtained by the method of finite elements, realized in the program "Ansoft HFSS". The vibrators represent themselves metallic conductors of the radius r_{in}, covered by the layer of the magnetodielectric of the thickness $r - r_{in}$. The materials of the covering for one and the other arms of the vibrators on the frequency $f_0 = 3\,\mathrm{GHz}$ have the following electrophysical parameters [5]: 1) **Al_2O_3**, $\varepsilon_1 = 10 - i0.015$, $\mu_1 = 1.0$; 2) ferrite **2CX 1**, $\varepsilon_2 = 10.6 - i0.068$, $\mu_2 = 24.0$.The calculations of the values of the surface impedance components give the following results at these parameters of the magnetodielectrics due to the corresponding formula from [4]: a) for $2L = 0.25\lambda_0$ and $\frac{r_{in}}{r} = 0.5$ $\bar{Z}_S^s = 10^{-6} + i0.09$, $\bar{Z}_S^a = 10^{-6} + i0.08$, b) for $2L = 0.4\lambda_0$ and $\frac{r_{in}}{r} = 0.88$ $\bar{Z}_S^s = 10^{-7} + i0.027$, $\bar{Z}_S^a = 10^{-8} + i0.025$. As it follows from the plots in Fig. 1, these values are close to the corresponding ratios between $\bar{X}_S^s$ and $\bar{X}_S^a$ for tuning the vibrators into resonance.

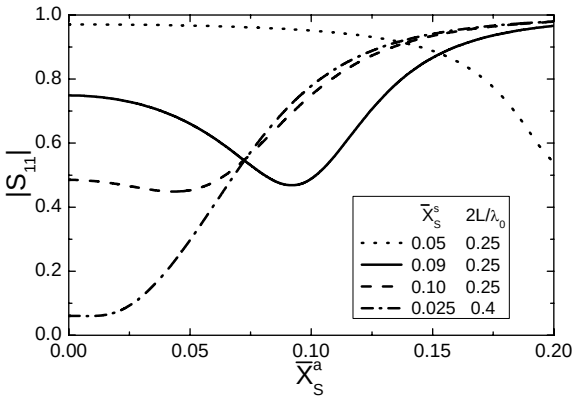


Fig. 1. The influence of the components of the vibrator asymmetrical surface impedance on $|S_{11}|$.

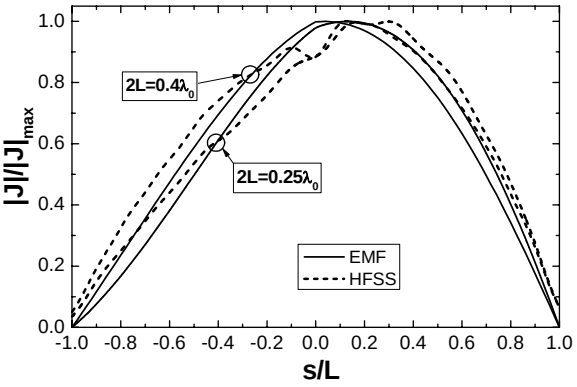


Fig. 2. The functions of the current distributions along the vibrators.

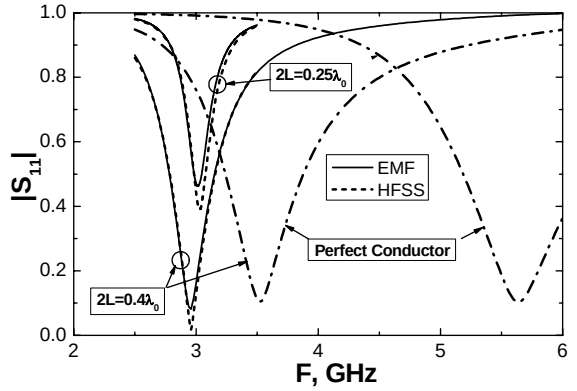


Fig. 3. The dependences $|S_{11}|$ from the frequency.

4. CONCLUSION

Thus the made investigations showed, that availability at vibrators of different electrical length of the asymmetrical distributed surface impedance allows to tune them into resonance with rather small values of the coefficient of reflection in the feeding line with the set wave resistance at a definite value of the operating frequency. Reliability and also the degree of preciseness of the represented approximate analytical expressions for the vibrators input characteristics have been proved by the comparison with the calculated data, obtained by the method of finite elements.

REFERENCES

1. Nesterenko M. V., Katrich V. A. & Dakhov V. M. 2005, 'Radiation field of a thin horizontal impedance vibrator in the lossy half-infinite medium over perfectly conducting plane', *Radiophysics and Radioastronomy*. **10**, 314-324.
2. Nesterenko M. V., Katrich V. A. & Dakhov V. M. and Berdnik S. L. 2008, 'Impedance vibrator with arbitrary point of excitation', *Electromagnetic waves: Progress In Electromagnetics Research B*, EMW Publishing, Cambridge, Massachusetts, USA. **05**, 275-290.
3. Nesterenko M. V. 2005, 'Scattering electromagnetic waves with thin vibrators with variable surface impedance', *Radiophysics and Radioastronomy*. **10**, 408-417.
4. Nesterenko M. V. 2002, 'Surface impedance of vibrators in thin-wire approximation', *Visnyk Kharkiv National University. Radiophysics and Electronics*. **544**, 47–49.
5. *Tables of Physical Values. Handbook*/ Editor Academic I.K. Kikoin. M.: Atomizdat, 1976.

THE RADIATOR OF K_u-BAND BASED ON INVERTED DIELECTRIC WAVEGUIDE

Mayboroda D. V., Pogarsky S. A., Saprykin I. I., Pshenichnaya S. V.

Karazin Kharkov National University, Kharkov, Ukraine
E-mail: Sergey.A.Pogarsky@univer.kharkov.ua

Abstract

The results of the experimental investigations of the single K_u-band radiator based on inverted strip dielectric waveguide are presented. The basic waveguide structure has a few advantages in comparing with other structures in K_u-band. The main of them is an ability of auxiliary elements arrangement. The investigating structure uses exactly this property. The radiator is a combination of two strip resonators, which are placed on both sides of a dielectric substrate. The essential advantage of this construction is the ability of frequency scanning of the main lobe in 26-35 GHz band.

Keywords: Radiator, inverted strip dielectric waveguide.

1. INTRODUCTION

The designing of systems for superfast processing of signals is actual problem of modern radioelectronic and computer technology. The successful decision of this problem defines by possibilities of transmitting of signals with spectral components of ultra high frequencies, super high frequencies and optical band frequencies. Therefore, the necessity of functional elements of these frequency bands designing is appearing.

The radiator systems and elements are widely used in modern radiotechnical equipment. It is very important to have ability to use the radiators of different types and forms, to account their arrangement in different types of the transmission lines and techniques of their excitation because these factors determine the efficiency of radiating systems and respectively parameters of receiving-transmitting equipment as a whole.

The strip radiators in combination with image isolated dielectric waveguide have high level of integral parameters in K_u band, they characterize of good adaptability to manufacture and reproducibility of characteristics with the series production [1,2].

Using an inverted strip dielectric waveguide (ISDWG) as basic transmission line in the radiating structures opens new possibilities to improve integral parameters of radiators [3,4]. The validity of this statement explains by essential character of inverted strip dielectric waveguide is less loss in millimeter band than another types of transmission lines.

Obviously, that the fundamental properties of these hybrid metal-dielectric structures may be determinate if the characteristics of single radiating element in combination with ISDWG are known. The investigation of characteristics of the single conducting radiator K_u band on ISDWG is the subject of present thesis.

2. ANALYSIS

The structure with single radiator in combination with ISDWG is represented in Fig. 1. The design consists of metalized basis - **1**, dielectric rod - **2**, dielectric substrate - **3**, conducting strips - **4**,**5**, placed on two sides of dielectric substrate **3** one above another. One of the ends of conducting strips **4**,**5** reaches the middle of dielectric rod **2**. Such arrangement provides the maximum transferring of SHF energy from transmission line, formed by elements **1**-**3**, to conducting strips **4**,**5**. Due to ISDWG is multimode structure, the excitation of radiator may be carry out at several frequencies, that leads to the multichannel work of examined radiator.

The properties of single radiator were determined experimentally. The design of radiator characterized as: dielectric rod made from the polystyrene with $\varepsilon = 2.5$ and with the cross-section 7×3 mm, the dielectric substrate made from alumina with $\varepsilon = 9.6$, conducting strips have the sizes 12×6.8 mm and 12×2.5 mm and they were made by the thin-film technology.

The excitation of the structure was realized with the help of rectangular waveguide with the cross-section 7.2×3.4 mm [4]. The $26 \div 35$ GHz frequency band was the operating range. In Fig. 2 the dependences of VSWR in operating range for two versions of the conducting strips (curve 1 corresponds to radia-

978-1-4244-7468-4/10/$26 ©2010 IEEE

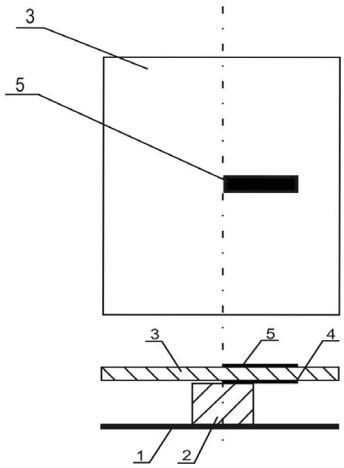


Fig. 1. The structure with single radiator based on ISDWG.

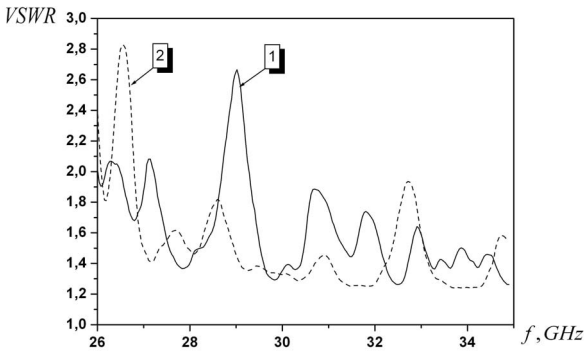


Fig. 2. The VSWR dependence in operating range of radiator with the different sizes of the conducting strips.

tor with sizes 12×2.5 mm, curve 2 corresponds to radiator with sizes 12×6.8 mm) are represented.

As it follows from the experimental results, the VSWR dependences in operating range have an oscillating character. One can observed the enough broadband frequency bands (channels) in the operating range with VSWR $\leq$ 1.4. As it follows from the represented results the channels with the values VSWR $\leq$ 1.4 are observed for both versions of geometrical sizes of strips.

It may be predicted that such structure radiate in the channels with minimum of VSWR values if the minimum of dissipative losses are observed in basic waveguiding structure. This fact finds it's acknowledgement in pattern characteristics of examined radiating structure.

The radiation patterns for two versions of the conducting strips sizes in frequency channels are given in Fig. 3, 4.

The characteristics represented in Fig. 3 correspond to radiator with sizes 12×2.5 mm (curves 1,2,3 are plotting at the frequencies 27.92 GHz, 29.6 GHz, 32.12 GHz, accordingly). As it follows from given data, the pattern characteristics are double-beam. It is evident that the radiation maximums are displaced from the normal line of structure, and the values of

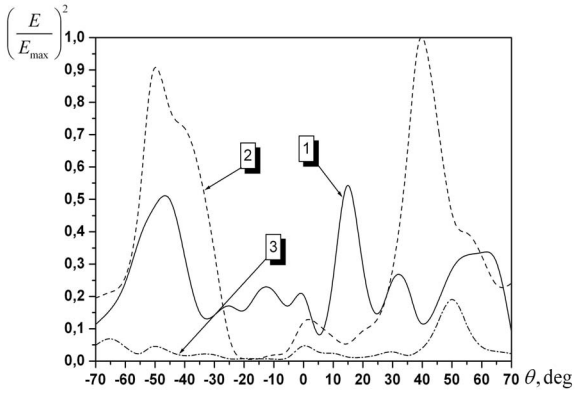


Fig. 3. Radiation pattern of radiator with 12×2.5 mm sizes of the conducting strips

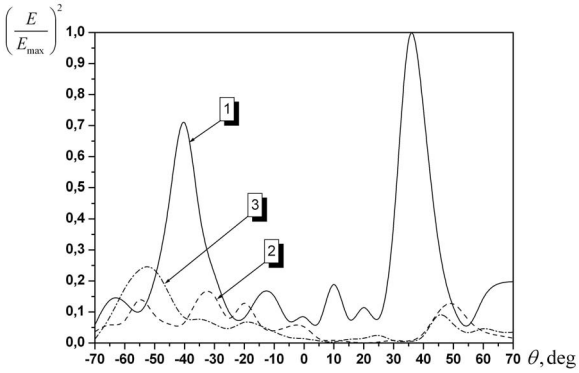


Fig. 4. Radiation pattern of radiator with 12×6.8 mm sizes of the conducting strips.

these displacements depend on the width of the conducting strips, frequency and they reach approximately $40^0 \div 50^0$, the beam width is $10^0 \div 15^0$ at 0.5 power level.

In the Fig. 4 the sizes of radiator are 12×6.8 mm (curves 1, 2, 3 are plotted at the frequencies 27 GHz, 31.2 GHz, 33 GHz accordingly).

Analyzing the data represented in Fig. 3, 4 one can note that the radiation effect is really observing near the frequencies with the minimum of VSWR values. The level of radiating power depends on geometry of strips. If one will compare the observed experimental results it may be establish that variations of conductive strips sizes lead to narrowing the width of lobes and to reducing of side lobe in pattern characteristics.

In Fig. 5,6 the pattern characteristics for investigated structure are represented.

In Fig. 5 (the curves 1, 2, 3 correspond to the frequencies of 27 GHz, 31.2 GHz, 33 GHz) and Fig. 6 (the curves 1, 2, 3 correspond to the frequencies of 27.92 GHz, 29.64 GHz, 32.12 GHz). These pattern characteristics were investigated in frequency ranges with maximum VSWR values for resonators with sizes 12×2.5 mm (Fig. 5) and 12×6.8 mm (Fig. 6).

Comparing the results represented in Fig. 3-6 it is obvious that frequency shift in the channel of radiation leads both to redistribution of energy and to the

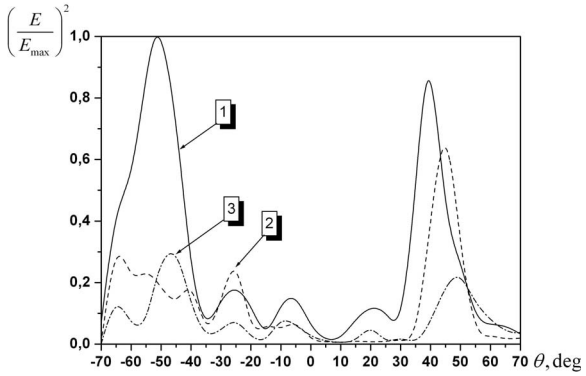


Fig. 5. Radiation pattern of radiator with 12×2.5 mm sizes of the conducting strips

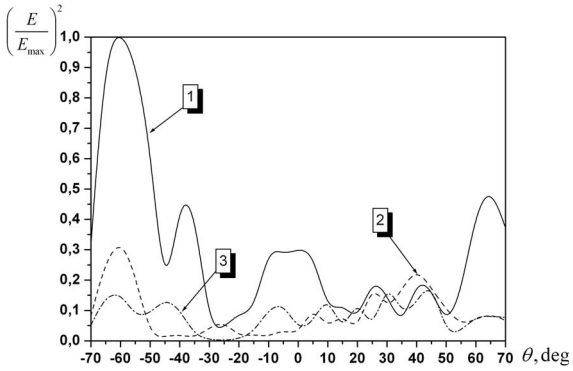


Fig. 6. Radiation pattern of radiator with 12×6.8 mm sizes of the conducting strips.

changes of pattern characteristics. These effects may be explained by multimode regime of ISDWG.

It may be state that the carried out experimental investigations confirm the successful possibility of inverted dielectric waveguide using as a basic transmission line in radiating structure design problem. The self-evident advantage of such design is the possibility of matching with internal devices in enough wide frequency band. The variation of radiator's parameters allows varying the level of radiating power and the form of pattern characteristics. The receive results allow to predict the designing of effective radiation systems with high level of integral characteristics.

REFERENCES

1. Katrich V., Saprykin I., Shaulov E., Chumachenko V. 1999, 'Radiating system based on isolate mirror-like dielectric waveguide', *Proc. 9th Int. Conf. CRIMICO-99*, Sevastopol, pp. 213 -214.
2. Katrich V., Mayboroda D., Pogarsky S., Pshenichnaya S., Saprykin I., Shaulov E. 2006 'Radiating characteristics of multielements hybrid metal-dielectric structure', *Proc. 16th Int. Conf. CRIMICO-2006*, Sevastopol, Vol. 2, pp. 477 -478.
3. James R., Henderson A., 'Dielectric image waveguide antenna array' *US Patent. Int*. Cl № 4, 507, 664. Mar. 26. 1985.
4. Katrich V., Mayboroda D., Pogarsky S., Pshenichnaya S., Saprykin I., Sukhov V. 2009 'Inverted strip dielectric waveguide with metal plane' *Proc. 19th Int. Conf. CRIMICO-2009*, Sevastopol, pp. 515 -516.

PROPER MODE OF EXCITATION FOR LARGE CURRENT RADIATORS

Pochanin G. P. and Pochanina I. Ye.

A.Ya. Usikov Institute for radiophysics and electronics of NAS of Ukraine,
Kharkiv, Ukraine.
E-mail: gpp@ire.kharkov.ua

Abstract

The aim of the experimental investigation is to compare efficiency of radiation in different modes of excitation.

Keywords: Large current radiator, UWB antennas, excitation of LCR.

1. INTRODUCTION

The process of forming of powerful pulses for UWB antennas excitation consists of two stages. The first one is storage stage. At that the energy necessary for pulse has to be accumulated. The second stage is stage of the pulse generating. A switching element changes its conductivity and it results in forming the pulse with a certain temporal parameters. In common a capacitor is used as an accumulating energy element. It is attractive because of it gives a possibility to store the energy for pulse quite long term.

However there is another well known way to store energy for a pulse. This is accumulation energy in inductance. At that the energy is accumulated in a magnetic field around the inductance. If the circuit is disconnected very quickly, a short pulse of electromotive force with a very high voltage raises at the terminals of inductance. The rise time and amplitude of the pulse depend on rate of change of the circuit resistance and difference between its values before and after switching off the current.

Energy storage in inductance in order to form pulses of electromagnetic field have been used in the earliest experiments on energy transmission by Nicola Tesla or radio communication by Oliver Lodge for example, [1]. There are modern scientific publications that describe use of this method of radiation for energy transmission [2] and for ground penetrating radiolocation [3]. The paper [4] contains description of the method of pulse signal generation which is used in these experiments.

This way of the pulse forming is inherent for the large current radiator (LCR) exactly. Since the inductance of the antenna prevents to fast rising of the current, exciting such an antenna by pulse with short front causes problems. At the same time it is not difficult to disconnect circuit with large current during the fractions of nanosecond. Since efficiency of the LCR radiation does not depend on whether the current rise or fall, based on the stopping of large current way of excitation is really inherent for LCR. It is attractive that the radiating element of LCR itself could be used as energy storing element of pulse generator.

2. IMPULSE GENERATION

The Figures 1 and 2 could help to understand peculiarity of the antenna driving. At the beginning the switch S is closed. When we apply voltage U_1 the current j flows through the radiator. As far as the radiator has inductance the current rise time is quite long. When the current riches its maximum (the maximum value depends on output impedance of the pulse source and could be very large) we open the switch. If the switching time is one or less nanosecond, the voltage U_2 across the switch S rises to very high amplitude. It is an electromotive force induced by current when we interrupt it in the circuit with an inductance. This electromotive force produces pulse of electromagnetic field that propagates of antenna. So, the idea is to store energy around the loop in form of magnetic field during quite long term (unlike the common case when the energy usually is stored in capacitance of a pulse generator) and to launch the energy in form of short pulse of electromagnetic wave into free space by means of switching off the switch S.

3. ANTENNA DESIGN

An appropriate driver for the LCR (Fig.2) was developed. Amplitude of electromotive force is 200 V and rise time could be in the range from 0.15 ns to 0.5 ns (fixed value). The picture of LCR is in figure 2. Width of the radiator is 7 cm and length is 9 cm (including a printed circuit board) and height is 3 cm. Several experiments were carried out to evaluate properties of LCR. The aim of the experiments was to compare efficiency of radiation in different modes of excitation.

978-1-4244-7468-4/10/$26 ©2010 IEEE

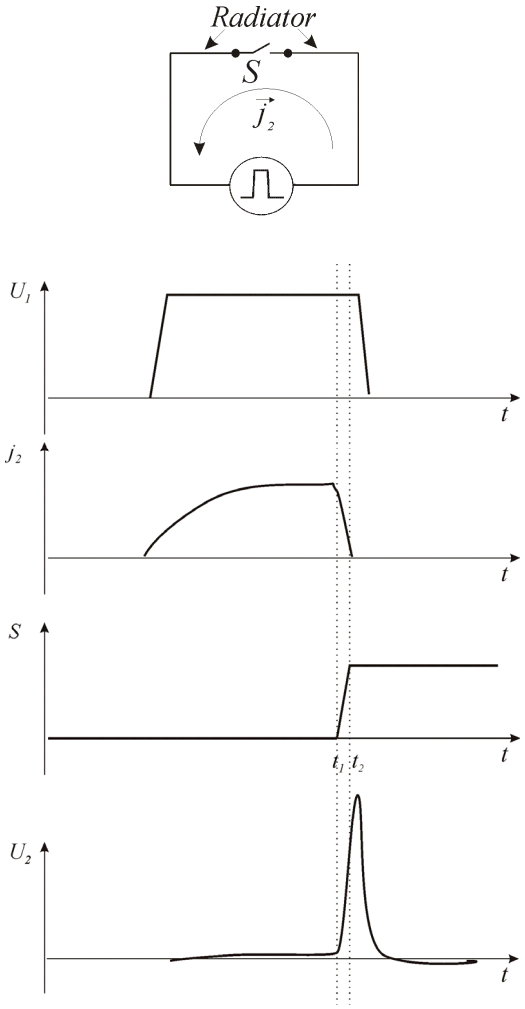


Fig. 1. Principle of short impulse generation with inductance.

4. MODES OF EXCITATION

4.1. MODE 1. ENERGY STORAGE IN LCR

The essence of the first mode is described above. Radiator is connected to the secondary winding of the transformer (Fig. 3). When voltage pulse U =12 V from the pulse generator is applied to the primary winding and switch is closed the current flows through the radiator. It rises quite slowly however it gets amplitude up to 10 A. It lasts for tens nanosecond. Than we switch off the S . LCR radiates. Shape of the radiated pulse at the distance 50 cm from the LCR is shown in Fig. 3.

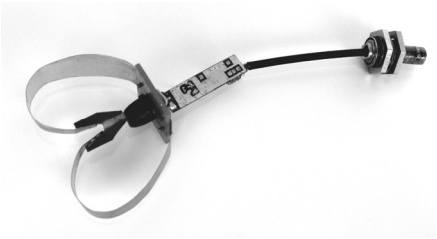


Fig. 2. Test model of the LCR.

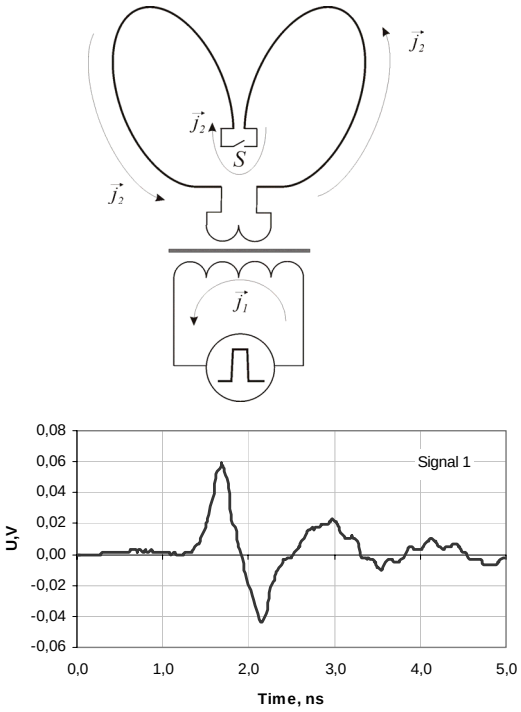


Fig. 3. Mode 1. Driving circuit and radiated signal.

4.2. MODE 2. ENERGY STORAGE IN A TRANSFORMER

The second mode rather is high voltage mode. It differs from the first one with following. The switch S is removed from the ends of antenna arms to the ends of the secondary winding (Fig. 4). In order to prevent the current flow through the radiator before the driving pulse is generated with S antenna arms are disconnected at the ends. The driving pulse is generated after interrupting current in the secondary winding. As a result the antenna radiates (Fig. 4).

4.3. MODE 3. ENERGY STORAGE IN A TRANSFORMER. LOADED ANTENNA

Third mode is between the large current mode and the high voltage mode. The driving signal arises at the end of the secondary winding of transformer (Fig. 5). The ends of the radiator are connected by means of resistor R=240 Ohms. The antenna radiates Signal 3 (Fig. 5) in this case.

4.4. MODE 3. IMPULSE FORMING IN A SEPARATED PULSE GENERATOR

The forth mode corresponds to usually used mode when the driving signal is formed in the independent pulse generator and then delivered to the radiator by means of feeder (Fig. 6). A pair of 50 Ohms coaxial cables was used for this. Their length is 0.6 m. Taking into account that pulse propagates from the switch S to the radiator for 3 ns it is reasonable to suppose that inductance of the radiator does not participate in the driving pulse generating. The antenna radiates Signal 4 (Fig. 6) in this case.

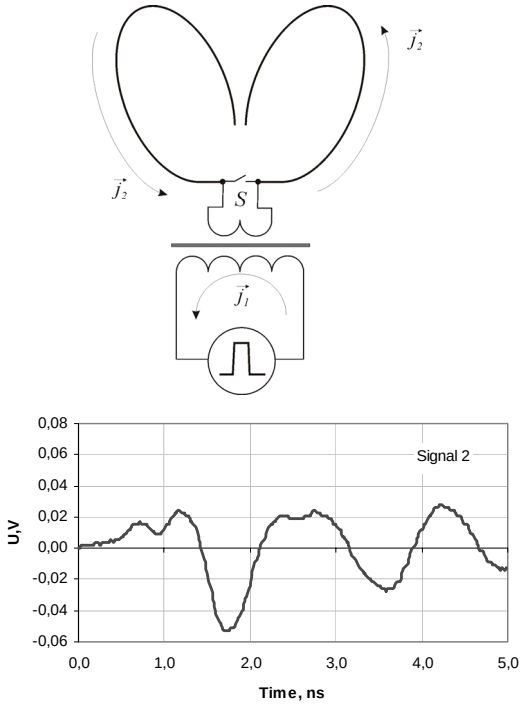


Fig. 4. Mode 2. Driving circuit and radiated signal.

CONCLUSIONS

Comparison of results of experiments shows that

- The large current mode is the most effective because of the largest amplitude of radiated field is generated in the large current mode (mode 1).
- It produces the shortest pulses in the form of the first derivative of the Gaussian pulse.

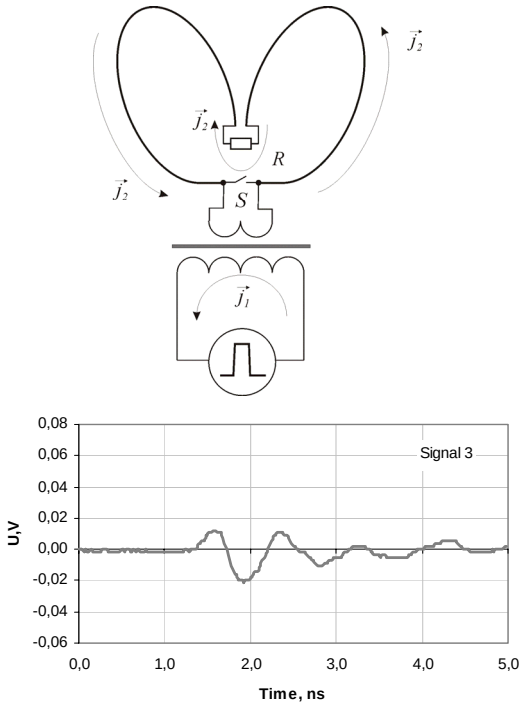


Fig. 5. Mode 3. Driving circuit and radiated signal.

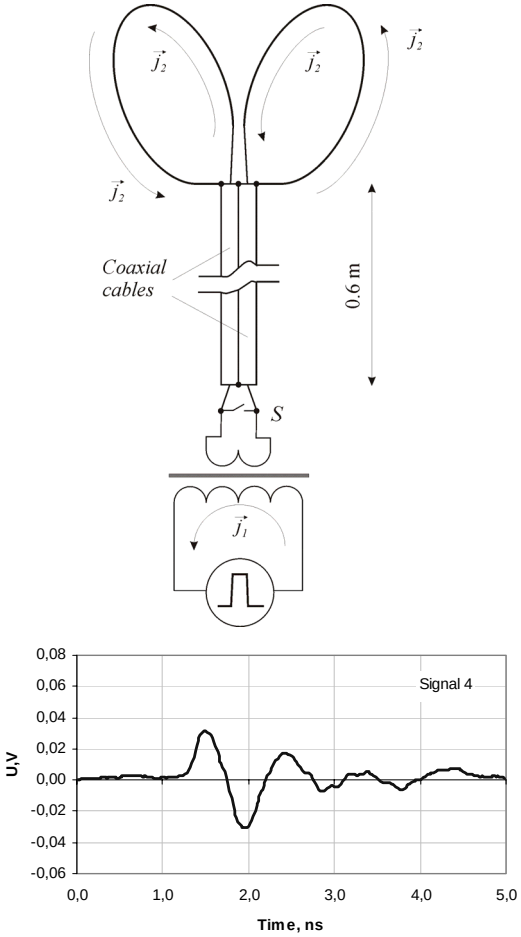


Fig. 6 Mode 4. Driving circuit and radiated signal.

- There are afterpulse oscillations in each of the signals. Nevertheless the lowest "ring" is in the large current mode.

Thus, the proper mode for LCR excitation is the large current mode.

REFERENCES

1. Lodge O.J. 'Electric telegraphy', US Patent 809154, Aug.16 1898. .
2. Boyko N.I., Bjrtsov A.V., Evdoshenko L.S. Zarochentsev A.I., Ivanov V.M., Evseev I.M. 2008, 'Generator of pulses with amplitude up to 1 MV and power up to 11 GW having radiator of spiral antennas', *Proc. 4th Intl. Conf. "Ultrawideband and Ultrashort Impulse Signals"* Sevastopol, 97-99.
3. Prokhorenko V.P., Ivashchuk V.E., Korsun S.V. 2004, 'Electromagnetic impulse radiator'. *Proc.2nd Intl. Workshop. "Ultrawideband and Ultrashort Impulse Signals"* Sevastopol, 244-245.
4. Nelin I.V. 2008, 'Comparison of two methods of generation of ultrawideband signals'. *Proc. 4th Intl. Conf. "Ultrawideband and Ultrashort Impulse Signals"* Sevastopol, 150-153.

GENERATOR OF WIDE-BAND PULSES WITH AMPLITUDE UP TO 20 KV AND PULSE REPETITION RATE UP TO 10^4 PULSES DESIGNED FOR OPERATION WITH VARIOUS RADIATORS

Boyko M. I., Bortsov A. V., Evdoshenko L. S., Ivanov V. M.

RDI "Molniya" NTU "KPI", Kharkov, Ukraine
E-mail: eft@kpi.kharkov.ua

Abstract

High-voltage generator of wideband pulses with amplitude up to 20 kV on the generator output and pulse repetition frequency up to 10^4 pls/s has been created. The pulses can be radiated with help of different radiators: TEM-horn, spiral antenna, V-antenna and others. The generator is implemented on the base of pulsed transformer with short transient response. Primary (in low-voltage circuit) switching is carried out with help of IGBT-transistors. High-voltage nanosecond switching is carried out by air multigap multichannel spark discharger.

Keywords: High-voltage generator, pulsed transformer, multigap multichannel spark discharger, IGBT-transistor, radiator.

Generators of high-voltage wide-band pulses with high (~10^4 pls/s and more) pulse repetition rate are promising for various technologies [1, 2].

The diagram of created generator is given in Figure 1.

Present-day transistor switches can afford power switching of energy from low-voltage energy storage C_0 into high-voltage storage C_h with pulse repetition (operation) rate up to 10^6 pls/s. Limiting factor is duration t_{PT} of transient response of pulsed transformer

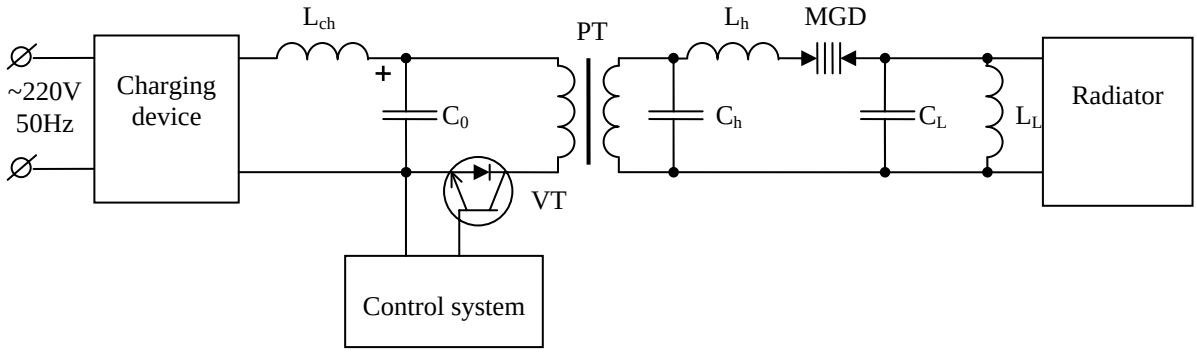
$$t_{PT} \approx \pi\sqrt{L_s C_h}\,,$$

where L_s – leakage inductance of PT relative to high-voltage winding. Difficult, but solvable, problem is the task to obtain t_{PT}~1 μs=10^{-6}s at transformation ratio $K_T=w_2/w_1\approx100$, $C_h=10^{-10}$F, where w_1, w_2 – the numbers of turns in low-voltage primary and high-voltage secondary windings of PT, respectively.

In the created generator in the transistor switch, IGBT transistors with free-wheeling diodes are used, which allows to switch currents ≈150-200 A during tens of nanoseconds.

The most critical element of the generator is high-voltage switch which should ensure switching times of few nanoseconds and less at pulse repetition rate f_r up to $f_r=10^4$pls/s (and more) for efficient operation of radiator.

As radiators on the output of the generator, TEM(T)-horns, helical antennas, V-antennas were successfully used.



C_0 – low-voltage storage capacitance; *VT* – transistor switch defining high pulse repetition frequency in high-voltage load; *PT* – pulsed step-up transformer; C_h – capacitance of high-voltage energy storage; MGD – multi-gap air discharger; L_h – spurious inductance; C_L, L_L – capacitance and inductance of load *LC*-loop.

Fig. 1. The diagram of created generator.

978-1-4244-7468-4/10/$26 ©2010 IEEE

Because characteristic electrical dimensions of high-voltage storage C_h are essentially less than 1 ns=10^{-9}s, there is no necessity to match it with radiator. This significantly simplifies the design of the generator.

Multi-gap multi-channel spark discharger created in our laboratory was used as high-voltage switch. The discharger ensures pulse repetition rate up to 10^4pls/s at working voltages up to 20 kV. Photo of this discharger is presented in Fig. 2.

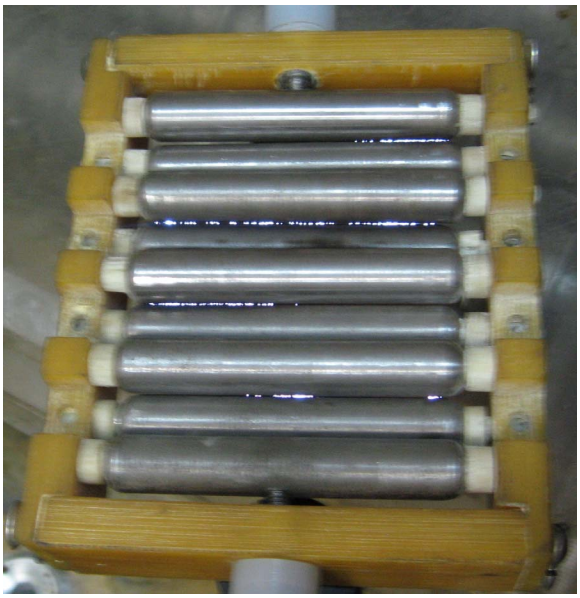


Fig. 2. Photo of multi-gap discharger.

This discharger was implemented as an air one and works under atmospheric pressure, which simplifies essentially its design and makes it easy to manufacture.

The following requirements allowing to increase pulse repetition frequency to maximal extent at the expense of quick recovery of electrical strength of gas in discharging gaps are realized in the discharger [3, 4]: multigapness; short times of fronts of pulses formed by this discharger; use of gas having short recovery times of electrical strength (air); improvement of conditions for displacement of base of sparks along electrodes from pulse to pulse (the conditions were created that spark channels should displace from pulse to pulse and shouldn't form along the trajectories that already took place), improved conditions for cooling and decay of plasma in spark channels after termination of each pulse.

Under conditions of frequency mode operation, minimal achievable switching time $t_{s.MGD}$≈10^{-9}s. This means that front duration t_f of pulses on radiator can be t_f≈$t_{s.MGD}$≈10^{-9}s.

Period T_L of own oscillations in L_LC_L-loop with L_L=10^{-6} H, C_L=10^{-12} F is

$$T_L = 2\pi\sqrt{L_L C_L} = 6{,}28\sqrt{10^{-6}\times 10^{-12}} = 6{,}28\cdot 10^{-9}\,\text{s}.$$

High-voltage capacitance storage of the generator can be approximately considered as a point source having low internal impedance. The generator can work with both directional and nondirectional radiators including multi-antenna radiators.

It should be noted that in this generator MGD and L_LC_L-loop are also radiators of electromagnetic pulses.

Structurally the generator consists of (includes) three main parts: generator of initial pulses, step-up pulsed transformer PT with high-voltage storage C_h and former of radiation, consisting of MGD, L_LC_L-loop and radiator itself of such or another design.

Overall dimensions of the generator of initial pulses: ≈400 mm×300 mm×200 mm. Dimensions of PT with C_h are ≈200 mm×150 mm×100 mm. Characteristic dimension of MGD is ≈100 mm, L_LC_L-loop has the same dimension. Characteristic dimension of the radiator is no more than 1000 mm.

The generator doesn't have scarce elements.

Under input impedance of radiator Z_{in}≈100 Ohm and voltage across its input U_{in}=20 kV, pulsed power P_{puls} at the input of radiator is

$$P_{puls}=U_{in}^2/Z_{in}=(2\ 10^4)^2/100=4\ 10^6\text{(W)}$$

and average power P_{av} at the input of radiator is $P_{av}=C_h\ U_{in}^2/2\ f_r$=$10^{-10}$F $(2\ 10^4\text{V})^2 10^4\text{s}^{-1}$/2=200 (W).

REFERENCES

1. Mesyats G.A. Pulse Power and Electronics. M.:Nauka, 2004.
2. Zheltov K. A., Pal'chevskii A. Yu., and Puchkov Yu. D. A Shaper of Multiply Repeated Picosecond High-Voltage Pulses in a Range of 10^{-10} s *Instruments and Experimental Techniques*, No. 4, 2009, pp. 102–105.
3. Boyko M.I, Evdoshenko L.S, Zarotchentsev A.I., Ivanov V.M., Tour A.I. High voltage spark gaps for technological purposes *Instruments and Experimental Techniques* No. 2, 2001, pp. 204–212.
4. Gerasimov A.I. Multichannel Spark Gaps with Control Bar Electrodes: Their Development and Application (A Review) *Instruments and Experimental Techniques*, No. 1, 2004, pp. 5–38.

INFLUENCE OF THE SCREEN ON THE RANGE PROPERTIES OF RAREFIED ARRAYS OF NEAR-OMNIDIRECTIONAL RADIATORS

Gorobets N. N. and Bulgakova A. A.

Karazin Kharkov National University, Kharkov, Ukraine
E-mail: Nikolay.N.Gorobets@univer.kharkov.ua

Abstract

The directional characteristics of arrays of isotropic radiators, Hertz dipoles and half-wave dipoles located above the screen at the arbitrary distance were theoretically investigated. To ensure minimum distortion of the form of ultra-wideband pulse signal radiated by the array, it is proposed to use the radiators of various lengths and arrange them at the different distances from the screen.

Keywords: Pattern, rarefied array, isotropic radiators, directional characteristics.

1. INTRODUCTION

At present time the parabolic reflector antennas are widely used as highly directive broadband antennas (as the antennas for space communication systems as ultra-wideband antennas for radar systems, subsurface sounding) [1]. This is primarily due to the fact that in such antennas the transformation of the inhomogeneities of spherical wave of radiator into inhomogeneous plane wave at the radiating aperture of the reflector in the transmit mode or the focus of the incident wave at the reflector at the focus of the parabola in receiving regime occurs regardless from the frequency of the electromagnetic wave (in practice, the restrictions, surely, occurs: at the low-frequency range, the size of reflector should be larger than the wavelength, and at the high-frequency range the manufacturing recourse of the reflector surface should not exceed $\lambda min/32$). At reflector radiation by UWB pulse signal, the distortion of the pulse form occurs because of the gain of a reflector antenna and, hence, its transfer function is proportional to the square of the electrical dimensions of the radiating aperture. In addition, the reflector antennas have the large volumes, which limit their use in UWB radar for subsurface radio sounding.

Thus, the requests almost lead to the necessary to find the alternatives to high gain antennas for UWB radio systems. It is obvious that as such variants the plane or conformal antenna arrays of near-omnidirectional radiators can be used. The principal feature of arrays in comparison with reflector antennas is the distortion of the signal due to a larger number of different factors. A fundamental influence on the directional characteristics are two factors:

- Change of the pattern form and energy characteristics of the radiator (an element of the array in the frequency range) due to the finite length of the radiator;
- Change of the form of radiation pattern and energy characteristics of the antenna array with a fixed distance between the radiators due to the changes of electrical values both the distance between radiators and electrical dimensions array in the frequency range.

Physical phenomena and limitations associated with the first factor studied in [2] for the case of a linear wire dipole of finite length. The determining factor for the solution of the formulated problem of creating a planar UWB antenna array of such radiators is the formation of zero in the direction of the normal to the radiator at frequencies at which its electrical length is an even number of quarter wavelengths. Obviously, this circumstance can be overcome using linear radiators of different lengths in the array.

Peculiarities of the directional patterns of arrays of linear near-omnidirectional radiators with change of frequency in a very wide range studied by us [3] and it was shown that in co-phase arrays at high frequencies, the direction of the main maximum of pattern is not changed. The dependence of the directivity gain of the electrical antenna length first increases to the maximum achievable value, and then oscillates with decreasing amplitude and in the limit this value is equal to the number of radiators.

Clearly, these conclusions require clarification in the case of antenna arrays with plane screens, creating unidirectional radiation. Indeed, according to the method of images, linear vibrator, located parallel to the screen, will form a null in the direction of normal to the screen, when the electrical distance between the vibrator and the screen is equal to an even number of quarter wavelength in the free space.

The purpose of this report is to study the directional characteristics of co-phase arrays and near-omnidirectional radiators located above the screen at an arbitrary height.

978-1-4244-7468-4/10/$26 ©2010 IEEE

2. ANALYSIS OF THE CALCULATION RESULTS

As in [3], the pattern of the studied radiating systems will be considered in the simplest case for analysis of linear-phase equidistant arrays, and to find the directivity gain by integration of the power radiation pattern

$$D_m = 1 \Big/ \int_0^{\pi/2} \left|F\left(\theta\right)\right|^2 \cos\theta d\theta$$

The influence of the screen will be taken into account by the method of images.

According to calculations by the geometric theory of diffraction [4], the method of images satisfactory describes the directional characteristics of the radiators with plane finite screens at the size of the screen, the edges of which are separated from the radiator to 0,5 ... 1 wavelengths. Let us first analyze the influence of the screen on the pattern sparse array for the most important practical case when the distance between the radiator and the screen is equal to a quarter wavelength. This distance defining the height of the antenna is the minimum distance at which the local maximum gain of the arrays is provided. To illustrate the qualitative changes in the radiation pattern when changing the distance between the radiators in Fig. 1 shows the pattern of the in-phase equidistant array of isotropic radiators excited by currents of equal amplitude for different distances between the radiators. The first version of $d/\lambda = 0.5$ illustrates the directional pattern of a classical array, the second one with $d/\lambda = 1$ shows the features of the pattern of the array with a maximum gain - a significant reduction in the width of the main lobe and the growth of the far sidelobes.

The third variant illustrates the case of very sparse array of $d/\lambda = 10$, when the pattern has interference (diffraction) lobes. The figure shows that in the whole range of distances between the radiator within a 1–20 the main maximum of the pattern is directed, as expected, along the normal to the array. The directions of diffraction and sidelobes are changed with changing d/λ. Consequently, when the array is excited by UWB pulse signal, the smallest distortion of the pulse occur in the direction of normal to the array. In other directions in the case of very sparse array, the pulse shape and spectral characteristics of the signal will be changed significantly.

The changes of signal parameters in the direction of normal to the array occur due to changes in the gain of the radiating system. Fig. 2 shows the calculated dependence of gain from the electrical length of the array of isotropic radiators, spaced at $\lambda/4$ from the flat screen. It is seen that the maximum gain occurs when the distance between the radiators is a little bit less than the wavelength and with further increase in the distance or decrease in the wavelength, the gain changes slightly. Consequently, in the spectrum of

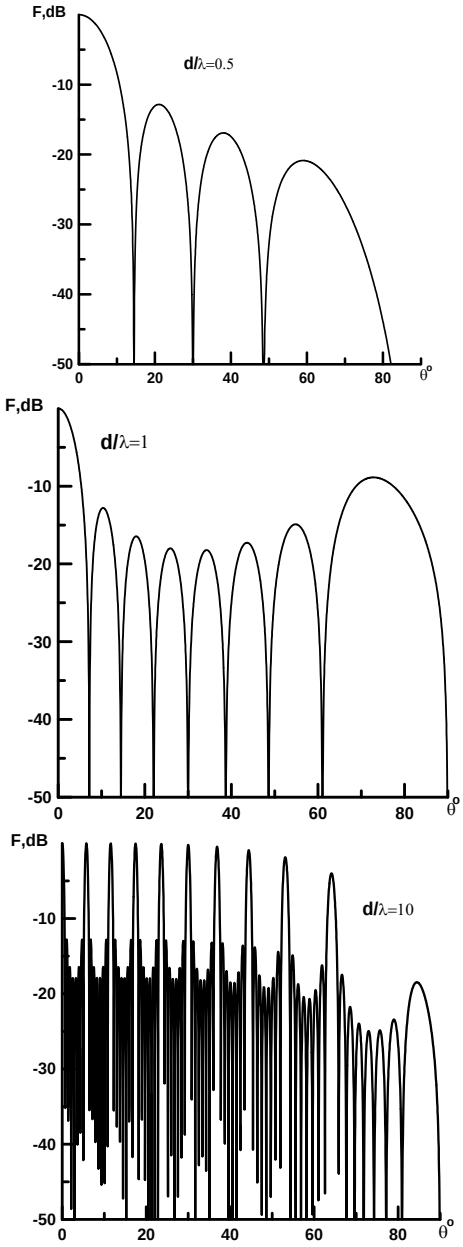


Fig. 1. The radiation patterns of a linear array of eight isotropic radiators located above the screen when $h/\lambda = 0.25$.

ultra-wideband impulse signal, low-frequency components will be increase, while the high frequency components will be changed insignificantly during radiation due to directivity of the array.

The same result can be obtained by accounting the directivity of radiators. Fig. 3 shows the dependence of gain of equidistant array of 8 radiators in the form of isotropic radiators, Hertz dipoles and half-wave dipoles from the distance between the radiators. It can be seen from Fig. 3, that in the low-frequency range the directivity of radiators does not influence significantly on the amplitudes of spectral components. In the high-frequency range, the influence of radiator directivity (the element of antenna array) is greater,

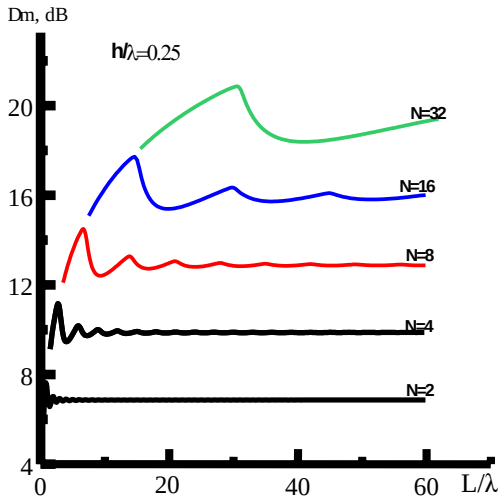


Fig. 2. Dependencies of the gain from the electrical length of antenna array.

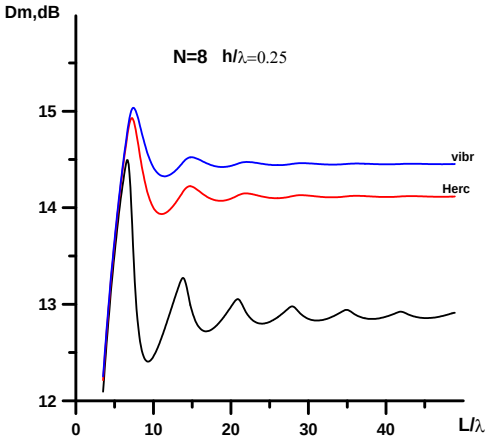


Fig. 3. Dependences of gain of array, consisting 8 radiators, versus d / λ.

namely: the greater radiator directivity, the less variation of amplitude of high-frequency spectral components. The same results were obtained for big distances from the array and screen.

Thus, narrow-beam plane antenna arrays can be realized with minimal distortions of the form of a pulse signal in the direction of normal to the array. In the case of using the screens, it is necessary to place the radiators of the array at the different distances from the screen.

3. CONCLUSION

The radiation pattern and gain of linear co-phase equidistant arrays was theoretically investigated in dependence from its number, distance between them and distances from the array to screen. It was shown that minimum distortion of the ultra-wideband pulse signal occurs in the direction of normal to the array. In the case of very short pulses, the necessary to use the radiators of difference length and place them on different distances from the screen can appear.

REFERENCES

1. *Pproblems of Surface Penetrating Radiolocation* 2005, Ed. by prof. A.Yu. Grinev. Moscov. Radiotechnique, 416. (in Russian)
2. Gorobets N.N., Nechesa A.V. 1999, Superwide-Band Signal Distortion Caused by Linear Dipole Antennas. //*Telecommunications and Radio Engineering*, vol.53, N 3, 36-41.
3. Gorobets N.N., Bulgakova A.A. 2008, Directivity Characteristics of Rarefied Antenna Arrays. // *Vestnik of Kharkov National University – Radiophysics and Electronics*. № 834,89-94 (in Russian)
4. Gorobets N.N., Yeliseyeva N.P. 2009, *Diffraction of Radiation of the Wire Antenna on the Rectangular and Corner Screens*. Kharkiv, Kharkiv V.N. Karazin National University -380. (in Russian)

THE GENERATION BY GUNN DIODES BASED ON THE GAN, INN, ALN TED'S IN BIHARMONIC REGIME

Storozhenko I. P. and Arkusha Yu. V.

Karazin Kharkov National University, Kharkov, Ukraine
E-mail: storozhenko_igor@mail.ru

Abstract

The frequency and power capabilities of the nitride semiconductor-A3B5-based Gunn diodes are evaluated using a temperature model of the intervalley electron transfer. Prospects, problems and characteristics of the nitride semiconductors in TED's for the harmonic and biharmonic modes are discussed.

1. INTRODUCTION

The efficient method to increase the frequency cutoff of Gunn diodes (TED's) is a biharmonic mode (generation of harmonics). In this regard the A_3B_5 nitride Gunn diodes characteristics are of interest. The nitride semiconductors have a high mobility and relaxation rate of electrons. The transport characteristics of AlN, InN, GaN have been investigated in [1]. These results reveal about perceptively of AlN, InN and GaN for submillimeter-wave Gunn diodes. Microwave generation of the fundamental harmonic via the mechanism of semiconductor nitrides Gunn diodes is found out theoretically in [2]. However, experimentally the oscillations haven't been obtained in Gunn diodes based on semiconductors nitride. This work's purpose is to investigate the characteristics of InN, GaN and AlN Gunn diodes in harmonic and biharmonic modes using some mathematical simulation methods.

2. BASIC PART

The temperature simulation wurtzite InN, AlN, and GaN Gunn diode [3].is being used.

The frequency limitation in ideal accumulation transit mode of InN, AlN, and GaN diodes is very high (Fig. 1). This is because of the small periods of electrons relaxation, compared with common semiconductors A_3B_5 (GaAs, InP); including the intervals of the transitions of electrons from the G-valley to the side-valleys and backwards. Allowing for the 2nd harmonic does not increase essentially the efficiency and the ultimate frequency of generation, by contrast to GaAs. It is worth mentioning that the above evaluation is made regardless of the special heterogeneities, which are the main cause limiting the LSA mode in frequency. It is known that because of the special inertia effects, the LSA mode is not the one of the highest frequency in TED's The highest frequencies of generation in TED's based on GaAs and InP are achieved for the resonance-transit mode.

Therefore the 2nd stage of investigation dealt with the modeling of devices with special heterogeneities. In InN, GaN and AlN TED's there are the same modes as in similar-type devices based on the other semiconductors A_3B_5, namely: the domain mode, the mode with the enriched layers drift and the mode with the increasing waves of volume charge.

The main feature of those TEDs' working is a high value of the threshold electric field E_n, esp. in AlN. This leads to great difficulties in the electron gas heating near cathode, its thermal insulation in contact with anode and in decreasing the temperature of a crystal lattice as well.

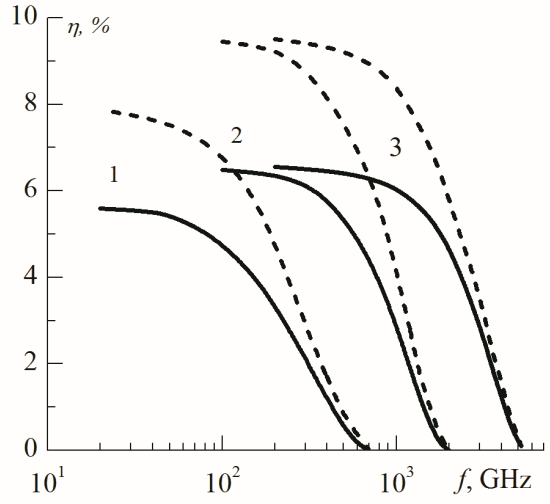


Fig. 1. Efficiency of ideal accumulation transit mode of TED's for fundamental harmonic (solid line) and biharmonic (first and second harmonics) mode (dotted line): 1 – InN; 2 – GaN; 3 – AlN.

978-1-4244-7468-4/10/$26 ©2010 IEEE

In order to heat up the electric gas in n^+-n^--n-n^+ devices, the region of a lower concentration of donators n^- near cathode has to have a greater length and the gradient of ionized admixtures concentration, compared with devices based on other semiconductors A_3B_5. Besides, when the oscillations of current are generated in AlN and GaN TED's, the maximal strength of electric field in the n-n^+ anode contact reaches 10^3 кV·cm^{-1}. The electron gas in the anode contact remains heated. The charge fluctuations are carried off into anode, and the transit region's length thus increases. For this reason, the optimal frequency of generation f_0 is lowered in all devices concerning the minimal velocity of electrons on the dependence $V(E)$.

In the semiconductor nitrides, the optimal value of such a basic parameter of TED's as the Crammer criterion *nl* several times exceeds that in GaAs. It is so especially in AlN. For example, the electric domains do not appear in n^+-n^--n-n^+:AlN TED's at $nl < 6\cdot10^{12}$ cm^{-2} at all.

In n^+-n^--n-n^+:InN TED's, the depth of the domains penetration into the active region is a function of the applied voltage [4]. Because of this effect, the InN TED's on the basic harmonic possess two times work bandwidth of GaN и AlN TED's (fig. 2). E.g., the maximal frequency of generation in -n^--n-n^+:InN TED's with l_a=2.5 mcm is 192 GHz, and the optimal one is 60 GHz.

The highest ultimate frequency ≈600 GHz is achieved in $^+$-n^--n-n^+ TED's based on InN – that is, in the worst one of the discussed materials as regards the intervalley electron transfer inertia. However, the energy gap in InN between the central Γ-valley and the closest to it that one in direction [<111>] is ≈1,68 eV at the room temperature, which is close enough to the forbidden zone width of ≈2 eV. Under those conditions the probability of the intervalley electron transfer to be overlapped by the ionization zone-zone is high. The TED's based on GaN are in an intermediate position in efficiency and frequencies of generation between InN and AlN. The maximal generation frequency in n^+-n^--n-n^+:GaN TED's may be 500–600 GHz.

The devices of a homogeneous profile of doping (рис. 3) are less efficient than those with a highohmmic heterogeneity close to cathode. But they can work in submm band as well. If the devices are placed in a double-contour (biharmonic mode), their efficiency and ultimate frequencies increase (Fig. 2, 3).

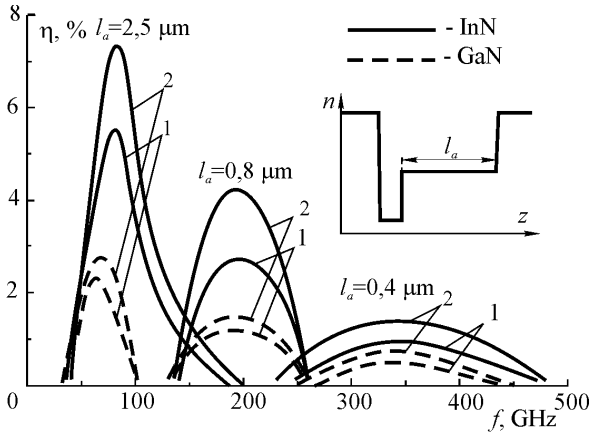


Fig. 2. Efficiency of n^+-n^--n-n^+ InN and GaN TED's: 1 – fundamental harmonic; 2 – biharmonic mode.

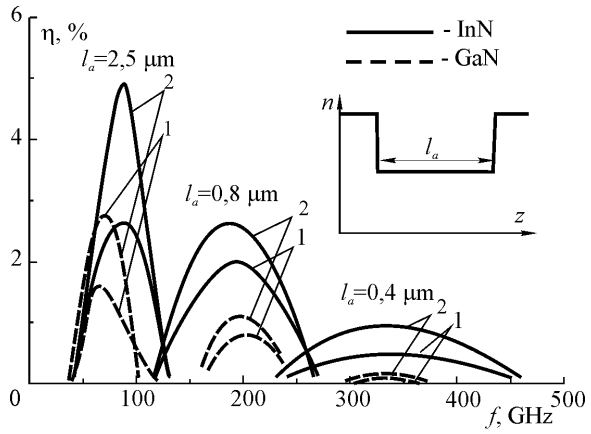


Fig. 3. Efficiency of n^+-n-n^+ InN and GaN TED's: 1 – fundamental harmonic; 2 – biharmonic mode.

4. CONCLUSION

Thus, semiconductors nitride GaN, InN and AlN are promising for sub-millimeter wave Gunn diodes in both fundamental and biharmonic modes because of the high velocity and small relaxation periods of electrons. However, in such devises there are certain problems of electrons heating near cathode, of electrons thermalization near anode, of the active region cooling. There is a good reason to believe that the approach presented is preferable enough to the well-known common methods.

REFERENCES

1. Farahmand M., Garetto C., Bellotti E., et al. 'Monte Carlo Simulation of Electron Transport in the III-Nitride Wurtzite Phase Materials System: Binaries and Ternaries,' *IEEE Transactions on electron devices*. 2001. V. 48, № 3. P. 535-542.
2. Alekseev E., Pavlidis D., 'Large–signal microwave performance of GaN–based NDR diode oscillators,' *Solid State Electronics*. 2000. Vol. 44. P. 941–947.
3. Storozhenko I.P., '$In_{0.4}Ga_{0.6}As$ Modeling the Gunn diodes based on variband semiconductors,' *Telecommunications and Engineering*. 2003. Vol. 59, № 1&2. Pp. 100–110
4. Storozhenko I.P., 'Initiation and Drift of the Space-Charge Waves in Devices Based on Variband $GaP_{x(z)}As_{1-x(z)}$ with the Intervalley Electron Transport,' *Telecommunications and Engineering*. 2008. Vol. 67, № 10. Pp. 881–894.

UWB ANTENNAS

AN ULTRAWIDEBAND 1−20 GHZ MODIFIED LOG-PERIODIC FEED

Dubrovka F. F. and Dolzhenko D. S.

National Technical University of Ukraine "Kyiv Polytechnic Institute",
Kyiv, Ukraine
E-mail: fedor.dubrovka@gmail.com, _light_@ukr.net

Abstract

Results of modeling and optimization of electrical characteristics of an ultra wideband modified log-periodic feed for axially symmetrical reflector antennas operating over frequency range 1-20 GHz are presented.

Keywords: Planar log-periodic antenna, log-periodic feed, ultrawideband axially symmetrical reflector antenna.

1. INTRODUCTION

There are a lot of articles and publications that deal with research and development of log-periodic antennas (LPA). In [1, 2, 3] influence of design parameters on the matching and radiation characteristics of LPA is analyzed in detail. But there are no words about the electrical characteristics of LPA with design parameters, such as width of the planar feedline and width of the flat dipoles, that change in non-log-periodic law.

For the optimal illumination of an axial-symmetric reflector antenna it is necessary to have a feed's axial-symmetric radiation pattern. To obtain such axial symmetry log-periodic antenna shoulders need to be moved apart through ψ-angle [4]. It is quite easy to design a log-periodic feed for operating frequency range 10:1. In this case a LPA feeding is performed by a coaxial line, outer conductor of which runs through the center line of the one of log-periodic elements and center conductor is attached to the another element [3]. There are huge amount of such log-periodic feeds due to the construction simplicity. But it is impossible with such method of feeding to obtain log-periodic feeds for operating in C- and K-bands with coverage 20:1. In [5] this problem is solved with the help of tapered line balun, which consists of a coaxial line with the outer conductor gradually opening up and finally tapered to form a balanced transmission line. This feeding system is too bulky and complicated for the geometry calculation and manufacturing. In [6] analysis of different log-periodic antenna arrays is performed. The author has shown, that in the case of the parallel feeding of the pair of elements in multielement arrays, increasing of the elements number decreases antenna impedance. Thus, a 50-Ohm feeding coax can be utilized.

The aim of this research is mathematical modeling and optimization of characteristics of ultra wideband reflector antenna feed, based on array in H-plane of two log-periodic antennas, that provides in the frequency range 1−20 GHz next parameters: VSWR ≤ 2.5 with coaxial feeder of 50 Ohm impedance; practically axial-symmetric radiation pattern and required frequency-independent −10dB beamwidth.

2. OPTIMIZATION RESULTS

The required feed −10dB beamwidth for given value of the ratio *F/D* = 0,5 can be defined in such a way [5]:

$$2\gamma_0 = 4 \cdot arctg((4 \cdot \frac{f}{D})^{-1}) = 102.5^0.$$

To provide $102{,}5^0$ −10dB beamwidth in E-plane values of log-periodic antenna parameters with the help of the tables [7] are defined as follows: τ = 0,904, $\sigma = 0{,}09$. It is well-known, that log-periodic antenna radiation pattern in H-plane is much more wider than in E-plane. That is why to obtain axial-symmetric radiation pattern the feed based on array in H-plane of two log-periodic antennas is used.

Calculations of the matching and radiation characteristics and also comparison analysis of four different planar log-periodic antennas (PLPA) are performed. These four PLPA are: a traditional PLPA; a PLPA with modified feedline; a PLPA with modified dipoles

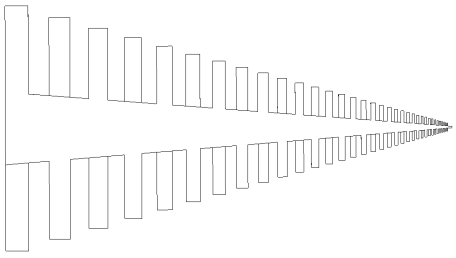


Fig. 1. Traditional PLPA structure.

978-1-4244-7468-4/10/$26 ©2010 IEEE

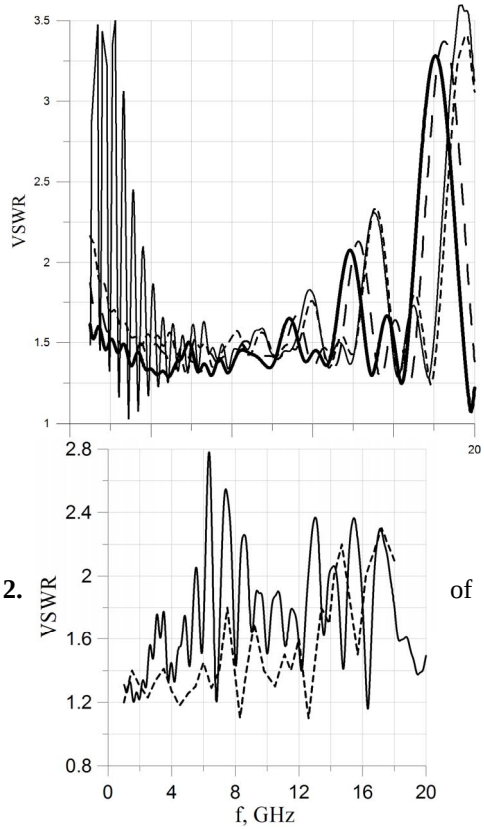


Fig. 2. of four

Fig. 6. Frequency dependence of SLL.

and a PLPA with both modified feedline and dipoles. The calculations show to what extent the main PLPA parameters should change in log-periodic manner. In a traditional PLPA (Fig.1), all parameters, namely, flat dipole length, flat dipoles width and planar feedline width change in log-periodic law. In all other PLPA the modified parameter means that this parameter changes by non-log-periodic law. For all models initial feedline and flat dipole width equals 1 mm and 0,5 mm respectively. In models with modified feedline the end feedline width equals 20 mm and in models with modified dipoles the end dipole width equals 8 mm.

Array consists of two log-periodic antennas in H-plane, fed by coaxial feeder of 50 Ohm impedance. Hence, the input impedance of the separate antenna due to the parallel connection is approximately 100 Ohm.

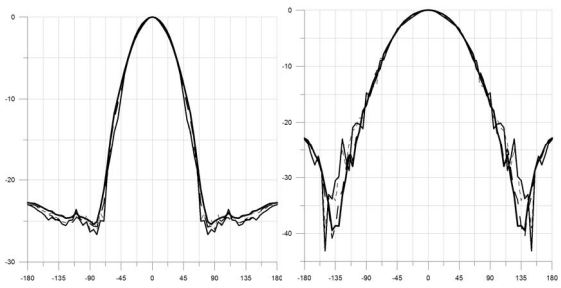


Fig. 3. Typical radiation pattern in E- and H-plane of four different PLPA.

The log-periodic feed construction modeling is performed using CST Microwave Studio software, based on FDTD method.

Curves of VSWR frequency dependences of the PLPA are shown in Fig. 2. It can be seen that matching characteristics of PLPA with both modified parameters is very similar to those of PLPA with modified feedline. But in comparison with traditional PLPA these structures have somewhat better values of VSWR.

Typical radiation patterns in E- and H-plane of the four different PLPA are shown in Fig. 3. Analyzing this curves one can state that changes of flat dipoles and feedline in non-log-periodic manner practically don't distort essentially radiation patterns.

Taking into account these results a PLPA with both modified parameters was chosen as the element for the array to be developed. To improve matching characteristics of this PLPA it was decided to move apart PLPA shoulders through some elevation angle in such a way that distance between elements gradually increases from about 1 mm near the apex to approximately 20 mm at the end of the structure. Frequency dependence of VSWR for PLPA with (dashed line) and without (solid line) shoulders moved apart is shown in Fig. 4. One can observed this approach has improved matching, especially in the frequency ranges 1−6 GHz and 17−20 GHz, but from 6 to 6,8 GHz VSWR values has become worse.

Analysis of the influence on VSWR and radiation pattern of the angle between two log-periodic antennas was carried out. Three values of this angle were chosen: 15^0, 25^0 and 35^0. Analyzing VSWR curves we have found, that angle increasing makes matching characteristics worse. It is obvious that angle increasing causes transverse dimensions increasing. Thus, the 15^0 angle is optimal in terms of VSWR and transverse dimensions. Analysis of radiation patterns for different angles shows, that for 15^0 angle the radiation pattern is asymmetric in the frequency range 1−8 GHz (difference between E- and H-plane −10dB beamwidth is greater than 20^0) and for the 35^0 angle the radiation pattern is asymmetric for 10−18 GHz (difference between E- and H-plane −10dB beamwidth is greater than 18^0). In contrary, for the 25^0 angle for all

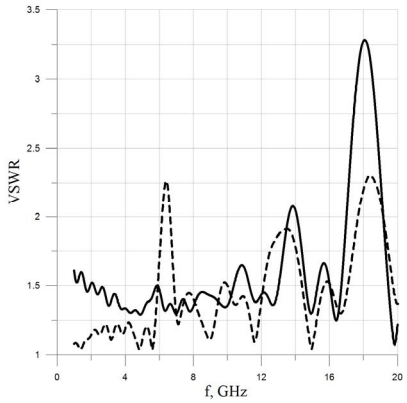


Fig. 4. Frequency dependence of VSWR for PLPA with and without moved apart elements.

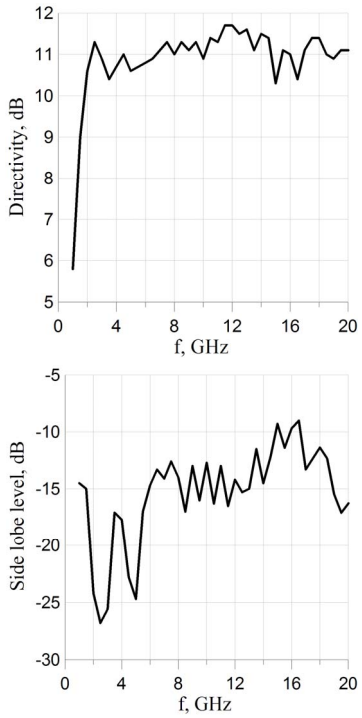


Fig. 5. Frequency dependence of directivity and side lobe level.

frequencies in the entire operating band the average difference between E- and H-plane −10dB beamwidth doesn't exceed 10 degrees. Thus, the 25^0 angle is optimal in terms of obtaining axial-symmetric radiation pattern. As for the 25^0 angle the matching characteristic is acceptable and radiation pattern is practically axial-symmetric, so this angle is chosen for the designing of the optimal log-periodic feed. We have found, that for this 25^0 angle the distance between center axis of log-periodic antennas is approximately λ/2. That is why to obtain practically axial-symmetric radiation pattern one must provide such angle between array elements to form approximately λ/2 distance between these elements.

Analysis of the main characteristics of the optimal log-periodic feed, which consists of two PLPA with both modified parameters with the λ/2 distance between center axes, was performed.

In general case due to the frequency changes the feed phase center moves against to the feeding point. But the log-periodic feed can be placed in such a way that reflector focus is located in the feed high-frequency part. Then distance from phase center to the focus in the entire frequency range will not exceed $\lambda/3$, which is acceptable for a number of applications [8].

Directivity of the feed versus frequency is shown in Fig. 5. It can be seen that average feed directivity is about 11 dB, except frequency band from 1 to 2 GHz, where this parameter falls drastically from 10,6 to 5,8 GHz. Frequency dependence of feed's side lobe level (SLL) is also presented in Fig. 5. In average theoretical maximum side lobe level is less than −14 dB, and only for the frequency band of 12−18 GHz this parameter is higher than −12 dB. Front-to-back ratio is less than −16 dB in the whole operating frequency range 1−20 GHz.

Comparison of theoretical and experimental results of VSWR was carried out. Curves of frequency dependence of theoretical (solid line) and experimental (dashed line) VSWR are presented in Fig. 6. Theoretical VSWR maximum values are less than 2,5 in entire frequency range 1−20 GHz, except for values f = 6,36 GHz (VSWR = 2,78) and f = 7,38 GHz (VSWR = 2,55). As for experimental results, they are much more better. Practical VSWR maximum values not exceed 2,3 in all operating frequency range.

5. CONCLUSIONS

Ultrawideband log-periodic feed, based on array in H-plane of two log-periodic antennas, for the reflector antenna with *F/D* = 0.5 is designed. In the frequency range 1−20 GHz developed feed provides VSWR ≤ 2.5 with coaxial feeder of 50 Ohm impedance; practically axial-symmetric radiation pattern with 90^0−100^0 −10dB beamwidth on the main polarization; approximately 11 dB directivity; acceptable phase center deviation; 16 dB noise immunity. This antenna may be recommended for usage in radiomonitoring systems with ultrawideband reflector antennas and ultrawideband systems of different purposes.

REFERENCES

1. DuHamel R. H., Isbell D. E. Broadband logarithmically periodic antenna structures. // *IRE National Convention Record*. – 1957. – pp. 119-128.
2. DuHamel R. H., Ore F. R. Logarithmically periodic antenna designs. // *IRE National Convention Record*. – 1958. – pp. 139-151.
3. Benenson L. S. Ultrawideband antennas. – 1964. – 415 p.
4. Milligan T. A. Modern antenna design. – 2005. – 613 p.
5. DuHamel R. H., Ore F. R. Log periodic feeds for lens and reflectors. // *IRE National Convention Record*. – 1959. – pp. 128 – 137.
6. DuHamel R. H., Berry D. G. Logarithmically periodic antenna arrays. // *IRE Wescon Convention Record*. – 1958. – pp. 161-174.
7. Stutzman Waren L. Antenna theory and design. – 1981. – 595 p.
8. Imbriale W.A. Optimum Designs of Broad and Narrow Band Parabolic Reflector Antennas Fed with Log-Periodic Dipole Arrays. // *IEEE Trans. Antennas Propagat.* – 1974. – Vol. 14. – pp. 201-205.

THE PLASMA ANTENNAS MOUNTED ON FRAGMENTS OF MOBILE OBJECTS

[1] Ovsyanikov V. V., [2] Ol'shevs'kiy O. L., [2] Popel' V. M., [2] Romanenko Y. D., [1] Ponomarenko Y. V., [1] Moroz S. N.

[1] Dniepropetrovsk National University named after O. Gonchar, Dniepropetrovsk, Ukraine
E-mail: ovsyan_viktor@mail.ru
[2] Yuzhnoe State Design Office named after M.K. Yangel, Dniepropetrovsk, Ukraine,
E-mail: kbu@public.ua.net

Abstract

Results of research of internal and external characteristics of the plasma aerials mounted on fragments of mobile objects are adduced. A number of features and advantages of such antennas is noted.

Keywords: Internal and external characteristics of the plasma aerial, mobile objects, features and advantages of the plasma antenna, conductivity, dielectric permeability, VSWR, the directional diagram, efficiency of the antenna.

1. INTRODUCTION

There are several studies on the interaction of microwaves with a cold plasma and the development of plasma antenna (PA) [1-5]. Published parameters of the simplest PA [5, 6]. However, the relevant question is to assess the radio and the electrodynamic parameters of the PA (input impedance, standing wave ratio, radiation pattern, efficiency, etc.), installed on more complex moving objects, such as airplanes, satellites and other bodies which affect in some way to these parameters to the PA. Especially significant is this influence, if the geometric parameters of a mobile object comparable or close to the operating wavelength of the PA. This paper presents the results of computer simulation of the above parameters of the loop plasma antennas (LPA), established on fragments of modern aircraft.

2. REFERENCE DATA FOR RESEARCH

The possibilities of modern computers and software environments do not allow you to quickly assess the electromagnetic characteristics of antennas are installed on the geometrically complex moving objects, such as airplanes, satellites, etc. Therefore, to speed up the computational results, resorted to the most characteristic simplified fragments of these objects.

2.1. FRAGMENTS MOBILE OBJECTS [7]

One of the fragments (A) plane is a cylinder with two wings, and mounted with a loop PA 1 (Fig. 1).

The second fragment (B) the aircraft is part of a cone with apex angle. At the top of the cone along its axis set loop of PA (Fig. 2).

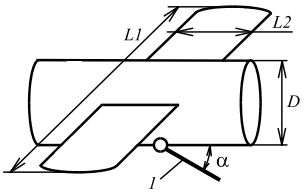


Fig. 1. A simplified fragment «A» of aircraft: α is angle of inclination of the plane of the LPA *1* to the surface of the cylinder of cylindrical part of the aircraft.

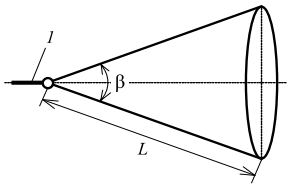


Fig. 2. A simplified fragment "B" of aircraft with a loop plasma antenna *1*.

2.2. RADIOPHYSICS CHARACTERISTICS OF COLD PLASMA

The conductivity σ and relative permittivity ε of a cold plasma, of which the PA consists, have a frequency dispersion and determined by known formulas [1]. These parameters were determined for the temperature of electronic components of the plasma $T_e = 10^4$ °K and the density of free charges in the plasma equal to $N_e = 10^{13}$ sm^{-3}. For this case σ ranged from approximately 10 to 200 mhos / m and

978-1-4244-7468-4/10/$26 ©2010 IEEE

relative dielectric constant ε ranging from $-3\cdot10^5$ to $-4\cdot10^3$. Calculations of microwave characteristics of the PA, the configuration of which is given in [2, 3, 6], installed on the fragments of the plane "A" and "B" have been implemented in a software environment FEKO.

3. Results of Calculations VSWR, Radiation Pattern and Efficiency

The calculated frequency characteristics of VSWR for the fragment "A" (Fig. 1) are shown in Fig. 3. Here d is height of LPA, D is diameter of the cylinder, L is length of the cylindrical part; L_1 is wingspan; L_2 is width of the wing.

As can be seen from the graphs, LPA, installed on the fragment "A" provides approximately 2 - 3 times more bandwidth than a similar configuration on the metal antenna, for example, of aluminum. The smaller the angle of LPA over the surface of the cylinder, the higher become the values of VSWR and deteriorating form of a VSWR frequency characteristic.

The calculated frequency characteristics of VSWR for the fragment B (Fig. 2) are shown in Fig. 4. Here $L = 2.5\lambda_0$.

As can be seen from the graphs of Fig. 4, LPA installed at the top of the cone segment "B" providing as in the previous case, approximately 2-3 times more bandwidth than a similar configuration of the antenna of aluminum. However, compared with the previous application, rum basic advanced schedule VSWR resonance is shifted to the right toward higher frequencies $d/\lambda = 0.35 - 0.45$. At the same time, for the values which equals 0.13–0.15 found a new resonance VSWR. Thus the LPA on a fragment of "B" is able to operate in two frequency bands with a relatively small electrical length $d/\lambda = 0.13 - 0.15$ and

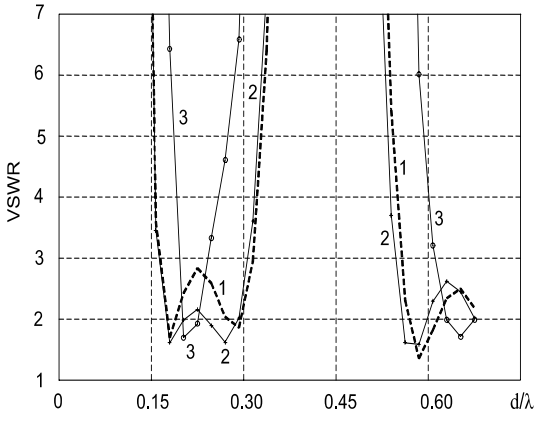


Fig. 3. The VSWR graphics in a frequency band of the loop plasma antenna (Fragment "A"), D/λ_0=2.9, L_1/λ_0=9.8, L_2/λ_0=1.7: 1 – LPA, $\alpha = 60^0$; 2 – LPA, $\alpha = 90^0$; 3 – antenna aluminum, $\alpha = 60^0$.

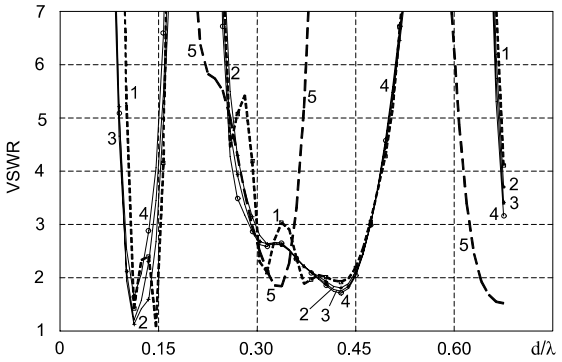


Fig. 4. The VSWR graphics in a frequency band, Fragment "B": 1 – $\beta = 0^0$; 2 – $\beta = 20^0$; 3 – $\beta = 40^0$; 4 – $\beta = 60^0$; 5 – $\beta = 20^0$. The antenna is executed from an aluminum tube with a configuration similar LPA.

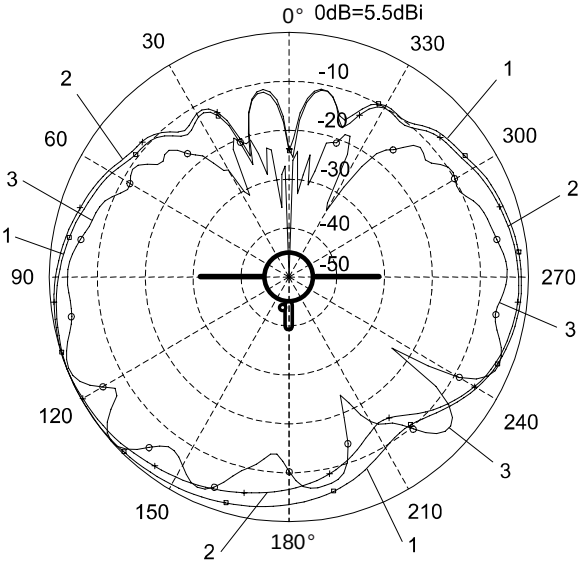


Fig. 5. The radiating pattern of the antenna system d/λ = 0,20 (Fragment "A"):
1 – $\alpha = 90^0$ (without wings);
2 – $\alpha = 60^0$ (without wings);
3 – $\alpha = 90^0$ (with wings).

$d/\lambda = 0.35 - 0.45$. With respect to the angle at the vertex of the cone, then it changes from 0 to 60 deg. little effect on the frequency dependence of VSWR LPA.

The calculated directivity patterns (in power) antenna system (fragment "A") (Fig. 1) at a constant length of the working wave λ_0 shown in Fig. 5.

As follows from graphs Fig. 5 at placing LPA as is shown in Fig. 1 plane wings, make considerable impact on formation of the radiation pattern (RP) round the case of the given fragment, that undoubtedly takes place by real planes with the similar electric sizes.

As follows from graphs Fig. 5 (graph 3) presence of wings of the plane leads to occurrence irregularity of RP in a direction opposite to a direction to the

Earth (deep failures of radiated or received power to – 30 … – 40 dB), and also to occurrence of some irregularity and in a direction to the Earth – 10 … – 20 dB in separate directions. As a whole it is possible to ascertain, that the power most part is thus radiated towards the Earth. The similar phenomenon takes place and for metal antennas. To reduce irregularity of RP it is necessary to choose optimum installation site of LPA, displacing it along a cylinder axis. Some asymmetry of the most loop antennas and its device of excitation explains asymmetry of RP concerning a vertical axis 0-180°.

The calculated directivity patterns (in power) antenna system (Fragment "B") (Fig. 2) at a constant length of the working wave λ_0 shown in Fig. 6.

As follows from comparing the graphs Fig. 6, with decreasing the angle increases the irregularity of RP. The most profound failures of power take place along the axis of the cone.

The calculated efficiency of antenna systems for fragments of the "A" and "B") (Fig. 1, Fig. 2) are shown in Fig. 7: curve 1 – cylinder (without wings), $d/\lambda_0 =$ 0,20, $\alpha = 60^0$; 2 – cone top, d/λ_0 = 0,35, $\beta = 20^0$.

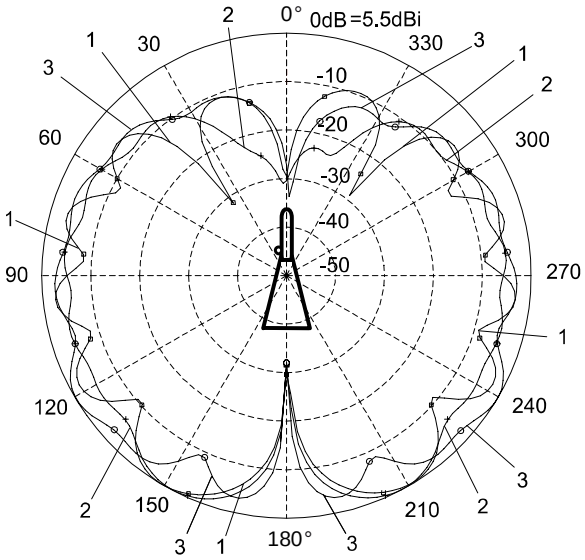


Fig. 6. The radiating pattern of the LPA placed in cone top, $d/\lambda = 0,35$ (Fragment "B"): $1 - \beta = 0^0$; $2 - \beta = 20^0$; $3 - \beta = 60^0$.

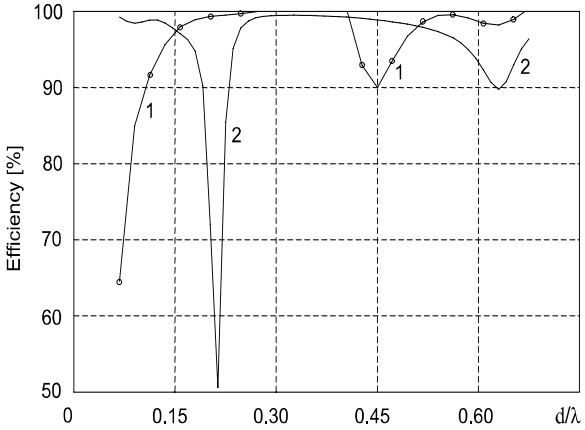


Fig. 7. The LPA efficiency.

3. CONCLUSION

It was found that LPA in both fragments A and B planes in terms of VSWR ≤ 2 have twice - three times wider frequency range than the usual loop, metal (aluminum) antenna, the additional resonance for a conical fragment "B" is thus found out. Obtain concrete numerical results for RP and effectiveness of the LPA, which are installed on the characteristic fragments of the plane.

ACKNOWLEDGMENTS

The authors thank the company EMSS and FEKO technical support team for granted by the opportunity to study and uses of the software FEKO.

REFERENCES

1. V.L. Ginzburg, *Propagation of Electromagnetic Waves on Plasma*, 1960, Moscow: GIPHML, p. 552. (in Russian).
2. Ovsyanikov V.V., Litvinov A.G., Malanchuk A.M. Antenna made of Plasma, The request it is offered on delivery of copyright certificate N 3566850 / 09 (044520), USSR, H01Q 1/00, 24.03. 1983.
3. V.V. Ovsyanikov. “Broadband Microwave Emitter on a Basis of Gas Discharge Plasma”, *Mag. Radiophysics and Radioastronomy*, Kharkiv. Vol. 6, No. 3, pp. 261-267, 2001. (in Russian).
4. Anderson T.R. 2002, ‘Electromagnetic Radiation from Frequency Driven and Transient Plasmas’, *IEEE International Symposium on EMS*, 19-23 August, Vol.1, 498-501.
5. Jenn D.C. 2003, Naval Postgraduate School, ‘Plasma antennas: Survey of Techniques and the Current State of the Art’, Prepared for: SPAWAR PMW 189 San Diego, CA.
6. Bezpalov A.Y., Gnatushenko V.V., Ovsyanikov V.V., and all. "Research Antenna Made of Gas Plasma on Microwave Band", *EuCAP'2010: The 4th Europ. Conf. on Antennas and Prop*. 12-16 April 2010, in Barcelona, Spain.
7. http://www.lockheedmartin.com.

COMPLEX PULSE RADIATION OF CIRCULAR TSA ARRAY WITH STEERING POLARITIES OF ELEMENT EXCITATION

[1] Kolchigin N. N., Kazansky O. V., Ivanchenko D. D.,
[2] Liang Jing Feng, He Shi, Zheng Yu

V.N. Karazin Kharkov National University, Kharkov, Ukraine
E-mail: [1] kolchigin@univer.kharkov.ua; [2] lyl212003@yahoo.com.cn

Abstract

A time-domain characteristic of the field radiated by a circular TSA array has been investigated in paper. The possibility of patterns synthesis by excitation polarities of circular array element has been showed. The results of experimental measurements have coincided with the simulation results.

Keywords: Circular antenna, plane antenna array, TSA pulse radiation, excitation polarities of circular array.

1. INTRODUCTION

A circular array is extended due to its omnipattern. Such antenna constructions are well known in literature for all direction excitation/receipt of monochromatic and poly-frequencies signals and this applies to radiolocation, geological detection and telecommunication. This antenna is distinguished by structural simplicity, easy fabrication and low material consumption. The application of these arrays in pulse regime provides high resolving ability due to short spatial pulse duration, and also represents possibilities of high penetration in different mediums. In addition, it needs high amount of information in radio communication, and then impulse with a short time interval can provide a higher sending/receiving quality then monochromatic signal [1,2]. Therefore, presented antennal system with circular impulse excitation can be applied to situations mentioned above.

2. PROBLEM DEFINITION

2.1. ARRAY CONSTRUCTION

Described array is a set of tapered slot antenna (TSA) on the general dielectric substrate and with independent excitations of antenna elements which are able to steer polarities pulse excitation. Each element is made of thin metal layer on dielectric substrate with slot tapered from the feeding to the edge of radiation. The slot width is taken by this way, in order to satisfy the condition of matching between the excited point and the feeder line (wave impedance of slot is set 50 Ohm at frequency of 3 GHz and the slot width should be 0.1 mm), and the width of radiation edge should satisfy the condition of matching between antenna slot and space medium (wave impedance 377 Ohm and the slot width should be 26 cm). Generally, this antenna is a disk with a series of radial slots and the feeding points in the centre of disk (Fig. 1).

Experimental operative embodiment had such parameters: thickness of copper layer 0.1 mm, the substrate was made of grass with thickness 1 mm and dielectric permittivity $\varepsilon = 4.25$. Elements are excited with gaussian pulse with duration of T = 1 ns and peak amplitude 25V .

2.2. CALCULATION AND EXPERIMENTAL METHODOLOGY

Each frequency in the spectrum of pulse was considered as relative monochromatic signal which excited from all TSA circular arrays. Each array element is represented as a series of inhomogeneous radiating rectangular apertures. But current distributing on each aperture is considered to be homogeneous. And then, radiated fields of each rectangular aperture are solved by the method (system of linear algebraic equation). The radiated field of the circular array is calculated as a sum of all the fields from each aperture.

Experimental measurement was carried out by using the described setup and a block diagram is presented on Fig. 1. Signals are excited from the pulse generator, the elements of the array are fed by the coaxial cable with wave impedance 50 Ohm. The basis of the generator with steerable signal polarities at antenna elements uses special steerable blocks (ST). Pulse signal is radiated from circular antenna array (A1) and receipted by tapered slot antenna A2, which can effectively receive a frequency band from 0.5 GHz to 5 GHz just as the spectrum of radiated impulse signal. And then a signal was transmitted to a stroboscopic oscillograph (SO) with a frequency band from 0 to 10 GHz by coaxial cable, and can detect signals with durations not less than 0.1 ns, the signal from oscillograph was digitized through Analog-

978-1-4244-7468-4/10/$26 ©2010 IEEE

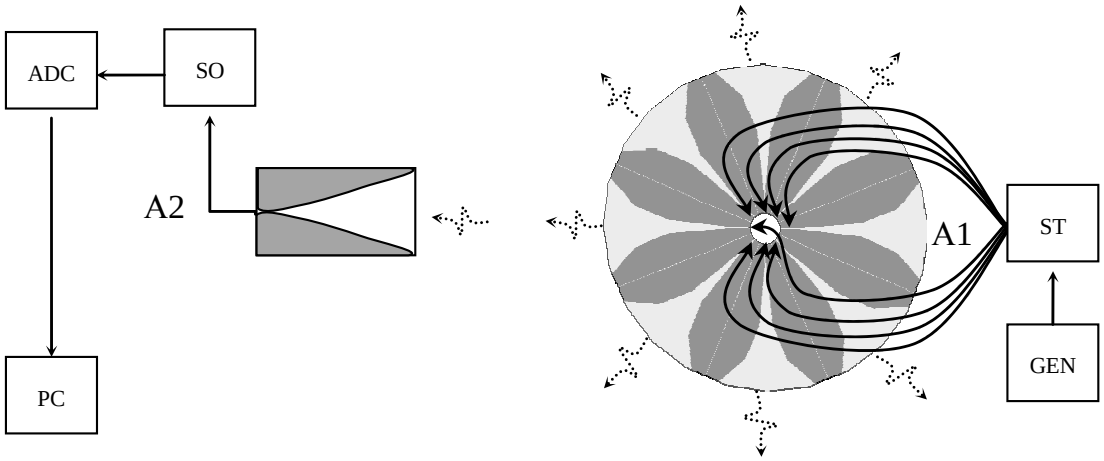


Fig. 1. Scheme of Experimental measurement, time-space characteristics of circular TSA array.

to-Digital Converter (ADC) with such parameters: number of digits-10 (1024 points), number of channels-16, input signal- unipolar 0..10 V or bipolar +/-10 V, maximal frequency transformation – 285 KHz, boot-manual or programmable. ADC was controlled by special developed program, which can make simultaneous observation and records specified quantity of points (up to 32000) through specified quantity of channels (up to 16) with specified frequency transformation. Numerical processing signal, input to personal computer (PC), is completed by 2 steps: average of 10 adjacent points, remove thermal noise and smooth form of the received signal, and another step is to adopt an average of 10 times to realize complete elimination of non-stationary noise. The antenna was placed above the ground at a height of 1m by measurement, and utilized "time window" to eliminate the influence of radiated field, the distance between the receiving and transmitting antennas is 3 meters.

The errors of the signal amplitude with these setups are: intrinsic noise of installation (~ 10 mV) and error of ADC (~ 4.88 mV). After applying the above algorithms of numerical processing, the influence of random fluctuation of the signal which exists in inherence of SO has lowered, and the noise has reduced by 3.16 times. Thus, the total error in amplitude is 3 mV.

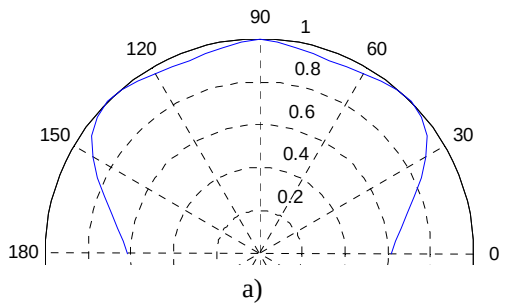
3. RESULTS

The results of numerical simulation radiation of 8 elements circular TSA array, where excited 4 elements, as well as experimental measurement are presented in the form of radiation peak power pattern in Fig. 2- 4 (E-plane), here we consider the cases of antenna elements excitation with the following polarities (indicated polarities are electrodes of input signal for array): Fig. 2 for the excitation of the array elements with type + - + - + - + - (constant polarities): Fig. 3 for excitation of the array elements with type + - - + + - - + (alternating polarities); Fig. 4 for excitation of the array elements with type + - + - - + - + (polarities changed on the middle of the array).

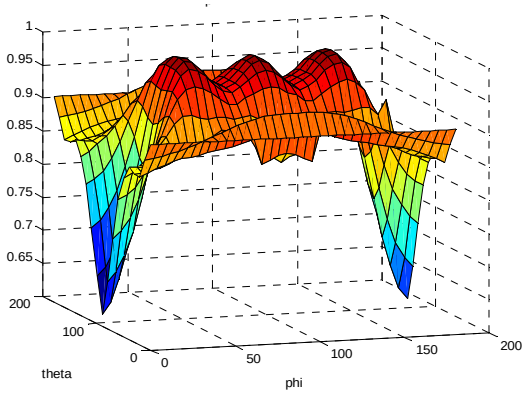
Numerical simulation showed that the synchronous excitation with the same polarities obtained isotropic radiation pattern, in this case just considered half circular array, the radiation pattern in the sector of angles $\pm 60^0$ is isotropic, and for further angles the magnitude of the radiated signal was decreased down to 0.7 at 70^0. Experimental measurement of circular array with analogical excitation confirms the change of the radiation pattern. Fig. 2 shows the radiation pattern of half array elements, and also gives a visual representation of the back excitation of the array elements. Hence, the inter-elemental interaction in the array is due to the interrelation of opposite array elements. Note that, the magnitude of excited signal and the radiation pattern are included in amplitude of excited signal, but in amplitude of the back excited signal, the coefficient of inter-elemental interactions between opposite elements is included too. Then it's easy to calculate this coefficient of interaction by the measurement, the design of array should take into account the coefficient of interaction between the opposite lying elements to ensure the desired magnitude of the radiated signal. And the interaction between neighboring elements should be also considered [5]. In this case, we are interested in the situation for omni-directional radiation/reception.

In another case, when polarities of excited signals are alternating, the radiation pattern has the form of lobed structure. The lobes are corresponding to elements of the array. For the angle of related intersections of two close elements occurs decreased amplitude of excited signal, up to complete disappearance, which is associated with the signals excited from adjacent elements with opposite polarities. Here the angle of observation is increased by 10^0 and amplitude of signal increases by 0.7 times, that is due to compensation of different degrees of excited signals from the array elements (Fig. 3). Experimental measurements of the radiation pattern confirm the simulation results.

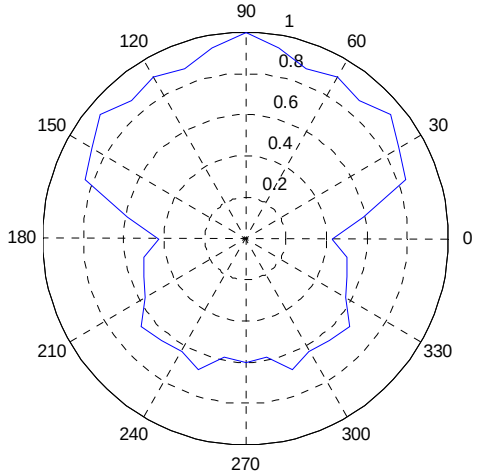
In the third case, signals of array elements are excited with different polarities changed on the middle of the array (Fig. 4).An identical radiation pattern is observed to the first case, when the signal of array elements were



a)

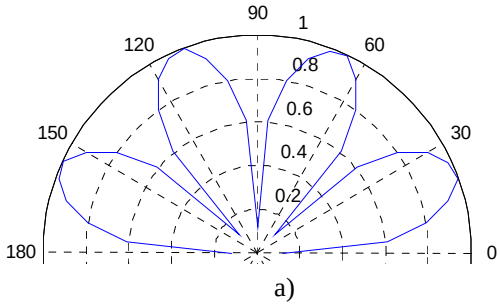


b)

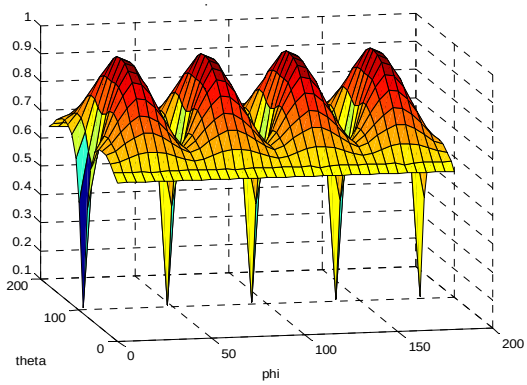


c)

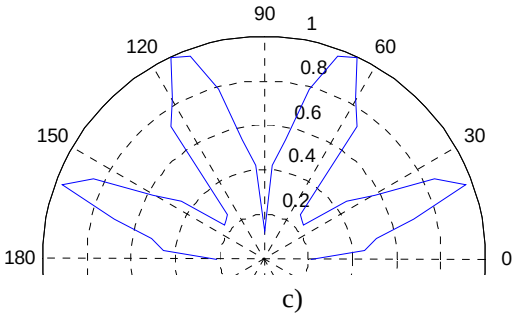
Fig. 2. Pattern for type of excitation + - + - + - + - case (a, b– calculation, c - experiment)



a)



b)



c)

Fig. 3. Pattern for type of excitation + - - + + - - + case (a, b– calculation, c - experiment).

excited with the same polarity, the middle of the pattern observed similar failures as the previous case, signals of different polarities eliminated mutually each other. The experiment meets the calculated values well, and has the same characteristics as the theorem of radiation pattern.

Thus, the possibility of changing the excited polarity of the array elements can synthesize radiation pattern, then it is able to provide the desired amplitude of radiated signal to a given sector of angles.

Organization of the antenna system as multi-layered semi circle TSA arrays in volume antenna which would solve issues as working with a large number of "goals" and to provide more detailed and quality management "goal" by working with several layers of the antenna system at the same time.

4. CONCLUSIONS

The possibility of changing the excited polarity of the array elements can synthesize radiation pattern, then it is able to provide the desired amplitude of radiated signal to a given sector of angles.

REFERENCES

1. *Suhovetskij B.I.* // Russian Federation Patent, 2093936 (13) C1.
2. USA patent N 4001834.

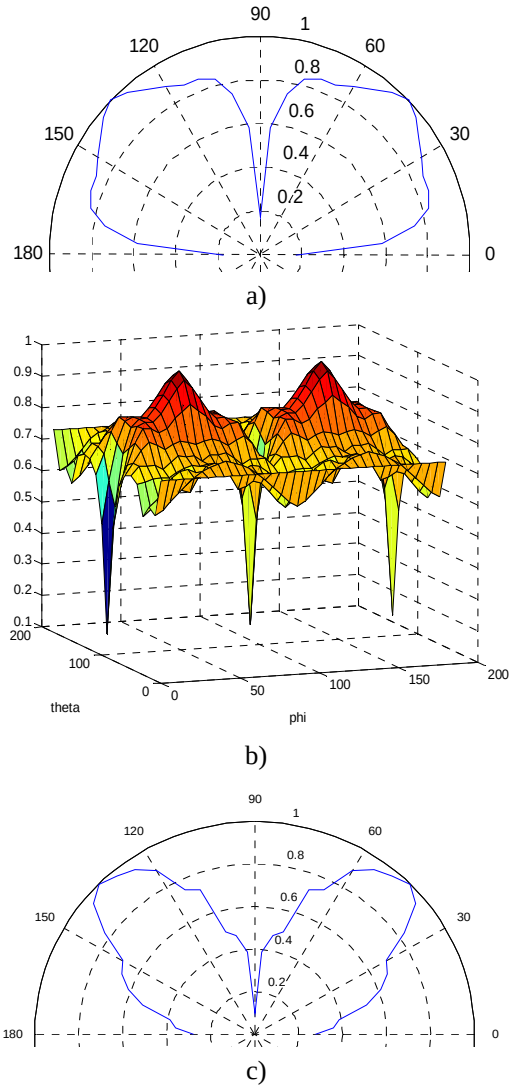


Fig. 4. Pattern for type of excitation + - + - - + - + case (a, b– calculation, c - experiment).

3. Butrym A.Yu., Kazansky O.V., 'Time Domain Tapered Slot Antenna Analysis,' *Ukrainian physical journal*, 2002, v. 47, № 6, P. 557-559.
4. 4. Butrym A.Yu., Kazansky O. V., Kolchigin N.N. 'Array of tapered slot antennas (TSA) for ultrawideband signals,' *An advances of modern radiophysics* . 2005. No 5. P. 60-64.
5. Kazansky O.V., Kolchigin N.N., Litvinov D.D., 'High power and ultrashort pulse forming,' *KhNU Bulletin. Radiophysics and electronics*, 2002. N 544. P. 217-222.
6. Kazansky O.V., 'An influence of mutual interaction on characteristics of signal radiated by antenna array, which excited by pulse,' *KhNU Bulletin. Radiophysics and electronics*. 2007 № 756. P. 57-60.

ARRAYED «VIVALDI» RADIATORS CHARACTERISTICS

[1] Yukhanov Y. V., Bolov R. B., Privalova T. Y.,
[2] Kondrat'eva A. P., Kurochkin A. P., Los' V. F.

[1]Taganrog Institute of Technology of Southern Federal University, Russia
[2] Joint-Stock Company "Radio Engineering Corporation "VEGA", Russia
E-mail: yu_yukhanov@mail.ru

Abstract

In this work, characteristics of ultra-wideband «Vivaldi» radiators in single use and also in array condition was investigated. One of the design features in this antenna is the original arousing detail, eliminating a resonator. There is a research about abilities of band enhancement using absorber. Significant bandwidth widening to the left of arrayed «Vivaldi» radiators in E-plane is demonstrated.

Keywords: «Vivaldi», antenna array, VSWR, radiation pattern.

Employment of ultra-wideband (UWB) or ultra-short pulse signals in radiolocation with high action radius allows to raise considerably self-descriptiveness of radio-systems, improve external noise immunity, provide secrecy and ability to detect objects under growth or a underlying terrain due to meaningful portion of probing videopulse energy at lower (about 10..100 MHz) frequencies. To realize such radars, antenna array (AA) with UWB radiators operating at referred above frequencies is necessary. Scanning sector of such AA for aerospace location is to belong to the range of

$$\theta = \pm(15...30)^\circ;\ \varphi = \pm(25...60)^\circ \qquad (1)$$

over a bandwidth

$$f \in [0.1...1.5]\ \text{GHz}. \qquad (2)$$

«Vivaldi» radiators are sufficient for this requests including beam width [1-7].

The **purpose** of this paper is a researches about «Vivaldi» radiators in single use and also with video pulse scanning antenna array (VPSAA) with characteristics, allowing to reach compromise between lower operating frequency, partial radiation pattern and necessity to minimize radiated pulses duration in comparison with arousing ones.

Antenna's sheets and arousing structure's shape and size, such as also width of regular slotline between antenna's main parts were scaleable definitions during electrodynamics modeling.

Prior approximate calculus with available methods [5, 6] of «Vivaldi» radiators allowed considerably reduce amount of variables to make next computations more rigorous method.

Final computer simulation was implemented with HFSS software.

In this work the original feeding system [8] was used to provide «monocycle» form of radiating pulse and to minimize signal length. Its realization was found in two cylinders with common central axe moved away from each other on a few distance. From one side there is an antenna plane and feeding coaxial line opposite (Fig. 1).

In accordance with theory of radiating systems enlarging exit aperture size causes not only reducing of bandwidth lower frequency f_L [2] but also partial radiation pattern narrowing that defines scanning sector. Last state in condition of fixed aperture size could be compensated in «Vivaldi» radiator by shortening its lengthway size that in turn initiates worse matching with open space and finally – attenuates radiation efficiency.

That's why all these requirements as to frequency f_L, beam width in E- and H-planes of partial radiation pattern and maximum radiation efficiency could be achieved only as result of compromise.

Results of computer simulation have demonstrated [8] necessity in «Vivaldi» antenna with dimensions 400x800 mm to provide f_H about 100 MHz with VSWR <3. However beam width of such element is very small and doesn't allow to provide scan in given angle range [1]. In addition, «Vivaldi» radiator is entering to the VPSAA composition of N elements, which spacing parameter d is selecting in condition of

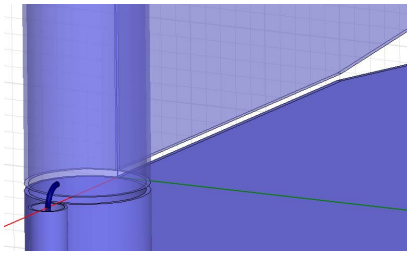


Fig. 1. Feeding system.

978-1-4244-7468-4/10/$26 ©2010 IEEE

absence grating lobes at the bandwidth highest frequency:

$$d < \frac{N-1}{N} \frac{\lambda_{\min}}{1+\left|\sin\theta_0\right|}, \qquad (3)$$

where θ_0 - scan angle, counting from a positive normal of array plane; $\lambda_{\min} = c/f_{\max}$ - minimal wavelength of VPSAA ($\lambda_{\min} = 20$ cm) – is the minimal considering wavelength for describing AA. Therefore d have not be greater than 10÷13 cm.

In connection with these factors in the work there is also a research of «Vivaldi» radiator with dimensions 100x200mm (Fig. 2).

VSWR frequency dependence of a single antenna is shown on Fig. 3 and the same for infinitely arrayed in E-plane on Fig. 4. Spacing parameter was given to be equal to the radiators width, that is 100mm.

We can notice considerable reducing the bandwidth lower frequency of the radiator in AA composition (see Fig. 4). On a level with this improvement there are anomalous bursts on the curve. It may be caused by «blinding» effect of AA [9].

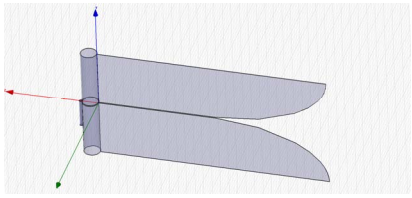


Fig.2. «Vivaldi» radiator.

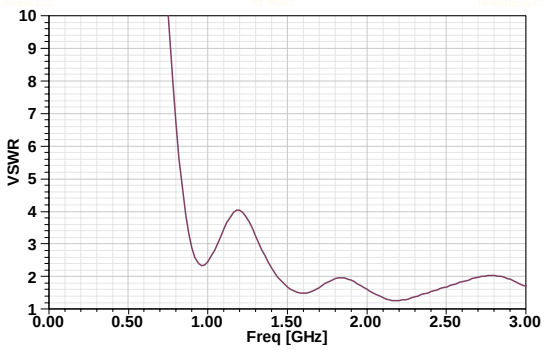


Fig. 3. VSWR frequency dependence of a single «Vivaldi» radiator.

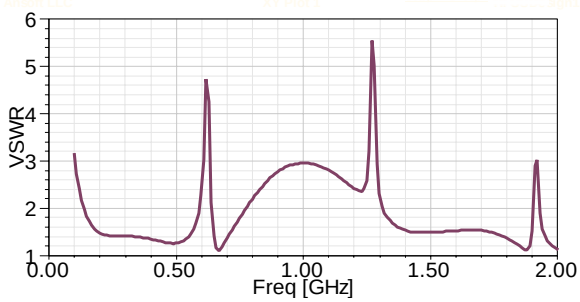


Fig. 4. VSWR frequency dependence of an arrayed «Vivaldi» radiator.

VSWR bursts results in reducing of AA gain on the same frequencies [see Fig. 5].

Absorber allocated on outside edges may produce significant improvements of VSWR and bandwidth characteristics [Fig. 6].

Computer simulation results of such antennas putted side by side in E-plane in array is shown on Fig. 7 and Fig. 8.

As we can see (Fig. 4, Fig. 7) presence of an absorber allowed to eliminate anomalous bursts of VSWR curve. Along with it a gain curve of the arrayed radiator with absorber also became smooth and kept its level the same during bandwidth (see Fig. 5, Fig. 8).

AA (10x5 elements) scan mode in E-plane was investigated in this work. Computation results have shown ability of arrayed «Vivaldi» radiator with dimensions 100x200mm and $d = 100$ mm in E-plane and 200mm in H-plane to effect scanning in the sector of $\pm 30^0$ right up to higher frequency of the band.

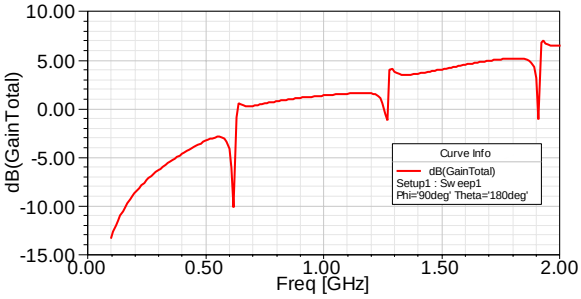


Fig. 5. Gain frequency dependence of an arrayed «Vivaldi» radiator without an absorber.

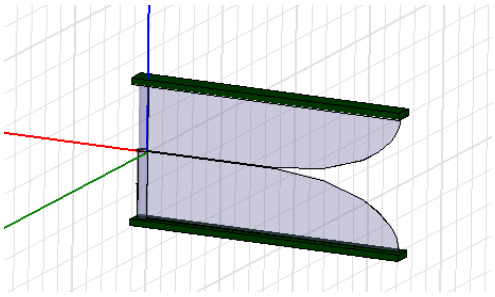


Fig. 6. VSWR frequency dependence of «Vivaldi» radiator with an absorber on outside edges.

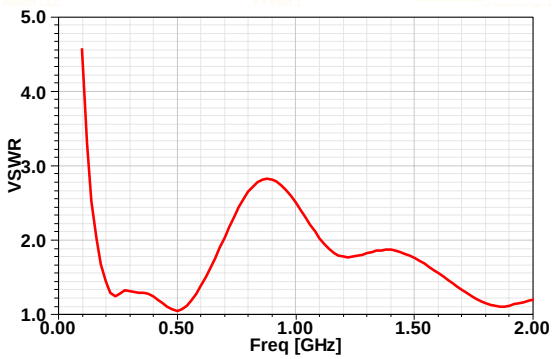


Fig. 7. VSWR frequency dependence of an arrayed «Vivaldi» radiator with absorber.

At scanning angles out of this range there are huge side lobes on radiation pattern. To illustrate it there is a radiation patterns of such VPSAA with an absorber at scan angles of 30^0 and 45^0 on Fig. 9 and Fig. 10.

Thus as a result of investigations there was shown that joining of the radiators to the array causes reduce of the band lower frequency 4-5 times. Absorber employment on outside edges of the radiators eliminates anomalous bursts on VSWR frequency dependence curves. At 1.5 GHz array with $d = 100$ mm in E-plane has a limitation of scan angle $\theta = 30°$.

REFERENCES

1. Schantz Hans, *The art and the science of ultrawideband antennas*. Art. House, Inc., USA, 2005.
2. D. Herskovitz, Wide, wider, widest. *Journal of Electronic Defense*. July 1995, pp.50-57.
3. C.E. Baum and E.G. Farr, Impulse radiating antennas, Ultra-wideband, short-pulse electromagnetics, Plenum Press. 1993, pp. 139-147.
4. J.Shin, D. Schaubert, A parameter Study of Stripline-fed Vivaldi Notch-antennas Arrays// *Trans. on Antennas and Propag.* 1999. Vol.47, N5, p.879.
5. R. Janaswamy, D. Schaubert, Analysis of Tapered Slot Antenna //*IEEE Trans. Antennas and Propag*., 1987, v. 35, no.9, pp. 1058-1065.
6. R .Janaswamy, An accurate moment model for the tapered slot antennas// *IEEE Trans. Antennas and Propag*., 1989, v. 37, no. 12, pp. 1523-1528.
7. N.P. Agrawall, G. Kumar, K.P. Ray, Wide-band planar monopole antennas// *IEEE Trans. Antennas and Propag*., 1998, v. 46, no. 2, pp. 294-295.
8. Bolov R.B., Kondratjeva A.P., Kurochkin A.P., Los' V.F., Privalova T.Yu., Yukhanov Yu.V., Ultrawideband radiators for scanning videopulse antenna arrays, *Antenny*, 2010, №2, p. 25-30. (In Russian)
9. Amitey N., Galindo V., Wu Ch., *Theory and analysis of phased antenna array*, M.: Mir, 1974, 455 p. (In Russian)

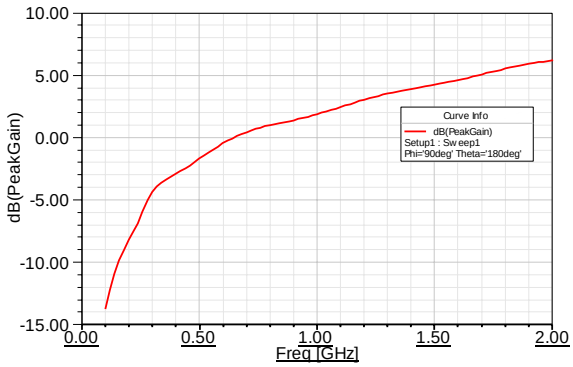


Fig. 8. Gain frequency dependence of an arrayed «Vivaldi» radiator with an absorber.

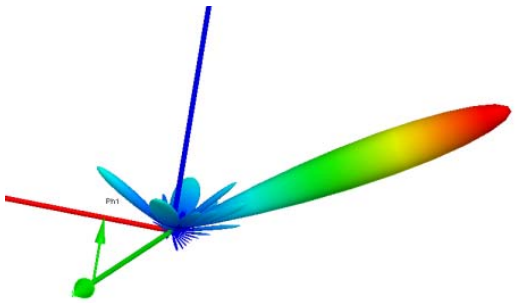


Fig. 9. Radiation pattern of the arrayed «Vivaldi» radiator of 10x5 elements with absorber at $\theta = 30°$.

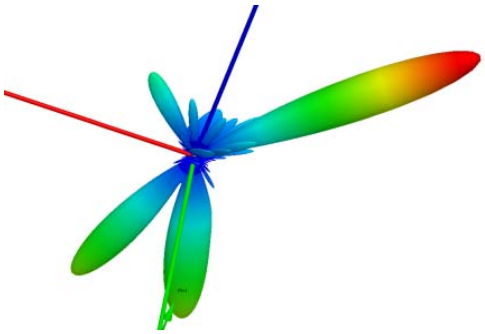


Fig. 10. Radiation pattern of the arrayed «Vivaldi» radiator of 10x5 elements with absorber at $\theta = 45°$.

THE CHARACTERISTICS ANALYSIS OF PATCH ANTENNA ARRAY Ku-BAND

[1] Golovin V. V., [2] Tyschuk Y. N., [3] Luk'yanchikov A. V. and [4] Toloknova E. U.

[1] Sevastopol National Technical University, Sevastopol, Ukraine
E-mail: v_golovin@mail.ru
[2] Sevastopol National Technical University, Sevastopol, Ukraine
E-mail: y.tyschuk@gmail.com
[3] Sevastopol National Technical University, Sevastopol, Ukraine
E-mail: brain75@mail.ru
[4] Sevastopol National Technical University, Sevastopol, Ukraine

Abstract

The construction of a broad-band patch antenna is offered. The rhomboid spacing chart of these irradiators in a few-element array is observed. The analysis of irradiation and input characteristics of the four-element array in Ku-band is carried out.

Keywords: Patch antenna, phased antenna.

1. INTRODUCTION

Intensive development of satellite telecommunication systems is coupled to growth of number of users and improvement of the subscriber's equipment. One of aspects of this problem is development of receiving antenna systems. Available alternative to traditionally used reflector parabolic antennas are the phased antennas (FA). Development of FA is an actual problem and is related to necessity of simplification of antenna system construction for cut down of its cost and competitiveness raise.

In the paper the results of the phased antenna cluster development constructed on the basis of the patch antenna are presented. Possibility of enhancement of the irradiators match strip at the changes in their construction is shown.

2. MAIN PART

Let's observe the rectangular plate (Fig. 1), had over the conducting substrate. The feeding point is on axis OX. Thus the right and left plate faces participate in radiation field shaping. In the paper the square plate is observed that allows at disposing of the second feeding point on axis OZ to obtain radiation from top and bottom faces of plate in order to obtain radiation at orthogonal polarization and at the given phase shift to obtain a radiation field of circular polarization. It will allow to exercise operation of radiation field polarization. So the important advantage of the rectangular patch antenna is possibility to generate two linear or circular polarizations of radiation field (right-hand or left side).

Main shortcoming of the presented antenna is a resonance-frequency behavior of its input impedance. The solution of this problem within a frequency band (10…12) GHz represents a complex task.

Radiation of the in-phase currents at the right and left plate faces (see Fig. 1) is possible to present in a form of the two-element array radiation. Its radiation pattern is described by the relationship [1]

$$E_X = E_{X1} + E_{X3} = F(\theta,\varphi) = f_{array}(\theta,\varphi)\cdot f_{el}(\theta,\varphi), \quad (1)$$

where

$$f_{array}(\theta,\varphi) = \mathrm{e}^{\mathrm{j}0.5ka\cdot\sin(\theta)\cdot\sin(\phi)} + \mathrm{e}^{-\mathrm{j}0.5ka\cdot\sin(\theta)\cdot\sin(\phi)}, \quad (2)$$

$$f_{el}(\theta,\varphi) = E_0 \times \left[e^{a\cdot u}\cdot\left(u\cdot\cos\left(\frac{v\cdot a}{2}\right) + v\cdot\sin\left(\frac{v\cdot a}{2}\right)\right) - \right.$$

$$\left. -u\cdot\cos\left(\frac{v\cdot a}{2}\right) + v\cdot\sin\left(\frac{v\cdot a}{2}\right)\right] \frac{e^{\left[\frac{a\cdot u}{2}\right]}}{\left[u^2+v^2\right]}; \quad (3)$$

$$v = \frac{m\cdot\pi}{a},\ u = jk\cdot\sin(\theta)\cdot\cos(\phi).$$

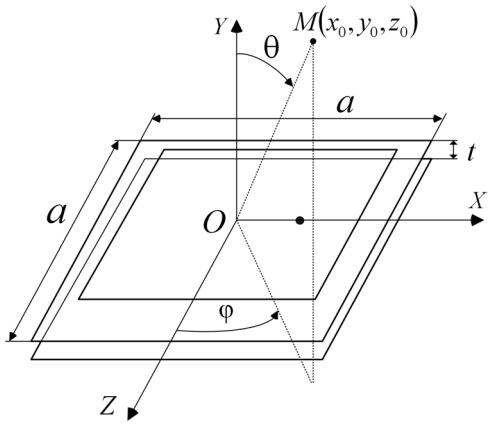


Fig. 1. Patch antenna model.

978-1-4244-7468-4/10/$26 ©2010 IEEE

After transformation to spherical axes, for components of a field of the basic polarization it will take advantage of relationships

$$\begin{cases} E_{\theta}\left(\theta,\phi\right) = E_{X} \cdot \cos\theta \cdot \cos\phi; \\ E_{\phi}\left(\theta,\phi\right) = -E_{X} \cdot \sin\phi. \end{cases} . \qquad (4)$$

The presented relationships (1)–(4) allow to calculate a radiation field of the square-topped plate on the basic polarization.

One of methods of enhancement of the irradiators match strip is caused by addition of longitudinal strips (Fig. 2, a) [2,3]. However it does not allow to ensure the matching in the wide frequency band. The researches have allowed to enhance the frequency properties of irradiator on Fig 2,a at the expense of modification of its construction (see Fig. 2, b).

For irradiator that presented on Fig. 2, b calculations of performances of the radiation field and an input impedance over the frequency band (10…12) GHz are carried out. All further calculations were led with application of the moments method. At the geometrical parameters chosen as a result of calculations following performances of patch antenna are obtained.

The antenna radiation pattern over the frequency band changes how is shown on Fig. 3. Dependence of the input impedance of the antenna on frequency is presented on Fig. 4. At antenna feed at one port (Fig. 2 see,) the radiation field in all frequency band has the linear polarisation. Directivity factor over the frequency band it is equal 4,5…7 dB.

The developed irradiator over the frequency band has stable directional performances. However,

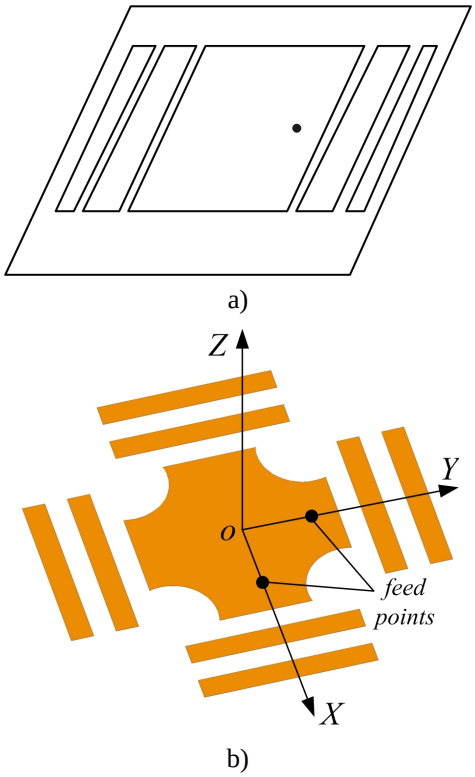


Fig. 2. Models of irradiators with enhanced match strip.

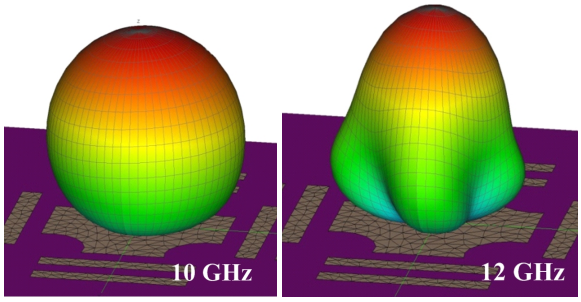


Fig. 3. The patch antenna radiation patterns.

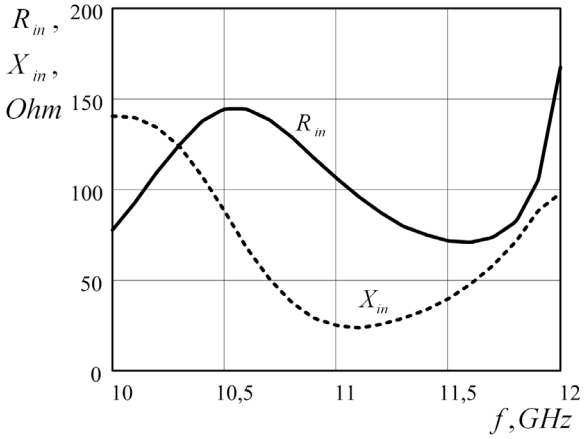


Fig. 4. The dependence of the antenna input impedance from frequency.

apparently from Fig. 4, the considerable variations of the input impedance of the antenna on frequency band boundaries do not allow to ensure in all frequency band the matching with VSWR<2. Thus the matching strip foots up to 10,5…11,8 GHz.

The further analysis will be spent for a four-element array of patch irradiators. In the array irradiators place on corners of a square rhomb. It has allowed to satisfy a requirement of missing of diffraction lobes in the array radiation pattern

$$d \le \frac{\lambda}{2\left(1+\sin\theta_{0}\right)},$$

where d – distance between irradiators, θ_{0} – a direction of a maximum of the radiation pattern concerning a normal line to the array.

For cophased array $d \le 1,4$ sm.

For the irradiators presented in Fig. 2,b two variants of their placing in the antenna array have been considered:

— without crossing of external matching elements in construction of irradiators;

— with crossing of external matching elements in construction of irradiators.

More stable characteristics in the frequency band are obtained for the second case.

The investigated four-element antenna array is presented in Fig. 5.

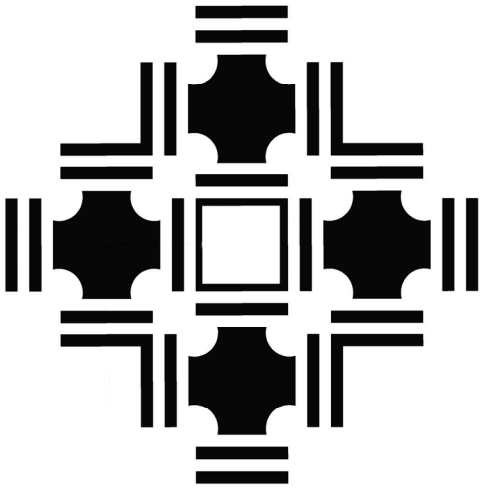


Fig. 5. The model of the four-element array antenna.

In the array with rhomboid disposing of irradiators the radiation pattern is characterized by the linear polarization, and also by the small dependence of radiation pattern main lobe width and side lobes level from frequency (see Fig. 6). The cross-polarization component level possess the value no more –25 dB, the main lobe width changes from within 10 % from the centre frequency (on which $\Delta\theta_{-3\,dB} = 35^\circ$), the side lobes level is not above –15 dB.

The analysis of the array input characteristics (Fig. 5) has allowed to obtain following results. At the rhomboid disposing of irradiators in the array the input characteristics of each array's element at the expense of the cross-effect became more stable in all operating frequency band (see Fig. 7) in comparison with the same performance for single irradiator (Fig. 4). At feed of each irradiator by the feeder with a wave resistance 80 Ohm, the VSWR value in all operating frequency band do not exceed two.

3. CONCLUSION

The four-element array constructed on the basis of the patch irradiator, had in rhomb corners is developed and theoretically explored.

The array allows to exercise control of the radiation field polarisation at the expense of switching and phrasing of two inputs of each irradiator.

Theoretical researches were led over the frequency band (10…12) GHz.

The radiation pattern of the developed antenna is characterised by the linear polarisation, at the mean of the radiation pattern main lobe width $\Delta\theta_{-3\,dB} = 35^\circ$; side lobes level is not above –17 dB and cross-polarization radiation level is no more then –25 dB.

At feed of each irradiator by the feeder with a wave resistance 80 Ohm, the VSWR value do not exceed two over the frequency band (10…12) GHz.

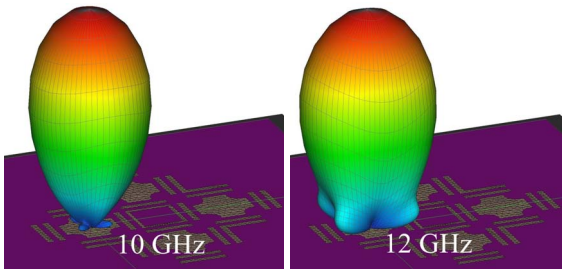


Fig. 6. The patch antenna radiation patterns.

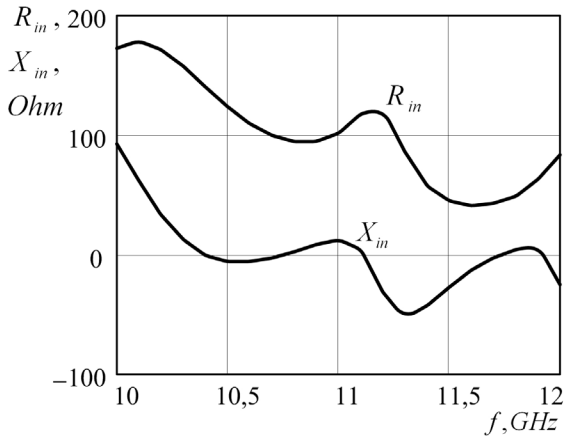


Fig. 7. The antenna array input impedance.

The further stage of researches is development of the phased antenna constructed on the basis of offered cluster.

REFERENCES

1. Lobkova L.M., Shestakov A.G., Shebetovsky V.G., 2006, 'Mathematical model of printed feed element', *Vestnik SevGTU. Informatica, electronica, svyaz'*, Sevastopol. PP. 119-123. (In Russian)
2. Lobkova L.M., Luk'yanchikov A.V. 2004, 'Characteristics of forming of radiation field of printed antennas in dual-frequency regime', *Electronica i Svyaz'*. Kyiv. № 22. PP. 129–135. (In Russian)
3. Shestkov A.G., Shebetovsky V.G., Luk'yanchikov A.V. 2005, "Experimental Research of Microstrip Radiator Characteristics', *Vestnik SevGTU. Informatica, electronica, svyaz'*, Sevastopol. PP. 122–126. (In Russian)

A NOVEL MINIATURIZED ULTRA WIDEBAND LOG-PERIODIC ANTENNA

[1] Luan Shan, [2] Liu Xiaofeng and [3] Qiu Jinghui

[1] Harbin Institute of Technology, Harbin, China
E-mail: luanshan.hit@gmail.com
[2] Harbin Institute of Technology, Harbin, China
E-mail: liuxiaofeng@hit.edu.cn
[3] Harbin Institute of Technology, Harbin, China
E-mail: qiujh@hit.edu.cn

Abstract

The log-periodical antenna (LPDA) is a kind of ultraw wide-band antennas. To achieve the purpose of miniaturization of the LPDA in radiate direction, this paper presents a novel structure log-periodically loaded with symmetrical meandering dipoles. The radiate direction is reduced to 46% of the conventional LDPA. The return loss is less than -10dB from 200MHz to 2GHz, according to the simulation results. A good directivity is also obtained that the gain ranges from 1.9dB to 7.2dB.

Keywords: Ultra wideband antenna, LPDA, miniaturization, meander.

1. INTRODUCTION

Modern communication system needs broadband, miniaturized and universal equipments. Thus to adapt the development trends of radioactive equipments, it has more significant reality sense to research on miniaturized broadband antenna.

At present, broadband antenna mainly includes ridged horn antenna, LPDA, TEM horn antenna, helical antenna and biconical antenna and so on. LPDA is a common and important broadband antenna, due to its non-frequency-dependent characteristic. However, in the conventional design, the physical size is restricted to the longest oscillator dipole with the lowest resonant frequency, which is quite large and constrains its application.

To realize the antenna miniaturization, many methods, including loading technology, fractal technology, meandering line technology etc. have been taken to reduce the size of antenna without reducing the antenna's performance. Loading technology needs to insert some components or networks in right place to change the current distribution of antenna and the electricity characteristic of antenna, which increases the complexity and cost, and reduces the antenna efficiency with extra energy loss. Space-filling propriety and self-similarity make fractal antenna have many advantages in constructing small-size antenna and broadband antenna. Meandering antenna also can have similar characteristic and even have better quality in some case. [1-2] Moreover, the construction of fractal antenna has comparative complexity. The antenna with meandering structure is relatively simple and low cost

2. DESIGN OF DIPOLE ANTENNA

At first, the meandering technology used in dipole antenna is researched.

A dipole antenna is designed, whose resonance frequency is 200MHz, with the structure-oscillator length l = 320 mm, section radius r = 5 mm, distance between two oscillator d = 20 mm. Based on the CST simulation, the resonance frequency of the dipole antenna is 200 MHz and gain is 2.061 dB.

Meandering technology is used in dipole antenna for miniature, and the structure is shown in Fig. 1.

The influence of main-arm length, vertical-arm length and secondary-arm length to antenna characteristics is researched separately.

2.1. THE INFLUENCE OF MAIN-ARM AND VERTICAL-ARM LENGTH TO ANTENNA CHARACTERISTICS

Five different meandering dipole antennas are designed, the structure parameters of which are shown in Table 1, and the oscillator length is 320mm (oscillator length =main-arm +vertical-arm+ secondary-arm).

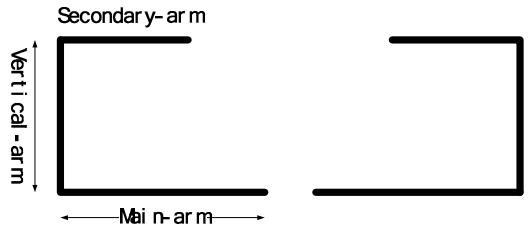


Fig. 1. Structure of meandering dipole antenna.

978-1-4244-7468-4/10/$26 ©2010 IEEE

Based on the CST simulation, the electrical length of the five antennas is shown in Table 1. Since the antenna oscillator is bent, its equivalent length is shorter than half of its resonant wavelength. Therefore, the electrical length of meandering dipole antenna is shorter than that of conventional dipole antenna (oscillator length l = 320mm, resonant frequency f = 200MHz). Meanwhile, the lower the ratio of main-arm length to oscillator length, the shorter the electrical length is. After the antenna oscillator is bent, the current direction of the main-arm is just opposite to that of the secondary-arm, and the current of the vertical-arm has no help for the gain on the radiation direction, which leads to the fact that the gain of the antenna is lower than the dipole antenna. The simulation results are shown in Table 1. When the vertical-arm length is the same, the lower the ratio of main-arm length to oscillator length, the lower the gain is.

Table 1. Structure and characteristics of meandering dipole 1-5.

Antenna	Main-arm length/whole oscillator length	Secondary-arm length/whole oscillator length	Electrical length	Gain (dB)
Meandering dipole 1	0.60	0.10	0.27	1.73
Meandering dipole 2	0.55	0.15	0.26	1.64
Meandering dipole 3	0.50	0.20	0.24	1.61
Meandering dipole 4	0.45	0.25	0.21	1.45
Meandering dipole 5	0.40	0.20	0.19	1.41

2.2. The Influence of Vertical-Arm Length to Antenna Characteristics

Five different meandering dipole antennas are designed, the structure parameters of which are shown in Table 2, and the oscillator length is 320mm.

Based on the CST simulation, the electrical length and gain of the five antennas are shown in Table 2. The vertical-arm length decides the coupling between main-arm and secondary-arm. The shorter the vertical-arm is, the higher the coupling is. When the ratio of main-arm length to oscillator length is the same, the lower the ratio of vertical-arm length to oscillator length is, the shorter the meandering LPDA's electrical length is. But there is little influence to the gain of meandering LPDA.

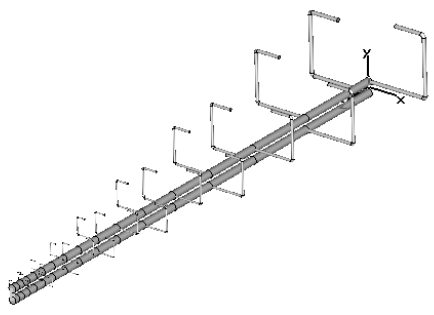


Fig. 2. Structure of meandering LPDA

Table 2. Structure and characteristics of meandering dipole 6-10.

Antenna	Main-arm length/whole oscillator length	Vertical-arm length/whole oscillator length	Electrical length	Gain (dB)
Meandering dipole 6	0.60	0.30	0.273	1.73
Meandering dipole 7	0.60	0.25	0.278	1.77
Meandering dipole 8	0.60	0.20	0.284	1.77
Meandering dipole 9	0.60	0.15	0.294	1.78
Meandering dipole 10	0.60	0.10	0.306	1.80

3. Design and Simulation of Meandering LPDA

Trough the results shown above, using meandering technology in dipole antenna for miniature is advisable. Since LPDA is composed by different dipole antennas with different resonant frequencies, meandering technology could be used in LPDA to achieve a miniaturized antenna. The structure of meandering LPDA is shown in Fig. 2.

This model is designed by CST software. In microwave bandwidth, the current is mainly at the surface of conductor. Oscillator arm and feeder in the model can be substituted by ideal conductor. Leading and reflection function of meandering oscillator unit is similar with that of dipole. So according to the parameter calculation equation of LPDA, considering the request of antenna engineer- frequency range is 200MHz ---2GHz, horizontal length is no more than 450mm and vertical length is no more than 1500mm, it can be achieved that scale factor $\tau = 0.83$ and space factor $\sigma = 0.14$, the number of dipole elements N is 16 , horizontal length is 344 mm, vertical length is 1345 mm, radius of feeding line is 10 mm, the thickest radius of oscillator is 5mm and the thinnest radius of that is 1 mm.

Based on the CST simulation, the voltage standing wave ratio(VSWR) is shown in Fig. 3. Between 200 MHz and 2 GHz, the reflection loss is less than –10dB. According to the radiate pattern (Fig. 4) , with the increase of frequency, the minor lobe of the antenna radiate pattern increases. But the main lobe width of antenna radiation is not influenced, and the directivity is good. The gain of meandering LPDA is shown in Fig. 8.

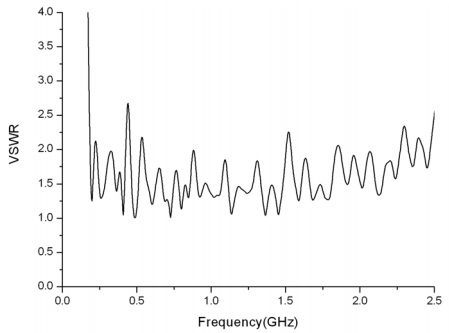
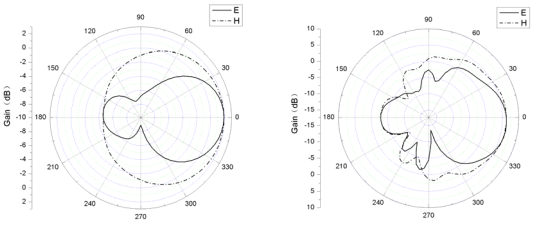
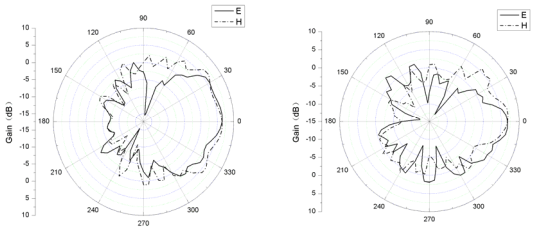


Fig. 3. VSWR of meandering LPDA



0.2GHz 0.6GHz



1.1GHz 2.0GHz

Fig. 4. The azimuth pattern of the LPDA

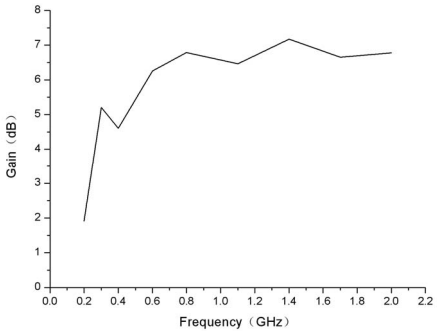


Fig. 5. The gain of the LPDA

In the case with same number of dipole element, the horizontal length of meandering LPDA is just 46% (344 mm) of the conventional LPDA. Compared to the other miniaturized LPDA, the meandering LPDA has obvious advantages on the aspect of miniaturization. (in Table 3.)

4. CONCLUSION

This paper takes the meandering method to research the miniaturization of LDPA, and design meandering LDPA with frequency between 200MHz and 2GHz, in which the reflection loss is less than -10dB , the directivity is good and the technical specification is ideal. But the gain in the low frequency is influenced and reduced. In the case with the same number of dipole elements, the horizontal length of meandering LDPA is just 46% of the conventional LDPA. Finite space is effectively filled and the design of the miniaturization of LDPA is achieved.

ACKNOWLEDGMENTS

The authors would like to express their sincere gratitude to CST Ltd, Germany, for providing the CST Training Center (Northeast China Region) at our university with a free package of CST MWS software. Meanwhile, the authors would like to thank Doctor Lin Shu for his help and suggestions.

REFERENCES

1. First Report and Order on UWB Transmission System, Revision of Part 15 of the Communications Rules Regarding Ultra-Wideband Transmission Systems 2002, FCC Std. Part 15 on UWB Transmission System.
2. H. Gemmeke, “Radio detection of ultra high-energy cosmic ray air showers”, in *Proc. Nuclear Science Symp. Conf. Rec.*, Oct. 23-29, 2005, vol.2, pp. 1080-1083.
3. Huang Jingjing, Xiao Zhiwen, Yangyang, He jianguo, and Liupeiguo, ‘A Miniaturized Antenna for Ground Penetrating Radar’, *ICMMT 2008*, pp. 1849-1850
4. Wang Hao, Wang Zhichen and Xing Feng, ‘Analysis of the Square Loop Log-Periodic Antenna’, *Journal of Information engineering University*, 2008, 9(3): 301-303(in Chinese).

Table 3. Comparison of different miniaturized methods for LPDA

Miniaturized Antenna	Lowest frequency	Largest horizontal size/λ_L	Miniaturization extent
Fractal LPDA[3]	250MHz	0.37	73%
Rectangular LPDA[4]	400MHz	0.31	60%
Meandering LPDA	200MHz	0.23	46%

THE DIRECTIVITY CHARACTERISTICS OF AN ANTENNA ARRAY RECEIVING THE UWB SIGNAL

Konovalenko A. A., Tokarsky P. L., Erin S. N.

Radio Astronomical Institute of National Academy of Science of Ukraine,
Kharkiv, Ukraine
E-mail: akonov@rinan.kharkov.ua, tokarsky@yandex.ru

Abstract

The power and directivity characteristics of the planar regular antenna array operating in mode of the receiving the UWB signal with uniform spectrum in frequency range of 3:1. Expressions for calculation of the directivity and the effective area of such an antenna array are obtained. Results of computations of the 5×5 array performance are presented.

Keywords: UWB signal; antenna array; effective area; radiation pattern; directivity; radiation efficiency; beam scanning.

1. INTRODUCTION

For the last decade, UWB signals have been increasingly applied when building various radio systems. The use of such signals in radiolocation, telecommunications and radio astronomy allows to noticeably enhance the resolution of radars [1], to augment significantly an information rate in communication channels [2,3], to obtain more information about structures and properties of extra-terrestrial radio sources [4]. The crucial devices of such systems are antennas which should radiate and/or receive the UWB signals with minimum distortions. Many works devoted to the development and investigations of various UWB antennas were published recently [5-7]. At the same time, a little attention is paid to the investigations of arrays working with UWB signals [7,8]. In particular, the directivity characteristics of phased arrays receiving such signals are insufficiently studied yet. In this work, we try somewhat to fill in this gap.

2. THEORY

The power delivered to a load of the arbitrary receiving antenna can be determined as

$$P_L(\theta,\phi) = \int_0^\infty S(f)\cdot A_e(\theta,\phi,f)\cdot \eta(f)\cdot K_P(f)\,df\,, \quad (1)$$

where $S(f)$ is the spectral power density of the plane wave incident from the direction (θ,ϕ) at the frequency *f*; $A_e(\theta,\phi,f)$ is the antenna effective area and $\eta(f)$ is the antenna efficiency; $K_P(f)$ is the transfer coefficient of a feed system taking into account the mismatch loss.

Indeed, Eq. (1) determines the directional antenna properties. The integrand here consists of four multipliers, of which each, in the general case, is frequency dependent and to some extent affects the integration result. Obviously, the strongest influence is of the factor $A_e(\theta,\phi,f)$, which depends on sizes and a structure of a radiating system. The frequency dependence $K_P(f)$ features the antenna as the frequency filter, dividing all the frequency continuum into two parts being a pass band and an attenuation band. When designing an antenna system, developers usually aim to make it, if possible, uniform at the pass band and close to zero at the attenuation band. Therefore we consider the radiator efficiency to be $\eta(f)=1$, and the frequency dependence of the transfer coefficient to look like $K_P(f)=1$ if $f_L \le f \le f_H$ and $K_P(f)=0$ otherwise. Besides, we assume the power spectrum of the incident wave to be uniform $S(f)=S_0$. Taking into account the assumptions, expression (1) can be rewritten as

$$P_L(\theta,\phi,\Delta f) = S_0\int_{f_L}^{f_H} A_e(\theta,\phi,f)\,df = S_0 A_e(\theta,\phi,\Delta f)\Delta f$$

with $\Delta f = f_H - f_L$

$$A_e(\theta,\phi,\Delta f) = \frac{1}{\Delta f}\int_{f_L}^{f_H} A_e(\theta,\phi,f)\,df\,. \quad (2)$$

Let us apply the obtained expression for the analysis of power parameters and directional properties of the planar regular array located above the infinite flat perfectly conducting screen coinciding with the plane $z=0$ at Cartesian coordinates. In order not to deal with a fixed type of the array element, we will assume

978-1-4244-7468-4/10/$26 ©2010 IEEE

the array to be consisted of identical perfect isotropic radiators with horizontal polarization of waves being received by them. In this case, the far field of the *n*-th element operating in a transmit mode is described as

$$\dot{E}_n(R,\theta,\phi,f) = \frac{Z_0}{2R}\dot{I}_n\Phi_n(\theta,\phi,f)\exp\left(-\mathrm{j}\frac{2\pi f}{c}R\right)$$

where $\dot{I}_n$ is the complex current amplitude at the *n*-th element input; $c \approx 3\cdot 10^8\ ms^{-1}$ is the light speed in free space; Z_0 is the characteristic impedance of free space; (R,θ,ϕ) are coordinates of the observation point at a spherical system of coordinates; $\Phi_n(\theta,\phi,f)$ is the radiation pattern of the *n*-th element at the common system of coordinates

$$\Phi_n(\theta,\phi,f) = \frac{4\pi f}{c}l_{en}\ \sin\left(\frac{2\pi f}{c}z_n\cos\theta\right)\times$$
$$\times\exp\left(\mathrm{j}\frac{2\pi f}{c}(x_n\sin\theta\cos\phi + y_n\sin\theta\sin\phi)\right).$$

The far field, the directivity gain and the antenna array effective area are

$$\dot{E}(R,\theta,\phi,f) = \frac{Z_0}{2R}\exp\left(-\mathrm{j}\frac{2\pi f}{c}R\right)\sum_{n=1}^{N}\dot{I}_n\Phi_n(\theta,\phi,f)$$

$$D(\theta,\phi,f) = \frac{2\pi R^2}{Z_0 P_\Sigma}\left|\dot{E}(R,\theta,\phi,f)\right|^2 \qquad (3)$$

$$A_e(\theta,\phi,f) = \frac{c^2}{4\pi f^2}D(\theta,\phi,f) \qquad (4)$$

where $P_\Sigma = \frac{1}{2}\sum_{m=1}^{N}\sum_{n=1}^{N}\dot{I}_m^*\dot{I}_n R_{\Sigma mn}$ is radiated power, and $R_{\Sigma mn}$ are the mutual radiation resistances between array elements.

For isotropic elements placed above the perfect ground, which are considered here, these resistances can be obtained by equation

$$R_{\Sigma mn} = \frac{Z_0 f}{2c}\left[\frac{l_{em}l_{en}}{R_{mn}}\sin\left(\frac{2\pi f}{c}R_{mn}\right) - \right.$$
$$\left. - \frac{l_{em}l_{en}}{R'_{mn}}\sin\left(\frac{2\pi f}{c}R'_{mn}\right)\right], \qquad (5)$$

where R_{mn} and R'_{mn} are direct and "mirror" distances between the *m*-th and *n*-th elements

$$R_{mn} = \sqrt{(x_n - x_m)^2 + (y_n - y_m)^2 + (z_n - z_m)^2}$$
$$R'_{mn} = \sqrt{(x_n - x_m)^2 + (y_n - y_m)^2 + (z_n + z_m)^2}\ .$$

3. Numerical Example

This techniques was applied for the analysis of the performance of a subarray of the new large Ukrainian radio telescope [3] being under construction, which is intended for operation at the frequency range of 10…70 MHz. The subarray is a square array comprising $N = 5\times 5$ identical elements located in knots of a square grid with a step of $d = 3.75$ m at a height of $h = 1.6$ m above ground. It has a parallel excitation system that contains switched-line phase shifters. The main beam of the array factor in each of principal planes can be oriented in the nine following directions: $\theta_0 = 0^\circ$; 7°; 14°; 21.4°; 29°; 37.4°; 46.7°; 58.1° and 76.1°. Fig.1 shows the frequency dependences of the directivity $D(\theta_0,\phi_0,f)$ and the normalized effective area of the array $A_e(\theta_0,\phi_0,f)/A_0$ ($A_0 = N\,d^2$ is the array square), wish is calculated by the Eqs. (3) and (4) respectively.

Fig. 2 shows angle dependences of the normalized effective area of the array at the 3 fixed frequencies 20 MHz, 40 MHz and 60 MHz (dashed, dotted and dash-dot lines respectively), obtained by the Eq. (4), and of the array receiving UWB signal with the uniform spectrum covering the frequency band from 20 MHz to 60 MHz (solid line), obtained by the Eq. (2).

4. Conclusion

As a result of in-band averaging, the radiation pattern of antenna array receiving the UWB signal takes a smoothed shape in the field of side lobes, with their

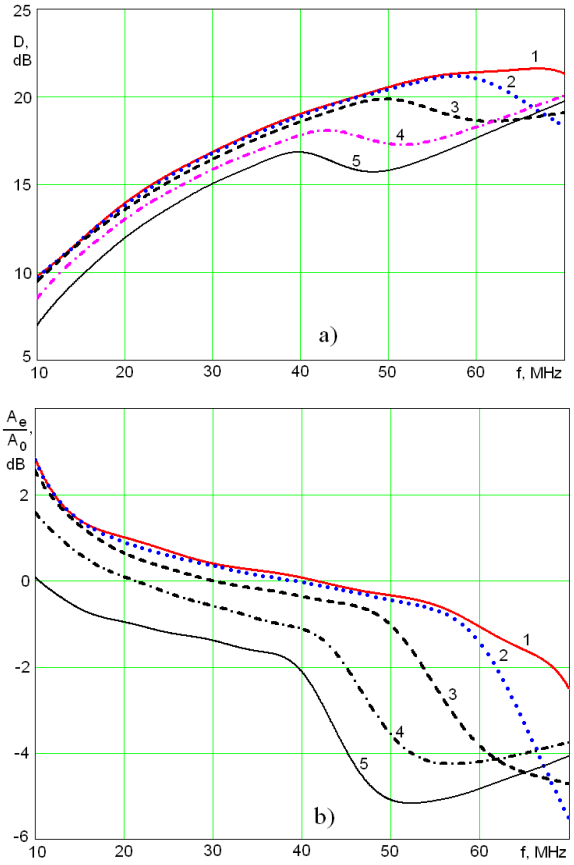


Fig. 1. Directivity gain (a) and effective area (b) of antenna array vs. frequency for different beam directions: 1–$\theta_0 = 0^\circ$; 2–$\theta_0 = 14^\circ$; 3–$\theta_0 = 29^\circ$; 4–$\theta_0 = 46.7^\circ$; 5–$\theta_0 = 58.1^\circ$ at $\phi_0 = 0^\circ$

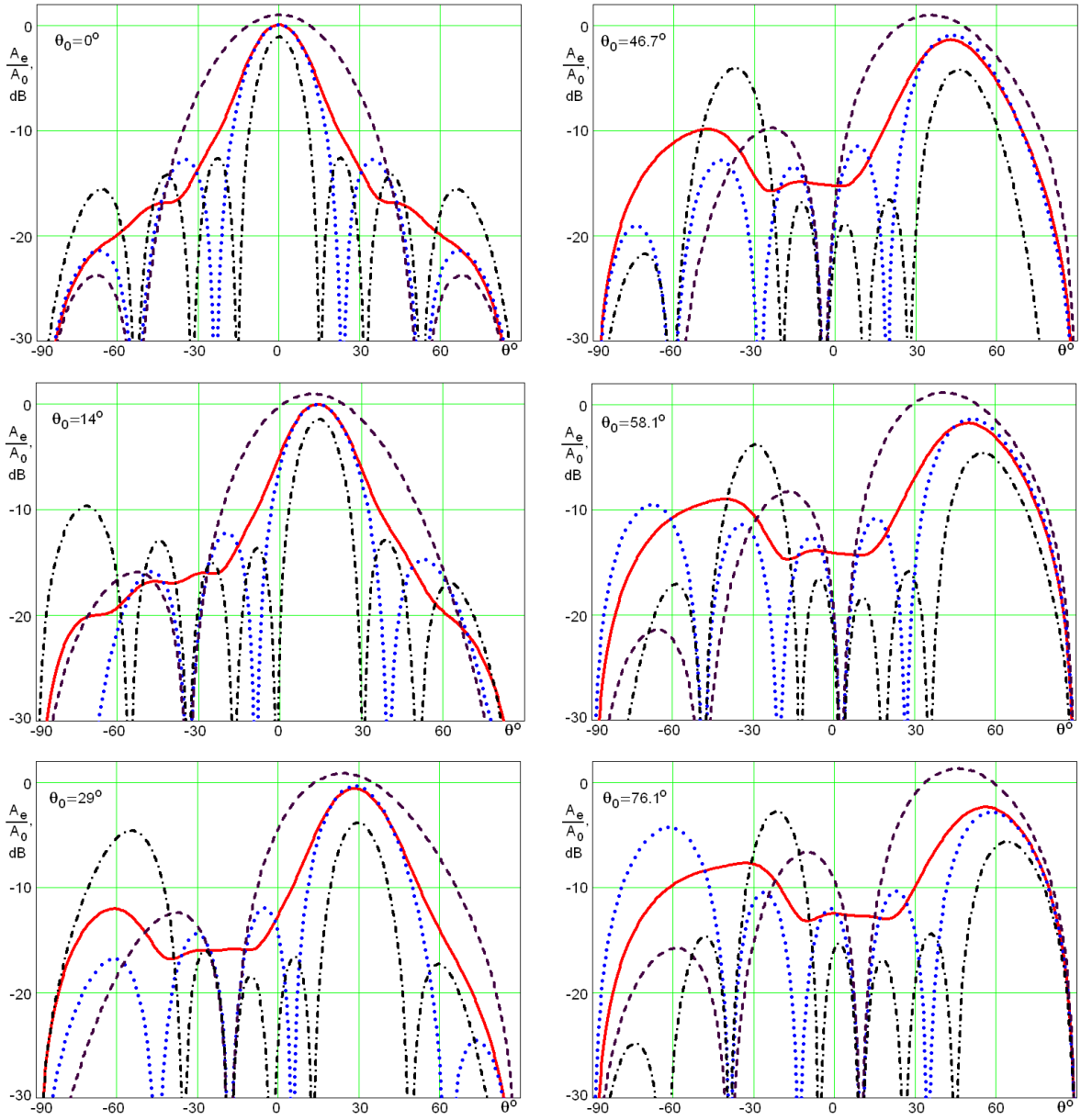


Fig. 2. Radiation patterns in terms of the normalized effective area of the 5×5 antenna array receiving UWB signal with the uniform spectrum covering the frequency band from 20 MHz to 60 MHz for six different main beam directions $\theta_0 = 0^\circ;\ 14^\circ;\ 29^\circ;\ 46.7^\circ;\ 58.1^\circ$ and 76.1° at $\phi_0 = 0^\circ$

levels noticeably decreased. Therewith its peak effective area is close in quantity to the effective area of the same array receiving a simple harmonic wave at the central frequency of band.

REFERENCES

1. *Ultra-wideband Radar Technology*, Ed. by James D. Taylor, 2000, New York: CRC Press.
2. *Ultra Wideband Systems. Technologies and Applications*, 2006, Ed. by Robert Aiello and Anuj Batra, New York: Elsevier Inc.
3. Immoreev I.J., Sudakov A.A. 2002, Ultra-Wideband Communication System with High Data Rate, *Radio Physics and Radio Astronomy*, **7**, 466.
4. Lecacheux A., Konovalenko A.A., Rucker H.O. 2004, Using Large Radio Telescopes at decameter wavelengths, *Planetary and Space Sci.*, **52**, 1357.
5. Schantz H.G. 2005, *Art and Science of Ultrawideband Antennas*, Boston: Artech House.
6. Ghosh, D. et al. 2006, Transmission and Reception by Ultra-Wideband (UWB) Antennas, *IEEE Antennas and Propagation Magazine*, **48**, 67.
7. Chavka G. 2006, Power Parameters of Ultra-Wideband Antenna Array, Proc. Of the 3rd Int. Conf. Ultra Wideband and Ultra Short Impulses Signals (UWBUSIS'2006), Sevastopol, 223.
8. Ellingson S.W., 2005, Antennas for the Next Generation of Low-Frequency Radio Telescopes, *IEEE Trans. Antennas and Propagat.*, **53**, 2480.

ELECTROMAGNETIC COMPATIBILITY. ELECTROMAGNETIC METROLOGY

STANDARD COMPLEX FOR REPRODUCTION AND TRANSMISSION OF UNIT SIZES OF PULSE ELECTRIC AND MAGNETIC INTENSITIES IN ULTRASHORT PULSE RANGE

Sakharov K. Yu., Mikheev O. V., Turkin V. A., Dobrotvorsky M. I., Aleshko A. I.

All-Russian Research Institute for Optophysical Measurements, VNIIOFI, Moscow,
Russia, Ozernaya street, 46, tel. 437-28-47,
E-mail: sax-M12@vniiofi.ru

Abstract

Standard complex for reproduction and transmission of unit sizes of pulse electric and magnetic intensities with pulse leading-edge time no more than 20 ps has been presented. Field-forming system "cone over plane" excited by step voltage signal with amplitude 20 V has been used. Pulse electric intensity has been measured with strip transducer.

Keywords: UWB-SP, strip transducer, primary standard, cone field-forming system.

1. INTRODUCTION

Present work is the continuation of the investigation cycles connected with study of possibilities of generation and measurement of standard electromagnetic pulses with pulse leading-edge time of the order of tens and units of picoseconds.

In [1, 2] the creation principles of primary standard of ultrashort electromagnetic pulses (UWB-SP) have been developed and the selection of standard field-forming system (FS) in the form of circular cone over plane has been proved. In [3] preliminary results of development of cone field-forming system (CFS) by means of strip transducer have been presented. When exiting of the CFS by generator with pulse leading – edge time (on level 0,1 - 0,9 from maximum value) 23,6 ps, pulse leading-edge time at the transducer output was 25,1 ps. On the basis of obtained results the possibility of EMP production in FS with pulse leading-edge time 20 ps has been proved.

2. WORK PURPOSE

Purpose of present work is the creation of the standard complex for reproduction and transmission of unit sizes of pulse electric and magnetic intensities with pulse leading-edge time no more than 20 ps.

3. DEVELOPMENT AND CREATION OF THE STANDARD COMPLEX

The standard complex for reproduction and transmission of unit sizes of pulse electric and magnetic intensities with pulse leading-edge time no more than 20 ps has been developed and created. The standard complex has been approved as the secondary standard, it is recorded in the Register of the secondary Russian standards and it is numbered as VET148-2-2009.

The standard complex includes: cone field-forming system (CFS), set of edge generators of voltage pulses, set of couplers for measurement of voltage pulse parameters in cone field-forming system, measuring system of pulse electromagnetic fields with ultrashort pulse leading-edge time for transmission of unit sizes, digital stroboscopic signal analyzer Tektronix CSA 8000B, mobile shielded cab.

The block diagram of the standard complex is presented in Fig. 1. Exterior view of the standard complex is presented in Fig. 2.

The standard complex has following metrological performance: leading-edge time of reproduced electromagnetic pulses is no more than 19 ps; amplitude of electric intensity pulses is no less than 30 V/m, amplitude of magnetic intensity pulses is no less than 75 mA/m, duration of field pulses is no less 1 ns, extended reproduction uncertainty of maximal value of field pulse intensity is no more than 6.5 %.

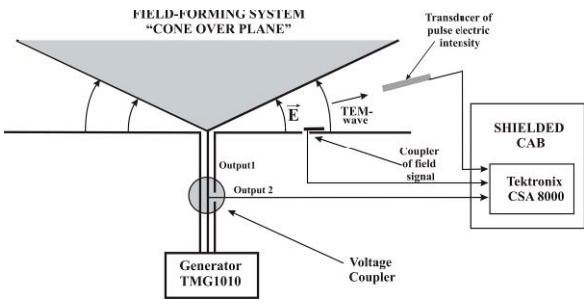


Fig. 1. The block diagram of the standard complex.

978-1-4244-7468-4/10/$26 ©2010 IEEE

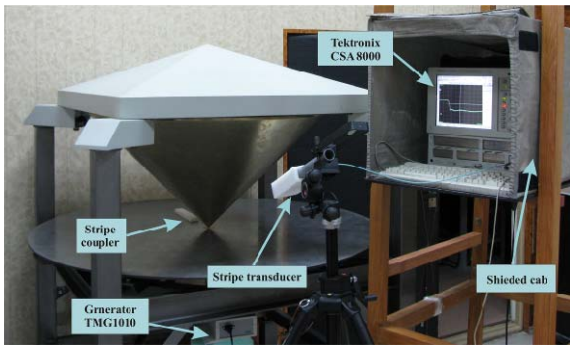


Fig. 2. Exterior view of the standard complex.

Oscillograms of reproduced pulse in the CFS operating area at the output of the strip transducer IPPL-L and exiting generator TMG1010 (at the CFS input) are presented in Fig. 3 and Fig. 4.

The standard complex permits metrological assurance of existing and perspective critical engineering of the support of the population security and life activity and the main objects, technologies of treatment, holding, transmission and information security, base and critical military, special and manufacturing technologies. The standard complex provides traceability of the parameters of ultrashort electromagnetic pulses and development of new types of ultrawideband pulse radio engineering, new types of the radio communication, radiolocation of high resolution, search and detection of plastic mines, electromagnetic compatibility in the area of pulse electromagnetic fields.

4. CONCLUSION

Obtained results show that the created standard complex provides for reproduction and transmission of unit sizes of pulse electric and magnetic intensities with pulse leading-edge time no more than 20 ps

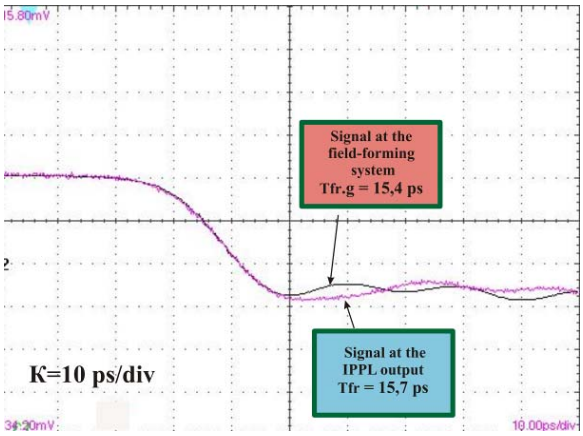


Fig. 3. Oscillogram of reproduced pulse in the CFS operating area at the output of the strip transducer IPPL-L and exiting generator TMG1010 (at the CFS input).

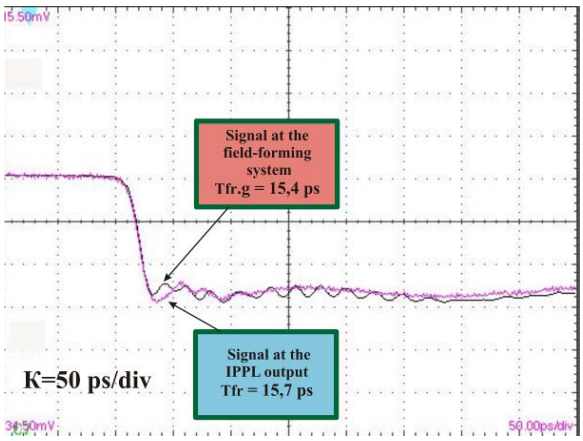


Fig. 4. Oscillogram of reproduced pulse in the CFS operating area at the output of the strip transducer IPPL-L and exiting generator TMG1010 (at the CFS input).

REFERENCES

1. Sakharov K.Yu. 2005, 'Creation principles of primary standard of ultrashort electromagnetic pulses', *Technology EMC*. № 3, 12-16.
2. Sakharov K.Yu. 2005, 'Field-forming system selection of standard of ultrashort electromagnetic pulses', *Technology EMC*. № 3, 17-26.
3. Sakharov K.Yu., Mikheev O.V., Turkin V.A., Aleshko A.I. 2007, 'Experimental results for generation of standard electromagnetic pulses with pulse leading-edge time of tens picoseconds', *Technology EMC*. № 1, 17-26.

SOFTWARE FOR PROCESSING METROLOGICAL CERTIFICATION RESULTS OF SHORT IMPULSE GAUGES

Skoblikov O. Y.

Research and Design Institute "Molniya",
National Technical University "Kharkiv Polytechnic Institute", Kharkiv, Ukraine
E-mail: oleksii.skoblikov@gmail.com

Abstract

"Etalon-PEMF" and "Etalon-TN" are used for metrological certification of gauges for fast processes, pulse electromagnetic fields, currents and voltages in particular. The current metrological standard GOST 8.207-2008 presupposes quite a big amount of routine calculations for the gauge certification, which makes the process very labor-intensive and increases error probability.

The specialized software "Metrological statistics", developed by the author, enables to solve this problem, extracting the data from oscilloscope images, processing all the necessary calculations and creating certification reports.

Keywords: Electromagnetic fields, gauges, metrological certification, data processing, specialized software.

1. INTRODUCTION

1.1. "ETALON-PEMF"

In 2005-2006 Research and Design Institute "Molniya" constructed, certificated and implemented the Initial Etalon of Ukraine for the maximum values of pulse electric (V/m) and pulse magnetic (A/m) fields ("Etalon-PEMF"). The main purpose of "Etalon-PEMF" is metrological certification and verification of gauges for pulse electric and magnetic fields, which are used at the proof ground of R&D Institute "Molniya" and other similar organizations of CIS [1].

1.2. "ETALON TN"

In addition to the primary function, "Etalon-PEMF" can also be applied for metrological certification of gauges for high pulse voltages and currents. This can be achieved by using pulse voltages and currents from the striplines of "Etalon-PEMF". In such a case "Etalon-PEMF" becomes the source for maximum values of high pulse voltages (V) and high pulse currents (A) and is titled "Etalon-TN".

1.3. THE PROCESS OF CERTIFICATION

As the structures of "Etalon-PEMF" and "Etalon-TN" have lots in common, the procedure of the certification of gauges for pulse electric and magnetic fields, voltages and currents does not contain any significant differences. It is divided into two phases: parameter measurement by the certifying gauge and processing the data measured.

GOST 8.207-2008 [2] demands to conduct a set of tests (at least 10) for each value of the etalon parameter (electric or magnetic field, voltage or current). Normally, 3-5 values of the etalon parameter are used to cover the whole operating range of the gauge during the certification. Every impulse for each etalon value is measured by the gauge and stored by a recorder, which is an oscilloscope placed within a shielded chamber. Therefore, we get 30-50 images of pulse curves at the end of the first phase.

During the second phase, each curve has to be processed in order to get amplitude-time parameters (ATP) of the impulse. ATP are then used to compute the transition factor. Finally, a set of curves enable to estimate the measurement error rates.

The second phase of gauge certification, obviously, involves high amount of routine calculations, therefore manual processing of data received during the first phase causes some serious problems:

- the error of visual estimation of the ATP;
- possible mistakes in calculations;
- low speed of processing the measured data;
- high labor demands for processing the curves;
- high labor demands for preparing the gauge certification reports.

The listed problems can be partially or fully solved by specialized software running on a PC, however there were no such computer programs until recently.

978-1-4244-7468-4/10/$26 ©2010 IEEE

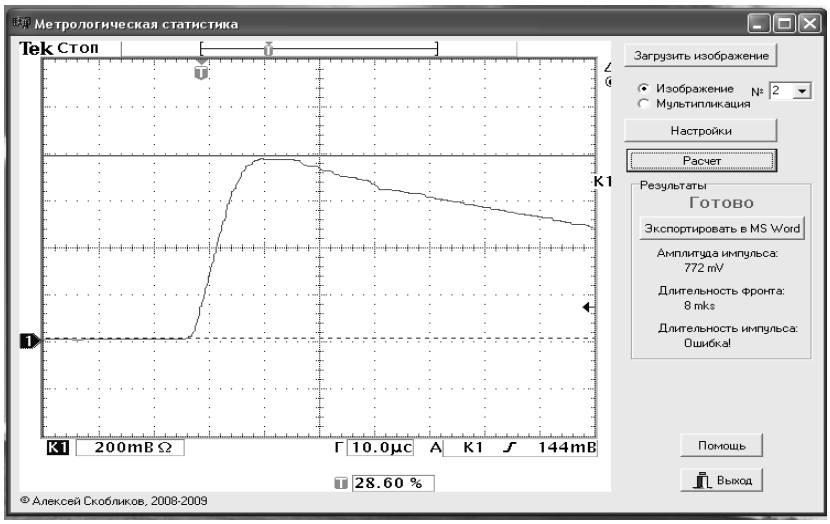


Fig. 1. The main window of the "Metrological statistics" software

2. "METROLOGICAL STATISTICS"

2.1. MAIN FUNCTIONS

Developing "Metrological statistics" computer program (Fig. 1), the author focused himself on solving the problems listed above, meanwhile strictly adhering the metrological certification methodic, assigned in the current standard [2].

As a result the software possesses the following functions:

- automatic processing of a set of pulse curves according to the current standard GOST 8.207-2008 [2];
- graphic pulse ATP estimation;
- automatic division values and pulse polarity detection;
- pulse curve smoothing;
- transition factor calculation for the certifying gauge, based on the results of analysis for measured data;
- measurement error and uncertainty calculation;
- certification reports generation in Microsoft Word format;
- specialized mode for self-testing.

The further few subchapters are devoted to the brief description of the distinctive features of "Metrological statistics" software.

2.1.1. Source data

In order to process automatically the curves, received during the first phase of the certification procedure, they should be saved in the memory of oscilloscope. The saved data then should be transferred from the oscilloscope memory to graphic files on a PC hard drive. Thereby, the program uses graphic files of BMP, TIFF or PDF formats on its input.

"Metrological statistics" processes graphic estimation of ATP of a pulse, therefore the correct structure of source images is of utmost importance. Currently, "Metrological statistics" is optimized to be used with Tektronix TDS-3052B oscilloscope; however it can be readjusted easily to any other one by editing oscilloscope settings of the program.

2.1.2. Basic calculations

After the source pulse curves are loaded to the program and the "Calculate" button is pressed, the program processes the computation of pulses ATP, transition factor of the certifying gauge and measurement error estimation according to the following algorithm [4]:

1. Pulse ATP are calculated:
   a. Impulse amplitude.
   b. Impulse front duration. The program leaves the possibility to be adjusted for various standards:
      - 0 – 1 of the amplitude value;
      - 0.1 – 0.9 of the amplitude value;
      - 0.1 – 0.8 of the amplitude value.
   c. Impulse duration (at the level 0.5 of the amplitude value).

After the computation of pulse ATP is finished, they are displayed in the "Results" section of the program main window.

2. Based on the impulse ATP the transition factor of the certifying gauge is computed. The transition factor appears to be the main characteristic of a gauge.
3. The measurement errors are estimated as follows:

$$S_{\Sigma} = \sqrt{\sum_{i=1}^{m} \frac{\Theta_i^2}{3} + \left[S(\tilde{K}_{np}) \right]^2}, \qquad (1)$$

where S_{Σ} – total standard deviation of the measurement result; $S(\tilde{K}_{np})$ – standard deviation of the gauge transition factor; Θ_i – the limit of *i*-th non-exceptional systematic inaccuracy (the constant characteristics for the "Etalon-PEMF" and "Etalon-TN" installations).

$$S(\bar{K}_{np}) = \sqrt{\frac{\sum_{i=1}^{n}(K_{np_i} - \bar{K}_{np})^2}{n(n-1)}}, \qquad (2)$$

where n – the number of measurements for one etalon value (n usually equals 10), K_{np_i} – gauge transition factor, calculated based on the i-th pulse curve; $\tilde{K}_{np_i}$ – mean value of the gauge transition factor.

The limit of random error, non-exclusive systematic error and the limit of the measurement result error are calculated in addition to the listed parameters [4].

2.2. Additional Functions

The program possesses a set of additional functions which make an impact on the further automation and simplification of user routine operations while working with the program and increase the precision of the received results.

2.2.1. Pulse curve smoothing

Real pulse electric processes involve low-frequency harmonics, which define the form of the impulse, as well as high-frequency ones, which lay over the form as noise. The last ones do not influence significantly the form of the impulse; however they can cause some error during the graphic analysis of the impulse.

The program possesses the function which abates the error, via pulse curve smoothing according to the current standard GOST 17512-82 [3]

2.2.2. Automatic detection for the division values

In order to save the time and avoid possible mistakes in user input "Metrological statistics" possesses the function of automatic detection for the division values and pulse polarity from the curve image.

2.2.3. Processing a set of curves

According to the current standard [2], the minimal set of measurements for each etalon value should contain at least 10 curves, therefore the program enables processing the measured data in packet mode. A user just needs to select the necessary number of graphic files in the dialog window and press "Calculate" button. The program will then compute ATP and measurement errors for each curve and estimate the transition factor of the gauge.

2.2.4. Time-amplitude parameters visualization

Any of the calculated ATP can be graphically displayed on the analyzed curve. In order to setup this and many other parameters, the "Settings" window (Fig. 2) should be used.

2.3. Report Creation

After all the necessary parameters are calculated the "ready to issue" certification reports [4] can be created. These reports involve final as well as intermediate values of the calculated parameters. The reports also contain the complete methodic for computation of every parameter during the gauge cer-

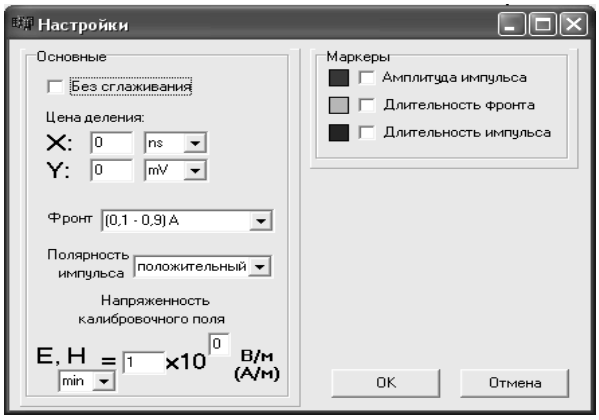


Fig. 2. Settings window

tification, therefore it is possible to monitor the correctness of the calculated results.

3. Conclusion

"Metrological certification" software is registered in the State Department of Intellectual Property and testified in practice with "Etalon-PEMF" and "Etalon-TN" during 1.5 years. The program appeared to be an effective tool for gauge metrological certification automation. These days the program is being applied as an integral part of "Etalon-PEMF" and "Etalon-TN". All together they create the automated pulse electromagnetic processes measurement unity supporting system of Ukraine.

References

1. Nemchenko Yu.S., Knyazyev V.V., Kravchenko V.I. and Lisnoy I.P. The development of the pulse electromagnetic processes measurement unity supporting system in Ukraine // *IEEE 2006 Third International Conference on Ultra wideband and Ultrashort Impulse Signals.* September 18 – 22, 2006. – Sevastopol, Ukraine, - p. 363-366.
2. GOST 8.207-2008 "Direct measurements with multiple observations. Methods of processing the results of observations. Basic principles."
3. GOST 17512-82 "Electric equipment and installations for 3 kV and higher. Measuring methods during high voltage test"
4. Skoblikov O.Y. Processing statistic data automation during the metrological certification of the instrumentations. // Bulletin of NTU "KhPI". Topical issue: "Techniques and physics of powerful voltages" № 11, 2009, Kharkiv, Ukraine

THE "TEM" METHOD OF CALIBRATION OF THE PULSE HIGH VOLTAGE DIVIDER

Kniaziev V. V., Kravchenko V. I., Niemchenko Yu. S., Lisnoy I. P.

National Technical University "Kharkiv Polytechnic Institute"
Res. & Des. Institute "Molniya", Kharkiv, Ukraine
E-mail: knyaz2@i.ua

Abstract

The article describes a TEM-method for calibrating high-voltage pulse dividers. The method is based on Etalon-EMP use. It presents the results of method use for determining transient response form and rise time of five types of high-dividers of various designs. The article shows the advantages of this method compared with the known methods.

Keywords: High-voltage pulse dividers, transient response, rise time, metrological certification.

1. INTRODUCTION

World practice of metrological certification (MC) of impulse voltages measuring devices, usually voltage dividers of different type (VD), consists in compulsory experimental determination of following characteristics:

– form and time parameters of transient response (TR), including TR rise time (. T_r^{TR} .);

– division factor K_d on impulse voltage. Herewith TR of VD is determined by special generators of unit voltage steps (GUVS), as a rule, relatively low voltage. GUVS used in Ukraine usually have output voltage up to 400 V. Specified parameters for high and very high voltage dividers are currently estimated by indirect methods. For example, K_d is more accurately determined at high pulse voltage (HV) using standard test sphere-gap voltmeter (SGV) [1, 2].

Both stages have difficulties, especially at MC of VD meant for voltage pulses measurement with amplitude of more than 500 kV. The difficulties are:

1) This kind of VD typically has a coefficient $K_d \geq 10000$, so that a digital oscilloscope could be connected to VD low-voltage shoulder. In this case VD output voltage in TR determination has a small value (units or tens of millivolts); this does not allow us determining TR parameters with the required accuracy (error is not more than few percents) in conditions when valid signal is accompanied with various types of noise.

2) The process of determining K_d with SVG is connected with such problems:

– SGV for voltages over 500 kV should have a minimum diameter of 0.5 m. These types of SGV as a rule are cumbersome, stationary structures weighing over 500 kg;

- procedure for MC using SGV includes definition of 50% breakdown voltage, which requires long period of time due to the necessity of statistic data set;

– breakdown voltage of SVG is sensitive to the influence of external climatic factors (pressure, humidity, ambient temperature, various types of radiation)

– accuracy in measuring HV using SVG not less than 3%, and the total accuracy of metrological certification results of VD not less than 5%.

In addition, SGV is applicable only for specific types of standardized pulses of microsecond range [1, 2]. It is not suitable for pulses with different parameters, such as the nanosecond range.

Therefore, to enhance the capacity of MC for arbitrary pulse shapes, as well as simplify the procedure of MC and obtain more reliable data of VD parameters, an alternative method was developed [3].

The method has no fundamental limitations in time and amplitude range of VD. Now, this method realized for nanosecond time range of voltages from 1 kV to 50 kV. It should be noted that for such parameters carrying out MC using SGV is impossible.

2. DESCRIPTION OF THE TEM METHOD

For carrying out the metrological certification of pulse high-voltage dividers (HVD) a method based on the use of the "Etalon-EMP" [4] is developed and implemented. Structurally, "Etalon- EMP" consists of high voltage (50 kV) energy storage, high-speed switch (response time 2 ns), field-forming structure (FS) as a TEM cell (with impedance of 50 Ohm), the matching load, a electric field converter (the time of transition characteristics is less than 0.2 ns), a digital storage oscilloscope DPO4041 (cutoff frequency – 1 GHz), a personal computer combined with an oscilloscope to a network, software for processing measurement results. The voltage between the electrodes FS has a form of

978-1-4244-7468-4/10/$26 ©2010 IEEE

bi-exponential impulse with an amplitude of 1 to 50 kV, a rise time of 8 ns and a duration of half-decay time 127 μs.

The method of metrological certification of HVD is the experimental determination of the form and rise time of the transient response (TR), the division factor HVD and, in some cases, the duration of TR by the simultaneous recording of amplitude-time electric field parameters and amplitude-time parameters of the signal from the low-voltage shoulder of calibrated HVD. In metrological certification of Etalon-CH an univocal correspondence with the electric field parameters in FS and the voltage between electrodes of FS, which is supplied to the HVD is found. HVD division factor is determined for each registered pair of signals. Statistical analysis is performed for a sample of not less than 10 observations. The value of the expanded uncertainty of the divider evaluation result is less than 5% [5], with the potential to reduce it by constructive improvement of the energy elements of the standard and the use of recording equipment with higher metrological characteristics. In addition, there is an opportunity to certification HVD without reference to the standardized form of voltage, which is regulated by IEC 60052:2002 [1]. These features provide significant advantages of TEM - method in comparison with traditional methods.

3. Results of Calibration

The method was tested in the study of 5 species of HVD, namely: OVD-6, OVD-10, OVD-50 and OVD-300 (ohmic VD at 6, 10, 50, 300 kV) and CVD-10 (capacitive VD 10 kV). According to the study in addition to determining the parameters of TR constructive improvements were held that allowed to improve the shape TR and reduce its rise time.

Studies of VD were conducted by the method of repeated observations using statistics results set of 10 pulses at each studied level.

Experimental data were analyzed using a personal computer program developed for automated processing “Metrology statistic" [6], that allows to process data set automatically. Typical oscillograms obtained in metrological certification of VD are shown in Fig. 1 – Fig. 5.

All the oscillograms (Fig. 1 – Fig. 5) show that curve No. 1 refers to the voltage of the meter SPEFV-EC output, and curve No. 2 – to the voltage of certified voltage divider output.

The got results allow to define all meaningful metrology descriptions of dividers directly from oscillograms. Therefore, the offered method can be named “direct”.

A method has not limitations on peak or on temporal parameters. For example, it can be realized on unique high-voltage Simulation which are described in compendium [7].

The received oscillograms allow making justified conclusion on the rise time of transient response of

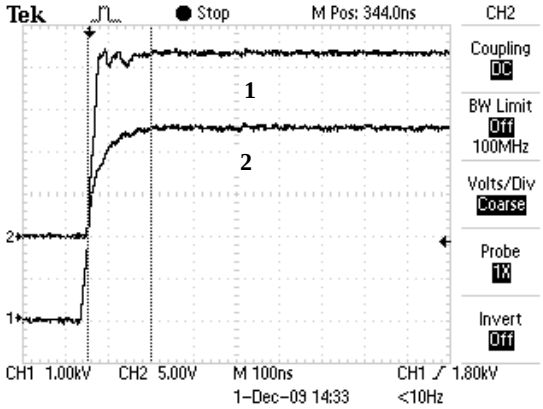


Fig. 1. Oscillogram of voltage OVD-6 with the pressure in high-voltage switch 2,5 atm., voltage 5 kV and oscilloscope bandwidth of 100 MHz.

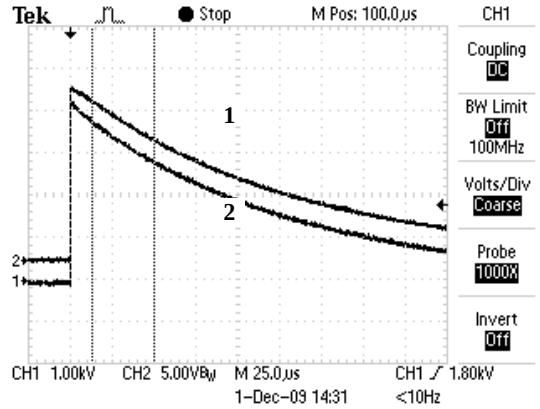


Fig. 2. Oscillograms of decay part of voltage pulse measured with OVD-6.

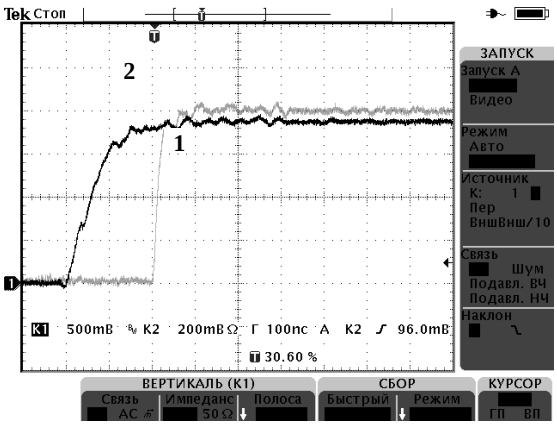


Fig. 3. Oscillogram of voltage SVD-10 with the pressure in high-voltage switch 0 atm., voltage 5 kV and oscilloscope bandwidth of 100 MHz.

the divider and the division factor. In the process of study, we managed to identify the need of making changes in the integrating circuit for some samples of VD. As a result, fluctuations in the front part have been mitigated, that significantly improved metrological characteristics of these dividers.

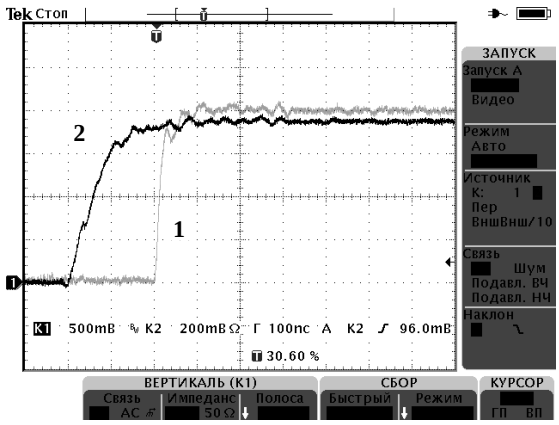


Fig. 4. Oscillogram of voltage OVD-300 with the pressure in high-voltage switch 6,5 atm., voltage 20 kV and oscilloscope bandwidth of 20 MHz.

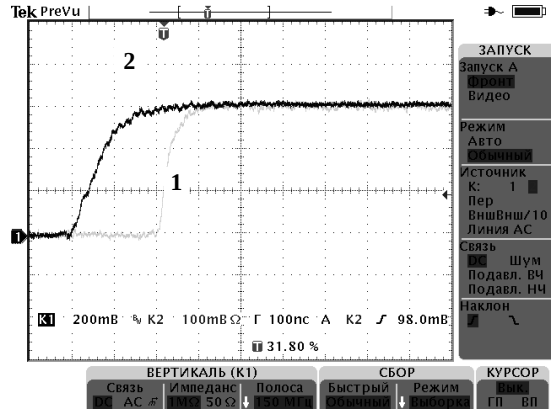


Fig. 5. Oscillogram voltage OVD-300, with the pressure in high-voltage switch, 0 atm., voltage 5 kV, bandwidth of oscilloscope 150 MHz and switching of integrating circuit on the output of OVD-300.

CONCLUSIONS

The results of studies of transient response form of 5 types of VD showed that Etalon-CH, created by the completion of Etalon-EMF, allows you to receive full information about metrological characteristics of voltage dividers of nanosecond range in the voltage range from 1 to 50 kV.

Amplitude-temporal parameters of the Etalon-CH enable to determine a VD division factor of any type with a division factor to 10000. At the same time, we determine the form of transient response. Thus, Etalon-CH can be considered as volt pulse etalon.

The application of stabilizing blocks in Etalon-CH and automated methods of processing provides measurement accuracy of amplitude-time parameters of certified VD less than 3%. In the next refinement of Etalon-CH it possible to reduce measurements accuracy up to 1%.

These results clearly show the advantages of the proposed TEM-method and the effectiveness of established Standard "Etalon-CH".

REFERENCES

1. IEC 60052:2002 «Voltage measurement by means of standard air gaps».
2. GOST 17512-82 Electric equipment and installations for 3 kV and higher. Measuring methods during high - voltage tests.
3. Knyazyev V.V., Kravchenko V.I., Lisnoy I.P. and Nemchenko Yu.S. The search for alternative methods of metrological certification of high-voltage pulse measuring devices. *Proceedings of the National Symposium with International participation of "Metrology and metrological support 2009»*, (Sozopol, September 10-14, 2009), TC – Sofia, Bulgaria 2009, p. 456-460.
4. Nemchenko Yu.S., Knyazyev V.V., Kravchenko V.I. and Lisnoy I.P. The development of the pulse electromagnetic processes measurement unity supporting system in Ukraine // *IEEE 2006 Third International Conference on Ultra wideband and Ultra short Impulse Signals.* September 18 – 22, 2006. – Sevastopol, Ukraine, - p. 363-366.
5. Zaharov I.P., Kniaziev V.V., Shevchenko N.S. The procedure of estimating uncertainty of measurement of attenuator division factor on Etalon-CH. *The System of Information Processing* Edition 4(85), (2010), p.126-129.
6. Program for PC, "Metrology statistic", Certificate No. 33321 from 17.05.2010 Department of Science and Education of Ukraine.
7. IEC 61000-4-32:2002 EMC – Part 4-32: Testing and measurement techniques – High – altitude electromagnetic pulse (HEMP). Simulation compendium.

SOME APPROACHES TO THE DEVELOPMENT OF ABSORBING MATERIALS FOR ULTRAWIDEBAND SYSTEMS

[1,2] Bibikov S. B., [1,3] Smolnikova O. N., [4] Menshova S. B., [1,3] Prokof'ev M. V., [1] Orlov V. V.

[1] "RPE Radiosrtim" Ltd., Volokolamskoe Shosse 4, 125993, Moscow, Russia
(info@radiostrim.ru)
[2] Institute of Biochemical Physics of RAS, Kosygina St., 4, 119334, Moscow, Russia
[3] Moscow Aviation Institute, Volokolamskoe Shosse 4, 125993, Moscow, Russia
[4] The Kuznetsk Institute of information and control technology
(branch of Penza state university), Kuznetsk of Penza region

Abstract

The paper presents the main approaches and results in the improvement of broadband and ultrawideband (UWB) radio absorbing materials used for UWB systems.

New composite materials on the basis of polyurethane foam and new ultradispersed carbonic fillers are developed. The frequency dispersion of dielectric permittivity of the received materials has been investigated. The effectiveness of gradient-resistance absorbers with the use of ultra-dispersed graphite fillers of new generation has been confirmed.

The way of decrease in frequency of a resonance of domain walls in MHz area has been found to expand a frequency range of radio absorbing materials down.

Keywords: Microwave absorbers, electromagnetic compatibility, conductive composite, ferrites, anechoic chambers.

1. INTRODUCTION

The development of modern ultrawideband (UWB) radio systems requires the development of new and modernization of existing measuring instruments, as well as new challenges associated with the problems of electromagnetic compatibility. These problems cannot be solved without application of UWB radio shielding and radio absorbing materials in radio engineering systems, the equipment and test benches.

For today theoretical principles are in detail developed and practical technologies of reception of microwave absorbers for various regions of a radio spectrum are mastered. Recently conducted studies of materials based on nanostructured composite thin film structures (see, e.g., [1]), but the problem of creating ultra-wideband PRM for frequencies $10^6...10^{11}$ MHz is still very relevant. Practice shows that the approach involving the use of resistive materials for ultrawideband applications [2], will be very useful because of its adaptability, flexibility of implementation and cost effectiveness. Also, the development of radio frequency absorbers for low-frequency range-based approach uses of high magnetic permeability, has not yet been exhausted, and requires further study.

2. BULK- RESISTANCE MATERIALS

One of the tasks, which must be solved with the construction of the radio absorbing materials, is the account of the dispersion of dielectric permittivity and magnetic permeability.

Let's consider one of the widely used approaches to obtaining microwave absorbers based on materials with Joule losses, or the so-called bulk-resistive materials. One of the advantages of this approach is the adaptability to obtain electrically conductive composite materials and the possibility of building structures on the basis of gradient materials with different concentrations of the conducting phases.

2.1. DISPERSION OF DIELECTRIC PERMITTIVITY

The material in question in the work consists of polyurethane foam (PUF) with the ultra-dispersed carbonic filler, introduced into the system in an amount providing the percolation threshold. To give the properties of non-flammable material is processed with a special compound does not influence the radiotechnical characteristics. Particles of carbon material substantially less than the wavelength, the skin layer, and form a continuous quasi-graphite conductive mesh. The final dc conductivity and all the features in the microwave range depend on the amount of carbon filler, structure, thickness and length of conducting

978-1-4244-7468-4/10/$26 ©2010 IEEE

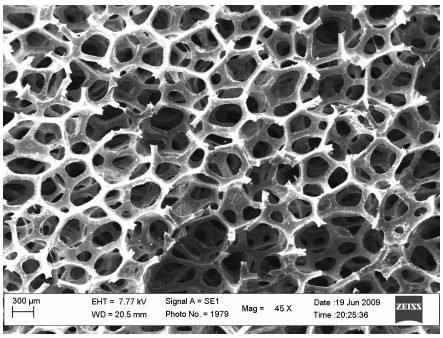


Fig. 1. Structure of resistive material on the basis of polyurethane.

clusters. Such material can be considered uniform on the electrical properties (although this may be the subject of a separate study), and isotropic.

Often at calculations of similar not magnetic structures consider that the material is completely characterized at macro scope level in two parameters: dielectric constant ε' = Re (ε^*) and the specific bulk electrical conductivity σ_V, independent of frequency in the studied range of frequencies. In some cases, these assumptions are justified, because the conductivity of the medium in the radio frequency σ(ω) differs slightly from that of the σ_0 in dc regime, while the imaginary part of dielectric constant independent of frequency as $\varepsilon'' \sim \omega^{-1}$ [3]. However, in some cases the condition $\sigma(\omega) \approx \sigma_0$ is not observed exactly. At the same time, during the construction of the flat multilayer constructions, where the resonance wave effects are completely essential, it is necessary to know the precise dispersion law of the generalized dielectric constant: $\varepsilon^*(\omega) = \varepsilon'(\omega) - j\cdot\varepsilon''(\omega)$.

Furthermore, frequently it is necessary to determine the function of the frequency dependence of dielectric constant for the correct extrapolation of experimental data into the extended frequency domain. Thus, for instance, the frequency spectrum of many UWB devices, in particular, geo-radars, stretches into region $10^7 \ldots 10^{10}$ Hz. Characterization of conductive foam is convenient to produce contactless method in the microwave range. With the measurements of such materials in the sub-gigahertz region noncontact method requires the large sizes of irradiators and models, and contact method is characterized by the poor reproducibility of results of measurements and requires special conditions for guaranteeing the electrical contacts. Determine the magnitude of the permittivity at low frequencies is possible, if you know the dispersion in the microwave range.

The analysis of a dispersion of dielectric permeability on an example of a material "the Mokh", made on the basis of electrically conductive polyurethane foam ("Radiostrim" Ltd.) is resulted below.

Measurements were performed at the Institute for Theoretical and Applied Electrodynamics RAS (Russia) using a vector measuring circuits Rohde & Schwarz ZVA40. A modified antenna. P6-23M was used as the irradiator.

Figure 2 (solid curves) shows the experimental plots ε' and ε", obtained from the measured values of the complex transmission coefficient for a flat sheet in an free space. Samples differ from each other the maintenance of the spending phase adsorbed on polymer and forming the electrically conducting clusters. Filling increases in an order to sample $C_1 > C_2 > C_3$.

The structure is logical to describe by the modified Maxwell-Wagner polarization model of the inhomogeneous medium [4]:

$$\varepsilon^* = \varepsilon_\infty + \frac{j\cdot\sigma_V}{\omega} + \frac{\varepsilon_c - \varepsilon_\infty}{1+\left(j\omega\tau\right)^{1-\alpha}}, \qquad (1)$$

where ε_c and ε_∞ – the dielectric constant at low and high frequency limits, respectively, τ – time of relaxation, and a dimensionless exponent (1 – α) characterizes the distribution of relaxation times, with α = 0 blur of relaxation is absent. After decomposing (1) to the real and imaginary parts, it is possible to find the parameters of model. Fig. 2 shows the curves of the real ε'and imaginary ε" parts of the permittivity, obtained both experimentally and from the calculation of (dotted line) by formula (1) with certain parameters τ, α, σ_V, ε_c and ε_∞. The parameters are given in Table 1.

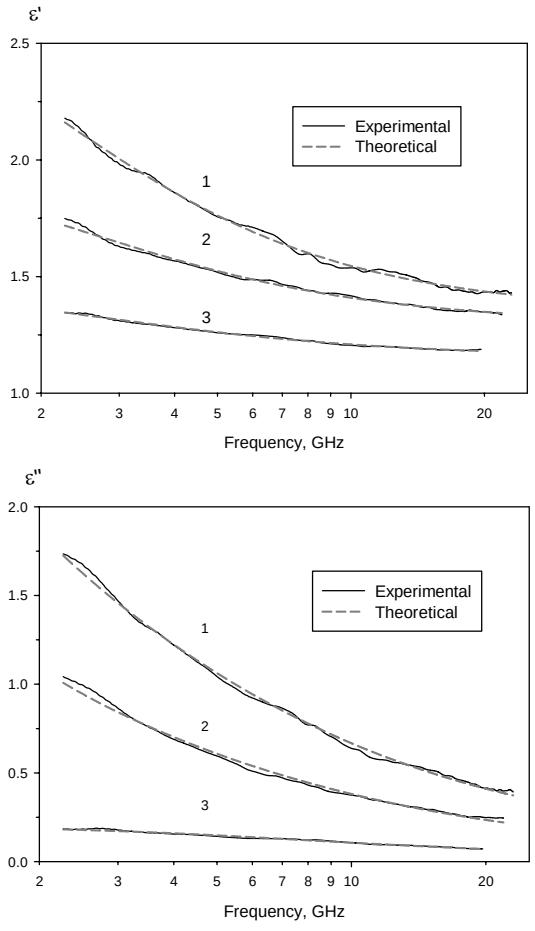


Fig. 2. Dependence of ε', ε" the basis of material "Mokh" from the frequency.

Table 1. Parameters of dispersion.

Specimen	τ, ns	σ_V , $\Omega^{-1}m^{-1}$	Δε	ε∞
1	0.47	0.126	1.73	1.33
2	0.39	0.084	0.79	1.29
3	0.36	0.006	0.33	1.15

At $\alpha \approx 0.17$ theoretically constructed curves simultaneously well coincide with experimental values ε' and ε".

The analysis shows that for the investigated samples last member in expression (3) is defining character of frequency dependence while the contribution of through conductivity σ_V is less.

2.2. SHAPED MICROWAVE ABSORBERS

The shaped SHF absorbers are multilayer or pyramidal structures (Fig. 3).

Figure 4 shows the frequency dependence of resistive material of the pyramidal type, developed by "Radiostrim" Ltd. on the basis of the investigated conductive polyurethane foams. Measurements were performed in the free space on the measuring stand of the Institute of Theoretical and Applied Electrodynamics RAS on the basis of a vector meter Rohde & Schwarz ZVA40. Characteristics for materials of "Mokh-P" type in height of 70, 250 and 330 mm are shown.



Fig. 3. View of microwave absorber "Mokh P-70".

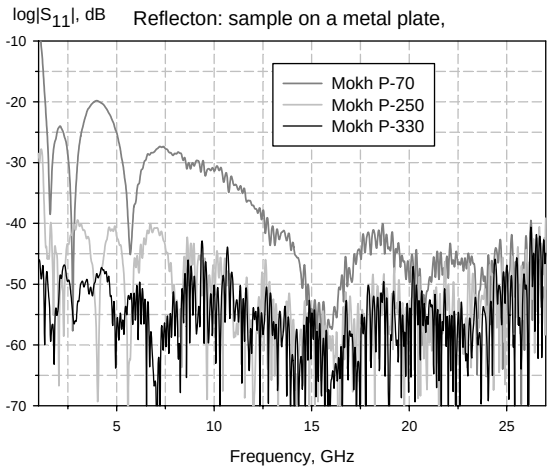


Fig. 4. Reflectivity of microwave absorbers of "Mokh" type (the samples on metal plate).

For equipment of anechoic chambers the microwave absorbers must possess the lowered combustibility. Therefore the represented materials are processed by the specially developed solution, which ensures non-flammability, with the retention of radiotechnical characteristics.

3. SCATTERING MATERIALS

Materials based on quasi random dipole structures have a radio absorbing and partially radio scattering properties. The distinctive special feature of such materials is the relatively isotropic nature of reflection coefficient, insignificant weight, possibility of the shelter of the objects of any form, increase the efficiency and wide bandwidth with the use of multilayer gradient construction.

Figure 5 shows typical frequency response in the band 2-26 GHz of microwave absorber of carpet type "Ternovnik": MO (basic version), 2MO (upgraded to work in the high-frequency region) and MO-20 (the most functional material). In RPE "Radiostrim" there is developed the material of the carpet type of series "Ternovnik-TG", which is characterized by lowered combustibility and increased strength.

4. SOFT MAGNETIC MATERIALS

To ensure electromagnetic compatibility and testing a number of UWB devices, for example, a georadar with the central frequency less then ≈200 MHz and for equipment of proper anechoic chambers, it is necessary to use radio shielding and absorbing materials of a range of frequencies from MHz to GHz. Because of the geometric limitations absorbers of resistance type are here unacceptable; therefore it is necessary to use materials with the high magnetic losses. We obtained the materials on the basis of modified nickel-zinc ferrites, which are characterized by an increase in the losses with the resonance of domain walls in the MHz region due to the special structure of the ferrite grains.

The magnetic spectrum of materials actually is the sum of contributions of a spectrum of a natural ferromagnetic resonance and a resonance of domain borders. Moreover the nature of the latter depends not only on the magnetic parameters of material (field of anisotropy, saturation magnetization), but also of parameters of structure (geometry of grains, the parameters of the wall of domain) [5]. The spectrum of magnetic susceptibility, defined resonance of domain boundaries can be described by the expression:

$$\chi = \chi_0 \left(1 - \frac{\omega^2}{\omega_0^2} - j \frac{\omega}{\omega_{rel}} \right)^{-1} \qquad (2)$$

where the resonance frequency of domain walls

$$\omega_0 = (\zeta/m)^{-1} \qquad (3)$$

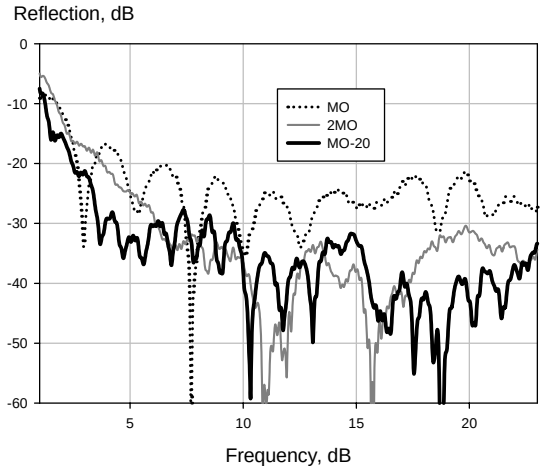


Fig. 5. Reflectivity of microwave absorbers "Ternovnik" (the samples on metal plate).

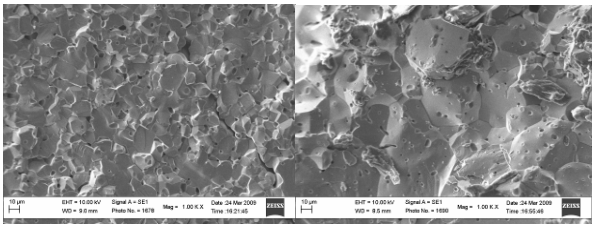


Fig. 6. The structure of the material (on the left - the original, right - doped by Bi_2O_3)

ζ – coefficient of "magnetic" elasticity, depending on initial magnetization and the sizes of the domains d, χ_0 – initial static susceptibility, ω_{rel} – frequency of a relaxation of displacement of walls, m – effective mass of the domain wall.

Figure 6 shows the structure of the material obtained by different technological processes - with addition of bismuth compounds and without them.

The spectrum of magnetic permeability is resulted on Fig. 7. Appropriate reflection coefficients of the ferrite materials "Rif" with thickness 8.8 mm on the metal plate are shown in Fig. 8. Measurements were performed in a coaxial measuring cell, which is a continuation of coaxial tract.

ACKNOWLEDGMENTS

In order to ensure the functionality of UWB systems appropriate to use radio absorbing material, ensuring optimum dissipation of electromagnetic energy, taking into account the dispersion of electrical and magnetic characteristics of materials.

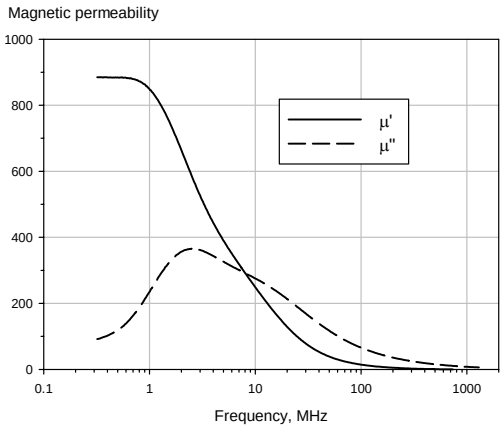


Fig. 7. Complex magnetic permeability of the modified ferrite material of type "Rif".

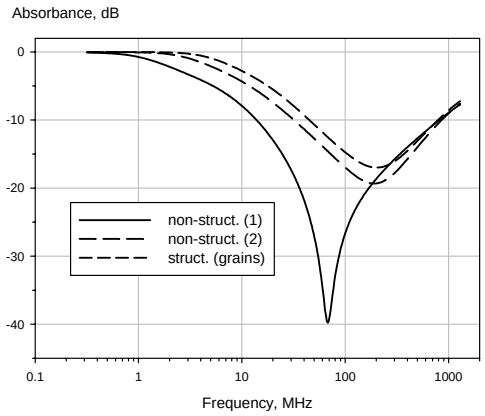


Fig. 8. Reflectivity of ferrite-based material "Rif" (the samples on metal plate).

REFERENCES

1. L. Lutzev, etc. Nanotechnics. 2008, **2,** p.37-43.
2. Titov A. N., Bibikov S. B., Kulikovskij Ed.I. Proceedings of the Four International Conference on Ultrawideband and Ultrashort Impulse Signals, 2008, Sevastopol, Ukraine, pp. 248-250.
3. L.D. Landau and E.M. Lifshitz, Electrodynamics of Continuous Media, Course of Theoretical Physics, Vol. 8 (Pergamon, New York, 1975).
4. Oreshkin P.T. Physics of semiconductors and dielectrics. Moscow: High School. 1977. 448p.
5. A.Gurevich and G.Melkov. Magnetic oscillations and waves. Moscow: Nauka, 1994, pp.464.

PARAMETRIC STUDY OF IMPULSE HIGH VOLTAGE DISCHARGE

Berdin S. A., Galchenko D. A,. Zagvozdkin B. V., Karelin S. Yu., Magda I. I., Mukhin V. S., Soshenko V. A.

Institute of Plasma Electronics and New Acceleration Methods of NSC KhIPT
NASU, 1, Academicheskaya Str., Kharkov, 61108, Ukraine.
E-mail: magda@kipt.kharkov.ua; тел. +38-057-751-2669

Abstract

Features and results of experimental parametrical study of high-voltage breakdown in dense dielectric media are considered. Influence of temporal characteristics of the test system to breakdown parameters of dielectric is shown. Design and performance data of voltage and current sensors together with algorithm for experimental data processing are discussed.

Keywords: Ultra-short impulse, voltage and current sensors, high-voltage breakdown, ultra-wideband forming system.

1. INTRODUCTION

The electric breakdown in a dielectric media relates with the condition that the carrier of charge gains its energy in the electric field of an external source sufficient for ionization of molecules. As a result, a number of carriers and electric current in dielectric avalanchely increase.

To the present time, numerous researches of high-voltage (HV) breakdown in dielectrics in stationary and slowly changing electric fields are curried out. Nevertheless, the temporary parameters of breakdown in dielectric media of high density produced by HV impulse of nano- and subnanosecond duration are studied insufficiently [1,2]. Providing the researches in the voltage range of hundreds kV allow to obtain fundamental results necessary in many areas of science and engineering. Investigation of a breakdown in extreme electric fields of nano- and sub-nanosecond duration has some specific features which are considered below.

2. REALIZATION OF INVESTIGATION

Formation of a breakdown implements in the test chamber where the gap between electrodes is filled with necessary substance. Schematics of investigation facility is shown in Fig. 1. The facility contains the HV impulse source, pulse forming system, preliminary peaker, test chamber, and load. Variation of voltage and current in the interelectrode gap provides the data of the studied process. Since the breakdown time is greatly determined by the rise-time of the voltage impulse over the gap, the system contains a preliminary peaker that provides impulses with the rise-time less than 0.5 ns. Small time of the breakdown process (10^{-9}-10^{-10} ns) demands ultra-wideband (UWB) quality of the system. In our case, it is implemented as a HV coaxial waveguide with a wave impedance of 75 Ohm. The impulse power source (Marx generator) is also implemented as a coaxial system [3]. General view of the facility is shown in Fig. 2.

Technique of researches requires complex solution of a series of interdependent problems:

- choice of the geometry and dimensions of the UWB system,
- design and calibration of the electrical and magnetic field sensors, technique and instrumentation for measurement the sensors' parameters,
- development an algorithm for processing the experimental data.

3. PROCESSES IN DISCHARGE GAP

The coaxial HV (U_0=500 kV) system generally is non-uniform because of a necessity to use switches. Up to the moment of their breakdown, the reflection waves are formed in the system obstructing to process of the obtained data. It is expedient to consider physical processes arising in the coaxial system at a breakdown of the intere-

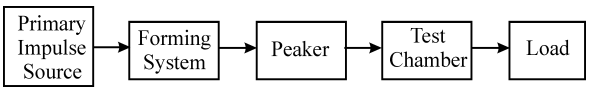


Fig. 1. Schematics of investigation.

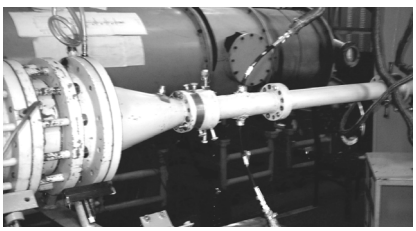


Fig. 2. Facility for HV investigation.

978-1-4244-7468-4/10/$26 ©2010 IEEE

lectrode gap more detaily. Let's use the simplified equivalent circuit of our installation shown in Fig. 3. The impulse generator coupled to a series of losses coaxial lines L1…L4, discharge gap *Rg*(*t*), and load resistor R_{load} is used as the primary voltage source. Presentation of the discharge gap as a resistor with varying resistance is quite justified since the discharge has dropping characteristic. The time delay in every coaxial line makes 3 ns. A 1 kV voltage impulse source has internal resistance of 1 Ohm, and the pulse rise-time of 4 ns. The system operation is simulated with the help of the Micro-Cap 7 software.

Fig. 4 demonstrates: a) the gap resistance varying in time, b) the voltage in points 1 (continuous line) and 2 (dotted lines), c), the voltage impulse over the discharge gap. The gap resistance decreases from 1 MOhm down 1 Ohm within the time interval 8-9 ns.

The signal from the generator travels through the line L1 and in the area of the sensor arranged in point 1. Then the signal passes through the line L2 to the switch and reflects since at this time the gap resistance $R_g(t)$ is high (Fig. 4a). The time delay equals the double transit time in the line L2. The voltage amplitude over the gap arises. Then, in regard with Fig.4a, the breakdown development in the discharge gap results in reduction of the resistance $R_g(t)$, and, accordingly, the reflection impulse decreases. The discharge current arises in the discharge gap. The voltage at the second electrode of the discharge gap in point 2 (Fig. 4b, dotted line) increases, while the voltage over the discharge gap drops (Fig. 4c). Obviously, measurement of the instantaneous voltages and currents in the discharge gap helps to determine the time variation of the resistance R_g.

Thus, the results of simulation of the breakdown of the gap display the presence of a time-delay for the wave traveling between the discharge gaps and sensors allows to separate in time the amplitudes of direct and reflected waves, and receive information on the breakdown process. The delay time should exceed the rise-time of the arriving pulse.

4. PARAMETERS OF HIGH-VOLTAGE IMPULSES

The measurement technique for measurement the HV impulses of sub-nanosecond time range is based on indirect method of measurements of the electrical or magnetic components of electromagnetic fields (EMF) in the UWB system. In this regard, we have studied and designed a series of UWB voltage and currents sensors [4].

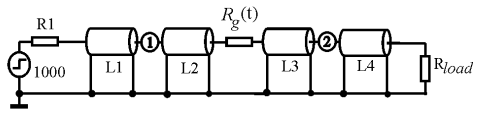
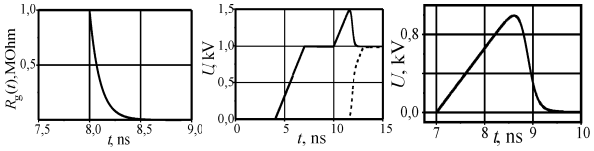


Fig. 3. Equivalent circuit of the studied system.



a) b) c)

Fig. 4. Simulation results.

The equivalent circuits of sensors and their design are shown in Fig. 5a-d. Structurally the sensors are executed on the basis of N-type connectors placed on the external electrode of the coaxial system. The equivalent circuit of the sensor of the electrical component of EMF contains the capacitors C1 and C2, resistance R1, coaxial cable L1, and input resistance of the oscilloscope R2. A differential equation of such divider looks like:

$$\frac{dU_{in}}{dt} = k\left(\frac{dU_{out}}{dt} + \frac{U_{in}}{T}\right) \qquad (1)$$

where $k = \dfrac{C1+C2}{C1} = 1 + \dfrac{C2}{C1}$ is the output voltage ratio, and *T* is the time constant of the divider equal to $T = \left(C1 + C2\right)\cdot(R1 + R2)$.

Depending on a value of the time constant *T* there are three operation modes of a capacitive voltage divider:

- proportional (integrating) voltage divider,
- voltage divider with partial integration,
- differentiating divider.

In the proportional divider $T >> t_p$, where t_p is the pulse duration. In this case, the second addendum in an equation (1) can be neglected, and the voltage output is:

$$U_{\text{out}} = \frac{1}{k}U_{\text{in}}.$$

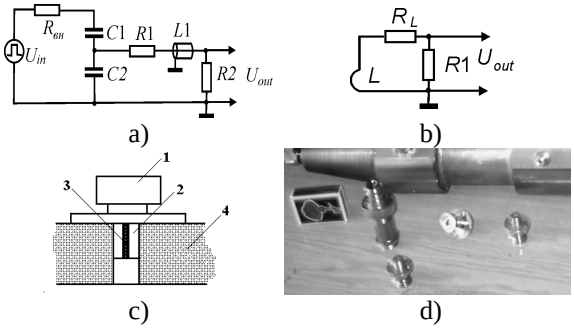
Thus, the voltage output of the divider is proportional to the input voltage.

The voltage divider with partial integration can be realized when the time constant *T* is commensurable with pulse duration t_p. In this case, the divider behavior is described by full equation (1) without any simplifications, and the output voltage is described by equation:

$$U_{\text{out}} = T\left(\frac{1}{k}\frac{dU_{\text{in}}}{dt} - \frac{dU_{\text{out}}}{dt}\right).$$

Let's restore the original signal with the help of (1):

$$U_{\text{in}} = k\int_0^t\left(\frac{U_{\text{out}}}{T} + \frac{dU_{\text{out}}}{dt}\right)dt = k\left(\int_0^t\frac{U_{\text{out}}}{T}\,dt + U_{\text{out}}\right).$$



a) b) c) d)

Fig. 5. a) equivalent circuit of electric field sensor, - b) equivalent circuit of magnetic field sensor, c) design of sensor, d) general view of sensors and facility.

The differentiating voltage divider is implemented at $T << t_p$, that allows to neglect the first addend in equation (1), and then:

$$U_{out} = \frac{T}{k}\frac{dU_{in}}{dt} = T_1\frac{dU_{in}}{dt},$$

where $T_1 = C1R2$.

The output voltage of this sensor is proportional to the derivative of the input voltage and the time constant of the sensor *T1*. The voltage incoming to the sensor is restored by integration:

$$U_{in} = \frac{1}{T_1}\int_0^t U_{out}dt$$

The operational modes of the electrical field sensor and procedure of signal recovery are implemented in the magnetic fields sensor. Their feature is the sensitiveness to the electric current direction in the coaxial system.

Checking of the impulse characteristics of sensors is implemented on a special bench. Its design represents the coaxial line matched to the impulse source with the rise-time 80 and 250 ps.

Fig. 6 shows a dotted line of the restored impulse of the differentiating sensor. The original signal is shown in this figure by a continuous line. The experimental results demonstrate that the differentiating sensor provides measurements with sub-ns time resolutions.

The calibration scheme of the sensors installed into the experimental facility is shown in Fig.7. The calibration implements the voltage step-impulse produced by the capacitor discharge to the load. In this case, the capacitor is made of the central conductor of the coaxial line. The rise-time of the pulse is determined by a value of the resistor R2

5. Algorithm of Calculations of Discharge Gap Resistance and Experimental Results

The initial data for calculation of non-stationary resistance are the signals from inductive and capacitive sensors positioned before and after the discharge gap.

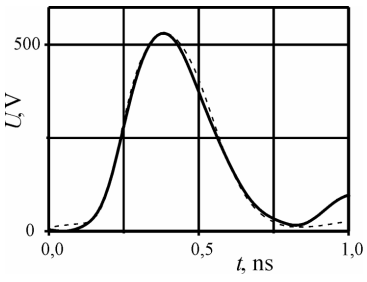


Fig. 6. Calibration impulse.

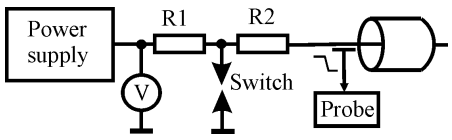


Fig. 7. Schematics of experimental circuit for sensor calibration.

Preliminary procedure of the data processing includes the data recovery with the use of the results of measurements, registration of the delay time in the coaxial system and measurement cables.

Calculation of the voltage amplitudes of the direct and returned waves before the discharge gap to be made accordingly**:**

$$\begin{cases} U_{in} = 0.5\left(U + U_I\right) \\ U_{out} = 0.5\left(U - U_I\right) \end{cases},$$

Where U and UI are accordingly the voltages measured by the capacitive and induction sensors.

The given operation allows to eliminate a signal, reflected from the discharge gap what dilates a range of the pulse rise-time supplied to the discharge gap.

Dependence of the discharge gap resistance on time is:

$$R_g = Z\frac{2\left(U_1 - U_2\right)}{U_2} = 2Z\left(\frac{U_1}{U_2} - 1\right),$$

where U_1 and U_2 are the voltage accordingly before and after the discharge gap, Z is the wave impedance of the coaxial line.

The experimental results of the breakdown process in oil, and calculation of the discharge gap resistance are shown in Fig.8. The experimental technique shown in Fig.8 provides to study the breakdown in dielectric media developed in nano- and subnanosecond time range.

6. Conclusion

The experimental set-up and research techniques for study the parameters of HV breakdown in nano- and subnanosecond time range are considered. The breakdown processes in UWB coaxial chamber are analyzed. It is shown that measurement of the voltage over the discharge gap can be executed by means of introduction of the additional delay time between points of measurements and electrodes of the studied discharge gap. The operational modes of the measurement sensors and recovery methods of the HV impulse amplitude are determined. The experimental data of the breakdown development and processing algorithm for experimental data recovery that determines the breakdown time-delay and the resistance dynamics of the discharge gap are shown. The ability to process the signals in wide time range is the peculiarity of the algorithm.

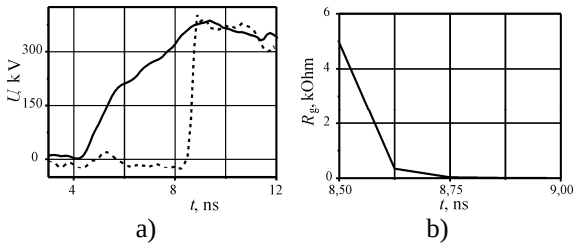


Fig. 8. a) Experimental results of discharge in transformer oil, b) calculated resistance of the discharge gap.

REFERENCES

1. Kromphoz H., Hatfield L., Hausten M., Spears J., Kristiansen M. 2003, 'Nanosecond pulsed breakdown for point-plane geometries at moderate voltage', *Ultra-Wideband Short-Pulse Electromagnetics 6*, Edited by Mokole et al., Kluwer Academic / Plenum Publishers, 409-414.
2. Kromphoz H., Hatfield L., Short B., Kristiansen M. 2002, 'Sub-nanosecond gas breakdown phenomena in the voltage regime below 15kV', *Ultra-Wideband Short-Pulse Electromagnetics 5*, Edited by P. D. Smith., S. R. Cloude, Academic/Plenum Publishers, 437-443.
3. Gladkov V.S., Magda I.I., Melnikov P.N., Rudakov V.V. 2009, 'A Megavolt Frequency Generator Pulses with an FWHM duration of 30 nanoseconds', *Instruments and Experimental Technics*, V.52, No 3, 53-59.
4. Berdin S.A., Karelin S.Yu., Korenev V.V., Magda I.I., Muchin V.S., Naboka A.M., Soshenko V.V. 2010, 'Measurement of subnanosecond impulse electromagnetic fields in coaxial waveguides', *20-th Int. Conf. "MW and communication technologies"*, 12-16 Sept., Sevastopol. Vol.2, No.516.

IMPULSE SUB-NANOSECOND REFLECTOMETRY

[1] Berdin S. A., [1] Karelin S. Yu., [1] Korenev V. G., [1] Magda I. I., [1] Mukhin V. S., [2] Naboka A. M., [1] Soshenko V. A.

[1]Institute of Plasma Electronics and New Acceleration Methods of NSC KhIPT
NASU, 1, Academicheskaya Str., Kharkov, 61108, Ukraine.
E-mail: magda@kipt.kharkov.ua; тел. +38-057-751-2669
[2]Institute of Electrophysics and Radiation Technologies NASU.
28, Chernyshevskaya Str, P.B.8812, Kharkov, 61002, Ukraine.

Abstract

Features of impulse reflectometry using sub-nanoseconds pulses are considered. Impacts of non-uniformities in the system to the measured signal parameters are analyzed. An algorithm for observed data processing that takes into account the test signal envelope and numerous reflections originating in non-uniform system is proposed.

Keywords: Sub-nanosecond, impulse reflectometry, non-uniform systems, ultra-wideband systems.

1. INTRODUCTION

A technology of measurement the parameters of systems, that uses a response to the initial signal bears the name reflectometry. Variation of the method is impulse reflectometry (IRM) [1], which uses the time delay and amplitude of the initial and reflect signals to define the location and discontinuity parameters of the system. Now reflectometry is applied for studying the systems with high temporal resolution [2], in particular, for debugging and matching of impulse antennas [3]. Functional units that provide the IRM supplement some of digital oscilloscopes. Very important to note that for several investigations, it is required large amplitudes of the test signal (up to a some kV) what is not possible for serial instruments. Therefore these researches are connected with creation of new algorithms for data processing.

2. MAIN PART

Traditional circuit for carrying on measurements using a method of IRM is shown in Fig. 1. The signal of the test generator is injected into the investigated system, and spreads through it with the phase velocity determined by the parameters of the transmission line. The reflected wave originates at the non-uniformities. The reflectivity factor K of this wave depends on the amplitudes of incident V_{IN} and reflected V_R waves, and the wave impedances of the line Z_0 and non-uniformity Z_{IN}:

$$K = (V_R - V_{IN})/V_R \quad (1)$$

$$Z_{IN} = Z_0(1+K)/(1-K) \quad (2)$$

The measured signal presents the net amplitude of these waves. At study of an extended homogeneous system, there are no special requirements to parameters of the test signal, therefore the obtained data processing has not practical difficulties.

Application of the method for study of ultra-wideband systems requires providing measurements in sub-nanosecond time range, and accordingly, formation of the test signals with sub-nanosecond rise-time. To the present time, the technical possibilities allow to generate the test signals with an envelope close to a step-function. However the interfering fields that originate in the investigating system due to discontinuities create errors in the processing data.

Let's consider an impact of a form of the exploring impulse at research of non-homogeneous tract when the processing algorithms of IRM for exponential (Fig. 2a) and oscillatory (Fig. 2b) exploring impulses are known. Fig. 2c and Fig. 2d demonstrate the results of calculation in regard with formulas (1) and (2) of the wave impedance of a homogeneous tract with the wave impedance of 50 Ohm coupled to the load resistance of 200 Ohm.

Thus, these calculations allow to receive acceptable results, when the test signal has the form close to a step-function, and the tested system has only one non-uniformity. At the same time, a well-shaped rise-time of the test impulse defines the accuracy of the discon-

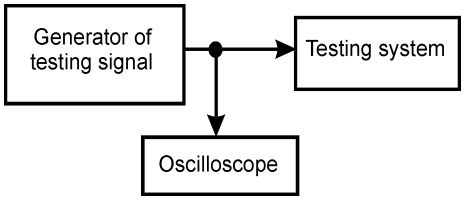


Fig. 1. Reflectometry setup

978-1-4244-7468-4/10/$26 ©2010 IEEE

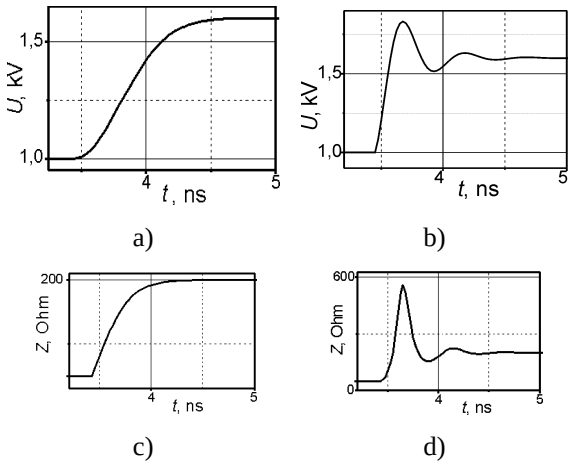


Fig. 2. Test signals with different rise-time and calculated impedances.

tinuity location. The presence of oscillatory process at the rise-time of the test signal leads to considerable errors (Fig. 2d).

In Fig.3a the dependence of the reflected signal in a coaxial line with the serial resistance of 50-20050-200-50 Ohms is shown. The rise-time of the testing impulse is of 20 ps. The result of calculation of the wave impedance according formulas (1) and (2) is shown in Fig.3b. It can be seen that the obtained data allow to define only a value of the first jump of a resistance, and calculations that take into account further non-uniformities have very large divergency with the initial data even for very small rise-time. The presence of oscillations in the real test signal aggravates the result more, and does not allow to use the obtained data.

Thus, a study of ultra-wideband system requires taking into account the forms of both the test signal and the reflections originating at non-uniformities. In this regard, a processing algorithm for IRM of picoseconds time-scale has been designed.

To start the algorithm it is required to provide a time-delay for the test signal at the input of the studied system. Its value should exceed the time of relaxation of the test signal in the system. The presence of the delay helps to introduce the envelope of the test signal into processing procedure. In our experiments, this delay is provided by a coaxial cable matched to the input of the tested system and is of 5 ns. The data obtained for an UWB system are shown in Fig.4. A signal registered by the oscilloscope can be divided

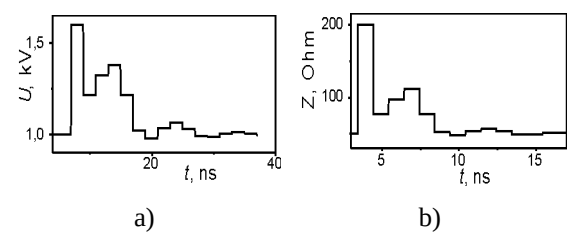


Fig. 3. a) Reflected signal, b) restored impedance

into three temporal zones I-III. In zone I (up to 5 ns), the test signal travels down the coaxial cable to the oscilloscope. An envelope of the test signal U_i is recorded in this zone. In zone II, the test signal enters the input of the studied system, and the amplitude of the plane part of the pulse V_0 is registered being the normalizing amplitude for further definition of the wave impedance of the tested system. In zone III (for our case, it exceeds 10 ns), the reflected signal V_i enters the oscilloscope and forms the data array for calculation of the current wave impedance Z_i.

The processing procedure of the experimental data is the following. Let the input data contain n values of the signal amplitude V_i where $j=1…n$, measured with the time-step Δt. The measured transmission line is divided on n sections with the wave impedance Z_j and a step $\Delta l=v\Delta t/2$, where v – is the wave velocity in the system. The reflection from non-uniform sections of the signal traveling in forward direction is defined by the reflection factor $K_j=(Z_j–Z_{j-1})/(Z_j+Z_{j-1})$.

During the processing procedure of the experimental data, Table 1 is formed, where dependence of the reflected signal amplitudes on time and distance from the beginning of the line is described. Every i-th line of the table corresponds to a value of the signal at the distance $l=i\Delta l$ from the line input, and every j-th column corresponds to a value of the signal at $t=j\Delta t/2$. Every unit of the table $U_{i,j}^k$ (k – is the number of the step, where a value of the table unit is evaluated) corresponds to two variables: $(U_{i,j}^k)_{in}$ - is the direct signal moving from the beginning of the line to its end, and $(U_{i,j}^k)_{out}$ - is the backward signal moving from the end of the line to its input.

An order of calculation is the following. At zero step (k=0), the upper left unit of the table: $(U_{00}^k)_{in}=V_0$ and $(U_{00}^k)_{out}=0$ is filled, and a value of the wave impedance of the coaxial cable Z_0 (known a priori) is written. At each subsequent k-step the following operations is fulfilled:

1. The k-th reflection factor is estimated as the first approximation:

$$K_k=(V_k–V_0)/V_0,$$

where V_k – is the signal amplitude at the system input.

2. The amplitudes of the direct and backward sig-

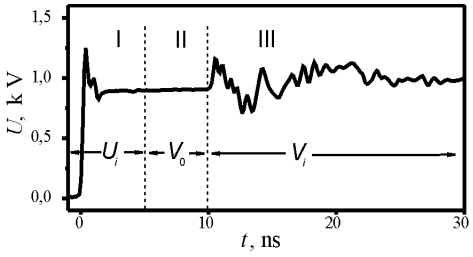


Fig. 4. Reflectometry of signal of ultra-wideband forming system.

nals appropriate for *k*-th step are estimated (Table 1.):

$$\left(U_{i,j}^{k}\right)_{in}=\begin{cases}(1-K_{k-1})\cdot\left(U_{i-1,j-1}^{k}\right)_{in}-K_{k-1}\cdot\left(U_{i-1,j}^{k}\right)_{out} & j\geq 2\\ U_{i/2} & j=1\end{cases}$$

$$\left(U_{i,j}^{k}\right)_{out}=K_{k}\cdot\left(U_{i-1,j}^{k}\right)_{in}+(1+K_{k})\cdot\left(U_{i-1,j+1}^{k}\right)_{out}$$

where $U_{i/2}$ is the test signal amplitude at the center of the time interval *i*. Values $U_{i/2}$ for the fractional indexes are evaluated with the help of linear interpolation.

3. The divergency between the measured and calculated signals is defined:

$$E=V_{k}-V_{0}-\left(U_{2k+1,1}^{k}\right)_{out}$$

4. The k-th reflection factor is corrected:

$$K_{k}=K_{k}+K_{fb}(E/V_{0}),$$

where $K_{fb}\leq 1$ is selected from the condition of calculation stability.

Table 1. Table of calculation.

		V_0		V_1		V_2		V_3		V_4		V_5	
	Z_1	$U^0_{1,1}$	$U^1_{2,1}$	$U^1_{3,1}$	$U^2_{4,1}$	$U^2_{5,1}$	$U^3_{6,1}$	$U^3_{7,1}$	$U^4_{8,1}$	$U^4_{9,1}$	$U^5_{10,1}$	$U^5_{11,1}$	…
K_1	Z_2	0	$U^1_{2,2}$	$U^2_{3,2}$	$U^2_{4,2}$	$U^3_{5,2}$	$U^3_{6,2}$	$U^4_{7,2}$	$U^4_{8,2}$	$U^5_{9,2}$	$U^5_{10,2}$	…	
K_2	Z_3	0	0	$U^2_{3,3}$	$U^3_{4,3}$	$U^3_{5,3}$	$U^4_{6,3}$	$U^4_{7,3}$	$U^5_{8,3}$	$U^5_{9,3}$	…		
K_3	Z_4	0	0	0	$U^3_{4,4}$	$U^4_{5,4}$	$U^4_{6,4}$	$U^5_{7,4}$	$U^5_{8,4}$	…			
K_4	Z_5	0	0	0	0	$U^4_{5,5}$	$U^5_{6,5}$	$U^5_{7,5}$	…				
K_5	Z_6	0	0	0	0	0	$U^5_{6,6}$	…					
K_6	Z_7	0	0	0	0	0	0						

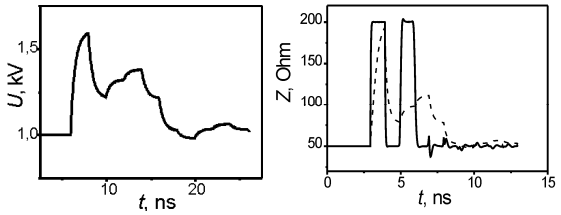
5. Operations from 2 to 4 are repeated till one of conditions are fulfilled: $|E|<\varepsilon$, where ε is the required accuracy, and a number of the fulfilled operations does not exceed a specified value.

6. The *k*-th wave impedance is calculated:

$$Z_{k}=Z_{k-1}(1+K_{k})/(1-K_{k}).$$

Thus, as a result of execution of the algorithm the array Z_k (distribution of the wave impedance along the line length) is obtained.

The IRM signal in the non-uniform system (50-200-50-200-50 Ohm) is shown in Fig. 5a. The results of calculation of the wave impedance according (1) and (2) (dotted lines), and also according the proposed algorithm (solid line) are shown in Fig. 5b. It is obvious that the use of the algorithm helps to locate the non-uniformities in the tract, and reduce the errors in estimation of their values.



a) b)

Fig. 5. a) Reflectometry signal, b) result of impedance calculation.

3. CONCLUSION

The disadvantages of traditional approach to data processing by means of impulse reflectometry are discussed. The algorithm of data processing that permits to take into account the test signal envelope and numerous reflections originating in the systems with several non-uniformities is proposed.

REFERENCES

1. Kushnir F.V. 1983, 'Electoradioizmereniya', Leningrad, Energoatomizdat. 320.
2. Dick A. R., MacGregor S.J., Pate R. C. 2002, 'Transmission line switch design for the investigation of sub-nanosecond electrical breakdown', Measurement Science Technology, 13. 539-546.
3. Bowen L. H., Farr E. G. 2000, 'Experimental result of optimizing the location of feed arms in collapsible IRA and a solid IRA', Sensor and Note 450. 1-14.

SCALE ELECTRODYNAMIC MODELING OF ULTRA WIDEBAND SYSTEMS

[1,2] Titov A. N., [1] Gribanov A. N.

[1] V. Tikhomirov scientific research institute of instrument design (NIIP), Zhukovsky, Russia. E-mail:niip@niip.ru
[2] Moscow institute of a radio engineering, electronics and automatics (MIREA), Moscow, Russia. E-mail:mirea@mirea.ru

Abstract

Rules which observance is necessary at performance of scale modeling narrow-band and ultra wideband electrodynamics systems are shown.

Keywords: Scale electrodynamics modeling, electrodynamics similarity, scale model, scaling factor.

1. INTRODUCTION

Scale electrodynamics modeling is widely applied at designing antennas and microwave devices, and also at experimental researches of processes of reflection and dispersion of electromagnetic waves. It allows to carry out, for example, on models in laboratory conditions experimental processing of bulky antennae which are characteristic for rather long-wave ranges and also, to research on models with the convenient sizes tiny antennae of millimeter and submillimeter ranges. Scale modeling is irreplaceable means which allows to choose variants of accommodation of numerous antennae on various objects long before creation of these objects, and also to look questions of electromagnetic compatibility.

The opportunity of electrodynamics modeling for the first time has been shown by Abraham M. in 1919 [1]. The opportunity of electrodynamics modeling is based on linearity of Maxwell equations which describe all the electrodynamics phenomena in linear matters. The theoretical substantiation of a principle of electrodynamics similarity is shown, for example, in [2]. In books [3,4] conditions of scale modeling of antennae and reflectors of electromagnetic waves with reference to harmonious processes are described. In the general view the principle of electrodynamics modeling can be formulated as follows: *scaling of space is equivalent to scaling of time and on the contrary*.

2. PARAMETERS OF SCALING

In Table 1 parameters of electrodynamics modeling for a case of signals sine wave are shown. It is necessary to understand a signal as electric currents, voltage, electric-field strength and magnetic-field strength. This table with sufficient accuracy for practice can be used and in case of nonsine wave signals provided that the relative width of a spectrum of a signal is less 0.1. In this and the subsequent tables the index "O" means "original", and the index "M" means «model».

Table 1. Modeling parameters for narrow-band signal

№	Description of parameter	Original	Model
1	Frequency	f_O	$f_M=f_O*m$
2	Wavelength	λ_O	$\lambda_M=\lambda_O/m$
3	Linear size	l_O	$l_M=l_O/m$
4	Far-field range for directional antenna	R_O	$R_M=R_O/m$
5	Dielectric constant	ε_O	$\varepsilon_M=\varepsilon_O$
6	Permeability	μ_O	$\mu_M=\mu_O$
7	Conductivity	σ_O	$\sigma_M=\sigma_O*m$
8	Active resistance	R_O	$R_M=R_O$
9	Reactive resistance	X_O	$X_M=X_O$
10	Complex impedance	Z_O	$Z_M=Z_O$
11	Capacity	C_O	$C_M=C_O/m$
12	Inductance	L_O	$L_M=L_O/m$
13	Radar cross section	σ_O	$\sigma_M=\sigma_O/m^2$
14	Antenna power gain	G_O	$G_M=G_O$
15	Wave number	k_O	$k_M=k_O*m$
16	Phase velocity of an electromagnetic-wave propagation	u_{FO}	$u_{FM}=u_{FO}$
17	Characteristic impedance of transmission line	ρ_O	$\rho_M=\rho_O$
18	Antenna effective area	S_O	$S_M=S_O/m^2$

978-1-4244-7468-4/10/$26 ©2010 IEEE

In all cases the factor of scaling is designated through «m» which can accept any positive value.

In Table 2 features of electrodynamics modeling for a case of ultra wide band signals are shown. Parameters are shown for a case when the frequency domain is considered.

Table 2. Modeling parameters for ultra wideband signal (frequency domain).

№	Description of parameter	Original	Model
1	Min frequency of radio spectrum	f_{minO}	$f_{minM}=f_{minO}*m$
2	Max frequency of radio spectrum	f_{maxO}	$f_{maxM}=f_{maxO}*m$
3	Spectral density	$S_O(f)$	$S_M(mf)=S_O(f)$
4	Amplitude-frequency characteristic	$K_O(f)$	$K_M(mf)=K_O(f)$
5	Phase-frequency characteristic	$\varphi_O(f)$	$\varphi_M(mf)=\varphi_O(f)$
6	Information band Δf	Δf_O	$\Delta f_M=\Delta f_O*m$
7	Linear size	l_O	$l_M=l_O/m$
8	Far-field boundary for directional antenna	R_O	$R_M=R_O/m$

In Table 3 parameters of modeling for a case when the time domain is of interest are shown.

REFERENCES

1. Abraham M. 'Ein Satz uber Modelle von Antennen', *Mittlg, der Phys. ges. Zurich*, 1919, v.19, S. 17.
2. Fedorov N.N. '*Bases of electrodynamics*': A manual for high schools. – Moscow.: Vishaja shkola, 1980. (in Russian)
3. R.S. Johnson, Ed '*Antenna Engineering Handbook*', 3th Ed 1994.
4. Maizels E.N., Torgovanov V.A. '*Measurement of characteristics of dispersion of the radar target*'. Under M.A. Kolosov, Ed. -Moscow.: Sov. radio, 1972. (in Russian)
5. Balanis, Constantine A., Ed '*Modern Antenna Handbook*', John Wiley & Sons, Inc., 2008.

Table 3. Modeling parameters for ultra wide band signal (time domain).

№	Description of parameter	Original	Model
1	Time	t_O	$t_M=t_O/m$
2	Linear size	l_O	$l_M=l_O/m$
3	Diagram of electric signal from impulse generator	$U_O(t)$	$U_M(t)=U_O(t/m)$
4	Diagram of emitted oscillation in far field region	$E_O(t)$	$E_M(t)=E_O(t/m)$
5	Impulse responses	$h_O(t)$	$h_M(t)=h_O(t/m)$
6	Autocorrelation functions of ultra wide band signal	$R_O(\tau)$	$R_M(\tau)=R_O(\tau/m)$

SAMPLING DURATION FOR NOISY SIGNAL CONVERSION

[1] Ruban V. P., [2] Pochanin G. P.

A.Ya. Usikov Institute of radiophysics and electronics of NAS of Ukraine,
Kharkiv, Ukraine
E-mail: [1] ruban@ire.kharkov.ua, [2] gpp@ire.kharkov.ua.

Abstract

A selection of the working band (sampling duration) of the sampler for optimal recording of noisy videopulse radar signals has been considered in the present work.

Keywords: Sampler, videopulse signal, noise level, correlation coefficient.

1. INTRODUCTION

In most cases the data processing, such as averaging and filtering, is not sufficient for detecting noisy UWB pulse radar signals, which amplitude is comparable with noise level and less in the prescribed working frequency band of the receiver [1]. That is why it's necessary to find a new possibility of increasing the signal-noise ratio, and decreasing the noise level of the receiver.

The sampling method of signal recording is mainly used in UWB videopulse radar [2]. Therefore let's consider the problem of weak signal recording namely by stroboscopic (sampling) receivers.

It is known that the noise level of the sampler depends on the working bandwidth of the receiver. The working bandwidth of the sampler is chosen taking into account the cutoff frequency of the received signal spectrum, as well as requirements of the measurement error [3]. The more precise measurement should be taken, the wider working bandwidth should be. At the same time, the noise level at the receiver input increases with widening the working bandwidth. And in its turn this leads to desensitization. And moreover, at low signal-noise ratios the accuracy of measurements is significantly worse, despite the fact that the signal spectrum and the working bandwidth are matched. So, the extension of the working bandwidth on receiving of weak signals leads to the degradation of the measurement accuracy instead of the desired increase.

The present work is aimed to define a selection criterion of the sampler working bandwidth, accounting the weak signal receiving features.

2. MODEL AND ANALYSIS

The given problem is solved by using an approximate (simplified) sampler model, having the true formula of periodical signal conversion [4]:

$$U(\theta) = \int_{-\tau/2}^{\tau/2} u(t + nT_R + \theta + T_0)dt\,, \qquad (1)$$

where $U(\theta)$ is the average signal amplitude at time θ, τ is the sampling duration, T_R is the signal time, T_0 is the time delay, n is the sampling number.

Let's consider the recording of Gaussian signals, as well as the first and the second derivatives of the Gaussian pulse. In the model a detected signal is the sum of the unnoisy signal and the noise voltage- $u(t) = u_i(t) + u_n(t)$. For comparing the converted signal $U(\theta)$ and the detected signal $u_i(t)$ it was assumed that $\theta = t$ and there was used the correlation coefficient function $R_{U,ui_i} = \dfrac{\mathrm{cov}(U, u_i)}{\sigma_U \sigma_{ui}}$, where $\mathrm{cov}(U, u_i)$ was the covariance of signals $U(t)$ and $u_i(t)$, σ_U and σ_{ui} was the standard deviation of $U(t)$ and $u_i(t)$, respectively.

Judging by the maximal value of the function R_{U,ui_i}, it is clearly seen the degree of «similarity» of the ideal no $u(t)$ ise-free signal and a signal converted by the sampler with a sampling duration τ. Therefore, the correlation coefficient may serve for estimation of converted signal distortion.

Graphs (Fig. 1) of dependences of signal correlation on the sampling duration for given noise levels at the sampler input have been plotted by calculation results of the function of correlation coefficient for three signal types. In these calculations the noise level σ was normalized to the peak signal amplitude - $u_{\max}$, and the sampling duration τ was normalized to δ, which is the pulse duration at the level $0.5u_{\max}$.

As is obvious from these graphs, the maximal correlation coefficient is for each noise level. This is due to the fact that in a wide working band of the sampler, where $\tau << \delta$, the noise essentially distorts a received waveform. And in a more narrow band, where $\tau > \delta$, signals are essentially distorted because high frequencies of the signal spectrum are behind the

978-1-4244-7468-4/10/$26 ©2010 IEEE

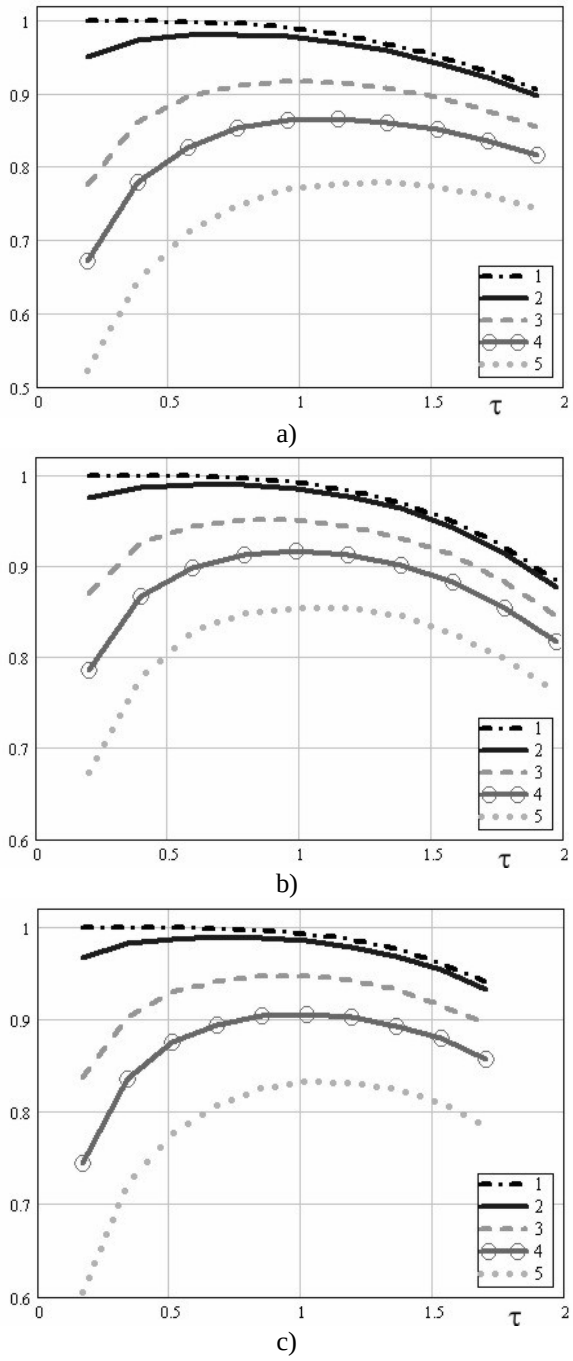


Fig. 1 Dependences of the correlation coefficient of the converted signal and the following signals: a – Gaussian signal, b – signal of Gaussian derivative, c – signal of the second derivative of the Gaussian function on the sampling duration at the noise level: 1 – 0; 2 – 0.2; 3 – 0.5; 4 – 0.7; 5 – 1.

working band of the sampler. Also it is seen from graphs that when increasing the noise level the signal correlation decreases, and the maximum of correlation curve moves towards a long sampling duration.

It's obvious that at a given noise level at the sampler input the sampling duration will fit with the maximum of correlation curve.

Based on this criterion, graphs of dependence of optimal sampling duration on the noise level for three signal types have been plotted for selection of sampling duration.

It's well seen in graphs that when the noise level drops to zero, the optimal sampling duration tends to values, corresponding to classical interpretation.

3. Conversion Error

It is difficult to judge the degree of amplitude distortions of a converted signal by static quantities (correlation coefficients). To estimate the error of signal conversion we have compared amplitudes of the original recording signal and a converted signal at maximal distinction between them. As it has turned out, these time points of maximal distinction coincide with signal extremums. Thereat, it has been proposed to estimate the measurement error of signal amplitude by relative units (relative to the peak-maximum) at time points, coincident with signal extremums.

Dependences of the conversion error of peak signal on sampling duration for three signal types are shown in Fig. 3.

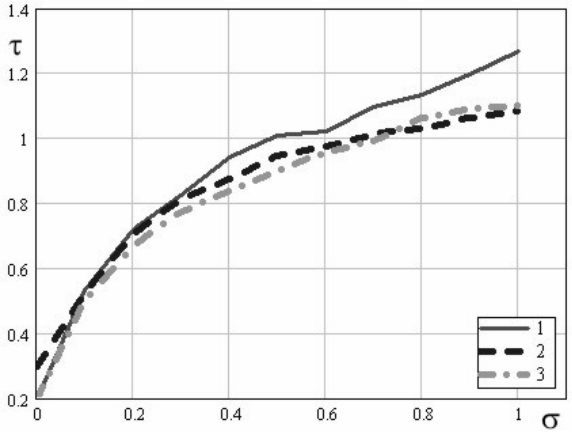


Fig. 2 Dependences of optimal sampling duration on the noise level: 1 – for the Gaussian signal, 2 – for the Gaussian derivative, 3 – for the second derivative.

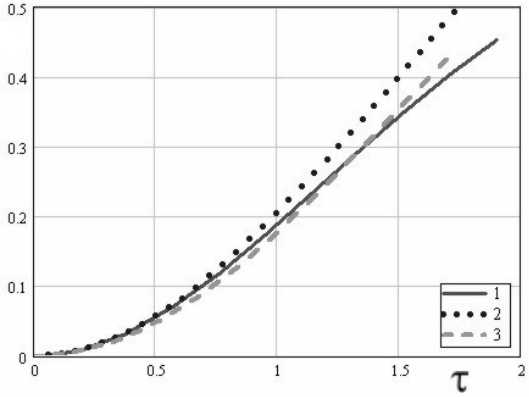


Fig. 3 Conversion errors of: 1 – the Gaussian signal, 2 – the Gaussian derivative, 3 – the second derivative.

These diagrams allow determining the maximum distinction of the converted signal when selecting an optimal sampling duration.

Thus, for example, at signal detection which waveform is the Gaussian derivative, and the noise level at sampler input is $\sigma = 0.7$, an optimal sampling duration is $\tau = 1$ (defined from the diagram in Fig. 2). At this sampling duration the maximal amplitude of a converted signal will differ by 20% from a signal at sampler input. A signal converted by the sampler, which sampling duration is determined by the condition [4], is shown in Fig. 4a. And a signal converted by the sampler which sampling duration equals to 1, is shown in Fig. 4b.

It's clearly seen in diagrams that the increase of sampling duration leads to a sufficient increase of signal-noise ratio. At that the converted waveform has changed very slightly.

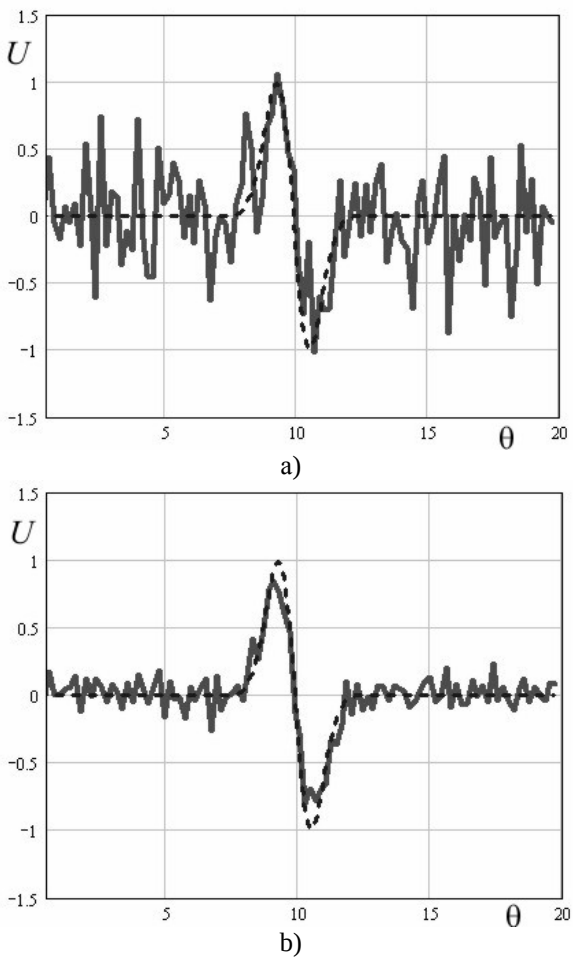


Fig.4 Converted signals (a – at sampling duration 0.1; b – at sampling duration 1; the input signal is marked by dashed line).

4. CONCLUSION

So, dependences of correlation coefficients of the converted signal on sampling duration (for three signal types) have been calculated and analyzed by using a simple sampler model.

It has been suggested to use the maximal correlation coefficient as a selection criterion of sampling duration of the sampler, taking into account the noise level at input.

Dependences of the error of signal conversion on sampling duration have been calculated.

The examined approach permits to evaluate a degree of distortion of the noisy signal being detected with an optimal for the given noise level sampling duration, as well as to determine a sampling duration of the sampler judging by a permissible error of signal conversion, and to evaluate the noise level, at which the cross-correlation of original and converted signals is maximal.

REFERENCES

1. 'Problems of subsurface radiolocation.' Ed. By A.Yu. Grinev. 2005, *Moscow, Radiotehnika*.
2. 'Ground Penetrating Radar Theory and Applications'. Ed. by H. Jol 2009, *ELSEVIER*.
3. Astanin L.Yu., Kostylev A.A. 1989, *Basic principles of ultrawideband radiolocation measurements*, Moscow, Radio i Svyaz'.
4. Ryabinin Yu.A. 1972, *Sampling oscillography*, Moscow, Sov. Radio.

WIDE-BAND MEASURING COMPLEX DESIGNED FOR REMOTE CONTROL OF THERMAL RADIO RADIATION PRODUCED BY COKE-OVEN BATTERIES

[1] Bykov V. N., [1] Grichaniuk A. M., [1] Ivanchenko D. D., [1] Krayushkin V. A., [2] Zhyravsky A. A., [2] Fedorova S. V., [3] Hudokormov A. P., [3] Rjapovol E. V., [1] Berezhnaya T. D.

[1] V.N. Karazin Kharkov National University, Kharkov, Ukraine
[2] UCHIN, Kharkov, Ukraine
[3] AKHZ, Avdeevka, Ukraine

Abstract

The research contains a well-grounded necessity to use remote control over average temperatures of coke-oven batteries applying the radiowave method through optically opaque and partially transparent screens for electromagnetic waves.

Keywords: Radiometric (RM) and infrared (IR) band of electromagnetic waves, remote control of temperatures, coke-oven battery.

1. INTRODUCTION

The modern technologies of coke production provide for regular measurement and further regulation of temperatures inside a coke-oven battery according to the specified operative conditions. The methods of temperature measurement inside a coke-oven battery may be classified into contact and remote measurement methods. The former is carried out with the help of thermometers and -couples, the latter – with the help of ardometers.

Contact measurement methods provide for the distribution and regular replacement of these thermometers and -couples only in case of complete furnace unloading (which is not always possible).

That is why the application of remote measurement methods becomes topical. Though to apply these methods it is necessary to open the hatch of the battery (which is possible only within short intervals of time in case of furnace charge loading or coke unloading).

One of the effective means to measure temperatures of a certain object through optically opaque and partially transparent screens for radio waves is the employment of probing in infrared and radio band [1].

The research aims to determine the intensity of thermal radiation (produced by the coke-oven battery within the period of its functioning) applying the radiowave method.

To determine the intensity of thermal radiation the wide-band measuring complex (WBMC) is used. The WBMC consists of:

- radiometric (RM) sensor of millimeter-long waveband (MW);
- RM sensor of infrared (IR) band;
- thermometer (thermocouple).

The WBMC on a movable platform is shown in Fig.1.

The RM sensor of MW consists of a parabolic double-optical Cassegrain antenna and a modulation

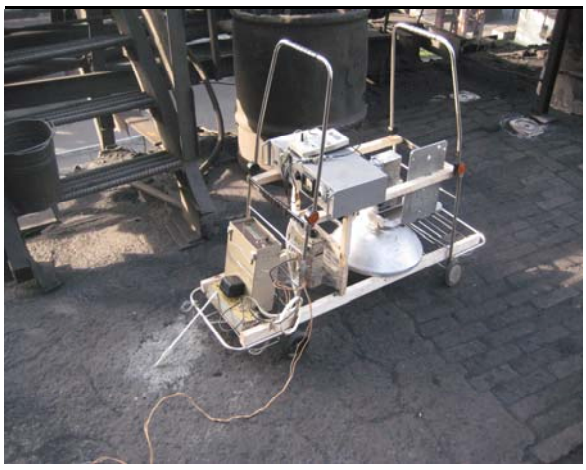


Fig. 1. The Wide-Band Measuring Complex.

RM tuned-radio-frequency receiver of eight-millimeter waveband (which was designed by the Public Research Institution “Aisberg”, Kyiv [2]). The fluctuating sensitivity of this RM sensor is $\delta T \leq 0,02\,K$ for the period of integration $\tau = 1\,s$.

978-1-4244-7468-4/10/$26 ©2010 IEEE

The pyrometrical RM sensor of IR band ($(2 \div 14)\,\mu k$) can measure thermodynamic temperatures within the range of $(-20 \div +200)\,^0C$ with the possible measuring uncertainty of ±1,5°C.

2. METHODOLOGY OF MEASUREMENTS

The measurement of radiobrightness temperature of radiation produced by the heated furnace charge (coke) is carried out in several stages.

Stage 1. Calibration of the measuring equipment. The WBMC equipment is set on the top of the coke-oven battery with the thermodynamic temperatures which are constantly checked (Fig. 1) with the help of a mercury thermometer within the temperature range of $(0-150)\,^0$C with the possible measuring uncertainty of $\pm 1\,^0$C. The obtained data of the mercury thermometer is fixed according to the data of both the IR and RM sensors.

The IR sensor is used for temperature measurement of the coating surface of the battery in three bands: HF wave – ($(2-5)\,\mu k$), long wavelength – ($(7-14)\,\mu k$) as well as integrated band which includes the first two bands. The data of the thermodynamic temperatures of the coating surface is checked by the digital measuring equipment with the measuring range of $(-20 \div +200)\,^0C)$.

The data of a sagittary moving-coil microammeter M4205 (with the measuring range of $(-100 \pm +100)\,\mu A$ and scale factor of 2,5) and a digital voltmeter (with the measuring range of ±20 Watt) (both the microammeter and the voltmeter are located at the outlet of the low-frequency part of the RM sensor) serves as the data of the RM sensor of MW.

The calibration of the WBMC equipment takes place only after the equipment has been heated for half an hour, before and after every stage of the measuring procedure and if there is such a necessity during any stage of this measuring procedure.

Stage 2. Measurement of the intensity distribution of radiobrightness radiation and temperature on the top of the coke-oven battery across the motion of the charging crane i.e. along the heating channel.

The WBMC on a movable platform is transferred towards the prime vertical. The receiving antenna of the RM sensor is located in such a way that its center coincides with the center of the heating channel (Fig. 2) among the peepholes. That is how the level of radiothermal radiation is measured. After the measurement of RM-temperature the IR sensor is set there (instead of the RM sensor) and the thermodynamic temperature is being measured.

Simultaneously with the above mentioned measurements the temperature inside the channels is checked with the help of an ardometer (without peepholes).

Stage 3. Measurement of intensity distribution of radiobrightness radiation and temperature on the top of the coke-oven battery along the motion of the charging crane (Fig. 2) i.e. across the heating channels and coke cameras.

The WBMC on a movable platform is located between the channels. The radiobrightness temperature is measured through the RM as well as IR sensors; these sensors are also used to measure the temperature above the coke camera. At the same time the temperature inside the channels is checked with the help of the ardometer.

Stage 4. Measurement of temporary changes of radiobrightness and thermodynamic temperatures at certain places on the surface of the coke-oven battery.

The WBMC on a movable platform is located in a certain place so that the RM antenna is above the channel between the peepholes. The radiobrightness temperature is measured for equal periods of time.

3. MEASURING RESULTS

Fig. 3 shows results of the measurement of radiobrightness and IR temperatures along the heating channel.



Fig. 2. Temperature measurement across and along the heating channel.

Fig. 3 shows results of the measurement through the ardometer. At the bottom of the graph the location of the typical surface heterogeneities (1) rails, 2) charging hatches and 3) metal strainers) is stated. The temperature at the places where the rails and strainers are located was not measured. The nature of

the interdependence of the temperature measured with the help of RM and IR sensors coincides. It is important to state that near the charging hatches the temperature measured with the help of the IR sensor and the level of the radiobrightness radiation in the eight-millimeter band increase.

The minimum radiobrightness and IR temperature are those measured above the strainers. The temperature distribution measured with the help of the ardometer has the same character of $\pm 30^0$C with the temperature decrease of 60^0C towards the edges of the heating channel. The data obtained from the RM sensor is highly dependent on the surface heterogeneities and has greater temperature drop in the center of the heating channel (up to 60^0C).

4. CONCLUSIONS

1. The research contains a well-grounded necessity to use remote control over average temperatures of coke-oven batteries applying the radiowave method through optically opaque and partially transparent screens for electromagnetic waves.
2. The research states the reasonability of radiometric measurements in several wavebands: eight-millimeter – and IR band (the temperature integrated channel).
3. According to the results of the model measurements of the electromagnetic wave advancing level in the IR band and radiothermal radiation level in MW through the given grogs, we may draw to a conclusion about great losses (~ 60 dB) and relatively low level of radiation from the surface furnace charge as the emittance of the furnace charge is close to the that of an absolute black body.
4. The comparison of the experimental results obtained with the help of the WBMC on the one hand and the results obtained with the help of the ardometer on the other shows that the WBMC has sufficient sensitivity to establish connection of the data obtained from the device with the thermal changes inside the coke cameras:
   - temperature distribution along the surface of the coke-oven battery and
   - changes of radiothermal radiation during coke unloading, furnace charge loading and canting of heating channels may be definied.
5. The comparative analysis of these results shows that the measurement with the help of the WBMC allows to determine the integrated temperature of the whole coke-oven battery (whose radiation is measured through the WBMC).
6. The WBMC helps to increase efficiency and self-descriptiveness of the measurement. It allows to

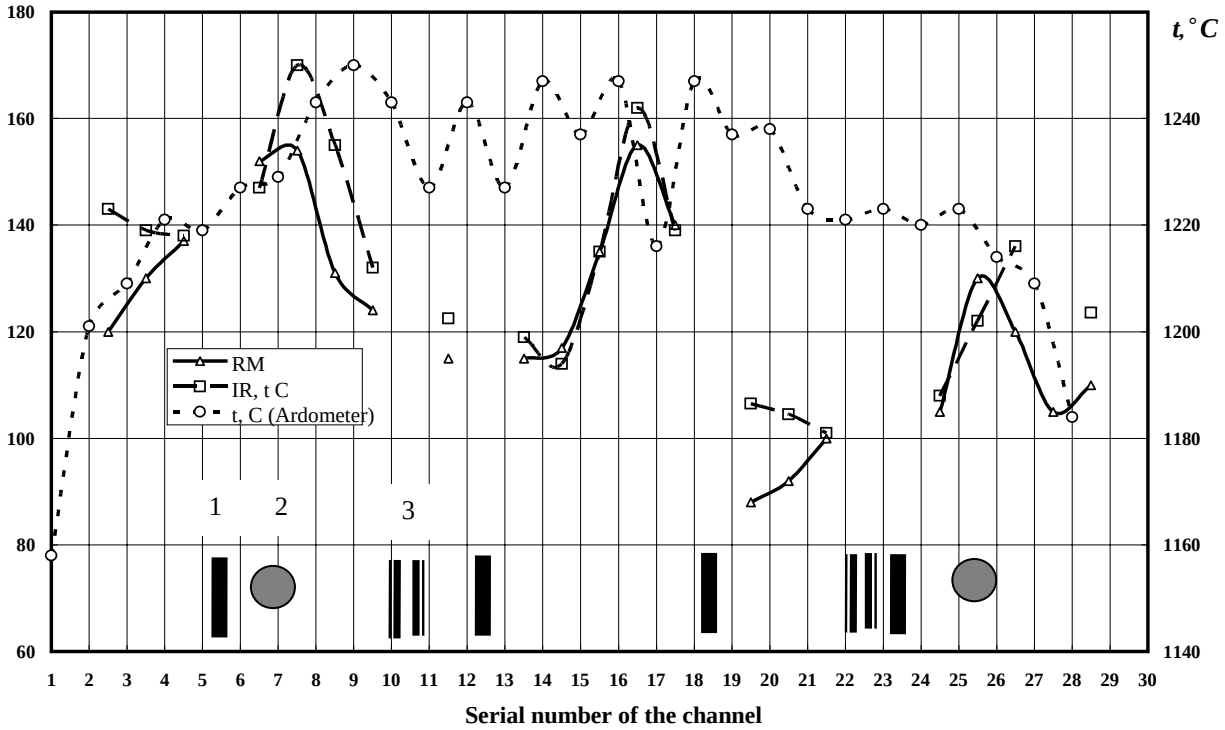


Fig. 3. Results of the measurement along the heating channel.

determine the temperature of the furnace charge (owning to the measurement above the coke camera) more precisely.

REFERENCES

1. V.I. Antyfeev, V.N. Bykov, A.M. Grichaniuk, D.D. Ivanchenko, V.A. Krayushkin. A Scanning Measuring Radiometry Complex with Computer Control // *Proc. 6th International Conference on Antenna Theory and Techniques* (ICATT`07). – Sevastopol (Ukraine), September 17–21, 2007. – P. 486–488.
2. V.P. Gorishniak, A.G. Denisov, S.E. Kuzmin, V.N. Radzikhovsky, B.M. Shevchuk. Passive multichannel millimeter-waves imaging system // *The Fifth International Kharkov Symposium on Physics and Engineering of Microwaves, Millimeter and Submillimeter Waves. Symposium Proceedings*. – V.1. Kharkov (Ukraine), June 21–26, 2004. – P. 202–204.

CELEBRATING ANNIVERSARIES

TO 90TH ANNIVERSARY OF PROF. YAKOV S. SHIFRIN



Life Fellow IEEE, founder of the statistical antenna theory, Professor Yakov Solomonovich Shifrin was born in the town Mstislavl (Belarus) on April 23, 1920. In 1941, he graduated with honors from the Leningrad State University with specialty in physics. Yakov Solomonovich is a man of unbending spirit and morality. He took part in the Great Patriotic War of 1941-1945, fighting against fascism. In 1944-1945, he had been a commander of radar units. He had been the first lecturer of radiolocation with the Sevastopol school of antiaircraft artillery in 1945-1948.

The main scientific and pedagogic activity of Yakov Solomonovich was associated with the Artillery Radio Engineering Academy in Kharkov where he had worked since 1948 to 1980. In 1953, he received a degree of candidate of sciences (equivalent of PhD), and in 1965, he defended a doctoral thesis (DSc). In 1966, he was elected a full professor. Since 1951 to 1956 he had worked as a lecturer and since 1956 to 1980 he had been Head of the chair of antennas and propagation at this academy. After he retired from the Armed Forces from 1980 to date, Yakov Solomonovich has been worked with the Kharkov National University of Radio Electronics. He is a founder of the powerful scientific school on the theory of antennas and propagation. Prof. Shifrin has trained 16 Doctors of sciences (Dr-Sci) and over 40 candidates of sciences (equivalent of PhD).

Yakov Solomonovich has made fundamental contributions to science in a number of directions of modern radio physics. He is a founder of a new scientific direction - the statistical theory of antenna. Widely known is his monograph "Questions of the statistical theory of antennas," published in 1970 and immediately after its release translated and published in the USA as “Statistical Antenna Theory” (Golem Press, USA, 1971). Owing to this, the monograph became worldwide recognized and appreciated.

He is author and co-author of the textbook on antennas, the handbook on antenna techniques, 16 monographs and over 200 scientific papers and articles.

After the Soviet Union disintegrated, Yakov Solomonovich initiated and was an active organizer of international conferences on antenna theory and technique (ICATT). In 2002, he initiated a new conference on ultrawideband and ultrashort impulse signals (UWBUSIS). Now he is honorary chairman of UWBUSIS conference. Also, he was one of the organizers of the East-Ukraine and Kharkov Joint Chapters of Ukraine Section IEEE.

Now Yakov Solomonovich is a very respected person and an outstanding scientist and educator. He is the founder and undisputed leader of strong scientific school. His scientific work is awarded with the A.S. Popov prize USSR, he is the Honorary worker of science and techniques of Ukraine. He was elected an honorary professor of the Kharkov National University of Radio Electronics, the Sevastopol National Technical University, the Taganrog Technological Institute of the South Federal University, and an honorary doctor of the V.N. Karazin Kharkov National University. He is President of the Ukrainian National Antenna Association and Academician of the international Academy of Sciences of Applied Radio Electronics. In 1998, he was the first in Ukraine and the first among antenna specialists in UIS who was elected Fellow IEEE (with citation “For fundamental contribution to the antenna theory and technology”); since 2008 he has been Life Fellow IEEE. Prof. Yakov S. Shifrin is an organizer and president of the Ukrainian National Antenna Association.

Organizing committee is very pleased to send greetings to dear Yakov Solomonovich on occasion of his great anniversary and to wish him all the success and good health.

978-1-4244-7468-4/10/$26 ©2010 IEEE

A

Aleshko A. I. 254
Alexin S. G. 177
Almakadma T. 162
Alpert T. 168
Altunc Serhat 138
Amosova A. I. 16
Andreev M. V. 116
Angermann L. 68
Antyufeyeva M. S. 134
Arkusha Yu. V. 226
Averin S. V. 209

B

Badeev V. A. 156
Bardou N. 209
Barilko M. S. 171
Batrakov D. O. 113
Batrakova A. G. 113
Baum Carl E. 12,138
Berdin S. A. 266, 270
Berdnik S. L. 212
Berezhnaya T. D. 278
Berroth M. 168
Bezrukova E. G. 132
Bibikov S. B. 262
Blinova N. K. 82
Bolov R. B. 240
Bortsov A. V. 221
Borulko V. F. 116
Boyko M. I. 221
Buchenauer C. Jerald 138
Bulgakova A. A. 223
Bunin S. G. 141
Butrym A. Yu. 49, 71, 119

C

Chernogor L. F. 105
Christodoulou Christos G. 138
Churikov D. V. 54,59,62
Collin St. 209

D

Dakhov V. M. 212
Dobrotvorsky M. I. 254
Dolzhenko D. S. 230
Drobakhin O. O. 177
Dubrovka F. F. 45, 230
Dumin O. M. 99
Dumina O. O. 99

E

Erin S. N. 249
Evdoshenko L. S. 221

F

Fedorova S. V. 278

G

Gaikovich K. P. 90, 156
Gaikovich P. K. 90, 156
Galchenko D. A. 266
Galkin O. E. 90
Gardner R. L 30, 93,197
Golovin D. V. 113
Golovin V. V. 243
Gorobets N. N. 96, 223
Grabina V. A. 34
Gribanov A. N. 273
Grichaniuk A. M. 278
Grözing M. 168

H

Harlanov A. V. 206
He Shi 236
Hudokormov A. P. 278

I

Ilyin N. V., 144
Immoreev I. Ya. 40
Ivanchenko D. D. 236, 278
Ivanov V. M. 221

K

Kaliberda M. E. 85
Kalinin V. I. 165
Karelin S. Yu. 266, 270
Katrich V. A. 99, 212
Kazansky O. V. 192, 236
Khakhinov V. V. 144
Kholodov V. I. 99
Khoroshun V. V. 111
Kniaziev V. V. 259
Kochetov B. A. 71
Kolchigin N. N. 34, 192, 236
Kondrat'eva A. P. 240
Konovalenko A. A. 249
Korenev V. G. 270
Korepanov A. L. 195
Kostyleva V. V. 171, 174
Kravchenko O. V. 22
Kravchenko V. F. 22, 54,59
Kravchenko V. I. 259

Krayushkin V. A. 278
Krivchikova A. A. 16
Kumar Prashanth 138
Kurochkin A. P. 240

L

Lang F. 168
Lazorenko O. V. 105
Legenkiy M. N. 119
Liang Jing Feng 236
Lisnoy I. P. 259
Liu Xiaofeng 246
Los’ V. F. 240
Luan Shan 246
Luk'yanchikov A. V. 243
Lyakhovsky A. A. 82

M

Magda I. I. 266, 270
Maksimovitch Ye. S. 156
Masini M. 168
Mayboroda D. V. 215
Menshova S. B. 262
Mikheev O. V. 254
Mitrofanov D. G. 183
Moroz S. N. 233
Mukhin V. S. 266, 270
Myakinkov A. V. 147, 150

N

Naboka A. M. 270
Nesterenko M. V. 99, 212
Niemchenko Yu. S. 259
Nikolaev V. A. 171, 174
Numerov M. A. 159

O

Ochotnikov D. A. 201
Ol'shevs’kiy O. L. 233
Orlov V. V. 262
Ovsyanikov V. V. 233

P

Pardo F. 209
Pasiuga V. N. 34, 192
Pavlikov V. V. 74
Pazynin V. L. 16
Pelouard J. L. 209
Petrov D. A.. 65
Pochanin G. P. 218, 275
Pochanina I. Ye. 218
Pogarsky S. A. 85, 215
Ponomarchuk S. N. 144
Ponomarenko Y. V. 233
Popel’ V. M. 233
Privalova T. Y. 240
Prohorkin A. G. 189
Prokof'ev M. V. 262
Prudyus I. N. 88
Pshenichnaya S. V. 212, 215

Q

Qiu Jinghui 246

R

Reznikov A. E. 132
Rjapovol E. V. 278
Romanenko Y. D. 233
Ropiak C. A. 93
Ruban V. P. 275
Rudenchik A. E. 132
Rutkas A. G. 102

S

Safin A. R 22
Sakharov K. Yu. 254
Saprykin I. I. 215
Schamiloglu Edl 138
Shafalyuk O. S. 122
Shckorbatov Y. G. 34, 192
Shirokov I. B. 195
Shkvyrya Y. 153
Shostko I. S. 162
Simachev A. A. 113
Simachova O. N. 129
Sinitsyn R. B. 48
Sirenko Y. K. 16, 122
Skoblikov O. Y. 256
Slesareva A. V. 195
Smirnova D. M. 147, 150
Smolnikova O. N. 262
Soshenko V. A. 266, 270
Stasjuk N. N. 96
Storozhenko I. P. 226
Stoudt D. C.. 197
Sumin M. I. 90
Sumyk M. M. 88
Sushko A. Ju. 45
Syvozalizov N. A. 109

T

Titov A. N., 273
Tokarsky P. L. 249
Toloknova E. U. 243

Tretyakov O.A. 99, 134
Turkin V. A. 254
Tyschuk Y. N. 243

V

Varyanitza-Roshchupkina L. A. 125
Velychko L. G. 122
Vlasenko L. A. 102
Vlasik S. N. 180
Volkomirskaya L. B. 132
Volosyuk V. K. 74, 77
Vygolov S. A. 159

W

Wang C. 186
Wei Y. 186

Y

Yang Y. 186
Yankevych R. V. 88
Yanovsky F. J. 48
Yastrebov Yu. V. 171, 174
Yatsuk L. P. 82
Yatsyk M. V. 68
Yatsyk V. V. 68
Yermakov G. V. 180
Ying R. 186
Yukhanov Y. V. 240

Z

Zagvozdkin B. V. 266
Zheng Yu 236
Zhyravsky A. A. 278
Ziganshin E. G. 159
Zima I. I. 180

НАУКОВЕ ВИДАННЯ

2010 5th International Conference on ULTRAWIDEBAND AND ULTRASHORT IMPULSE SIGNALS September 6-10, 2010, Sevastopol, Ukraine

ЗБІРНИК НАУКОВИХ ПРАЦЬ

Відповідальні секретар: Хардіков В.В.
Комп'ютерне верстання: Хардіков В.В., Кочетов Б.А.
Макет обкладинки: Антюфєєва М.С.

Підписано до друку 27.07.2010. Формат 60×84/8
Папір офсетний. Друк ризографічний.
Ум. друк. арк. 31,21. Обл.-вид. арк. 39,01.
Тираж 130 пр.
Ціна договірна.

Харківський національний університет імені В.Н. Каразіна
Україна, 61077, м. Харків, пл. Свободи, 4

Надруковано ХНУ імені В.Н. Каразіна
61077, Харків, пл. Свободи, 4.
Тел. 705-24-32.
Свідоцтво про державну реєстрацію ДК №3367 від 13.01.09